Interfaces between pavement layers in bituminous mixtures

Thomas Attia

N° d'ordre NNT : 2020LYSET001

THESE de DOCTORAT DE L'UNIVERSITE DE LYON
opérée au sein de l'
École Nationale des Travaux Publics de l'État

Ecole Doctorale N° 162
Mécanique, Énergétique, Génie Civil et Acoustique (MEGA)

Spécialité / discipline de doctorat : Génie Civil

Soutenue publiquement le 21/01/2020, par :
Thomas Attia

Interfaces entre couches de chaussée en enrobé bitumineux

Devant le jury composé de :

MADEO, Angela	Prof., INSA Lyon	Présidente
PETIT, Christophe	Prof., Université de Limoges	Rapporteur
ZOFKA, Adam	Prof., IBDiM, Pologne	Rapporteur
POUGET, Simon	Dr, Eiffage Infrastructures	Examinateur
DI BENEDETTO, Hervé	Prof., University of Lyon/ENTPE	Directeur de thèse
SAUZÉAT, Cédric	HDR, University of Lyon/ENTPE	Co-directeur

NNT order number: 2020LYSET001

DOCTORAL THESIS OF THE UNIVERSITY OF LYON
prepared at
École Nationale des Travaux Publics de l'État

Doctoral School N° 162
Mécanique, Énergétique, Génie Civil et Acoustique (MEGA)

Specialty: Civil Engineering

Publicly defended the 21st of January 2020 by:
Thomas Attia

Interfaces between pavement layers in bituminous mixtures

Before the committee composed of:

MADEO, Angela	Prof., INSA Lyon	President
PETIT, Christophe	Prof., University of Limoges	Reviewer
ZOFKA, Adam	Prof., IBDiM, Poland	Reviewer
POUGET, Simon	PhD, Eiffage Infrastructures	Examiner
DI BENEDETTO, Hervé	Prof., University of Lyon/ENTPE	Advisor
SAUZÉAT, Cédric	HDR, University of Lyon/ENTPE	Co-Advisor

TABLE OF CONTENTS

REMERCIEMENTS

« Partout le cerveau des hommes cesse aujourd'hui ironiquement de comprendre que la véritable garantie de la personne réside non dans un effort personnel isolé, mais dans la solidarité des hommes. Mais ce terrible isolement aura infailliblement une fin, et tous comprendront à la fois combien leur détachement les uns des autres était peu naturel. […] Mais, d'ici là, il faut néanmoins maintenir l'étendard et, ne fût-ce qu'individuellement, l'homme doit donner de temps en temps l'exemple de tirer son âme de l'isolement au service de l'amour fraternel, dût-il passer pour un simple d'esprit. Cela pour que ne meure pas la grande idée… » Fiodor Dostoïevski, *Les Frères Karamazov*

Je tiens à remercier ici toutes les institutions et toutes les personnes qui ont contribué à la réalisation de cette thèse. Et bien que cette partie soit la dernière que j'ai écrite, soyez sûrs qu'elle m'est très chère.

Je tiens à remercier tout d'abord les financeurs de la thèse : l'entreprise Eiffage Infrastructures associée à l'École Nationale des Travaux Publics de l'État (ENTPE) dans le cadre d'une chaire industrielle, qui ont tous deux su voir un intérêt à cette thèse.

Je remercie le personnel du laboratoire central d'Eiffage à Corbas pour leur aide, notamment Jean-Paul Desgrange, qui a fabriqué toutes mes plaques de matériaux, et Florent Schrevel, qui a réalisé les essais avec le *DSR* sur mes bitumes. Parmi les membres d'Eiffage, je suis également très reconnaissant à François Olard et Simon Pouget qui ont suivi ma thèse de près et avec qui j'ai beaucoup échangé. Ces discussions ont toujours été positives et ont grandement contribué à mon raisonnement et à mon travail. Il est important qu'ils sachent que leur sympathie et leurs encouragements tout au long de cette thèse m'ont sincèrement touché.

J'ai passé près de cinq ans à l'ENTPE et il est évident que j'ai beaucoup bénéficié des ressources, humaines ou non, de l'école. Que ce soit pour des choses essentielles, et je remercie Sonia Cenille pour mes inscriptions, Francette Pignard, pour mes contrats et ma soutenance, Antonella Alotta Sartout, Marie-Victoire Baussant, Fanny Blancon, Emmanuelle Dubois Trepat, Hélène Nguyen, pour tous les ordres de mission, bons de commande et autres lourdeurs administratives qu'elles ont rendues plus légères ; ou pour des choses qui sont moins essentielles mais tout de même sympathiques comme la présence d'un gymnase pour le futsal, d'une salle de musculation et d'un restaurant universitaire.

Je remercie ensuite Prof. Angela Madeo et Dr. Simon Pouget d'avoir accepté de faire partie de mon jury de thèse. Et je remercie plus particulièrement Prof. Christophe Petit et Prof. Adam Zofka pour avoir accepté d'être les rapporteurs de cette thèse.

De toute évidence, cette thèse n'aurait ressemblé en rien à ce qu'elle est si je n'avais pas été encadré par Hervé Di Benedetto et Cédric Sauzéat. Ils ont réussi à faire évoluer mon niveau d'exigence avec mon travail, notamment d'un point de vue scientifique, car eux-mêmes sont des exemples de rigueur et d'honnêteté intellectuelle. J'ai beaucoup appris à leurs côtés et j'ai été très heureux de travailler avec eux. Hervé recherche toujours le meilleur chez les autres, avec son dynamisme caractéristique et communicatif. Sa sympathie et sa confiance m'ont été chères pendant les moments difficiles de cette thèse (et aussi pendant les week-ends ski). Quant à Cédric, il m'a fallu deux ou trois ans pour arriver à discerner ce qui était de l'ironie de ce qui n'en était pas dans ses paroles. Ce qui n'en était pas m'a toujours été très utile, ses connaissances pratiques et théoriques ainsi que sa disponibilité ont débloqué bien des situations qui me semblaient sans issues. Et ce qui était effectivement de l'ironie m'a toujours fait rire.

Je remercie les techniciens du laboratoire A de l'ENTPE, notamment Stéphane Cointet et Frédéric Sallet qui m'ont beaucoup aidé au cours de cette thèse pour les petits travaux que quelqu'un d'assez peu débrouillard, comme moi au début de cette thèse, aurait mis une éternité à faire ou pour les grandes manœuvres sur les presses hydrauliques et enceintes climatiques qui nécessitaient leurs connaissances techniques et leur sens pratique. Merci aussi à Joachim Blanc-Gonnet pour toute l'aide avec l'électronique, l'informatique ou l'utilisation des caméras. Et merci à Alexandra Elbakyan pour l'idéal de la science qu'elle représente.

Je remercie également les étudiants que j'ai encadrés en stage de master, Viet Hai Nguyen et Phu Ngoc Vu, pour leur aide précieuse dans mes expériences, mes analyses et leur compréhension. Je les félicite encore pour leur réussite et leur souhaite une bonne continuation.

Au sein de la partie du LTDS qui se trouve à l'ENTPE (ex-LGCB) règne une ambiance conviviale qui rend agréables les journées de travail, grâce à tous les chercheurs, techniciens, post-doctorants, doctorants et stagiaires qui y travaillent.

J'ai eu beaucoup de plaisir à partager des moments avec mes collègues doctorants, notamment grâce à l'association des doctorants et docteurs de l'école, l'ALD²ENTPE. Même si nos discussions étaient parfois scientifiques et intéressantes (surtout au sein de l'équipe bitume), je me souviendrai surtout des amitiés forgées au futsal, autour de parties animées de mots croisés ou aux championnats du monde de Perudo, des discussions à propos des playoffs NBA, à propos des différences entre football européen et sud-américain, à propos de géopolitique ou à propos du quotidien. Alvaro, Lucas, Diego, Salvo, Viet, Jean-Claude, Pierre, Minh Duc, Kevin, Florian, Lucile, Abhilash, Fionn, Simon, Matthieu, Pascal, Mike, Carlos, Nicole, Eric, pour les docteurs, Reuber, Gabriel, Thang, Jean-Marie, Yasmina, Andrei, Stefano, Thibaud, Mohamed pour ceux qui le seront bientôt (je leur souhaite), j'ai été très heureux de vous côtoyer. J'ai également une pensée chaleureuse pour les doctorants que je n'ai pas cités, les nouveaux arrivants, les stagiaires, et ainsi que pour les chercheurs avec qui j'ai échangé amicalement au cours de ma thèse.

Je remercie enfin mes parents, Christel et Joël, ma sœur Maé, ma grand-mère Simone, toute ma famille et mes amis pour leur soutien indéfectible tout au long de cette thèse.

ABSTRACT

Several cases of premature degradation of road structures were connected with the debonding of their layers, especially in the upper part of the structures where they are often made of bituminous mixtures. The application of a tack coat at the interface between the layers usually ensures a good bond between the layers and in the road design methods, pavement layers in bituminous mixtures are considered perfectly bonded. However, this simplistic assumption corresponds to the most favourable case and the road design methods can sometimes misestimate the actual structure lifetime.

The purpose of this thesis is the characterisation of the thermomechanical behaviour of interfaces between pavement layers. It has been carried out in the framework of the industrial chair between the company Eiffage Infrastructures (France) and the University of Lyon/ENTPE (France).

A literature review about the interfaces between pavement layers has been conducted. It highlights the importance of the state of bonding at the interface and it presents the previous experimental approaches to the study of interfaces with the models that have been developed.

An innovative experimental device, named 2T3C Hollow Cylinder Apparatus (2T3C HCA), has been designed during this work. It applies torsion and tension-compression, independently or simultaneously, to hollow cylinder samples with two layers and an interface. It is a homogeneous test with which many load paths can be tested. The major feature of the 2T3C HCA is the use of 3D Digital Image Correlation (3D DIC), an optical measurement technique, to find the displacements at the surface of the sample. A specific analysis method has been introduced to find the vertical and horizontal displacement gaps at the interface from the 3D DIC results. This method also allows finding the strain in the bituminous mixtures.

An experimental campaign was performed on different interface configurations with four different mixtures and three type of tack coats at different dosages. Tests in the small strain domain and monotonic shear failure tests were carried out.

Advanced complex modulus tests in the small strain domain were done with the 2T3C HCA to find the complex moduli of the bituminous mixtures and the complex interface stiffnesses both in tension-compression mode and in shear mode. The mixtures behaviour was modelled with the 2S2P1D model (2 Springs, 2 Parabolic elements, 1 Dashpot). The interfaces behaviour was not linear viscoelastic at the tested amplitudes. A new model, the DBN_{PDSC} model (DBN model with Plastic Dissipation for Small Cycles), was introduced and used to describe the interfaces. No conclusions could be drawn on the effect of the type of mixture or of the type of tack coat on the interface behaviour in the small strain domain.

A nonlinearity test was performed and it confirmed that the interface behaviour was not linear viscoelastic, but it was not possible isolate the effect of the amplitude of the displacement gap on the complex interfaces stiffness because of apparent damage. From the results of an oligocyclic test, the norm of the complex interface stiffness decreased rapidly after a few number of cycles. However, the interface recovered its strength almost entirely after rest periods showing that reversible phenomena are partially responsible for the apparent damage of the interfaces.

The interface behaviour for large deformations was observed using monotonic shear failure tests. The influence of the rotation speed, of the normal stress, of the aggregate interlocking, of the type of tack coat and of its dosage on the interface shear strength were identified.

Keywords: interfaces; road structures; bituminous materials; 3D DIC; experimental results; small strain; failure.

RÉSUMÉ

Les chaussées routières et aéroportuaires sont des structures possédant plusieurs couches. Dans les méthodes actuelles de dimensionnement, les couches réalisées en enrobé bitumineux sont considérées parfaitement collées entre elles. Cette hypothèse simplificatrice constitue le cas le plus favorable du comportement de la chaussée, prise dans son ensemble. En effet, lorsque les couches sont collées, elles agissent d'un seul tenant, avec une rigidité globale importante. En pratique, des couches d'accrochage, souvent faites avec des émulsions de bitume, sont appliquées aux interfaces entre les couches pour garantir le collage. Cependant, de nombreuses dégradations prématurées de chaussées ont été reliées au décollement des couches les unes par rapport aux autres. Au-delà de leur rôle dans la favorisation des échanges à l'intérieur des sociétés, les infrastructures routières représentent un patrimoine d'une valeur immense dont l'entretien et la réparation entraînent des dépenses importantes. Un dimensionnement précis permet de réduire ces coûts d'entretien ou au minimum de mieux les anticiper. C'est pour cela que le comportement des interfaces entre couches de chaussée doit être mieux pris en compte dans le dimensionnement des chaussées.

L'intérêt porté par la communauté scientifique aux interfaces remonte aux années 1970. Les premières observations de décollement entre les couches datent de cette époque et coïncident avec l'augmentation des charges liées au trafic et avec le développement des couches minces en surface. Les premiers tests mécaniques pour étudier les interfaces entre couches de chaussées furent des essais de cisaillement dans l'objet essentiel était la détermination de la contrainte maximale à laquelle peut résister une interface. Bien que ce type d'essai permette de comparer la résistance de différentes configurations d'interfaces, il n'est pas vraiment représentatif de la manière dont les chaussées se dégradent en réalité, à l'exception des pistes d'atterrissage d'aéroport où les efforts peuvent être très importants. Les tests cycliques développés plus récemment imitent mieux les sollicitations cycliques liées au trafic ou au climat auxquelles sont soumises les chaussées et permettent d'évaluer la résistance des interfaces à la fatigue. Cependant, la plupart des tests actuels sur les interfaces sont inhomogènes ce qui peut conduire à des analyses biaisées des résultats. Un essai adapté à l'étude des interfaces doit donc être capable d'appliquer des sollicitations cycliques et de manière homogène.

L'objectif de cette thèse est l'étude du comportement thermomécanique des interfaces entre couches de chaussée en enrobé bitumineux. Elle a été réalisée au Laboratoire de Tribologie et de Dynamique des Systèmes (LTDS, UMR 5513 CNRS) au sein de l'Université de Lyon à l'École Nationale des Travaux Publics de l'État (ENTPE). Cette thèse fait partie de la Chaire Eiffage, une chaire industrielle marquant la collaboration de l'entreprise Eiffage Infrastructures (France) et de l'ENTPE sur le thème des structures et matériaux de chaussée.

Un dispositif expérimental innovant est conçu et mis en place à l'ENTPE. Il se nomme 2T3C (Torsion-Traction-Compression sur Cylindre Creux). Il permet d'appliquer indépendamment des chargements de torsion et de traction-compression sur des éprouvettes cylindriques creuses composées de deux couches d'enrobé bitumineux avec une interface entre les couches. Les essais peuvent être cycliques et c'est un test homogène. La composante principale du 2T3C est l'utilisation de la Corrélation d'Images Numériques 3D (CIN 3D), une technique de mesure optique, pour observer les déplacements à la surface des échantillons. Une méthode d'analyse spécifique a été développée afin de trouver les déformations dans les enrobés bitumineux et le déplacement relatif entre les couches au niveau de l'interface.

Avec cet appareil, une campagne expérimentale a été conduite pour étudier le comportement des interfaces dans le domaine des petites déformations et à la rupture. Plusieurs configurations d'interface ont été testées avec plusieurs types d'enrobés bitumineux et différentes couches d'accrochage à plusieurs dosages. Les résultats des essais dans les petites déformations doivent permettre de trouver un modèle pour les interfaces qui puisse être utilisé dans de futures méthodes de dimensionnement. Les essais de

rupture avaient pour but de trouver les configurations optimales de matériaux qui entraînaient la meilleure résistance de l'interface soumise à un chargement monotone de cisaillement.

Dans le premier chapitre du mémoire de thèse, une étude bibliographique présente les structures de chaussée pour mieux souligner l'importance des couches d'accrochage.

Les couches supérieures des chaussées sont généralement réalisées en matériaux liés comme le béton de ciment ou les enrobés bitumineux car leur résistance mécanique est très importante. Mais lorsqu'ils sont soumis à des sollicitations répétées, liées au trafic ou au climat, ces matériaux peuvent se fissurer, notamment par fatigue. Des études numériques ont montré que le collage parfait des couches diminue les contraintes de traction maximale à l'intérieur des couches, en comparaison avec le cas où les interfaces sont parfaitement glissantes, ce qui augmente de manière significative la durée de vie des structures routières.

Les méthodes de dimensionnement des chaussées varient d'un pays à l'autre. Si certaines sont totalement empiriques, les méthodes dites « rationnelles », où le comportement de la chaussée est obtenu à partir de modèles de structures et des lois de comportement des matériaux, se font de plus en plus présentes. Mais même dans les plus complètes (aux États-Unis et en France), les interfaces entre couches en enrobé bitumineux sont considérées parfaitement collées entre elles dans les calculs. Cela correspond au cas le plus favorable mais pas au plus réaliste.

De nombreux essais ont été développés pour tester les interfaces entre couches de chaussées. Des tests *in situ* permettent de surveiller l'évolution de l'état de dégradation des interfaces dans des structures routières en utilisation. Mais les informations obtenues avec ces tests sont limitées puisque les conditions expérimentales ne peuvent pas être contrôlées. En laboratoire, plusieurs types d'essais mécaniques ont été inventés afin de créer des états de contraintes complexes à l'interface, représentatifs des chargements appliqués par les véhicules. Parmi eux se trouvent les essais de cisaillement, les essais de torsion, les essais de flexion, les essais de traction, les essais de traction-compression, les essais de fendage de coin, … Ces essais en laboratoire ont permis d'étudier l'influence de la température, de la vitesse de chargement, du type de couche d'accrochage ou encore du type d'enrobé sur le comportement des interfaces. Peu de ces essais sont homogènes. À l'aide des résultats expérimentaux, plusieurs modèles ont été développés qui décrivent adéquatement le comportement des interfaces à la rupture pour des chargements monotones ou pour des essais de fatigue.

Dans le deuxième chapitre du mémoire de thèse, la conception du dispositif expérimental 2T3C est présentée.

Les essais sur cylindre creux présentent l'avantage de pouvoir être considérés homogènes avec une bonne approximation si les dimensions de l'échantillon sont bien choisies. En se basant sur de précédentes études sur les essais sur cylindre creux, et en prenant en compte la taille du volume élémentaire représentatif des enrobés bitumineux et d'autres considérations pratiques, les dimensions des échantillons sont choisies comme suit : diamètre extérieur de 17,2 cm, diamètre intérieur de 12,2 cm pour une épaisseur de 2,5 cm et une hauteur de 12,5 cm. Pour la présente étude des interfaces entre couches de chaussée, les échantillons sont composés de deux couches d'enrobé bitumineux avec une couche d'accrochage à l'interface.

Des pièces mécaniques ont été dessinées et réalisées pour permettre la transmission des chargements de torsion et de traction-compression créés par une presse hydraulique vers les échantillons. Des systèmes de centrage assurent l'alignement des axes de l'échantillon et de la presse hydraulique. Une enceinte thermique avec des fenêtres sur ses côtés peut être installée autour de l'échantillon pour maîtriser sa température.

Les systèmes de mesure du 2T3C sont les suivants :

- le capteur de force axiale de la presse (plage de mesure : ± 100 kN) ;
- le capteur de position verticale du piston de la presse (plage de mesure : ± 75 mm) ;
- le capteur de couple de la presse (plage de mesure : ± 2000 N.m) ;
- le capteur d'angle de rotation du piston de la presse (plage de mesure : ± 45 °) ;

- les capteurs sans-contact (plage de mesure : 0-1 mm) : au nombre de quatre, ils permettent de mesurer le déplacement global entre le haut et le bas de l'échantillon, deux d'entre eux mesurent le déplacement vertical et les deux autres le déplacement horizontal lié à la rotation ;
- la CIN 3D : quatre caméras, deux de chaque côté de l'échantillon, prennent des images pendant les tests mécaniques. Un algorithme de corrélation trouve ensuite le champ de déplacement en trois dimensions sur toute la surface à chaque instant où des images sont prises.

Une méthode d'analyse des résultats de la CIN 3D a été mise au point afin de trouver, à partir du champ de déplacement, les déformations dans les deux couches d'enrobés et les sauts de déplacement verticaux et horizontaux au niveau de l'interface, définis comme les déplacements relatifs entre le bas de la couche supérieure et le haut de la couche inférieure. Cette méthode est basée sur l'utilisation de valeurs moyennes calculées sur des bandes à la surface de l'échantillon. L'hypothèse d'homogénéité des déformations, confirmée expérimentalement, est ensuite invoquée pour trouver des formules simples reliant les déformations à la distribution spatiale des déplacements dans l'échantillon. Une étude paramétrique a permis d'identifier les paramètres de calcul de la CIN 3D les plus adéquats pour cette méthode d'analyse.

Le troisième chapitre du mémoire présente la campagne expérimentale réalisée durant cette thèse.

Quatre enrobés bitumineux (BBSG3 et BB5 en couche supérieure, EME2 et GB5 en couche inférieure) représentatifs des matériaux utilisés en couches de surface ou en couche d'assise et trois émulsions (à base de bitume pur, de bitume modifié au SBS ou de bitume modifié au latex) ont été employés pour créer huit configurations d'interface différentes. Les matériaux sont fabriqués en laboratoire par plaque de 60x40x15 cm^3 à l'aide d'un compacteur à roue. Une fois que la couche inférieure d'enrobé a été compactée et s'est refroidie, l'émulsion de la couche d'accrochage est appliquée à l'aide d'une brosse. Après la rupture de l'émulsion, la couche supérieure est compactée à chaud sur la couche d'accrochage. Trois échantillons cylindriques creux du 2T3C peuvent être carottés dans chaque plaque.

Pour étudier l'effet de l'engrènement à l'interface, quatre configurations sont testées. La même couche d'accrochage est utilisée à chaque fois mais avec différents enrobés dans les couches. Les enrobés étudiés ont soit une courbe granulométrique continue (BBSG3 et EME2) soit une courbe granulométrique discontinue (BB5 et GB5). Les quatre possibilités (couche supérieure avec une courbe continue ou discontinue, sur couche inférieure avec une courbe continue ou discontinue) sont testées.

Trois configurations sont utilisées pour évaluer l'influence du dosage en couche d'accrochage. Les enrobés sont les mêmes et l'émulsion utilisée est une émulsion de bitume pur. Les trois dosages en bitume résiduel au niveau de l'interface sont 250, 350 et 450 g/m^2.

Enfin, trois configurations permettent d'étudier l'effet du type de couche d'accrochage. Les enrobés sont les mêmes dans les trois configurations mais l'émulsion de la couche d'accrochage est réalisée à partir de bitume pur, à partir de bitume modifié au SBS ou bien à partir de bitume modifié au latex.

Plusieurs protocoles de tests sont définis pour l'étude du comportement thermomécanique des interfaces dans le domaine des petites déformations. Un essai avancé de module complexe est réalisé sur chaque échantillon : des sollicitations cycliques sinusoïdales sont appliquées à plusieurs fréquences (entre 0,01 et 0,3 Hz) et pour plusieurs températures (de 10 à 40 °C), en rotation avec une légère contrainte de compression constante puis en traction-compression avec un couple nul. Aussi, des tests de non-linéarité sont conduits en appliquant des sollicitations cycliques en rotation à différentes amplitudes sur l'échantillon, la fréquence et la température étant fixées. Un protocole de test oligocyclique est également présenté et consiste en l'application de quelques dizaines de cycles à la même amplitude sur un échantillon, à fréquence et température fixées.

Pour étudier la rupture des échantillons, des essais de torsion à vitesse de rotation constante sont effectués. Une contrainte normale constante est appliquée pendant le test, sa valeur étant 0, 0,25 ou 1 MPa selon l'échantillon.

Des tests complémentaires sont également réalisés : des tests de module complexe en traction-compression sur des éprouvettes d'enrobé bitumineux cylindriques et un test de module complexe sur bitume avec un rhéomètre à cisaillement dynamique (*Dynamic Shear Rheometer*, *DSR* en anglais).

Dans le quatrième chapitre, les résultats des tests en petites déformations sont présentés et analysés.

Les signaux obtenus lors des tests cycliques ont été approximés par des signaux sinusoïdaux parfaits afin de calculer les modules complexes dans les couches d'enrobé et les rigidités d'interface complexes, pour les modes de cisaillement et de traction-compression. La rigidité d'interface complexe est obtenue à partir des signaux de contraintes et de sauts de déplacement.

Pour les essais avancés de module complexe, le Principe d'Équivalence Temps-Température (PETT) a été vérifié pour les enrobés bitumineux mais aussi pour les interfaces, pour les modes de cisaillement et de traction-compression. Les coefficients de translations pour le PETT sont décrits à l'aide de l'équation WLF. Le modèle 2S2P1D a été utilisé pour décrire le comportement viscoélastique linéaire des enrobés dans les couches, dans les modes de cisaillement et de traction-compression. L'absence de données expérimentales aux hautes fréquences et basses températures dans l'essai avancé de module complexe a rendu difficile la calibration des modèles dans cette zone. La comparaison des résultats d'essais avancés de module complexe réalisés avec le 2T3C avec les résultats d'essais de module complexe en traction-compression sur des éprouvettes d'enrobé cylindriques a fait apparaître des différences dans les comportements des enrobés obtenus avec les deux essais. Celles-ci pourraient être dus à la différence de pourcentage de vides entre les deux échantillons ou à l'anisotropie du comportement des enrobés liée à leur compaction, les éprouvettes des deux tests étant carottées dans des directions différentes.

Le comportement des interfaces obtenus avec l'essai avancé de module complexe s'est révélé ne pas être viscoélastique linéaire, ni dans le mode de cisaillement ni dans le mode de traction-compression. Un nouveau modèle, le modèle DBN_{PDSC} (en anglais, *DBN model with Plastic Dissipation for Small Cycles*, en français, modèle DBN avec dissipation plastique pour cycles en petites déformations) est introduit pour décrire le comportement des interfaces. Il est basé sur le modèle DBN et correspond à un modèle de Kelvin-Voigt généralisé avec l'ajout de dissipation d'énergie plastique dans les ressorts. Pour les configurations avec des couches d'accrochage réalisées en émulsion de bitume pur, la calibration du modèle DBN_{PDSC} a été effectuée en se basant sur les résultats de l'essai de module complexe réalisé avec le *DSR* sur le bitume constitutif des émulsions. Il n'a pas été possible d'identifier une influence du type d'enrobés, du type ou du dosage de couche d'accrochage sur le comportement des interfaces en petites déformations.

Le test de non-linéarité a montré que le comportement des interfaces changeait suivant l'amplitude des cycles appliqués. Un endommagement apparent a été observé au cours de l'essai. Lors du test oligocyclique, réalisé à la même amplitude que l'essai avancé de module complexe, la norme de la rigidité d'interface complexe a chuté rapidement, dès les premiers cycles. Mais cette diminution est en partie réversible puisque la quasi-totalité de la norme de la rigidité a été récupérée après un temps de repos suffisant.

Dans le cinquième et dernier chapitre du manuscrit, les résultats des essais de rupture en cisaillement monotone sont présentés et analysés.

Sur les 27 échantillons testés, 26 ont rompu au niveau de l'interface. Dans tous les essais un maximum de contrainte de cisaillement a été observé, ce maximum est nommé résistance au cisaillement de l'interface.

A partir de trois échantillons de la même configuration testés à des vitesses différentes, il a été observé que la résistance au cisaillement de l'interface augmentait avec la vitesse de rotation suivant une loi de puissance.

A partir des résultats obtenus sur trois différentes configurations d'interface pour chacune desquelles des échantillons ont été testés avec trois contraintes normales de compression différentes (0, 0,25 et 1 MPa) à la même vitesse de rotation, la dépendance de la résistance au cisaillement à la contrainte

normale a pu être identifiée. Une loi linéaire, le critère de rupture de Mohr-Coulomb, a permis de décrire l'augmentation de la résistance au cisaillement avec la contrainte normale.

Les résultats pour les quatre configurations avec des enrobés différents dans les couches ont montré que la configuration avec un enrobé ayant une courbe granulométrique continue compacté sur un enrobé à courbe granulométrique discontinue présentait la plus haute résistance au cisaillement. Les autres configurations ont présenté des résistances similaires.

En ce qui concerne les configurations avec une couche d'accrochage en émulsion de bitume pur, le dosage le plus faible testé (250 g/m^2) a montré une résistance au cisaillement plus faible que les deux autres dosages (350 et 450 g/m^2).

Pour les trois configurations avec des couches d'accrochage différentes, l'interface avec la couche d'accrochage réalisée en émulsion de bitume modifié au SBS présentait la plus faible résistance au cisaillement, comparée aux couches d'accrochage en émulsion de bitume pur et en émulsion de bitume modifié au latex.

En conclusion, le comportement thermomécanique des interfaces entre couches de chaussée en enrobé bitumineux a pu être observé à l'aide d'essais en petites déformations et en grandes déformations. Ces essais ont notamment été réalisés avec l'appareil 2T3C mis au point dans cette thèse. Cet appareil permet de tester une grande variété de chemins de contraintes en appliquant indépendamment de la torsion et de la traction-compression sur des éprouvettes cylindriques creuses composées de deux couches. L'utilisation de la CIN 3D couplée à une nouvelle méthode d'analyse développée dans cette thèse permet d'obtenir les déformations dans les couches d'enrobés et les déplacements relatifs au niveau de l'interface, dans les modes de cisaillement et de traction-compression.

Une importante campagne expérimentale a été conduite avec le 2T3C pour étudier huit configurations d'interface, avec quatre types d'enrobés et trois couches d'accrochages appliquées à différents dosages. Un total de 27 échantillons a été testé.

Des essais avancés de module complexe ont été réalisés sur toutes les éprouvettes. Ils ont consisté en l'application d'un chargement sinusoïdal à quatre fréquences différentes (de 0,01 à 0,3 Hz) et à quatre températures différentes (de 10 à 40 °C), à chaque fois en torsion (avec une légère contrainte de compression maintenue constante) puis en traction-compression (avec un couple nul). Ces cycles ont été réalisés dans le domaine des petites déformations, avec une amplitude de déplacement globale appliquée entre le haut et le bas des échantillons correspondant à une déformation de 200 µm/m pour un échantillon de même dimension que ceux du 2T3C mais qui ne serait composé que d'un seul matériau homogène. Les conclusions suivantes peuvent être tirées de ces essais :

- Les modules complexe en traction-compression et en cisaillement des enrobés ont été obtenus avec la CIN 3D. Les quatre enrobés testés ont respectés le PETT, en mode de cisaillement et en mode de traction-compression. Ils ont été modélisés en utilisant le modèle viscoélastique linéaire 2S2P1D. L'absence de résultats expérimentaux aux hautes fréquences et basses températures a rendu difficile la calibration des modèles dans cette zone.
- Les modules complexes de traction-compression obtenus avec le 2T3C pour deux des enrobés testés ont été comparés avec les modules obtenus à partir d'essais de traction-compression sur des éprouvettes cylindriques de ces mêmes enrobés. Des différences significatives ont été observées entre les deux essais. Elles pourraient être expliquées par l'anisotropie du comportement des enrobés bitumineux compactés en laboratoire ou par une différence de pourcentage de vides entre les deux éprouvettes.
- Les sauts de déplacement à l'interface, définis comme le déplacement relatif entre le bas de la couche supérieure et le haut de la couche inférieure au niveau de l'interface, ont été trouvés à partir de la méthode d'analyse des résultats de la CIN 3D développée dans cette thèse. Quand les chargements sinusoïdaux ont été appliqués, les sauts de déplacement étaient également sinusoïdaux. Les amplitudes de saut de déplacement vertical observées pendant les tests étaient comprises entre 0,5 et 4 µm. Les amplitudes de saut de déplacement horizontal observées pendant les tests étaient comprises entre 2 et 10 µm.

- Les rigidités d'interface complexes dans les modes de cisaillement et de traction-compression ont été définies et calculées pour les essais avancés de module complexe. Les huit configurations d'interface respectaient le PETT dans les modes de cisaillement et de traction-compression.
- Le comportement des interfaces à l'amplitude testée n'était pas viscoélastique linéaire.
- Un nouveau modèle, le modèle DBN_{PDSC} (en anglais, *DBN model with Plastic Dissipation for Small Cycles*, en français, modèle DBN avec dissipation plastique pour cycles en petites déformations) a été introduit pour décrire les interfaces. Il est basé sur le modèle DBN avec l'addition de dissipation d'énergie plastique dans les éléments élasto-plastiques. Ce modèle a permis de décrire adéquatement le comportement des interfaces dans les modes de cisaillement et de traction-compression. Aucune influence du type d'enrobé bitumineux dans les couches, du type ou du dosage en couche d'accrochage sur le comportement de l'interface dans le domaine des petites déformations n'a pu être identifié.
- Le comportement des interfaces avec une couche d'accrochage en émulsion de bitume pure a pu être modélisé avec le modèle DBN_{PDSC} en se basant sur les résultats d'un essai de module complexe de cisaillement réalisé avec un *DSR* sur le bitume de l'émulsion.

Toujours dans le domaine des petites déformations, un test de non-linéarité a été réalisé sur un échantillon avec une interface en appliquant des cycles sinusoïdaux en rotation (à 0,1 Hz et 20 °C) à différentes amplitudes. Il a été observé que :

- Pour des amplitudes de saut de déplacement entre 3 et 10 µm, la norme de la rigidité d'interface complexe de cisaillement a diminué lorsque l'amplitude des cycles augmentait. L'angle de phase n'a pas varié significativement.
- L'interface s'est apparemment endommagée durant le test de non-linéarité rendant impossible l'identification de l'effet de la valeur de l'amplitude du saut de déplacement sur la rigidité d'interface complexe de cisaillement.

De plus, un test oligocyclique a été réalisé sur le même échantillon pour surveiller l'évolution de la rigidité d'interface complexe de cisaillement lors d'un chargement cyclique répété quelques dizaines de fois (à 0,1 Hz et 20 °C). L'amplitude des cycles étaient la même que dans l'essai avancé de module complexe. Il a été trouvé que :

- La norme de la rigidité d'interface complexe de cisaillement a diminué rapidement. L'angle de phase a augmenté durant le test. La norme a perdu près de 50 % de sa valeur initiale après 50 cycles. Ce résultat confirme que le comportement de l'interface n'est pas viscoélastique linéaire à cette amplitude.
- La norme de la rigidité d'interface complexe de cisaillement a récupéré rapidement après la fin des cycles, regagnant 90 % de sa valeur initiale après seulement 1 h de repos et 98 % après 24 h. Ceci prouve que des phénomènes réversibles sont en partie responsables de la chute de la norme de la rigidité d'interface complexe de cisaillement et qu'ils doivent être pris en compte dans les essais cycliques sur les interfaces.

Après les tests en petites déformations, des tests de rupture de cisaillement monotone ont été conduits pour évaluer la résistance au cisaillement de l'interface. Les essais ont été réalisés à vitesse de rotation constante (0,02, 0,067 ou 0,2 %/s en taux de déformation global) avec une contrainte verticale maintenue constante (0, 0,25 ou 1 MPa). La température des essais était la même pour tous les essais, proche de 20 °C.

- Sur les 27 échantillons testés, 26 se sont rompus au niveau de l'interface. Dans tous les essais, la contrainte de cisaillement a atteint un maximum avant de diminuer. La résistance au cisaillement de l'interface est définie comme la contrainte maximale observée pendant l'essai.
- Pour les trois vitesses de rotations testées sur la même configuration d'interface, la résistance au cisaillement a augmenté avec la vitesse de rotation suivant une loi de puissance comme cela a été déjà observé dans la littérature scientifique.
- L'ajout d'une contrainte normale de compression pendant les essais a augmenté la résistance de l'interface au cisaillement et a aussi augmenté la valeur du saut de déplacement horizontal pour lequel ce maximum de contrainte est observé. Le critère de rupture de Mohr-Coulomb a été utilisé pour modéliser le comportement des interfaces à la rupture.

- L’engrènement a eu un effet sur la résistance au cisaillement. La configuration optimale d’enrobés bitumineux était celle où un enrobé avec une courbe granulométrique continue a été compacté sur un enrobé avec une courbe granulométrique discontinue. Ce résultat concorde avec un raisonnement simple sur l’engrènement trouvé dans la littérature scientifique. Les autres configurations ont montré des résistances au cisaillement moindres.
- Un dosage insuffisant en couche d’accrochage a conduit à une diminution de la résistance au cisaillement des interfaces. Le dosage de 250 g/m² en bitume résiduel a montré de moins bons résultats que les dosages de 350 et 450 g/m², alors que c’est le dosage minimum recommandé dans la norme française pour les enrobés bitumineux de cette configuration.
- La modification du bitume utilisé dans les émulsions, que ce soit avec le SBS ou avec le latex n’ont pas fait augmenté significativement la résistance au cisaillement des interfaces. A partir des résultats sur un faible nombre d’échantillon, il semble que la modification au SBS a même fait diminuer la résistance de l’interface.

INTRODUCTION

The behaviour of a road structure depends strongly on the state of bonding at the interfaces between its layers. Numerous premature degradations of road structures were connected with the debonding of the layers. As roads in good condition are essential to the functioning of a society, they have a significant value. Any reparation is very costly, in addition of being time- and energy-consuming and should be avoided if possible, carefully anticipated if not. Standards exist in many countries concerning the application of a tack coat at the interface to ensure a good bond of the layers. But the design methods, even the most rational ones, do not take properly into account the mechanical behaviour of interfaces. The layers between bituminous mixtures are indeed considered perfectly bonded which is the most favourable case and might lead to an overestimation of the pavement lifetime. More realistic interface behaviours must be implemented in the design methods.

The scientific community began to pay attention to the interfaces in the late 1970's when the use of surface layers began to be frequent. The first mechanical tests were developed at that time. A majority of them characterised the bond between the layers by the maximum stress that the interface can endure. If this approach is useful to compare interface configurations (type and dosage of tack coat, mixtures in the layers), it does not represent well the actual damage mechanisms in a pavement except for structures that endure heavy loads, like airport runways for instance. Recently, cyclic tests were developed to mimic the iterative aspect of vehicle traffic and evaluate the interface resistance to fatigue. However, most of the tests on interfaces are inhomogeneous which can bias their analysis. An adequate test to determine the behaviour of interfaces should be homogeneous and able to perform cyclic testing.

The objective of this thesis is to study the thermomechanical behaviour of interfaces between pavement layers. This thesis has been carried out in the *Laboratoire de Triblogie et Dynamique des Systèmes* (LTDS, UMR 5513) at the University of Lyon/*École Nationale des Travaux Publics de l'État* (ENTPE). It was part of an industrial chair dedicated to pavement materials and structures, co-signed by the company Eiffage Infrastructures (France) and the University of Lyon/ENTPE (France).

An innovative experimental device named 2T3C Hollow Cylinder Apparatus (2T3C HCA) has been developed in this work. It allows applying complex loadings on hollow cylinder samples composed of two layers and an interface. It is a homogeneous test and cyclic loadings can be applied in tension-compression mode and in shear mode, independently or simultaneously, in order to reproduce adequately the loadings induced by traffic. A novel approach to the characterisation of the interfaces is made possible thanks to the use of 3D Digital Image Correlation (3D DIC). A specific analysis method has been introduced to obtain the mechanical properties of the interfaces and of the mixtures in both layers from 3D DIC results.

With this new apparatus, an experimental campaign has been performed to investigate the behaviour of interfaces in the small strain domain and at failure. Multiple interface configurations have been tested with different bituminous mixtures in the layers and different tack coats at the interface. The results of the tests in the small strain domain are expected to allow finding a precise model of interfaces that could be used in future design methods. The failure tests aimed at finding the optimal configuration of materials for the interface regarding its shear resistance to monotonic loadings.

This manuscript is divided in five chapters.

After this introduction, Chapter 1 is a literature review about interfaces between pavement layers. It first describes the pavement structures to better highlight the importance of the interfaces between the

layers. The previous mechanical testing performed on interfaces are then presented. The different factors influencing the interface behaviour that were identified from these tests are also introduced. The existing approaches to model the thermomechanical behaviour of interfaces are outlined.

In Chapter 2, the design of the 2T3C HCA is thoroughly described. The theoretical frame of hollow cylinder test is recalled to support the design choices made for the apparatus. A complete description of the 2T3C HCA and of its measurement systems is made in this chapter. In particular, the 3D DIC principle is presented and the specific analysis method developed to obtain the interfaces properties with this technique is introduced.

Chapter 3 presents the performed experimental campaign. The important properties of the tested materials and the sample fabrication process are described. The procedures of the different tests, in the small strain domain or at failure, are then carefully explained.

The results of the tests in the small strain domain are found in Chapter 4. The methods to find the behaviour of the bituminous mixtures and of the interfaces are presented. The modelling approaches, different for mixtures and interfaces, are explained and applied to the experimental results.

Chapter 5 shows the results of the monotonic shear failure tests performed with 2T3C HCA. The influence of the different interface configurations on the interface shear strength are identified.

Finally, this manuscript ends with a conclusion that emphasises the findings of this thesis and that outlines perspectives for future work.

Chapter 1 - Literature review

This chapter presents a literature review of the current understanding of interfaces between pavement layers. As it will be explained subsequently, interfaces play a major role in road structures. The first section of this chapter is therefore an overview on road structures and serves as an introduction to interfaces. In a second section, the different experimental approaches to understand the interface behaviour are presented with a distinction between *in situ* tests and laboratory tests. The testing enables the identification of the factors influencing the interface behaviour and the most important of them will be explained in the third section. Finally, the existing models of interfaces will be summarized in the fourth and last section.

1.1. Introduction on road structures

1.1.1.Background

History of road structures begins with history of civilization. The first roads were basically tracks cut through the woods or shaped by the footsteps on which men or animals used to carry goods. The socio-economic development induced merchandise exchanges between the first settlements, creating a need for better mobility. Earth levelling and stone paving were among the first building techniques used to facilitate transport, even before the wheel invention. The use of stone for pavements has been observed in the ruins of the ancient cities of Mohenjo-Daro (Pakistan) and Ur (Iraq) that throve 6000 years ago, it also existed in Cretan, Egyptian, Persian and Indian civilizations. During the Antiquity, Romans built and maintained a large network of roads for economic and military purposes. In the year 312BC, the construction of the *Via Appia* begun (Figure 1.1): it is the oldest roman road built with a consistent design. It had a layered structure (Adam 1989), usual for all roman roadways, with, from bottom to top:

- a layer of stones called *statumen* used to solidify the base and placed on the natural ground, levelled or dug in a trench;
- a thick layer of sand, sometimes mixed with gravel or clay, called *rudus*;
- a surface made of gravel or compacted pebbles, sometimes of hard stone laid in a curve profile.

The whole structure was about 1 to 1.5 m thick. Surfacing with paving stones was systematic in the cities but not on the country sections. When lacking of large stones, Romans would use rows of timber to make the base of their roads, like on the *via Mansuerisca* (in Belgium now). These constructions would prove to stand the test of time as some of them are still in use today. Similar structures were built in India and in China in the same period (*The New Encyclopaedia Britannica* 2006).

Figure 1.1 - Via Appia leaving Rome near the Villa of the Quintilii (Adam 1989)

After the fall of the Roman Empire, when the barbaric invasions multiplied, roads deteriorated due to a lack of maintenance all across Europe. It is only under the reign of Charlemagne (9th century) that European roads started their revival but it is really from the 15th century that they gained attention (Berthelot 1885). The rationalization of roads network started in the 18th century in France with the creation of the *corps des ponts et chaussées* in 1716 by Philippe d'Orléans. This administration has been in charge of the building, the maintenance and the administration of roads on the territory ever since. Among their engineers was Pierre Trésaguet who wrote in 1775 a *memorandum* explaining how roads were built at that time. He described road structures having (Arbellot 1973):

- a base layer composed of large stones placed on their edge at the bottom of a trench dug in the ground;
- a layer of smaller broken stones, compacted to remove voids;
- a surface layer of small stones crushed to the size of a walnut (about 3 cm).

The whole structure was about 30 cm deep which constitutes a real difference compared to roman structures.

A major breakthrough in the way of thinking road structures was achieved by a Scottish engineer of the beginning of the 19th century, John McAdam. We owe him the structure named "macadam" after its designer, still broadly used nowadays (Figure 1.2). Unhappy with the state of the roads in Great Britain, he wanted to introduce a scientific method for the road construction (McAdam 1821). According to him, the soil was strong enough to carry the loads of the carriages on the condition that it was completely dry, preventing any degradation related to the frost and thaw. So, the placement of large stones on the ground was an unnecessary expense and even a mistake since it could not protect sufficiently the soil from water infiltrations. Besides, roads should be raised above the ground and not put in a trench where water infiltrations are more liable to occur. And to guaranty a protection from rain water, broken stones, never to be mixed with clay, chalk or any material that could conduct water, should be laid upon the ground in a layer 5 or 6 inches high (15 cm). Only broken stones smaller than a square inch (about 6,3 cm^2) were to be used. This dimension was related to the contact surface of a wheel with the road surface, McAdam arguing that large stones moved because of the wheels passing on it when a structure composed of small stones would only compact itself (McAdam 1819). Macadam structures developed very rapidly in the United States of America (USA) and proved to be very resistant to frost and thaw.

Figure 1.2 - Macadam road in Marshall county, IN, USA

During the 19th century, rail transportation competed with road transportation in industrial countries. It is only when motor vehicles spread than roads were again at the centre of attention. The high speed of these vehicles created large dust clouds and removed the small stones from the surface of the macadam roads. A flat surface with good adherence became necessary. John Henry Cassell, whose business was the making of rainwater-pipes and gutters, patented a bituminous material called “lava stone” in 1834 which was used for waterproofing and then for paving. The surface of macadam structures was sealed with a layer of this tar mixed with sand to prevent dust dispersion and water infiltrations. These tar-bound macadam (or “tarmacadam”) structures were laid in the USA starting from the 1860’s (not to be mistaken with “Tarmac” that designates a mix of tar with solidified hot slag coming from blast-furnaces, patented in 1902 by Edgar Purnell Hooley (Hooley 1903)). Bituminous concrete, a mix of tar and stones laid as surface layer on the roads, appeared in the 1860’s in the USA (Alsing 1868; Bailey 1869; De Smedt 1870) under the name of asphalt concrete. In that same time, the first road paved with cement concrete was built in 1865 in Scotland, forty years after Portland cement invention. These paving materials were not broadly used until the beginning of the 20th century and the actual development of automobile traffic (Figure 1.3). The type of materials used for roads has remained the same up to now but many efforts were done to better understand the behaviour of these materials and to enhance their quality by modifying the components (aggregates, cement or bitumen) or by optimizing their proportion in the mixtures. Construction techniques have also been continuously improved for more efficiency. It is also mostly during the 20th century that design methods were created and that they became more and more rational.

Figure 1.3 - A47 highway, made of bituminous concrete, between Lyon and Saint-Etienne, France

Roman built roads with a layered structure: this concept is still relevant today, the main changes are the materials they are made of, the role given to the layers and the road design methods.

1.1.2.Road materials

Every layer of a road structure has a different function and they are therefore all made of different materials. In the previous section we saw how the discovery of some of them changed significantly the way of thinking roads structures. This section focuses on the basic components of a modern road structure as a first step in the understanding of how the whole works.

1.1.2.1. Natural ground

Starting from the bottom, the ground on which the road is built is of uttermost importance. A durable road structure cannot be thought without a solid base that can endure the loadings created by the traffic. As roads are needed everywhere, all types of soils have to be considered, from bog to solid rock, from clay to sand. Unfortunately, it is not possible to build roads on bog and neither on grounds that cannot support high loads or that are very sensitive to hydric conditions. When the road layout cannot be changed, draining the ground or replacing it with another material are possible solutions. Also, it is sometimes necessary to improve the strength of the upper parts of the ground so that the construction machines might work without difficulties. In this case, the soil can be mixed with hydraulic binders such as lime or cement and put back on the ground.

1.1.2.2. Aggregates

Aggregates is the name given to the mineral components used in road constructions, by themselves or in the composition of bound materials. If stone pavement was an early method to make the road surface, this technique has been forsaken since and large stones (maximal size superior to 5 cm) are not used anymore. The classification of the aggregates is based on their maximal size, approximatively as follows: when it is superior to 2 cm they are called pebbles, when it is between 5 mm and 2 cm they are called gravel, when it is inferior to 5 mm they are classified as sand. A special class exists for very thin components, called filler, typically when their maximal size is inferior to 50 µm. Filler is always found with pebbles, gravel or sand. It is mostly responsible of the aggregate capacity to absorb water and it is essential to the realization of bituminous mixtures.

Stones and gravel can be used alone in a layer but they can be mixed together or with sand as well. Important indicators of the quality of these components are their resistance to mechanical loadings, to smoothing (when used in the surface layer) and to frost and thaw. These characteristics are verified with specific tests (Corté and Di Benedetto 2004) before they are used in a road. Their shape, their mineral composition and the proportion of filler are also monitored. Aggregates can be extracted directly from river alluvium or obtained from the breaking of rocks in careers. Recycled aggregates from old pavements or buildings are also more and more used in the making of new bound materials. These different sources a large variety of aggregates, with many different petrographic compositions.

1.1.2.3. Hydraulically bound materials

Road structures must diffuse the traffic loading to the natural ground. It requires a stiff material and this is why hydraulically bound materials are often used. Hydraulic binders react with water to form stable and rigid materials. Among them are cement and lime, obtained by heating at a very high temperature a mix of specific minerals. More hydraulic binders can also be obtained by adding industrial by-products (like furnace slag or fly ashes) to cement or lime.

Hydraulically bound materials are obtained by mixing aggregates with hydraulic binders and water. After the binder reacts with water, a stiff and resistant material is obtained. It is possible to use only

sand with hydraulic binders or only gravel with hydraulic binder. Cement concrete is a particular hydraulically bound material obtained with a mix of cement, water, gravel and sand. The aggregates used in the mixes must follow different requirements especially regarding their mechanical resistance. A careful attention is given to the grain size distribution since it is the granular skeleton that bears the compressive loads of the whole material. The maximal size of aggregate is about 20 mm in this kind of materials. Industrial by-products such as slag from furnaces are sometimes used as aggregates. The final material must have a good workability, it should also be tested in laboratory to determine its strength and its resistance to fatigue, which is the repetition of an important number of cycles at small strain amplitude until failure.

1.1.2.4. Bituminous materials

Hydrocarbon binders

A hydrocarbon binder is a mix of various hydrocarbons with high molecular weight forming a viscous liquid when heated and a glassy solid when cooled down. They are found in different forms. Many hydrocarbon binders are derived from petroleum, which is the result of the decay of algae and other living forms for millions of years in a confined environment under high temperatures. Natural asphalt is a heavy petroleum that can be found at the earth's surface in asphalt lakes, the most famous being the Pitch lake situated in Trinidad-and-Tobago (Figure 1.4). Bitumen is a hydrocarbon binder too; it designates the heavier parts resulting from the petroleum refining process. Historically, hydrocarbon binders, not always related to petroleum, were called tar or pitch. For instance, coal tar is a by-product of the coking process in the coal industry and represented an important part of the binders of road structures (like tarmacadam) in the beginning of the 20th century until bitumen from petroleum refining became abundant.

Figure 1.4 - Pitch lake in La Brea, Trinidad-and-Tobago (Credits: Grueslayer @Wikipedia, CC BY-SA 4.0)

Hydrocarbon binders are very stable to water and have been used for thousand years for waterproofing structures. In Mohenjo-Daro (Pakistan) a water tank was built with natural asphalt in the 3rd millennium BC. In India, some paved streets were grouted with asphalt in the 1st century (The New Encyclopaedia Britannica 2006). This property is the main reason why bituminous materials were applied on road surfaces in the first place, along with the absence of dust compared to macadam structures. Their very high sensitivity to temperatures is a great advantage for road construction since it is very easy to work these materials at high temperature and they become very stiff when they cool

down. Their ductility, their resistance to fracture at low temperature, their resistance to fatigue and how their properties change with time are tested before they are used.

Nowadays, bitumens obtained from petroleum are the most used in the road structures. Depending on their provenance, their chemical composition varies and it is quite difficult to describe. A bitumen is a mix of molecules with a continuous evolution of their molar masses and polarity (Lesueur 2002). The molecules with the higher densities and polarities are called asphaltenes, they are often identified by their insolubility in heptane and they give the colour black to the bitumen. Schematically, a bitumen is a colloidal dispersion of asphaltenes in an oil made of lighter molecules (Figure 1.5). Asphaltenes are polar and tend to create bonds between them. The structures they create this way are responsible for the viscous properties of bituminous materials.

It is possible to improve the stiffness of bitumen by adding polymers like latex in it. Polymers swells and attracts the light oils, creating a polymer phase without asphaltenes and thus concentrating asphaltenes in the rest of the bitumen which improves the bond between them and the overall stiffness of the mix. Other adjuvants exist to reduce the bitumen viscosity.

A noticeable property of bitumen exposed to outdoor conditions is the ageing process. Under the effect of rain, oxygen from the air and Sun, the bitumen composition changes, the proportion of asphaltenes increases and the binder becomes stiffer but also more fragile.

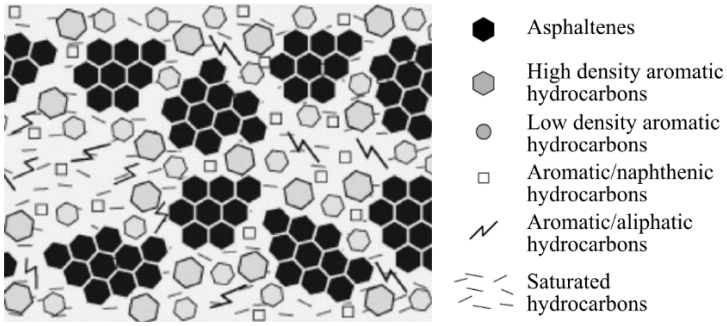

Figure 1.5 - Schematic representation of bitumen molecular structure (translated from Corté and Di Benedetto 2004)

Bituminous mixtures

Hydrocarbon binders are rarely employed by themselves in road structures. They are usually mixed with aggregates to form bituminous mixtures. The mixing is usually done at high temperature with pre-heated and dried aggregates. The aggregates count for about 95 % of the mixture weight, they form a granular skeleton in the mixture, enhancing its strength. The mix of the bitumen and of the filler added with the aggregates constitutes a mastic which can be considered as a binder rigidified by the thin mineral particles present in the bitumen. The grain size distribution of a mixture has a direct influence on its stiffness and on its resistance to permanent deformations, it is always chosen carefully and so is the bitumen content of the mixture. The shape of the aggregates also has an influence on the permanent deformation resistance. The closer the layer is to the surface the higher is the required hardness of the aggregates. Industrial by-products like rubber from worn out tyres or Recycled Asphalt Pavement (RAP) are sometimes substituted to the aggregates.

The aggregate distribution and binder content of the mix depend on the type of layer it is used in. The mixtures must be stiff and have a high resistance to fatigue. Their resistance to permanent deformations, to frost and thaw, their workability and their resistance to water are assessed before their utilisation.

The mechanical behaviour of bituminous mixtures depends on the temperature, the loading speed, the amplitude of loading and the number of cycles applied. Different type of behaviours can be identified (Figure 1.6). When small strain are applied a few times, the bituminous mixtures present a Linear

ViscoElastic (LVE) behaviour (presented in section 1.4.1.1). When small strain cycles are applied many times, the mixtures are damaged through a fatigue process. High amplitudes of loadings lead to the mixture failure and repeated cycles at medium amplitudes create permanent deformations in the material. The limitations of these domains are not precisely definite and depend heavily on the temperature and the loading speed.

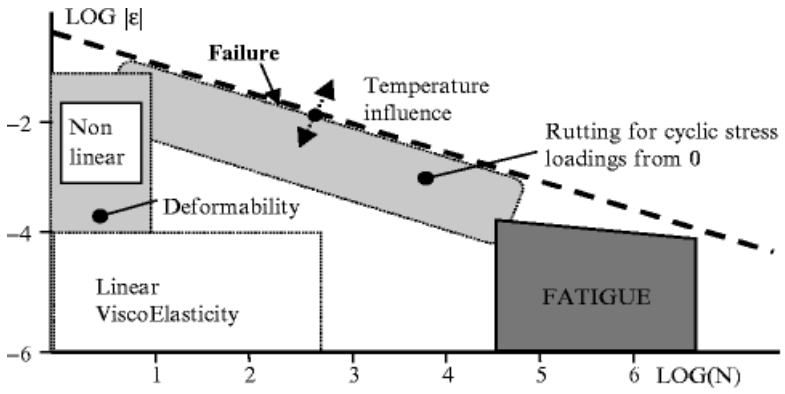

Figure 1.6 - Schematic representation of the mechanical behaviour domains for bituminous mixtures depending on the loading amplitude $|\varepsilon|$ and on the number of cycles applied N (Di Benedetto et al. 2013)

Bituminous emulsions

Water and bitumen are not miscible fluids but it is possible to create an emulsion of bitumen in water with the help of an emulsifying agent. Small particles of bitumen are stabilized by the emulsifying agent and solubilized in the water in a proportion that can reach 70 % of the total emulsion volume. Still, the emulsion viscosity is close to water, even at ambient temperature. Emulsions are used for the making of bituminous mixtures at low temperatures: the aggregates and the emulsion are mixed, laid on the road and after some time, the emulsifying interacts with the aggregates surface and release the bitumen. The water in the emulsion disappears (it is said that the emulsion has broken) leaving a bituminous mixture with the same properties as a conventional mixture. But emulsions are also used by themselves as tack coats to bond the road structure layers together. The bitumen in the emulsions can be pure or modified with polymers. The type of emulsifying agent and its dosage are chosen to have an acceptable viscosity and a good breaking time for the emulsion.

Figure 1.7 - Application of a bituminous emulsion as a tack coat using sprayers

1.1.3. Types of road structures

Road structures are layered structures (Figure 1.8). Each layer has a different role and can be made of different materials with different thicknesses. There is a large variety of structures but it is possible to identify three types of layers from their role (LCPC and SETRA 1994):

- the surface course: it is the superior layer of the structure, in direct contact with vehicle traffic and climate conditions. It must be waterproof to preserve the remaining of the structure. From the surface course depends the quality of usage of the road: it should be very flat and guarantee a good adherence with the vehicle tyres. Additionally, some surface courses have noise cancelling properties or important draining capacities. The surface layer is sometimes divided in two sub layers, the wearing course on top and the binder course. The materials used are usually bituminous mixtures or cement concrete.

- the base course: located under the surface course, its role is to improve the strength of the structure. It diffuses the loads created by traffic and climate from the surface layer to the lower layers in order to minimize the deformation of the ground. This layer can sometimes be divided in two or three sublayers that are made of bituminous mixtures, hydraulically bound materials or only aggregates. A subbase layer made of unbound granular material can sometimes be found under a base course.

- the subgrade layer: it is the transition layer between the natural ground, on which it is laid directly, and the upper road structure. It must ensure the circulation of construction engines and it has to protect the lower layer from frost. It is made of the natural ground by itself or treated with hydraulic binders to improve the stiffness of the layer.

At the interface between some layers, especially at the top of the structure and when there is a layer in a bound material, a tack coat is applied. It binds together the layers so that they act mechanically as one.

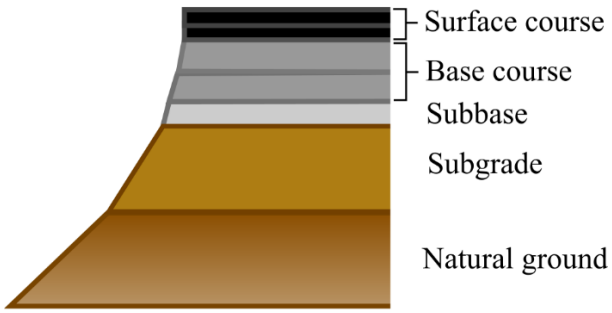

Figure 1.8 - Scheme of a road structure with typical layers

Depending on the projected traffic, on the climate conditions and on the type of natural ground, the layers will not be made of the same material or with the same thickness. A few examples of common structures used in France are described in the French design guide (LCPC and SETRA 1994) and presented in the following.

Flexible pavements are made of a surface layer in bituminous mixture (5 cm), a base course also in bituminous mixture (15 cm), a subbase layer in unbound granular material (20 cm) and the subgrade.

Thick bituminous pavements are used for heavy traffic conditions; they have a surface layer in bituminous material (5 cm) and a base layer entirely constituted of bituminous mixtures (from 15 to 40 cm) laid on the subgrade.

Mixed structures possess a surface layer in bituminous mixture (5 cm), a base course divided in two layers, one in bituminous mixture (15 cm) and one in hydraulically bound material (30 cm) on the subgrade.

Inverted structures have a surface layer in bituminous mixture (5 cm), a base course divided in three: bituminous mixture (15 cm) then unbound granular material (12 cm) and hydraulically bound material (35 cm) at the bottom placed on the subgrade.

In the USA, two types of structures are described in the design guide: the flexible pavements, that are close to the ones presented above with a surface layer in bituminous mixture, and the rigid pavements (NCHRP 2004).

Rigid pavements are made of a surface layer made of cement concrete (25 cm), a base course in bituminous mixture or cement concrete (15 cm) with or without a subbase in unbound granular materials (20 cm).

Bituminous mixtures and cement concrete are both adequate for road construction. The choice of flexible or rigid pavement depends on the designer preferences. In the USA, rigid pavements are very common when they are rare in France. It is possible to argue that the bituminous mixtures viscosity induces a slight increase in vehicle fuel consumption (Pouget *et al.* 2012) compared to cement concrete when used as a surface layer but they might have "self-healing" properties that are beneficial for fatigue resistance.

1.1.4. Loading and damage of road structures

The two main source of impairing of road structures are traffic and climate (Di Benedetto and Corté 2005).

Traffic induces loadings in the vertical direction related to the weight of the vehicles and loadings in the horizontal directions related to the acceleration and deceleration of the vehicles or to the direction changes in turns or roundabouts. The vertical loadings create flexion at the scale of the whole structure: in the upper part the materials are compressed and in the lower part tensile stresses appear. But if a layer is not bonded to the other ones, tensile stresses can be found at the bottom of the layer. The loading depends of the nature of the vehicle (weight, type of wheels) and of its speed. In the French design method, the standard axle representing a heavyweight double-wheel is modelled by a vertical pressure of 0.662 MPa applied on two discs 12.5 cm in diameter with their centres separated by 37.5 cm (LCPC and SETRA 1994). It does not include any horizontal components. The order of magnitude of strains in the structure are usually small (*in situ* measurements indicate that they are inferior to 10^{-4}) because of the stiffness of the layers' materials. Using finite element models, it is possible to compute the stress tensor components in the whole structure that cannot be found by measurement. When the loading is a simple wheel, represented by one of the two discs of the standard axle in the French design method, the results show a complex state of stress when the wheel is passing (Clec'h 2010) on a standard flexible pavement. Under the wheel and close to the surface, the structure undergoes compressive stresses. Under the wheel but deeper in the structure, shear components are also present and the compressive stresses gradually become tensile stresses. When moving away from the wheel, the shear components are more important.

Climate loadings are multiple. The rainwater flow can disorganize the structure of unbound materials. On bound materials like bituminous mixtures or cement concrete, water has almost no effect. The Sun and the oxygen present in the air can alter the properties of the materials bounded with hydrocarbon binders through the ageing process that makes the bitumen stiffer but also more susceptible to fracture. Temperature is the most important climatic factor to take into account. It changes the viscoelastic properties of the hydrocarbon binders in a dramatic fashion. When subjected to low temperatures, they even become fragile. Some road materials can dilate when temperature changes: it is the case for hydraulically bound materials and materials bound with hydrocarbon binders. When the deformation is impossible then stresses appear in the materials. Finally, low temperatures combined

with water lead to frost and thaw where the water present in the structure freezes, and thus expands, creating mechanical stresses in the structure.

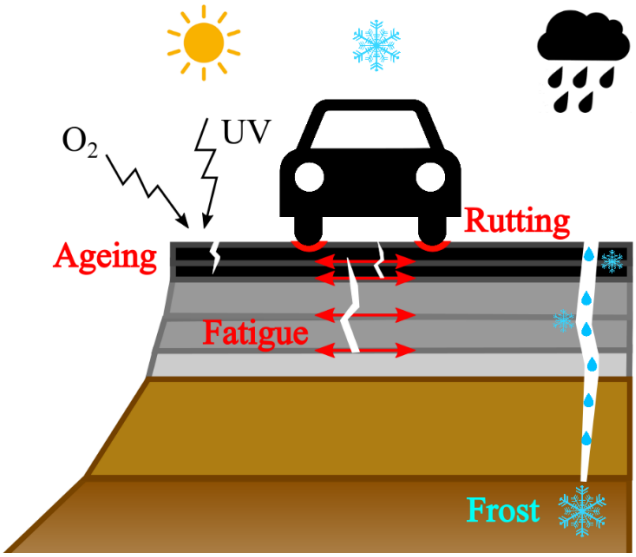

Figure 1.9 - Damage processes in a road subjected to traffic and climate loadings

All these loadings damage the structure following different processes (LCPC 1998) as illustrated in Figure 1.9.

Fatigue cracking is the result of the accumulation of a very important number of vehicle passages. Each passage alters slightly the materials and it is only after a long period that cracks appear (Figure 1.10). Bound materials are liable to break by fatigue. Cracks are devastating in a road structure; they can lead to the complete failure of the structure. They let the rainwater flow inside the structure, soak the lower materials and destabilize them, effects aggravated if water freezes. The presence of cracks at the surface is also the first step in potholes creation. Cracks often happen at the bottom of the layers, where they can be subjected to tensile stresses, and at the bottom of the structure if all the layers are perfectly bonded. Cracks born in the lower layers can propagate to the surface and be as dangerous as surface layer fractures. This is called the bottom-up cracking (or reflective cracking) in opposition to the top-down cracking when the crack is created at the surface of the road and propagate inside the structure. Fractures caused by fatigue are one of the main cause of road structure damage. Design methods ensure that strain levels are low enough to have a long lifetime.

Permanent deformations, leading to rutting, may appear after an important number of vehicle passages. There are two types of rutting: large radius rutting and small radius rutting (Figure 1.10). Large radius rutting is observed at the scale of a traffic lane; it is caused by the deformation of the soil under the structure. If the road structure is stiff enough then it can be avoided. Small radius rutting is visible in the tyre tread on surface layers made of bituminous mixture. They are caused by the complex and heavy loadings related to traffic and the viscous behaviour of bituminous materials. When temperatures are high, rutting is more liable to occur. A mix design with a small bitumen content, a low void ratio and an adequate granular distribution can prevent this kind of rutting.

Figure 1.10 - Crack on the surface of the road on the left, small radius rutting on the right

Some surface layers are very thin especially when they are made of bituminous mixture. If the bonding with the base course is not done properly then they undergo important loadings that can lead to a direct fracture of the layer after a few passages and thus with a different process than fatigue failure.

The aggregates of the surface layer bound materials can be ripped from their binder, leaving it alone against the traffic and climate conditions. In this situation, bituminous materials age quicker and become more subjected to fractures that can propagate inside the structure. Also, the aggregates get polished with time, reducing the adherence with the vehicle tyres.

1.1.5.Design of road structures

Each country defines their own method to design roads. They can be classified in two categories:

-empirical methods: based on previous experience, the designer chooses one type of structure and select the thicknesses of the different layers taking into account the climate conditions and the nature of traffic, generally with abacuses.

-rational methods: based on the knowledge of road materials behaviour and using mechanical calculations, it is possible to find how the structure behaves when it is subjected to a loading and validate the structure or not. The designer has to choose the type of structure based on experience but the thicknesses of the layers are chosen so that the structure is viable according to the model.

In addition to the design methods, national standards concerning the materials employed or the construction techniques are followed when building a road. The global tendency is to make the design methods more and more rational but today there are still significant differences as in the three examples described below in France, in the USA and in the United Kingdom.

The French design method is a rational method. First, a design lifetime is chosen, 20 or 30 years, and an equivalent number of heavy goods vehicles is determined to represent the traffic. A pre-design is selected by considering a previous and analogous situation. The strain and stresses in this structure are calculated with the Burmister method that assumes layers are elastic (Burmister 1945) usually using the Alizé software (developed by the *Laboratoire Central des Ponts et Chaussées (LCPC)*, now named *Ifsttar)*. The loading represents the static action of a standard heavyweight axle as a vertical pressure. The materials modulus and Poisson's ratio are found from laboratory tests. The classification of the subgrade is an important input parameter; its strength impacts the whole structure. The layers can be considered fully bonded or fully unbonded depending on the type of materials of the layers, for instance layers in bituminous mixtures are considered fully bonded together. An intermediate case exists; it is the so called half-bonded condition which corresponds to an average of the results of the calculations for the whole structure when the layers are bonded and when they are not. The strains obtained in the different layers are compared to the maximum admissible strain of each material to endure the fatigue due to the number of passages previously chosen. If the structure fails, then new thicknesses are chosen

and calculations are done again. If it adequately reacts to the mechanical loading, the structure resistance to frost and thaw still has to be verified. Based on the type and thicknesses of layers and considering typical winter temperatures, the frost depth in the ground is calculated and it must not induce too much frost in the natural ground. If the design fails to do so, then new thicknesses must be chosen. If it succeeds, then the structural design is validated.

The American design method had been empirical until 2002 and was based on full-size experiments on trial sections performed in the 1950's by the American Association of State Highway Officials (AASHO). It can be now qualified as a semi-empirical method since it includes mechanical calculations based on the multilayer elastic theory of Burmister, with the assumption that all layers are bonded together. The initial design must be chosen by the designer and verified for permanent deformation (rutting), fatigue cracking, thermal cracking (NCHRP 2004). A precisely timed estimation of traffic and climate is required. The calculations are iterative and allow predicting year by year how the structure evolves. The designer makes sure the structure is adequate for its intended service by choosing the right materials and layer thicknesses with a try and error methodology.

In the United Kingdom, the design method is purely empirical. The designer choses a design lifetime and a traffic prevision. The structure can be a flexible pavement or a rigid pavement as in the American method. Based on the subgrade stiffness, abacuses are used to choose the thicknesses of the layers (The Highways Agency *et al.* 2006). Frost and thaw resistance is also verified.

1.1.6. Importance of interfaces in road structures

The interface between two pavement layers is the contact surface of the two layers. This simple definition is adequate when thinking at the structure's scale. But it makes less sense when looking closely at this area. As explained before, the layers of a road structure are made of different materials that are usually composed of aggregates (bonded or not). The aggregates of the different layers can be tangled up after compaction but the layers do not perfectly assemble. So, what seemed to be a continuous contact surface looks more like many contact areas surrounded by voids.

It is more complicated when one or two of the layers are made of bituminous materials. Bituminous mixtures are used in the upper layers of the road, often in the surface course, close to the external loadings. In order to protect the thin and fragile surface layers, a tack coat is usually applied between the surface course and the base course in order to bond them together so that they act as one from a mechanical point of view. This tack coat is made with bituminous emulsions in most cases but aggregates precoated with bitumen or geogrids are added to prevent the reflective cracking. The tack coat adheres to the lower layer and when the upper layer in bituminous mixture is laid at high temperature, the bitumen of the tack coat and the bitumens of the layers can be partially mixed. The aggregates of both layers are also entangled at the interface. This explains why, when thinking about the interface at a scale smaller the structure's scale, some authors would rather define an interphase between pavement layers, constituted of the tack coat and thin thicknesses of the adjacent layers (Ktari 2016).

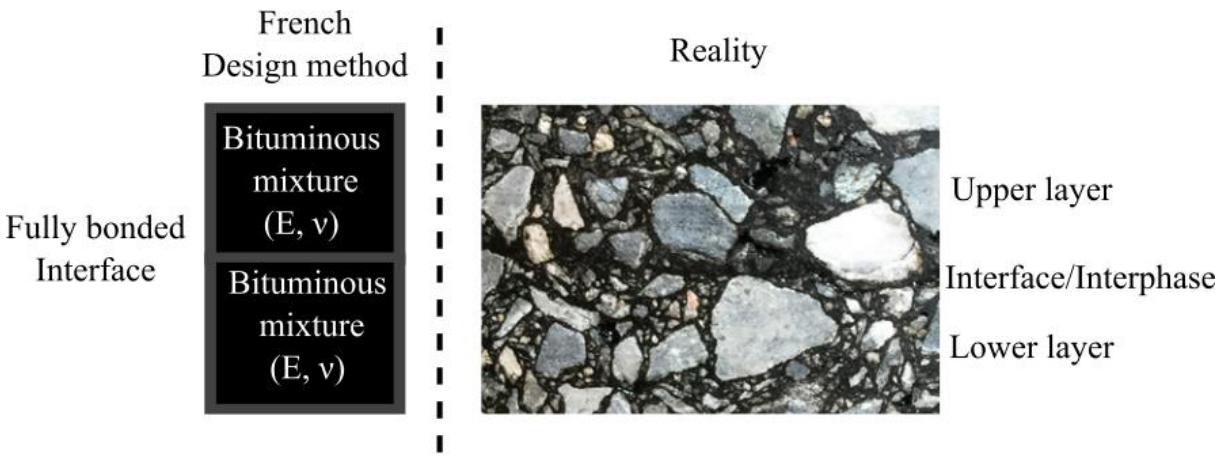

Figure 1.11 - Interface between bituminous mixtures layers: model in the French design method on the left, picture of a sawn bi-layered road material on the right

In the rational design methods presented in the previous section, the layers in bituminous mixtures are considered perfectly bonded at their interface for the mechanical calculations (Figure 1.11). This means that there is a continuity of the displacements at the interface, *i.e.* that there is no relative displacement between the layers. This is the most favourable case for the upper layer because it reduces the tensile strain in its lower part. Using the software Alizé, it is possible to evaluate the impact of the debonding of elastic layers on the strain distribution in a standard French road structure (Diakhaté 2007). The results show that the bonding of the layers guarantee that the surface course is not subjected to tensile strain (Figure 1.12). The bonding also reduces the strain at the bottom of each layer, leading to an increased lifetime. These significant results show that a rigorous knowledge of the interface behaviour is necessary for a sensible road design.

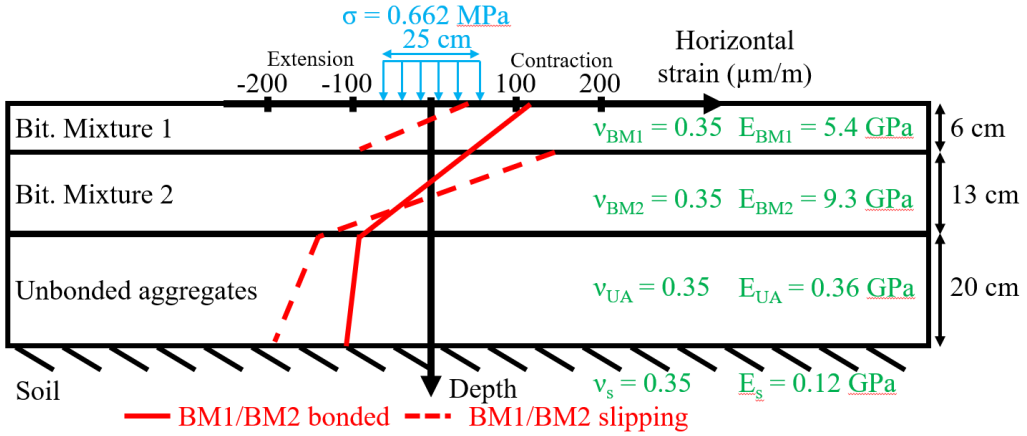

Figure 1.12 - Effect of the interface condition between bituminous mixtures layers on horizontal strain distribution in a road structure (Diakhaté 2007)

Standards usually set the frame for the application of tack coats so that the assumption of fully bonded layers makes sense. They are different in every country, in every state in the USA. In France, the application conditions are described in the norm NF P 98-150-1. After a careful cleaning of the surface a bitumen emulsion must be applied with a minimal residual dosage depending of the type of mixture used as surface layer, varying from 250 g/m² to 350 g/m². The minimal dosages are raised if the surface is rough, drilled or if there is a geogrid. Construction trucks must not pass on the tack coat until after its breaking to prevent the removal of material. Yet, premature degradations (happening prior to the expiration of the design lifetime) linked with the debonding of interfaces were reported (Blomberg 2014). In 1986, in France, it seemed that more than 5 % of the road network was affected, which

represented 1,000 km of roads (Meunier 1986). It is really difficult to get such an estimation but even 5 % of the network represent a significant patrimonial value at the scale of a country.

The way interfaces are treated in the rational design methods must then evolve. For the mechanical calculations, interfaces should be modelled more precisely. A better understanding of their behaviour is necessary to find the intermediate case between fully bonded and fully unbonded that is the closest to the reality and that will provide the best assessment of a structure lifetime. An intermediate case for the calculation of strain in elastic structures is found when allowing relative displacements at the interface proportional to the stresses applied. In the simple case where only shear displacements are considered in a plane problem, the proportionality coefficient between shear stress τ at the interface (MPa) and shear relative displacement between the layers Δu (mm) is called the interface stiffness and is noted K (MPa/mm) (Equation 1.1).

$$\tau = K.\Delta u \tag{1.1}$$

The higher the interface stiffness is, the lower are the relative displacements for the same stresses. The limit case of fully bonded layers correspond to K being nil, and the unbonded case correspond to very great values of K. Uzan *et al.* implemented numerically such an interface condition and showed a continuous evolution of the strain distribution in the structure between the two cases (Uzan *et al.* 1978). An important part of the mechanical testing of interface aims at finding the interface stiffness. Introducing this interface stiffness in the mechanical calculations in the design methods could be a first step in their rationalization. However, this approach assumes that interfaces have an elastic behaviour and that their thickness is nil when tack coats are made of viscoelastic bituminous materials and have a thickness.

The fatigue rupture of interfaces could also be taken into account when designing pavement. First the interface would be considered healthy (not necessarily fully bonded) and after a certain number of vehicle passages corresponding to the fatigue strength of the interface, the interface would be considered deteriorated and another calculation should be made to predict the structure behaviour until the complete failure. From experimental results for the interface fatigue, Petit *et al.* showed that interface failure is likely to happen before the fatigue of the materials in the layers when an horizontal loading representing the acceleration of a vehicle is considered, confirming the interest of the aforementioned approach (Petit *et al.* 2009).

Today's design methods do not take properly interfaces into account. Because of this, in some cases, they fail to predict roads lifetime efficiently. Different paths towards their improvement are possible: adding a horizontal loading representing the vehicles acceleration, implementing a more realistic behaviour of interfaces in the mechanical calculations or considering the fatigue failure of interfaces. These improvements call for a better understanding of the interfaces behaviour. The next section will present the experimental attempts to characterize the interfaces.

1.2. Mechanical testing of interfaces between pavement layers

1.2.1. In situ tests

One of the main aspect of interfaces testing is the monitoring of the state of bonding between the layers in actual road structures. This is one of the indicators of the overall health of the structure. It makes it possible to know if maintenance operations are required immediately, or not, which is a major issue in today's road industry. While waiting for the development of fully instrumented roads, several experimental protocol performed *in situ* can give access to the state of bonding at the interfaces.

1.2.1.1. Coring

The visual observation of core samples can give an overview of the state of the materials in the road structure but also of the state of the interfaces. The coring must be performed perpendicularly to the surface and throughout the structure (Figure 1.13). Core samples are removed from the core drilling machine or from the road using a clamp.

Figure 1.13 - Core drilling machine in use

Following the French valuation rule (LCPC 1996b), interface quality depends on whether the core sample is in two parts after the drilling. If it is not, the bond is considered good or quite good if the sample can be separated manually afterwards. If it is in two parts and that the surfaces of the layers are smooth, the interface is unbonded, and not because of the drilling. This simple test gives a simple answer to the question of the bond at the interface, fully bonded or fully unbonded as in the design method.

1.2.1.2. Tensile adhesive test and torque bond test

The tensile adhesive test and the torque bond test are performed directly at the road surface and allow evaluating the strength of the interface the closest to the surface of the structure. A coring is realized in the upper layer of the road up to a few centimetres in the layer underneath. Then a cap is glued to the surface of the inner core, which is not extracted. Specific devices can then apply either tension or a torque (Figure 1.14) until the failure of the interface. The axial force or the torque needed to break the interface characterize the interface bond strength. The torque is applied manually at a constant rate until failure. The torque bond test is a standard in the United Kingdom (clause 951 in (Highways England 2019)).

Figure 1.14 - Torque bond test device

The results of such destructive tests cannot be used directly in the design methods. Indeed, they do not give information on the interface mechanical behaviour when a loading corresponding to a vehicle is applied to the structure. But they can compare the strength of different interfaces. Unfortunately, tensile tests and torque tests suffer of a high variability (Godard *et al.* 2015).

1.2.1.3. Ovalization test

The ovalization test consists in coring the road and placing sensors at different depths inside the obtained hole (Figure 1.15). A moving load is then applied next to the sensors and the diameter variations are measured. Strain is then obtained from the diameter variations (LCPC 1995). Strain at the top and at the bottom of each layer is extrapolated from the experimental results and if there are discrepancies at the level of an interface the bonding is considered imperfect. The value of the difference between the strain at the level of the interface is not exploited, the conclusion of this test is that the interface is bonded or unbonded. This test is a standard in France (NF P-98-203-1).

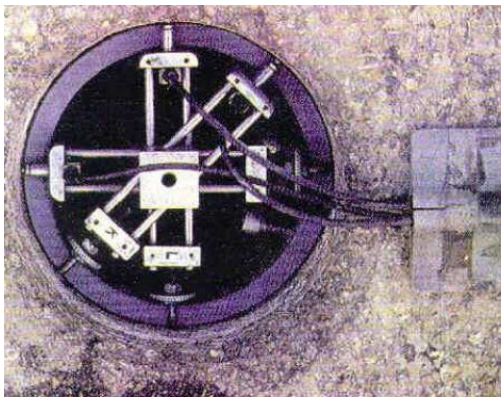

Figure 1.15 - Ovalization test sensors in the cored road structure

1.2.1.4. Radar monitoring of the road structure

The radar method consists in sending electromagnetic pulses in the road and recording the reflected signal. Electromagnetic wave propagates in the road materials but are reflected at the interface between two different materials. The signal analysis allows obtaining the type of material and the thickness of each layer. The interpretation tells if the layers are bonded or not (LCPC 1996a). The advantage of this method is that the traffic does not need to be interrupted to perform the tests, the results are obtained continuously on long distances.

Figure 1.16 - Radar monitoring apparatus on a vehicle

1.2.1.5. Heavy Weight Deflectometer (HWD)

The principle of the HWD (Figure 1.17) is to drop a heavy weight on the surface of the road. The pressure wave created by the impact propagates in the structure and deform the road surface. Geophones are set on the surface at known distances from the impact: they measure accelerations but the displacements are deduced from them. The deflection basin is obtained by plotting the maximal displacement recorded by each geophone versus the distance to the impact. A back analysis computes the mechanical properties of the materials in the layers (STAC 2014).

Figure 1.17 - Heavy Weight Deflectometer on a runway (STAC 2014)

Using the maximum deflection measured for all geophones, it is possible to tell apart a sound interface from an unbonded interface (Sadoun *et al.* 2016). The defect at the interface induces higher deflections. It is possible to locate the areas with unbonded interface but no analysis exists to have a more precise assessment of the interface behaviour.

1.2.2. Laboratory tests

If *in situ* tests are useful for efficient and quick assessments of interface bonding in structures in use, the information obtained on the interface behaviour is limited. It is indeed impossible to control the testing conditions (temperature, mechanical loading, …) without a specific equipment that is usually difficult to move and thus to use on actual roads. The testing of interfaces in laboratory is a major research topic since the beginning of the 1970's. After a brief numerical evaluation of the state of stress at the level of an interface between pavements layers, the different approaches developed to understand the interfaces behaviour will be presented. These laboratory tests can be used to study laboratory made materials but also materials extracted from pavements in use or from experimental sections.

1.2.2.1. Stress state at the interface between pavement layers

Measuring the mechanical response of an interface subjected to moving load inside a pavement in use is a difficult task. Strain in the layers can be monitored using various instruments such as strain gauges, optical fibres (Gaborit *et al.* 2014) or the ovalization test presented above. The interface response (strain gap) can only be obtained indirectly using extrapolations. The stresses can be measured using pressure cells (Al-Qadi *et al.* 2004) but only in one direction and it is not possible to find the shear stresses at the interface for instance.

This explains why numerical methods are used to evaluate the state of stresses at the interface. Of course, when modelling the structure, the interface is considered as fully bonded or fully unbonded since it is the easiest way to make the calculations. It is nothing but a simplistic assumption that gives a first approximation of the stresses at the interface. Stresses are complex to represent since they are different in every point of the pavement and that the stress tensor has got six independent components. Moreover, the results depend strongly of the model: because of the choice of the loading applied to represent a vehicle (amplitude, directions, application surface, static or dynamic) or because of the type of layers of the structure (thicknesses, material, mechanical behaviour).

The results of a simple numerical simulation using the Burmister model with the software Alizé is presented here. The static loading represents a standard French double-wheel axle: a vertical pressure of 0.662 MPa is applied on two discs with a diameter of 25 cm and their centre separated by 37.5 cm. This represents a total load of 65 kN. A flexible pavement structure commonly found in France was chosen for the simulation. The materials and the problem geometry are presented in Figure 1.18. The layers are elastic and fully bonded at their interfaces. The sign convention for stress is the soil mechanics convention with compressive stresses being negative.

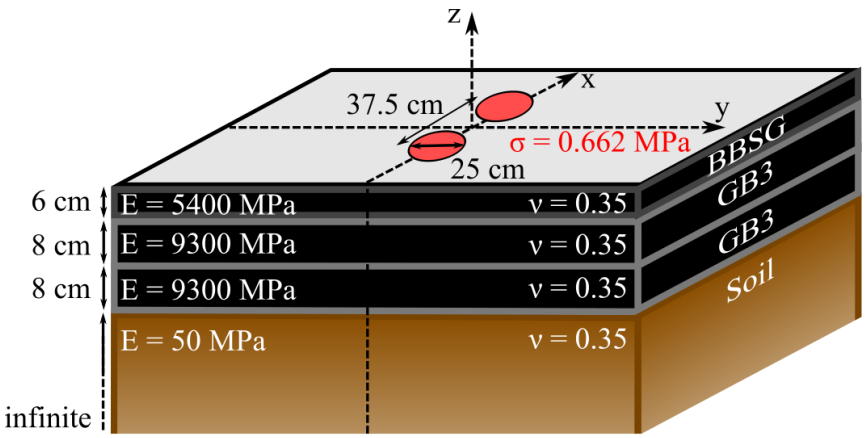

Figure 1.18 - Common flexible pavement structure model with standard double-wheel axle loading

In the simulation, y is the longitudinal axis corresponding to the traffic direction, x is the transversal axis and z the vertical axis. The results are plotted at the depth of 6 cm corresponding to the position of the first interface (Figure 1.19).

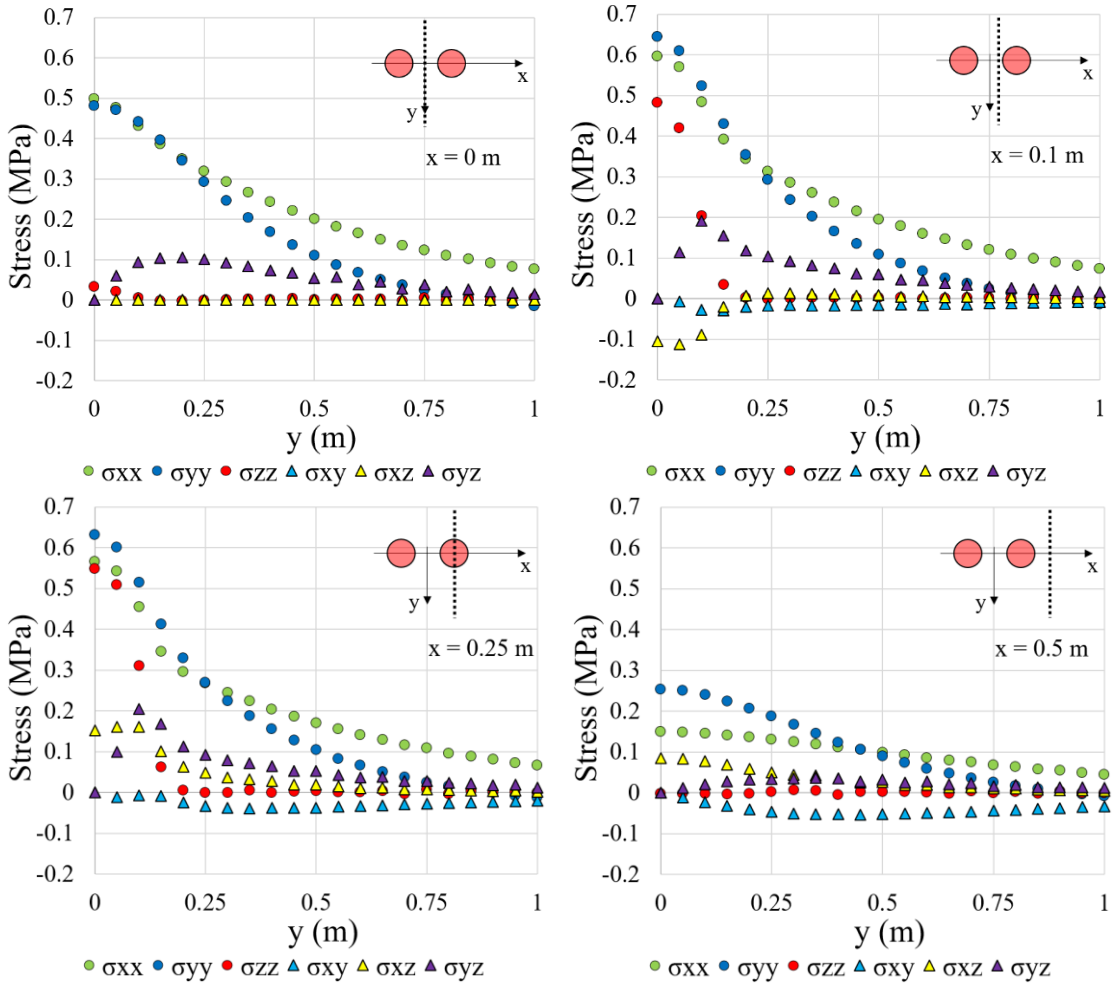

Figure 1.19 - Stress tensor components at the level of the interface between surface course and base course (z = 0.06 m) in the flexible pavement model at a distance x from the longitudinal axis: top left corner x = 0 m; top right corner x = 0.1 m; bottom left corner x = 0.25 m; bottom right corner x = 0.5 m

The relative importance of the stress tensor components depends on the position in the pavement. For instance, when comparing the vertical stress σ_{zz} and the shear stress σ_{yz}, the vertical stress is almost nil between the two wheels where the shear stress can be as high as 0.1 MPa but under the centre of a wheel the vertical stress is maximum, close to 0.6 MPa where the shear stress is nil. There are also points where the vertical stress and the shear stress have the same value, for instance under the extremity of a wheel (Figure 1.19, bottom left corner). When considering more stress tensor components, the stress state becomes even more difficult to describe. A more advanced numerical study conducted by D'Andrea and Tozzo shows well the complexity of the stress state at the interfaces depending of the position in the pavement (D'Andrea and Tozzo 2016b). The mechanical testing of interfaces has thus always been performed by simplifying the stress state at the interface, testing only one or two stress tensor components at a time.

1.2.2.2. Shear tests

The bond failure observed at the interface occurs more often in areas subjected to high horizontal loadings due to the acceleration, to the braking or to the turning of vehicles. Based on this observation an important part of the mechanical testing focused on the behaviour of interfaces subjected to shear stresses.

Guillotine test

The "guillotine test" is among the first tests specifically designed for the study of interfaces. It was developed by Leutner at the end of the 1970's (Leutner 1979). A bi-layered cylindrical sample is fixed horizontally on its lower part, under the interface. A vertical force is then applied on the upper part of the sample until the interface bond fails (Figure 1.20). In its original design, it is not possible to apply a normal stress to the interface nor to perform cyclic tests. The interface thickness in the test is defined by the gap between the part of the device that clamps the lower layer and the part of the device that applies the axial force on the upper layer. It is 1 mm in the original design. This device has been replicated in different laboratories sometimes with modifications (Raab and Partl 2004; Sholar *et al.* 2004; Miró Recasens *et al.* 2005; Collop *et al.* 2009).

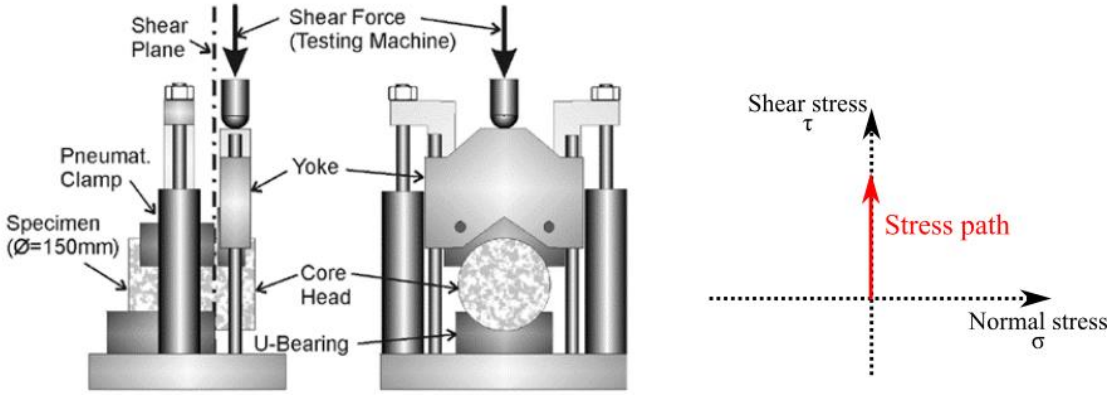

Figure 1.20 - Guillotine test: the LPDS (Layer-Parallel Direct Shear) test device (Raab and Partl 2004) with stress path on the right

The most common modification is the possibility of adding normal stress at the interface during the shear test. It is usually constant (Romanoschi 1999; West *et al.* 2005; D'Andrea *et al.* 2013) but Zofka *et al.* developed a guillotine test with a constant normal stiffness condition where the normal stress is proportional to the normal displacements at the interface during the shear test (Zofka *et al.* 2015). The gap width and the test speed can also be modified (Raab *et al.* 2009). Some tests can apply dynamic loadings (Hristov 2018b). It is interesting to notice that this test is inhomogeneous since the shear stress at the edge of the interface is nil, and this is the case of all shear tests where the interface is in contact with a free edge.

Shear box test

The shear box test stems from the soil mechanics testing device called Casagrande box. A bi-layered sample, usually prismatic, is placed into a box in two parts (Figure 1.21) (Hughes 1986; Canestrari *et al.* 2005). The lower part moves under the action of an actuator while the upper part is fixed. The shear force endured by the upper part is measured along with the vertical displacement. A constant load can be applied on the upper part of the sample during the test. The interface thickness is defined by the gap between the two parts of the device.

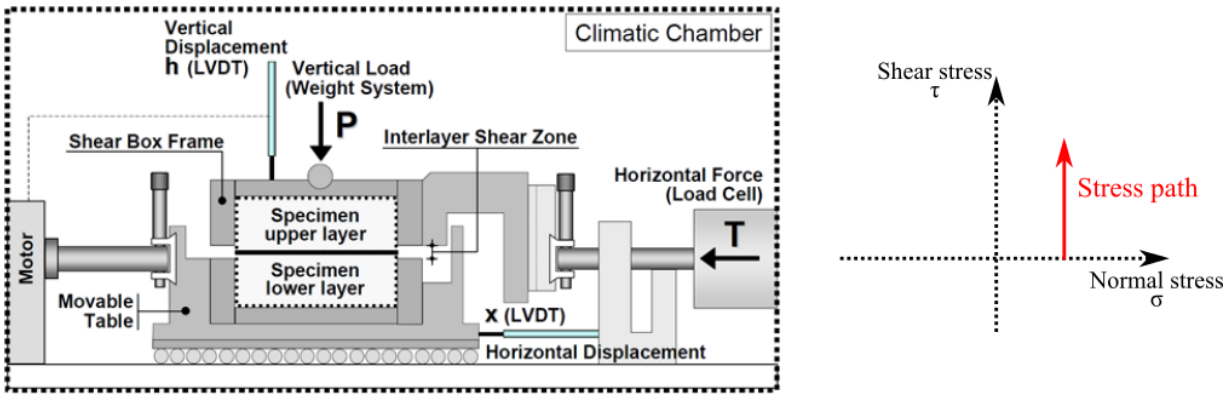

Figure 1.21 - Shear box test: the ASTRA test device (Canestrari *et al.* 2005) with stress path on the right

Functioning on a similar principle than shear box tests, the Superpave Shear Tester (SST) developed at the Louisiana State University (USA) allows controlling independently the vertical and horizontal forces applied to the interface using two actuators (Mohammad *et al.* 2002).

Inclined Shear test

Applying a normal load to the interface while applying a shear force using only one axial actuator is possible if there is an angle α between the interface normal direction and the force direction. The ratio between shear and normal loads is $tan\ \alpha$ under the condition that the horizontal displacements are allowed between top and bottom of the sample, *i.e.* at the interface. This condition can be met by placing the whole device on a ball bearing plate. It is the principle of inclined shear tests (Figure 1.22). The samples are made of two layers and can be cylindrical or prismatic. The gap between the device parts defines once again the interface thickness and the zone where shear is applied. The angle α is sometimes adjustable (Romanoschi and Metcalf 2001; Tozzo *et al.* 2016).

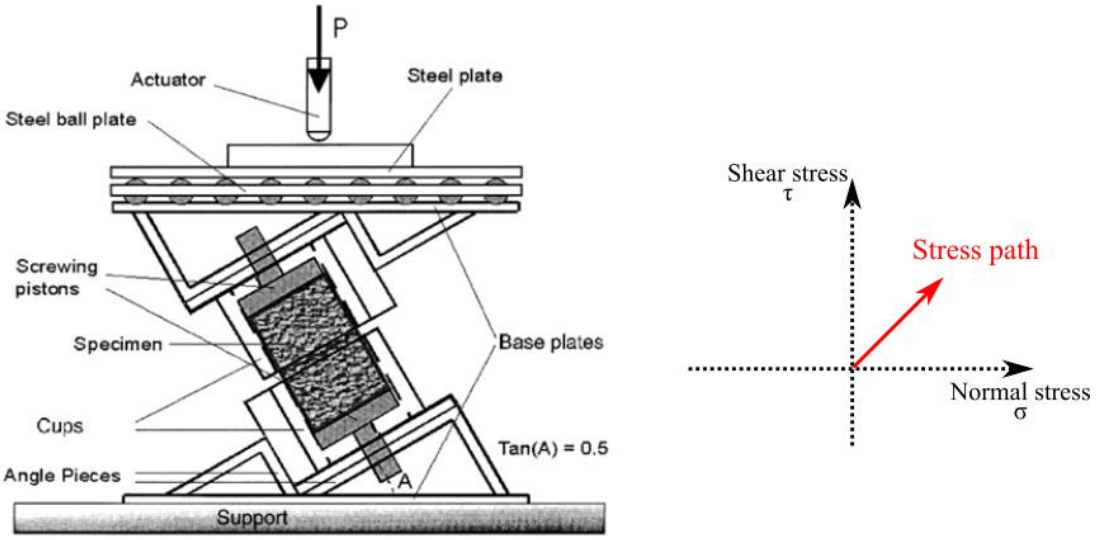

Figure 1.22 - Inclined shear test: the shear fatigue test (Romanoschi and Metcalf 2001) with stress path on the right

Double Shear Test

One of the disadvantage of the guillotine test is the flexion of the sample. The Double Shear Test (DST) developed at the University of Limoges (France) can apply shear to two interfaces simultaneously and without flexion (Figure 1.23) (Diakhaté 2007). The samples have to be symmetrical and are made by gluing two similar bi-layered samples at their head. The obtained sample has got two interfaces

between the same materials. The shear load is imposed to the middle part of the sample. Another DST has been developed at the North Carolina State University (USA) (Safavizadeh and Kim 2014). This test configuration makes it possible to use imaging techniques to study the deformation or the cracking at the interface.

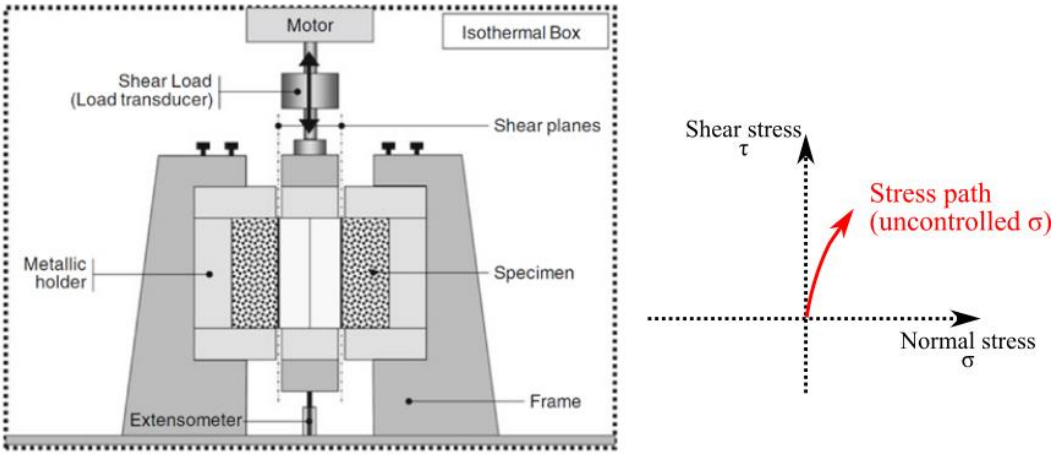

Figure 1.23 - Double Shear Test, developed at the University of Limoges (schematic from Canestrari et al. 2013) with stress path on the right

Double Notch Shear test

Using only one axial actuator, it is possible to design a sample where shear stress is found at the interface. In the Double Notch Shear test, a bi-layered sample is placed in a vertical position so that the axial force direction is in the interface plane (Ktari 2016). Two notches are cut, one in the upper layer and one in the lower layer (Figure 1.24). When the upper part is pulled up, the interface between the notches is subjected to shear.

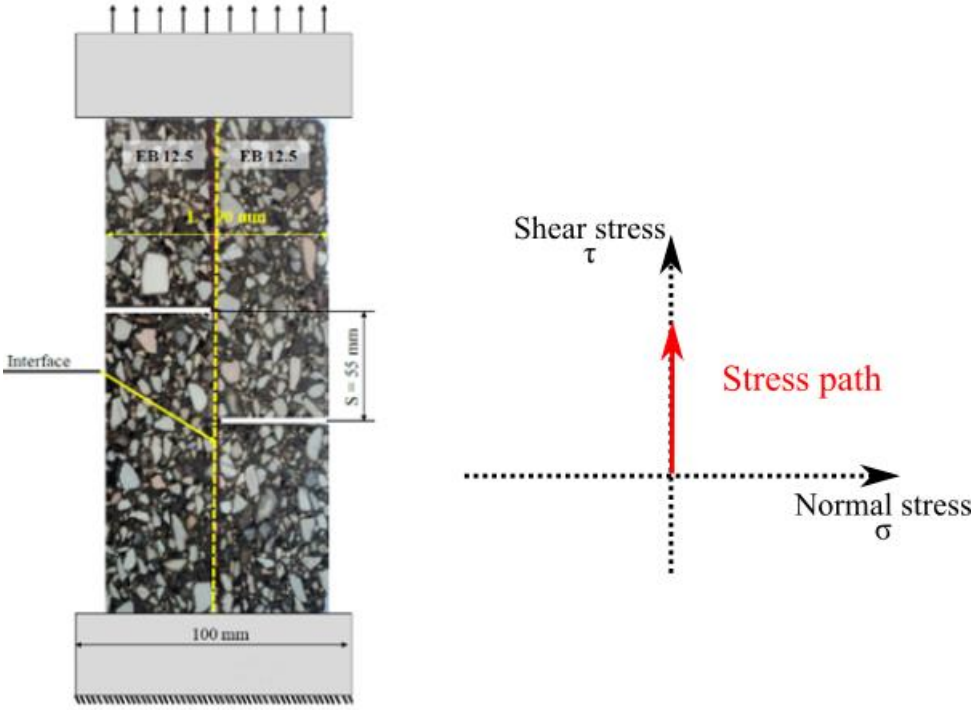

Figure 1.24 - Double Notch Shear test (adapted from (Ktari 2016)) with stress path on the right

1.2.2.3. Torsion tests

Based on the same principle as the *in situ* test, the torsion test on cylindrical samples made in laboratory is mainly used to study the shear strength of interfaces. The lower part is fixed while a torque is applied to the upper part of the sample. The torque can be applied manually (Destrée *et al.* 2012) but adaptations were designed to perform automatically a constant torque rate (Diakhaté 2007; Collop *et al.* 2011). The main issue with this test is its repeatability, even when the torque is applied automatically (Godard *et al.* 2015). Moreover, the shear stress field is heterogeneous since the shear stress is nil in the centre of the sample and maximal at the border.

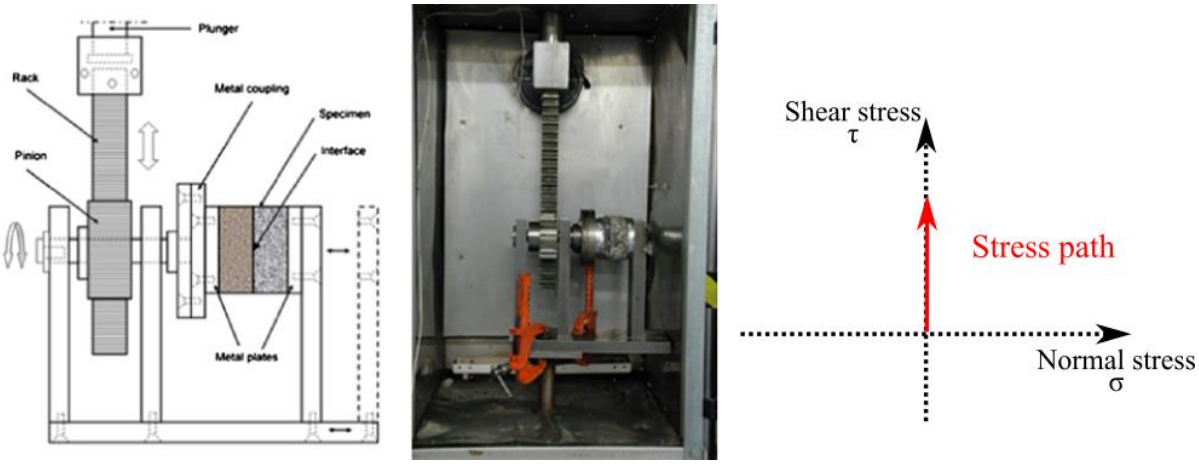

Figure 1.25 - Automatic torque test: schematic diagram and picture (Collop *et al.* 2011) with stress path on the right

1.2.2.4. Flexural tests

Flexural tests reproduce the flexion of the layers observed in a road structure when it is subjected to a vertical load. They were first developed to test the cracking resistance of bituminous mixtures. The samples are beams placed on supports and vertically loaded. Tensile stresses appear at the bottom of the beam and the stresses at the interface are quite similar to those in a real pavement presented in section 1.2.2.1. Different types of flexural tests exist. In the three-point bending test, the vertical loading is applied at the centre of the beam between two supports. This test has been used to evaluate the fracture process of interfaces by applying a monotonic vertical load until failure (Molenaar *et al.* 1986) and the crack retarding effect of a geogrid at the interface (Lee 2008; Pasquini *et al.* 2013; Canestrari *et al.* 2015). For the four-point bending test, the vertical load is divided in two and applied symmetrically (Figure 1.26). The four-point bending test presents the advantage of applying a pure flexion in the middle of the beam. It has been used to study the geogrids at the interface (Ferrotti *et al.* 2012; Canestrari et al. 2015; Zofka *et al.* 2017) or the effect of water on the bonding of interfaces between cement concrete layers and bituminous layers (Hun 2012). The Digital Image Correlation (DIC) can be used to observe the crack propagation (Safavizadeh and Kim 2014).

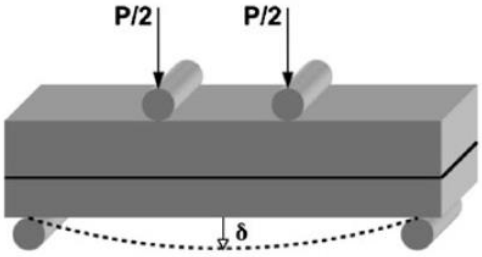

Figure 1.26 - A flexural test: the four-point bending test (Canestrari *et al.* 2015)

There is also a five-point bending test where the vertical loading is divided in two as in the four-point bending test but where there are now three supports with the beam embedded in the middle support. This test has been used to study the deck covering of bridges and the interactions between the bituminous mixture and the steel deck (Pouget 2011).

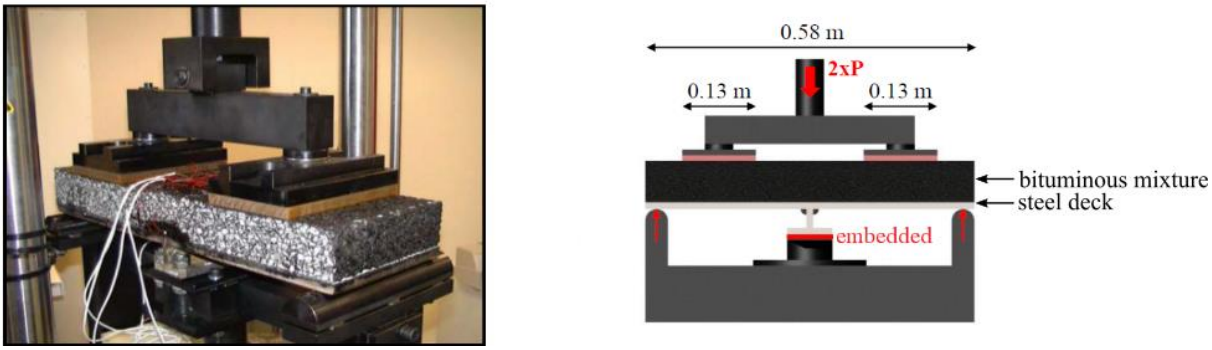

Figure 1.27 - Five-point bending test: on the left, a picture and on the right the descriptive schematic (adapted from (Pouget 2011))

1.2.2.5. Tensile tests

Interfaces are sometimes subjected to tensile stresses that tend to open the crack as presented in Figure 1.28. This type of loading is not necessarily the most degrading for the interfaces since it is normally small in amplitude compared to shear stresses. However, it could be predominant in the disbonding of thin wearing courses. But even if in some cases it is not the most representative damage mode, traction tests can give useful indications on the bonding strength at the interface.

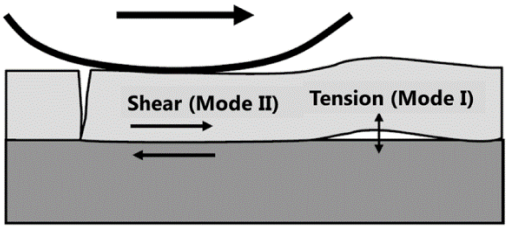

Figure 1.28 - Pavement interface debonding modes (C. Petit *et al.* 2018)

The principle of tensile tests in laboratory is the same that for *in situ* tests: the lower part of a bi-layered sample is fixed while the upper part is pulled off (Figure 1.29) (Destrée *et al.* 2012). The head of the sample is glued to a pulling mechanism. The sample can be prismatic or cylindrical. Digital Image Correlation can be used to study the displacement near the interface (Ktari *et al.* 2016).

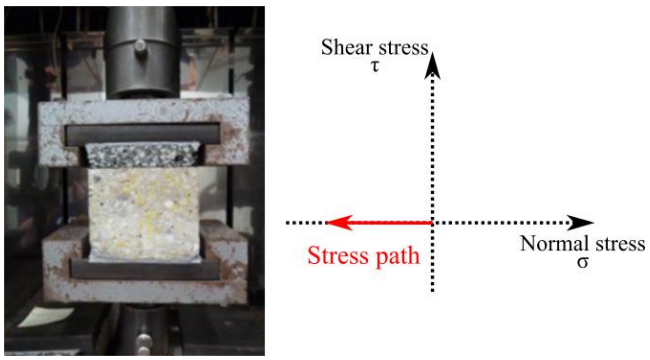

Figure 1.29 - Tensile test (Destrée *et al.* 2012) with stress path on the right

1.2.2.6. Tension-compression tests

Tension-compression tests are often used to characterize the viscoelastic behaviour of bituminous mixtures. A sample, usually cylindrical, is glued to aluminium caps and installed on a hydraulic press. For the interface testing, the setup is the same with a bi-layered sample but the instrumentation has to be different. Freire *et al.* used two sets of extensometers of different lengths placed across the interface to isolate the displacement at the interface from the displacement due to the deformation of the bituminous mixtures, identical in the upper and lower layers (Figure 1.30) (Freire *et al.* 2018). Cyclic testing is performed to study the behaviour of the interface.

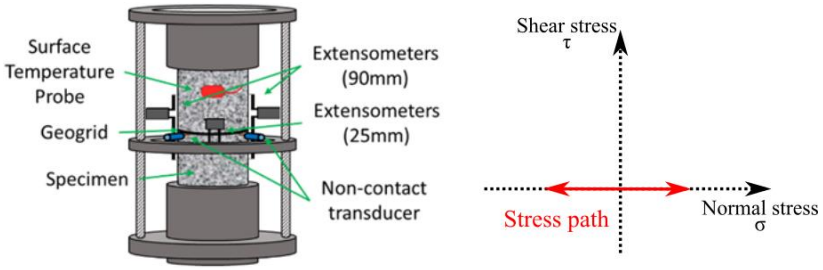

Figure 1.30 - Tension-compression test on a bi-layered sample with interface in the middle (Freire *et al.* 2018) with stress path on the right

1.2.2.7. Wedge splitting tests

First introduced for the study of concrete fracture (Linsbauer and Tschegg 1986; Brühwiler and Wittmann 1990), the wedge splitting test consists in cracking a sample using a wedge. A notch is cut in the head of the sample where the wedge is introduced. Then a vertical load is applied and partly converted in horizontal forces by the wedge, creating tensile stresses at the crack tip, in addition to the stress created by the remaining vertical loading. This test has also been used to test the interfaces between pavement layers with the notch placed at the interface (Figure 1.31) (Tschegg *et al.* 1995).

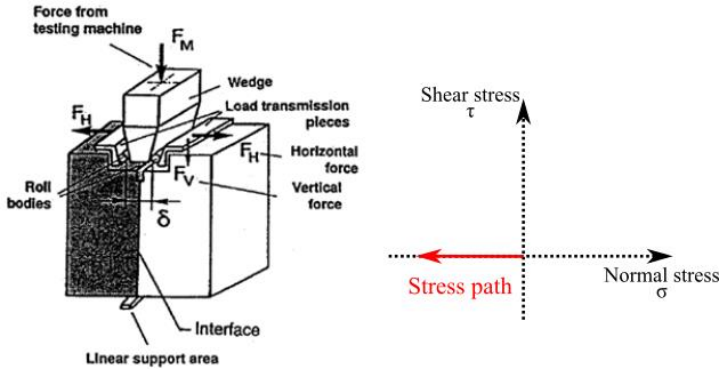

Figure 1.31 - Wedge splitting test (Tschegg *et al.* 1995) with stress path on the right

1.3. Important factors for interface behaviour

The mechanical testing of the interfaces has identified some of the factors impacting the interface behaviour (in the small strain domain, for fatigue failure, for monotonic failure tests and other types behaviours). The most important ones are explained hereafter for interfaces between layers in bituminous mixtures.

1.3.1. Temperature and loading speed

Bituminous materials present a thermo-viscoelastic behaviour meaning that their mechanical response depends on the temperature and on the loading speed. When studying interfaces between bituminous mixtures, these two parameters should be carefully taken into account, particularly when a tack coat made of bituminous materials is applied between the layers. It happens that the dependency in these two parameters is sometimes related. A majority of bituminous mixtures respects the Time-Temperature Superposition Principle (TTSP) that states that the behaviour is the same when the material is at low temperatures than when it is loaded quickly, and inversely that the behaviour is the same when the material is at high temperatures than when it is loaded slowly. It is well-known that the bituminous materials are more rigid when their temperature is low or when a load is applied quickly.

These thermo-viscoelastic properties are found again in the interface behaviour. Temperature effects on interface behaviour have been broadly studied. Concerning the monotonic failure tests, the shear resistance of interfaces (which is the maximum shear stress the interface can endure) increases when temperature diminishes (Mohammad *et al.* 2002; Canestrari and Santagata 2005; Bae *et al.* 2010). The shear stiffness, which is the ratio between shear stress and shear displacement at the interface, also increases when temperatures are low (Canestrari and Santagata 2005). For cyclic tests, the shear stiffness is defined as the ratio between the amplitude of shear stress and the amplitude of shear displacement. The cyclic shear stiffness is higher when the temperatures are low (Raab et al. 2017; Hristov 2018a). It seems that the fatigue performance of interfaces is higher at low temperatures (Collop *et al.* 2011; Isailović *et al.* 2017) meaning that the number of cycles before failure is higher.

Concerning the loading speed, inversely to temperature, it is when the loading speed is the highest than the shear resistance is maximal (Canestrari *et al.* 2005; 2013). The shear stiffness for cyclic tests also proves to be higher when the test frequency increases (Hristov 2018a) and the same observation is possible for the tension-compression cyclic tests (Freire *et al.* 2018). The influence of frequency on the fatigue resistance of interfaces has not been specifically studied.

The TTSP has been verified for the interface shear strength (Cho and Kim 2016; Graziani *et al.* 2017) and for the interface shear stiffness in cyclic tests (Cho and Kim 2016; Hristov 2018a).

1.3.2. Type of tack coat

The tack coat is the major constituent of the interface when it is present. It is of course possible not to apply tack coats between the pavement layers when building a road structure. But in this case, the interface bond is weakened. This has been observed experimentally for the resistance to shear monotonic failure (Canestrari and Santagata 2005; Collop *et al.* 2011; D'Andrea *et al.* 2013) and for the shear fatigue resistance (Diakhaté *et al.* 2011).

Tack coats are usually made of bituminous emulsions. The behaviour of an interface with a tack coat mainly depends on the dosage of residual binder at the interface and on the type of binder used.

For given bituminous mixtures layers and temperature, there is an optimum dosage in residual tack coat to obtain the best shear strength. The optimum value can be very different depending of the bituminous mixtures in the layers: it varies from 250 g/m^2 to 400 g/m^2 in (Raposeiras *et al.* 2012). If the dosage is too low, there is not enough tack coat to bond the two layers together. This effect is more visible at low temperatures. But if there is too much tack coat, a slippage plane can be created in the tack coat and prevent the interlocking of the aggregates from both layers, thus weakening the interface, especially at high temperatures. Generally, the influence of tack coat is less visible at high temperatures compared to the influence of the type of bituminous mixtures (Mohammad *et al.* 2002). Regrettably, few researches focused on the influence of the tack coat dosage on shear fatigue resistance or on the behaviour of interfaces in the small strain domain. The mechanisms implicated might be very different than the ones controlling the interface failure during monotonic tests. A larger influence of the tack coat bitumen compared to the interlocking effect can be expected.

Concerning the type of binder used for the tack coat, it is possible to find a correlation between the viscosity of the bitumen and the interface behaviour. Stiffer bitumen lead to higher shear strength

(Mohammad *et al.* 2002; Mohammad *et al.* 2012) and higher fatigue resistance (Diakhaté 2007). So it could be expected that tack coat made with bitumen modified with polymers, stiffer than pure bitumen, could improve the shear strength of interfaces. Yet the experimental evidence shows a moderate, if not negative, effect of bitumen modification with polymers (Collop *et al.* 2011; Canestrari *et al.* 2013; Godard *et al.* 2015).

The influence of application conditions of tack coats made of bituminous emulsion has been studied in laboratory to identify the right practices on a road construction site. A careful cleaning of the application surface is usually prescribed. Yet, Mohammad *et al.* observed that the application of a bituminous emulsion on a surface with sand on it led to lightly higher interface shear resistance (L. N. Mohammad *et al.* 2012). It could be that the bitumen and sand mix together to form a mastic with an increased stiffness. A dry surface is also prescribed before applying the tack coat. The water has indeed a negative influence on the interface shear strength (Hun 2012; Mohammad *et al.* 2012).

Tack coats are not always made using bituminous emulsions.

Pure bitumen tack coats and bituminous emulsions tack coat differ only by the application technique of a bitumen at the interface. The comparison between pure bitumens and emulsions is not easy given that the bitumens used are usually different. Testing different pure bitumens and different emulsions, it seems that the shear resistances are close for both types of tack coats (Mohammad *et al.* 2002).

Certain types of tack coats are designed to prevent the propagation of cracks from the base course to the surface course (reflective cracking). It is a concern when a layer has to be compacted on an existing old pavement where there are cracks at its surface because it leads to stress concentrations at the bottom of the new layer. Different methods exist to prevent the reflective cracking. A Stress Absorbing Membrane Interlayer (SAMI) is made of rubber bitumen applied on the lower layer with precoated aggregates compacted upon it on which the upper layer is laid. The SAMI does prevent the reflective cracking as it is verified with flexural tests but it reduces significantly the shear resistance of the interface resulting in mechanically independent layers (Molenaar 1986). Chips of a certain size can increase the interface shear strength, certainly due to the rough surface they create (D'Andrea *et al.* 2013) but it depends on the bituminous mixture used as the lower layer.

Geogrids are made of glass or carbon fibres arranged in mesh impregnated in a polymer resin, in the most general case. They are placed at the interface to prevent reflective cracking. Bituminous emulsion is applied on each side of the grid with an important dosage to cover it sufficiently (Figure 1.32). The interface shear strength is lowered if geogrids are placed at the interface (Ferrotti *et al.* 2016) but the reflective cracking resistance is improved as well as the fatigue resistance of bi-layered beams tested with flexural tests (Ferrotti *et al.* 2012; Safavizadeh and Kim 2014). The geogrid interface still respects the TTSP for both the interface shear strength and the shear stiffness in cyclic tests (Cho *et al.* 2017).

Figure 1.32 - Geogrid placed on a mixture with bituminous emulsion sprayed on it

1.3.3. Type of bituminous mixtures layers

An important part of the interface behaviour is guided by the bituminous mixtures of the pavement layers. Without any tack coat, the interface presents a certain shear strength because of the

interpenetration of the binders of the layers if the upper layer is laid at a high temperature and also because of the interlocking effect. After compaction, the lower layer is relatively rough depending on the aggregate size distribution, the binder content and the compaction process. The interlocking effect is related to the way that the aggregates of the two layers entangle. In some cases, the contact surface of the layers is optimum and it improves the interface shear strength.

For the simple example of bituminous mixtures being either rough or smooth, four interface configurations are possible (smooth on smooth, smooth on rough, rough on smooth, rough on rough, see Figure 1.33). Under the simplistic approximation than rough mixtures have got larger aggregates than smooth mixtures, the configuration smooth on rough seems to be the more resistant. Indeed, the rough surface of the lower layer has got "valleys" in which the small aggregates of the smooth upper layer can easily be placed in. The contact surface is more important than with a smooth lower layer with smaller "valleys". The rough upper layers create too much voids (partially filled with tack coat) that are not favourable to the interlocking effect.

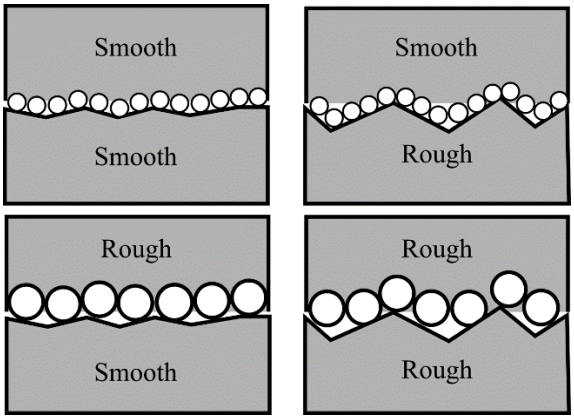

Figure 1.33 - Schematics of interlocking configurations with only smooth or rough bituminous mixtures layers

This simple reasoning is the base of a study conducted by Raab *et al.* where model materials were used to represent the bituminous mixtures. The aggregates of the mixtures were replaced by steel balls, large ones (9.5 mm in diameter) for rough mixtures and small ones (5.5 mm) for smooth mixtures. No tack coat was applied at the interface. The results show that the configuration smooth on rough presents the higher shear strength as expected, more than the configurations smooth on smooth, rough on rough and rough on smooth in that order (Raab *et al.* 2012).

The difference in roughness between the usual bituminous mixtures is not as visible as in Figure 1.33. There are several measurement techniques to define the roughness of a surface. One of the simplest one, used *in situ* or in laboratory, is the sand patch test (or volumetric method). It is a European standard (NF EN 13036-1). A small stack of sand of a known weight is placed on the mixture surface and spread in a circular shape so that the surface of the circle is perfectly flat, the sand filling the "valleys". The diameter of the circle gives access to the Mean Texture Depth (MTD) of the mixture.

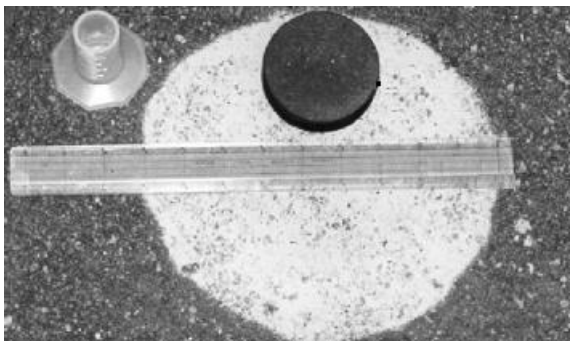

Figure 1.34 - Sand patch test (NF EN 13036-1)

Advanced measurement methods such as laser profilometry (Ech *et al.* 2007) or fringe projection (Léandry *et al.* 2012) create 3D representations of bituminous mixtures surfaces. From the 3D cartography, it is possible to calculate several roughness parameters as defined in the ISO standards 4287 and 13565. For instance, there are the Roughness Average (R_a) and the Root Mean Square Roughness (R_q) that represent the average depth of a "valley"; the Maximum Height of the Profile (R_t); the Skewness (R_{sk}) that describes the asymmetry in the distribution of "valleys" and "peaks"; or the Kurtosis (R_{ku}) that indicates the sharpness of the "peaks".

The average roughness R_a of the layers has got a significant influence on the interface shear strength. Raposeiras *et al.* studied interfaces between mixtures with different roughness and tack coats at different dosages. The lowest roughness for the lower layer was obtained by sawing the surface before compacting the upper layer and it gave the worst interface shear strength whatever the upper layer was made of. The R_a was measured using the sand patch test and varied between 0.05 and 0.3 mm, the sawn surface having a value close to 0.01 mm. The maximum shear strengths were obtained for lower layer with intermediate roughness: if the layer is too rough, the tack coat does not successfully fill the voids at the interface and cannot assume its role (Raposeiras *et al*. 2012). The latter argument concurs with a similar observation of sandblasted surfaces having a higher roughness but that led to less resistant interfaces compared to a sawn surface (Raab and Partl 2004).

D'Andrea *et al.* also studied the effect of the roughness of the lower layer. Different surface treatments were performed such as chipping, smoothing, de-bitumening or using a tooth compacter roller. The roughness parameters of the treated surfaces were obtained using laser profilometry. The same mixture was then compacted above the interface. The results show that the treatments that increased the average roughness parameter R_a increased the interface shear strength except for the de-bitumening treatment that removed the action of lower layer bitumen. The comparison between the treatments showed that a higher R_a is not a guarantee of higher shear strength. But a correlation was found between the interface shear strength and the Kurtosis parameter showing that a surface with sharper peaks leads to more interlocking (D'Andrea *et al.* 2013).

Thanks to Digital Image Correlation, Ktari *et al.* defined the Intermediate Transition Zone (ITZ, thought as an interphase) as the zone where strain is concentrated around the interface. The ITZ is typically 3 mm high for the materials studied, considering the vertical strain in a tensile test. Using fringe projection to obtain the roughness parameters of a mixture surface, a certain correlation was found between the maximum height of the profile R_t and the ITZ height in the three tested samples made of the same material (Ktari *et al.* 2016).

1.4. Interface behaviour modelling

Based on the experimental observations and the identified factors influencing the interface behaviour, several mechanical models were proposed for the interfaces. The experimental approaches focused on cyclic testing at small strain amplitude, on monotonic failure tests and on fatigue testing of interfaces. The models proposed for each of these tests will be presented in the following sections.

1.4.1. Small strain domain

1.4.1.1. Linear viscoelasticity

The bituminous materials such as bituminous mixtures or pure bitumen present a Linear ViscoElastic (LVE) behaviour when subjected to a small number of loading at small strain amplitude (Corté and Di Benedetto 2004) and, *a priori*, interfaces might do too.

The mechanical response of a LVE material depends on the history of loading that it has been subjected to. A LVE material respects, by definition, the Boltzmann superposition principle (Boltzmann 1874). It states that if a loading σ_1 creates a response ε_1 in the material and if a loading σ_2 creates a response ε_2 then a linear combination of the loadings $\alpha\sigma_1 + \beta\sigma_2$ creates a response that is the linear

combination $\alpha\varepsilon_1 + \beta\varepsilon_2$ where α and β are real numbers. The classical characterization of a LVE material is given by its creep function. The creep function *f(t)*, where *t* is the time, is the strain response to a unit stress loading *H(t)* defined in Equation 1.2.

$$H(t) = \begin{cases} 0 & if\ t < 0 \\ 1 & if\ t \geq 0 \end{cases} \qquad (1.2)$$

A creep experiment is performed to obtain the creep function. A constant stress σ_0 is applied instantly at a time t_0 and maintained ay this value (Figure 1.35). Given that the material respects the Boltzmann principle, the strain response to the creep experiment is simply the creep function multiplied by σ_0. In the most general case, the creep function can vary with the time t_0 but for non-ageing materials, it does not.

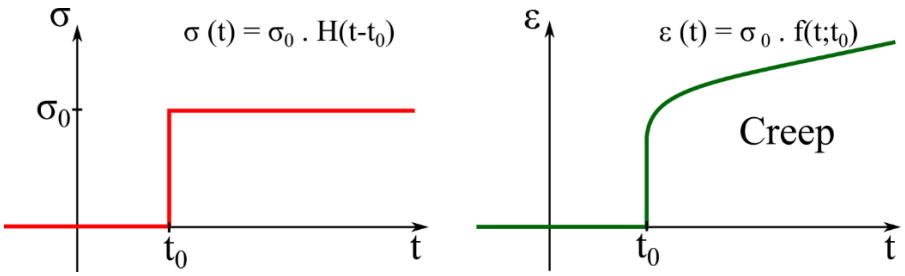

Figure 1.35 - Creep function for a LVE material

The creep function describes completely the behaviour of a LVE material but it is sometimes convenient to introduce the relaxation function that is the stress response *r(t)* to a unit strain loading *H(t)*. Similarly to the creep experiment, a relaxation experiment can be performed to obtain the relaxation function (Figure 1.36). The knowledge of only one of these two functions is enough to describe completely the LVE behaviour.

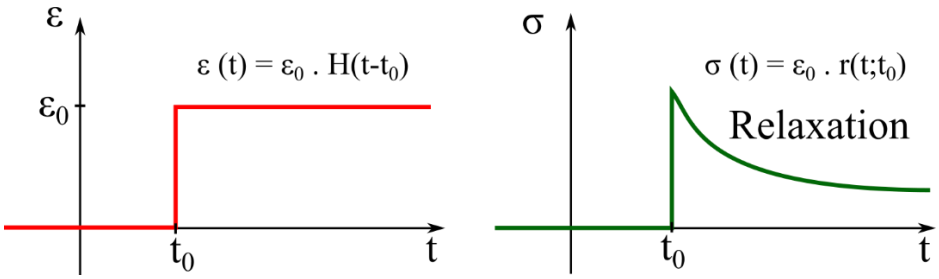

Figure 1.36 - Relaxation function for a LVE material

Using the Boltzmann superposition principle, it is possible to derive the analytical response of a non-ageing LVE material to any stress loading *σ(t)* using the creep function (Equation 1.3) or any strain loading *ε(t)* using the relaxation function (Equation 1.4).

$$\varepsilon(t) = \frac{d}{dt}\left(\int_0^t f(t-\tau).\sigma(\tau)d\tau\right) \qquad (1.3)$$

$$\sigma(t) = \frac{d}{dt}\left(\int_0^t r(t-\tau).\varepsilon(\tau)d\tau\right) \qquad (1.4)$$

The Laplace-Carson transform is practical when studying LVE materials because it simplifies the equations. The transformed function $\tilde{f}$ is a function of the complex variable p. It is defined in Equation 1.5 as the transformation of a locally integrable, real function *f* nil for negative values.

$$\tilde{f}(p) = p\int_0^{+\infty} f(t)e^{-pt}dt \tag{1.5}$$

Using the properties of the Laplace-Carson transformation, it is possible to rewrite Equation (1.2) in Equation (1.6) and Equation (1.4) in Equation (1.7) and then to find a relation between creep and relaxation functions in Equation 1.8.

$$\tilde{\varepsilon}(p) = \tilde{f}(p)\,\tilde{\sigma}(p) \tag{1.6}$$

$$\tilde{\sigma}(p) = \tilde{r}(p)\,\tilde{\varepsilon}(p) \tag{1.7}$$

$$\tilde{r}(p)\tilde{f}(p) = 1 \tag{1.8}$$

Analytical models were developed to represent the LVE materials. A large number of them can be constructed using the elemental bricks that are the spring and the dashpot (also known as damper) (Figure 1.37).

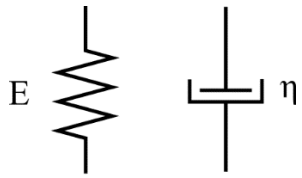

Figure 1.37 - Schematics of the elementary LVE models: the spring on the left, the dashpot on the right

The relationship between stress and strain for a spring is Equation 1.9 where E is the spring stiffness.

$$\sigma(t) = E\,\varepsilon(t) \tag{1.9}$$

The relaxation function after Laplace-Carson transformation of a spring is then as in Equation 1.10.

$$\tilde{r}(p) = E \tag{1.10}$$

Similarly, the relationship between stress and strain for a dashpot is Equation 1.11 where η is the dashpot viscosity.

$$\sigma(t) = \eta\,\frac{d\varepsilon}{dt}(t) \tag{1.11}$$

The relaxation function after Laplace-Carson transformation of a spring is then as in Equation 1.12.

$$\tilde{r}(p) = \eta p \tag{1.12}$$

Several rheological models can be constructed from springs and dashpots assembled in serial or in parallel. For instance the generalised Kelvin-Voigt model is the assembly in serial of a certain number *n* of simple elements constituted of one dashpot and one spring in parallel as illustrated in Figure 1.38.

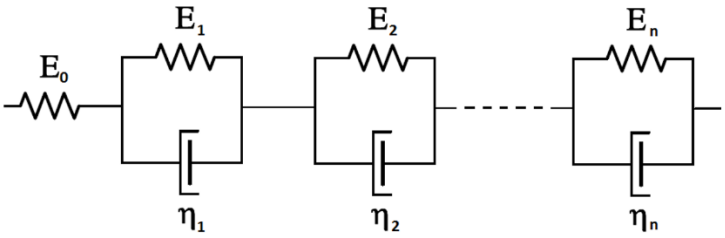

Figure 1.38 - Schematic of the generalised Kelvin-Voigt model with n elements

Using the notations of Figure 1.38, the relaxation function of the generalised Kelvin-Voigt model transformed by Laplace-Carson is given in Equation 1.13.

$$\tilde{r}(p) = \left(\frac{1}{E_0} + \sum_{i=1}^{n} \frac{1}{E_i + p\eta_i} \right)^{-1} \tag{1.13}$$

Any LVE material can be modelled by a generalised Kelvin-Voigt model with a sufficient number of elements and it is also the case for bituminous mixtures (Corté and Di Benedetto 2004). Accurate models can be obtained by adding another elementary brick called the parabolic element (Figure 1.39). The use of such elements reduces the number of parameters to describe adequately the LVE behaviour of bituminous mixtures compared to a generalised Kelvin-Voigt model.

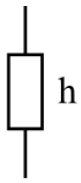

Figure 1.39 - Schematic of a parabolic element

The creep function of a parabolic element is given in Equation 1.14 with h and τ being the element parameters ($0 < h < 1$) and a being a constant.

$$f(t) = a\left(\frac{t}{\tau}\right)^{h} \tag{1.14}$$

The relaxation function of the parabolic element transformed with Laplace-Carson is Equation 1.15, with Γ being the gamma function.

$$\tilde{r}(p) = \frac{(p\tau)^{h}}{a\Gamma(h+1)} \tag{1.15}$$

The 2S2P1D (2 Springs, 2 Parabolic elements, 1 Dashpot) model was introduced as an improvement of the Huet-Sayegh model (Sayegh 1965) for a better modelling of bituminous binders at high temperatures and low frequencies (Olard and Di Benedetto 2003). It is illustrated in Figure 1.40.

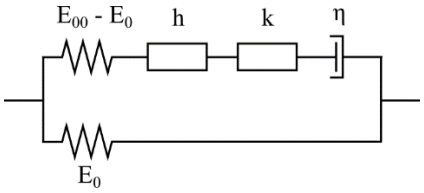

Figure 1.40 - Schematic of the 2S2P1D model

The constants of the parabolic elements in the 2S2P1D model (denoted by a in Equation 1.14) are chosen so that the relaxation function transformed by Laplace-Carson is Equation 1.16. The parameters τ of the two parabolic elements are chosen to be identical. β derives from the dashpot viscosity η with the relation $\beta = (\eta/\tau)/(E_{00}-E_0)$.

$$\tilde{r}(p) = E_0 + \frac{E_{00} - E_0}{1 + \delta(p\tau)^{-h} + (p\tau)^{-k} + (p\beta\tau)^{-1}} \quad (1.16)$$

In Equation 1.16, the seven constants of the 2S2P1D model can be identified. E_{00} is the static modulus which is the asymptotic value for low frequencies, E_0 is the glassy modulus which is the asymptotic value for high frequencies. k, h and δ are calibration parameters related to the parabolic elements. τ is a characteristic time and β a viscosity parameter.

1.4.1.2. Complex modulus

The creep or relaxation experiments are impossible to perform in reality since a perfect Heaviside strain or stress loading cannot be applied and because the measurements should theoretically be performed for an infinite time to obtain the creep function. An easier way to observe the behaviour of a LVE material is by applying a sinusoidal loading. This is the principle of the complex modulus test. A sinusoidal strain is imposed to a LVE material with an angular frequency ω (and thus with a frequency $f = \omega/2\pi$) as in Equation 1.17, starting from a time $t = 0$ *s*.

$$\varepsilon(t) = \varepsilon_0 \cos(\omega t)\, H(t) \quad (1.17)$$

It is possible to derive the stress response using Equation 1.4. The stress response is divided in two terms: a transient response and an asymptotic harmonic response. After a short period of time, a few cycles for bituminous mixtures (Gayte *et al.* 2016), the transient response is negligible compared to the harmonic response. The stress signal is then sinusoidal with a phase lag φ_E compared to the strain signal as in Equation 1.18.

$$\sigma(t) = \sigma_0 \cos(\omega t + \varphi_E)\, H(t) \quad (1.18)$$

The complex modulus E^* at the angular frequency ω is then defined as in Equation 1.19 where i is the imaginary unit ($i^2 = -1$) and illustrated in Figure 1.41. It is possible to prove that the complex modulus at the angular frequency ω is the Laplace-Carson transformation of the relaxation function of the LVE material, calculated for the complex number $p = i\omega$ (Salençon 2009).

$$E^*(\omega) = \frac{\sigma_0}{\varepsilon_0} e^{i\varphi_E} = |E^*|(\omega) e^{i\varphi(\omega)} = \tilde{r}(p = i\omega) \quad (1.19)$$

From Equation 1.19, it is possible to identify the complex modulus norm $|E^*|(\omega)$ that is the ratio between stress amplitude and strain amplitude and the phase angle $\varphi(\omega)$ that is the phase lag between the stress and strain signals. Both these quantities depend on the frequency.

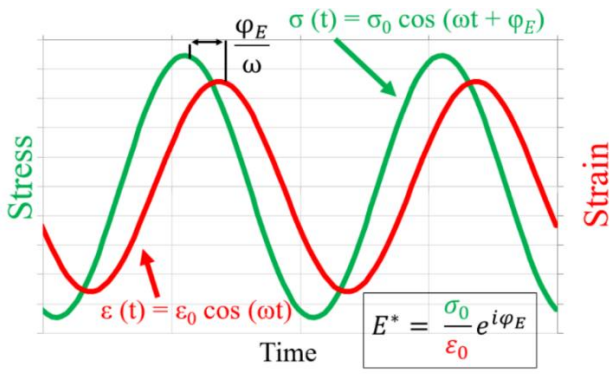

Figure 1.41 - Illustration of complex modulus definition

The phase angle varies between 0 and 90° meaning that the strain always lags behind the stress. Viscous energy dissipation is related with the phase angle, a higher phase angle inducing higher dissipation. An interesting property concerning the complex modulus is that there is a relationship between $|E^*|(\omega)$ and $\varphi(\omega)$. These two real functions derive indeed from a single real function that is the relaxation function $r(t)$. An approximation of this relationship well supported by experimental results is presented in Equation 1.20 (Booij and Thoone 1982).

$$\varphi(\omega) \approx \frac{\pi}{2}\left(\frac{d\ln|E^*(u)|}{d\ln u}\right)(\omega) \qquad (1.20)$$

1.4.1.3. *Time-Temperature Superposition Principle (TTSP) for complex modulus*

The complex modulus of bituminous materials depends on the frequency but also on the temperature. To describe completely the LVE behaviour, complex modulus tests are performed at different frequencies and at different temperatures. All the results are presented on specific diagrams such as the Black diagram where the complex modulus norm $|E^*|$ is plotted versus the phase angle φ or the Cole-Cole diagram where the imaginary part of the complex modulus is plotted versus its real part. The Time-Temperature Superposition Principle (TTSP) is verified if there is a unique curve (meaning that there are no discontinuities between tests at different temperatures) in these diagrams. Additionally, isothermal curves are obtained by plotting the complex modulus norm $|E^*|$ or the phase angle φ versus the frequency ω for each temperature.

If the TTSP is verified, it is possible to select one isothermal curve obtained for the temperature T_{ref} and shift the other isothermal curves along the angular frequency ω axis so that a unique continuous curve is created (Figure 1.42). This curve is called the mastercurve of either the complex modulus norm or the phase angle at the reference temperature T_{ref}. For a tested temperature T, the associated shift factor is written a_T.

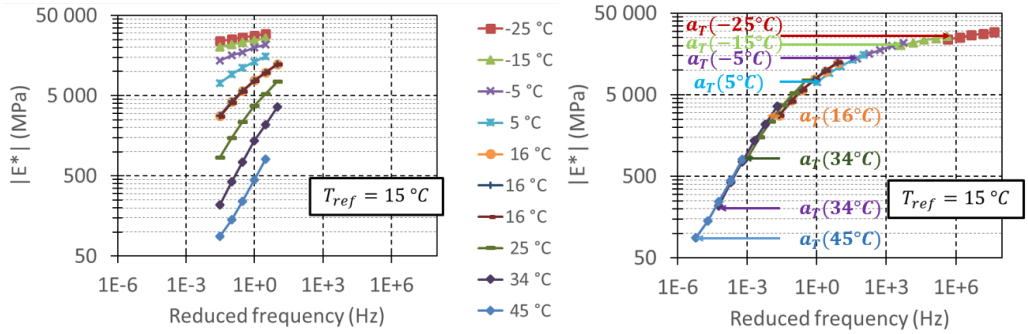

Figure 1.42 - Construction of complex modulus norm $|E^*|$ mastercurve of a bituminous mixture: isothermal curves on the left, mastercurve on the right (Gayte 2016)

The TTSP implies that the dependency of the complex modulus on temperature and frequency can be reduced to one variable as presented in Equation 1.21 where g is a real function.

$$E^*(\omega, T) = E^*(\omega . g(T)) \tag{1.21}$$

For a given temperature T and a given angular frequency ω, one obtains a value of complex modulus. At a chosen reference temperature T_{ref}, there exists a unique equivalent angular frequency ω_{eq} such as the complex modulus is the same than for T and ω. The equivalent angular frequency ω_{eq} (also called reduced angular frequency) is given in Equation 1.22 where it is also possible to identify the shift factor a_T necessary to build the mastercurves.

$$E^*(\omega, T) = E^*\left(\omega_{eq}, T_{ref}\right) \Leftrightarrow \omega_{eq} = \omega . \frac{g(T)}{g(T_{ref})} = \omega . a_T\left(T, T_{ref}\right) \tag{1.22}$$

The relationship between the shift factors and the temperature can be modelled using the Williams-Landel-Ferry (WLF) equation (Williams *et al.* 1955) (Equation 1.23, where "log" represents the logarithm with base 10). It introduces two constants C_1 and C_2. It has been proved to correctly describe the TTSP principle for bituminous materials (Corté and Di Benedetto 2004).

$$\log a_T = -\frac{C_1(T - T_{ref})}{C_2 + T - T_{ref}} \tag{1.23}$$

Other equations can be used to describe the dependency of the shift factors on the temperature like the Arrhenius law (Equation 1.24) that introduces one parameter E_a that is the activation energy of the material. In Equation 1.24, R represents the gas constant (8.314 $J.K^{-1}.mol^{-1}$).

$$\log a_T = \frac{E_a}{R}\left(\frac{1}{T} - \frac{1}{T_{ref}}\right) \tag{1.24}$$

For a temperature inferior to the reference temperature, the shift factor a_T is superior to 1 for bituminous materials (it is also the case in Equations 1.23 and 1.24). As expected, this means that at the reference temperature, a behaviour equivalent to the one at a lower temperature is found for higher frequencies, since the equivalent frequency is the original frequency multiplied by the shift factor.

1.4.1.4. LVE modelling of interfaces

The LVE domain for bituminous materials depends on the temperature, the loading speed and the type of materials. The order of magnitude of the amplitude limit of the LVE domain is 100 µm/m for bituminous mixtures and 10,000 µm/m for bitumens (Airey *et al.* 2003). As interfaces between pavement layers are closely related to the behaviour of these materials, it can be hypothesized that interfaces present a LVE behaviour in the small strain domain too. It has already been showed that a numerical model of the pavement considering that the interface is a layer of a LVE material is very satisfying to predict the actual structure response (Grellet *et al.* 2018).

Several shear cyclic tests were performed on interfaces and it has always been verified that the mechanical response (stress or strain) to a sinusoidal loading was also a sinusoidal loading *(Diakhate et al.* 2006; Tozzo *et al.* 2014; Isailović *et al.* 2017; Raab *et al.* 2017; Hristov 2018b). The complex shear interface stiffness is commonly defined using Equation 1.25 where τ_0 is the amplitude of shear stress cycles, Δu_0 is the amplitude of shear relative displacement at the interface and φ_K is the phase lag between the stress and displacement signals. The complex shear stiffness norm $|K^*|(\omega)$ and the complex shear

stiffness phase angle $\varphi_K(\omega)$ are identified in the same way as for the complex modulus. The phase angle has not been thoroughly studied (Diakhaté 2007; Diakhaté *et al.* 2011; Isailović *et al.* 2017).

$$K^*(\omega) = \frac{\tau_0}{\Delta u_0} e^{i\varphi_K} = |K^*|(\omega) e^{i\varphi_K(\omega)} \quad (1.25)$$

Based on the shear interface stiffness during the initial cycles of fatigue tests conducted by Diakhaté *et al.* where fatigue tests were realized at different stress amplitudes, it can be seen that the initial shear stiffness is rather constant for shear stress amplitudes lower than 1 MPa at 10 °C and 20 °C for interfaces with a tack coat in bituminous emulsion tested at 10 Hz. This is a first order of magnitude for the LVE domain limit even if it is a high value compared to the interface shear strength (Diakhaté *et al.* 2011). However, an amplitude sweep test conducted by Isailović *et al.* on a guillotine test at 10 Hz at 10 °C and 20 °C tend to show that there is no LVE domain. The shear displacement at the interface ranged from 0.005 mm to 0.2 mm for a gap of 1 mm, and the shear interface stiffness always decreased with the increasing amplitude (Isailović *et al.* 2017).

Hristov employed a guillotine test to perform complex modulus tests at small strain amplitude on an interface at different frequencies (from 0.1 Hz to 10 Hz) and temperatures (from -10 °C to 50 °C). The amplitude of shear displacement was between 0.03 mm at -10 °C and 0.15 mm at 50 °C. The TTSP was verified and the mastercurve of the complex interface stiffness norm was obtained. The dependency of the shift factors a_T with the temperature T was modelled using the Arrhenius law. The mastercurve of the complex interface stiffness norm was modelled using a sigmoid function similar as Equation 1.26 where G_0 is the maximum value of the complex interface stiffness norm, G_{00} the minimum value, a and b two parameters, f the frequency and a_T the shift factor for temperature T.

$$|G^*| = G_0 + \frac{G_{00} - G_0}{1 + \exp(a.\log(a_T.f) + b)} \quad (1.26)$$

Only one shear amplitude was tested per couple of temperature and frequency and it is not possible to determine whether the behaviour is LVE (Hristov 2018a).

Using a complex modulus test in tension-compression at different frequencies (from 0.003 Hz to 10 Hz) and temperatures (from -25 °C to 52 °C), Freire *et al.* obtained the complex interface stiffness in the normal direction for different alleged values of interface thickness (Figure 1.43, where the interface stiffnesses are normalized by the asymptotic values). A geogrid was placed at the interface with bitumen emulsion. They observed that the complex interface stiffness could be modelled using the 2S2P1D model. The tests were realized at only one amplitude and it is not sure if the complex interface stiffness changes with the amplitude of load cycles which would exclude the LVE behaviour (Freire *et al.* 2018).

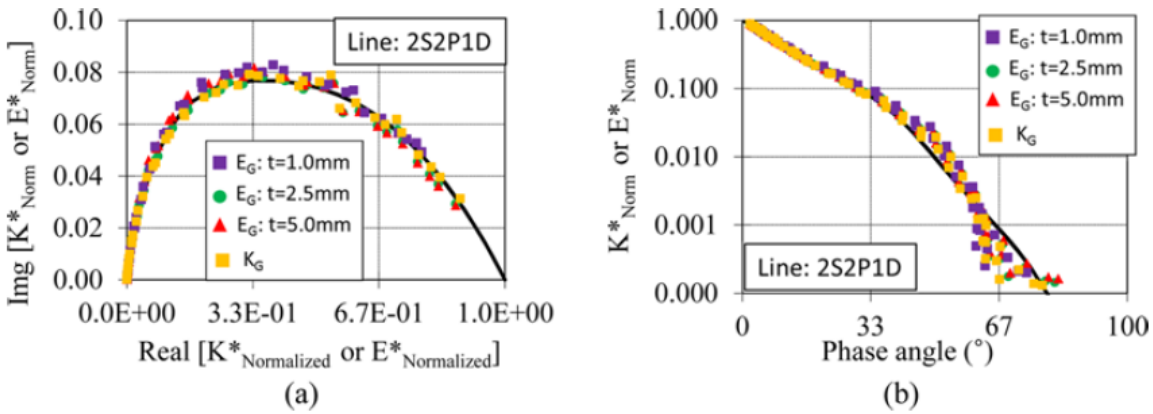

Figure 1.43 - Interface normalized complex modulus (E^*_{norm}) and complex modulus stiffness (K^*_{norm}) (points) and 2S2P1D model (line): (a) Cole-Cole plan, (b) Black diagram (Freire *et al.* 2018)

1.4.2. Fatigue

When they are subjected to a high number of loading cycles at small strain amplitude, interfaces deteriorate slowly until failure. The number of cycles until failure for one given interface depends on the temperature, the loading frequency, the application of normal stress, the amplitude of load cycles, the loading shape but also on the failure criterion chosen to determine when the interface is fatigued.

Fatigue tests on bituminous mixtures or binder can be divided in three stages regarding the evolution of complex modulus norm with the number of cycles applied. During a first stage, there is a rapid decrease of the complex modulus norm. During a second stage, the modulus decreases slowly and regularly. In the final stage, cracks propagate rapidly and the modulus decreases very rapidly. Those three stages are sometimes observed when testing interfaces in shear mode without normal stress (Figure 1.45). When a compressive stress is applied to the interface, the interlocking effect induces changes in the stages like an increase of the interface stiffness norm during the first stage (Tozzo *et al.* 2014) or a residual shear stiffness at the end of the second stage (Isailović *et al.* 2017).

The classical failure criterion for fatigue tests on interfaces is the diminution of the complex interface stiffness norm by 50 % of its initial value. Similarly, the criterion can be when the shear stress amplitude decreases by half for displacement controlled tests (Collop *et al.* 2011) or when the shear displacement reaches a certain value for stress controlled tests (Romanoschi and Metcalf 2001). When identifying the three stages of the fatigue test, a criterion for failure can be the number of cycles when the second stage ends and the third one begins whether there is a residual stiffness or not (Diakhaté 2007; Isailović *et al.* 2017).

Like for the bituminous mixtures fatigue tests, an energetic analysis of the interface fatigue test can be conducted. The viscous energy w_i dissipated during the cycle i of a fatigue test can be calculated using Equation 1.27 where τ_i is the shear stress amplitude at the cycle i, Δu_i is the amplitude of the shear displacement at the cycle i and φ_i is the phase lag between stress and displacement signal.

$$w_i = \pi \, \tau_i \, \Delta u_i \, sin \, \varphi_i \tag{1.27}$$

The energy dissipated per cycle changes slowly at the beginning of the fatigue test and an energetic criterion for fatigue failure would be the moment when the evolution changes rapidly (Diakhaté 2007).

Once a failure criterion is chosen, it is possible to evaluate the influence of the different parameters on the fatigue resistance of interfaces. The classical analysis of fatigue aims at finding a fatigue law that links the amplitude of load cycles with the number of cycles at failure. It is usually a power function like Equation 1.28 where τ is the shear stress amplitude, N the number of cycles at failure, a and b the law parameters. Equation 1.28 describes tests where the stress cycles are applied at a constant amplitude (Diakhaté 2007; Collop *et al.* 2011; Canestrari *et al.* 2013; Isailović *et al.* 2017). When the shear displacement cycles are applied at a constant amplitude, the fatigue law is the same than Equation 1.28 with Δu the shear displacement amplitude instead of τ.

$$\tau = aN^b \tag{1.28}$$

This law describes adequately the fatigue of interfaces as in Figure 1.44. The parameters depend on the temperature and on the normal stress.

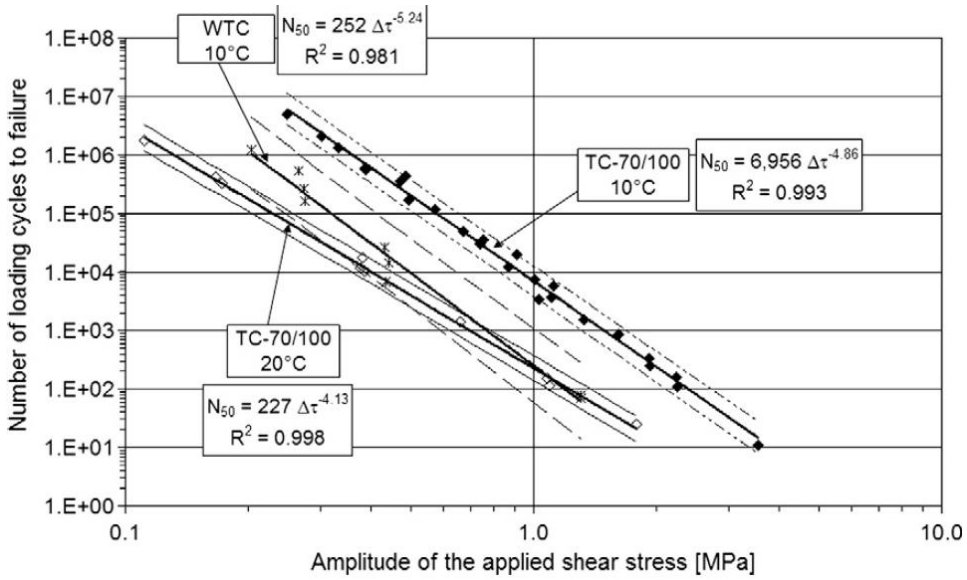

Figure 1.44 - Fatigue laws for interface shear tests at constant stress amplitude for interfaces Without Tack Coat (WTC) or with a Tack Coat in 70/100 bitumen (TC-70/100) (Diakhaté *et al.* 2011)

The influence of the normal stress using a shear fatigue test can also be modelled using a power function such as Equation 1.29 with *c* and *d* the parameters of the law (Tozzo *et al.* 2014; D'Andrea and Tozzo 2016a). *c* and *d* may vary with the temperature.

$$\log N = c\tau^{0.75} + d\sigma^{0.75} \quad (1.29)$$

Diakhaté introduced a simple model to describe the evolution of the interface shear stiffness with the number of cycles applied. The second stage and the third stage are modelled by two straight lines. Based on experimental results it is possible to obtain the initial interface shear stiffness, the slopes of the two lines and the number of cycles at failure with the amplitude of shear stress load cycles, the temperature and the type of material as inputs. The obtained model for one interface test is presented in Figure 1.45 along with experimental data (Diakhaté 2007).

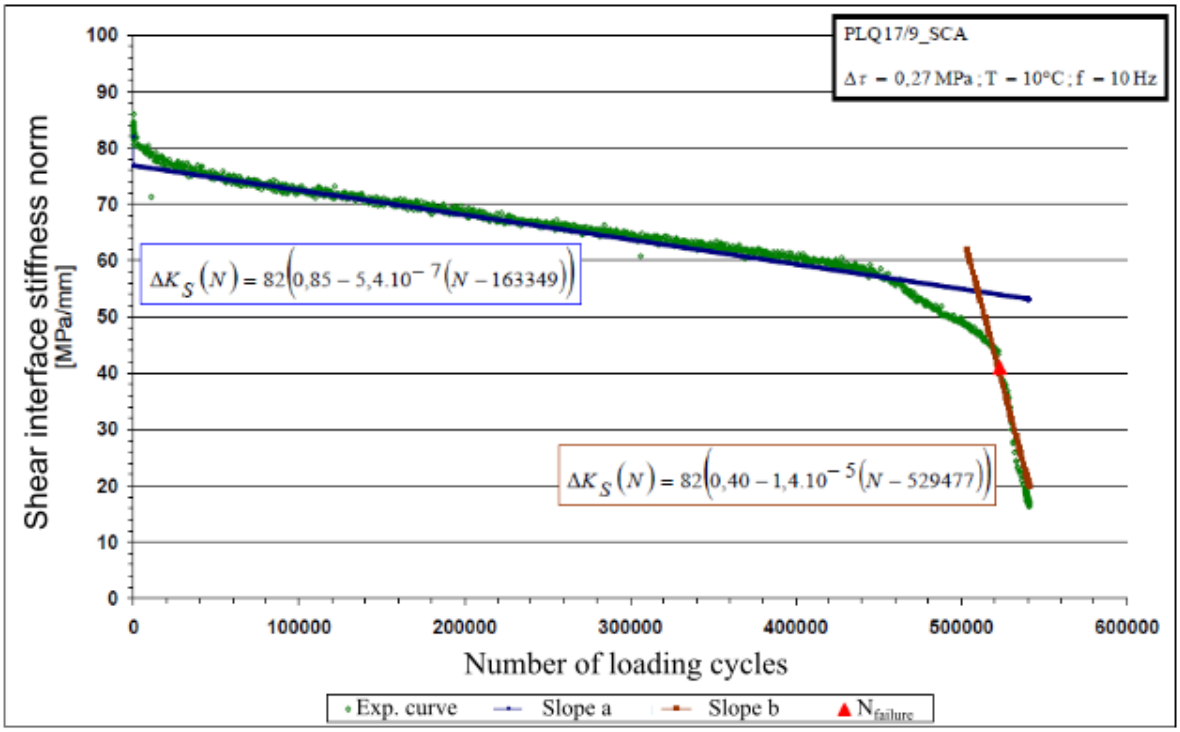

Figure 1.45 - Bilinear model for interface shear stiffness evolution during a fatigue test (translated from (Diakhaté 2007))

Up to now, no study was performed to evaluate the biasing effects observed during a fatigue test on interfaces where the cycles are applied without rest periods. It has been showed for bituminous mixtures and binders that the decrease of complex modulus norm during such fatigue tests was partially caused by reversible phenomena, different from proper, irreversible damage, such as self-heating, nonlinearities of the material behaviour or thixotropy (Mangiafico 2014; Babadopulos 2017; Babadopulos *et al.* 2019).

For fatigue tests where macro cracking is monitored, the evolution of the crack length with the number of cycles can be modelled using the Paris law, presented in Equation 1.30 where a is the crack length, N is the number of cycles, ΔK is the amplitude of the stress intensity factor on one cycle, C and m are the law parameters and depend on the type of material.

$$\frac{da}{dN} = C\Delta K^n \tag{1.30}$$

This approach was used to model the interface crack evolution in a double shear test and in a modified guillotine test, with the crack length measured using Digital Image Correlation (DIC) (Safavizadeh 2015).

1.4.3. Monotonic failure

The important factors that influence the interface shear strength (which is the maximum shear stress that the interface can endure) are the temperature, the loading speed, the normal stress and the type of tack coat and bituminous mixtures layers. Several laws have been proposed to describe the influence of these factors.

Concerning the dependency in the loading speed, Canestrari *et al.* proposed a power law as Equation (1.31) where τ is the interface shear strength, v is the loading speed, a and b the parameters of the law.

$$\tau = a\, v^b \tag{1.31}$$

The loading speed (mm/s) can be replaced by the strain rate (mm/m/s) by assuming an interface thickness. This law has been verified experimentally (Canestrari *et al.* 2013).

As in the small strain domain, the interface shear strength respects the TTSP meaning that the strength is higher for high loading speed but also for low temperatures (and inversely, the strength is lower for low loading speed and high temperatures). The reduced loading speed v_{red} is used to build a mastercurve at a given reference temperature. It is expressed in Equation 1.32 where v is the actual loading speed and $a_{T0}(T)$ is the shift factor for temperature T at the reference temperature T_0.

$$v_{red} = a_{T_0}(T)\, v \tag{1.32}$$

The shift factors are used to shift the isothermal curves to create the interface shear strength mastercurve as the one presented in Figure 1.46. The WLF equation can be used to fit the values of shift factors (Canestrari *et al.* 2016).

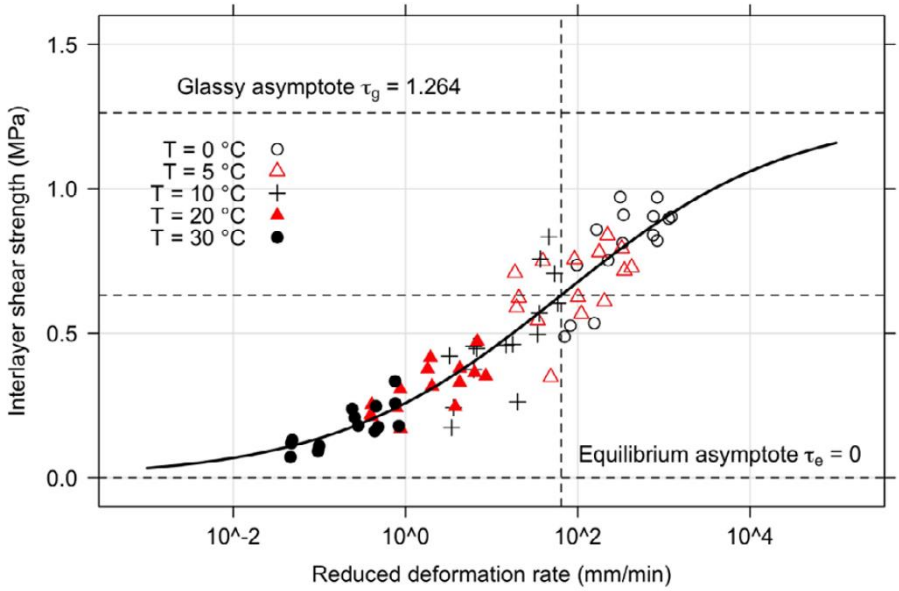

Figure 1.46 - Interface shear strength mastercurve with model in continous line (Canestrari *et al.* 2016)

The mastercurve can be modelled with a sigmoidal function, similar to Equation 1.26 for interface shear stiffness for cyclic tests. Such a function is presented in Equation 1.33 where τ_g is the glassy asymptote obtained for high loading speed, τ_e is the equilibrium asymptote obtained for low loading speed, α_1 and α_2 are the equation parameters.

$$\tau = \tau_e + \frac{\tau_g - \tau_e}{1 + \exp(-(\alpha_1 + \alpha_2 \log v_{red}))} \tag{1.33}$$

The equilibrium shear strength can be assumed nil for a simpler model that still fits correctly the mastercurve (Canestrari *et al.* 2016).

When a normal stress is applied to the interface during a shear failure test, the interface shear strength is modified. Under compressive stress, the interface is more resistant to shear failure. The Mohr-Coulomb failure criterion is broadly used in the soils mechanics. Its expression is Equation 1.34 where τ is the interface shear strength, σ is the normal stress (positive if it is a compressive stress), C, the cohesion, and φ, the angle of internal friction, are the criterion parameters.

$$\tau = C + \sigma \tan \varphi \tag{1.34}$$

This criterion has been proved to describe adequately the interface shear strength evolution (Canestrari *et al.* 2005).

To describe an interface subjected to tensile and shear stresses in a plane, Ktari introduced an innovative model based on a cohesive damage law used in the study of laminated composite (Allix *et al.* 1995). This model describes the interface at the mesoscale and at the macroscale. It takes into account damage processes in the two directions as shown in Equation 1.35 where σ is the normal stress, τ the shear stress, Δu_n the vertical displacement jump at the interface, Δu_s the horizontal displacement jump at the interface, k_n the interface normal stiffness, k_s the interface shear stiffness, d_n and d_s the damage variables in normal and shear directions.

$$\begin{pmatrix} \sigma \\ \tau \end{pmatrix} = \begin{pmatrix} k_n(1-d_n) & 0 \\ 0 & k_s(1-d_s) \end{pmatrix} \begin{pmatrix} \Delta u_n \\ \Delta u_s \end{pmatrix} \tag{1.35}$$

The evolution of damage variables, which is not presented here, is related to energetic criteria and takes into account a delay between loading and damage. Tensile stresses can damage the interface but not the compressive stresses. The model has been implemented numerically and confronted with experimental data from monotonic failure tests (Ktari 2016).

At the mesoscale, the interface geometry can be represented by the real surface geometry, obtained for instance using a fringe projection method on the mixture surface, or by an idealized geometry in a finite element software. Local stiffnesses between the layers at the level of the interface are derived from the mechanical behaviour of the tack coat bitumen. The model describes very well the interface behaviour during traction tests where the roughness does not have any influence. For shear tests, the model matches the experimental data best with the realistic geometry.

It is possible to derive a macroscale model from the mesoscale model. The interface in the macroscale model is now smooth and the macroscale interface stiffnesses in normal and shear directions can be calculated from the local stiffnesses and the mesoscale roughness, *i.e.* the interface mesoscale geometry (Figure 1.47).

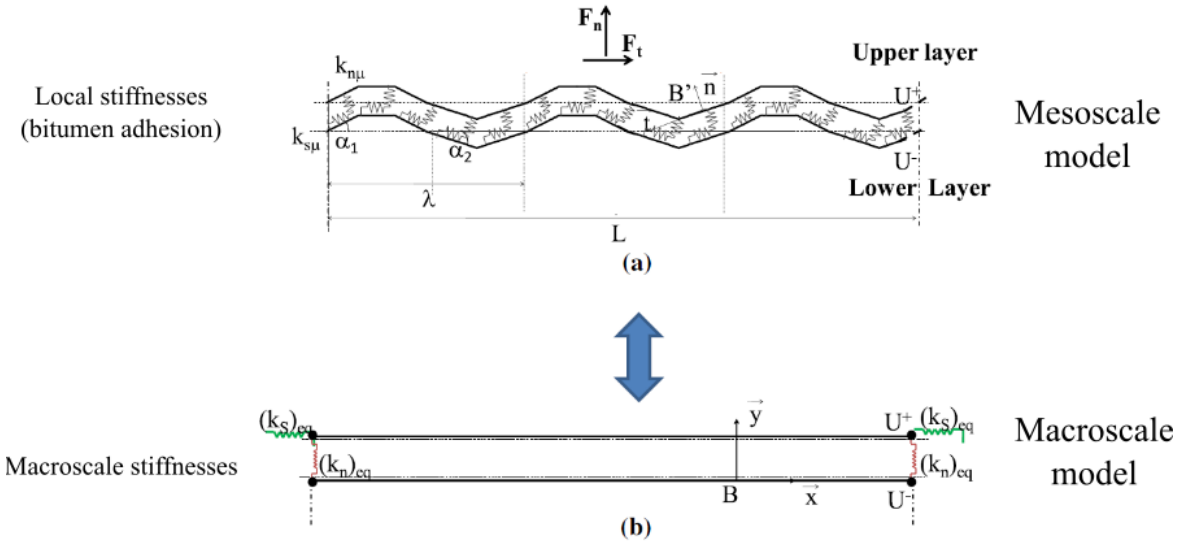

Figure 1.47 - Meso-model (with an ideal trapeziodal geometry) and macro-model of interface (adapted from Ktari *et al.* 2017)

The macroscale model is better at representing the shear tests for large displacements (Figure 1.48). And it is of course very convenient for structure calculations (Ktari *et al.* 2017).

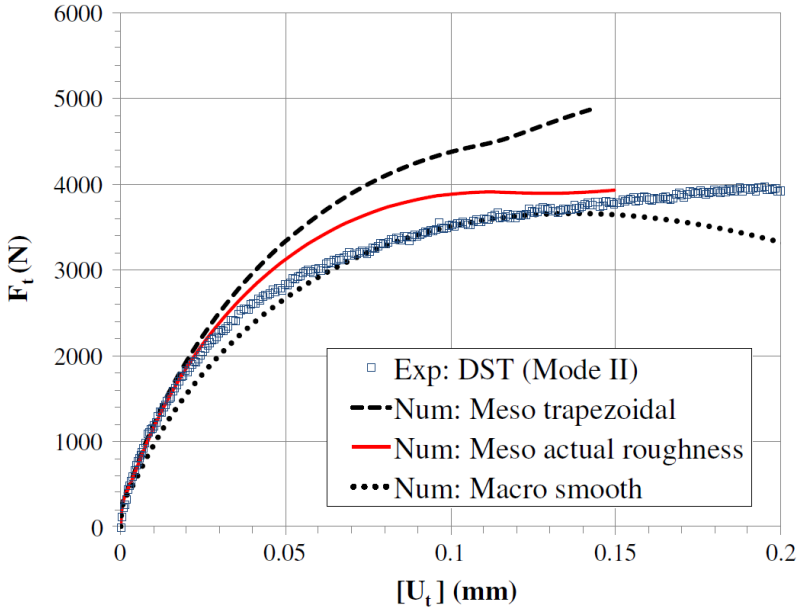

Figure 1.48 - Comparison of numerical simulation using meso- and macro- models with experimental data from a monotonic shear failure test performed with the Double Shear Test (DST) (Ktari *et al.* 2017)

1.5. Conclusion

Road structures are layered structures. The upper layers of the structures are usually made of bound materials like cement concrete or bituminous mixtures because of their exceptional mechanical resistance. However, when subjected to climate and traffic loadings, these materials are liable to be cracked, especially through a fatigue process. Bonding the layers together with tack coats reduces this risk since it diminishes the tensile stresses in the layers and this can extend significantly the structure lifetime. Yet, even the most rational design methods give no importance to the interfaces condition, assuming for instance that the bituminous mixtures layers will be perfectly bonded forever in spite of the field evidence.

Better design methods must take into account realistic behaviours of interfaces and this calls for a better understanding of their mechanical behaviour. Tests performed *in situ* give interesting but limited information since the testing conditions cannot be controlled. The experimental work performed in laboratory showed that the interface behaviour is complex, that it depends on many factors like the temperature, the loading speed, the amplitude of loading, the type of bituminous mixtures, the type of tack coats, the type of loading and the repetition of loadings. The influence of these factors has been extensively studied with a great variety of testing devices. Nevertheless, compared to the actual stress state at the interface, these devices apply simplistic loadings. In addition, most of them are not homogeneous which causes approximations for the stress valuation and few of them introduced direct measurements of the deformation at the interface. Adequate models have been obtained for fatigue and monotonic failure tests and in comparison, the knowledge on the interface behaviour in the small strain domain remains very thin, whereas it is very important in the design of a road structure.

This literature review presented the state of the art of the understanding of interfaces between pavement layers (especially between pavement layers in bituminous mixtures). It brought out the limit of current design methods. It showed that valuable data concerning the interface behaviour could be gathered through laboratory testing but that improvements are still possible. The next chapter describes a new experimental device developed at the University of Lyon/*École Nationale des Travaux Publics*

de l'État (ENTPE) for the purposes of gaining a deeper insight into interfaces mechanical behaviour and, hopefully, contributing to the betterment of road design.

Chapter 2 - 2T3C Hollow Cylinder Apparatus (2T3C HCA)

This chapter introduces the testing device developed at the University of Lyon/ENTPE for the study of interfaces between pavement layers. It is named *Torsion-Traction-Compression sur Cylindre Creux* (*TTCCC*, or *2T3C*) in French, meaning Torsion-Tension-Compression on Hollow Cylinder. Because it is a hollow cylinder apparatus, its complete name is "2T3C Hollow Cylinder Apparatus" (2T3C HCA). The first section of this chapter presents the principles and the design of the 2T3C HCA. The second section describes the measurement systems of this device. The third and final section focuses on one of these measurement systems, the Digital Image Correlation (DIC) and most precisely on the specific analysis method developed at the ENTPE for the study of interfaces.

2.1. 2T3C HCA design

2.1.1. Principle of hollow cylinder tests

Hollow cylinder apparatuses have been extensively used for the study of earth materials like soils or sands (Hight *et al*. 1983; Sauzéat 2003; Duttine *et al.* 2007). The samples are made inside an impervious membrane, placed in a pressurized atmosphere or in a pressurized water tank. A confinement pressure has to be applied to the hollow cylinder samples to maintain their shape. Vertical forces and shear torsional loadings can then be applied to the sample through mechanical actuators. The hollow cylinder shape ensures that the shear stress created in the sample does not vary significantly in the thickness of the sample.

Using the continuum mechanics frame, it is possible to model the hollow cylinder test. The reference configuration is a hollow cylinder with a height h, an external radius R_e and an internal radius R_i as illustrated in Figure 2.1. Its thickness t is defined as $t = R_e - R_i$. The cylindrical coordinates (r, θ, z) associated with the cylinder are chosen to describe the test with an associated vector basis $(\underline{e}_r, \underline{e}_\theta, \underline{e}_z)$ and an origin O taken as the centre of the lower surface of the cylinder. The vertical displacements of points of the lower surface are nil but the displacements in the surface plane are allowed. A constant pressure P is applied to the vertical edges of the hollow cylinder, both on the inside and on the outside. A resultant force F along the (Oz) axis with a torque T around the (Oz) axis are applied to the upper surface of the hollow cylinder.

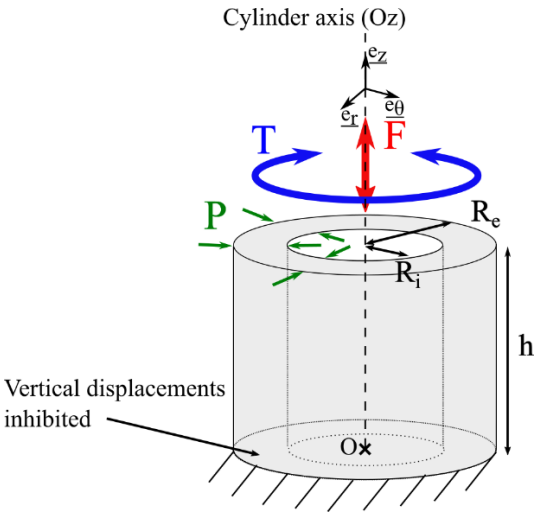

Figure 2.1 - Schematic representation of a hollow cylinder test

With this model, strain and stresses are independent from the coordinates θ and z.

With the assumption that the cylinder remains a cylinder after transformation, the displacement field $\underline{u}$ is as presented in Equation 2.1 in the cylindrical coordinates (where a quantity underlined once is vector).

$$\underline{u}(r,\theta,z) = \left(u_r(r), u_\theta(r,z), u_z(z)\right) \tag{2.1}$$

With the hypothesis of small displacements, the infinitesimal strain tensor $\underline{\underline{\varepsilon}}$ is defined in Equation 2.2 (where a quantity underlined twice is a tensor of order 2) in the vector basis ($\underline{e}_r$, $\underline{e}_\theta$, $\underline{e}_z$).

$$\underline{\underline{\varepsilon}} = \frac{1}{2}\left(\underline{\underline{grad}}(\underline{u}) + {}^t\underline{\underline{grad}}(\underline{u})\right) = \begin{pmatrix} \varepsilon_{rr} & \varepsilon_{r\theta} & \varepsilon_{rz} \\ \varepsilon_{r\theta} & \varepsilon_{\theta\theta} & \varepsilon_{\theta z} \\ \varepsilon_{rz} & \varepsilon_{\theta z} & \varepsilon_{zz} \end{pmatrix} \tag{2.2}$$

In the case of a hollow cylinder test, using Equation 2.1, the infinitesimal strain tensor $\underline{\underline{\varepsilon}}$ becomes as in Equation 2.3 in the vector basis ($\underline{e}_r$, $\underline{e}_\theta$, $\underline{e}_z$).

$$\underline{\underline{\varepsilon}} = \begin{pmatrix} \dfrac{\partial u_r}{\partial r} & \dfrac{1}{2}\left(\dfrac{\partial u_\theta}{\partial r} - \dfrac{u_\theta}{r}\right) & 0 \\ \dfrac{1}{2}\left(\dfrac{\partial u_\theta}{\partial r} - \dfrac{u_\theta}{r}\right) & \dfrac{u_r}{r} & \dfrac{1}{2}\dfrac{\partial u_\theta}{\partial z} \\ 0 & \dfrac{1}{2}\dfrac{\partial u_\theta}{\partial z} & \dfrac{\partial u_z}{\partial z} \end{pmatrix} \tag{2.3}$$

The stress tensor $\underline{\underline{\sigma}}$ can be written as in Equation 2.4 in the vector basis ($\underline{e}_r$, $\underline{e}_\theta$, $\underline{e}_z$). The sign convention in this manuscript is the convention of soils mechanics with compressive stresses being positive.

$$\underline{\underline{\sigma}} = \begin{pmatrix} \sigma_{rr} & \tau_{r\theta} & \tau_{rz} \\ \tau_{r\theta} & \sigma_{\theta\theta} & \tau_{\theta z} \\ \tau_{rz} & \tau_{\theta z} & \sigma_{zz} \end{pmatrix} \tag{2.4}$$

In order to link the stress tensor components with the external force *F*, the equilibrium of the upper surface of the hollow cylinder (surface normal to $\underline{e_z}$), projected on the direction $\underline{e_z}$ of the cylinder axis, is expressed in Equation 2.5.

$$F = \int \sigma_{zz} dS = \int_{r=R_i}^{R_e} \int_{\theta=0}^{2\pi} \sigma_{zz}(r, \theta, z = h)\, r\, d\theta dr \qquad (2.5)$$

For the torque *T* applied to the hollow cylinder, it is accessible by writing the momentum equilibrium of the upper surface relatively to the point O, projected on the direction $\underline{e_z}$, leading to Equation 2.6.

$$\begin{aligned} T &= \int \left(r\underline{e_r} + z\underline{e_z}\right) \wedge \left(\underline{\underline{\sigma}}.\underline{e_z}\right) dS\,.\,\underline{e_z} \\ &= \int_{r=R_i}^{R_e} \int_{\theta=0}^{2\pi} \tau_{\theta z}(r, \theta, z = h)\, r^2\, d\theta dr \end{aligned} \qquad (2.6)$$

Additional hypotheses are necessary to obtain simpler formulae for *F* and *T*.

If the assumption of a homogeneous stress field is made, the stress tensor component σ_{zz} is given in Equation 2.7 and the stress tensor component $\tau_{\theta z}$ in Equation 2.8.

$$\sigma_{zz} = \frac{F}{\left(\pi R_e^2 - \pi R_i^2\right)} \qquad (2.7)$$

$$\tau_{\theta z} = \frac{3T}{2\pi\left(R_e^3 - R_i^3\right)} \qquad (2.8)$$

If an isotropic linear elastic behaviour is supposed, then the constitutive equation of the material is the Hooke's law (Equation 2.9, where λ and μ are the Lamé constants of the material and $\underline{\underline{I}}$ represents the identity tensor of order two).

$$\underline{\underline{\sigma}} = \lambda\, tr\, (\underline{\underline{\varepsilon}})\underline{\underline{I}} + 2\mu\underline{\underline{\varepsilon}} \qquad (2.9)$$

Using Equation 2.3, the stress tensor can be written in the vector basis ($\underline{e_r}$, $\underline{e_\theta}$, $\underline{e_z}$) as in Equation 2.10.

$$\underline{\underline{\sigma}}(r, \theta, z) = \begin{pmatrix} \sigma_{rr}(r) & 0 & 0 \\ 0 & \sigma_{\theta\theta}(r) & \tau_{\theta z}(r) \\ 0 & \tau_{\theta z}(r) & \sigma_{zz} \end{pmatrix} \qquad (2.10)$$

And in this case the stress component σ_{zz} is actually the same than in the homogeneous case (Equation 2.7) but the stress tensor component $\tau_{\theta z}$ is now as in Equation 2.11.

$$\tau_{\theta z}(r) = \frac{2T}{\pi\left(R_e^4 - R_i^4\right)} r \qquad (2.11)$$

In both cases, homogeneous or isotropic linear elastic, using the balance of linear momentum, it is possible to derive the expressions of the other stress components (Equations 2.12 and 2.13).

$$\sigma_{r\theta} = \sigma_{rz} = 0 \qquad (2.12)$$

$$\sigma_{rr} = \sigma_{\theta\theta} = P \tag{2.13}$$

The state of stress in the sample can then be represented on an infinitesimal volume of material as in Figure 2.2.

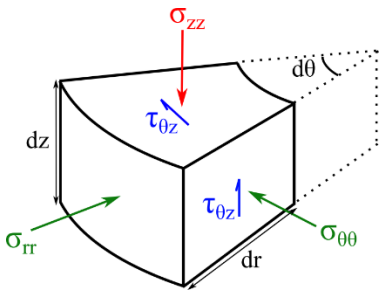

Figure 2.2 - Surface forces applied on an infinitesimal volume of material in a hollow cylinder test

In the hollow cylinder test, three independent stresses can be applied and it is possible to study the effect of rotation of principal stresses axes thanks to various stress paths. This has been done on materials like sand (Sauzéat 2003) but also on bituminous mixtures (Buttlar *et al.* 1999) for which hollow cylinder tests were used to study permanent deformation (Sousa 1986; Brown *et al.* 2013). As bituminous mixtures are coherent materials, it is not necessary to maintain the samples in impervious membranes and the external pressure is sometimes absent. In this case, only compression and shear can be applied to the mixture (Sousa 1986; Rueda *et al*. 2017).

The 2T3C HCA principle is the same than for a classical hollow cylinder test but with a bi-layered sample. All the equations presented above remain unchanged except in the area of the interface. It is chosen not to apply an external pressure on the side of the samples so that direct measurements can be conducted on the sample surface, in the interface area. As P = 0 and from Equations 2.12 and 2.13, the stress tensor in the 2T3C HCA sample is then as in Equation 2.14 where only components σ_{zz} and $\tau_{\theta z}$ are different from zero.

$$\underline{\underline{\sigma}} = \begin{pmatrix} 0 & 0 & 0 \\ 0 & 0 & \tau_{\theta z} \\ 0 & \tau_{\theta z} & \sigma_{zz} \end{pmatrix} \tag{2.14}$$

All stress paths are possible in the $\tau_{\theta z}$-σ_{zz} plane as presented in Figure 2.3, within the maximal achievable stress limits.

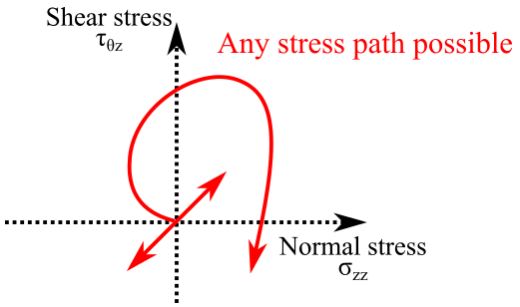

Figure 2.3 - Possible stress paths for the 2T3C HCA tests

2.1.2.Sample dimensions

The choice of sample dimensions is an equilibrium between having a good homogeneity of stresses, a good test repeatability, the maximum shear strength achievable and taking into account practical considerations.

Homogeneous tests, where the stress field and the strain field do not depend on the position, are very interesting since they give a direct access to the material properties without a complicated analysis and without restrictive assumptions. Hight *et al.* studied the repartition of stresses in a sand hollow cylinder sample subjected to a difference of pressure between the outside and the inside surfaces. The curvature of the sample and the friction at the ends of the sample proved to be important sources of inhomogeneity of the stress distribution. Using an indicator of the homogeneity of stresses based on the difference between the maximum value and the average value of stress tensor components in the thickness of the sample, it was concluded that the ratio of inner radius to outer radius should be superior to 0.8. However, this study supposed that the repartition of shear stresses in the thickness was uniform which is not a realistic assumption given that it is not even the case in the simple isotropic linear elastic case (Hight *et al*. 1983).

In the study of Sayao and Vaid, the material behaviour was supposed to be isotropic linear elastic for the shear stress calculation. The pressure on the outer surface and on the inner surface of the hollow cylinder were identical, like for the 2T3C HCA where the pressures are nil. A new indicator has been proposed. It is related to the ratio between principal stresses in the thickness. This indicator is named β_R and is defined in Equation 2.15 where R_{max}, R_{min} and R_{avg} are, respectively, the maximal, the minimal and the average ratio between the higher and the lower principal stresses in the thickness of the sample. The lower it is, the less heterogeneity there is in the thickness.

$$\beta_R = \frac{R_{max} - R_{min}}{R_{avg}} \tag{2.15}$$

It was shown that whereas an indicator involving only a ratio between maximal and minimal shear stress in the thickness seemed low enough, β_R could be unsatisfyingly high.

Based on this indicator and for a sample with a thickness between 20 mm and 26 mm, it is recommended that the ratio between inner and outer radius of the sample is between 0.65 and 0.82 and that the ratio between height of the sample and external diameter should be between 1.8 and 2.2 in order to obtain a homogeneous stress field (Sayao and Vaid 1991). These recommendations were taken into account in the 2T3C HCA design.

In order to apply a shear stress high enough to break the interface, the surface of the sample of the 2T3C HCA should be as small as possible. This implies that the thickness of the sample is thin. However, bituminous mixtures are heterogeneous materials, mixes of bitumen and aggregates. When they are modelled as a homogeneous material using the continuum mechanics frame, the tested sample volume should be large compared to a Representative Elementary Volume (REV) containing multiple aggregates in order to correctly represent the whole mix. Having a small sample compared to the aggregate size could decrease the test repeatability. For cement concrete, the REV is found to be at least 3 times larger than the nominal maximum aggregate size (NMAS) (Bazant 1989; Van Vliet 2000; Gitman *et al*. 2007). For bituminous mixtures, Romero *et al.* studied the size of a sample for the Superpave Shear Tester and found that a cylindrical sample with a 150 mm diameter and a 50 mm height was enough to have a good repeatability for a mixture with a NMAS of 25 mm (Romero and Masad 2001). In the previous example, the smallest dimension is only twice as big as the NMAS. Brown *et al.* chose a wall thickness of 50 mm, 5 times the NMAS, for their hollow cylinder test (Brown *et al*. 2013) when Sousa used samples with a 12.5 mm thickness (Sousa 1986) and Rueda *et al.* tested samples with a 25.4 mm thickness for a material with a NMAS of 9.3 mm (Rueda *et al*. 2017).

Regarding the previous conclusions, the thickness of the 2T3C HCA samples was chosen to be about 2.5 times bigger than the NMAS which seems to be the minimal size to guarantee a good test repeatability on bituminous mixtures. Many bituminous mixtures have a NMAS of 10 mm so the thickness of 25 mm is chosen. It also falls in the range studied by Sayao and Vaid. For torsion tests, the

principal dimension is the cylinder perimeter which is 54 cm (for the external perimeter) to be compared with the NMAS of 10 mm.

The laboratory made hollow cylinder samples of the 2T3C HCA are to be cored in a bi-layered slab 60 cm long, 40 cm wide and 15 cm high using a French wheel compactor (NF EN 12697-33+A1:2007). As the compaction is uneven on the sides of the slab, 5 cm of material are removed from the edges. This leaves a 50 x 30 cm^2 slab for the samples to be cored in (Figure 2.4). The maximal external diameter for a standard core drill to obtain 3 samples out of this slab is 182 mm and it leads to an external diameter of the 2T3C HCA samples of about 172 mm.

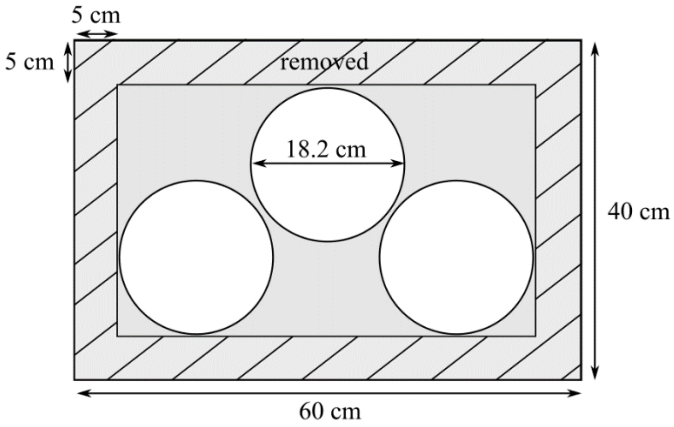

Figure 2.4 - Schematic of a laboratory made slab of bituminous mixture (NF EN 12697-33+A1) with 2T3C HCA samples cored out

In order to get a 25 mm thickness, the standard core drill of 122 mm in external diameter is chosen. The height of the sample is the height of the slab minus the parts sawn from the extremities of the sample.

The final dimensions of the hollow cylinder samples of the 2T3C HCA are: 172 mm for the external diameter (86 mm for the external radius), 122 mm for the internal diameter (61 mm for the inner radius) and thus a thickness of 25 mm (Figure 2.5). The sample height is close to 125 mm.

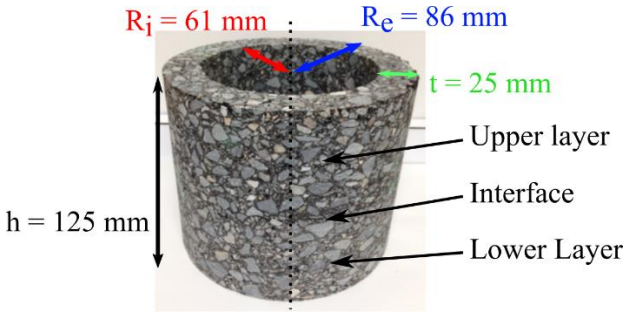

Figure 2.5 - 2T3C HCA sample dimensions

The thickness is between 20 and 26 mm and the ratio of inner radius to outer radius is 0.71 which is between 0.65 and 0.82. These dimensions ensure a good homogeneity of stresses in the sample. Stresses can be calculated using Equations 2.7 and 2.8 and are constant in the whole sample (in the mixture layers and at the interface). The ratio between height of the sample to outer diameter is here 0.73 which is far from the range of 1.8 to 2.2 recommended by Sayao and Vaid. This indicates that measurements should not be done in the areas close to the edges of the specimen. Even more so because the samples are glued at their extremities which is a different situation from the theoretical frame described in section 2.1.1.

2.1.3. Design of mechanical parts and climate chamber

A servohydraulic press (Instron 8800 MTL 8998) with an actuator that can generate independently an axial force and a torque is used to apply the loadings to the sample (Figure 2.6). This press was previously used to perform hollow cylinder tests on sand (Cazacliu 1996; Sauzéat 2003; Duttine *et al.* 2007). Because bituminous mixtures can be much stiffer than sand and because no confinement is required in the 2T3C HCA, new mechanical parts had to be designed to transfer the loadings from the press to the sample.

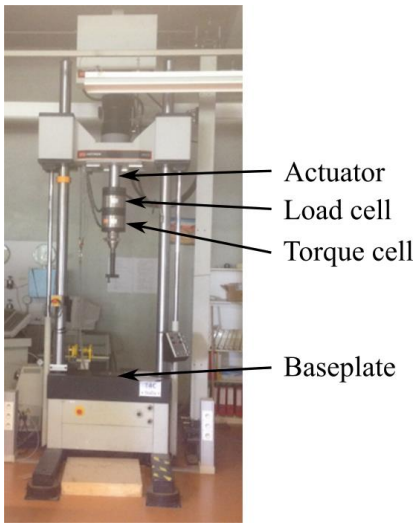

Figure 2.6 - Servohydraulic press used in the 2T3C HCA

The principle constraint for the design of the mechanical parts of the 2T3C HCA was the necessity to place a climate chamber around the sample. The chamber dimensions and the parts dimensions were chosen simultaneously. After a pre-design process where the concepts of the parts were defined, the final design and the machining were performed in collaboration with the local company REMT specialised in precision machining.

The global scheme of the 2T3C HCA is presented in Figure 2.7 with its most important dimensions. All the parts are made of stainless steel (except the aluminium caps) and they are designed to withstand the maximal loadings that can be applied by the hydraulic press. They are connected with each other using multiple screws in order to block the relative rotations. Some parts were left open so that the air could flow inside the sample.

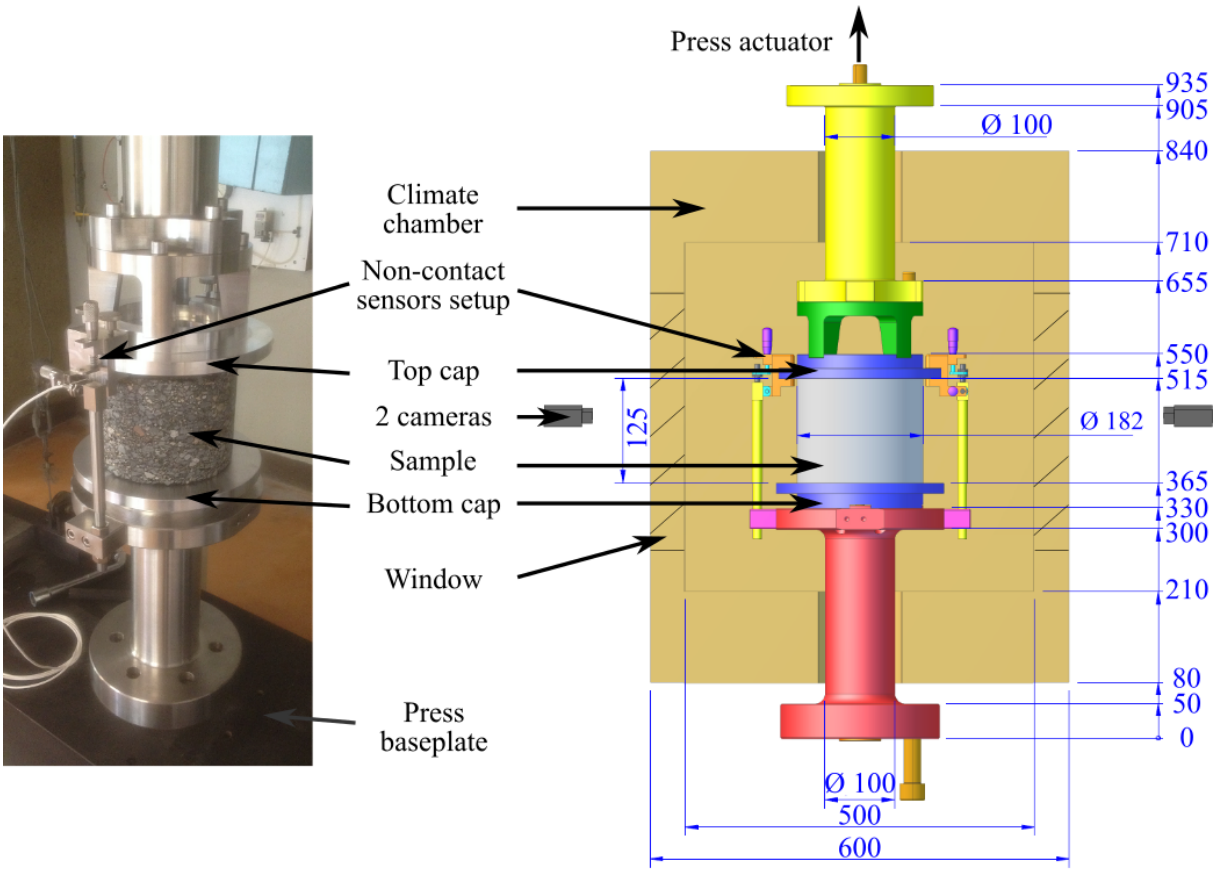

Figure 2.7 - Picture (on the left) and scheme (on the right) of the 2T3C HCA parts with a sample (dimensions in mm)

The 2T3C HCA samples are glued with epoxy resin to the aluminium caps (Figure 2.8). The caps were designed for hollow cylinder samples with variable dimensions (minimal internal diameter of 105 mm and maximal external diameter of 235 mm). A hole allows the air to circulate efficiently inside the hollow cylinder to guarantee a good temperature homogeneity in the sample.

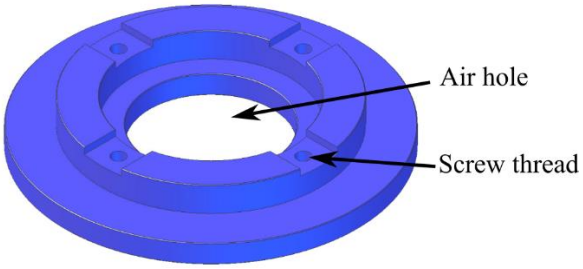

Figure 2.8 - 3D model of an aluminium cap for 2T3C HCA (bottom view, the samples are glued on the opposite and smooth side)

All the parts are designed to be centred with the press axis. However, the sample axis must also be aligned with the press axis. A specific device was produced (Figure 2.9) for this purpose. It ensures that the caps and the samples are centred during the gluing. This device can be used for samples with different sizes thanks to adjustable screws.

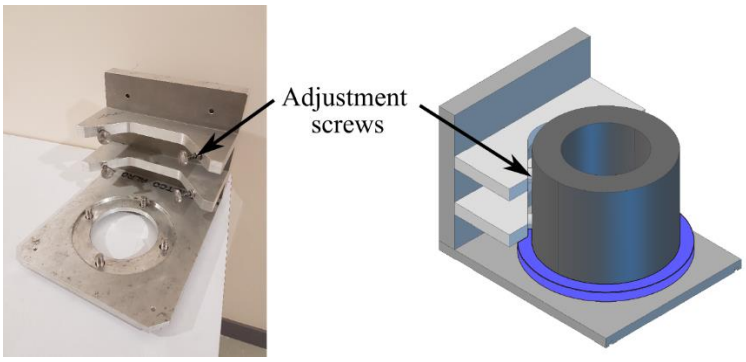

Figure 2.9 - Centring device for the gluing of 2T3C HCA samples (picture on the left, 3D model with the sample on a cap on the right)

After the sample is glued to the first cap (the top cap) using this device, it is fixed to the upper parts of the 2T3C HCA. The gluing of the second cap (the bottom cap) is performed directly on the press.

In the 2T3C HCA, the displacements between the top cap and the bottom cap are measured with non-contact sensors. They are fixed to the top cap using a fastener shown in Figure 2.10. Adjustment knobs make it possible to control precisely (within 1 µm) the distance between the sensors and their targets at the beginning of a test. The targets are located on an aluminium part fixed to the bottom cap.

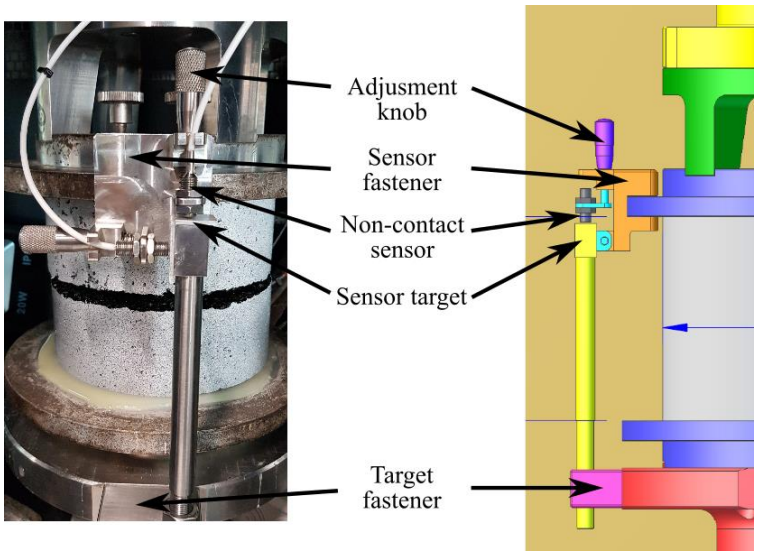

Figure 2.10 - Non-contact sensors setup (picture of the front view on the left, scheme of the side view on the right)

The climate chamber (Figure 2.11) was designed and made by the company BiA which answered a call for tender. It can regulate the temperature from -20 °C to 60 °C which is a classical range for tests on bituminous mixtures but it does not control the hygrometric conditions. Considering the gap between the columns of the press, the dimensions of the interior of the climate chamber were chosen as 600 mm for the width (maximum achievable), 500 mm for the height and 500 mm for the depth. Apertures with adjustable pieces of insulation allow the mechanical parts of the 2T3C HCA and the sensors cables to go through the chamber walls without air leaks.

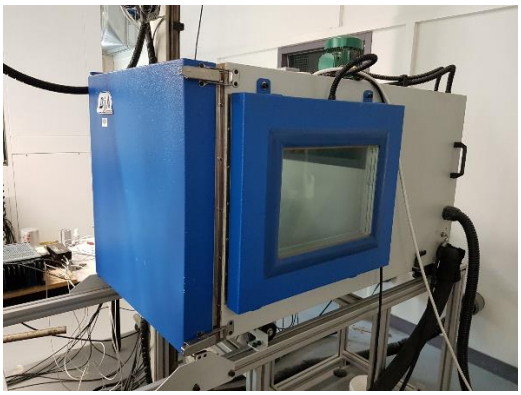

Figure 2.11 - Climate chamber for 2T3C HCA with windows on its sides

The principle feature of the climate chamber is the presence of two windows (400 mm x 400 mm each) on its sides so that pictures of the sample can be taken during tests with a controlled temperature. The interior of the climate chamber is painted in a matte black to prevent reflections on the sample and thermal resistances were imbedded in the window frame to prevent condensation at low temperatures by heating the window. The windows are centred on the useful volume. They are made of a thick multi-layered glass to lower their thermal conductivity and reduce the risk of condensation. A previous study showed that Digital Image Correlation (DIC) results were not affected by the presence of such a glass in front of the sample (Attia 2015) in accordance with the numerous examples of DIC being used with glasses between the cameras and the sample (Lyons *et al.* 1996; Eitner *et al.* 2010; Pinto *et al.* 2015).

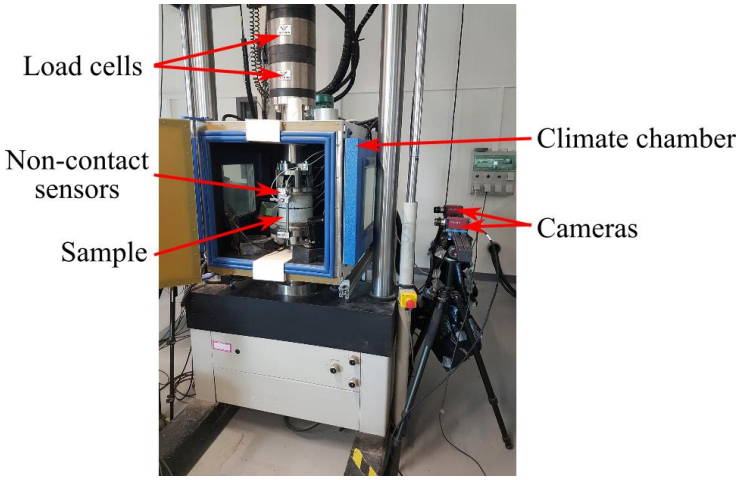

Figure 2.12 - Picture of the 2T3C HCA

In summary, the 2T3C HCA applies torsion and tension-compression but no confinement to hollow cylinder samples. The sample dimensions were chosen so that the stress state can be considered homogeneous and so that the sample is large compared to the representative elementary volume of bituminous mixtures ensuring *a priori* the repeatability of the test. The absence of confinement enables the optical measurement of the interface deformation. A climate chamber with windows allows cameras to take pictures of the interface even when the sample temperature is controlled. Special parts were also designed so that non-contact sensors can measure the displacement between the top and the bottom of the sample. A global picture of the 2T3C HCA is presented in Figure 2.12 with all its elements. The different measurement systems used during the tests are precisely described in the next section.

2.2. Measurement systems

2.2.1. Axial load cell, torque cell, position sensor and rotation angle sensor

Embedded in the hydraulic press actuator (Figure 2.6), two load cells give access to the values of the axial force and of the torque applied to the sample.

The axial load cell can measure dynamic forces up to ± 100 kN. For homogeneous stresses, using Equation 2.7, the maximal vertical stress σ_{zz} measurable for a 2T3C HCA sample is 8.67 MPa. The torque cell can measure torque up to ± 2000 Nm. The maximum measurable shear stress $\tau_{\theta z}$ related to torsion is then 2.33 MPa using Equation 2.8 for the homogeneous case.

Along with these load cells, two other sensors measure the actuator vertical position within a range of ± 75 mm and the rotation angle of the actuator within a range of ± 45 °.

A retrofit was conducted to modernise the press control system of the hydraulic press. The press sensors were calibrated during this operation. It is possible to control independently the axial force and the torque following any possible path, monotonic, cyclic or else. The axial force can be controlled with an estimated accuracy of 0.01 kN and the torque with an estimated accuracy of 0.1 Nm.

2.2.2.Non-contact sensors

Two pairs of non-contact sensors allow measuring the global displacements between the top and the bottom of the samples, more precisely between the top cap and the bottom cap (Figure 2.13).

These non-contact sensors work with eddy currents (Foucault's currents). They measure the distance between a metallic target and themselves. They can measure displacements with an accuracy of about 0.1 µm on a 1000 µm range. A calibration is performed before they are used with a target in the same material than the actual targets. It is important that the target and the sensor are correctly aligned and this is ensured by the 2T3C HCA setup depicted in Figure 2.10.

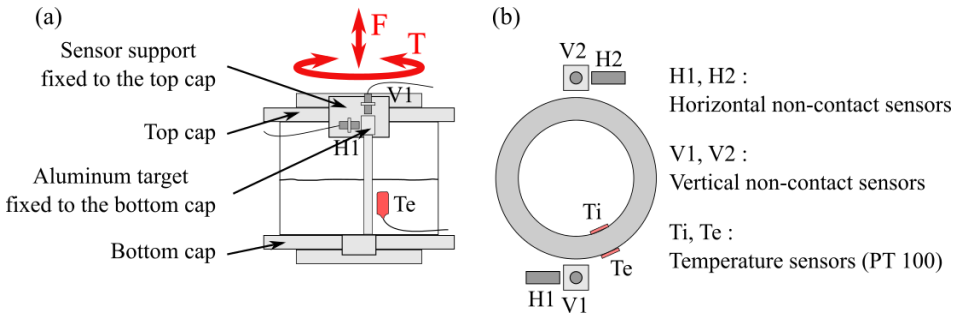

Figure 2.13 - 2T3C HCA sample instrumentation: (a) side view, (b) top view

Sensors are fixed to the top cap and their aluminium target is fixed to the bottom cap. On each side of the sample there is one pair of non-contact sensors with one sensor that measures vertical displacement and one sensor that measures the horizontal displacement related to the rotation (Figure 2.13). The value of global vertical displacement is taken as the average of the values of the two sensors measuring the vertical displacement (V1 and V2 in Figure 2.13). The global horizontal displacement related to the rotation is obtained in a similar way (with H1 and H2 in Figure 2.13). The rotation displacement at the level of the sample is proportional to the rotation displacement measured by non-contact sensors with a coefficient equal to the ratio of external diameter of the hollow cylinder (86 mm) to the distance of the non-contact sensors from the centre (153 mm). Tests can be performed by the hydraulic press under displacement control using the non-contact sensors values.

2.2.3.Temperature probes

Two PT100 sensors are used to measure temperature during the test (Figure 2.14).

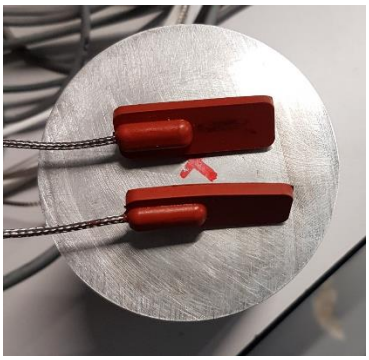

Figure 2.14 - PT100 sensors

They were calibrated so that their measurement range is between - 50 °C and 100 °C. They are placed on the surface of the sample using rubber band. One of them is located inside the hollow cylinder and the other one is located on the outside of the hollow cylinder, across the thickness of the sample as presented in Figure 2.13. It is thus possible to check the homogeneity of the temperature field in the sample, assuming the thickness is small.

2.2.4.Digital Image Correlation (DIC)

3D DIC finds the displacements in the three dimensions at the surface of the hollow cylinder during 2T3C HCA tests. A specific analysis method is used to compute the displacement gaps at the interface and the strain in the bituminous mixtures layers. This section presents the principle of 3D DIC and the experimental setup in the 2T3C HCA.

2.2.4.1. Principle of in-plane DIC

Digital Image Correlation is a non-destructive and non-intrusive measurement technique. It gives access to the displacement field at the surface of a deformable material. A digital camera takes pictures of a sample before and after its transformation. In-plane DIC only works for pictures of a plane surface with the displacement occurring in its plane. The idea of DIC is to select a point in the reference picture, which is the picture taken before the transformation, and locate it in the deformed pictures, taken after transformation, to then deduce its displacement.

First, an area of interest is defined in the reference picture: it corresponds to all the points where the calculations will be made, its size is usually of the same order of magnitude as the sample dimensions. Then, a subset of the reference picture is chosen around a selected point M_0 of which we want to know the displacement, called the point of interest (Figure 2.15). It is a small square, with sides usually a few dozen pixels long (the length represented by a pixel depending on the camera sensor and on the distance between the camera and the surface). A correlation algorithm is then run to find the subset in the deformed picture that looks the most like the reference subset. The centre M of the deformed subset is then obtained and the displacement is defined as the vector $\underline{M_0M}$.

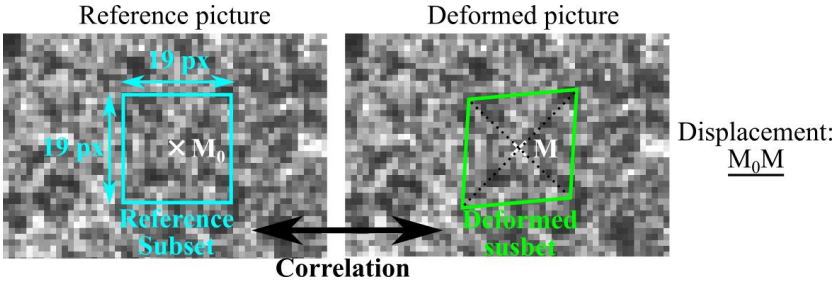

Figure 2.15 - Illustration of DIC principle

Usually the pictures are monochromatic and each pixel is represented by its grey level, a number between 0 (black) and 255 (white) for an 8-bit colour depth. An interpolation is performed on the area of interest to obtain the analytical function *I(x,y)* of grey level for non-integer values of pixel positions *(x,y)* in the picture. Examples of interpolations are presented in Figure 2.16.

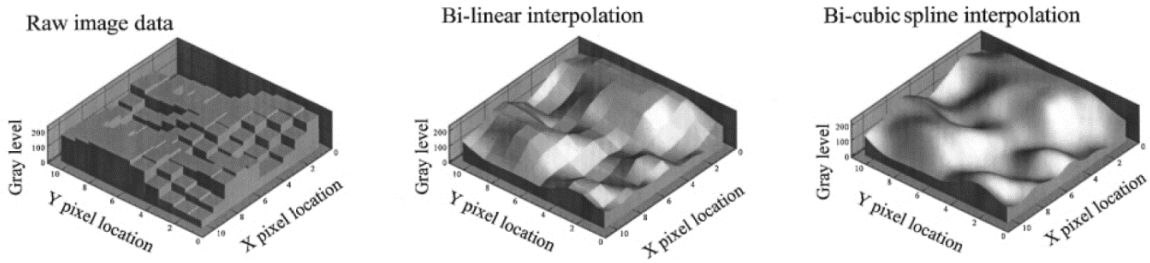

Figure 2.16 - Three representations of the grey level intensity values (Sutton *et al*. 2000)

Different correlation algorithms exist. The criterion *C* used for the Sum of Squared Differences (SSD) correlation method is defined as in Equation 2.16. Other criterions exist like the magnitude of intensity value difference, the cross-correlation or the normalized cross-correlation.

$$C = \int_{S_0} [I_0(x_0 + \Delta x, y_0 + \Delta y) - I(x_0 + \Delta x + \varepsilon, y_0 + \Delta y + \zeta)]^2 \, dS \qquad (2.16)$$

In Equation 2.16,

- S_0 is the reference subset
- x_0 and y_0 are the coordinates of the point of interest M_0
- Δx and Δy are the variables of integration, they describe the positions of all the points of the reference subset
- $I_0(x,y)$ is the grey level intensity in the reference picture of the point with the coordinates (x,y), and I is the grey level intensity in the deformed picture
- ε and ζ represent the displacement of M_0.

C is a function of x_0, y_0, ε and ζ. The lower C is, the more alike the reference subset around M_0 and the deformed subset around the point $M(x_0+\varepsilon,y_0+\zeta)$ are. For each point M_0, the goal of the correlation algorithm is to find the values of ε and ζ that lead to the lowest possible value of C.

To improve the criterion, two correlation parameters a and b are introduced to compensate for eventual changes in the global lighting of the surface, in scale and in mean value. The adjusted grey level intensity I^* in the deformed picture is searched as a linear function of I: $I^* = aI+b$.

To take into account an infinitesimal transformation of the shape of the reference subset from a square into a parallelogram, the values ε and ζ are defined as in Equation 2.17 and Equation 2.18 where u is the displacement component along the x axis and v the displacement component along the y axis.

$$\varepsilon = u + \Delta x \frac{\partial u}{\partial x} + \Delta y \frac{\partial u}{\partial y} \qquad (2.17)$$

$$\zeta = v + \Delta x \frac{\partial v}{\partial x} + \Delta y \frac{\partial v}{\partial y} \qquad (2.18)$$

The final criterion C is thus a function of x_0, y_0, u, v, $\frac{\partial u}{\partial x}, \frac{\partial u}{\partial y}, \frac{\partial v}{\partial x}, \frac{\partial v}{\partial y}$, a and b. For a given $M_0(x_0,y_0)$, the algorithm finds the set of parameters that minimizes C and keeps only the values of displacement u and v corresponding to the displacement vector $\underline{M_0M}(u,v)$. These displacement values are expressed in number of pixels and they still have to be converted in a length (in meters) by means of a calibration,

usually conducted before the test. A grid of known mesh is captured in the actual test configuration and a simple algorithm relates a number of pixels to a length.

DIC accuracy is about 1/100th of a pixel in the best case scenario. The subset size is of most importance for DIC accuracy. With small subsets, the calculation time is short and it is possible to know the displacement of a lot of points but there is an important random noise and the correlation does not always succeed. The noise is diminished with large subsets but less information is obtained on the area of interest because of the subset overlapping. However, the optimal subset size strongly depends on the surface aspect. The correlation algorithm can only work efficiently if the studied surface presents a random pattern. If not, a subset could correspond to different parts of the materials. Some materials present naturally a random pattern at their interface and it seems that sawn bituminous mixtures do too because of the random distribution of aggregates and bitumen (Figure 2.17, on the left). But the scale of the heterogeneities does not allow the study of small deformations.

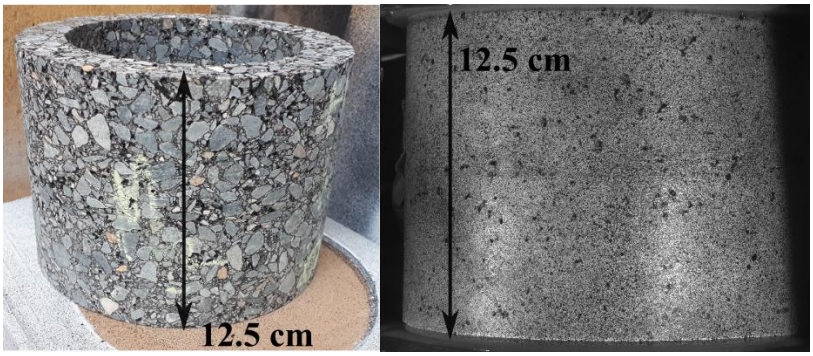

Figure 2.17 - 2T3C HCA samples, with sawn surface on the left, with a speckle pattern on the right

So a speckle pattern is usually applied on bituminous mixtures to improve DIC accuracy (Romeo 2013). A thin coat of white paint is applied to cover the surface. A black speckle pattern is then created using an aerosol spray (Figure 2.17, on the right). The speckles are small, distributed randomly and the contrast between the speckles and the white paint is good. This ensures that the correlation algorithm converges even for small subsets and small deformations.

2.2.4.2. Principle of 3D DIC: stereocorrelation

3D DIC measures the displacements in the three dimensions. And like humans that need two eyes to see in three dimensions, two pictures of the same surface must be taken at the same time, at each state of deformation, for stereocorrelation to find the 3D displacements. The points of view of the two cameras must have a minimum angle between them but it must not be too important because the point of interests have to be seen by the two cameras.

Before a test with 3D DIC, a stereocalibration of the camera system is needed. Its purpose is to find the equations that link the spatial position of a point of the studied surface to the pixels of the images taken by the two cameras where it can be seen. These equations depend on the relative position and orientation of the cameras and on the parameters related to the digital sensors of the cameras. The stereocalibration consists in taking pictures of a target, usually with black dots (some of them are markers) on a white background arranged in a mesh of known dimensions (Figure 2.18).

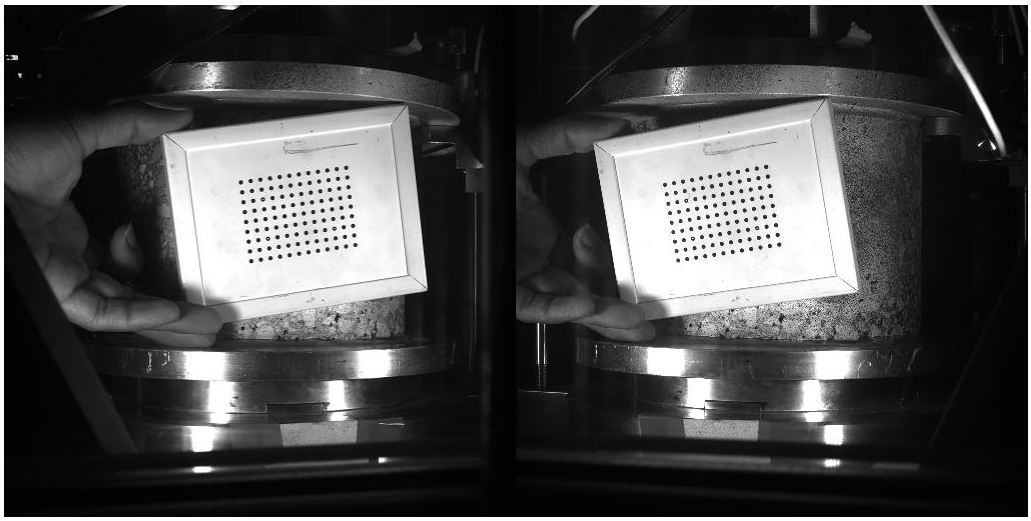

Figure 2.18 - Pictures of the calibration grid for stereocorrelation taken at the same time by two different cameras (one on the left, and one on the right)

Pictures are taken with different grid orientations in the three dimensions. About 15 pictures are necessary to obtain the parameters of the cameras using a specific program. After this calibration, one pixel on one of the two images can be associated with the spatial position of the material that it represents. This position is expressed in a coordinate system related to the studied surface but can then be expressed in a coordinate system related to one of the cameras.

3D DIC can be used to profile surfaces in three dimensions. The principle is to find the tangent plane of each point of the studied surface to recreate the 3D cartography. Around each point of interest, a subset is chosen in the picture taken by one of the two cameras. The subset is then projected on a virtual plane, also called candidate plane, defined by parameters controlling its position and orientation. From the spatial location of the subset projection, using the calibration results, a back projection is performed to associate a subset in the second picture to the subset projection, and thus to the subset in the first picture (Figure 2.19).

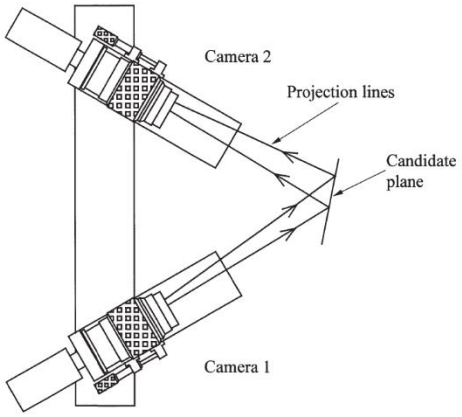

Figure 2.19 - Back projection principle for 3D profiling with 3D DIC (Sutton *et al*. 2000)

When the candidate plane is tangent to the surface at the point of interest, the two subsets should represent the same part of the material and be very similar. A correlation algorithm is then used to find the parameters of the candidate plane that results in the best resemblance of the original subset and of the back projected subset with a criterion similar to the one presented in section 2.2.4.1. These parameters define the tangent plane to the surface at the point of interest. The 3D surface is then obtained from all the tangent planes of the surface.

The principle of the calculation of displacements in three dimensions requires two virtual planes (Figure 2.20). One pair of pictures is taken in the reference state and one pair of pictures is taken in the deformed state. The area of interest is defined in the picture taken by the first camera (chosen arbitrarily) in the reference state. Around each point of interest, a subset is defined. A first virtual plane, called candidate plane, is introduced. It is used to define a back projected subset in the picture of the second camera in the reference state.

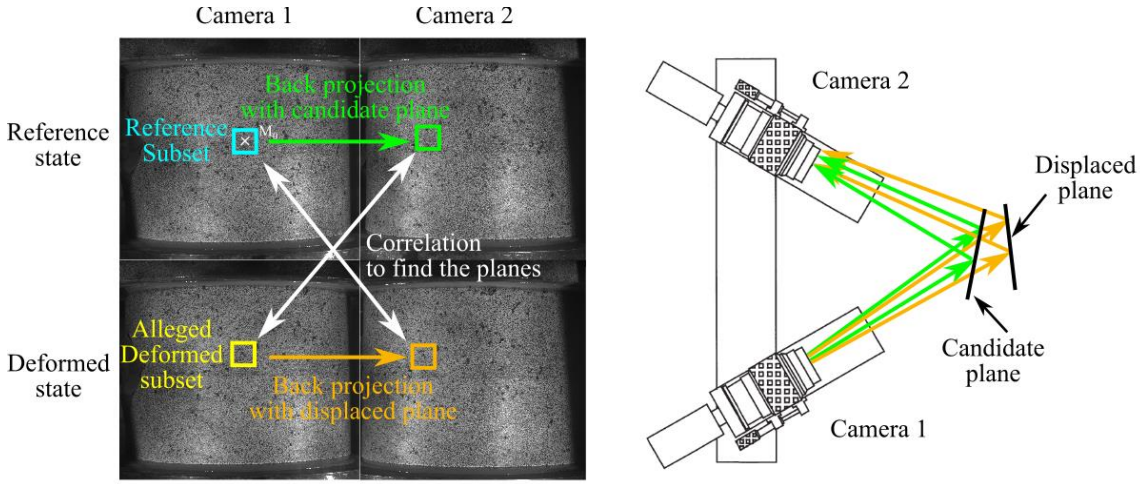

Figure 2.20 - Principle of 3D DIC

In the deformed state, a deformed subset is arbitrarily chosen in the picture taken by the first camera. A second virtual plane, called displaced plane, is introduced to project this subset on the picture taken by the second camera in the deformed state. At this point, there are four subsets in four different images. The correlation algorithm finds then the deformed subset and the parameters of the two planes that gives the four most similar subsets. The displacements of the point of interest are then deduced from the relative positions and orientations of the candidate plane and of the displaced plane. They are expressed in the coordinate system related to the 3D profile of the surface.

2.2.4.3. 3D DIC setup in the 2T3C HCA

The 3D DIC is used in the 2T3C HCA. Two pairs of CCD cameras Pike F-421B/C are placed on each side of the sample as presented in Figure 2.21. They are placed on rigid and adjustable supports. Their resolution is 4 Mpx and their maximum capture frequency is 10 Hz. They are placed at a distance of 60 cm from the surface of the samples and they are separated by 30 cm, the angle between their optical axis (pan angle) is then about 30 °. At this distance and knowing the sensor characteristics one pixel on a picture of the sample represents 151 µm of material. Birgisson *et al.* showed that an accuracy of 1/100th was accessible experimentally for in-plane displacements (Birgisson *et al.* 2009). It would represent an accuracy of 1.51 µm in the 2T3C HCA test.

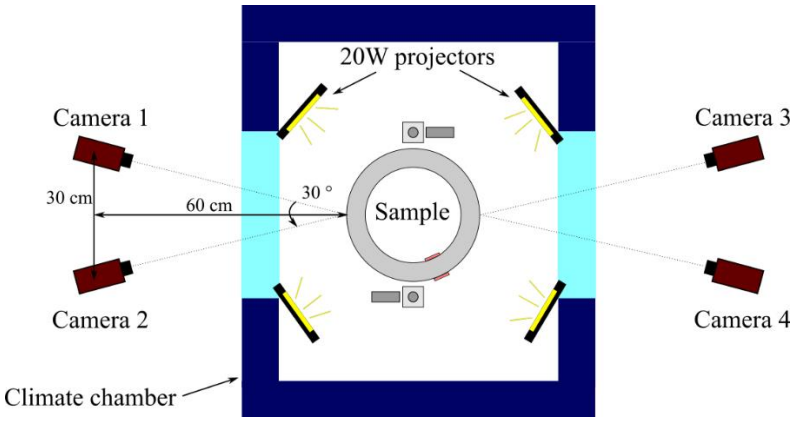

Figure 2.21 - 3D DIC setup in the 2T3C HCA test

Lighting is performed by four 20W LED projectors that are placed inside the climate chamber. The colour of the projector is a cold white. They ensure a good contrast between the speckle pattern and the white covering of the sample. There is a door at the front of the climate chamber to calibrate the system with all the other elements at their place. It is very important that the cameras are not moved after the stereocalibration is performed. The calibration is realized with a grid with 12 * 9 dots separated by 5 mm (presented in Figure 2.18).

The programs Vic Snap (for picture acquisition) and Vic 3D (for correlation), both developed by Correlated Solutions, were used to perform 3D DIC.

Vic Snap allows choosing the capture time of a picture (the aperture time, about 6 ms in the 2T3C HCA tests) in order to adjust the luminosity. It can program the picture acquisition according to a precise timeline and acquire analogic data each time a picture is taken.

Vic 3D assumes all the correlation functions after the tests. It performs the stereocalibration from the pictures of the grid. Different tools are available to draw the area of interest on the reference image (Figure 2.22). For the correlation, it allows choosing the subset size, the calculation step between the points of interest and the start point of calculation. The results can be expressed in various coordinate systems, and especially in the cylindrical coordinates associated to a cylindrical surface. This feature has been used for the 2T3C HCA tests. Different analysis tools are also available for obtaining the averages of displacements on a line or on a surface and to extract displacements profile along a line.

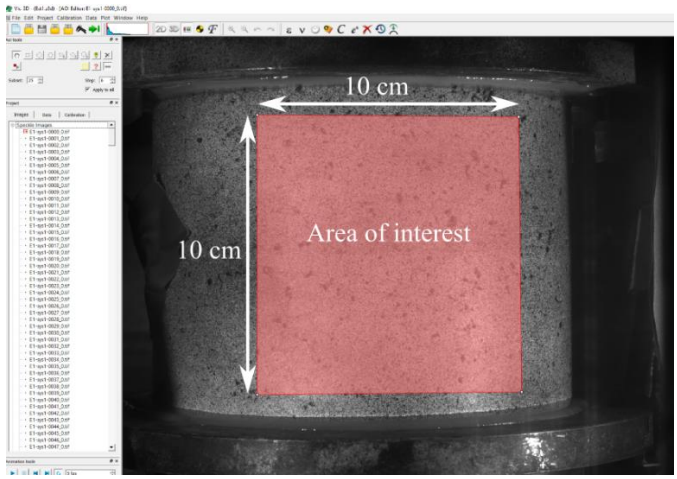

Figure 2.22 - Area of interest on a 2T3C HCA sample in the Vic 3D interface

The area of interest is chosen to represent about 10 x 10 cm^2 of the hollow cylinder surface, centered on the interface and limited in height so that the points close to the glued extremities of the sample are not taken into account in the calculations (Figure 2.22). The subset size is fixed at 25 pixels x 25 pixels

and the step between two points of interest is 6 pixels (justification in section 2.3.2). A rough estimation of the number of calculation points would be 10,000 per picture.

A function exist in Vic 3D to compute the local strain from the displacement. But the displacement results for small deformations for bituminous mixtures can be quite dispersed because of the difference of behaviour between aggregates and bitumen and because of a calculation noise. The computation of strain with Vic 3D is then not accurate for small strain because of a high variability between close points of interests. An analysis method of the displacement results from 3D DIC is proposed in section 2.3.1. It allows finding the strain tensor components ε_{zz}, $\varepsilon_{\theta z}$, $\varepsilon_{\theta\theta}$ in the layers and the relative displacements at the interface in the vertical direction Δu_z and in the horizontal direction Δu_θ.

2.2.5.Recapitulation and acquisition systems

A recapitulation of all the measurement systems and measured quantities with the 2T3C HCA is presented in Table 2.1.

Table 2.1 - Measured quantities with 2T3C HCA

Measurement system	Measured quantities	Symbol	Unit
Axial load cell	Axial force	F	kN
	→ Vertical stress	σ_{zz}	MPa
Actuator position sensor	Vertical position	Z	mm
Torque cell	Torque	T	Nm
	→ Shear stress	$\tau_{\theta z}$	MPa
Rotation angle sensor	Rotation angle	Θ	°
Non-contact sensors	Global vertical displacement in the sample	u_{z_g}	µm
	Global rotation displacement in the sample	u_{θ_g}	µm
PT100 probes	Inner surface temperature	T_i	°C
	Outer surface temperature	T_e	°C
3D DIC	Displacement field	(u_r,u_θ,u_z)	mm
	→ Vertical strain	ε_{zz}	µm/m
	→ Shear strain	$\varepsilon_{\theta z}$	µm/m
	→ Radial strain	$\varepsilon_{\theta\theta}$	µm/m
	→ Vertical displacement gap at the interface	Δu_z	mm
	→ Horizontal displacement gap at the interface	Δu_θ	mm

The press control system that regulates the hydraulic group presents two acquisition card: one for the measurements related to axial displacements and forces and one for the measurements related to rotations and torques. They possess four channels each. The axial force and actuator vertical position measurements take two of the first card channels. The two vertical non-contact sensors are connected into the two remaining channels. Similarly, the torque cell, the rotation angle sensor and the two horizontal non-contact sensors are connected in the four channels of the second acquisition card. An additional analogical card in the press control system can output the eight channels.

The cameras have their own acquisition card that controls the picture capturing. This acquisition card presents eight analogical input channels. The measurements obtained with the press control system are inputted in the camera acquisiton card so that they are acquired at the same time than a picture is taken. It has been verified that the derivation of these channels induced a negligible time lag (inferior to 1 ms).

An external acquisition card with 16 channels is also used to obtain all the measurements, apart from the digital pictures, on only one acquisition card. The eight channels from the press control system and the two temperature probes are the input of this external card.

A global scheme explaining the different acquisition systems is presented in Figure 2.23.

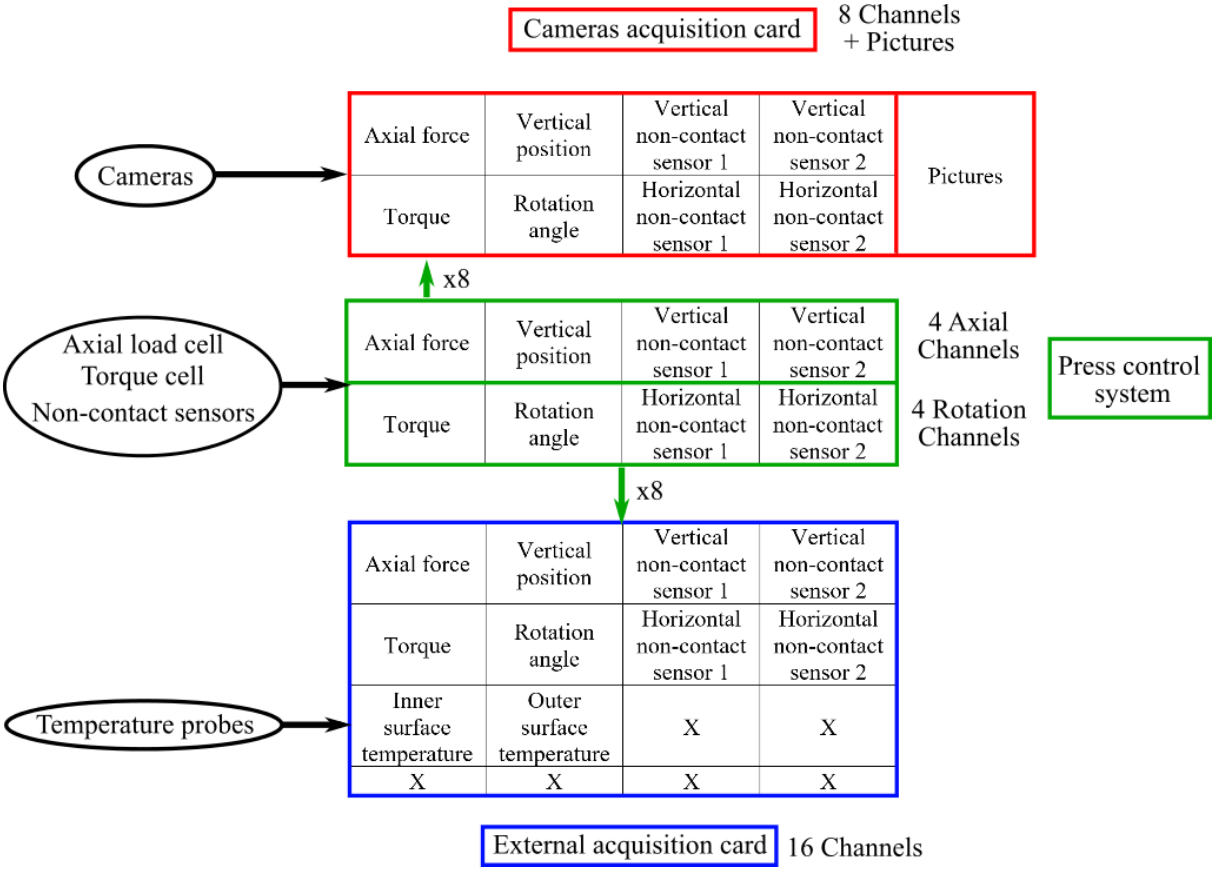

Figure 2.23 - Acquisition systems in the 2T3C HCA

2.3. Analysis of DIC results for bituminous mixtures and interfaces

In order to improve the accuracy of strain calculation in the bituminous mixtures layers and to find the displacement gap at the interface, a specific analysis method of the 3D DIC results has been developed at the University of Lyon/ENTPE during this thesis. In this section, its principle is explained

and the results of a parametrical study to optimise the method are presented. In this section only, a positive vertical displacement corresponds to an extension.

2.3.1. Computation of strain in the layers and of displacement gaps at the interface

2.3.1.1. Computation of the strain tensor components ε_{zz}, $\varepsilon_{\theta z}$, of the vertical displacement gap at the interface Δu_z and of the horizontal displacement gap at the interface Δu_θ

Using Vic 3D, the displacements in the three dimensions at the surface of deformed hollow cylinders can be expressed in the cylindrical coordinates: (u_r, u_θ, u_z). There exists a calculation noise in the displacement field related to the correlation. To illustrate this point, a small experiment was performed. It consisted in applying no loading to a 2T3C HCA sample. Pictures were taken quickly after the beginning of the test so that they all represented the same state of deformation. Vertical displacements obtained with 3D DIC at the surface are presented in Figure 2.24. It can be seen that even when no deformation is applied to the sample the DIC results show displacements different from 0, varying between + 2 µm and – 2 µm.

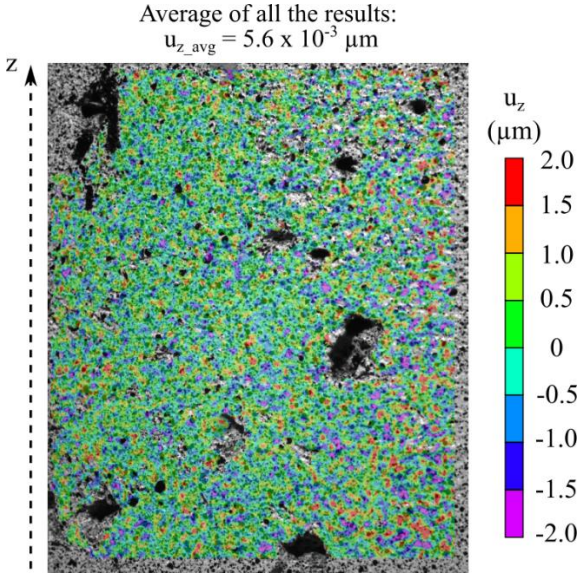

Figure 2.24 - Calculation noise for the vertical displacement u_z obtained with 3D DIC when no deformation is applied compared to the reference state

Yet the average of the displacements values for all the points of interest is close to 0 since it is 5.6 x 10^{-3} µm. The idea of the proposed analysis method is to use averaged displacements values to find the strain in the bituminous mixtures layers and to deduce the displacement gap at the interface.

First, horizontal strips are drawn using a Vic 3D tool on a deformed picture of a 2T3C HCA sample with two layers and an interface where the displacements are already calculated (Figure 2.25). The strips are 100 mm long and 4 mm high. There are 12 strips in each layer for 2T3C HCA samples, the number of strips can be adapted for samples with different dimensions. The averaged value u_{z_avg} of the vertical displacements of all the points in a strip is then affected to the coordinate z_{centre} of the centre of this strip. 12 points in the diagram z-u_z are then obtained in each layer.

From Equation 2.3 in section 2.1.1, the strain tensor component ε_{zz} expression is given in Equation 2.19 where u_z is the vertical displacement.

$$\varepsilon_{zz} = \frac{\partial u_z}{\partial z} \tag{2.19}$$

As the sample dimensions were chosen so that the test is homogeneous (section 2.1.2), the strain field is uniform in the bituminous mixtures layers and the vertical displacement is then a linear function of the z coordinate: $u_z = z.\varepsilon_{zz} + b$ with b a parameter independent from z. The slope of this line gives a direct access to the strain tensor component ε_{zz}.

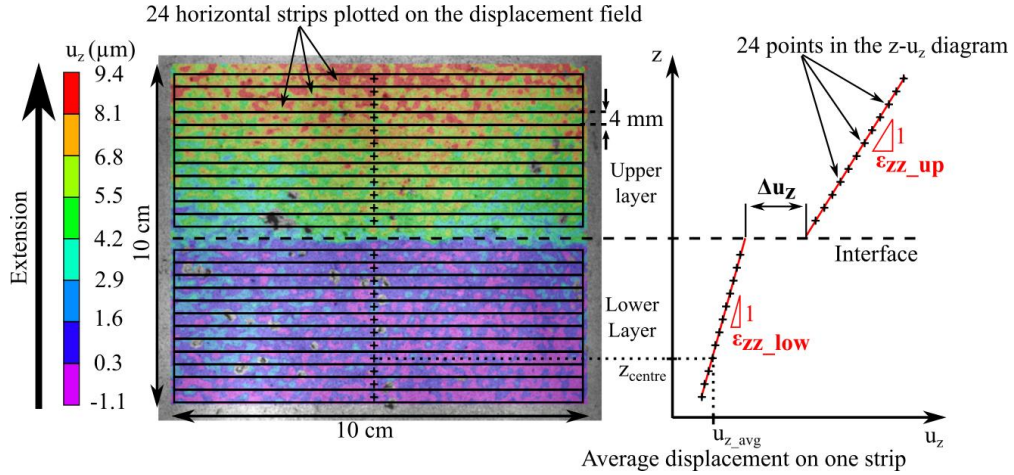

Figure 2.25 - Illustration of the analysis method to compute ε_{zz} in each layer and the displacement gap Δu_z at the interface (picture with a global extension of the sample of 12.5 µm and no rotation)

Two linear regressions are then performed to obtain the slope and thus the strain tensor component ε_{zz} in each layer. It is observed that the two lines found this way do not intersect at the position of the interface (determined visually, see section 2.3.2.3). The end of the upper line corresponds to the vertical displacement at the bottom of the upper layer when the end of the lower line is the vertical displacement at the top of the lower layer. The difference in these displacements is named vertical displacement gap Δu_z and characterises the interface deformation. This definition implies that the interface has no thickness but it is possible to find negative vertical displacement gaps corresponding to a "contraction" of the interface. Examples of values observed during a real experiment in the small strain domain are shown in Figure 2.26. It can be seen that the assumption of homogeneity of the sample is valid. It is only for very low global displacements (less than 1 µm between top and bottom of a layer) that linear regressions might fail.

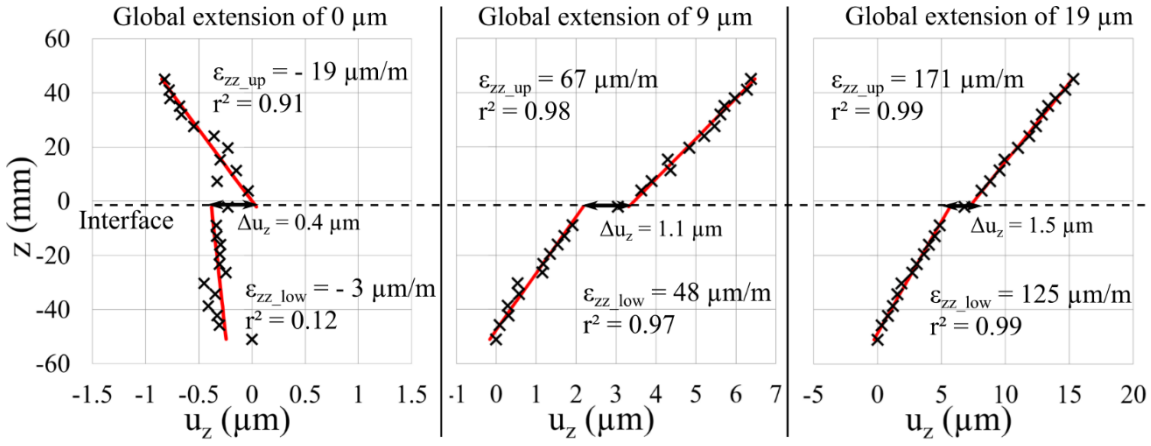

Figure 2.26 - Examples of computations of ε_{zz} in each asphalt layers and the displacement gap Δu_z at the interface for three states of deformation (from a cyclic tension-compression test with no shear stress, sample D/C-2, T = 10 °C, f = 0.3 Hz, see Chapter 3)

A similar procedure is performed to find the strain tensor component $\varepsilon_{\theta z}$ in each asphalt layers and the displacement gap Δu_θ at the interface using this time Equation 2.20 (derived from Equation 2.3) and the results of 3D DIC for the component u_θ of the displacement field.

$$\varepsilon_{\theta z} = \frac{1}{2}\frac{\partial u_\theta}{\partial z} \tag{2.20}$$

Indeed, as the test is homogeneous, the strain field is uniform in the bituminous mixtures layers and the horizontal displacement is then a linear function of the *z* coordinate: $u_\theta = z.2\varepsilon_{\theta z} + c$ with *c* a parameter independent from *z*.

The same horizontal strips are used for the study of ε_{zz} and $\varepsilon_{\theta z}$. Examples of calculation for $\varepsilon_{\theta z}$ and Δu_θ are presented in Figure 2.27.

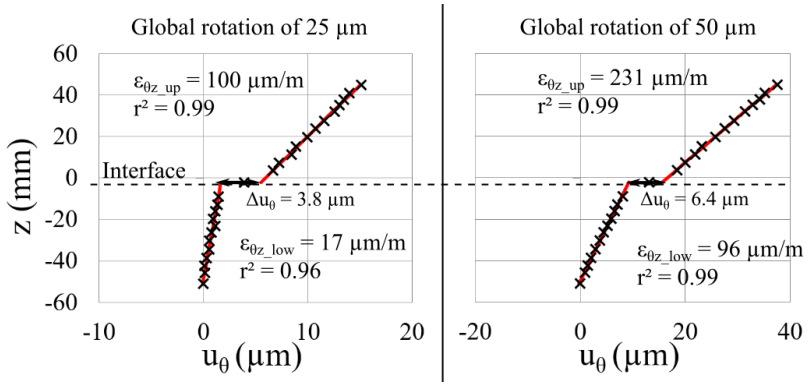

Figure 2.27 - Examples of computations of $\varepsilon_{\theta z}$ in each asphalt layers and the displacement gap Δu_θ at the interface for two states of deformation (from a cyclic torsion test with no vertical stress, sample D/C-2, T = 10 °C, f = 0.01 Hz, see Chapter 3)

Once these calculations are performed with the two pairs of cameras, a value of each quantity is obtained for each side of the sample. The two pairs of cameras are synchronized and the averaged values of ε_{zz}, $\varepsilon_{\theta z}$, Δu_z, Δu_θ can then be calculated. So for each of these quantities, only one result is obtained for each state of deformation (from four synchronized pictures: two pictures of one side and two pictures of the other side).

2.3.1.2. Computation of the strain tensor component $\varepsilon_{\theta\theta}$

From Equation 2.3, the strain tensor component $\varepsilon_{\theta\theta}$ in a layer can be written as in Equation 2.21 in a hollow cylinder test.

$$\varepsilon_{\theta\theta} = \frac{u_r}{r} \tag{2.21}$$

The displacement component u_r in the layers is obtained with 3D DIC but it is very small for tests in the small strain domain, close to the calculation noise. So a direct calculation induces a high variability of the results. As the 2T3C HCA sample remains in a shape of a hollow cylinder during a test, the strain tensor component $\varepsilon_{\theta\theta}$ is also equal to the relative variation of the external perimeter of the cylinder between deformed and reference state. A method to obtain $\varepsilon_{\theta\theta}$ from this property was developed.

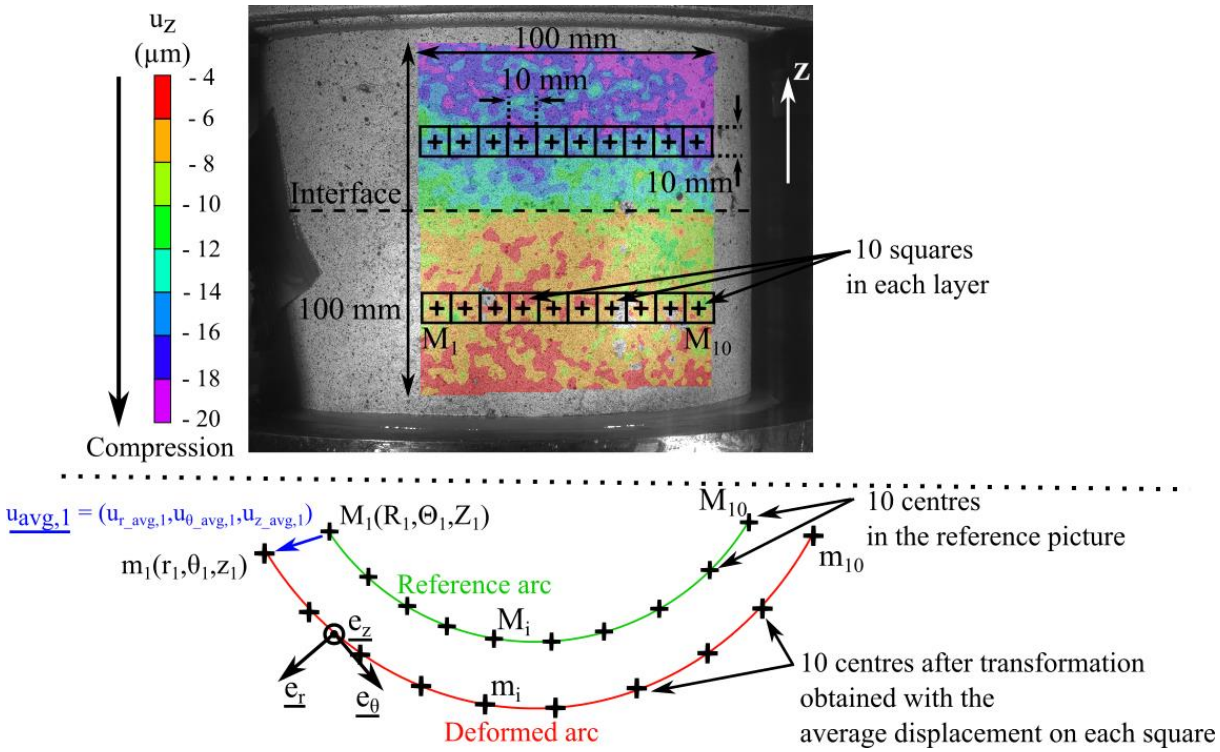

Figure 2.28 - Illustration of the analysis method to compute $\varepsilon_{\theta\theta}$ in each layer (picture with a global compression of the sample of 25 µm and no rotation)

In each layer, about 10 squares (10 mm sides) are drawn on the reference picture so that the central points of the strips are situated along an arc at the surface of the sample (Figure 2.28). The position of the centres M_i (R_i,Θ_i,Z_i) of the squares in the reference picture are known as a result of 3D DIC. The length L of the reference arc is obtained using Equation 2.22.

$$L = \sum_{i=1}^{9} \left\| \underline{M_i M_{i+1}} \right\| \tag{2.22}$$

For each state of deformation, the average values of the three displacement components in each square ($u_{r\_avg,i}$,$u_{\theta\_avg,i}$, $u_{z\_avg,i}$) are affected to the centre M_i of the square. The coordinates of the centre $m_i(r_i,\theta_i,z_i)$ after transformation are obtained using these average values as presented in Equations 2.23, 2.24 and 2.25.

$$r_i = R_i + u_{r\_avg,i} \tag{2.23}$$

$$\theta_i = \Theta_i + \frac{u_{\theta\_avg,i}}{R_i} \tag{2.24}$$

$$z_i = Z_i + u_{z\_avg,i} \tag{2.25}$$

In a hollow cylinder test, the centres m_i of the squares after transformation are also situated along an arc, called the deformed arc. The length l of the deformed arc is obtained using Equation 2.26.

$$l = \sum_{i=1}^{9} \left\| \underline{m_i m_{i+1}} \right\| \tag{2.26}$$

The strain tensor component $\varepsilon_{\theta\theta}$ is then obtained with Equation 2.27 as the relative variation of the length of the arc.

$$\varepsilon_{\theta\theta} = \frac{l}{L} - 1 \tag{2.27}$$

At each state of deformation, the value of $\varepsilon_{\theta\theta}$ is obtained in the two layers. Finally, as for the previous analysis method, the average of the values obtained for the two sides of the sample is calculated.

This strain component $\varepsilon_{\theta\theta}$ was not calculated in this thesis.

2.3.2. Parametrical study

Using the previous analysis method, it is possible to obtain the strain tensor components ε_{zz}, $\varepsilon_{\theta z}$, $\varepsilon_{\theta\theta}$, the vertical displacement gap Δu_z and the horizontal displacement gap Δu_θ at the interface. These values depend on the 3D DIC results and thus on the correlation parameters like the size of the subsets and the step between two points of interest. The computation of the displacement gaps Δu_z and Δu_θ also depend on the selected interface position for the displacement gaps calculation.

The influence of these parameters are quantified using a simple test. A 2T3C HCA sample was subjected to a global rotation of 50 µm with no vertical stress applied to the sample. The sample is named LAT-1; it is presented in Chapter 3. Pictures were taken in the reference state and in the deformed state. The method presented in section 2.3.1.1 was performed to obtain $\varepsilon_{\theta z}$ in both layers and Δu_θ at the interface in the deformed picture. The same deformed picture was used in all the different cases with the exact same shapes and positions of the strips, except for the study of the influence of the interface location.

2.3.2.1. Influence of the subset size

In order to compare the analysis method results for different subset sizes, the overlap of the subsets was fixed, meaning that the proportion that two adjacent subsets have in common is the same in all cases. The calculation step was set to be a quarter of the subset size as it is commonly prescribed. Subset sizes from 9 pixels x 9 pixels to 65 pixels x 65 pixels were used for the correlation. The analysis was then performed to obtain $\varepsilon_{\theta z}$ in both layers and Δu_θ at the interface in the deformed picture. All the results are presented in Table 2.2 where $\overline{x}$ represents the average of the quantity x obtained for all the different subset sizes.

Table 2.2 - Influence of subset size on the analysis results to find the strain tensor component $\varepsilon_{\theta z}$ and the horizontal displacement gap Δu_θ at the interface

Subset size (pixels)	**Step (pixels)**	**Shear strain in the upper layer**		**Shear strain in the lower layer**		**Horizontal displacement gap at the interface**	
		$\boldsymbol{\varepsilon_{\theta z\_up}}$ **(µm/m)**	$\left\lvert\frac{\varepsilon_{\theta z\_up}-\bar{\varepsilon}_{\theta z\_up}}{\bar{\varepsilon}_{\theta z\_up}}\right\rvert$ **(%)**	$\boldsymbol{\varepsilon_{\theta z\_low}}$ **(µm/m)**	$\left\lvert\frac{\varepsilon_{\theta z\_low}-\bar{\varepsilon}_{\theta z\_low}}{\bar{\varepsilon}_{\theta z\_low}}\right\rvert$ **(%)**	$\boldsymbol{\Delta u_\theta}$ **(µm)**	$\left\lvert\frac{\Delta u_\theta-\overline{\Delta u_\theta}}{\overline{\Delta u_\theta}}\right\rvert$ **(%)**
9	2	251.6	3.4	177.9	6.0	9.5	13.5
13	3	240.7	1.1	191.1	1.0	7.8	6.8
17	4	245.6	0.9	188.1	0.6	8.0	4.3
21	5	244.7	0.5	185.5	2.0	8.5	1.9
25	6	241.1	1.0	187.8	0.7	8.5	2.0
29	7	240.5	1.2	187.9	0.7	8.5	2.5
33	8	241.7	0.7	187.9	0.7	8.5	2.0
37	9	242.2	0.5	191.0	0.9	8.3	0.4
41	10	242.3	0.5	192.8	1.9	8.2	1.3
53	13	243.7	0.1	195.7	3.4	8.0	4.6
65	16	243.7	0.1	195.7	3.4	8.0	4.5
Average		$\bar{\varepsilon}_{\theta z\_up}$ = 243.4 µm/m		$\bar{\varepsilon}_{\theta z\_low}$ = 189.2 µm/m		$\overline{\Delta u_\theta}$ = 8.3 µm	

The relative gaps to the average for the strain tensor component $\varepsilon_{\theta z}$ in the layers and for the horizontal displacement gap Δu_θ at the interface are plotted in Figure 2.29 versus the subset size. It can be seen that the relative gap is very low for $\varepsilon_{\theta z}$ for all the subset sizes, in both layers. For the displacement gap Δu_θ, the relative gap increases when the subset size is too small or too large. It is inferior to 3 % for subsets between 21 and 41 pixels.

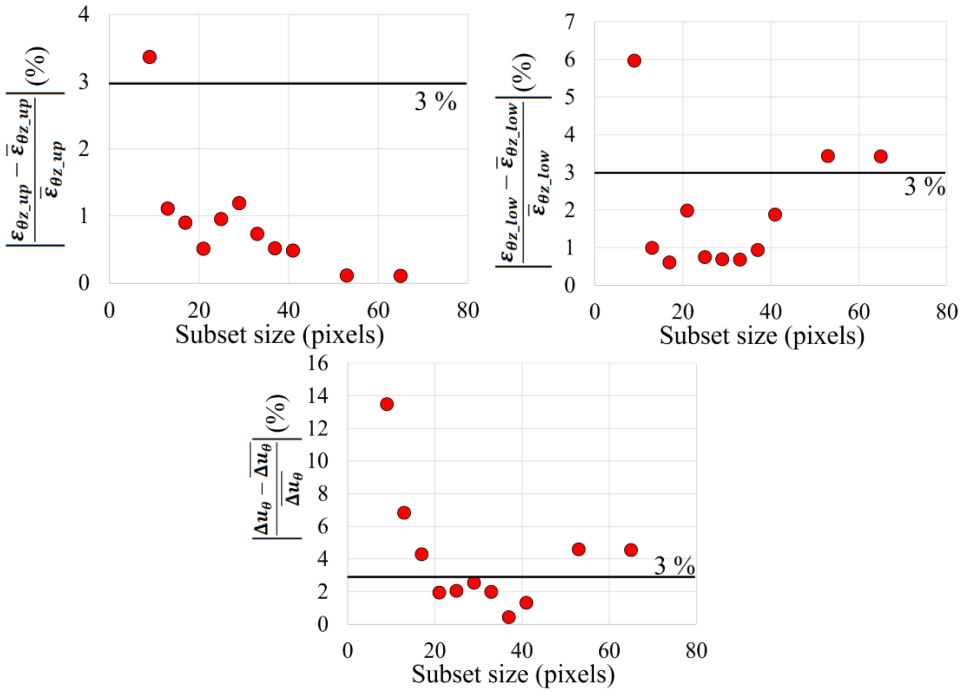

Figure 2.29 - Relative gap to the average for the strain tensor component $\varepsilon_{\theta z}$ in the layers (top left, in the upper layer and top right, in the lower layer) and for the horizontal displacement gap Δu_θ at the interface (bottom) obtained with different subset sizes

Based on these results, the size of a subset is fixed at 25 pixels: it induces low relative gaps to the average for Δu_θ and it enables a large number of calculation.

2.3.2.2. Influence of the calculation step

The subset size is now 25 pixels. The step was previously chosen to be a quarter of the subset; it is now varying from 1 pixel to 10 pixels. All the results are presented in Table 2.3 where $\overline{x}$ represents the average of the quantity x obtained for all the different subset sizes.

Table 2.3 - Influence of the calculation step on the analysis results to find the strain tensor component $\varepsilon_{\theta z}$ and the horizontal displacement gap Δu_θ at the interface

Subset size (pixels)	**Step (pixels)**	**Shear strain in the upper layer**		**Shear strain in the lower layer**		**Horizontal displacement gap at the interface**	
		$\boldsymbol{\varepsilon_{\theta z\_up}}$ **(µm/m)**	$\left\lvert\frac{\varepsilon_{\theta z\_up}-\bar{\varepsilon}_{\theta z\_up}}{\bar{\varepsilon}_{\theta z\_up}}\right\rvert$ **(%)**	$\boldsymbol{\varepsilon_{\theta z\_low}}$ **(µm/m)**	$\left\lvert\frac{\varepsilon_{\theta z\_low}-\bar{\varepsilon}_{\theta z\_low}}{\bar{\varepsilon}_{\theta z\_low}}\right\rvert$ **(%)**	$\boldsymbol{\Delta u_\theta}$ **(µm)**	$\left\lvert\frac{\Delta u_\theta-\overline{\Delta u_\theta}}{\overline{\Delta u_\theta}}\right\rvert$ **(%)**
25	1	240.6	0.0	187.7	0.0	8.5	0.2
25	2	240.9	0.1	187.8	0.1	8.5	0.1
25	3	240.7	0.0	186.8	0.5	8.6	0.9
25	4	240.3	0.1	187.2	0.2	8.6	0.4
25	5	239.4	0.5	186.8	0.4	8.7	1.8
25	6	241.1	0.2	187.9	0.1	8.5	0.1
25	7	240.4	0.1	187.4	0.1	8.6	0.7
25	8	241.4	0.3	189.3	0.9	8.3	3.2
25	10	241.0	0.1	187.7	0.0	8.5	0.7
Average		$\bar{\varepsilon}_{\theta z\_up}$ = 240.6 µm/m		$\bar{\varepsilon}_{\theta z\_low}$ = 187.6 µm/m		$\overline{\Delta u_\theta}$ = 8.5 µm	

The relative gaps to the average for the strain tensor component $\varepsilon_{\theta z}$ in the layers and for the horizontal displacement gap Δu_θ at the interface are plotted in Figure 2.30 versus the calculation step. The relative gaps are low in every case (inferior to 3 %) indicating a small influence of the calculation step on the results.

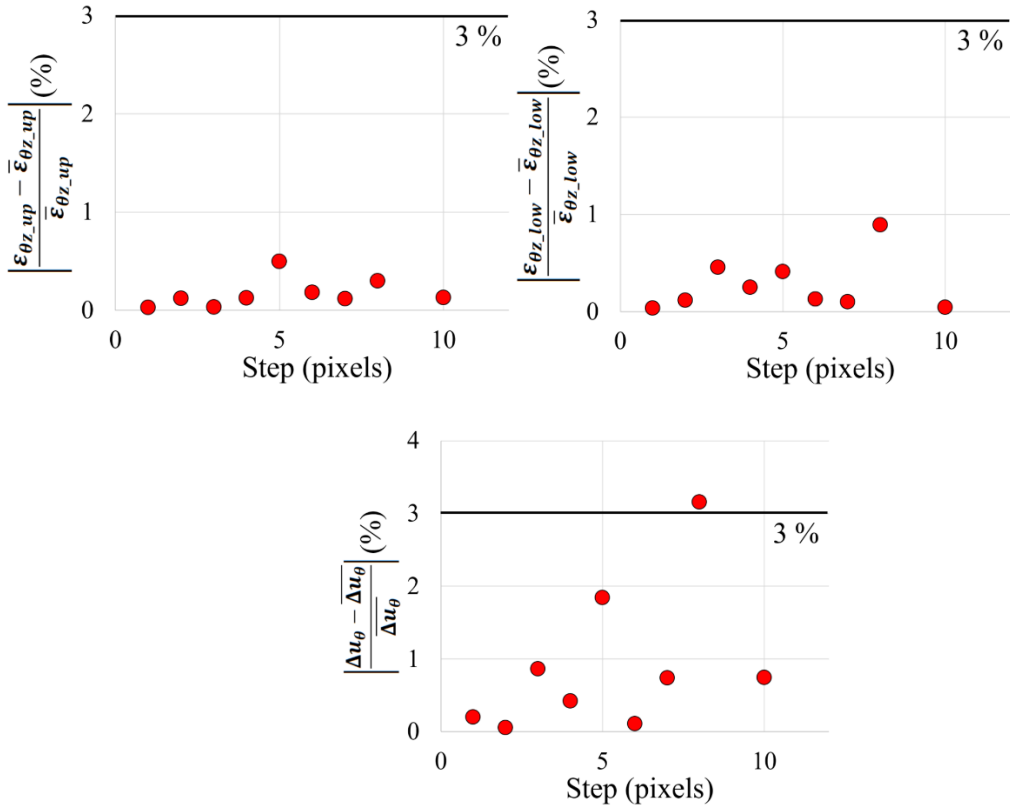

Figure 2.30 - Relative gap to the average for the strain tensor component $\varepsilon_{\theta z}$ in the layers (top left, in the upper layer and top right, in the lower layer) and for the horizontal displacement gap Δu_θ at the interface (bottom) obtained with different calculation steps

The calculation step is chosen to be 6 pixels which is the commonly prescribed value of a quarter of the subset size. It ensures a good precision and an acceptable calculation time compared to lower values.

2.3.2.3. Influence of the selection of the interface position

In the developed analysis method, the calculation of the displacement gaps at the interface Δu_z and Δu_θ depends on the position of the interface along the z axis of the cylinder. It is determined visually as the position where colour changes rapidly using the DIC colour scale for displacements values, meaning that this is the area with the highest displacement gradients in the picture (Figure 2.31). In order to obtain a coordinate z for the interface, a strip is plotted on the deformed picture with its centre placed in what seems to be the centre of the colour change zone. Vic 3D can retrieve the coordinates of this centre for further analysis. This point is chosen in the deformed picture where the displacement gradient is the highest to obtain the strongest colour change and its position stays the same for all the other analysed pictures.

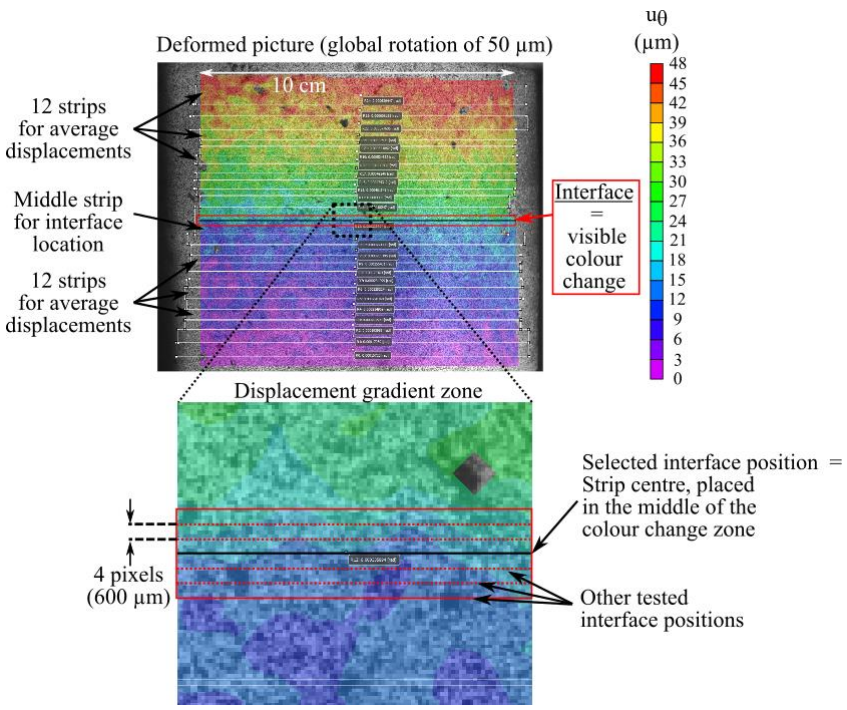

Figure 2.31 - Selection of interface position for displacement gaps calculation

As it is difficult to precisely locate the interface, different interface positions were tested to evaluate the error that it could induce. The 2T3C HCA sample LAT-1 was subjected to a global rotation of 50 µm. Pictures were taken in the reference state and in the deformed state. The procedure is similar to the test presented in sections 2.3.2.1 and 2.3.2.2 but it is a different one in this section. The 3D DIC was applied to find the displacements with a subset size of 25 pixels and a calculation step of 6 pixels.

The initial guess for interface location is taken as the reference, and then positions situated 4, 8 and 12 pixels above the initial guess and 4, 8 and 12 pixels below (Figure 2.31) were used to perform the analysis method presented in section 2.3.1.1 to obtain $\varepsilon_{\theta z}$ in both layers and Δu_θ at the interface. The distance between the highest and the lowest position is 24 pixels. It is close to the subset size (25 pixels) meaning that the displacements of two points separated by 24 pixels are calculated with subsets that do not overlap. As an order of magnitude, the tack coat thickness can be estimated to be inferior to 1 mm with a visual inspection of sample without speckle pattern, when 24 pixels represent 3.6 mm.

The strips in the layers are the same for all the cases. All the results are presented in Table 2.4 where $\overline{x}$ represents the average of the quantity x obtained for all the different subset sizes.

Table 2.4 - Influence of the interface position on the analysis results to find the strain tensor component $\varepsilon_{\theta z}$ and the horizontal displacement gap Δu_θ at the interface

Subset size/Step (pixels /pixels)	Interface distance to reference (pixels)	Shear strain in the upper layer		Shear strain in the lower layer		Horizontal displacement gap at the interface	
		$\varepsilon_{\theta z\_up}$ (µm/m)	$\left\lvert\frac{\varepsilon_{\theta z\_up}-\bar{\varepsilon}_{\theta z\_up}}{\bar{\varepsilon}_{\theta z\_up}}\right\rvert$ (%)	$\varepsilon_{\theta z\_low}$ (µm/m)	$\left\lvert\frac{\varepsilon_{\theta z\_low}-\bar{\varepsilon}_{\theta z\_low}}{\bar{\varepsilon}_{\theta z\_low}}\right\rvert$ (%)	Δu_θ (µm)	$\left\lvert\frac{\Delta u_\theta-\overline{\Delta u_\theta}}{\overline{\Delta u_\theta}}\right\rvert$ (%)
25/6	-12	259.0	0.0	114.2	0.0	8.4	0.2
25/6	-8	259.0	0.0	114.2	0.0	8.6	0.1
25/6	-4	259.0	0.0	114.2	0.0	8.7	0.9
25/6	0	259.0	0.0	114.2	0.0	8.9	0.4
25/6	+4	259.0	0.0	114.2	0.0	9.0	1.8
25/6	+8	259.0	0.0	114.2	0.0	9.1	0.1
25/6	+12	259.0	0.0	114.2	0.0	9.4	0.7
Average		$\bar{\varepsilon}_{\theta z\_up}$ = 259.0 µm/m		$\bar{\varepsilon}_{\theta z\_low}$ = 114.2 µm/m		$\overline{\Delta u_\theta}$ = 8.5 µm	

As expected, the values for $\varepsilon_{\theta z}$ in both layers stay identical because they do not depend on the interface location. The values of Δu_θ depend linearly on the interface position. It can be seen in Figure 2.32 that the relative gap to the average is inferior to 6 % in all the tested cases. It is close or inferior to 3 % when the distance to the reference is inferior to 8 pixels (1.2 mm).

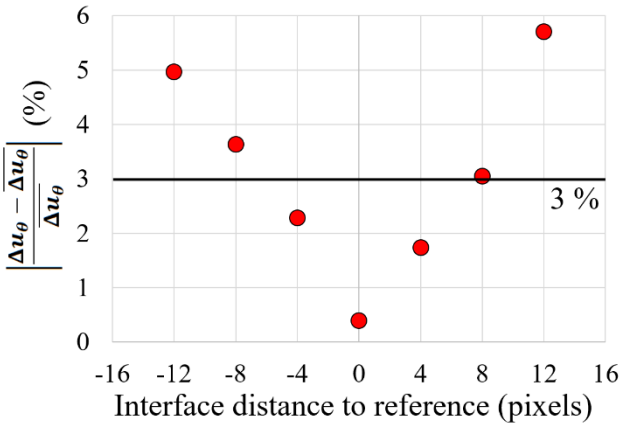

Figure 2.32 - Relative gap to the average for the horizontal displacement gap Δu_θ at the interface obtained with different interface positions

The order of magnitude of the influence of the interface position on the displacement gap results is thus evaluated at ± 5 %.

2.4. Conclusion

A new hollow cylinder apparatus named 2T3C HCA has been designed and developed at the University of Lyon/ENTPE, inspired by former hollow cylinder tests on sands. It can apply independently torsion and tension-compression to samples constituted of two layers thanks to a hydraulic press. No confinement pressure is applied to the samples. Sample dimensions are 86 mm for the external radius, 61 mm for the inner radius and 125 mm for the height. They have been chosen so

that the stresses are homogenous and so that the sample is sufficiently large compared to the bituminous mixture representative elementary volume, ensuring the repeatability of the tests *a priori*.

A climate chamber controls the temperature of the samples during the tests, which is verified with temperature probes on the sample surface. The chamber has windows on its sides so that 3D Digital Image Correlation (3D DIC), an optical measurement method, can compute the displacements in the three dimensions at the surface of the sample. The global displacements between top and bottom of the sample are also measured using non-contact sensors. The axial force and the torque applied are monitored using the hydraulic press load cells.

A specific analysis method has been developed to find the displacement gaps at the interface in the vertical direction Δu_z and in the horizontal direction Δu_θ from the displacement field found with 3D DIC. It is also possible to obtain the value of the strain tensor components ε_{zz}, $\varepsilon_{\theta z}$ and $\varepsilon_{\theta\theta}$ in both layers. These procedures have been performed on real interfaces and have proved to be consistent. This statement is supported by a parametrical study ensuring that the method is properly optimised.

The next chapter presents the experimental campaign performed with the 2T3C HCA and its associated analyses above-mentioned. The objective of this campaign is to study interfaces behaviour in the small strain domain as well as their failure behaviour. The influence of the bituminous materials chosen for the layers and for the tack coat are evaluated, hoping to find an optimal combination.

Chapter 3 - Experimental campaign

Using the 2T3C HCA apparatus developed at the University of Lyon/ENTPE presented in Chapter 2, an experimental campaign was performed to improve the knowledge on interfaces behaviour.

The objectives of this campaign are:

- the study of the thermomechanical behaviour of interfaces between bituminous mixtures layers in the small strain domain;
- the study of the failure behaviour of interfaces between bituminous mixtures layers under shear monotonic loading.

Eight interface configurations were tested to identify the influence on interfaces behaviour of:

- the bituminous mixtures;
- the tack coat dosage;
- the tack coat type.

In this chapter, the tested materials (bituminous mixtures, bituminous emulsions and the different configurations of bi-layered materials) are thoroughly presented as well as the fabrication process of the samples. The experimental procedures followed in this campaign are then explained. The 2T3C HCA tests in the small strain domain, the monotonic failure tests performed with 2T3C HCA and the complementary tests done on the bituminous mixtures and on the bitumens are precisely described. An overview of all performed tests is available at the end of the chapter.

3.1. Tested materials

3.1.1. Sample fabrication

The materials of this experimental campaign were made by the company Eiffage Infrastructures in their central laboratory situated in Corbas (France). Bi-layered slabs composed of two bituminous mixtures layers with a tack coat at their interface were produced. Slab dimensions are 600 mm in length, 400 mm in width and 150 mm in height with the interface located at mid-height. The bituminous mixtures layers were compacted using a French wheel compactor (Figure 3.1) following the standard NF EN 12697-33+A1:2007.

Figure 3.1 - French wheel compactor (NF EN 12697-33+A1:2007)

The fabrication process begins with the compaction of the lower layer of bituminous mixture in a mould that represents half a slab (600 x 400 x 75 mm^3). The compaction is performed with the mixture heated at a high temperature (about 160 °C, it depends on the bitumen used in the mixture). This half of the slab is left at ambient temperature for 24 hours. Once it has cooled down, the sand patch test (NF EN 13036-1, presented in Chapter 1) is performed at the surface of the bituminous mixture to obtain its Mean Texture Depth (MTD). The sand is then removed using pressurised air.

Next, the tack coat is applied on the lower layer using a brush (Figure 3.2). The quantity of emulsion used is carefully monitored to reach the aimed residual bitumen content. Although the breaking time of the emulsions used is close to one hour, the tack coat is left to break for 24 hours. This rest time is due to practical constraints.

Figure 3.2 - Tack coat application on the lower layer of bituminous mixture using a brush

Finally, the bituminous mixture of the upper layer is compacted at high temperature upon the interface with the tack coat. The complete slab (600 x 400 x 150 mm^3) is then left to cool down at ambient temperature for another 24 hours before being removed from its mould. The sand patch test is also performed on the upper layer. After its fabrication, the bi-layered slab is transferred at the University of Lyon/ENTPE where the coring of the samples takes place maximum one month after the slab fabrication (Figure 3.3).

Figure 3.3 - Core drilling machine at the University of Lyon/ENTPE

The coring plan is presented in Figure 3.4. In each slab, three 2T3C HCA samples are cored vertically and four cylindrical samples of bituminous mixtures (without interface) are cored horizontally, two in each layer. The cylindrical samples have a diameter of 65 mm and a length of 150 mm. The names of the different slabs are presented in section 3.1.4. For a slab named X, the names of the samples are presented in Figure 3.4: the hollow cylinder samples are named X-1, X-2 and X-3; the cylindrical samples cored in the upper layer are named X-U1 and X-U2; and the cylindrical samples cored in the lower layer are named X-L1 and X-L2.

The first samples cored are the 2T3C HCA samples, starting with the inner coring using a 122 mm core drill and finishing with the outer coring with the 182 mm core drill. The slab is hold fixed using heavy wedges to prevent any movement during the coring but also during the core drill change to ensure that the hollow cylinders have a regular shape and are well centred. After the hollow cylinders are extracted, the cylindrical samples are cored in the bituminous mixtures layers.

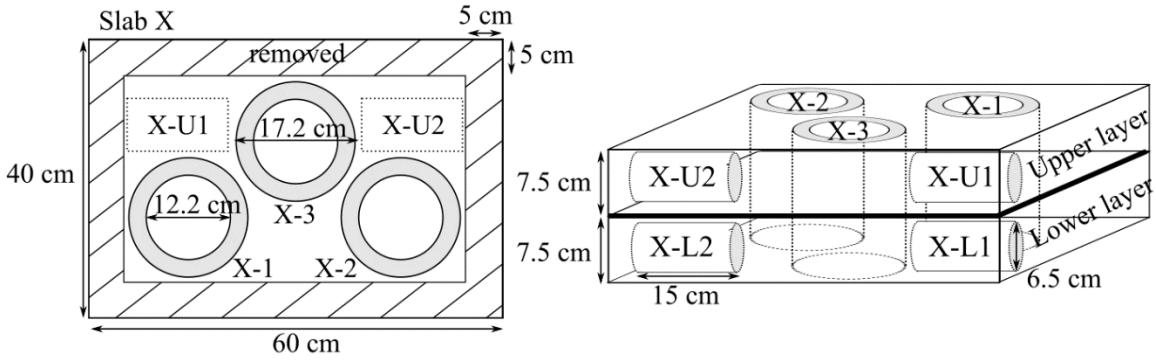

Figure 3.4 - Coring plan with sample names for a slab named X (top view on the left, side view on the right)

The samples are sawn at their extremities on about 1 cm on each side in such a way that the edges are parallel. Plain surfaces enhance the bonding between the samples and the aluminium caps; when the edges' parallelism makes it possible to centre correctly the samples and the caps. The samples are washed using water and left to dry for about two weeks. Their dimensions are then measured using a calliper (accuracy of 0.02 mm) and they are weighed using a balance (accuracy of 0.1 g).

A speckle pattern is applied on the 2T3C HCA samples with aerosol paint. Small spots of black paint are sprayed on a thin coat of white paint. The paints are matte to prevent glare on the pictures. The samples are then ready to be glued to the aluminium caps.

The 2T3C HCA sample production process is illustrated in Figure 3.5.

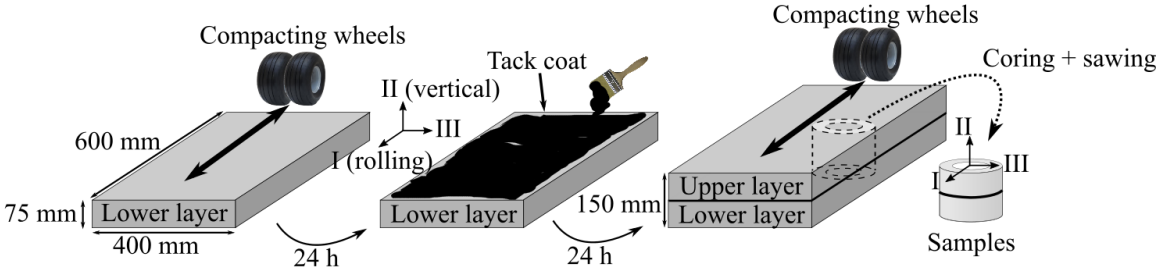

Figure 3.5 - 2T3C HCA sample fabrication process

3.1.2. Bituminous mixtures

Four different bituminous mixtures were used in this experimental campaign: BBSG3, BB5, EME2 and GB5. The bituminous mixtures were chosen to be representative of actual pavements. Two of them, BBSG3 and BB5, are commonly used in France as surface layers. The two others, EME2 and GB5, are used as base courses.

The BBSG3 mixture was made with a 50/70 bitumen. Its Nominal Maximum Aggregate Size (NMAS) is 10 mm. The aggregate size distribution curve is continuous (Figure 3.6, on the left), obtained from 0/4, 4/6 and 6/10 fractions coming from the Creuzeval quarry (France) and a 0/10 Recycled Aggregate Pavement (RAP) fraction. RAP aggregates represent 20 % of the mix weight. The total bitumen content (including RAP binder) is 5.4 % of the total mix weight.

The BB5 mixture was made with a bitumen modified with polymers (Biprène 61). Its NMAS is 10 mm and the aggregate size distribution curve is discontinuous (Figure 3.6, on the left), obtained from 0/2 sand from the Igé quarry (France), 6/10 pebbles from Creuzeval and a 0/10 RAP fraction. RAP aggregates represent 15 % of the mix weight. The total bitumen content (including RAP binder) is 5.1 % of the total mix weight.

The EME2 mixture was made with a 15/25 bitumen. Its NMAS is 14 mm and the aggregate size distribution curve is continuous (Figure 3.6, on the right), obtained from 0/4 sand from Igé, 4/6, 6/10 and 10/14 fractions from Creuzeval and a 0/10 RAP fraction. RAP aggregates represent 30 % of the mix weight. The total bitumen content (including RAP binder) is 5.6 % of the total mix weight.

The GB5 mixture was made with a bitumen modified with polymers (Biprène 41). Its NMAS is 14 mm and the aggregate size distribution curve is discontinuous (Figure 3.6, on the right), obtained from 0/4 sand from Igé, 10/14 pebbles from Creuzeval and a 0/10 RAP fraction. RAP aggregates represent 20 % of the mix weight. The total bitumen content (including RAP binder) is 4.3 % of the total mix weight.

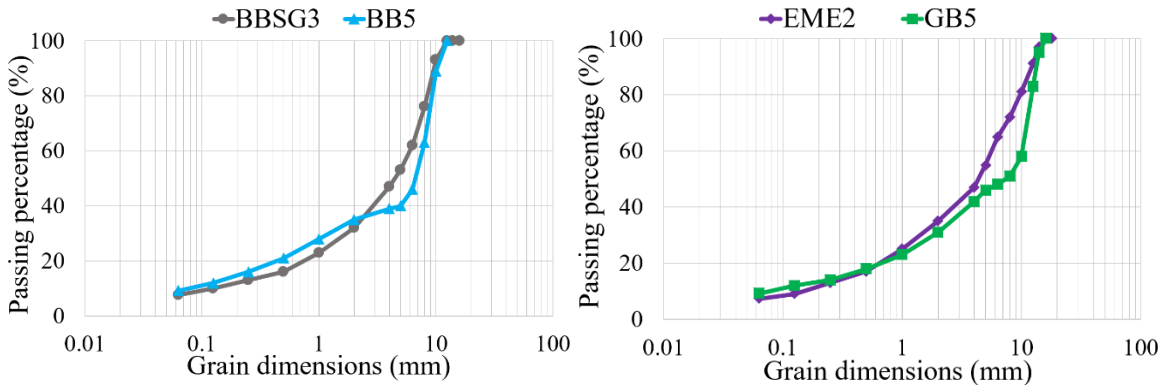

Figure 3.6 - Aggregate size distribution curves of the bituminous mixtures (surface layer mixtures on the left, base course mixtures on the right)

After the bi-layered slabs are compacted, cylindrical samples are cored in the bituminous mixture layers. Their dimensions and their weight are measured as explained in section 3.1.1. The air void content v of a sample is calculated using Equation 3.1 where ρ_m is the measured density of the samples including the air voids and ρ_b is the bulk density of the bituminous mixture calculated from the mix composition.

$$v = 1 - \frac{\rho_m}{\rho_b} \tag{3.1}$$

The cylindrical samples of bituminous mixtures are 65 mm in diameter and the layers are theoretically 75 mm high but when the layers are a little bit smaller, some samples have to be cored too close of the slab surface and do not have a regular shape (Figure 3.7). The air void content values are not calculated for these samples (12 samples out of 40) and they are not tested either. Sample HDO-L1 had a regular shape and was tested but its dimensions were not measured before the test.

Figure 3.7 - Cylindrical sample of bituminous mixture cored too close to the surface and unfit for testing

The air void content of the bituminous mixture samples are presented in Figure 3.8 (the sample names are explained in section 3.1.1). It can be seen that the air void content varies between 3.3 and 7.2 % for BBSG3, between 0.3 and 1.7 % for BB5, between 2 and 4.2 % for EME2 and between 1 and 2.5 % for GB5. In each slab the difference between the two samples of the same material is never more than 1 %. However, the variation of air void content in the same material from different slabs can be significant, like for the BBSG3 mixture in the slab C/D and in the slab SBS.

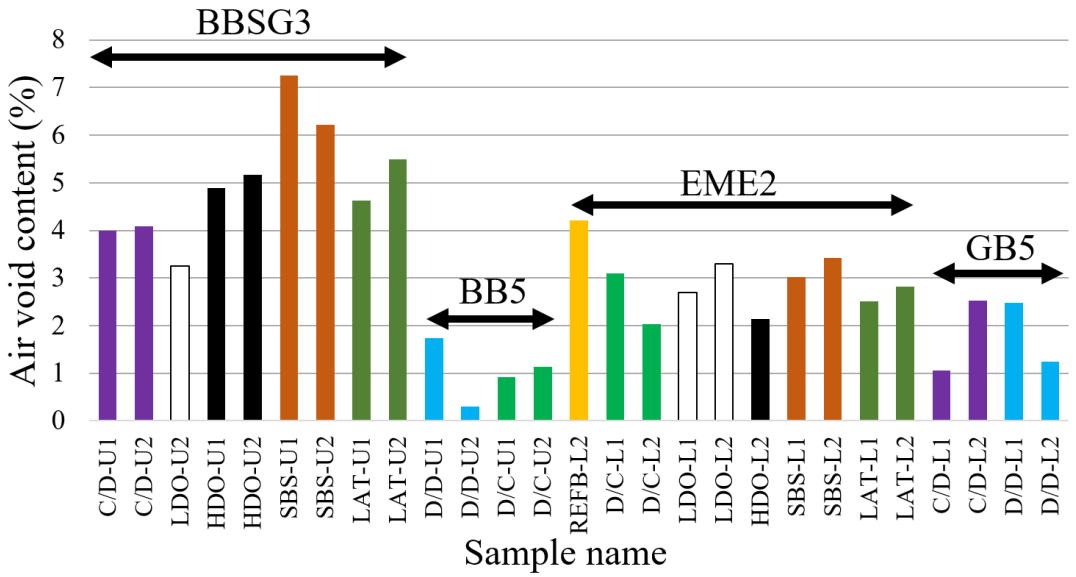

Figure 3.8 - Air void content in the cylindrical samples cored in the bituminous mixtures

Among the two mixtures used in the surface layers, one of them has a continuous grading curve (BBSG3) and the other one has a discontinuous grading curve (BB5). For the mixtures in the base course, EME2 has a continuous grading curve when GB5 has a discontinuous one. The reason behind this is the will to study the aggregate interlocking considering that mixtures with discontinuous grain size distributions would create surfaces rougher than surfaces of mixtures with a continuous grain size distribution. The Mean Texture Depths (MTDs) of the mixtures after compaction were obtained with the sand patch test for all the layers except for the upper layers of configurations REFA and REFB where the MTD measurement was not performed. The MTDs are presented in Figure 3.9 (the slab names are explained in section 3.1.4).

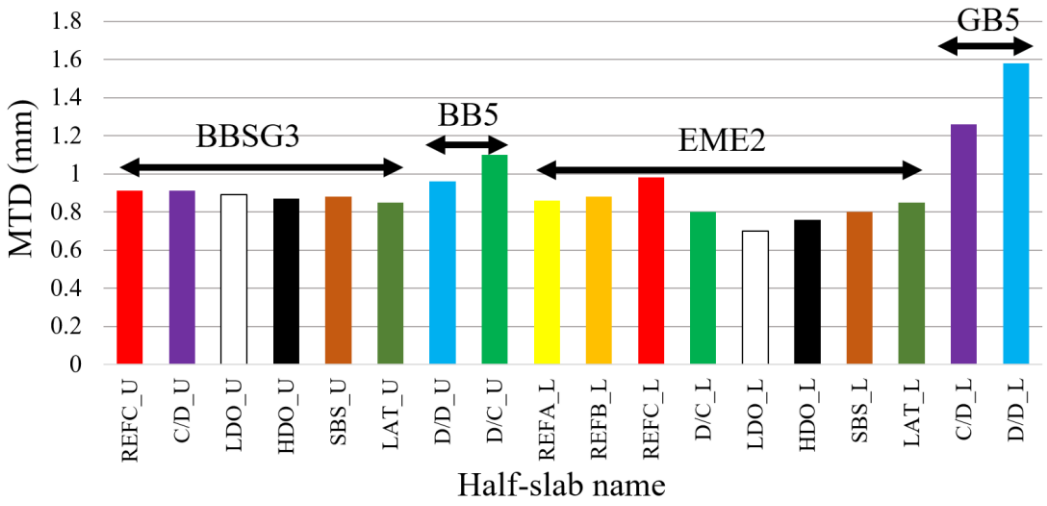

Figure 3.9 - Mean Texture Depth (MTD) of the bituminous mixtures obtained with the sand patch test (X_U is the upper layer of slab X, X_L its lower layer)

There are small differences between the MTDs of the same mixtures. The average value obtained for each mixture is presented in Table 3.1. The mixtures with discontinuous grain size distribution present a higher MTD than the mixtures with a continuous grain size distribution. However, if the difference is significant between EME2 and GB5, it is not the case between BBSG3 and BB5.

Table 3.1 - Average MTDs of the bituminous mixtures

Mixture	BBSG3	BB5	EME2	GB5
Average MTD (mm)	0.89	1.03	0.83	1.42

3.1.3. Bituminous emulsions

Three different bituminous emulsions were used in this campaign as tack coats.

The first one is a cationic emulsion of pure bitumen. The bitumen grade is 160/220 and the dosage in bitumen in the emulsion is 65 %. This emulsion was used to study the influence of the dosage of tack coat on the interface behaviour. The different dosages were obtained by applying more or less of this emulsion at the interface.

The second one is a cationic emulsion made with a bitumen modified with an elastomer named Styrene-Butadiene-Styrene (SBS). The bitumen before modification is the 160/220 bitumen used in the pure bitumen emulsion. The dosage of binder in the emulsion is 65 %.

The third one is a cationic emulsion made with a bitumen modified with latex. The bitumen before modification is the 160/220 bitumen used in the pure bitumen emulsion. The dosage of binder in the emulsion is 65 %.

3.1.4. Interface configurations

Eight interface configurations were tested (Table 3.2).

The reference configuration is a slab with a layer of BBSG3 over a layer of EME2. The tack coat at the interface is a pure bitumen emulsion with a residual binder content of 350 g/m^2. This configuration is used in the study of the three parameters considered in this campaign: the influence of the type of bituminous mixtures in the layers, the type of tack coat and the dosage of tack coat at the interface. For this configuration, named REF, three slabs were produced: REFA, REFB and REFC.

For each of the seven remaining configurations, one slab was produced. The name of the slab is the same than the name of the configuration written in Table 3.2. As explained in section 3.1.1, three 2T3C HCA samples are obtained from each slab.

Table 3.2 – Interface configurations

Name	Bituminous mixtures		Tack coat		Number of slabs	Number of 2T3C HCA samples
	Upper layer	Lower layer	Type	Residual bitumen (g/m^2)		
REF	BBSG3	EME2	Pure bitumen	350	3	9
C/D	BBSG3	GB5	Pure bitumen	350	1	3
D/D	BB5	GB5	Pure bitumen	350	1	3
D/C	BB5	EME2	Pure bitumen	350	1	3
LDO	BBSG3	EME2	Pure bitumen	250	1	3
HDO	BBSG3	EME2	Pure bitumen	450	1	3
SBS	BBSG3	EME2	SBS modified bitumen	350	1	3
LAT	BBSG3	EME2	Latex modified bitumen	350	1	3

3.1.4.1. Interface configurations to study the influence of the bituminous mixtures

The influence of the type of bituminous mixtures on the interface behaviour was tested with four configurations: REF, C/D, D/D and D/C. The tack coat is the same for these configurations: a pure bitumen emulsion with a residual binder content of 350 g/m^2. There are two mixtures for the upper layer (BBSG3 and BB5) and two mixtures for the lower layer (EME2 and GB5). The four possible configurations were tested. The configuration with a layer of BBSG3 over a layer of GB5 is named C/D as in Continuous aggregate size distribution curve over Discontinuous aggregate size distribution curve. Since BBSG3 and EME2 have a continuous gradation curve, they are designated with the letter C. And since BB5 and GB5 have a discontinuous gradation curve, they are designated with the letter D. The tested configurations are then C/D, D/D, D/C and the reference configuration REF with a layer of BBSG3 on a layer of EME2 (that would be C/C).

3.1.4.2. Interface configurations to study the influence of the tack coat dosage

The influence of the dosage of tack coat was investigated with three configurations. They have in common the type of bituminous mixtures, a layer of BBSG3 on a layer of EME2, and the type of tack coat, a pure bitumen emulsion. The residual binder contents tested were 250 g/m^2 for the configuration LDO (Low DOsage), 350 g/m^2 for the configuration REF and 450 g/m^2 for the configuration HDO (High DOsage). Following the French standard NF P 98-150-1, the minimum application rate is 250 g/m^2 for the bituminous mixtures used in this configuration. The tested dosages are all above the prescribed application rate.

3.1.4.3. Interface configurations to study the influence of the type of tack coat

Finally, the influence of the tack coat type was studied with three configurations. The bituminous mixtures are the same in these configurations with a layer of BBSG3 over a layer of EME2. The tack coat is either an emulsion of pure bitumen (configuration REF), an emulsion of SBS modified bitumen

(configuration SBS) or an emulsion of latex modified bitumen (configuration LAT). The residual binder content is 350 g/m^2 in all these configurations.

3.1.5.Bi-layered materials properties

The air void content of bi-layered 2T3C HCA samples can be calculated. Using a ruler (accuracy of 0.5 mm), the distance h_{low} between the interface and the bottom of the sample was measured. A bulk density of the sample was estimated using a blending law, knowing the bulk density of the bituminous mixtures and the proportion of the mixtures in the sample. The air void content v of a 2T3C HCA sample was calculated using Equation 3.2 where ρ_m is the measured density of the hollow cylinder sample (from its dimensions and weight), h is the total height of the sample, ρ_{b_l} is the bulk density of the lower layer and ρ_{b_u} is the bulk density of the upper layer.

$$v = 1 - \frac{\rho_m}{\frac{h_{low}}{h}\rho_{b\_l} + \frac{h - h_{low}}{h}\rho_{b\_u}} \tag{3.2}$$

The air void content of the bi-layered samples are presented in Figure 3.10, except for sample REFC-3 for which data was lost. This method has the advantage to give a unique value of air void content for each sample. However, this value might be less interesting than the air void content value in the bituminous mixtures layers calculated in section 3.1.2 since the latter one gives additional information on the state of compaction at the interface.

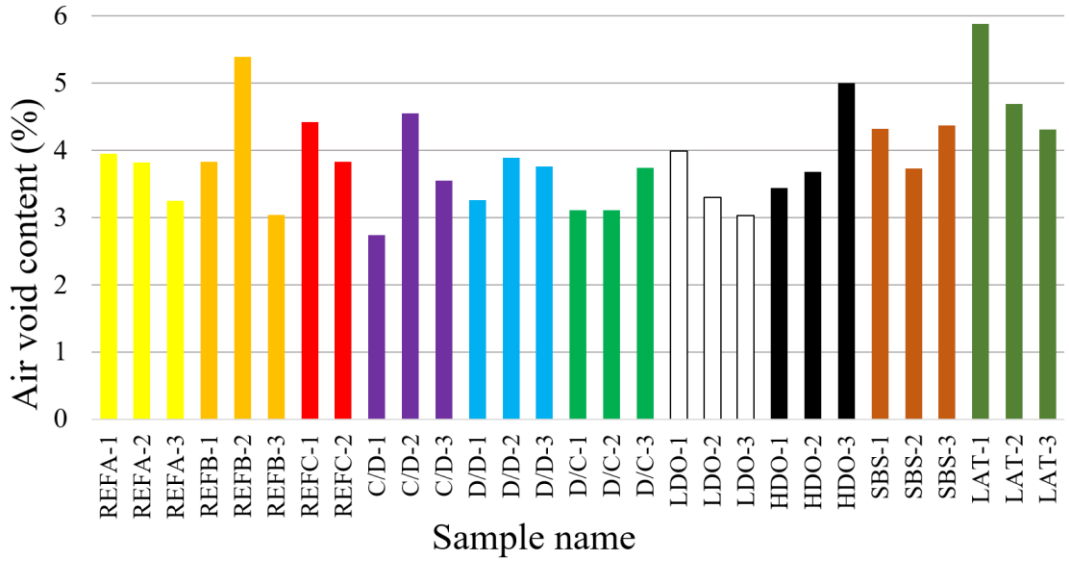

Figure 3.10 - Air void content of the 2T3C HCA samples

The actual residual binder contents calculated from the weight of emulsion applied are presented in Table 3.3 for all the slabs. The actual values are very close to the aimed values.

Table 3.3 - Actual residual binder content at the interface

Slab	REFA	REFB	REFC	C/D	D/D	D/C	LDO	HDO	SBS	LAT
Aimed residual binder (g/m²)	350	350	350	350	350	350	250	450	350	350
Actual residual binder (g/m²)	344.6	350.0	350.2	351.3	352.7	349.4	249.8	452.5	350.3	350.2

3.2. Experimental procedures

3.2.1. Procedures for tests in the small strain domain using 2T3C HCA

In order to study the behaviour of the interfaces in the small strain domain, three types of tests were conducted. An advanced complex modulus test was performed to obtain the mechanical properties of the bituminous mixtures layers and of the interface in shear mode and in tension-compression mode. An oligocyclic test and a nonlinearity test were performed to check if the interface presents a Linear ViscoElastic (LVE) behaviour in the advanced complex modulus test.

3.2.1.1. Advanced complex modulus test

To improve the road design methods, the behaviour of interfaces in the small strain domain must be studied. When a material presents a LVE behaviour in the small strain domain, it can be completely characterised by a complex modulus test. A similar test is then performed on the 2T3C HCA samples with an interface. The test described below is an advanced complex modulus test because the mechanical properties of the bituminous mixtures and of the interface, in shear mode and in tension-compression mode are obtained with the same test.

Sinusoidal cycles are applied to the sample. The amplitude of the cycles is controlled using the non-contact sensors that measure the global displacements between the top and the bottom of the sample. It is actually impossible to control directly the strain in the upper layer, in the lower layer or the displacement gap at the interface using the 2T3C HCA as these values are obtained after the 3D DIC analysis at the end of the tests. Even if it was possible to control one of these three values, the two others could not be controlled independently anyway.

Cycles are applied in rotation and then in the axial direction. While rotation cycles are applied, the axial force is maintained at a small compressive value (0.20 kN which is σ_{zz} = 20 kPa for 2T3C HCA samples) to prevent creep in tension. While axial cycles are applied, the torque is maintained nil.

The amplitude of the cycles is chosen as to create a global strain that would represent 200 µm/m if the sample was homogeneous. The cycles are centered around the zero value. For the rotation cycles, the global displacement amplitude applied with the horizontal non-contact sensors is 90 µm, equivalent to a rotation displacement of 50 µm at the level of the external surface of the hollow cylinder, representing a global shear strain $\varepsilon_{\theta z\_g}$ of 200 µm/m (see Chapter 2 for the equations, the sample height is considered equal to 125 mm for all of the samples in these calculations). For the axial cycles, the global vertical displacement amplitude applied is 25 µm representing a global vertical strain ε_{zz_g} of 200 µm/m. The amplitude of the cycles was chosen as the smallest amplitude for which the measurement of the vertical displacement gap at the interface using 3D DIC was possible. In a bituminous mixture, 200 µm/m is close to the LVE domain limit, depending on the temperature and the frequency (Mangiafico *et al.* 2017), the classical analyses of complex modulus tests being still relevant at this amplitude.

A temperature and frequency sweep is performed. Four frequencies (0.01, 0.03, 0.1 and 0.3 Hz) and four temperatures (10, 20, 30, 40 °C) are tested. The maximum frequency is chosen so that it would be possible to capture enough images per cycle using the cameras (they have a maximal capture frequency of 10 Hz). The other frequencies and the temperatures are then selected by taking into account the minimal and maximum values that are measurable with the press load cells.

At each temperature, five rotation cycles are performed for each of the tested frequency and then five axial cycles are performed at each of the tested frequency. Between the different frequencies and between the rotation test and the axial test, a rest period of one minute is imposed with a global displacement maintained nil. During the temperature changes (4 h), the torque is maintained nil and the axial stress is constant equal to a small compression (σ_{zz} = 20 kPa).

It is important to notice that although the global strain is controlled, the amplitude of the strain in the layers and the amplitude of the displacement gap at the interface is different for each couple of temperature and frequency. Indeed, the repartition of the displacements in the layers and at the interface depend on the ratio between the mixtures' complex moduli and the complex interface stiffness that vary with the temperature and with the frequency.

The advanced complex modulus test procedure is illustrated in Figure 3.11.

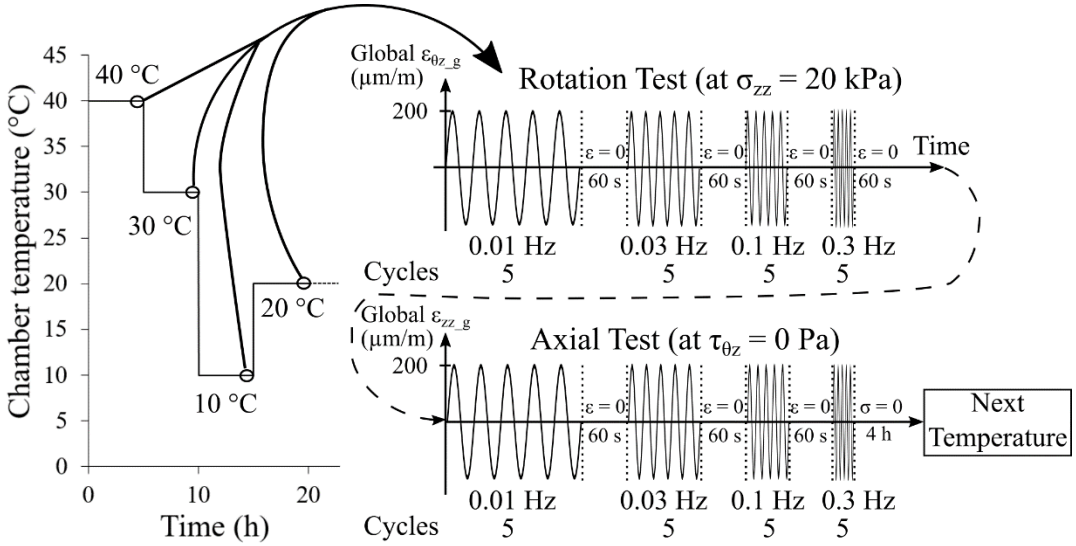

Figure 3.11 - Advanced complex modulus test procedure

For 3D DIC, each camera takes 50 pictures per cycle except for tests at 0.3 Hz where they capture 30 pictures per cycle. As there are four cameras, 7,200 pictures are taken at each temperature and thus 28,800 for the whole test. This represents about 120 Go of data for each sample which is a significant amount. A calibration of the 3D DIC system (as described in section 2.2.4.2) is performed at the beginning of each test. The data from the other sensors is also acquired as explained in Chapter 2.

3.2.1.2. Nonlinearity test

The nonlinearity test consists in applying sinusoidal cycles at different amplitudes on a 2T3C HCA sample.

Sinusoidal rotation cycles are applied using the non-contact sensors. Different amplitudes are tested: 45, 67, 90, 111 µm of global horizontal displacements that would represent, in the same order, 100, 150, 200, 250 µm/m of global shear strain $\varepsilon_{\theta z\_g}$ in a homogeneous sample with the same dimensions. The test frequency f is 0.1 Hz and the temperature T is 20 °C. Five cycles are applied at each amplitude, starting with the lowest amplitude. After all the amplitudes were applied, the lowest amplitude is tested again to check if the interface was damaged. Rest periods of ten minutes are imposed between each applied amplitude with a global displacement maintained nil. The axial stress is maintained at a small

compressive value (σ_{zz} = 20 kPa) during the whole test. The nonlinearity test procedure is illustrated in Figure 3.12.

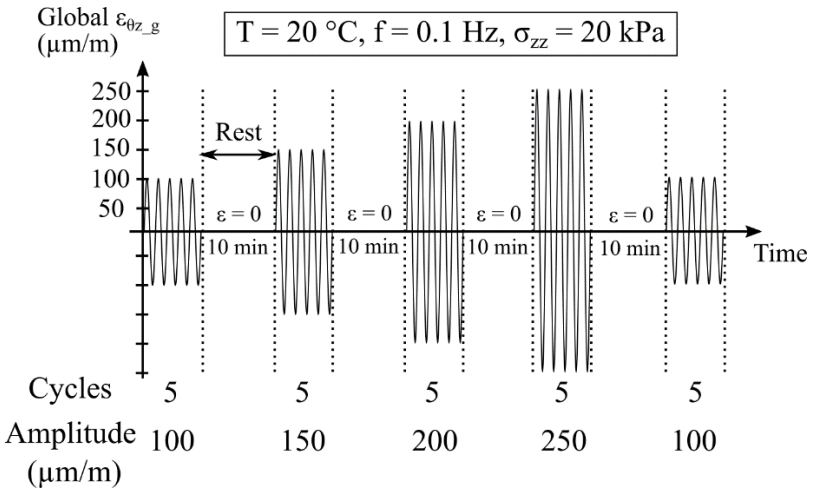

Figure 3.12 - Nonlinearity test procedure

Each camera captures 50 images per cycles for all the cycles of the nonlinearity test.

3.2.1.3. Oligocyclic test

The oligocyclic test consists in applying several dozens of rotation cycles separated by rest periods on a 2T3C HCA sample.

Sinusoidal rotation cycles are applied to the hollow cylinder sample using the horizontal non-contact sensors. The global horizontal displacement amplitude is 90 µm that would represent to a global shear strain $\varepsilon_{\theta z\_g}$ of 200 µm/m on a homogeneous sample with the same dimensions. This amplitude is the same than for the rotation test in the advanced complex modulus test. The cycles are applied at a frequency f of 0.1 Hz and at a temperature T of 20 °C. During the cycles and during the rest periods, the axial force is maintained at a small compressive value (σ_{zz} = 20 kPa).

In a first step, 52 cycles are applied to the sample before a rest period of 24 h is imposed. Next, another 52 cycles are performed. Once those last cycles have been carried out, a second rest period is applied during which few cycles are applied after different rest times to monitor the evolution of the interface behaviour. Three cycles are performed after a rest time of 30 s (counted from the end of the 52 cycles), three others after 60 s, 2 min, 4 min, 8 min, 16 min, 32 min and 1 hour of rest. The oligocyclic test procedure is presented in Figure 3.13.

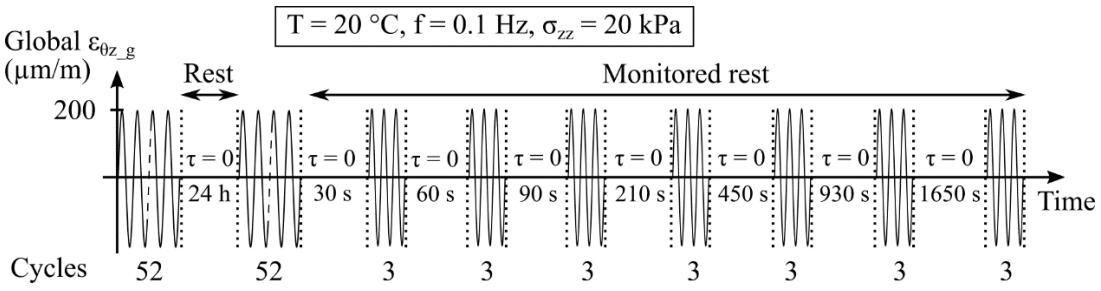

Figure 3.13 - Oligocyclic test procedure

During the sequences of 52 cycles, pictures of four consecutives cycles are acquired every eight cycles to limit the number of pictures to analyse. Pictures are taken throughout the sequences of three cycles. Each camera captures 50 pictures per cycle.

3.2.2. Procedure of monotonic shear failure test with 2T3C HCA

The aim of the monotonic shear failure test is to obtain the interface shear strength, that is the maximum shear stress that the interface can endure before it fails.

Torsion is applied at a constant angular velocity $\dot{\theta}$ to a 2T3C HCA sample until it fails. The angular velocity is measured using the press rotation angle sensor. The testing temperature T is 20 °C in most of the tests (see section 3.3). A constant vertical stress σ_{zz} is applied during the test, its value can be 0, 0.25 or 1 MPa depending on the sample (see section 3.3). As a reminder, in this manuscript, compressive stresses are positive.

The angular velocity $\dot{\theta}$ during the test is 0.033 °/s that would represent 200 µm/m/s or 0.02 %/s of global shear strain rate $\dot{\varepsilon}_{\theta z\_g}$ in a homogeneous sample with the same dimensions than a 2T3C HCA sample. The velocity was chosen so that the torque at failure is about half of the maximum value measurable with the press torque load cell (this maximum value being 2,000 Nm) when no compression is applied. The first three samples were tested at different angular velocities to find the actual test value (see section 3.3).

The monotonic shear failure test procedure is presented in Figure 3.14.

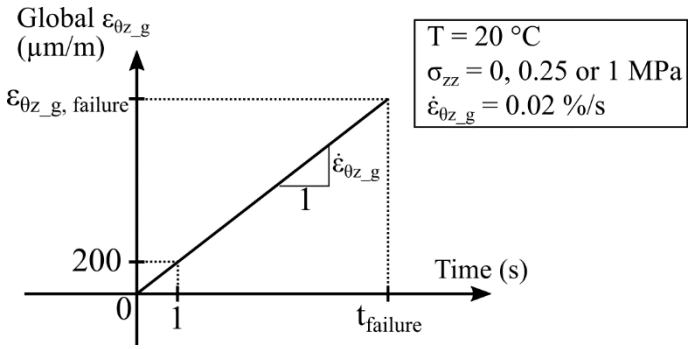

Figure 3.14 - Monotonic shear failure test procedure

Each camera captures two images per second until the sample fails. The 3D DIC analysis is conducted after the test is finished. The measurements of the other sensors are acquired each time a picture is taken.

3.2.3. Complementary tests

Two types of tests are performed on the bituminous mixtures and on the bitumens using other experimental devices than the 2T3C HCA.

A tension-compression complex modulus test is done on some of the cylindrical samples cored in the bituminous mixture layers. The results are compared with the ones of the advanced complex modulus test performed with 2T3C HCA.

A shear complex modulus test is performed on the bitumen used in the tack coats made of pure bitumen emulsion using a Dynamic Shear Rheometer (DSR). It enables to link the bitumen behaviour and the interface behaviour in the small strain domain

3.2.3.1. Tension-compression complex modulus test on bituminous mixtures

The tension-compression complex modulus test consists in applying axial sinusoidal cycles to a cylindrical sample of bituminous mixture using a hydraulic press (different from the one used for the 2T3C HCA). It is a homogeneous test. The amplitude of the cycles is 50 µm/m of axial strain ε_{zz}, centred around zero. It is controlled using three extensometers that have an angle of 120 ° between them (Figure 3.15). A climate chamber maintains the temperature constant during a test. The sample temperature is

monitored using a PT100 probe taped to the surface of the sample. Two non-contact sensors are situated across a diameter of the sample to find the radial strain. They measure displacements with an accuracy of 0.05 µm on a 500 µm range. An axial load cell measures the axial force applied to the sample up to 25 kN.

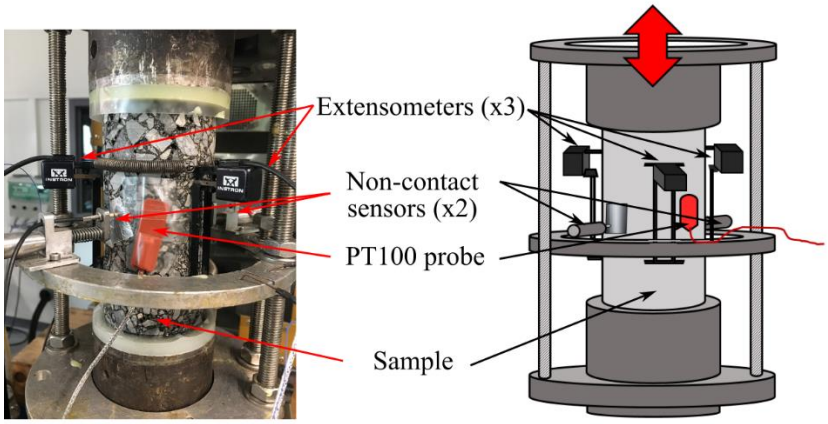

Figure 3.15 - Tension-compression complex modulus test instrumentation (picture on the left and schematic on the right)

Cycles are performed at eight different frequencies (0.003 Hz, 0.01 Hz, 0.03 Hz, 0.1 Hz, 0.3 Hz, 1 Hz, 3 Hz and 10 Hz) and eight different temperatures (-25 °C, -15 °C, -5 °C, 5 °C, 15 °C, 25 °C, 35 °C, 45 °C). The temperature 15 °C is tested three times, once at the beginning of the test, once in the middle and once at the end to check for potential damage. For a given temperature, the number of cycles applied for each frequency is presented in Figure 3.16. Between two frequencies, the axial strain ε_{zz} is maintained nil during five minutes. Between two temperatures, the axial stress σ_{zz} is maintained nil for the whole duration of the temperature change (5 h). The tension-compression complex modulus test procedure is presented in Figure 3.16.

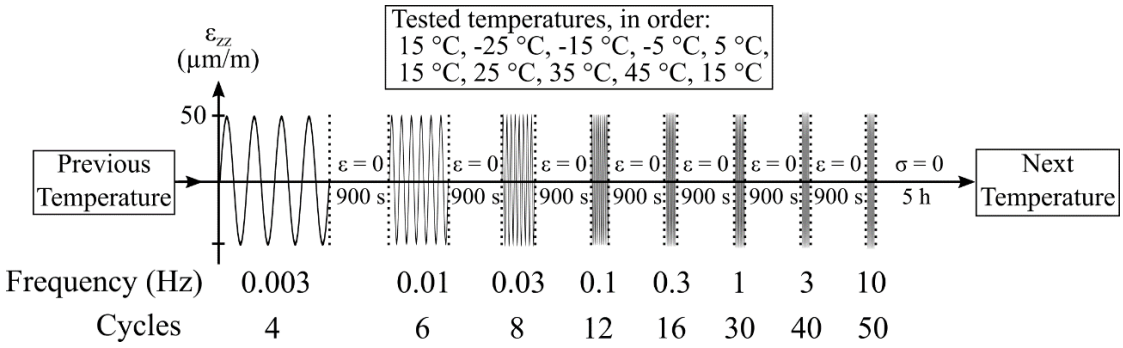

Figure 3.16 - Tension-compression complex modulus test procedure

Data is acquired throughout the test.

3.2.3.2. Complex modulus test on bitumens with the Dynamic Shear Rheometer (DSR)

The Dynamic Shear Rheometer (DSR) is a device that allows applying rotation cycles to a cylindrical sample of bitumen. The bitumen samples are located between two plates, the top plate moving while the bottom plate is fixed (Figure 3.17). The rotation angle and the torque are measured throughout the tests.

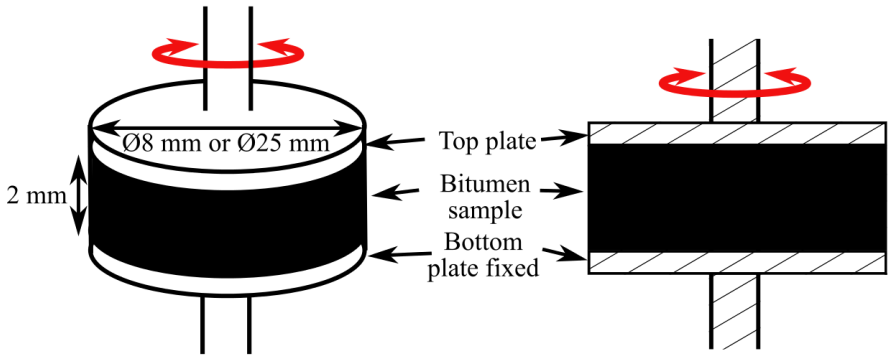

Figure 3.17 - Schematic of the Dynamic Shear Rheometer (DSR) test with the plate/plate geometry (side view on the left, cross-section on the right)

The DSR apparatus is operated by Eiffage Infrastructures at the central laboratory of Corbas (France). The DSR tests are performed with the plate/plate geometry. The sample diameter is 8 mm and its height is 2 mm for the lowest temperatures (up to 20 °C). For the other temperatures, the sample diameter is 25 mm and its height is 1 mm. This test is not homogeneous; the maximum strain value obtained at the edge of the sample is used for the analysis.

A shear complex modulus test with DSR consists in applying sinusoidal rotation cycles to a bitumen sample. The amplitude of the cycles is 0.1 %. The bitumen behaviour is LVE at this amplitude. Ten temperatures (-20 °C, -10 °C, 0 °C, 10 °C, 15 °C, 20 °C, 30 °C, 40 °C, 50 °C, 60 °C) and ten frequencies (0.01 Hz, 0.022 Hz, 0.046 Hz, 0.1 Hz, 0.22 Hz, 0.46 Hz, 1 Hz, 2.2 Hz, 4.6 Hz, 10 Hz) are tested. For each of the temperature, all of the frequencies are tested.

This test was carried out on the 160/220 bitumen used for emulsion of pure bitumen presented in section 3.1.3.

3.3. Overview of performed tests

An overview of the tests performed with the 2T3C HCA is presented in Table 3.4. The names of the samples and their composition are described in section 3.1.4. The samples REFA-1 and REFA-2 failed due to creep in tension during the first temperature change for the advanced complex modulus test and thus could not be tested. The pictures captured during the advanced complex modulus test on the sample LAT-2 could not be analysed. The sample LAT-3 was not tested. The tests in the small strain domain have the same procedures for all the samples (presented in section 3.2.1) but it is not the case for the monotonic shear failure tests where the normal stress or the strain rate are different depending on the sample.

The details of the monotonic shear failure tests performed on the 2T3C HCA samples are presented in Table 3.5. The samples REFA-3, REFB-1 and REFB-2 were used to find a suitable rotation speed for the other tests. The global shear strain rates were 0.2%/s for REFA-3, 0.07 %/s for REFB-1 and 0.02 %/s for REFB-2, they are calculated from the rotation speed as if the samples were homogeneous. Afterwards, all the tests were performed with a global shear strain rate of 0.02 %/s (200 µm/m/s). All the failure tests were done at an aimed temperature of 20 °C, except for samples REFC-1 and D/D-3 where the aimed temperature was 25 °C with the intention of checking the time-temperature superposition principle. The vertical stress applied was either 0, 0.25 or 1 MPa. Different vertical stresses were tested for samples of the same configuration (see Table 3.5 for details).

The complementary tests that were carried out on the bituminous mixtures and on the bitumens are presented in Table 3.6. Tension-compression complex modulus tests were performed on two samples of the bituminous mixtures of the configuration HDO. The 160/220 bitumen used for the emulsion in pure bitumen was tested with the DSR.

Table 3.4 - Tests performed with the 2T3C HCA

Sample Name	Advanced Complex Modulus test	Nonlinearity test	Oligocyclic test	Monotonic shear failure test
REFA-1				
REFA-2				
REFA-3	X			X
REFB-1	X			X
REFB-2	X			X
REFB-3	X			X
REFC-1	X			X
REFC-2	X			X
REFC-3	X			X
C/D-1	X			X
C/D-2	X			X
C/D-3	X			X
D/D-1	X			X
D/D-2	X			X
D/D-3	X			X
D/C-1	X			X
D/C-2	X			X
D/C-3	X			X
LDO-1	X			X
LDO-2	X			X
LDO-3	X			X
HDO-1	X			X
HDO-2	X			X
HDO-3	X			X
SBS-1	X			X
SBS-2	X			X
SBS-3	X			X
LAT-1	X	X	X	X
LAT-2	X			X
LAT-3				

Table 3.5 - Monotonic shear failure tests performed with the 2T3C HCA

Sample Name	**Global shear strain rate $\dot{\varepsilon}_{\theta z\_g}$ (%/s)**	**Aimed temperature (°C)**	**Vertical Stress (MPa)**
REFA-3	0.2	20	0
REFB-1	0.067	20	0
REFB-2	0.02	20	0
REFB-3	0.02	20	0.25
REFC-1	0.02	25	0
REFC-2	0.02	20	1
REFC-3	0.02	20	0.25
C/D-1	0.02	20	0
C/D-2	0.02	20	0
C/D-3	0.02	20	1
D/D-1	0.02	20	0
D/D-2	0.02	20	0
D/D-3	0.02	25	0
D/C-1	0.02	20	0
D/C-2	0.02	20	0.25
D/C-3	0.02	20	1
LDO-1	0.02	20	0
LDO-2	0.02	20	0.25
LDO-3	0.02	20	1
HDO-1	0.02	20	0
HDO-2	0.02	20	0
HDO-3	0.02	20	1
SBS-1	0.02	20	0
SBS-2	0.02	20	0
SBS-3	0.02	20	1
LAT-1	0.02	20	0
LAT-2	0.02	20	0

Table 3.6 - Complementary tests performed on the bituminous mixtures and the bitumens

Type of Material	**Sample Name**	**Tension-compression complex modulus test**	**Shear complex modulus test with DSR**
Bituminous Mixture	HDO-L1	X	
Bituminous Mixture	HDO-U1	X	
Bitumen	Bitumen 160/220		X

Chapter 4 - Small strain domain: results and analysis

In this chapter, the results of the tests performed in the small strain domain are presented. The analysis of an advanced complex modulus test is first presented as an example. The procedure to obtain the mechanical properties of the bituminous mixtures and of the interface are explained for this example. The Time-Temperature Superposition Principle is described as well as the different modelling approaches used for the bituminous mixtures and for the interfaces, for which a new model, the DBN_{PDSC} model, is introduced.

The linear viscoelastic behaviour of the bituminous mixtures is obtained with the 2T3C HCA. The mixtures are modelled with the 2S2P1D model. The results of the advanced complex modulus test with 2T3C HCA are then compared with the results of tension-compression complex modulus tests.

The thermomechanical behaviour of interfaces in the small strain domain is modelled using the DBN_{PDSC} model. The different factors that influence the interface behaviour in the small strain domain are exhibited. Finally, the results of the nonlinearity test and of the oligocyclic test bring new information on the interfaces behaviour.

4.1. Analysis of an advanced complex modulus test on one 2T3C HCA sample

The results of the advanced complex modulus test performed on the 2T3C HCA sample HDO-1 are presented in detail in this section as an example. The sample is made of a layer of the BBSG3 mixture on a layer of the EME2 mixture. The tack coat is made with a pure bitumen emulsion. The residual binder content at the interface is 450 g/m^2. Detailed information on these materials can be found in Chapter 3.

4.1.1. Calculation of the complex modulus in the bituminous mixtures and of the complex interface stiffness

4.1.1.1. Computation of the average values of strain, stress and displacement gap

At the end of the advanced complex modulus test, the 3D DIC analysis presented in section 2.3 is performed on the pictures taken during the test. In the advanced complex modulus test, rotation cycles and axial cycles are applied. For the rotation cycles, the shear strain in the upper layer $\varepsilon_{\theta z\_up\_1}$, the shear strain in the lower layer $\varepsilon_{\theta z\_low\_1}$ and the horizontal displacement gap at the interface Δu_{θ_1} are obtained on the side 1 of the sample after the 3D DIC analysis. The shear strain in the upper layer $\varepsilon_{\theta z\_up\_2}$, the shear strain in the lower layer $\varepsilon_{\theta z\_low\_2}$ and the horizontal displacement gap at the interface Δu_{θ_2} are also obtained on the other side of the sample, the side 2. The cameras are synchronized and it is thus possible to associate a quantity measured on one side to the same quantity measured on the other side at the same time. The retained values for further analyses are the average values of the two sides: the shear strain in the upper layer $\varepsilon_{\theta z\_up}$, the shear strain in the lower layer $\varepsilon_{\theta z\_low}$ and the horizontal displacement gap at the interface Δu_{θ} are obtained using Equations 4.1, 4.2 and 4.3. One value for each of these quantities is obtained each time pictures are taken simultaneously, which happens 50 times per cycle (30 times for cycles at 0.3 Hz).

$$\varepsilon_{\theta z\_up} = \frac{\varepsilon_{\theta z\_up\_1} + \varepsilon_{\theta z\_up\_2}}{2} \quad (4.1)$$

$$\varepsilon_{\theta z\_l} = \frac{\varepsilon_{\theta z\_low\_1} + \varepsilon_{\theta z\_low\_2}}{2} \quad (4.2)$$

$$\Delta u_{\theta} = \frac{\Delta u_{\theta\_1} + \Delta u_{\theta\_2}}{2} \quad (4.3)$$

For the axial cycles, the average values of the two sides of the vertical strain in the upper layer ε_{zz_up}, of the vertical strain in the lower layer ε_{zz_low} and of the vertical displacement gap at the interface Δu_z are calculated in a same manner.

The values of the axial force *F* and of the torque *T* applied to the sample are acquired when pictures are captured. As the test is homogeneous, the stresses are the same everywhere in the sample: in the mixtures layers and also at the interface. The axial stress σ_{zz} and the shear stress $\tau_{\theta z}$ are calculated with Equations 2.7 and 2.8 presented in section 2.1.1.

4.1.1.2. Sinusoidal fitting of the experimental signals using the least square method

In the advanced complex modulus test, the mechanical loadings are sinusoidal. If a material has a linear viscoelastic behaviour, then the mechanical response is also sinusoidal. The measurements of stress, of strain and of the displacement gaps are then fitted by sinusoidal signals using the least square method described below. The sinusoidal fitting works for signals centred around zero, *i.e.* for signals with a mean value nil on a cycle. The experimental signal $X(t_i)$ acquired at the time t_i are centred using Equation 4.4 where $X_c(t_i)$ is the centred signal at the time t_i and *N* is the number of acquisitions in the analysed cycles (if two cycles are treated and if there are 50 cycles per cycle, then *N* = 100).

$$X_c(t_i) = X(t_i) - \frac{1}{N}\sum_{i=1}^{N} X(t_i) \quad (4.4)$$

The time between two acquisitions is always constant and the number of acquisitions analysed is chosen to correspond to a whole number of cycles. In order to improve the fitting accuracy, cycles are analysed two by two (for instance, cycles 2 and 3, cycles 3 and 4, *etc*.).

The approximated sinusoidal signal *x* is searched with the form presented in Equation 4.5 where *A* and *B* are two constants and ω is the angular frequency of the signals (related to the applied frequency *f* by $\omega = 2\pi f$).

$$x(t_i) = A\sin(\omega t_i) + B\cos(\omega t_i) \quad (4.5)$$

The least square method consists in finding the constants *A* and *B* that minimise the coefficient *S* defined in Equation 4.6.

$$S = \sum_{i=1}^{N}\left(X_c(t_i) - x(t_i)\right)^2 = \sum_{i=1}^{N}\left(X_c(t_i) - A\sin(\omega t_i) - B\cos(\omega t_i)\right)^2 \quad (4.6)$$

The constants *A* and *B* should then verify the Equations 4.7 and 4.8.

$$\frac{\partial S}{\partial A} = 0 = \sum_{i=1}^{N} (2A\sin^2(\omega t_i) - 2X_c(t_i)\sin(\omega t_i) + 2\mathrm{B}\cos(\omega t_i)\sin(\omega t_i)) \quad (4.7)$$

$$\frac{\partial S}{\partial B} = 0 = \sum_{i=1}^{N} (2B\cos^2(\omega t_i) - 2X_c(t_i)\cos(\omega t_i) + 2\mathrm{A}\cos(\omega t_i)\sin(\omega t_i)) \quad (4.8)$$

One can notice that the second derivative of 4.6 with respect to A is positive (Equation 4.9) and that the relation presented in Equation 4.10 is verified for any couple *(A,B)*. This indicates that any critical point, *i.e.* any couple (*A,B*) verifying Equations 4.7 and 4.8, corresponds to a local minimum for *S*.

$$\frac{\partial^2 S}{\partial A^2} = \sum_{i=1}^{N} 2\sin^2(\omega t_i) \geq 0 \quad (4.9)$$

$$\frac{\partial^2 S}{\partial A^2}\frac{\partial^2 S}{\partial B^2} - \left(\frac{\partial^2 S}{\partial A \partial B}\right)^2 \geq 0 \quad (4.10)$$

It is possible to isolate *A* and *B* from Equations 4.7 and 4.8 and obtain their values, presented in Equations 4.11 and 4.12.

$$A = \frac{(\sum_{i=1}^{N} X_c(t_i)\cos(\omega t_i)) * (\sum_{i=1}^{N} \cos(\omega t_i)\sin(\omega t_i)) - (\sum_{i=1}^{N} X_c(t_i)\sin(\omega t_i)) * (\sum_{i=1}^{N} \cos^2(\omega t_i))}{(\sum_{i=1}^{N} \cos(\omega t_i)\sin(\omega t_i))^2 - (\sum_{i=1}^{N} \cos^2(\omega t_i)) * (\sum_{i=1}^{N} \sin^2(\omega t_i))} \quad (4.11)$$

$$B = \frac{(\sum_{i=1}^{N} X_c(t_i)\sin(\omega t_i)) * (\sum_{i=1}^{N} \cos(\omega t_i)\sin(\omega t_i)) - (\sum_{i=1}^{N} X_c(t_i)\cos(\omega t_i)) * (\sum_{i=1}^{N} \sin^2(\omega t_i))}{(\sum_{i=1}^{N} \cos(\omega t_i)\sin(\omega t_i))^2 - (\sum_{i=1}^{N} \cos^2(\omega t_i)) * (\sum_{i=1}^{N} \sin^2(\omega t_i))} \quad (4.12)$$

So there is a unique couple (*A,B*) that verifies Equations 4.7 and 4.8 and it corresponds to a local minimum for *S*. The fitting signal *x* is then expressed as in Equation 4.13 with x_0 its amplitude found using Equation 4.14 and φ_x its phase angle found with Equation 4.15.

$$x(t_i) = x_0\sin(\omega t_i + \varphi_x) \quad (4.13)$$

$$x_0 = \sqrt{A^2 + B^2} \quad (4.14)$$

$$\varphi_x = \cos^{-1}\left(\frac{A}{x_0}\right) \quad (4.15)$$

The least square approximation is performed on the average quantities presented above but also on the quantities obtained for each side of the sample to be able to compare the results on the opposite sides and check the test homogeneity.

An indicator *Q* of the quality of the fitting is expressed in Equation 4.16.

$$Q = \frac{1}{N}\sum_{i=1}^{N} \frac{|X_c(t_i) - x(t_i)|}{x_0} \quad (4.16)$$

The fitting is usually considered successful if *Q* is inferior to 15 %. If it is superior to 15 %, the signal is not taken into account into the analysis. Examples of experimental signals with their sinusoidal approximation fitted with the least square methods are presented for rotation cycles in Figure 4.1 and for axial cycles Figure 4.2, both are part of the advanced complex modulus test performed on the sample HDO-1.

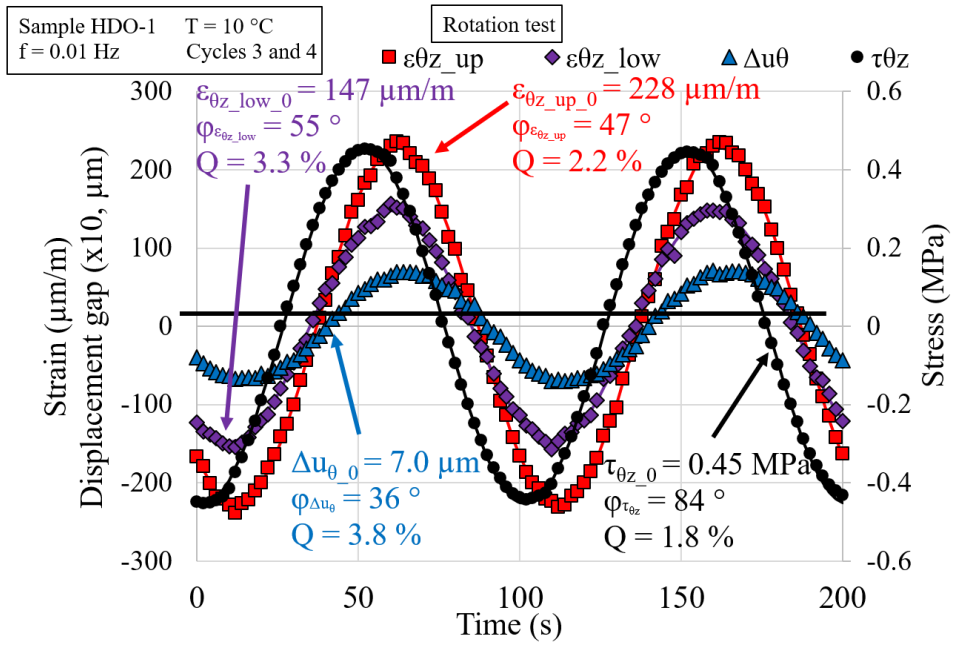

Figure 4.1 - Example of measurements (centred around zero, sinusoidal approximations in continuous lines) obtained with 2T3C HCA during rotation cycles in an advanced complex modulus test

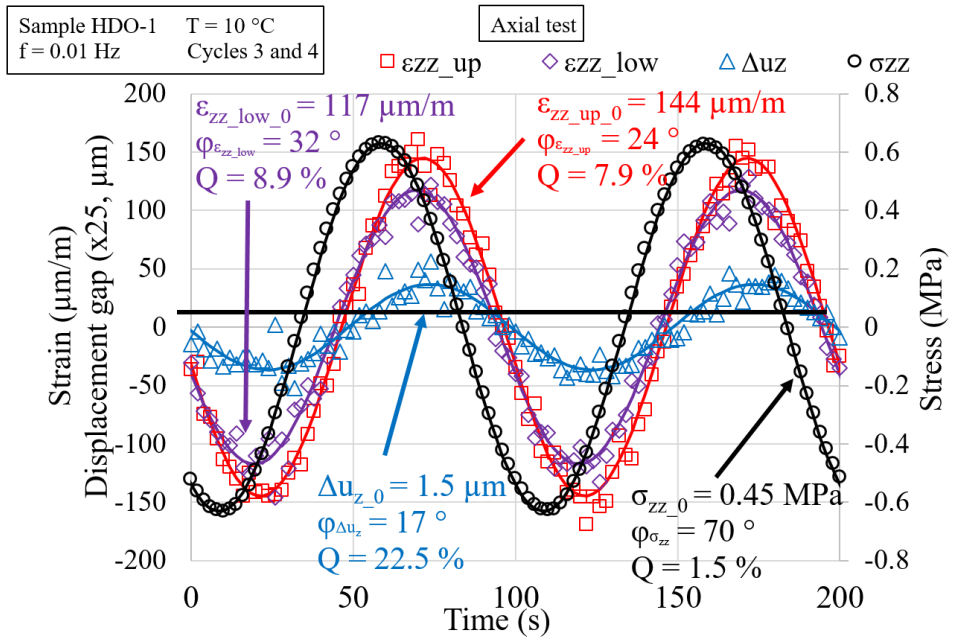

Figure 4.2 - Example of measurements (centred around zero, sinusoidal approximations in continuous lines) obtained with 2T3C HCA during axial cycles in an advanced complex modulus test

It can be seen on Figure 4.2 that the fitting quality indicator *Q* for the vertical displacement gap signal is superior to 15 % in the presented test. Vertical displacement gaps always have a small amplitude in the advanced complex modulus test, close to the accuracy of the 3D DIC analysis. Yet, as it can also be seen in Figure 4.2, the signal has still the shape of a sine. An exception was then created for the vertical displacement gap signals that were considered suitable for analysis if the fitting quality indicator was below 40 %.

4.1.1.3. Definition of the complex moduli in the bituminous mixtures and of the complex interface stiffnesses

Using the sinusoidal fitting of the average quantities calculated in section 4.1.1.2 (ε_{zz_up}, ε_{zz_low}, Δu_z, $\varepsilon_{\theta z\_up}$, $\varepsilon_{\theta z\_low}$, Δu_θ, σ_{zz}, $\tau_{\theta z}$), it is possible to calculate the complex moduli in the bituminous mixtures and the complex interface stiffnesses.

The axial complex modulus E^*_{zz} of a bituminous mixture at the angular frequency ω and at the temperature T is defined in the upper layer or in the lower layer using Equation 4.17 where σ_{zz_0} is the amplitude of the stress signal and $\varphi_{\sigma zz}$ is its phase angle, ε_{zz_0} is the amplitude of the vertical strain signal in the layer ($\varepsilon_{zz\_up\_0}$ in the upper layer; $\varepsilon_{zz\_low\_0}$ in the lower layer) and $\varphi_{\varepsilon zz}$ its phase angle ($\varphi_{\varepsilon zz\ \_up\_0}$ in the upper layer; $\varphi_{\varepsilon zz\ \_low\_0}$ in the lower layer). The axial complex modulus norm $|E^*_{zz}|$ is the ratio between stress amplitude and strain amplitude and the phase angle φ_E is the phase lag between the stress and strain signals. The axial complex modulus is calculated for the axial cycles.

$$E^*_{zz}(\omega, T) = |E^*_{zz}|e^{i\varphi_E} = \frac{\sigma_{zz\_0}}{\varepsilon_{zz\_0}} e^{i(\varphi_{\sigma zz} - \varphi_{\varepsilon zz})} \tag{4.17}$$

The normal complex interface stiffness K^*_{zz} at the angular frequency ω and at the temperature T is defined using Equation 4.18 where σ_{zz_0} is the amplitude of the stress signal and $\varphi_{\sigma zz}$ is its phase angle, Δu_{z_0} is the amplitude of the vertical displacement gap at the interface and $\varphi_{\Delta uz}$ its phase angle. The normal complex interface stiffness norm $|K^*_{zz}|$ is the ratio between stress amplitude and displacement gap amplitude and the phase angle φ_{Kzz} is the phase lag between the stress and displacement gap signals. The normal complex interface stiffness is calculated for the axial cycles. It is important to notice that following this definition, the unit for a complex interface stiffness is Pa/m when it is Pa for a complex modulus.

$$K^*_{zz}(\omega, T) = |K^*_{zz}|e^{i\varphi_{Kzz}} = \frac{\sigma_{zz\_0}}{\Delta u_{z\_0}} e^{i(\varphi_{\sigma zz} - \varphi_{\Delta uz})} \tag{4.18}$$

The shear complex modulus $G^*_{\theta z}$ of a bituminous mixture at the angular frequency ω and at the temperature T is defined in the upper layer or in the lower layer using Equation 4.19 where $\tau_{\theta z\_0}$ is the amplitude of the stress signal and $\varphi_{\tau\theta z}$ is its phase angle, $\varepsilon_{\theta z\_0}$ is the amplitude of the shear strain signal in the layer ($\varepsilon_{\theta z\_up\_0}$ in the upper layer; $\varepsilon_{\theta z\_low\_0}$ in the lower layer) and $\varphi_{\varepsilon\theta z}$ its phase angle ($\varphi_{\varepsilon\theta z\ \_up\_0}$ in the upper layer; $\varphi_{\varepsilon\theta z\ \_low\_0}$ in the lower layer). The shear complex modulus norm $|G^*_{\theta z}|$ is the ratio between stress amplitude and strain amplitude and the phase angle φ_G is the phase lag between the stress and strain signals. The shear complex modulus is calculated for the rotation cycles.

$$G^*_{\theta z}(\omega, T) = |G^*_{\theta z}|e^{i\varphi_G} = \frac{\tau_{\theta z\_0}}{2\varepsilon_{\theta z\_0}} e^{i(\varphi_{\tau\theta z} - \varphi_{\varepsilon\theta z})} \tag{4.19}$$

The shear complex interface stiffness $K^*_{\theta z}$ at the angular frequency ω and at the temperature T is defined using Equation 4.20 where $\tau_{\theta z\_0}$ is the amplitude of the stress signal and $\varphi_{\tau\theta z}$ is its phase angle, Δu_{θ_0} is the amplitude of the horizontal displacement gap at the interface and $\varphi_{\Delta u\theta}$ its phase angle. The shear complex interface stiffness norm $|K^*_{\theta z}|$ is the ratio between stress amplitude and displacement gap amplitude and the phase angle $\varphi_{K\theta z}$ is the phase lag between the stress and displacement gap signals. The shear complex interface stiffness is calculated for the rotation cycles.

$$K^*_{\theta z}(\omega, T) = |K^*_{\theta z}|e^{i\varphi_{K\theta z}} = \frac{\tau_{\theta z\_0}}{\Delta u_{\theta\_0}} e^{i(\varphi_{\tau\theta z} - \varphi_{\Delta u\theta})} \tag{4.20}$$

In an advanced complex modulus test, five cycles (rotation cycles or axial cycles) are applied at a given couple of temperature and frequency. Only the cycles 3 and 4 are fitted using the least square method presented in section 4.1.1.2. The obtained values are used to find the complex moduli in the layers and the complex interface stiffnesses at this couple of temperature and frequency. The first cycles

are not taken into account because of the transient effects. These effects are negligible after two cycles for the frequencies tested in the advanced complex modulus test (Gayte et al. 2016).

It is not sure *a priori* that the tested amplitudes correspond to loadings in the linear viscoelastic domain of the bituminous mixtures or of the interface. However, if the effects of nonlinearities are small, the mechanical response to sinusoidal loadings is still very close to sines and it is still possible to use the above definitions to define equivalent complex moduli or equivalent complex interface stiffnesses. The term "equivalent" will not be mentioned hereafter for reasons of simplicity.

The axial complex moduli of the bituminous mixtures of sample HDO-1, BBSG3 in the upper layer and EME2 in the lower layer, are presented in the Black space (norm of the axial complex modulus versus phase angle of the axial complex modulus) in Figure 4.3 (on the left). The shear complex moduli of the bituminous mixtures of the sample HDO-1 are presented in Figure 4.3 (on the right).

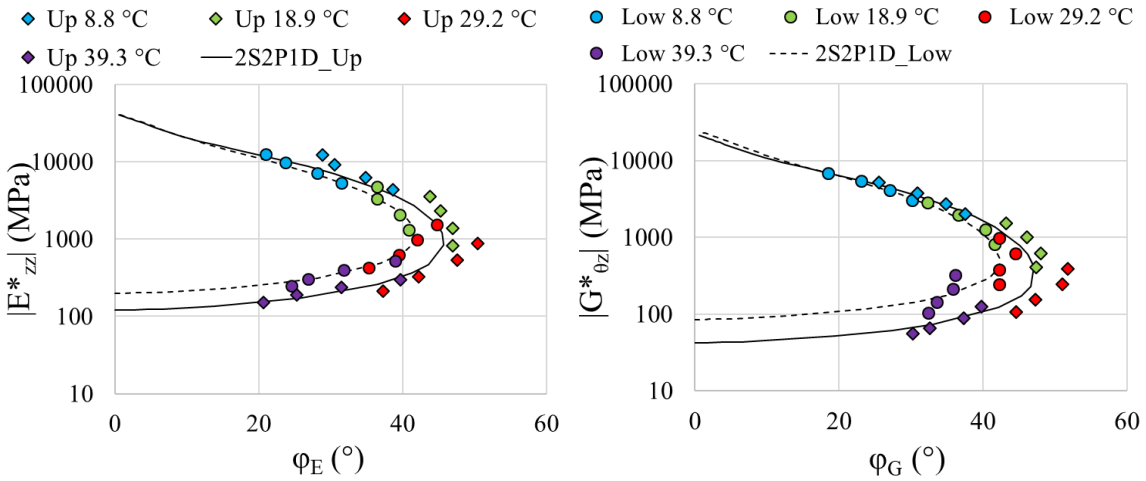

Figure 4.3 - Black diagram of the axial complex modulus (on the left) and shear complex modulus (on the right) of the bituminous mixtures of sample HDO-1, BBSG3 in the upper layer (Up) and EME2 in the lower layer (Low), obtained with the advanced complex modulus test with 2S2P1D models

The vertical strain amplitudes ε_{zz_0} in the bituminous mixtures layers measured during the axial cycles in the advanced complex modulus test on the sample HDO-1 are presented in Figure 4.4 (on the left). The shear strain amplitudes $\varepsilon_{\theta z\_0}$ in the bituminous mixtures layers during the rotation cycles are presented in Figure 4.4 (on the right). Because of the difference of behaviour between the mixtures, the strain amplitudes vary for each couple of temperature and frequency tested. It can be noticed on Figure 4.4 that the strain amplitude is higher in the bituminous mixture of the upper layer and it can be as high as 275 µm/m in the shear test.

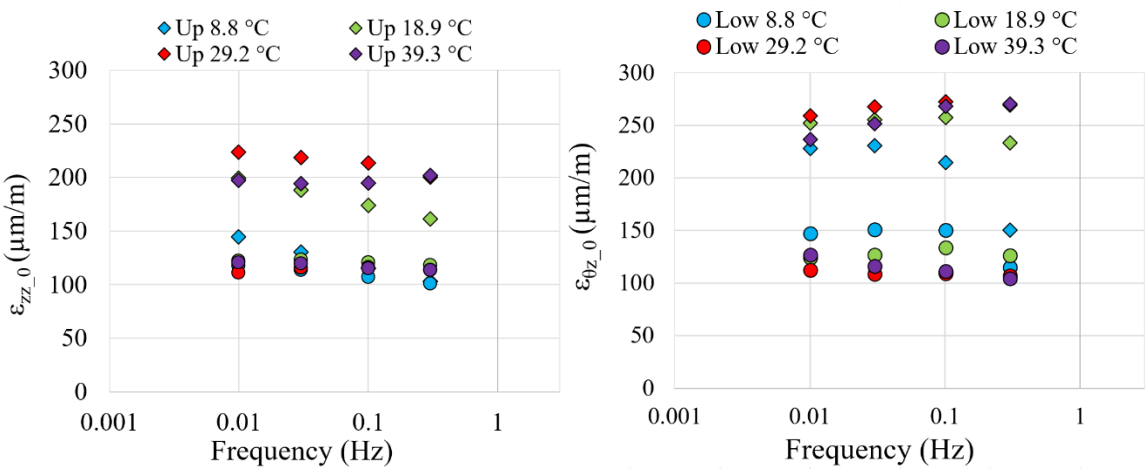

Figure 4.4 - Strain amplitude in the bituminous mixtures of sample HDO-1 in the advanced complex modulus test during axial cycles (on the left) and during rotation cycles (on the right)

The normal complex interface stiffness of the interface in the sample HDO-1 is presented in the Black space in Figure 4.5 (on the left). The Black diagram of the shear complex interface stiffness of the same interface can also be seen in Figure 4.5 (on the right).

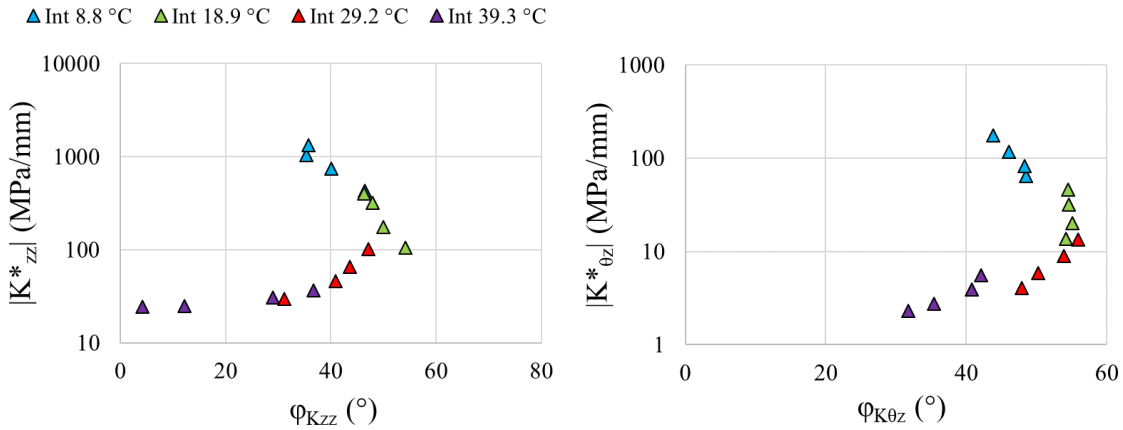

Figure 4.5 - Black diagram of the normal complex interface stiffness (on the left) and shear complex interface stiffness (on the right) of the interface in the sample HDO-1 obtained with the advanced complex modulus test

The amplitudes of the vertical displacement gap at the interface during the axial cycles can be found in Figure 4.6 (on the left). The horizontal displacement gap amplitude during the rotation cycles are also presented in Figure 4.6 (on the right).

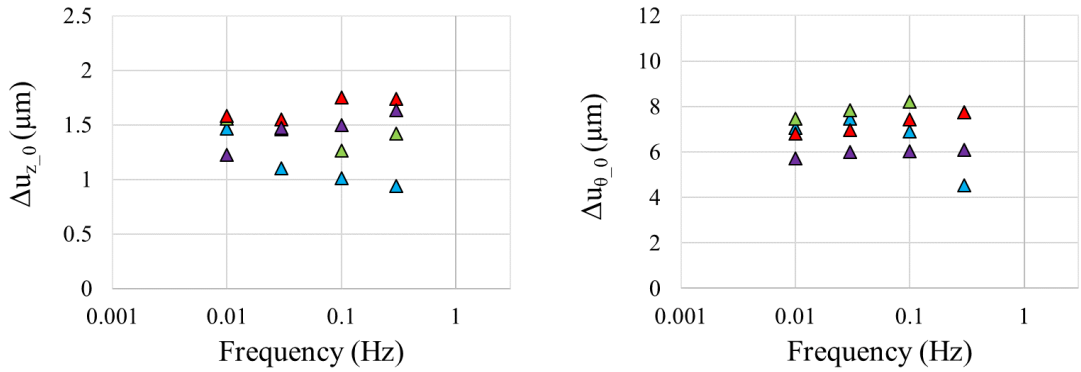

Figure 4.6 - Displacement gap amplitude at the interface in sample HDO-1 in the advanced complex modulus test: vertical displacement gap amplitude during axial cycles (on the left) and horizontal displacement gap amplitude during the rotation cycles (on the right)

4.1.2. Time-temperature superposition principle (TTSP)

The complex moduli of the bituminous mixtures presented in Figure 4.4 and the interface complex stiffnesses presented in Figure 4.5 form unique curves in the Black space when considering all the temperatures. This indicates that the TTSP is verified for the bituminous mixtures and for the interface, both in the tension-compression mode and in the shear mode.

As introduced in section 1.4.1.3, the master curves of the norm of the complex moduli and of the norm of the complex interface stiffnesses can then be built from the isothermal curves. The master curves are defined at a given reference temperature. The first reference temperature chosen for the master curves is the one measured during the test where the aimed temperature is 20 °C. For sample HDO-1, this experimental reference temperature was 18.9 °C. For each tested temperature T, the original tested frequencies of the isothermal curve at the temperature T are multiplied by an associated shift factor $a_T(T, T_{ref})$ so that the translated isothermal curves form a continuous curve. The construction of the axial complex modulus master curve of the bituminous mixture in the upper layer of the sample HDO-1 is illustrated in Figure 4.7.

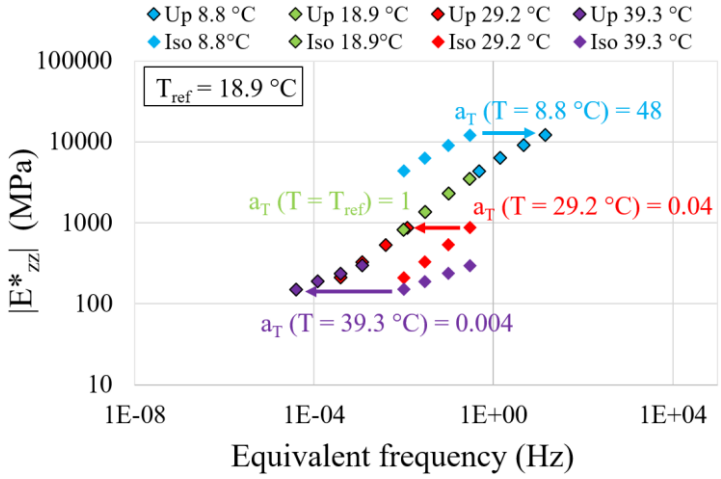

Figure 4.7 - Construction of the master curve of the axial complex modulus of the bituminous mixture in the upper layer of sample HDO-1 (BBSG3) at the experimental reference temperature of 18.9 °C

The shift factors a_T presented on Figure 4.7 for the experimental reference temperature are then approximated using the WLF equation presented in Equation 4.21 where C_1 and C_2 are constants and T_{ref} is the reference temperature.

$$\log a_T = -\frac{C_1(T - T_{ref})}{C_2 + T - T_{ref}} \tag{4.21}$$

The constants C_1 and C_2 that give the best fit to the shift factors are found with a least square method. For the bituminous mixture in the upper layer of the sample HDO-1, the WLF constants at T_{ref} = 18.9 °C are C_1 = 12.8 and C_2 = 87.8.

In order to compare the master curves of samples with different experimental reference temperatures, a common reference temperature is chosen: T'_{ref} = 15 °C. The WLF constants C'_1 and C'_2 at the new reference temperature T'_{ref} can be obtained from the WLF constants C_1 and C_2 at the experimental reference temperature T_{ref} using Equation 4.22 and 4.23.

$$C'_2 = C_2 + T'_{ref} - T_{ref} \tag{4.22}$$

$$C_1' = \frac{C_1 C_2}{C_2'} \tag{4.23}$$

Using these constants, it is possible to find shift factors and to plot the master curves at the new reference temperature T_{ref} = 15 °C. The master curves of the norm of the axial complex moduli of the bituminous mixtures of sample HDO-1 at the reference temperature of 15 °C are presented in Figure 4.8 (on the left). The master curves of the norm of the shear complex moduli of the bituminous mixtures of sample HDO-1 at the reference temperature of 15 °C are also presented in Figure 4.8 (on the right). The shift factors at the reference temperature of 15 °C used for the construction of the master curves are found in Figure 4.9 (with the shift factors for the axial modulus test on the left and the shift factors for the shear complex modulus on the right). The WLF equation constants used to calculate the shift factors can be found in Table 4.1 and Table 4.2.

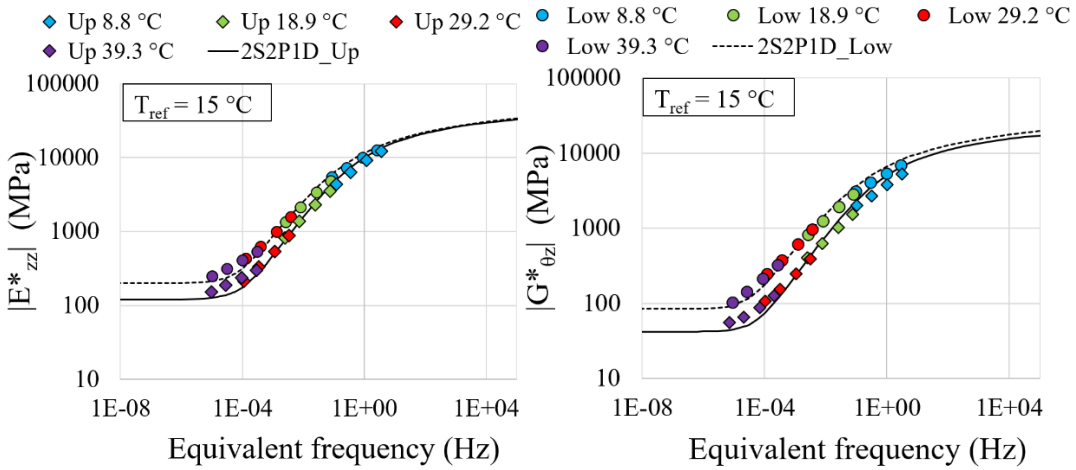

Figure 4.8 - Master curves of the norm of the axial complex moduli (on the left) and of the norm of the shear complex moduli (on the right) of the bituminous mixtures of sample HDO-1, BBSG3 in the upper layer (Up) and EME2 in the lower layer (Low), at the reference temperature of 15 °C with 2S2P1D models

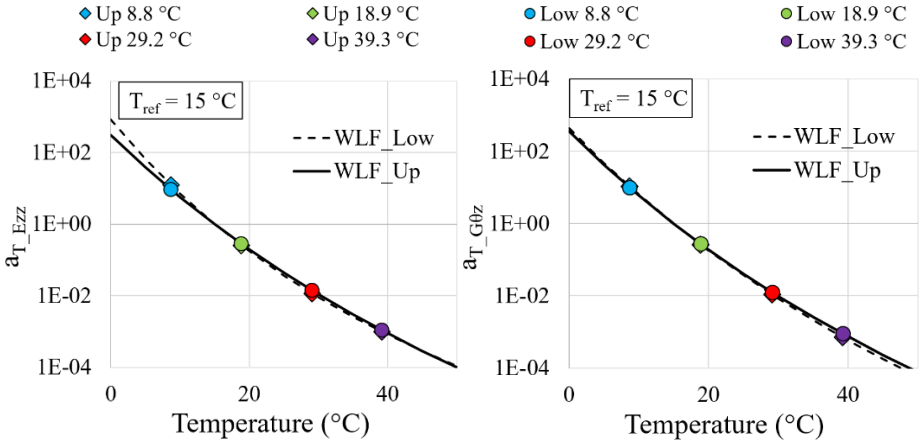

Figure 4.9 - Shift factors for the construction of the master curves of the axial complex modulus norm (on the left) and of the shear complex modulus norm (on the right) of the bituminous mixtures of sample HDO-1 at the reference temperature of 15 °C with corresponding WLF curve

The master curve of the norm of the normal complex interface stiffness in sample HDO-1 at the reference temperature of 15 °C is presented in Figure 4.10 (on the left). The master curve of the norm of the shear complex interface stiffness in sample HDO-1 at the reference temperature of 15 °C is also presented in Figure 4.10 (on the right). The shift factors used for the construction of the master curves

at the reference temperature of 15 °C are found in Figure 4.11 (with the shift factors for the axial modulus test on the left and the shift factors for the shear complex modulus on the right). The WLF equation constants used to calculate the shift factors can be found on Figure 4.11.

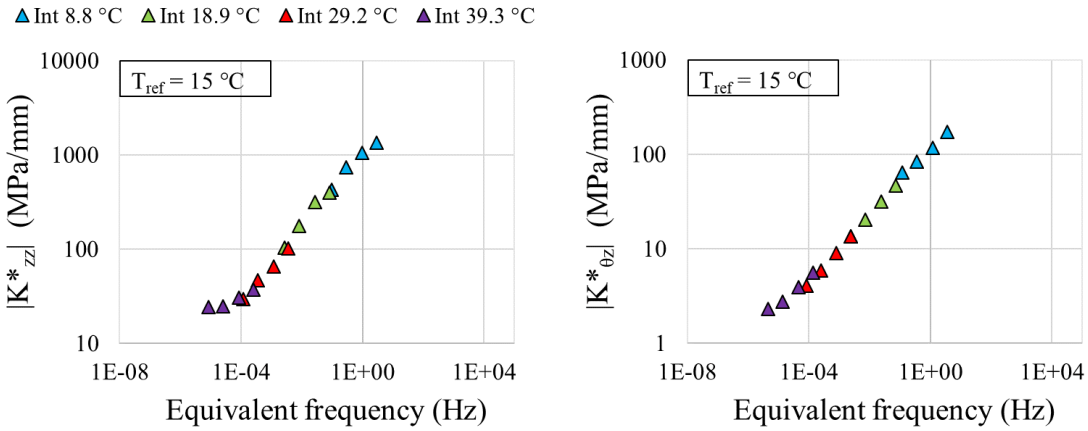

Figure 4.10 - Master curves of the norm of the normal complex interface stiffness (on the left) and of the shear complex interface stiffness (on the right) of the interface in the sample HDO-1 at the reference temperature of 15 °C

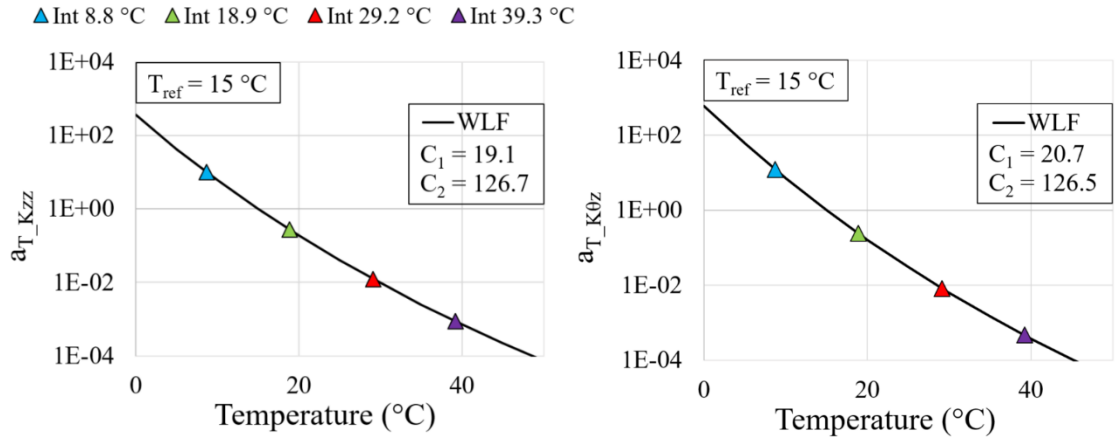

Figure 4.11 - Shift factors for the construction of the master curves of the normal complex interface stiffness norm (on the left) and of the shear complex interface stiffness norm (on the right) in sample HDO-1 at the reference temperature of 15 °C with corresponding WLF curve

It is also possible to build the master curves of the phase angle of the complex modulus of the mixtures and of the complex interface stiffnesses using the same shift factors than for their norm. The master curves of phase angle for the bituminous mixtures are presented in Figure 4.12 (on the left for the axial complex modulus and on the right for the shear complex modulus, on the right). The master curves of the phase angle of the complex interface stiffnesses are presented in Figure 4.13 (on the left for the normal complex interface stiffness and on the right for the shear complex interface stiffness).

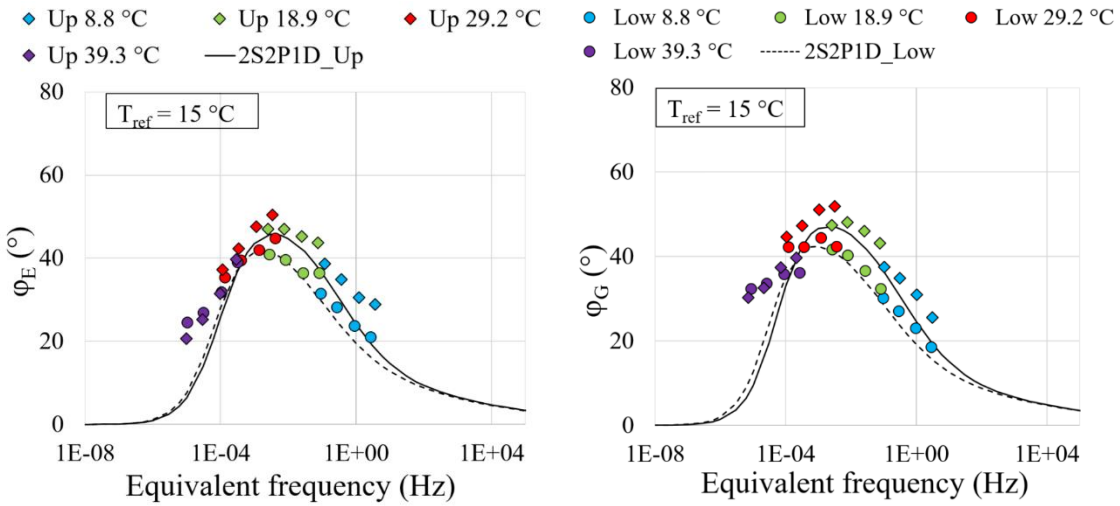

Figure 4.12 - Master curves of the phase angle of the axial complex moduli (on the left) and of the phase angle of the shear complex moduli (on the right) of the bituminous mixtures of sample HDO-1, BBSG3 in the upper layer (Up) and EME2 in the lower layer (Low), at the reference temperature of 15 °C with 2S2P1D models

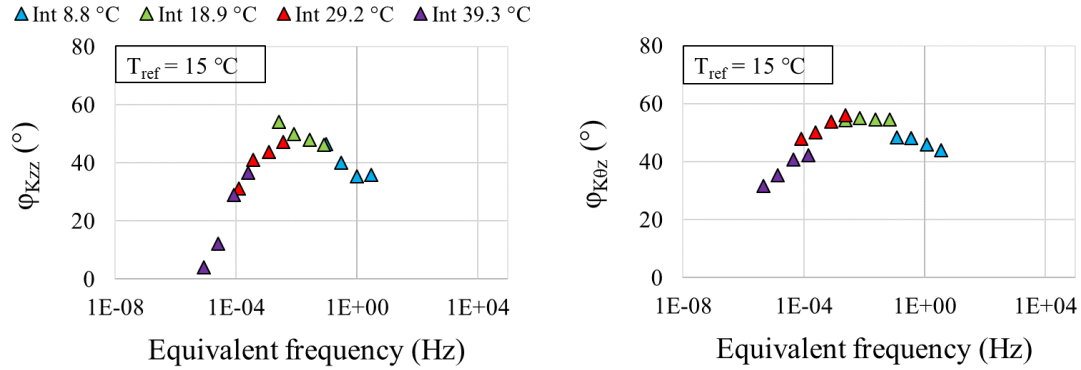

Figure 4.13 - Master curves of the phase angle of the normal complex interface stiffness (on the left) and of the phase angle of the shear complex interface stiffness (on the right) in sample HDO-1 at the reference temperature of 15 °C

4.1.3. Bituminous mixture modelling

The behaviour of bituminous mixtures in the small strain domain is modelled using the 2S2P1D model introduced in section 1.4.1.1, which is a linear viscoelastic model. The complex modulus E^*_{2S2P1D} in the 2S2P1D model is given in Equation 4.24 where the seven constants of the model can be identified: E_{00} is the static modulus, E_0 is the glassy modulus; k, h and δ are related to the parabolic elements; τ is a characteristic time and β a viscosity parameter.

$$E^*_{2S2P1D}(i\omega) = E_0 + \frac{E_{00} - E_0}{1 + \delta(i\omega\tau)^{-h} + (i\omega\tau)^{-k} + (i\omega\beta\tau)^{-1}} \qquad (4.24)$$

When the material respects the TTSP, the dependency of the complex modulus with the temperature T is implemented in the 2S2P1D model through the characteristic time τ. The evolution of τ with the temperature is found using Equation 4.25 where τ_0 is the value of τ at the reference temperature T_{ref} and a_T is the shift factor found when building the master curves at the same reference temperature. The shift factors are expressed using the WLF equation as explained in section 4.1.2.

$$\tau(T) = \tau(T_{ref}) * a_T(T, T_{ref}) = \tau_0 * a_T(T, T_{ref}) \qquad (4.25)$$

A calibration is conducted to find the seven constants (E_{00}, E_0, k, h, δ, β and τ_0) that ensure the best fit to the experimental results in the Black diagram and for the master curves of the norm and of the phase angle at a given reference temperature (T'_{ref} = 15 °C in our case). With the addition of the two constants C_1 and C_2 of the WLF equation at this reference temperature, one obtains the complete set of constants necessary to describe the LVE behaviour of bituminous mixtures.

The axial complex modulus and the shear complex modulus are modelled using the 2S2P1D model. For the axial complex modulus E^*_{zz} the set of constants is noted (E_{00}, E_0, k, h, δ, β and τ_E) and for the shear complex modulus $G^*_{\theta z}$ it is (G_{00}, G_0, k, h, δ, β and τ_G).

The constants used to describe the LVE behaviour of the bituminous mixtures of the sample HDO-1 with 2S2P1D model are presented in Table 4.1 for the axial complex modulus and in Table 4.2 for the shear complex modulus.

Table 4.1 - 2S2P1D constants and WLF equation constants for the axial complex modulus of the bituminous mixtures of sample HDO-1

Layer	Mixture	E_{00} (MPa)	E_0 (MPa)	k	h	δ	τ_E (s)	β	T_{ref} (°C)	C_1	C_2
Upper	BBSG3	120	42000	0.17	0.59	1.8	0.08	120	15	13.4	83.8
Lower	EME2	200	42000	0.18	0.57	2.1	0.2	90	15	18.4	125.8

Table 4.2 - 2S2P1D constants and WLF equation constants for the shear complex modulus of the bituminous mixtures of sample HDO-1

Layer	Mixture	G_{00} (MPa)	G_0 (MPa)	k	h	δ	τ_G (s)	β	T_{ref} (°C)	C_1	C_2
Upper	BBSG3	42	22000	0.17	0.58	1.8	0.07	130	15	19.6	126.2
Lower	EME2	85	25000	0.17	0.55	2.1	0.18	130	15	18.9	126.1

The 2S2P1D models of the bituminous mixtures of the sample HDO-1 are plotted along with the experimental results: they are presented in the Black space in Figure 4.3 (axial complex modulus on the left and shear complex modulus on the right), with the master curves of the norm of the complex modulus in Figure 4.8 (axial complex modulus on the left and shear complex modulus on the right) and with the master curves of the phase angle of the complex modulus in Figure 4.12 (axial complex modulus on the left and shear complex modulus on the right).

4.1.4. Interfaces modelling

As the bituminous mixtures and the bitumen (see below) situated at the interface between the layers can be modelled in the small strain domain using the linear viscoelastic model 2S2P1D, it would seem sensible to try to model the interface behaviour using the 2S2P1D model. However, as it will be shown in this section, the interface behaviour is not linear viscoelastic at the tested amplitude and it is thus impossible to use the 2S2P1D model. So a new model, the DBN_{PDSC} model, is introduced to describe the interface behaviour. Its definition and its calibration are presented in this section.

4.1.4.1. Shear complex modulus of the bitumen used in the pure bitumen emulsion

The bitumen used for the pure bitumen emulsion (tack coat used in all the configurations except for SBS and LAT) was tested with the DSR following the procedure presented in section 3.2.3.2. From the rotation angle and the torque measurements, it was possible to calculate its shear complex modulus. The Black diagram of the bitumen is presented in Figure 4.14.

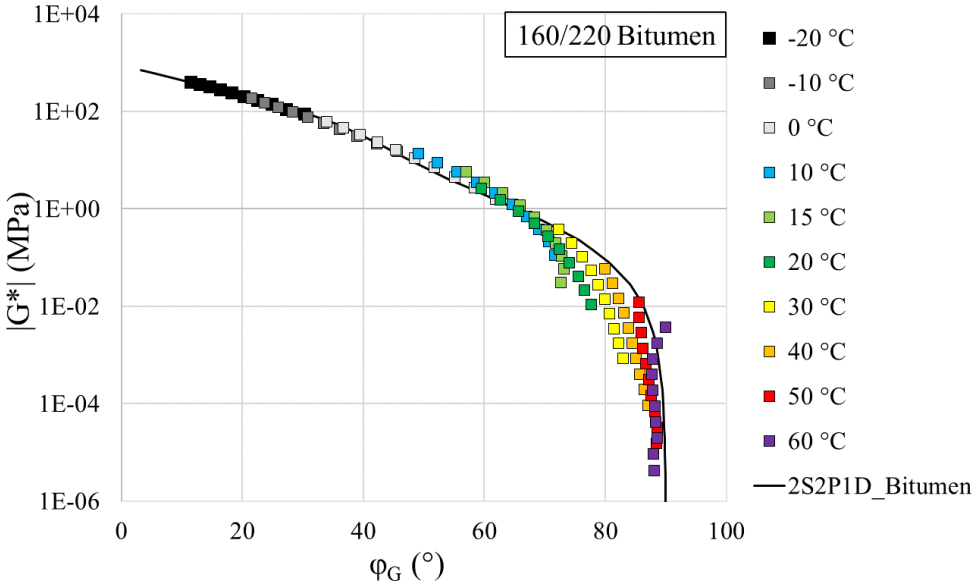

Figure 4.14 - Shear complex modulus of the 160/220 pure bitumen obtained with DSR represented in the Black space

From Figure 4.14, it seems that there is a unique curve in the Black diagram indicating that the TTSP is verified for this bitumen. The master curve of the norm of the shear complex modulus of the bitumen was then built at the reference temperature of 15 °C using shift factors as explained in section 4.1.2. This master curve is found in Figure 4.15 and the shift factors used for the construction of the master curve are presented in Figure 4.16

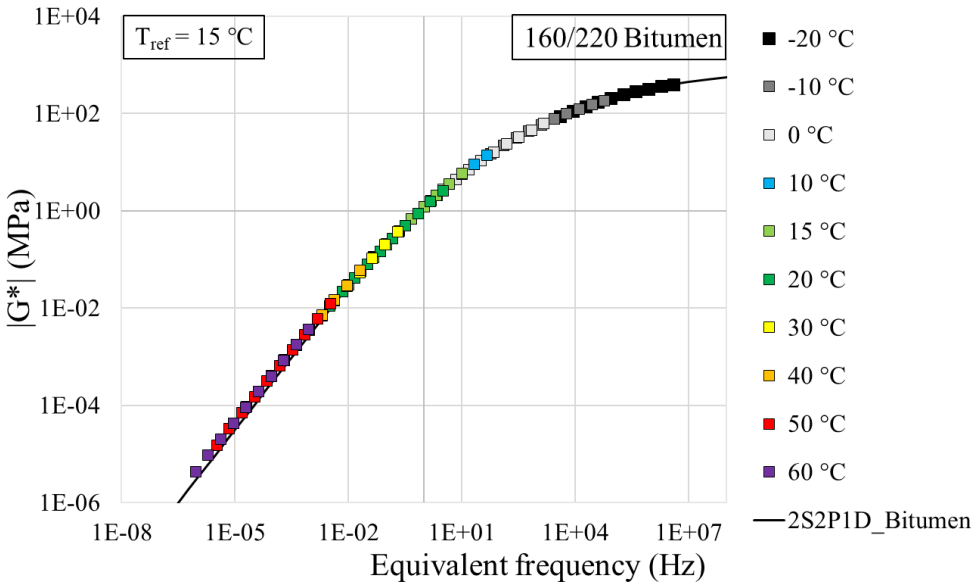

Figure 4.15 - Master curve of the norm of the shear complex modulus of the 160/220 pure bitumen at the reference temperature of 15 °C

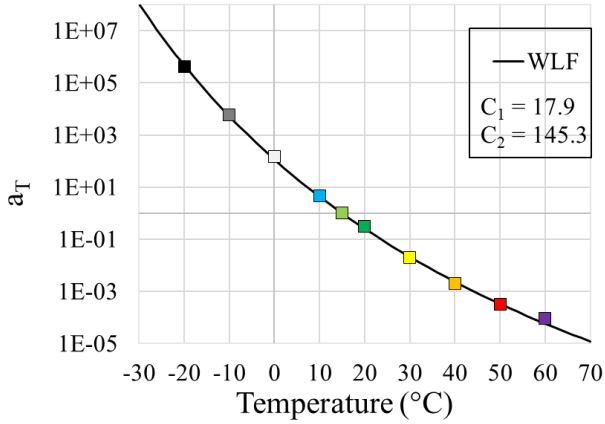

Figure 4.16 - Shift factors for the construction of the master curve of the shear complex modulus of the 160/220 pure bitumen at the reference temperature 15 °C with fitted WLF curve

The bitumen behaviour was then modelled using the 2S2P1D model as in section 4.1.3. The 2S2P1D constants and the WLF equation constants for the bitumen behaviour can be found in Table 4.3.

Table 4.3 - 2S2P1D constants and WLF equation constants for the shear complex modulus of the 160/220 pure bitumen

G_{00} (MPa)	G_0 (MPa)	k	h	δ	τ_G (s)	β	T_{ref} (°C)	C_1	C_2
0	850	0.2	0.53	2.3	2.10^{-6}	300	15	17.9	145.3

The value of the static modulus G_{00} is nil as it is always the case for pure bitumen (but not for mastic). The 2S2P1D model is plotted by the experimental data in the Black space in Figure 4.14 and for the master curve of the norm of the shear complex modulus in Figure 4.15.

4.1.4.2. Inadequacy of linear viscoelastic models to describe the behaviour of interfaces obtained with the advanced complex modulus test

The interface behaviour should depend on the behaviour of the bitumen of the tack coat. For bituminous mixtures, it has been shown that the mixture linear viscoelastic behaviour can be linked with the behaviour of its binder. The SHStS transformation (Shift, Homothetic expansion, Shift in time, Shift) has been developed to link the behaviour of the mixture with the behaviour of the binder (Di Benedetto *et al.* 2004). When both the mixture and the binder are modelled using 2S2P1D, the SHStS transformation implies that it the constants k, h, δ, β are the same in the two models.

Based on the same idea, an attempt to model the normal complex interface stiffness of sample HDO-1 using the 2S2P1D model was conducted with the same constants k, h, δ, β than for its binder (Table 4.3), the 160/220 pure bitumen. The 2S2P1D model definition for the complex modulus of mixtures given in Equation 4.24 is simply adapted for complex interface stiffness by changing the unit of the glassy and static modulus. Instead of the set of constants (E_{00}, E_0, k, h, δ, β, τ_E), the notations used for the normal complex interface stiffness are (K_{zz_00}, K_{zz_0}, k, h, δ, β, τ_{Kzz}) and the notations for the shear complex interface stiffness are ($K_{\theta z\_00}$, $K_{\theta z\_0}$, k, h, δ, β, $\tau_{K\theta z}$).

One model was fitted on the master curve of the norm of the normal complex interface stiffness of sample HDO-1. The model constants can be found in Table 4.4. The master curves of the normal complex interface stiffness are presented in Figure 4.17 with the 2S2P1D model (master curve of the norm on the left, and master curve of the phase angle on the right).

Table 4.4 - 2S2P1D constants and WLF equation constant for the normal complex interface stiffness in sample HDO-1

K_{zz_00} (MPa/mm)	K_{zz_0} (MPa/mm)	k	h	δ	τ_{Kzz} (s)	β	T_{ref} (°C)	C_1	C_2
22	7500	0.2	0.53	2.3	0.02	300	15	19.1	126.7

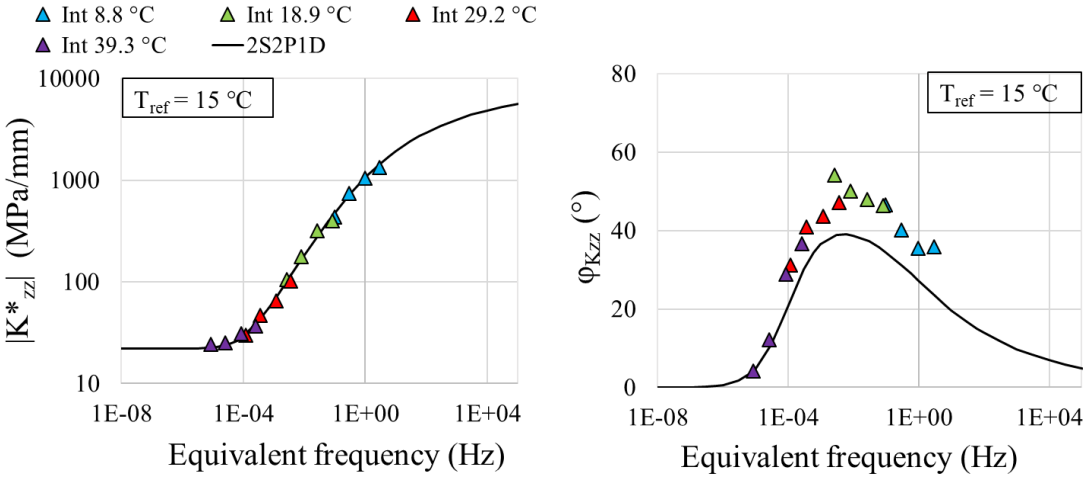

Figure 4.17 - Master curve of the norm (on the left) and of the phase angle (on the right) of the normal complex interface stiffness in sample HDO-1 with the 2S2P1D model fitted on the master curve of the norm

As it can be seen on Figure 4.17, the calibration succeeds for the norm of the complex interface stiffness, but it fails for the phase angle with an underestimation of about 10 °. The same observation can be done for the shear complex interface stiffness.

The fact that the model fits the norm but not the phase angle shows that the interface behaviour is not linear viscoelastic at the tested amplitudes. There is indeed a relationship between the norm and the phase angle of a complex modulus as defined in the linear viscoelastic theory. If a linear viscoelastic model fits the norm of the complex modulus, then it fits the phase angle of the complex modulus. A new model, that is not linear viscoelastic, is introduced in the next section to describe the interface behaviour.

4.1.4.3. DBN_{PDSC} model definition

The DBN model is a theoretical frame developed to describe a large class of behaviour of the bituminous materials. It is a generalization of the Kelvin-Voigt model (presented in section 1.4.1.1) with elastoplastic elements (noted EP) instead of springs (Neifar and Di Benedetto 2001). Different models were developed within this frame, for instance to describe the three dimensional behaviour of bituminous mixtures (Di Benedetto *et al.* 2007) or their thermo-viscoplastic behaviour (Gayte 2016).

The DBN_{PDSC} (DBN model with Plastic Dissipation for Small Cycles) model is introduced in this thesis using the framework of the DBN model. Its schematic representation is found in Figure 4.18. It corresponds to a generalised Kelvin-Voigt model with additional plastic dissipation in the springs, noted EP_i as in the DBN model. A single element of the DBN_{PDSC} model is presented in Figure 4.19 with useful notations.

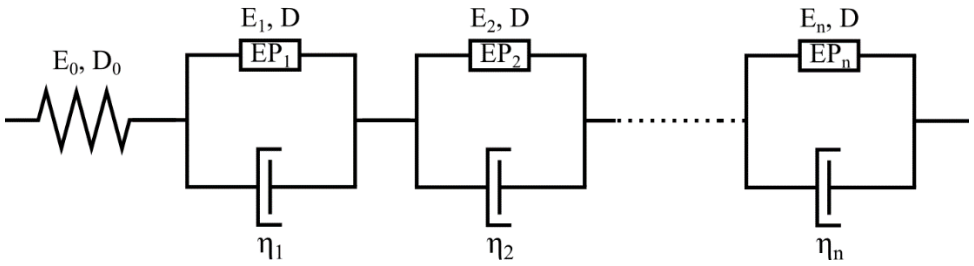

Figure 4.18 - Schematic representation of the DBN_{PDSC} model

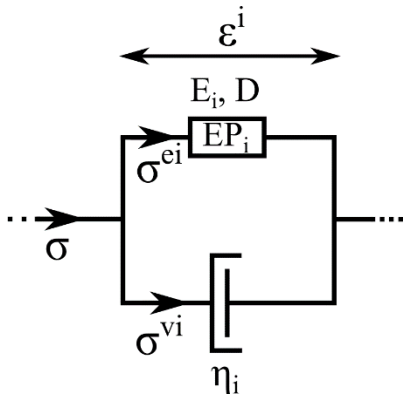

Figure 4.19 - Schematic representation of a single element of the DBN_{PDSC} model

In each element EP_i the stress σ^{ei} and the strain ε^i are simply related by Equation 4.26 where E_i is the element elastic modulus (Pa). The elastic modulus E_i does not depend on the strain amplitude in the DBN_{PDSC} model.

$$\sigma^{ei} = E_i \varepsilon^i \tag{4.26}$$

A similar relation exists for the spring E_0. The strain in this spring is noted ε^e.

For the linear dashpots, the Equation 4.27 links the stress σ^{vi} with the strain rate $\dot{\varepsilon}^i$, where η_i is the dashpot viscosity (Pa.s).

$$\sigma^{vi} = \eta_i \dot{\varepsilon}^i \tag{4.27}$$

The DBN_{PDSC} model is defined for cyclic loadings. When applying cyclic loading in a linear viscoelastic material, viscous energy is dissipated. If the cycles are sinusoidal, the energy per unit volume dissipated during one cycle (W^v) can be calculated as in Equation 4.28 where ε_0 is the strain amplitude, σ_0 the stress amplitude and φ is the phase angle of the complex modulus of the linear viscoelastic material. The viscous dissipation is illustrated in Figure 4.20 (on the right).

$$W^v = \pi \varepsilon_0 \sigma_0 \sin \varphi \tag{4.28}$$

For instance, in a linear dashpot subjected to a sinusoidal loading, the dissipated energy per unit volume in one cycle W^{vi} is given in Equation 4.29 where ε^i_0 is the strain amplitude and σ^{vi}_0 the stress amplitude in the dashpot.

$$W^{vi} = \pi \varepsilon_0^i \sigma_0^{vi} \tag{4.29}$$

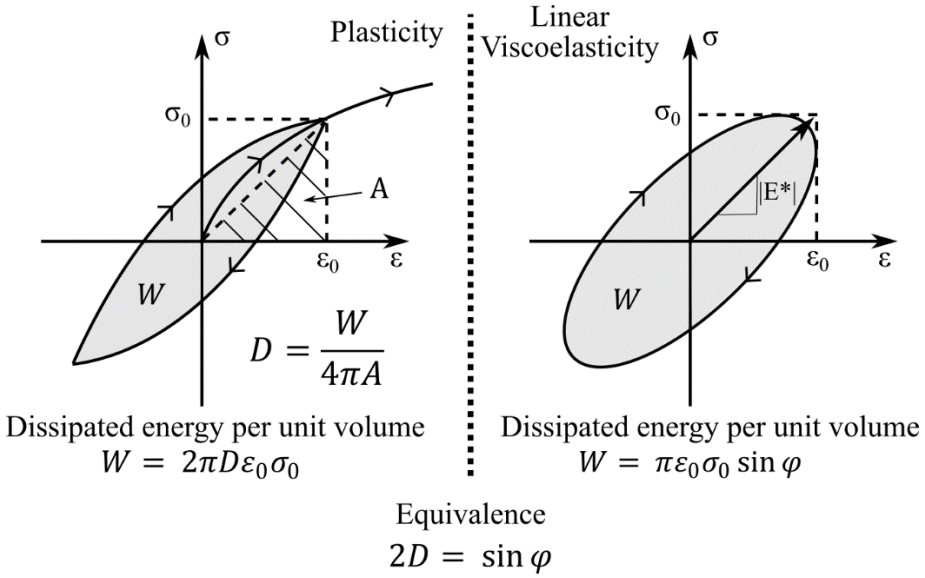

Figure 4.20 - Illustration of the analogy between plastic dissipation and viscous dissipation during a cycle

The general idea of the DBN_{PDSC} model is to add plastic dissipation in the non-viscous elements independently of the viscous dissipation happening in the dashpots. Plastic dissipation can be observed in sands for cycles at small strain amplitude (between 10^{-5} and 10^{-4} µm/m) where their behaviour is "hysteretic stabilised" (Sauzéat 2003). Using the same equations than for sands, the plastic energy per unit volume dissipated in an element EP_i in one cycle (W^{pi}) is defined in Equation 4.30 where D is a damping coefficient (illustrated in Figure 4.20).

$$W^{pi} = 2\pi D\varepsilon_0^i\sigma_0^{ei} \tag{4.30}$$

The damping coefficient D is chosen to be the same in every element EP_i but there is a different damping coefficient D_0 in the spring E_0 where a similar plastic dissipation is added. The coefficient D_0 depends on the strain amplitude ε^e_0 in the spring. As shown in Equation 4.31, a linear law is chosen to link D_0 and ε^e_0. The coefficient of proportionality depends on the amplitude of the total strain in the model ε_0 and on an angle φ_{NL_0} that is a parameter.

$$D_0(\varepsilon_0^e) = \frac{\sin\varphi_{NL\_0}}{2\varepsilon_0}\varepsilon_0^e \tag{4.31}$$

A similar law for the damping coefficient D is presented in Equation 4.32 but now D depends linearly on the total strain amplitude ε^v_0 in the elements different from the spring E_0 (at any time, the total strain ε in the model is $\varepsilon = \varepsilon^e + \varepsilon^v$). A parameter φ_{NL_00} is introduced in Equation 4.32.

$$D(\varepsilon_0^v) = \frac{\sin\varphi_{NL\_00}}{2\varepsilon_0}\varepsilon_0^v \tag{4.32}$$

The parameters φ_{NL_0} and φ_{NL_00} are chosen to be equal to the same value φ_{NL} in the following.

It is assumed that the addition of these dissipation coefficients does not affect the norm of the complex modulus of the model. The norm of the complex modulus $|E^*|(\omega)$ at the angular frequency ω can be calculated as for a classical generalised Kelvin-Voigt model with Equation 4.33 (that is derived from Equations 4.26 and 4.27).

$$|E^*|(\omega) = \left| \frac{1}{E_0} + \sum_{i=1}^{n} \frac{1}{E_i + i\omega\eta_i} \right|^{-1} \tag{4.33}$$

Using this value, it is possible to find the values of ε^e_0 and ε^v_0 with Equations 4.34 and 4.35 where σ_0 is the stress amplitude in the model.

$$\varepsilon_0^e = \frac{\sigma_0}{E_0} = \varepsilon_0 * \frac{|E^*|}{E_0} \tag{4.34}$$

$$\varepsilon_0^v = \varepsilon_0 \left| 1 - \frac{E^*}{E_0} \right| \tag{4.35}$$

The phase angle φ_{DBN} of the model DBN_{PDSC} at a given angular frequency ω is obtained from the total dissipation W in the model obtained in one cycle. The total dissipation W is simply the sum of all the dissipated energies per unit volume in the viscous elements (W^{vi}), in the elements EP_i (W^{pi}) and in the spring E_0 (W^{p0}) as presented in Equation 4.36.

$$W = W^{p0} + \sum_{i=1}^{n} \left(W^{pi} + W^{vi} \right) \tag{4.36}$$

Using the analogy with the dissipation in a linear viscoelastic material (Figure 4.20), the phase angle φ_{DBN} of the model DBN_{PDSC} is calculated with Equation 4.37.

$$\sin \varphi_{DBN} = \frac{W}{\pi \varepsilon_0 \sigma_0} \tag{4.37}$$

It is then possible to find an expression of the phase angle φ_{DBN} with the constants of the model. In the case of sinusoidal loadings, in an element of the DBN_{PDSC} model (such as the one presented in Figure 4.19) it is possible to find the relation between the stress amplitude σ_0 and the strain amplitude in the element ε^i_0 with Equation 4.38.

$$\varepsilon_0^i = \frac{\sigma_0}{\sqrt{E_i^2 + (\eta_i \omega)^2}} \tag{4.38}$$

Also, in the elements EP_i, Equation 4.39 can be derived, and in the dashpots, Equation 4.40.

$$\sigma_0^{ei} = E_i \varepsilon_0^i \tag{4.39}$$

$$\sigma_0^{vi} = \eta_i \omega \varepsilon_0^i \tag{4.40}$$

And the definition of the complex modulus of the complete model implies Equation 4.41.

$$\varepsilon_0 = \frac{\sigma_0}{|E^*|} \tag{4.41}$$

Now, from Equation 4.29 and using Equations 4.38, 4.40 and 4.41, the dissipation in a dashpot can be written as in Equation 4.42.

$$W^{vi} = \pi \varepsilon_0 \sigma_0 \frac{|E^*| \eta_i \omega}{E_i^2 + (\eta_i \omega)^2} \tag{4.42}$$

From Equation 4.30 and using Equations 4.38, 4.39 and 4.40, the dissipation in an element EPi can be written as in Equation 4.43.

$$W^{pi} = \pi \varepsilon_0 \sigma_0 \frac{2|E^*| D(\varepsilon_0^v) E_i}{E_i^2 + (\eta_i \omega)^2} \tag{4.43}$$

And the dissipation in the spring E_0 is as in Equation 4.44.

$$W^{p0} = \pi \varepsilon_0 \sigma_0 \frac{2|E^*| D_0(\varepsilon_0^e)}{E_0} \tag{4.44}$$

So finally, from Equations 4.36 and 4.37, using Equation 4.42, 4.43 and 4.44, an expression of the phase angle φ_{DBN} of the DBN_{PDSC} model is expressed in Equation 4.45.

$$\sin \varphi_{DBN} = |E^*|(\omega) \left(\frac{2D_0(\varepsilon_0^e)}{E_0} + \sum_{i=1}^{n} \frac{2D(\varepsilon_0^v) E_i + \eta_i \omega}{E_i^2 + (\eta_i \omega)^2} \right) \tag{4.45}$$

When the frequency tends to infinity, the phase angle φ_{DBN} tends to the angle φ_{NL}. From the Equations 4.31, 4.32, 4.34 and 4.34 it can also be seen that the phase angle φ_{DBN} does not depend on the global strain amplitude ε_0.

4.1.4.4. DBN_{PDSC} model calibration

First, a 2S2P1D model is fitted to the master curve of the complex interface stiffness as explained in section 4.1.4.2, using the pure bitumen 2S2P1D constants presented in Table 4.3 if the tack coat is made out of this bitumen. Then a Generalised Kelvin-Voigt (GKV) model is calibrated from the 2S2P1D model at the reference temperature of 15 °C with an existing optimisation procedure in the frequency domain (Tiouajni 2013; Gayte 2016). The number of elements in the GKV model is set at 25 in this thesis. It is a sufficient number of elements to describe correctly the bituminous materials in the small strain domain on a large frequency range. The elements constants are noted (K_{zz0}, K_{zzi}, η_i) for the normal complex interface stiffness and ($K_{\theta z0}$, $K_{\theta zi}$, η_i) for the shear complex interface stiffness where the unit of the stiffnesses is the Pa/m and the unit of the viscosities is the Pa.s/m. As explained in the previous section, the norm of the complex modulus of the DBN_{PDSC} model is the same than for a GKV model. So the elements constants in the DBN_{PDSC} are the same than for the GKV model.

For the example of the normal complex interface stiffness of sample HDO-1, the DBN_{PDSC} constants obtained from the 2S2P1D model (Table 4.4) can be found in Table 4.5.

Table 4.5 - DBN_{PDSC} constants of the normal complex interface stiffness in sample HDO-1

Element number	K_{zzi} (MPa/mm)	η_i (MPa.s/mm)	φ_{NL} (°)
0	7.5E+03	X	10
1	1.2E+06	1.0E-08	
2	1.3E+06	6.7E-08	
3	1.2E+06	3.4E-07	
4	1.1E+06	1.8E-06	
5	6.6E+05	6.1E-06	
6	5.2E+05	2.7E-05	
7	3.4E+05	1.0E-04	
8	2.5E+05	4.3E-04	
9	1.7E+05	1.6E-03	
10	1.2E+05	6.7E-03	
11	8.6E+04	2.6E-02	
12	6.0E+04	1.0E-01	
13	4.1E+04	4.0E-01	
14	2.8E+04	1.5E+00	
15	1.8E+04	5.7E+00	
16	1.1E+04	2.0E+01	
17	6.7E+03	6.7E+01	
18	3.6E+03	2.1E+02	
19	1.8E+03	5.8E+02	
20	8.5E+02	1.5E+03	
21	3.7E+02	3.8E+03	
22	1.6E+02	9.2E+03	
23	7.0E+01	2.3E+04	
24	5.9E+01	1.1E+05	
25	3.9E+02	4.1E+06	

The phase angle of the complex interface stiffness is calculated using the DBN_{PDSC} model as explained in section 4.1.4.3 with the quantities adapted for normal (respectively, shear) complex interface stiffnesses: the complex modulus E^* is replaced by the complex interface stiffness K^*_{zz} (resp. $K^*_{\theta z}$), the strain ε by the displacement gap Δu_z (resp. Δu_θ), the stress σ by σ_{zz} (resp. $\tau_{\theta z}$), the model elements constants (E_0, E_i, η_i) by the constants (K_{zz0}, K_{zzi}, η_i) (resp. ($K_{\theta z0}$, $K_{\theta zi}$, η_i)) with the units mentioned above. The DBN_{PDSC} is then fitted using the calibration parameter φ_{NL} on the Black diagram and on the master curve of the phase angle of the complex interface stiffness.

For the example of the normal complex interface stiffness in sample HDO-1, the angle φ_{NL} is found to be 10 ° which represents a damping coefficient of 8.6 %. The normal complex interface modulus with the DBN_{PDSC} model and the 2S2P1D model used for the calibration are plotted in the Black space in Figure 4.21 (on the left), the master curve of the norm of the normal complex interface stiffness with

the models is presented in Figure 4.22 (on the left) and the master curve of the phase angle with the models is in Figure 4.23 (on the left).

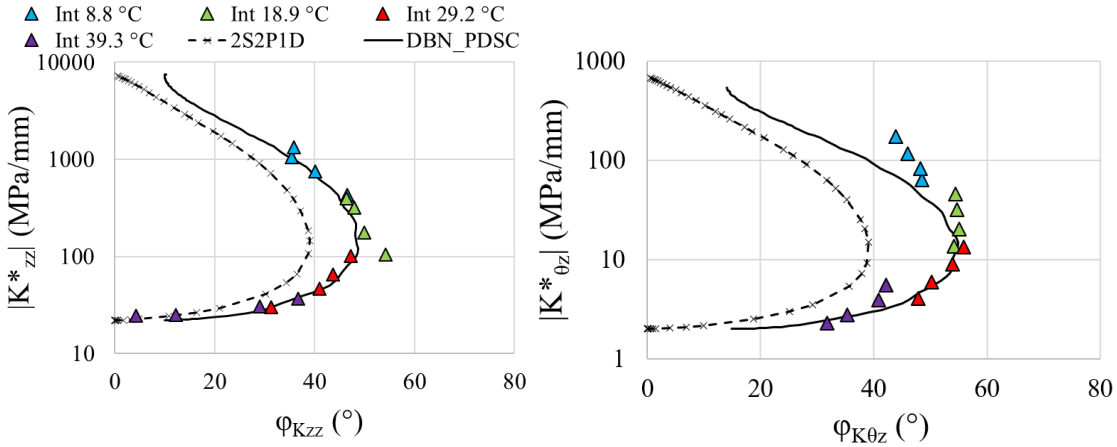

Figure 4.21 - Black diagram of the normal complex interface stiffness (on the left) and shear complex interface stiffness (on the right) of the interface in the sample HDO-1 with DBN_{PDSC} model and the 2S2P1D model used for the calibration

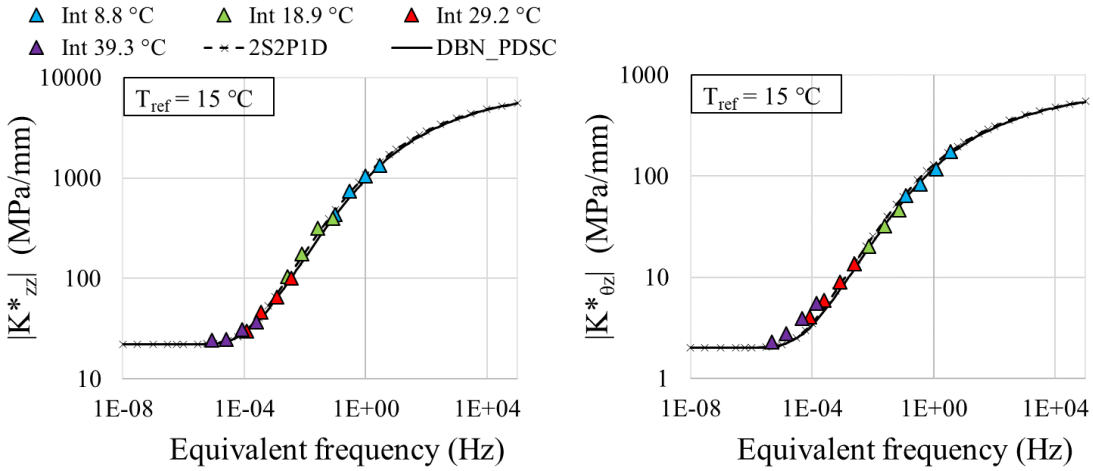

Figure 4.22 - Master curves of the norm of the normal complex interface stiffness (on the left) and of the shear complex interface stiffness (on the right) of the interface in the sample HDO-1 at the reference temperature of 15 °C with DBN_{PDSC} model and the 2S2P1D model used for the calibration

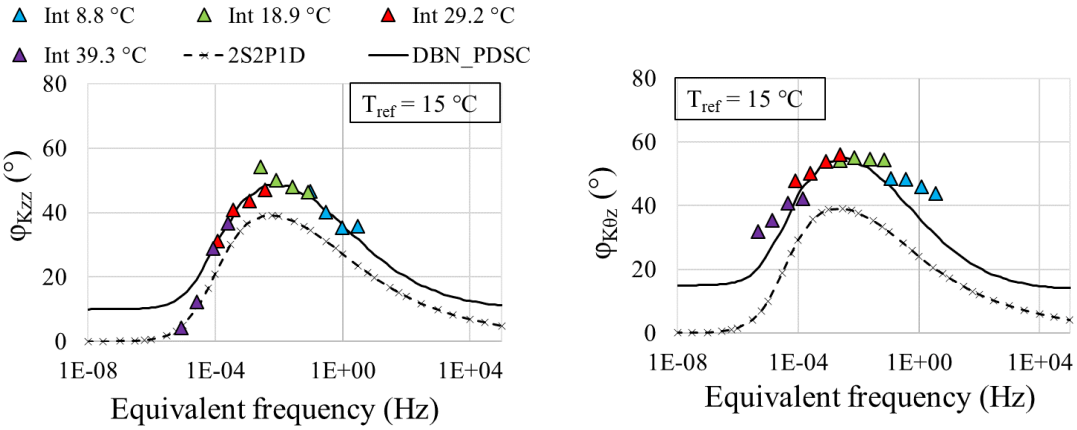

Figure 4.23 - Master curves of the phase angle of the normal complex interface stiffness (on the left) and of the shear complex interface stiffness (on the right) of the interface in the sample HDO-1 at the reference temperature of 15 °C with DBN_{PDSC} model and the 2S2P1D model used for the calibration

The same procedure is conducted to calibrate the DBN_{PDSC} model for the shear complex interface stiffness in sample HDO-1. The angle φ_{NL} is this time 15 ° which corresponds to a damping coefficient of 12.9 %. The constants of this DBN_{PDSC} model can be found in Appendix B. The model is plotted with the experimental results in the Black space in Figure 4.21 (on the right), with the master curve of the norm of the complex interface stiffness in Figure 4.22 (on the right) and with the master curve of the phase angle of the complex interface stiffness in Figure 4.23 (on the right).

4.2. Bituminous mixtures behaviour in the small strain domain

4.2.1.Modelling with 2S2P1D

The axial complex moduli and the shear complex moduli of the bituminous mixtures of the 2T3C HCA samples were obtained following the procedure described in section 4.1.1.

For the bituminous mixtures in the upper layer of the samples, the Black diagram of the axial complex modulus is presented in Figure 4.24 and the Black diagram of the shear complex modulus is presented in Figure 4.25.

For the bituminous mixtures in the lower layer of the samples, the Black diagram of the axial complex modulus is presented in Figure 4.26 and the Black diagram of the shear complex modulus is presented in Figure 4.27.

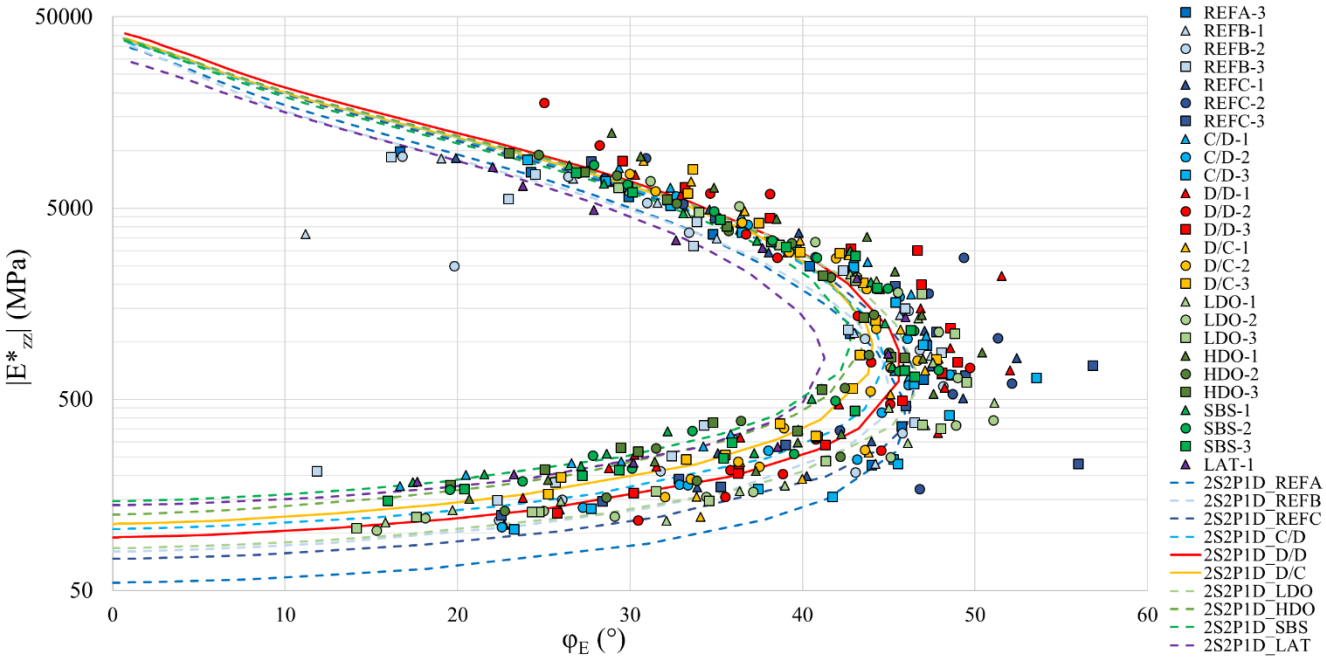

Figure 4.24 - Axial complex modulus of the bituminous mixtures in the upper layer of the 2T3C HCA samples represented in the Black space (BBSG3 mixtures are in blue or green, BB5 mixtures are in red or orange) with 2S2P1D models (one average model for each slab)

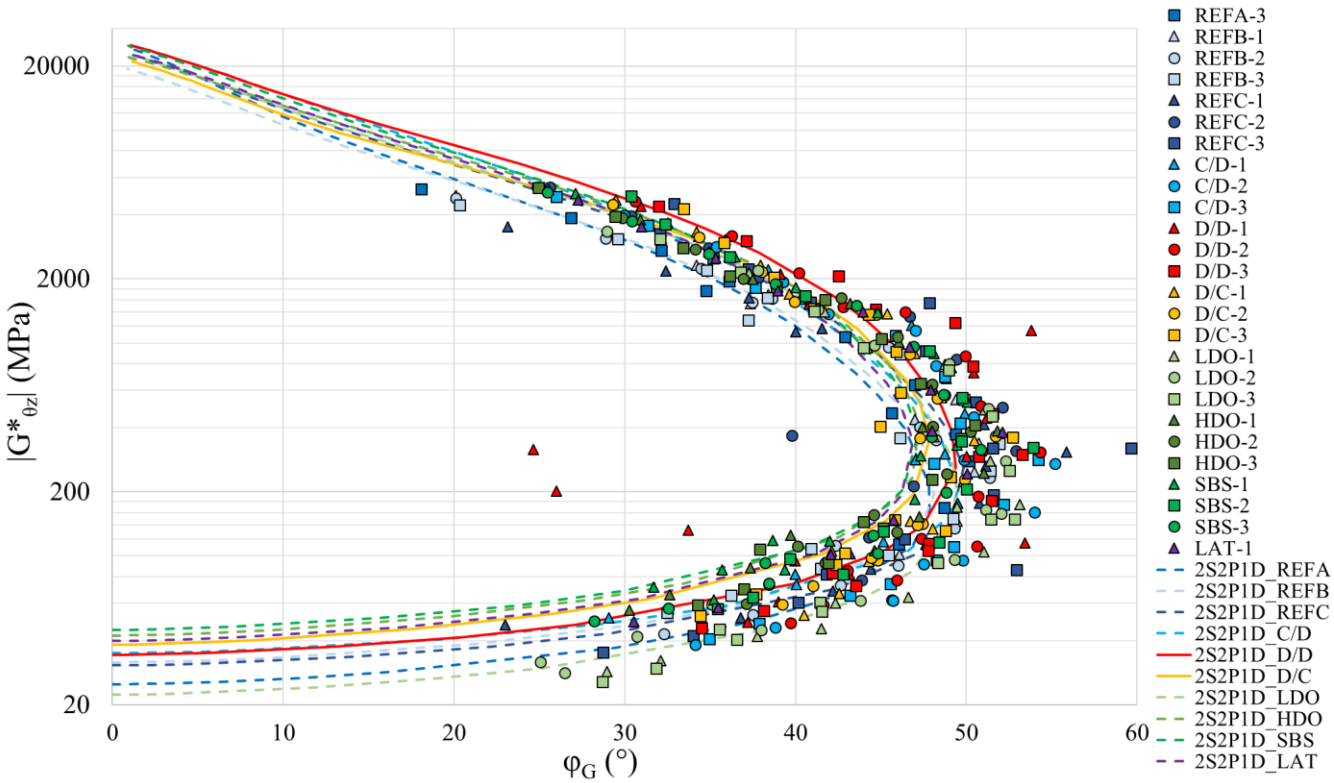

Figure 4.25 - Shear complex modulus of the bituminous mixtures in the upper layer of the 2T3C HCA samples represented in the Black space (BBSG3 mixtures are in blue or green, BB5 mixtures are in red or orange) with 2S2P1D models (one average model for each slab)

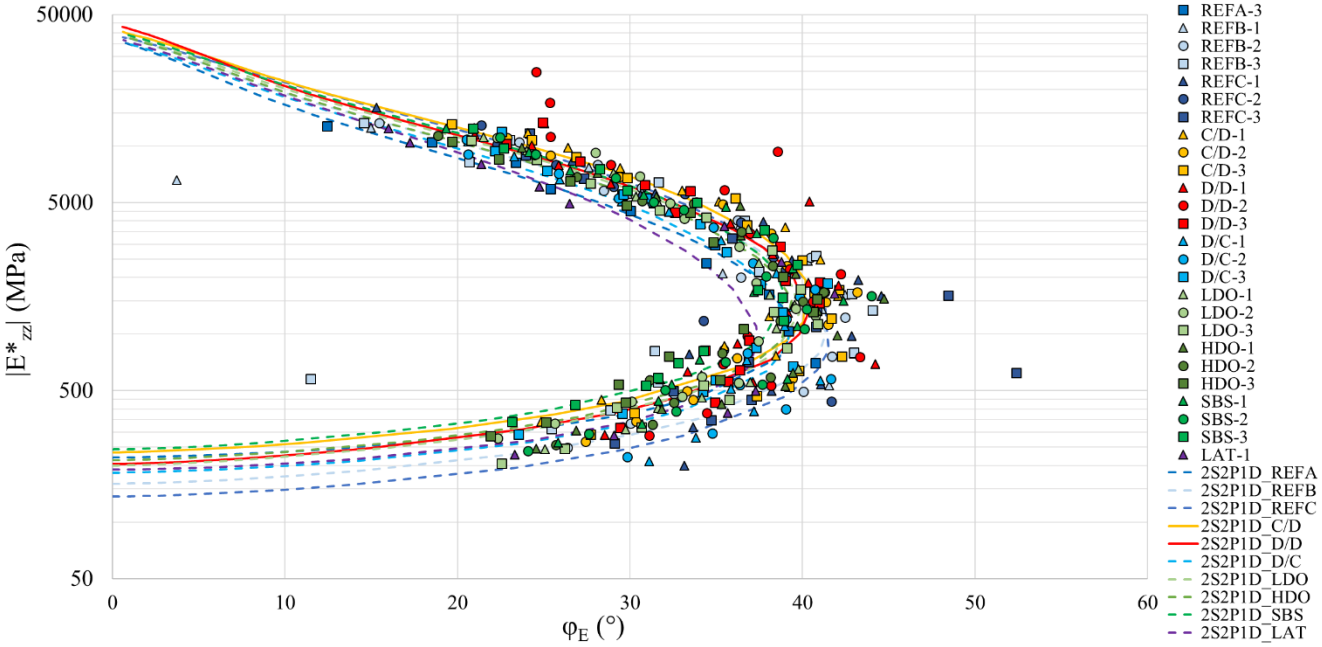

Figure 4.26 - Axial complex modulus of the bituminous mixtures in the lower layer of the 2T3C HCA samples represented in the Black space (EME2 mixtures are in blue or green, GB5 mixtures are in red or orange) with 2S2P1D models (one average model for each slab)

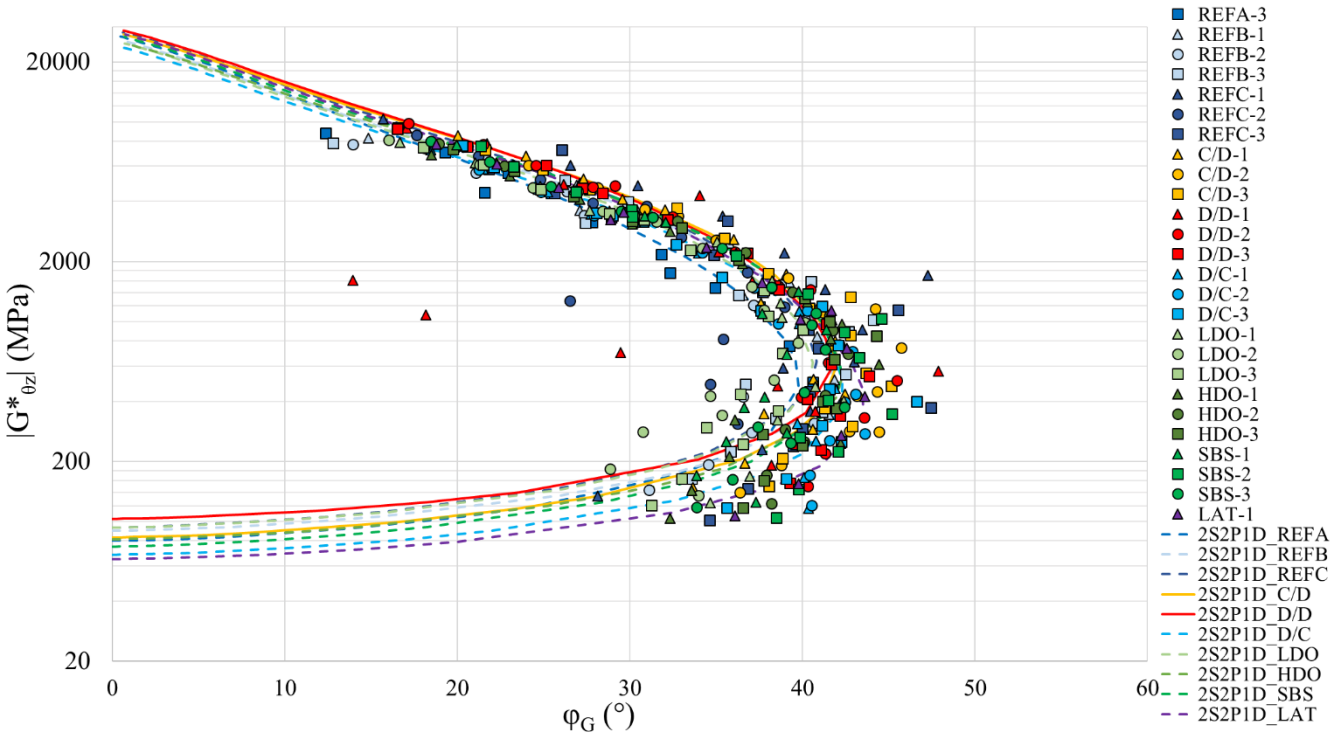

Figure 4.27 - Shear complex modulus of the bituminous mixtures in the lower layer of the 2T3C HCA samples represented in the Black space (EME2 mixtures are in blue or green, GB5 mixtures are in red or orange) with 2S2P1D models (one average model for each slab)

Unique curves were found on the Black diagrams of the axial complex modulus and of the shear complex modulus for all the bituminous mixtures (to look at the figures sample by sample, see Appendix A). So all the tested bituminous mixtures respected the TTSP.

The master curves of the bituminous mixtures were then built following the procedure presented in section 4.1.2, with the same reference temperature T_{ref} = 15 °C for all the samples.

For the bituminous mixtures in the upper layer of the samples, the master curve of the norm of the axial complex modulus is presented in Figure 4.28 and the master curve of the phase angle of the axial complex modulus can be found in Figure 4.29. The vertical strain amplitude in the mixtures during the axial cycles can be found in Figure 4.30 where they are plotted versus the equivalent frequency using the same shift factors than for the master curves. The master curve of the norm of the shear complex modulus is plotted in Figure 4.31 and the master curve of the phase angle of the shear complex modulus is found in Figure 4.32. The shear strain amplitude in the mixtures during the rotation cycles can be found in Figure 4.33.

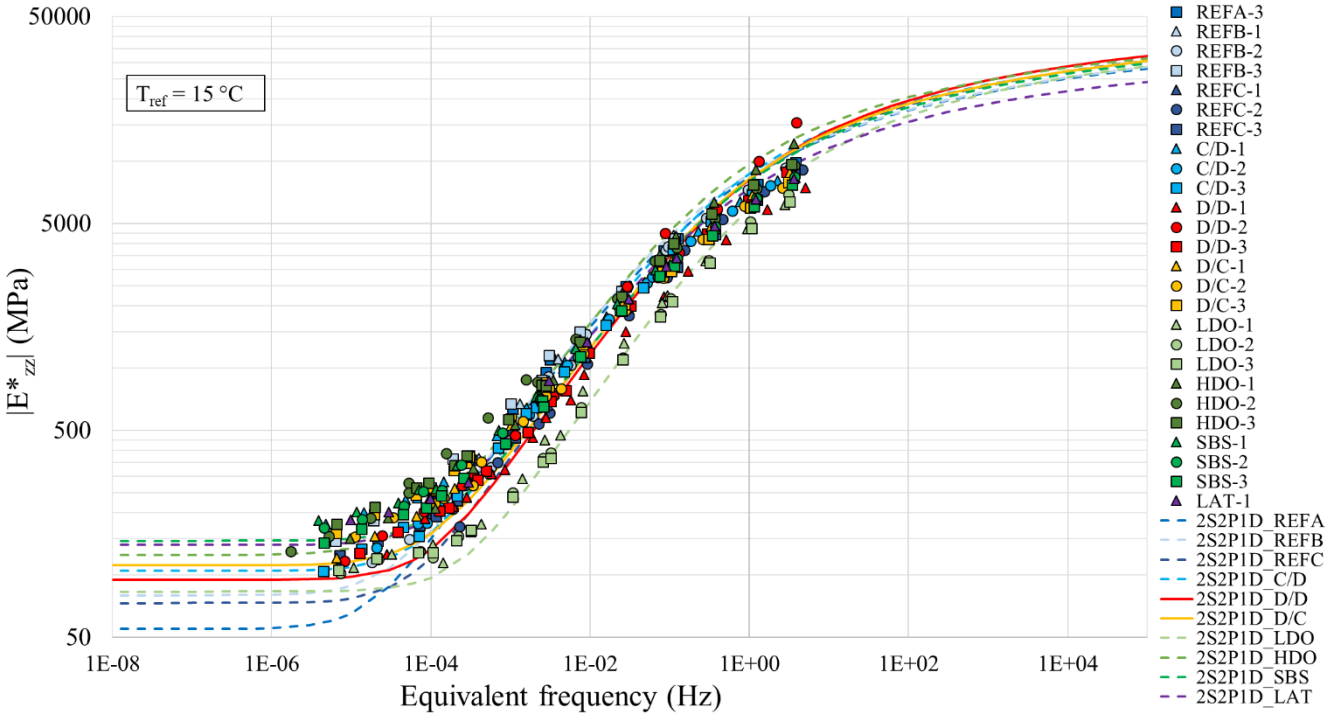

Figure 4.28 - Master curve of the norm of the axial complex modulus of the bituminous mixtures in the upper layer of the 2T3C HCA samples (BBSG3 mixtures are in blue or green, BB5 mixtures are in red or orange) with 2S2P1D models (one average model for each slab)

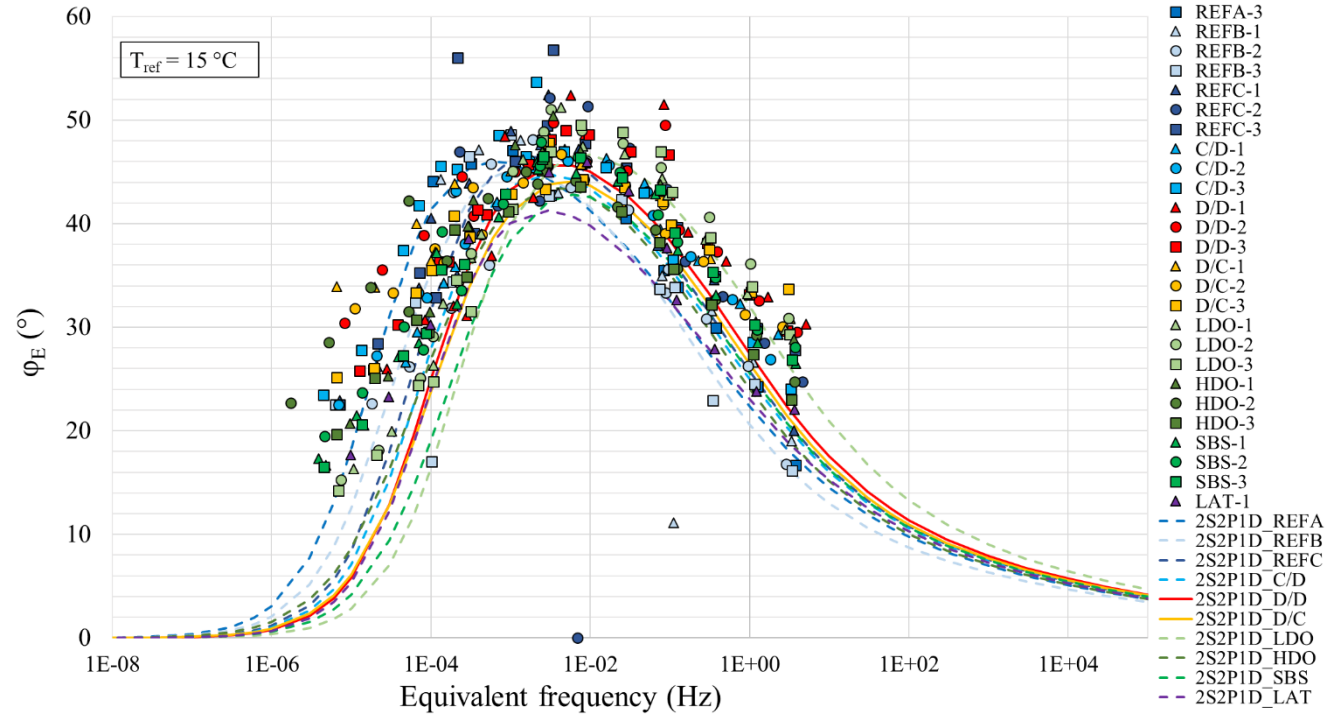

Figure 4.29 - Master curve of the phase angle of the axial complex modulus of the bituminous mixtures in the upper layer of the 2T3C HCA samples (BBSG3 mixtures are in blue or green, BB5 mixtures are in red or orange) with 2S2P1D models (one average model for each slab)

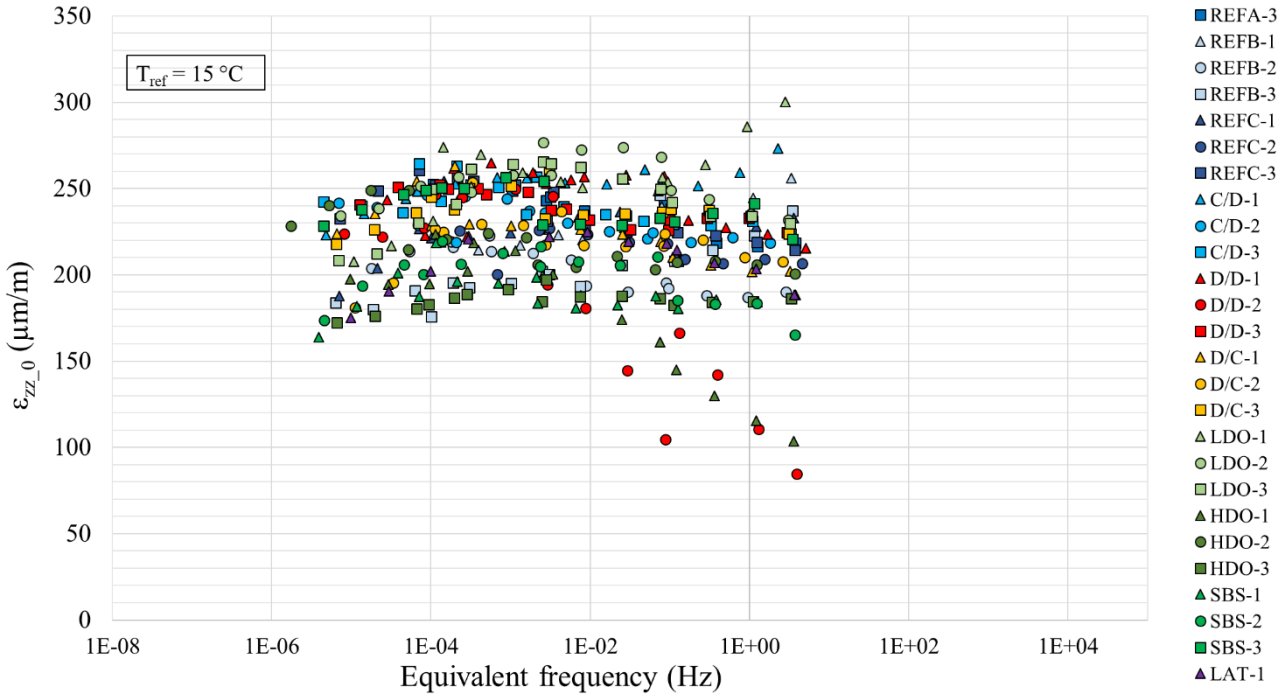

Figure 4.30 - Vertical strain amplitude during the axial cycles in the bituminous mixtures in the upper layer of the 2T3C HCA samples (BBSG3 mixtures are in blue or green, BB5 mixtures are in red or orange)

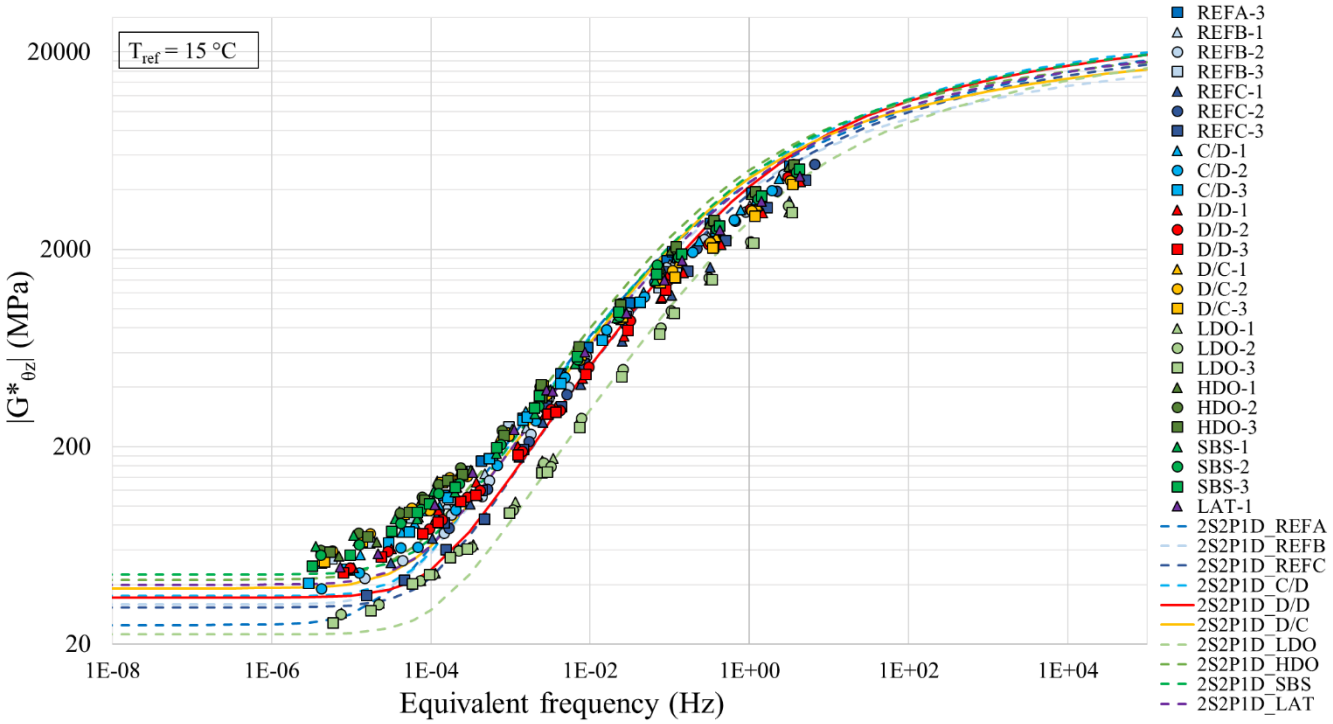

Figure 4.31 - Master curve of the norm of the shear complex modulus of the bituminous mixtures in the upper layer of the 2T3C HCA samples (BBSG3 mixtures are in blue or green, BB5 mixtures are in red or orange) with 2S2P1D models (one average model for each slab)

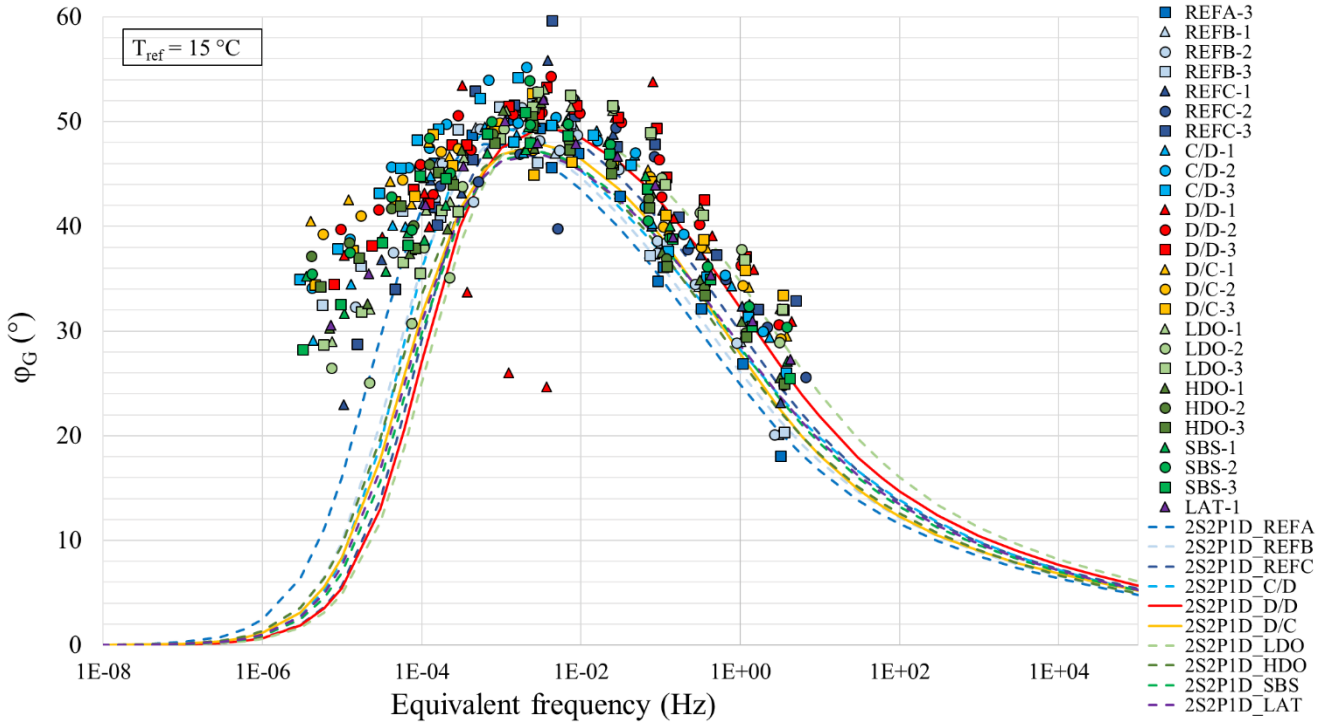

Figure 4.32 - Master curve of the phase angle of the shear complex modulus of the bituminous mixtures in the upper layer of the 2T3C HCA samples (BBSG3 mixtures are in blue or green, BB5 mixtures are in red or orange) with 2S2P1D models (one average model for each slab)

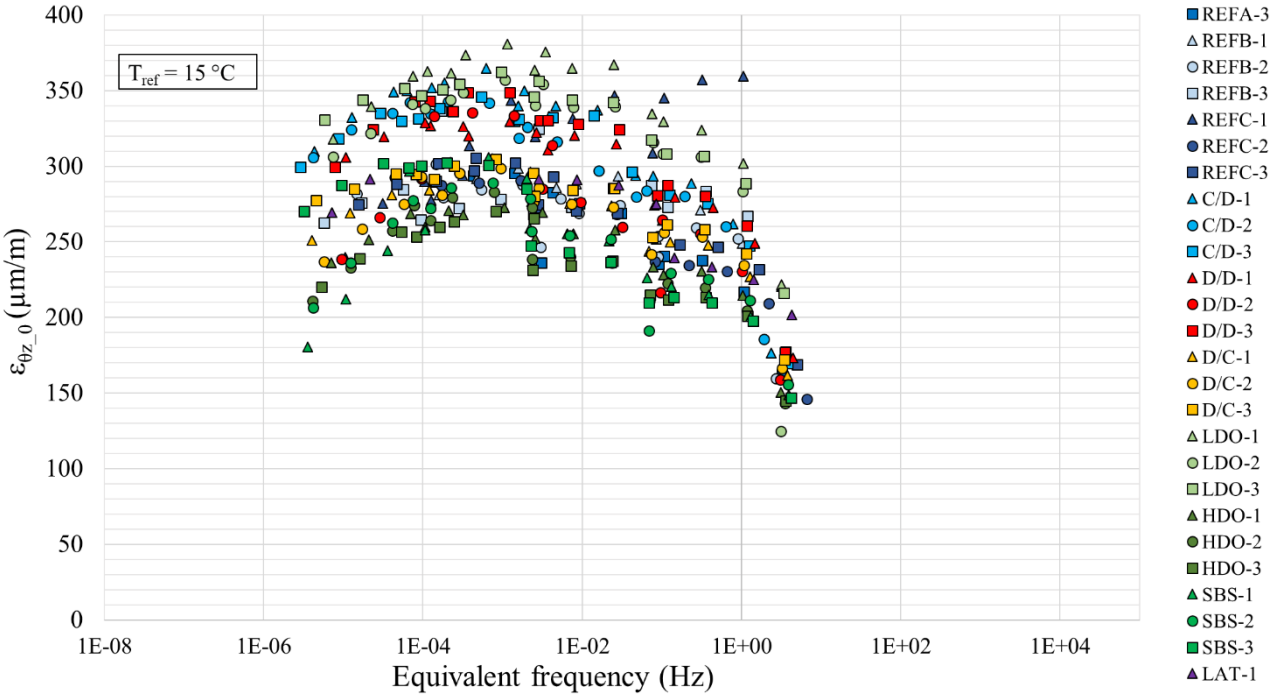

Figure 4.33 - Shear strain amplitude during the rotation cycles in the bituminous mixtures in the upper layer of the 2T3C HCA samples (BBSG3 mixtures are in blue or green, BB5 mixtures are in red or orange)

For the bituminous mixtures in the lower layer of the samples, the master curve of the norm of the axial complex modulus is presented in Figure 4.34 and the master curve of the phase angle of the axial complex modulus can be found in Figure 4.35. The vertical strain amplitude during the axial cycles are presented in Figure 4.36.The master curve of the norm of the shear complex modulus is plotted in Figure 4.37 and the master curve of the phase angle of the shear complex modulus is presented in Figure 4.38. The shear strain amplitude in the layers during the rotation cycles are found on Figure 4.39.

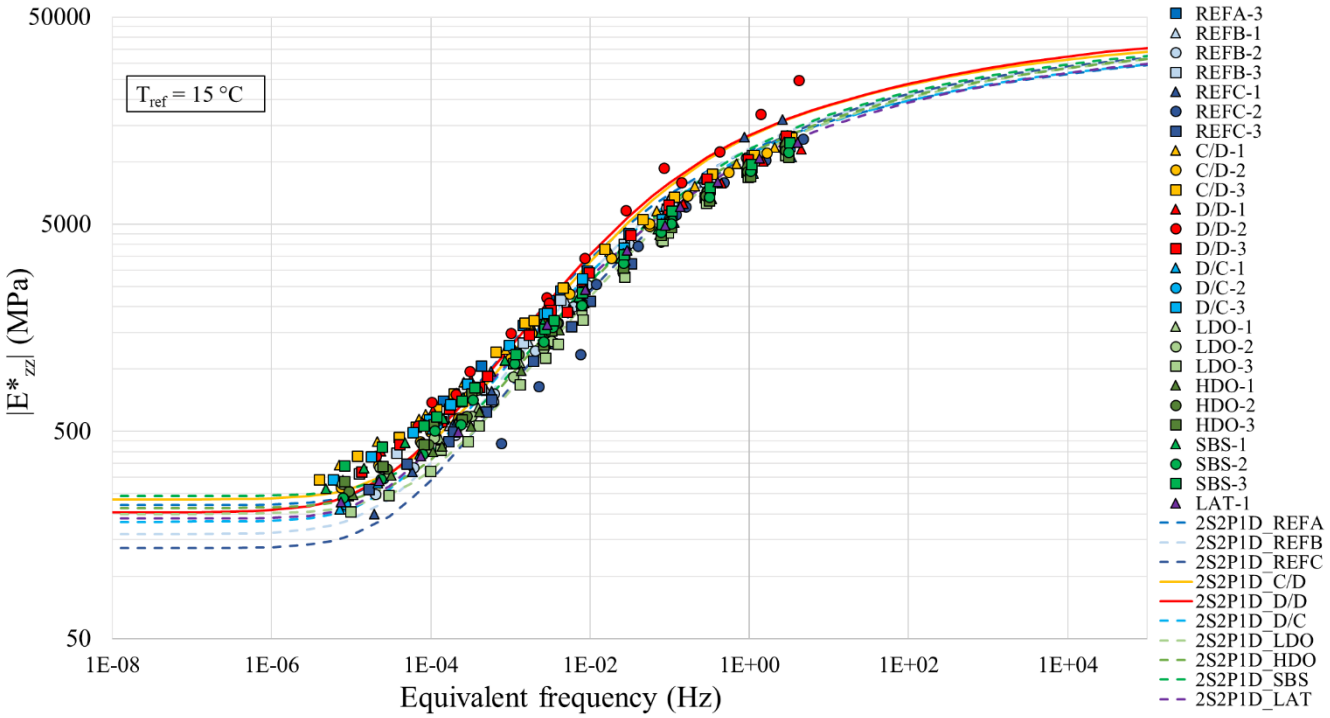

Figure 4.34 - Master curve of the norm of the axial complex modulus of the bituminous mixtures in the lower layer of the 2T3C HCA samples (EME2 mixtures are in blue or green, GB5 mixtures are in red or orange) with 2S2P1D models (one average model for each slab)

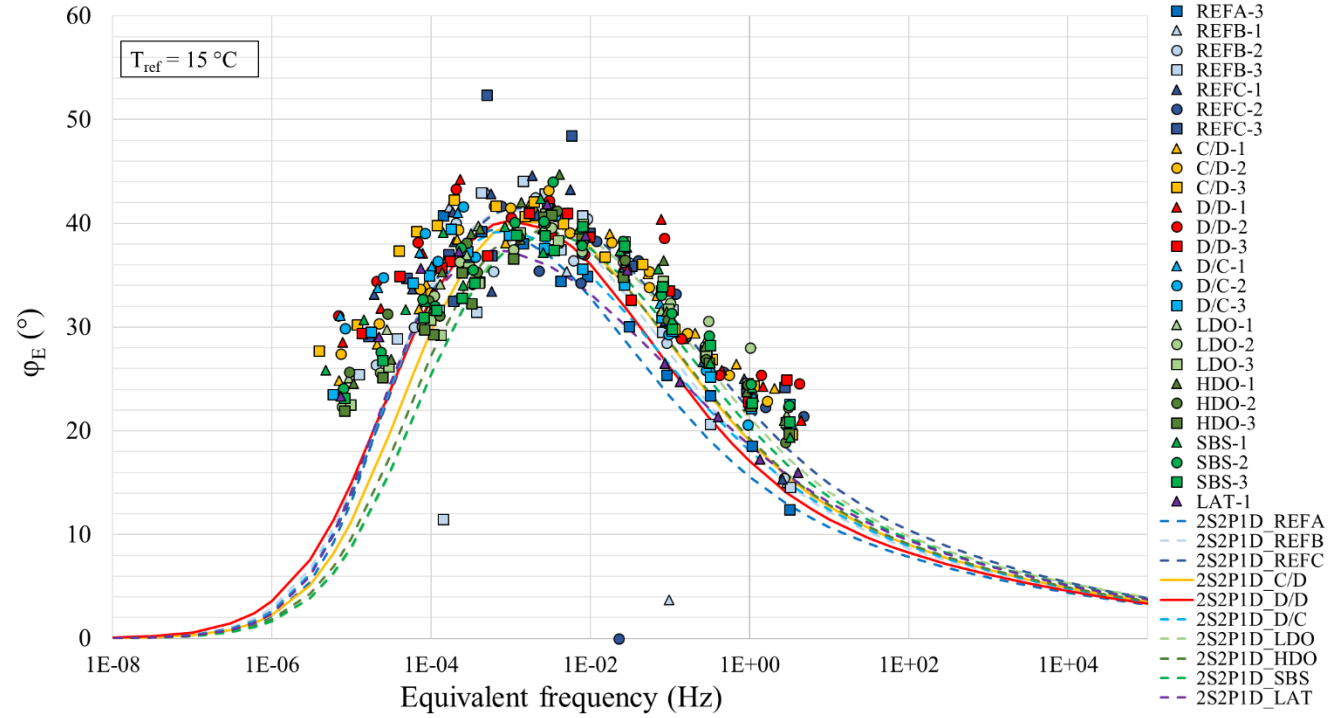

Figure 4.35 - Master curve of the phase angle of the axial complex modulus of the bituminous mixtures in the lower layer of the 2T3C HCA samples (EME2 mixtures are in blue or green, GB5 mixtures are in red or orange) with 2S2P1D models (one average model for each slab)

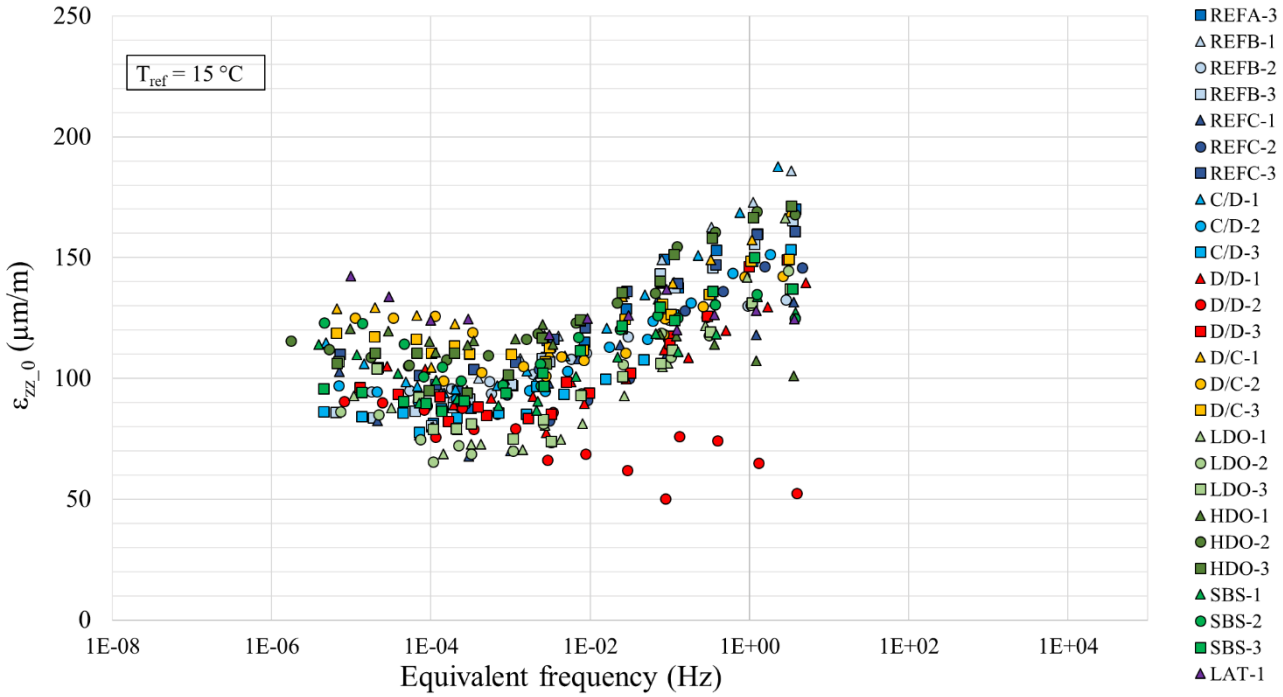

Figure 4.36 - Vertical strain amplitude during the axial cycles in the bituminous mixtures in the lower layer of the 2T3C HCA samples (EME2 mixtures are in blue or green, GB5 mixtures are in red or orange)

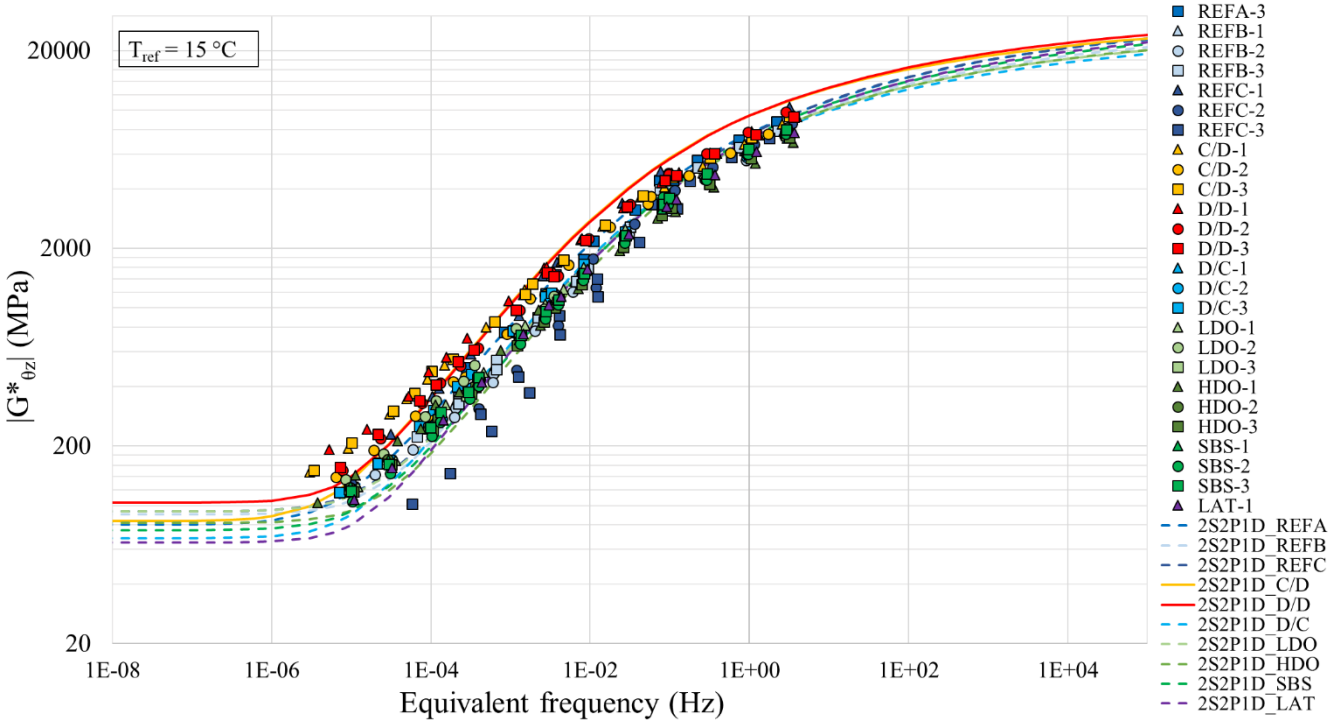

Figure 4.37 - Master curve of the norm of the shear complex modulus of the bituminous mixtures in the lower layer of the 2T3C HCA samples (EME2 mixtures are in blue or green, GB5 mixtures are in red or orange) with 2S2P1D models (one average model for each slab)

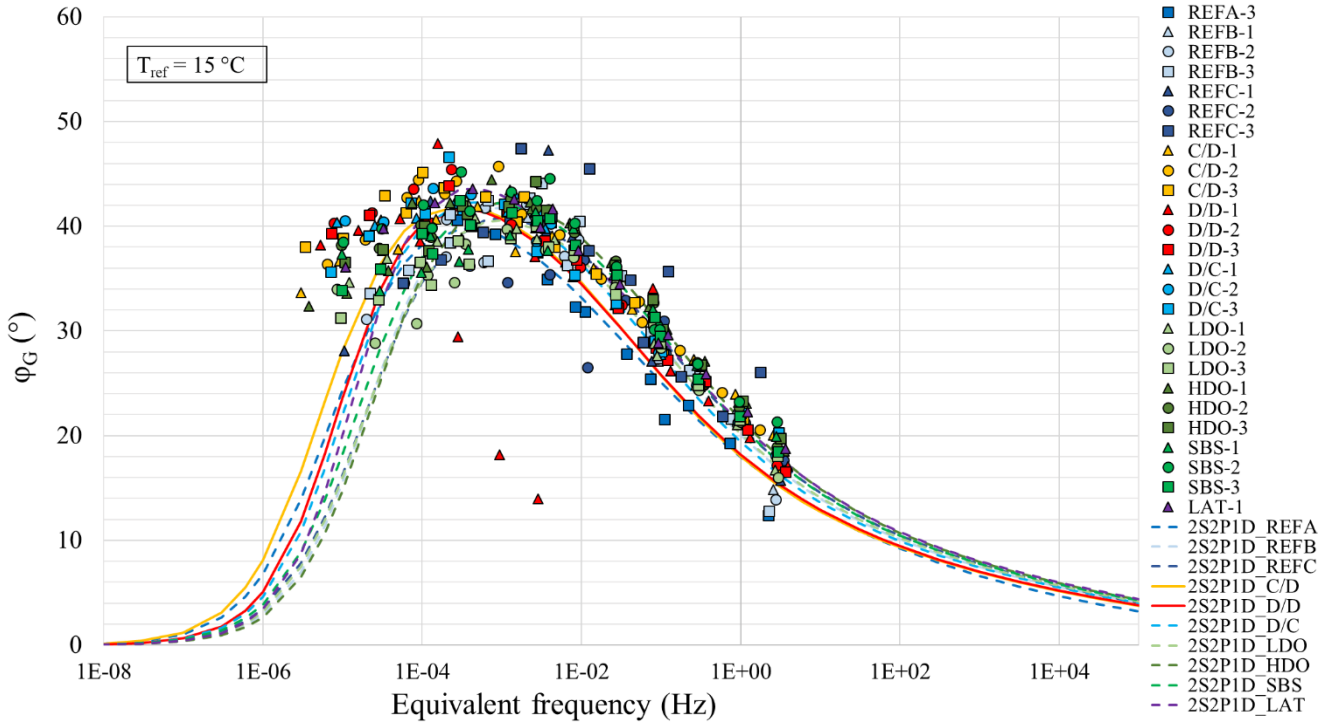

Figure 4.38 - Master curve of the phase angle of the shear complex modulus of the bituminous mixtures in the lower layer of the 2T3C HCA samples (EME2 mixtures are in blue or green, GB5 mixtures are in red or orange) with 2S2P1D models (one average model for each slab)

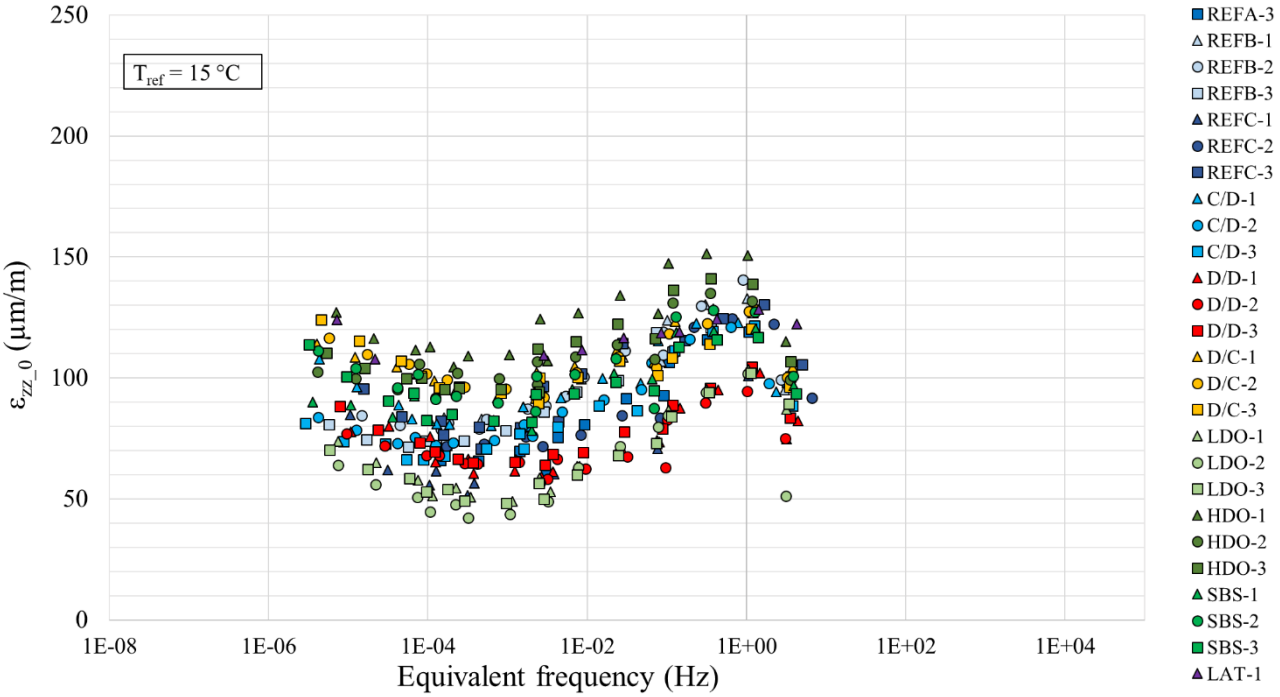

Figure 4.39 - Shear strain amplitude during the rotation cycles in the bituminous mixtures in the lower layer of the 2T3C HCA samples (EME2 mixtures are in blue or green, GB5 mixtures are in red or orange)

The bituminous mixtures were modelled using the 2S2P1D model as explained in section 4.1.3. The constants of the 2S2P1D model and of the WLF equation for each sample are found in Table 4.6 for the axial complex modulus of the mixtures in the upper layer, in Table 4.7 for the shear complex modulus of the mixtures in the upper layer, in Table 4.8 for the axial complex modulus of the mixtures in the lower layer and in Table 4.9 for the shear complex modulus of the mixtures in the lower layer. For the sake of clarity, one average 2S2P1D model is calculated for the same material of a single slab by

calculating the arithmetic mean of each constant of the 2S2P1D models obtained from the slab (one model per sample). The average 2S2P1D models are plotted on the previous figures with the experimental data (Figure 4.24 to Figure 4.39). The 2S2P1D model for each sample are plotted in Appendix A with the experimental data.

It is possible to notice small discrepancies between the 2S2P1D model and the experimental data for low and high equivalent frequencies on the master curves of the norm and of the phase angle of the complex moduli (Figure 4.28, Figure 4.29, Figure 4.31, Figure 4.32, Figure 4.34, Figure 4.35, Figure 4.37, Figure 4.38). This is partly due to the difficulty to calibrate the model in these regions with the limited frequency range where the advanced complex modulus test is performed. There are indeed few measurements at high frequencies and low temperatures inducing uncertainty for the calibration of parameters k and E_0. But this is also related to the apparition of nonlinearities in the behaviour of the bituminous mixtures because of the amplitude of the loadings. As it can be seen on Figure 4.30, Figure 4.33, Figure 4.36 and Figure 4.39, the strain amplitude in the layers is often superior to 100 µm/m which can be considered as the limit of the LVE domain for bituminous mixtures (Airey *et al.* 2003) but this limit could be even lower for the frequencies and temperatures (Mangiafico *et al.* 2017) tested in the advanced complex modulus test.

Table 4.6 - 2S2P1D and WLF constants for the axial complex modulus of the mixtures in the upper layer

Sample	Mixture	E_{00} (MPa)	E_0 (MPa)	k	h	δ	τ_E (s)	β	T_{ref} (°C)	C_1	C_2
REFA-3	BBSG3	55	37000	0.168	0.55	2.0	0.080	200	15	21.2	131.4
REFB-1	BBSG3	60	38000	0.174	0.57	2.2	0.090	160	15	17.7	115.1
REFB-2	BBSG3	70	38000	0.17	0.57	2.1	0.080	160	15	14.0	97.2
REFB-3	BBSG3	110	38000	0.17	0.59	2.6	0.150	130	15	20.8	131.0
REFB_avg	BBSG3	80	38000	0.171	0.58	2.3	0.107	150	15		
REFC-1	BBSG3	80	42000	0.168	0.57	2.0	0.060	180	15	15.8	95.9
REFC-2	BBSG3	45	38000	0.176	0.57	1.7	0.040	110	15	7.3	46.3
REFC-3	BBSG3	95	41000	0.17	0.57	2.1	0.050	130	15	19.5	122.3
REFC_avg	BBSG3	73	40333	0.171	0.57	1.9	0.050	140	15		
C/D-1	BBSG3	150	39000	0.17	0.57	1.8	0.070	100	15	16.3	98.9
C/D-2	BBSG3	90	37000	0.17	0.57	1.8	0.070	150	15	17.0	111.4
C/D-3	BBSG3	75	40000	0.176	0.56	1.8	0.060	150	15	20.8	131.9
C/D_avg	BBSG3	105	38667	0.172	0.57	1.8	0.067	133	15		
D/D-1	BB5	100	42000	0.17	0.56	2.0	0.025	100	15	7.5	46.2
D/D-2	BB5	95	44000	0.17	0.58	1.8	0.050	150	15	16.2	101.4
D/D-3	BB5	90	43000	0.17	0.58	1.8	0.040	200	15	19.2	133.9
D/D_avg	BB5	95	43000	0.17	0.57	1.9	0.038	150	15		
D/C-1	BB5	80	40000	0.16	0.58	1.7	0.050	300	15	19.8	125.6
D/C-2	BB5	115	41000	0.17	0.56	1.8	0.040	150	15	18.3	125.7
D/C-3	BB5	140	40000	0.17	0.58	2.0	0.050	120	15	19.7	125.8
D/C_avg	BB5	112	40333	0.167	0.57	1.8	0.047	190	15		
LDO-1	BBSG3	85	38000	0.17	0.57	1.8	0.018	100	15	18.5	125.3
LDO-2	BBSG3	75	42000	0.17	0.58	1.8	0.020	150	15	19.6	126.7
LDO-3	BBSG3	90	38000	0.17	0.58	1.8	0.015	140	15	19.6	126.2
LDO_avg	BBSG3	83	39333	0.17	0.58	1.8	0.018	130	15		
HDO-1	BBSG3	120	42000	0.17	0.59	1.8	0.080	120	15	13.4	83.8
HDO-2	BBSG3	105	38000	0.17	0.57	1.8	0.100	450	15	41.4	242.1
HDO-3	BBSG3	150	40000	0.17	0.58	1.8	0.080	150	15	20.0	125.7
HDO_avg	BBSG3	125	40000	0.17	0.58	1.8	0.087	240	15		
SBS-1	BBSG3	160	38000	0.17	0.58	2.1	0.060	150	15	21.1	125.4
SBS-2	BBSG3	150	42000	0.17	0.57	1.9	0.050	130	15	20.7	125.5
SBS-3	BBSG3	130	38000	0.17	0.57	1.8	0.040	150	15	24.6	153.4
SBS_avg	BBSG3	147	39333	0.17	0.57	1.9	0.050	143	15		
LAT-1	BBSG3	140	31000	0.17	0.54	1.8	0.080	120	15	19.0	126.1

Table 4.7 -2S2P1D and WLF constants for the shear complex modulus of the mixtures in the upper layer

Sample	Mixture	G_{00} (MPa)	G_0 (MPa)	k	h	δ	τ_G (s)	β	T_{ref} (°C)	C_1	C_2
REFA-3	BBSG3	25	26000	0.172	0.56	2.5	0.040	200	15	19.8	131.6
REFB-1	BBSG3	30	23000	0.172	0.57	2.1	0.040	120	15	17.0	115.3
REFB-2	BBSG3	25	18000	0.166	0.57	2.0	0.060	140	15	17.8	125.1
REFB-3	BBSG3	40	20000	0.170	0.54	2.0	0.060	100	15	21.1	130.9
REFB_avg	BBSG3	32	20333	0.169	0.56	2.0	0.053	120	15		
REFC-1	BBSG3	31	19000	0.164	0.57	2.3	0.040	100	15	14.8	94.7
REFC-2	BBSG3	35	26000	0.170	0.56	1.8	0.020	100	15	7.2	41.4
REFC-3	BBSG3	26	27000	0.176	0.57	2.0	0.015	120	15	9.8	58.6
REFC_avg	BBSG3	31	24000	0.170	0.57	2.0	0.025	107	15		
C/D-1	BBSG3	40	30000	0.170	0.56	2.2	0.030	150	15	16.6	98.9
C/D-2	BBSG3	30	26000	0.170	0.54	1.8	0.030	100	15	21.4	134.9
C/D-3	BBSG3	35	23000	0.200	0.53	1.9	0.040	100	15	21.9	131.7
C/D_avg	BBSG3	35	26333	0.180	0.54	2.0	0.033	117	15		
D/D-1	BB5	40	22000	0.170	0.58	1.8	0.030	110	15	12.4	75.7
D/D-2	BB5	35	30000	0.170	0.56	1.8	0.015	120	15	21.7	146.8
D/D-3	BB5	28	27000	0.160	0.58	1.8	0.020	150	15	20.2	131.5
D/D_avg	BB5	34	26333	0.167	0.57	1.8	0.022	127	15		
D/C-1	BB5	40	24000	0.170	0.57	1.8	0.035	120	15	21.0	125.0
D/C-2	BB5	40	22000	0.120	0.58	1.8	0.050	100	15	20.1	125.6
D/C-3	BB5	35	21000	0.170	0.58	1.8	0.060	200	15	20.6	125.7
D/C_avg	BB5	38	22333	0.153	0.58	1.8	0.048	140	15		
LDO-1	BBSG3	20	25000	0.170	0.56	1.8	0.008	200	15	19.5	125.6
LDO-2	BBSG3	25	23000	0.170	0.58	2.1	0.012	120	15	19.6	126.2
LDO-3	BBSG3	22	24000	0.170	0.58	2.1	0.010	200	15	20.0	125.7
LDO_avg	BBSG3	22	24000	0.170	0.57	2.0	0.010	173	15		
HDO-1	BBSG3	42	22000	0.170	0.58	1.8	0.070	130	15	19.6	126.2
HDO-2	BBSG3	40	24000	0.170	0.57	1.8	0.060	150	15	22.7	137.8
HDO-3	BBSG3	45	23000	0.170	0.57	1.8	0.060	120	15	20.5	125.6
HDO_avg	BBSG3	42	23000	0.170	0.57	1.8	0.063	133	15		
SBS-1	BBSG3	50	26000	0.170	0.58	1.9	0.030	150	15	21.3	124.8
SBS-2	BBSG3	45	24000	0.170	0.55	1.8	0.050	100	15	20.9	125.0
SBS-3	BBSG3	40	28000	0.170	0.56	2.1	0.030	150	15	22.0	127.5
SBS_avg	BBSG3	45	26000	0.170	0.56	1.9	0.037	133	15		
LAT-1	BBSG3	40	24000	0.170	0.56	1.9	0.035	150	15	18.6	116.6

Table 4.8 - 2S2P1D and WLF constants for the axial complex modulus of the mixtures in the lower layer

Sample	Mixture	E_{00} (MPa)	E_0 (MPa)	k	h	δ	τ_E (s)	β	T_{ref} (°C)	C_1	C_2
REFA-3	EME2	220	37000	0.168	0.55	2.3	0.50	90	15	19.8	131.6
REFB-1	EME2	110	38000	0.172	0.57	2.1	0.30	200	15	16.7	115.3
REFB-2	EME2	150	42000	0.170	0.57	2.2	0.25	200	15	13.8	97.5
REFB-3	EME2	220	39000	0.170	0.57	2.1	0.35	120	15	14.7	96.7
REFB_avg	EME2	160	39667	0.171	0.57	2.1	0.30	173	15		
REFC-1	EME2	110	35000	0.190	0.54	1.2	0.25	200	15	13.5	94.2
REFC-2	EME2	100	40000	0.170	0.55	1.8	0.10	300	15	3.0	22.8
REFC-3	EME2	200	42000	0.170	0.57	2.4	0.15	150	15	17.3	122.5
REFC_avg	EME2	137	39000	0.177	0.55	1.8	0.17	217	15		
C/D-1	GB5	270	42000	0.170	0.59	1.8	0.35	200	15	15.5	99.0
C/D-2	GB5	205	40000	0.170	0.57	1.8	0.25	200	15	20.3	138.9
C/D-3	GB5	230	43000	0.170	0.56	2.0	0.40	120	15	21.1	131.9
C/D_avg	GB5	235	41667	0.170	0.57	1.9	0.33	173	15		
D/D-1	GB5	200	44000	0.170	0.57	2.5	0.35	250	15	14.4	86.3
D/D-2	GB5	200	46000	0.170	0.58	1.8	0.50	200	15	16.6	101.3
D/D-3	GB5	210	44000	0.170	0.58	2.3	0.30	300	15	19.0	133.9
D/D_avg	GB5	203	44667	0.170	0.58	2.2	0.38	250	15		
D/C-1	EME2	160	35000	0.170	0.56	2.1	0.35	120	15	17.5	109.9
D/C-2	EME2	160	38000	0.170	0.53	2.1	0.20	180	15	19.1	125.3
D/C-3	EME2	230	38000	0.170	0.54	2.0	0.35	180	15	19.9	125.8
D/C_avg	EME2	183	37000	0.170	0.54	2.1	0.30	160	15		
LDO-1	EME2	200	41000	0.170	0.57	2.1	0.15	250	15	18.8	124.9
LDO-2	EME2	230	38000	0.170	0.56	1.8	0.17	280	15	19.5	126.2
LDO-3	EME2	170	41000	0.170	0.57	2.1	0.12	200	15	18.7	126.3
LDO_avg	EME2	200	40000	0.170	0.57	2.0	0.15	243	15		
HDO-1	EME2	200	42000	0.180	0.57	2.1	0.20	90	15	18.4	125.8
HDO-2	EME2	210	40000	0.170	0.57	2.1	0.25	180	15	18.8	125.7
HDO-3	EME2	230	37000	0.170	0.57	2.2	0.22	300	15	19.5	126.2
HDO_avg	EME2	213	39667	0.173	0.57	2.1	0.22	190	15		
SBS-1	EME2	230	41000	0.170	0.57	2.0	0.25	250	15	24.6	154.4
SBS-2	EME2	210	42000	0.170	0.55	1.9	0.12	250	15	19.2	125.1
SBS-3	EME2	290	39500	0.170	0.57	1.9	0.22	150	15	18.3	118.9
SBS_avg	EME2	243	40833	0.170	0.56	1.9	0.20	217	15		
LAT-1	EME2	190	38000	0.170	0.51	2.1	0.20	200	15	19.8	126.0

Table 4.9 -2S2P1D and WLF constants for the shear complex modulus of the mixtures in the lower layer

Sample	Mixture	G_{00} (MPa)	G_0 (MPa)	k	h	δ	τ_G (s)	β	T_{ref} (°C)	C_1	C_2
REFA-3	EME2	80	27500	0.200	0.55	2.6	0.40	250	15	16.8	132.1
REFB-1	EME2	80	24000	0.180	0.57	2.0	0.30	200	15	15.8	115.4
REFB-2	EME2	80	25000	0.174	0.57	2.3	0.25	200	15	14.0	99.1
REFB-3	EME2	110	30000	0.170	0.53	2.2	0.15	100	15	17.3	131.5
REFB_avg	EME2	90	26333	0.175	0.56	2.2	0.23	167	15		
REFC-1	EME2	85	31000	0.200	0.57	2.2	0.40	200	15	14.8	94.7
REFC-2	EME2	140	28000	0.170	0.55	1.9	0.10	160	15	5.7	41.5
REFC-3	EME2	55	28000	0.170	0.54	2.5	0.07	400	15	14.3	126.6
REFC_avg	EME2	93	29000	0.180	0.55	2.2	0.19	253	15		
C/D-1	GB5	75	29000	0.170	0.56	1.8	0.50	400	15	17.3	98.8
C/D-2	GB5	85	30000	0.165	0.53	2.1	0.30	130	15	20.2	135.1
C/D-3	GB5	90	26000	0.170	0.54	2.0	0.80	130	15	26.2	166.4
C/D_avg	GB5	83	28333	0.168	0.54	2.0	0.53	220	15		
D/D-1	GB5	110	26000	0.170	0.56	2.2	0.80	200	15	21.1	129.1
D/D-2	GB5	100	31000	0.170	0.53	1.8	0.30	130	15	30.1	206.3
D/D-3	GB5	100	32000	0.170	0.52	2.1	0.25	130	15	20.5	131.5
D/D_avg	GB5	103	29667	0.170	0.54	2.0	0.45	153	15		
D/C-1	EME2	75	25000	0.170	0.55	2.2	0.28	200	15	18.9	124.6
D/C-2	EME2	65	24000	0.170	0.53	2.0	0.25	180	15	16.8	112.7
D/C-3	EME2	65	24000	0.170	0.55	2.1	0.30	180	15	19.4	125.8
D/C_avg	EME2	68	24333	0.170	0.54	2.1	0.28	187	15		
LDO-1	EME2	70	26000	0.170	0.55	2.1	0.25	250	15	18.2	125.3
LDO-2	EME2	110	26000	0.170	0.55	2.1	0.20	200	15	19.2	126.3
LDO-3	EME2	100	25000	0.170	0.54	2.1	0.20	200	15	18.8	125.9
LDO_avg	EME2	93	25667	0.170	0.55	2.1	0.22	217	15		
HDO-1	EME2	85	25000	0.170	0.55	2.1	0.18	130	15	18.9	126.1
HDO-2	EME2	80	27000	0.170	0.56	2.1	0.20	220	15	18.4	123.2
HDO-3	EME2	80	25000	0.170	0.55	1.8	0.15	200	15	16.0	104.2
HDO_avg	EME2	82	25667	0.170	0.55	2.0	0.18	183	15		
SBS-1	EME2	90	30000	0.170	0.55	2.1	0.12	350	15	18.7	125.7
SBS-2	EME2	65	27000	0.170	0.55	2.1	0.18	140	15	18.4	124.7
SBS-3	EME2	70	26000	0.170	0.56	2.1	0.25	250	15	18.6	125.4
SBS_avg	EME2	75	27667	0.170	0.55	2.1	0.18	247	15		
LAT-1	EME2	65	28500	0.170	0.53	2.1	0.15	180	15	17.5	116.7

4.2.2. Comparison between advanced complex modulus test with 2T3C HCA and tension-compression complex modulus test on cylindrical samples

The tension-compression complex modulus test was performed on two cylindrical samples from the slab HDO. One sample, named HDO-U1, was cored horizontally in the upper layer of bituminous mixture (BBSG3), the other one, named HDO-L1, was cored horizontally in the lower layer (EME2). In Chapter 3 can be found the details of sample preparation (section 3.1.1), the characteristics of the bituminous mixtures and the air void ratio in the samples (section 3.1.2) as well as the test procedure (section 3.2.3.1).

During the test, the vertical strain is measured by three extensometers. The average value ε_{zz} of the three measurements is calculated and used in the test analysis. The vertical stress σ_{zz} is obtained from the hydraulic press load cell. The signals obtained during the tension-compression complex modulus test are approximated by sinusoidal signals with the same procedure than the one presented in section 4.1.1.2. The axial complex modulus obtained with the tension-compression test is noted $E^*_{T\text{-}C}$ and is defined as in Equation 4.17.

The sample HDO-1 is the 2T3C HCA sample cored the closest to the cylindrical samples of bituminous mixtures. The axial complex modulus $E^*_{2T3CHCA}$ of the bituminous mixtures of this sample were obtained and modelled with 2S2P1D and WLF equation in section 4.1.

The two values of the axial complex modulus obtained for each mixture with the two different tests are then compared. They are represented in the Black space in Figure 4.40 for the mixture in the upper layer (BBSG3) and in Figure 4.41 for the mixture in the lower layer (EME2).

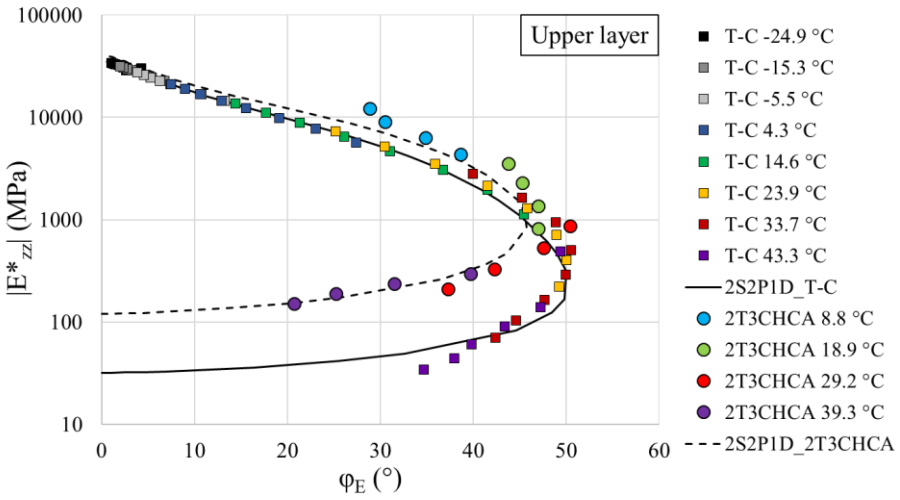

Figure 4.40 - Axial complex modulus in the upper layer of bituminous mixture (BBSG3) of the slab HDO obtained with tension-compression test (sample HDO-U1, noted T-C) and 2T3C HCA test (sample HDO-1, noted 2T3CHCA) represented in the Black space with 2S2P1D models

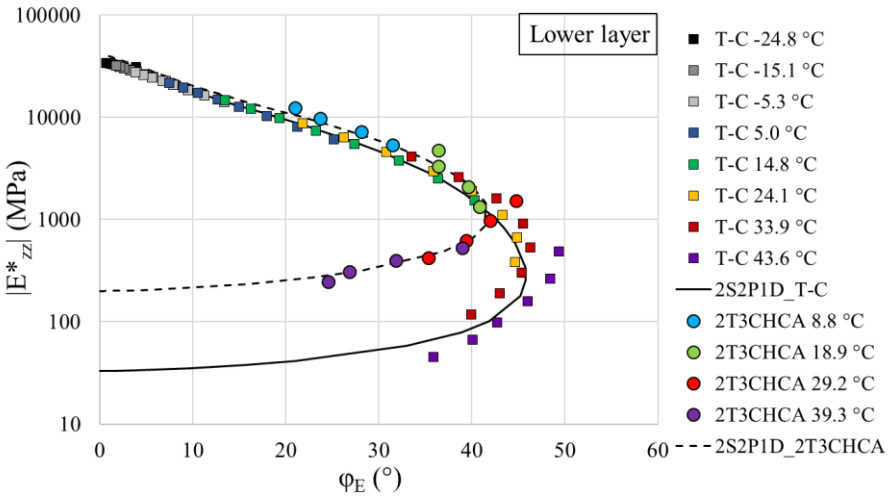

Figure 4.41 - Axial complex modulus in the lower layer of bituminous mixture (EME2) of the slab HDO obtained with tension-compression test (sample HDO-L1, noted T-C) and 2T3C HCA test (sample HDO-1, noted 2T3CHCA) represented in the Black space with 2S2P1D models

The different complex moduli were then modelled with the 2S2P1D model with the procedure explained in section 4.1.3. The bituminous mixtures respected the TTSP in both tests; the WLF equation was used to fit the shift factors at the reference temperature of 15 °C. The 2S2P1D constants and the WLF equation constants of the bituminous mixtures obtained from the two tests are presented in Table 4.10. The 2S2P1D models are plotted with the experimental results in Figure 4.40 and Figure 4.41.

Table 4.10 - 2S2P1D constants and WLF equation constants for the bituminous mixtures of the slab HDO obtained from tension-compression test (T-C) or 2T3C HCA test (2T3C)

Layer	**Mixture**	**Test**	**E_{00} (MPa)**	**E_0 (MPa)**	**k**	**h**	**δ**	**τ_E**	**β**	**T_{ref} (°C)**	**C_1**	**C_2**
Upper	BBSG3	2T3C	120	42000	0.17	0.59	1.8	0.08	120	15	13.4	83.8
Upper	BBSG3	T-C	32	36300	0.176	0.56	2	0.15	150	15	22.3	152.2
Lower	EME2	2T3C	200	42000	0.18	0.57	2.1	0.2	90	15	18.4	125.8
Lower	EME2	T-C	33	35500	0.19	0.55	2.1	0.4	350	15	21.4	147.4

It can be seen on Figure 4.40 and Figure 4.41 that the complex modulus at high temperatures are different between the two tests. From the 2S2P1D model calibration, it appears that the static modulus E_0 and the glassy modulus E_{00} are different, being higher in the 2T3C HCA test, when the other constants are very similar in the two tests. The constants E_0 and E_{00} are asymptotic moduli, their values depend on the granular skeleton of the mixtures and especially on the air void ratio. The normalized axial complex modulus $E^*_{zz\_norm}$ was then calculated to remove the influence of E_0 and E_{00} using Equation 4.46.

$$E^*_{zz\_norm} = \frac{E^*_{zz} - E_{00}}{E_0 - E_{00}} \qquad (4.46)$$

The normalized axial complex moduli are presented in the Black space in Figure 4.42 for the mixture in the upper layer and in Figure 4.43 for the mixture in the lower layer.

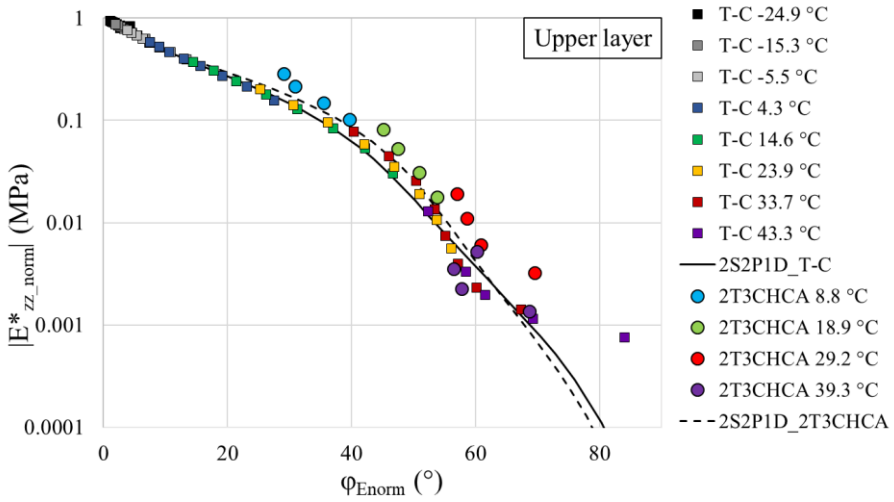

Figure 4.42 - Normalized axial complex modulus in the upper layer of bituminous mixture (BBSG3) of the slab HDO obtained with tension-compression test (sample HDO-U1, noted T-C) and 2T3C HCA test (sample HDO-1, noted 2T3CHCA) represented in the Black space with 2S2P1D models

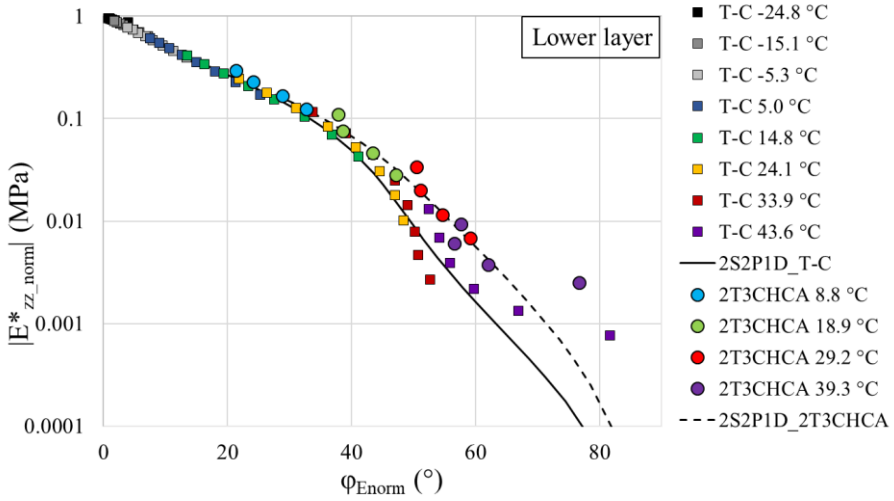

Figure 4.43 - Normalized axial complex modulus in the lower layer of bituminous mixture (EME2) of the slab HDO obtained with tension-compression test (sample HDO-L1, noted T-C) and 2T3C HCA test (sample HDO-1, noted 2T3CHCA) represented in the Black space with 2S2P1D models

As expected, there is a better match of the results of the two different tests with the representation of the normalized axial complex modulus. The differences observed for E_0 and E_{00} might be related to the air void ratio in the samples: the cylindrical samples tested with the tension-compression test (HDO-U1 and HDO-L1) are cored close to the extremities of the slab where the compaction is less efficient, inducing higher void ratios and lower E_0 and E_{00}. Moreover, the slab compaction process with the wheel compactor (see section 3.1.1) induces an anisotropic behaviour of the laboratory made bituminous mixtures (Di Benedetto *et al.* 2016). The axial complex modulus of the mixtures is indeed different if it is tested in the "rolling" direction (longitudinal direction) where the tension-compression samples were cored or in the "compaction" direction (vertical direction) where the 2T3C HCA sample was cored.

It can be seen on Figure 4.4 that the vertical strain amplitude during the cycles in the 2T3C HCA tests is about 200 µm/m in the upper layer and about 130 µm/m in the lower layer when the vertical strain amplitude during the tension-compression tests is always 50 µm/m. The effect of the nonlinearity of the behaviour of bituminous mixtures could then be observed between the two tests. However, when increasing the strain amplitude, the complex modulus of bituminous mixtures should decrease

(Mangiafico *et al.* 2017) which is the contrary of what is observed here. So this effect might not be preeminent.

4.3. Interfaces behaviour in the small strain domain

4.3.1. Modelling with DBN_{PDSC} model

The normal complex interface stiffness and the shear complex interface stiffness for all the samples were obtained from the advanced complex modulus test results following the procedure of section 4.1.

The Black diagrams of the normal complex interface stiffnesses of all the samples is presented in Figure 4.44. The shear complex interface stiffnesses of all the samples are presented in the Black space in Figure 4.45. The figures for each sample are presented individually in Appendix A.

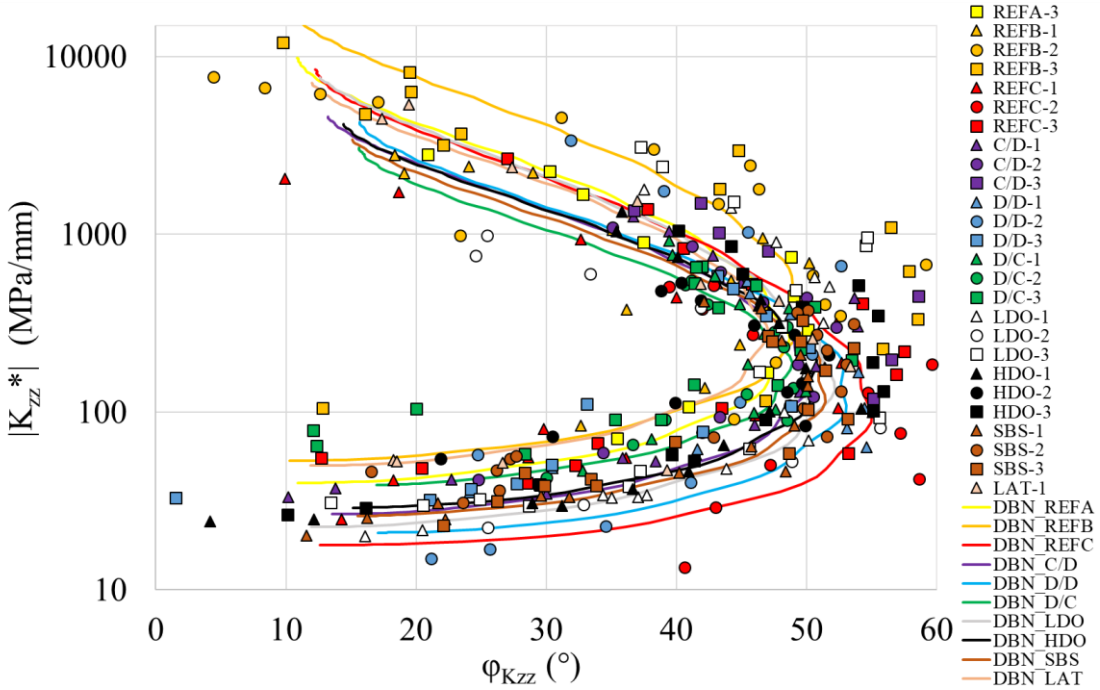

Figure 4.44 - Normal complex interface stiffness of the 2T3C HCA samples represented in the Black space with DBN_{PDSC} models (one average model for each slab)

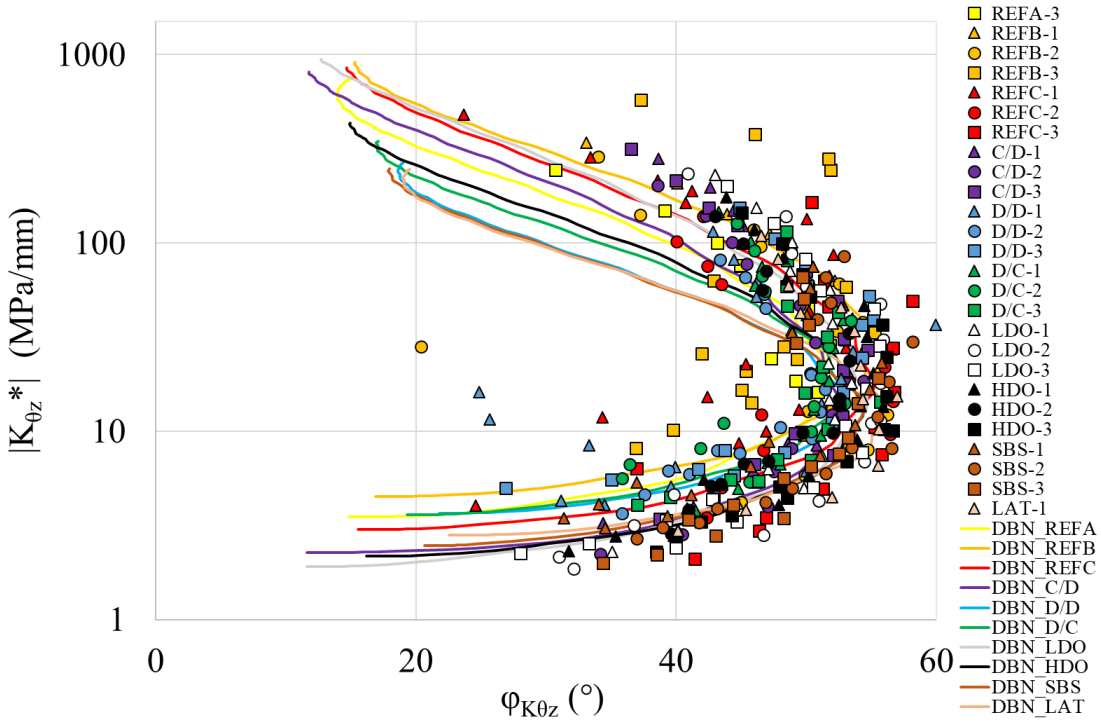

Figure 4.45 - Shear complex interface stiffness of the 2T3C HCA samples represented in the Black space with DBN_{PDSC} models (one average model for each slab)

From Figure 4.44 and Figure 4.45, the normal complex interface stiffness is roughly ten times higher than the shear complex interface stiffness, for all the interfaces. For the Black diagrams of the interface are unique curves, the interfaces respected the TTSP both in tension-compression mode and in shear mode. The master curves were then built as explained in section 4.1.2 at the reference temperature of 15 °C for all the samples.

The master curve of the norm of the normal complex interface stiffness is presented in Figure 4.46. The master curve of the phase angle of the normal complex interface stiffness can be found in Figure 4.47. The amplitude of the vertical displacement gap at the interface during the axial cycles is plotted versus the equivalent frequency in Figure 4.48.

The master curve of the norm of the shear complex interface stiffness is presented in Figure 4.49. The master curve of the phase angle of the shear complex interface stiffness can be found in Figure 4.50. The amplitude of the horizontal displacement gap at the interface during the rotation cycles is plotted versus the equivalent frequency in Figure 4.51.

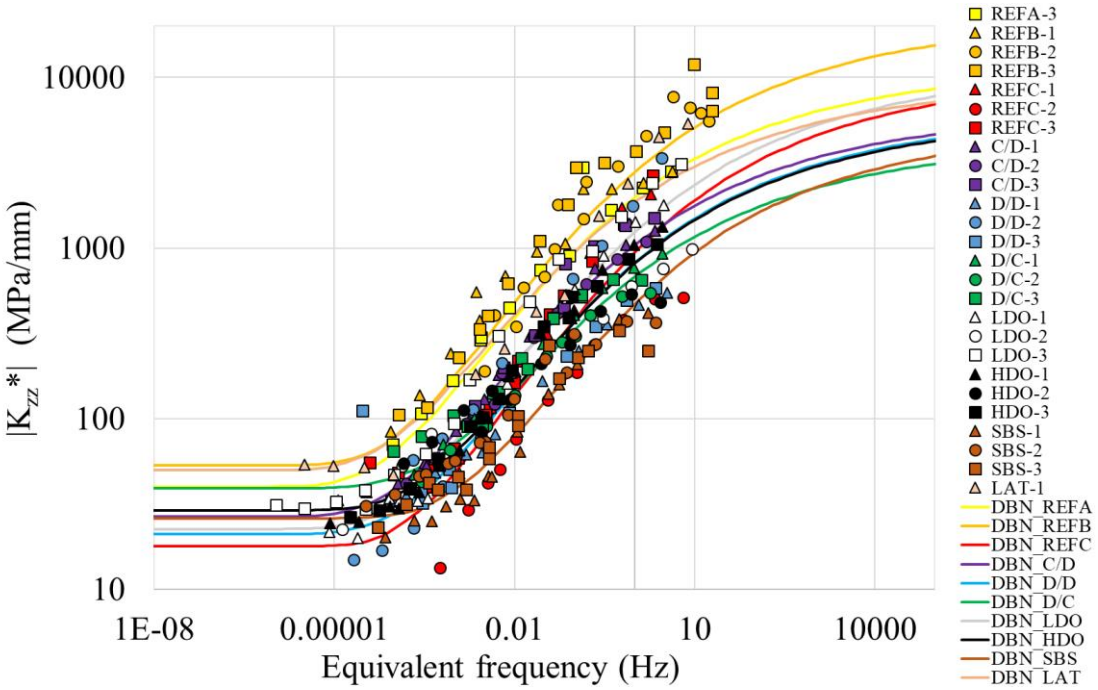

Figure 4.46 - Master curve of the norm of the normal complex interface modulus of the 2T3C HCA samples with DBN_{PDSC} models (one average model for each slab)

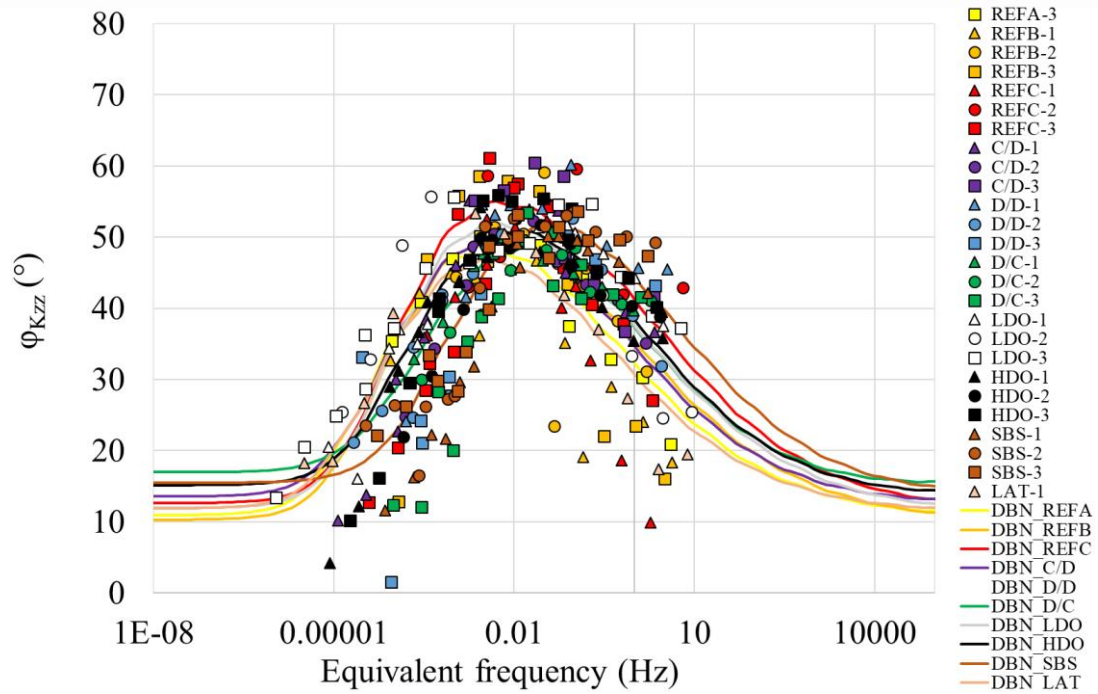

Figure 4.47 - Master curve of the phase angle of the normal complex interface modulus of the 2T3C HCA samples with DBN_{PDSC} models (one average model for each slab)

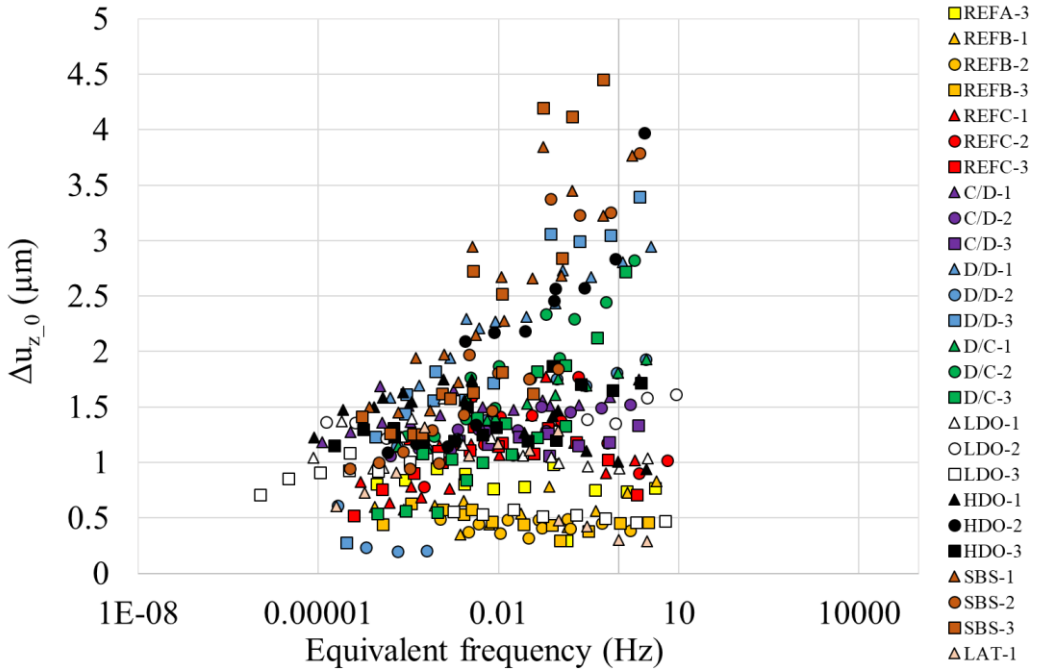

Figure 4.48 - Vertical displacement gap amplitude during the axial cycles at the interface of the 2T3C HCA samples

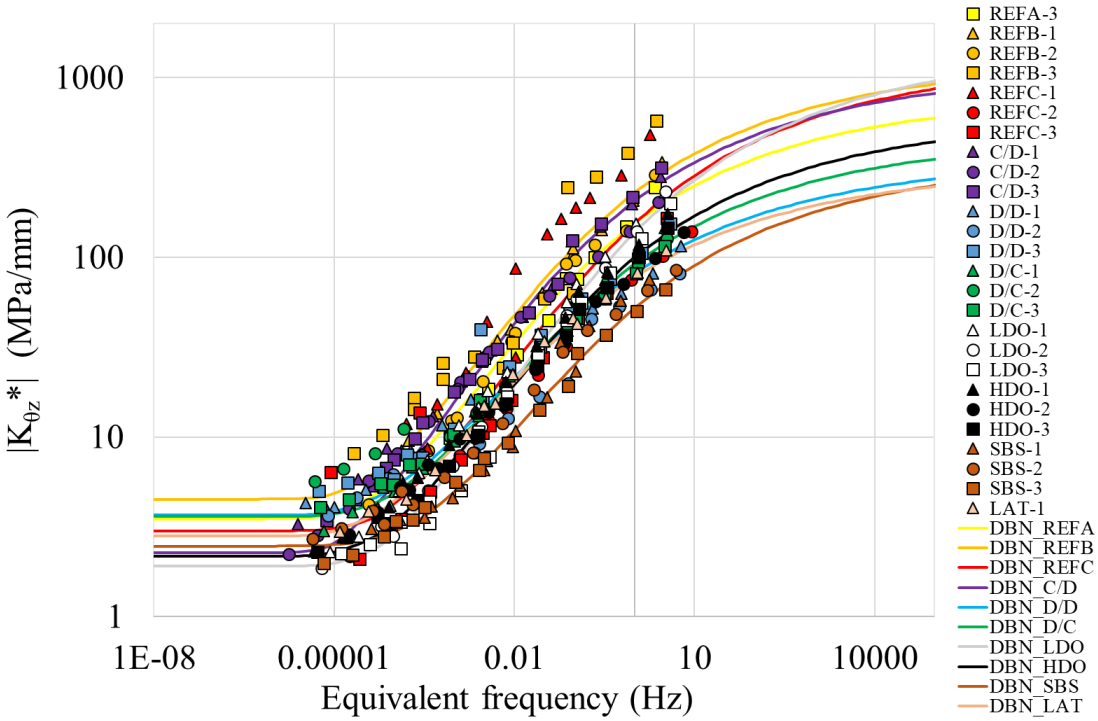

Figure 4.49 - Master curve of the norm of the shear complex interface modulus of the 2T3C HCA samples with DBN_{PDSC} models (one average model for each slab)

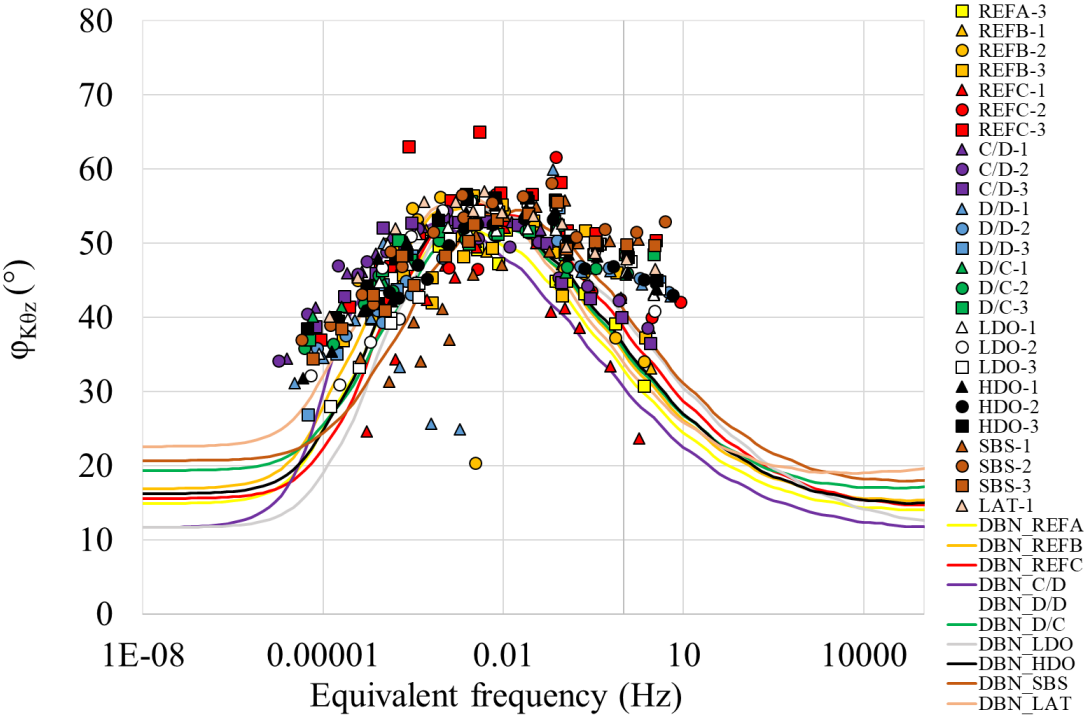

Figure 4.50 - Master curve of the phase angle of the shear complex interface modulus of the 2T3C HCA samples with DBN_{PDSC} models (one average model for each slab)

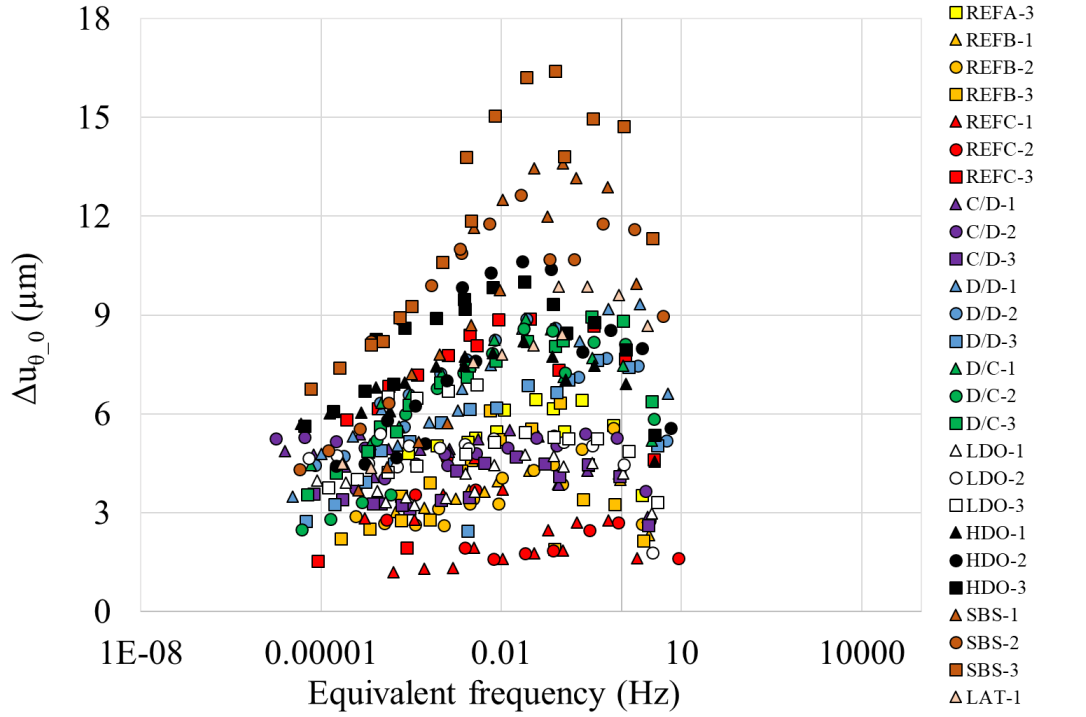

Figure 4.51 - Horizontal displacement gap amplitude during the rotation cycles at the interface of the 2T3C HCA samples

From Figure 4.48 and Figure 4.51, it is possible to see that the vertical displacement gap amplitude during the axial cycles is generally lower than the horizontal displacement gap amplitude during the rotation cycles. The vertical displacement gap amplitude is sometimes as low as 0.5 µm. For these cycles, even if the sinusoidal approximation is considered satisfying, there might be a variability in the phase angle measurement as it can be seen on the Black diagram of the normal complex interface stiffness (Figure 4.44) or on the master curve of the phase angle (Figure 4.47). The vertical displacement

gap amplitude is close to 1 µm as a first approximation and the horizontal displacement gap amplitude can be 10 µm. Now, if the tack coat is considered to be a homogeneous layer of binder, its thickness can be approximated from its dosage. As the bitumen density is close to 1,000 kg/m^3, the average dosage in the 2T3C HCA samples of 350 g/m^2 leads to a thickness of 350 µm. For a homogeneous layer 350 µm thick, a vertical displacement gap of 1 µm corresponds to a vertical strain of about 0.3 % (3,000 µm/m) and a horizontal displacement gap of 10 µm to a shear strain of about 1.5 % (15,000 µm/m). These strain amplitudes are close to the limit of the linear viscoelastic domain for the bitumens that is 1 % (10,000 µm/m), as an order of magnitude, but that depends strongly on the temperature and frequency. The limit could be lower for the tested temperature and frequencies in the 2T3C HCA (Babadopulos 2017).

The interface behaviour is then modelled with the DBN$_{PDSC}$ model as explained in section 4.1.4.4. The first step in the modelling is the calibration of a 2S2P1D model on the master curve of the norm of the complex interface stiffnesses. Then a generalised Kelvin-Voigt model (GKV) with 25 elements is calibrated from the 2S2P1D model. The phase angle of the DBN$_{PDSC}$ model is then modified by adding plastic dissipation.

For clarity's sake, for each slab, one average DBN$_{PDSC}$ model is calculated for the normal complex interface stiffness and another one is calculated for the shear complex interface stiffness. For each frequency, one value of norm of complex interface stiffness and one value of phase angle are obtained for each sample with the DBN$_{PDSC}$ model. The values for all the samples of the same slab are averaged frequency by frequency to create the average model for the slab. The average DBN$_{PDSC}$ models are represented with the experimental data in Figure 4.44, Figure 4.45, Figure 4.46, Figure 4.47, Figure 4.49 and Figure 4.50. The figures where each sample is presented independently with its own DBN$_{PDSC}$ model can be found in Appendix A.

The DBN$_{PDSC}$ model requires 25 couples (K_{zzi}, η_i) (or 25 couples ($K_{\theta zi}$, η_i)) and the constants (K_{zz0}, φ_{NL}) (or the constants ($K_{\theta z0}$, φ_{NL})) which represents 52 constants per model. In order to compare the different interfaces, the 2S2P1D models constants used for the calibration are presented in this section. There are only nine constants for each interface (including the WLF equation constants) and they successfully represent the norm of the complex interface stiffness guaranteeing their physical meaning. As a reminder, the constants of the GKV model (and thus of the DBN$_{PDSC}$ model) are actually chosen so that the GKV is as close as possible from the 2S2P1D. In addition, the parameter φ_{NL} of the DBN$_{PDSC}$ model will also be analysed. The 2S2P1D constants and φ_{NL} for the normal complex interface stiffness of every sample are presented in Table 4.11. The 2S2P1D constants and φ_{NL} for the shear complex interface stiffness of every sample are presented in Table 4.12. The DBN$_{PDSC}$ constants for each sample can be found in Appendix B.

Table 4.11 - 2S2P1D and WLF constants for the normal complex interface stiffnesses with DBN_{PDSC} parameter φ_{NL}

Sample	K_{zz_00} (MPa/mm)	K_{zz_0} (MPa/mm)	k	h	δ	τ_{Kzz} (s)	β	T_{ref} (°C)	C_1	C_2	φ_{NL} (°)
REFA-3	40	11000	0.2	0.53	2.3	0.060	300	15	21.8	131.3	11
REFB-1	40	12000	0.2	0.53	2.3	0.100	300	15	19.3	115.0	6
REFB-2	40	26000	0.2	0.53	2.3	0.010	300	15	3.9	40.5	8
REFB-3	80	25000	0.2	0.53	2.3	0.020	300	15	20.0	130.9	17
REFC-1	20	17000	0.2	0.53	2.3	0.005	300	15	11.4	94.4	8
REFC-2	4	3000	0.2	0.53	2.3	0.020	300	15	3.3	22.7	15
REFC-3	30	10000	0.2	0.53	2.3	0.012	300	15	16.2	134.2	15
C/D-1	30	6000	0.2	0.53	2.3	0.050	300	15	11.3	71.7	14
C/D-2	25	6500	0.2	0.53	2.3	0.030	300	15	12.8	92.9	14
C/D-3	25	5500	0.2	0.53	2.3	0.100	300	15	17.0	132.5	13
D/D-1	25	2500	0.2	0.53	2.3	0.050	300	15	13.1	86.4	23
D/D-2	13	12000	0.2	0.53	2.3	0.020	300	15	14.0	100.5	14
D/D-3	25	3000	0.2	0.53	2.3	0.040	300	15	16.8	134.1	19
D/C-1	35	4500	0.2	0.53	2.3	0.040	300	15	9.5	66.3	16
D/C-2	32	4200	0.2	0.53	2.3	0.020	300	15	15.4	126.1	16
D/C-3	50	3500	0.2	0.53	2.3	0.100	300	15	12.5	126.5	20
LDO-1	20	15000	0.2	0.53	2.3	0.005	300	15	19.2	125.6	8
LDO-2	18	3500	0.2	0.53	2.3	0.100	300	15	28.5	126.5	12
LDO-3	30	14000	0.2	0.53	2.3	0.020	300	15	24.5	125.6	16
HDO-1	22	7500	0.2	0.53	2.3	0.020	300	15	19.1	126.7	10
HDO-2	40	4000	0.2	0.53	2.3	0.030	300	15	18.4	126.4	18
HDO-3	25	5500	0.2	0.53	2.3	0.035	300	15	17.3	126.5	18
SBS-1	20	5500	0.2	0.53	2.3	0.005	300	15	10.4	92.9	12
SBS-2	30	4500	0.2	0.53	2.3	0.012	300	15	12.0	93.5	19
SBS-3	28	5000	0.2	0.53	2.3	0.007	300	15	14.3	126.7	16
LAT-1	50	9000	0.2	0.53	2.3	0.100	300	15	15.7	82.8	12

Table 4.12 - 2S2P1D and WLF constants for the shear complex interface stiffnesses with DBN_{PDSC} parameter φ_{NL}

Sample	$K_{\theta z\_00}$ (MPa/mm)	$K_{\theta z\_0}$ (MPa/mm)	k	h	δ	$\tau_{K\theta z}$ (s)	β	T_{ref} (°C)	C_1	C_2	φ_{NL} (°)
REFA-3	3.5	750	0.2	0.53	2.3	0.1000	300	15	16.8	132.0	15
REFB-1	4.5	1200	0.2	0.53	2.3	0.0600	300	15	16.6	115.3	17
REFB-2	3.0	800	0.2	0.53	2.3	0.1000	300	15	12.5	97.8	18
REFB-3	6.0	1500	0.2	0.53	2.3	0.1000	300	15	17.3	131.3	16
REFC-1	5.0	2500	0.2	0.53	2.3	0.0150	300	15	11.3	94.3	10
REFC-2	2.5	420	0.2	0.53	2.3	0.0600	300	15	7.5	39.7	21
REFC-3	1.5	600	0.2	0.53	2.3	0.0360	300	15	18.9	122.4	16
C/D-1	2.5	1000	0.2	0.53	2.3	0.1000	300	15	17.7	98.7	13
C/D-2	1.8	600	0.2	0.53	2.3	0.3000	300	15	21.0	116.9	10
C/D-3	2.5	1500	0.2	0.53	2.3	0.0500	300	15	19.4	132.3	12
D/D-1	4.0	300	0.2	0.53	2.3	0.2000	300	15	16.3	88.2	25
D/D-2	3.0	200	0.2	0.53	2.3	0.8000	300	15	11.9	67.2	21
D/D-3	4.0	500	0.2	0.53	2.3	0.1000	300	15	21.2	131.4	21
D/C-1	2.8	500	0.2	0.53	2.3	0.1000	300	15	19.7	125.7	17
D/C-2	4.0	425	0.2	0.53	2.3	0.1000	300	15	19.9	120.8	20
D/C-3	4.0	400	0.2	0.53	2.3	0.1000	300	15	19.9	125.8	22
LDO-1	2.0	950	0.2	0.53	2.3	0.0400	300	15	17.3	110.9	12
LDO-2	1.8	1200	0.2	0.53	2.3	0.0150	300	15	20.0	126.0	13
LDO-3	2.0	2000	0.2	0.53	2.3	0.0025	300	15	11.1	68.7	10
HDO-1	2.0	700	0.2	0.53	2.3	0.0500	300	15	20.7	126.5	15
HDO-2	2.5	400	0.2	0.53	2.3	0.0800	300	15	7.3	39.7	17
HDO-3	2.0	600	0.2	0.53	2.3	0.0500	300	15	20.6	126.1	17
SBS-1	2.8	450	0.2	0.53	2.3	0.0100	300	15	14.8	125.9	20
SBS-2	2.6	300	0.2	0.53	2.3	0.0800	300	15	15.2	85.4	23
SBS-3	2.0	250	0.2	0.53	2.3	0.0800	300	15	19.7	125.7	20
LAT-1	2.8	300	0.2	0.53	2.3	0.2500	300	15	18.3	126.2	23

4.3.2. Influential factors

As it can be seen in Table 4.11 and Table 4.12, the constants *k*, *h*, *δ*, and *β* of the pure bitumen (Table 4.3) were used to model the interfaces with a tack coat made of the emulsion of pure bitumen but also the interfaces with tack coat in modified emulsions (configurations SBS and LAT). The explanation to this fact is not the absence of modification of the viscoelastic properties of the bitumen, it is only a modelling choice that allowed fitting the master curve of the norm of complex interface stiffnesses properly on the limited frequency range tested with 2T3C HCA. The modified bitumens were not tested with DSR.

The asymptotic moduli of the 2S2P1D models for the normal complex interface stiffness are represented in Figure 4.52 (on the left) where the glassy modulus K_{zz_0} is represented versus the static modulus K_{zz_00}. For the shear complex interface stiffness, the glassy modulus $K_{\theta z\_0}$ is represented versus the static modulus $K_{\theta z\_00}$ on Figure 4.52 (on the right).

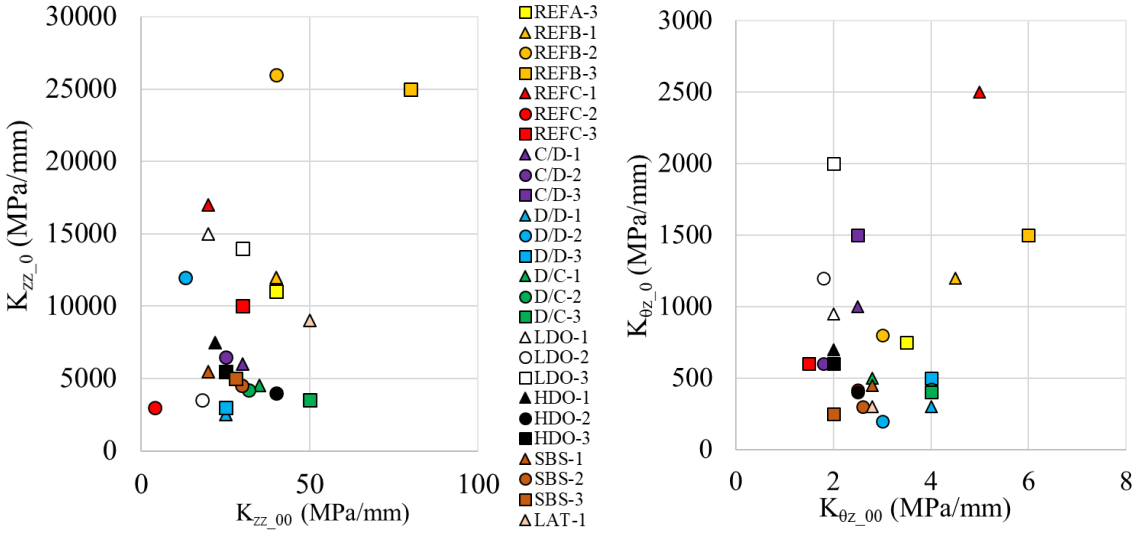

Figure 4.52 - Glassy modulus plotted versus the static modulus (2S2P1D constants) for the normal complex interface stiffness (on the left) and for the shear complex interface stiffness (on the right)

When studying more carefully the influence of the tack coat dosage on the shear complex interface stiffness, it is possible to observe a tendency. The glassy modulus $K_{\theta z\_0}$ is plotted versus the tack coat dosage on Figure 4.53 for the configurations REFA, REFB, REFC, LDO and HDO. In these configurations, the bituminous mixtures in the upper layer and in the lower layer are the same. The bituminous emulsion is a pure bitumen emulsion in each case but dosage of residual binder at the interface differs.

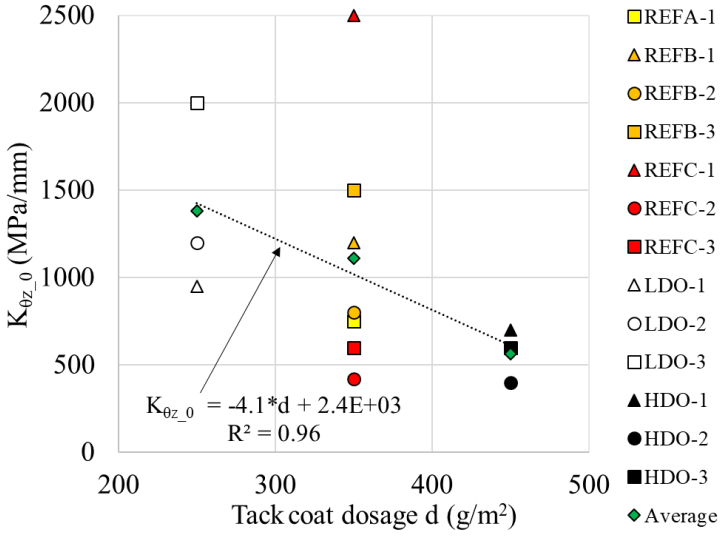

Figure 4.53 - Glassy modulus of the shear complex interface stiffness for different tack coat dosages

For each dosage, the average of the glassy modulus is calculated from the value obtained for each sample at this dosage. A linear regression successfully links the tack coat dosage with these average values as it can be seen on Figure 4.53. This observation can be simply explained if the tack coat is thought as a homogeneous layer of binder. In this case, the displacement gap at the interface is the total displacement between the top and the bottom of this layer. If the tack coat dosage is increased, the layer

thickness e is increased, proportionally if the tack coat is perfectly distributed at the interface. If the complex modulus of the binder G^* stays the same, the displacement gap is increased proportionally with e since the layer is homogeneous. So the complex interface stiffness K^* decreases proportionally with e following Equation 4.47 which is observed on Figure 4.53.

$$K^* = \frac{G^*}{e} \tag{4.47}$$

It was not possible to observe the effect on the normal complex interface stiffness.

There is actually a high variability of the value of the asymptotic moduli (Figure 4.52), even for samples from the same slab (for instance REFB, REFC). It was impossible to determine if there is an influence of the other interface configurations on these asymptotic moduli. This variability can be related to the lack of data at high frequencies and low temperatures that makes it difficult to calibrate the 2S2P1D models, especially the glassy modulus. But also to a difference in the behaviours of the different samples of the same slab.

No influence of the interface configurations could be observed on the constant φ_{NL} of the DBN_{PDSC} model. The values for φ_{NL} were between 6 and 25 ° which represent damping coefficients between 5 and 21 %.

4.3.3. Nonlinearity of interfaces behaviour

4.3.3.1. Nonlinearity test results

The nonlinearity test was performed on the sample LAT-1 following the procedure described in section 3.2.1.2. Sinusoidal rotation cycles were applied at different amplitudes but at the same temperature and the same frequency on the 2T3C HCA sample. The shear complex interface stiffness was obtained as explained in section 4.1.1.

The norm of the shear complex interface stiffness is plotted versus the horizontal displacement gap amplitude Δu_{θ_0} in Figure 4.54. The evolution of the phase angle of the shear complex interface stiffness with the displacement gap amplitude can be found in Figure 4.55.

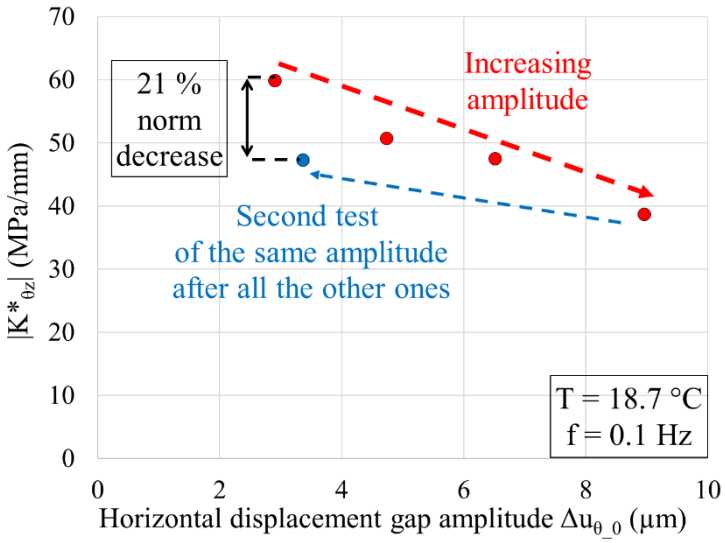

Figure 4.54 - Norm of the shear complex interface stiffness versus the horizontal displacement gap amplitude at the interface during the nonlinearity test on sample LAT-1

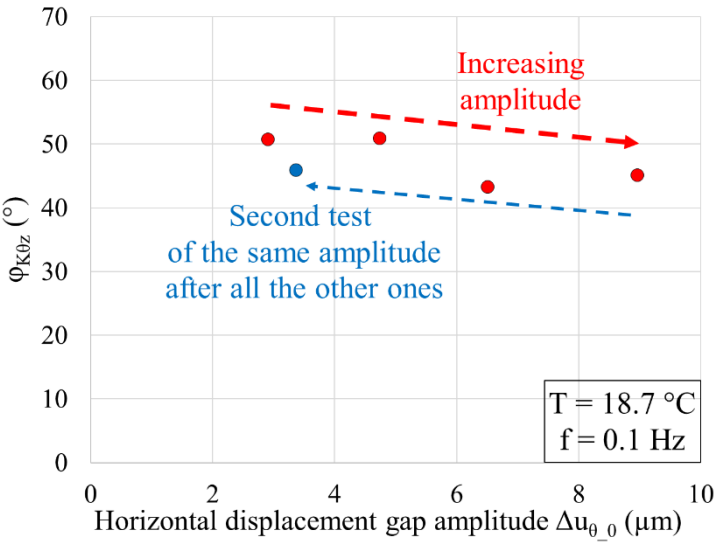

Figure 4.55 - Norm of the shear complex interface stiffness versus the horizontal displacement gap amplitude at the interface during the nonlinearity test on sample LAT-1

The tested amplitudes were between 2 and 9 µm which corresponds to the range of amplitude observed in the advanced complex modulus test (Figure 4.51). From Figure 4.54, it can be seen that the norm of the modulus decreased with the increasing displacement gap, it lost 35 % between the lowest amplitude (2.9 µm) and the highest (9.0 µm). This result concurs with the observations of the nonlinearities in the behaviour of bituminous binders and mixtures in the small strain domain (Mangiafico et al. 2017; L. F. de A. L. Babadopulos et al. 2019). No clear tendency of the variation of the phase angle can be observed in Figure 4.55.

After all the amplitudes were tested, the first amplitude, the smallest, is tested again. As it can be seen on Figure 4.54, the norm of the complex modulus lost 21 % of its initial value between the beginning and the end of the test. This shows that the interface got possibly damaged during the test and did not recover during the rest periods between the cycles at different amplitudes. So the decrease in modulus observed in Figure 4.54 is not only related to a change of displacement gap amplitude. The results of this test suggests that the rest periods between the frequencies during the advanced complex modulus test should be increased.

4.3.3.2. Oligocyclic test results

Following the nonlinearity test, the behaviour of an interface subjected to repeated sinusoidal cycles is evaluated with the oligocyclic test. The test procedure is described in section 3.2.1.3. The oligocyclic test was performed on the sample LAT-1. Sinusoidal rotation cycles are applied to the sample at 0.1 Hz and at the temperature of 20 °C. The global strain amplitude for the cycles is the same than in the advanced complex modulus test. The shear complex interface stiffness was obtained following the procedure presented in section 4.1.1 except that all the cycles were analysed one by one.

The evolution of the shear complex interface stiffness during the first 50 cycles applied is presented in Figure 4.56 (as explained in section 3.2.1.3, pictures were not captured during some cycles to reduce the amount of data to analyse).

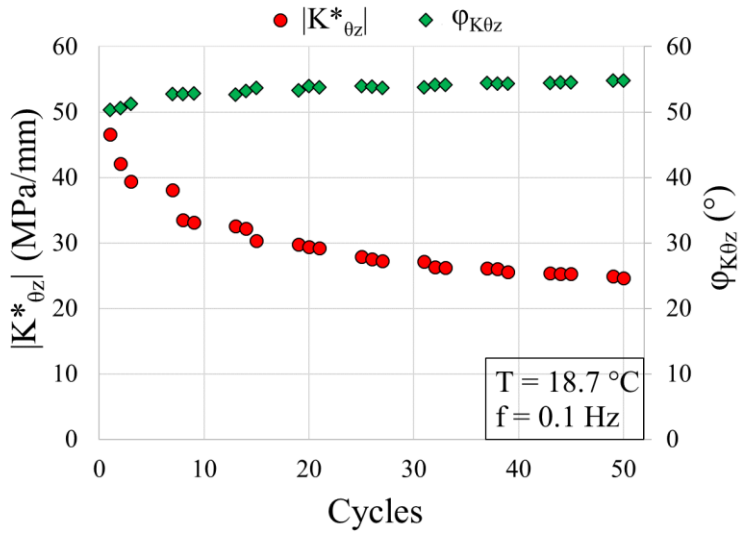

Figure 4.56 - Shear complex interface stiffness evolution during the first 50 cycles applied in the oligocyclic test on sample LAT-1

The norm of the shear complex interface stiffness decreased rapidly: it lost 28 % of its initial value after 9 cycles and 47 % after 50 cycles. The phase angle gained 4.5 ° during the first 50 cycles. This confirms that at the amplitude tested during the advanced complex modulus test (and for the temperature and frequency presented in this section), the interface behaviour is not linear viscoelastic.

After a rest period of 24 hours, a second round of cycles were applied again and then few cycles were performed during a rest period to monitor the shear complex interface stiffness. The shear complex interface stiffness evolution with the time during the whole test is plotted in Figure 4.57.

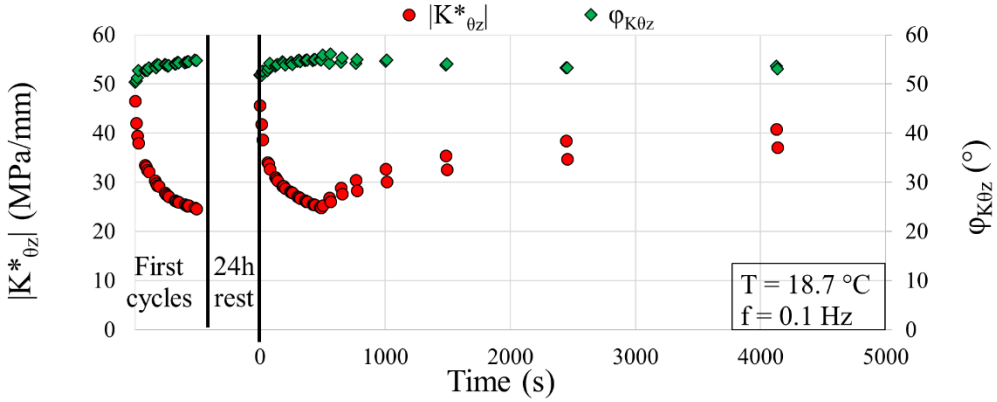

Figure 4.57 - Evolution of the shear complex interface stiffness during the oligocyclic test on sample LAT-1

After the 24 h rest period, the interface had almost completely recovered: the value of the complex interface stiffness norm was 98 % of the initial value. The value of the phase angle was 51.8 ° when it was initially 50.3 °. During the second round of cycles the norm of the interface stiffness decreased rapidly again until it reached 55 % of its initial value after 50 cycles. During the rest period, the interface recovered: the norm of the complex interface stiffness was 70 % of its initial value after a 15 min rest and 90 % after 1 h when the monitoring ended. The loss of the norm of the complex stiffness observed during the cyclic loading is thus partly reversible. This observation has already been made for fatigue tests on bituminous binders and mixtures (Babadopulos *et al.* 2019).

The evolution of the horizontal displacement gap amplitude during the oligocyclic test is plotted in Figure 4.58.

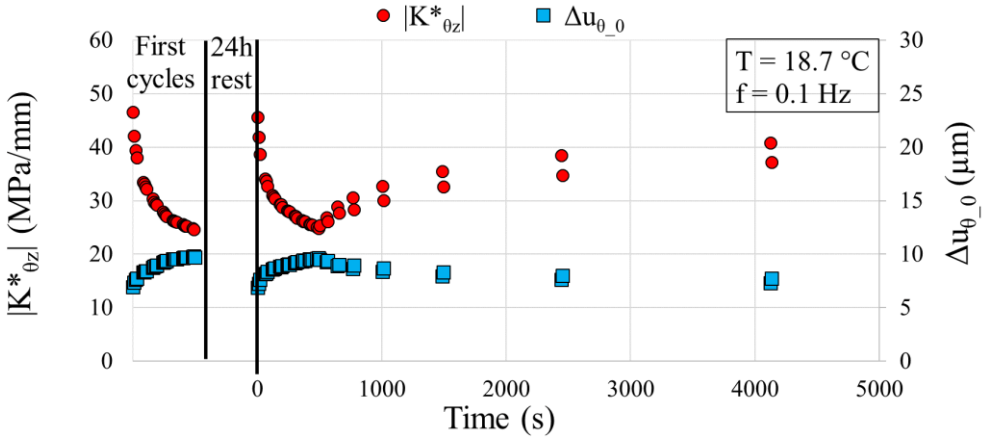

Figure 4.58 - Evolution of the complex interface stiffness and of the horizontal displacement gap amplitude during the oligocyclic test on sample LAT-1

The initial displacement gap amplitude value was close to 7 µm and it grew throughout the cycles until it reached its maximal value of about 10 µm for the last cycle. The fact that the displacement gap amplitude is not constant during the test is related to the procedure of the test where the amplitude of the global displacement between the top and the bottom of the sample is maintained constant during a test. The increase in displacement gap amplitude means that the relative loss of norm of complex interface stiffness during the cycles was more important than the relative loss of norm of the complex modulus in the bituminous mixtures layers.

This is confirmed when looking at the evolution of the shear complex modulus in the bituminous mixtures layers during the test, presented in Figure 4.59 for the mixture in the upper layer and in Figure 4.60 for the mixture in the lower layer. The norm of the modulus in the upper layer decreased of about 25 % after 50 cycles and the norm in the lower layer of only 10 %. The shear strain amplitude is higher in the upper layer, as shown in Figure 4.61, explaining why the modulus decreased more in the upper layer. The strain amplitude was almost constant in the upper layer during the cycles when the amplitude in the lower layer decreased of about 20 % after 50 cycles, compensating for the increase of displacement gap the interface.

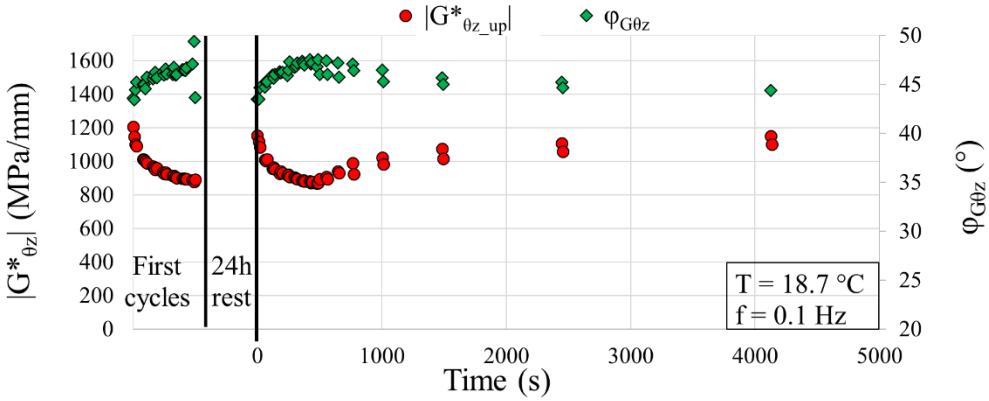

Figure 4.59 - Evolution of the shear complex modulus of the bituminous mixture in the upper layer during the oligocyclic test on sample LAT-1

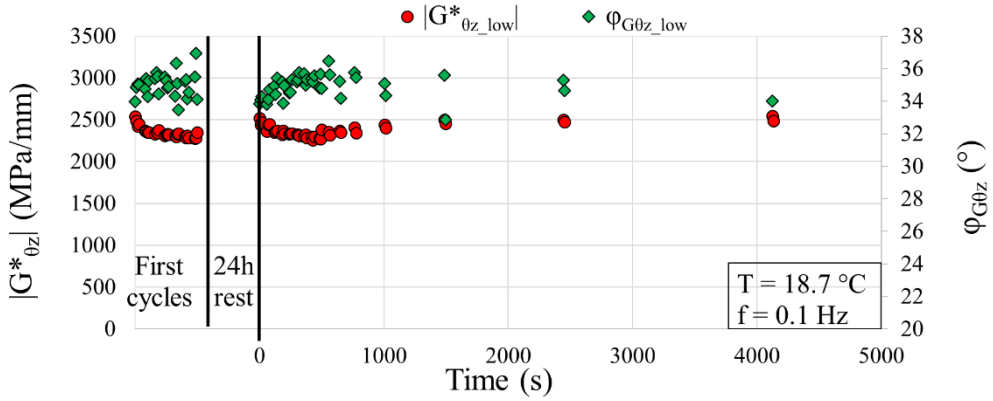

Figure 4.60 - Evolution of the shear complex modulus of the bituminous mixture in the lower layer during the oligocyclic test on sample LAT-1

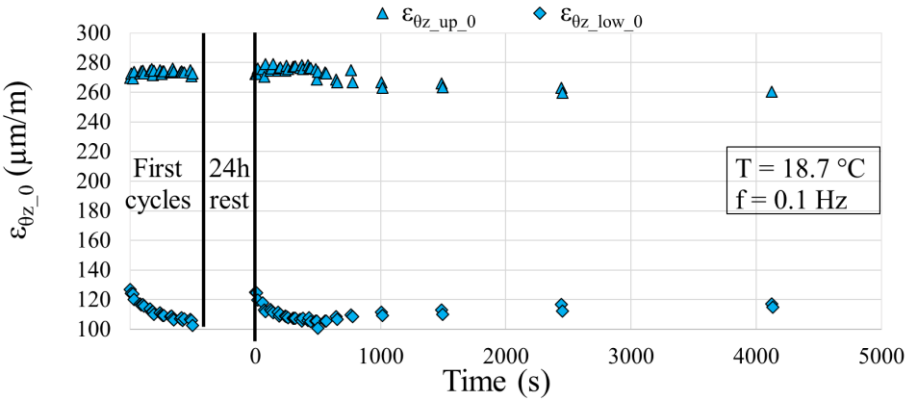

Figure 4.61 - Evolution of the vertical strain amplitude in the bituminous mixture layers during the oligocyclic test

4.4. Conclusions

Using the 2T3CHCA, advanced complex modulus tests were performed on bi-layered samples representing different interface configurations. With these tests, the complex modulus of the bituminous mixtures and the complex interface stiffness in the small strain domain were obtained both in shear mode and in tension-compression mode.

The bituminous mixtures respected the TTSP. They were modelled using the 2S2P1D model. Their behaviour was linear viscoelastic. A comparison between a tension-compression complex modulus test on cylindrical samples and the advanced complex modulus test with 2T3C HCA showed differences between the results of the two tests that could be explained by the void ratio in the samples or the anisotropy of the bituminous mixtures.

The interfaces respected the TTSP. However, their behaviour is not linear viscoelastic at the tested amplitudes, as confirmed by the nonlinearity and oligocyclic tests. A new model was developed to describe their behaviour. It is called DBN_{PDSC} (DBN model with Plastic Dissipation for Small Cycles) and is based on the addition of plastic dissipation in the springs of a generalised Kelvin-Voigt model. The interfaces with pure bitumen emulsion could be modelled using the viscoelastic properties of the pure bitumen. If the dosage of tack coat seems to have an influence on the shear complex interface stiffness, it was not possible to evaluate the influence of the other factors on the interface behaviour in the small strain domain.

Chapter 5 - Monotonic shear failure tests: results and analysis

In this chapter, the results of the monotonic shear failure tests performed during the experimental campaign are presented. First, the results a monotonic failure test conducted on one sample are explained and analysed in detail. The interface shear strength and the displacement gaps at the interface at the maximum shear stress are identified.

After this introductory example, the influence of the test factors on the interface failure behaviour is evaluated through the comparison of tests performed at different rotation speeds and with different vertical stresses.

Finally, the influence of the type of bituminous mixtures in the layers, of the dosage of tack coat and of the type of tack coat used at the interface are investigated.

5.1. Analysis of a monotonic shear failure test on one 2T3C HCA sample

The results of the monotonic shear failure test on the 2T3C HCA sample HDO-1 are presented in detail in this section as an example of the analyses conducted in this chapter. The sample is composed of a layer of the BBSG3 mixture on a layer of the EME2 mixture. The tack coat is made of a pure bitumen emulsion. The residual binder dosage at the interface is 450 g/m^2. Detailed information on these materials can be found in Chapter 3.

The vertical stress in the sample was maintained nil while rotation at a constant speed was applied to the sample. A constant rotation speed of 0.033 °/s was maintained throughout the test using the hydraulic press rotation angle sensor, corresponding to a global shear strain rate $\dot{\varepsilon}_{\theta z\_g}$ that would be 0.02 %/s in a homogeneous sample with the same dimensions than a 2T3C HCA sample. The measured test temperature was 18.5 °C.

During the torsion test, pictures are captured for the 3D DIC analysis. The vertical strain and the shear strain in the bituminous mixtures layers (ε_{zz_low}, ε_{zz_up}, $\varepsilon_{\theta z\_low}$, $\varepsilon_{\theta z\_up}$), the horizontal and vertical displacement gap at the interface (Δu_z, Δu_θ) are obtained after the test following the procedure described in section 2.3.1. One value of each of these quantities is obtained on each side of the sample. But as the cameras from both side of the samples are synchronised, the average value from both sides can be calculated. These values are the ones used in the following analyses. Each time pictures are captured, the axial force and the torque values are also acquired. The vertical stress σ_{zz} and the shear stress $\tau_{\theta z}$ are then calculated with the formulae in the homogeneous case presented in Equations 2.7 and 2.8.

5.1.1. Failure of the sample HDO-1

Four pictures taken with one of the four cameras during the monotonic shear failure test on sample HDO-1 are presented in Figure 5.1. The first one was captured at the beginning of the test and the other ones 25.5, 83 and 163 s later.

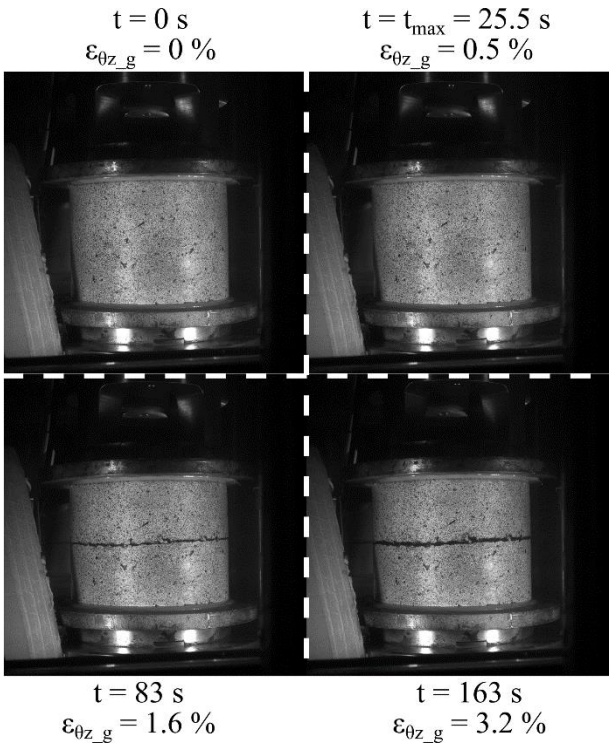

Figure 5.1 - Pictures taken at different times during the monotonic shear failure test on sample HDO-1

It is possible to see in Figure 5.1 that the sample broke at the interface between the layers. This observation was the same for all the samples at the exception of sample HDO-3 in which the upper layer of bituminous mixtures failed before the interface (the results for this sample were not analysed).

For large deformation, the upper part of the sample elevated relatively to the lower part. This is explained by the aggregates overriding at the level of the interface so that a horizontal relative displacement between the layers could happen. As the vertical stress was maintained constant, vertical displacements were indeed allowed.

5.1.2. Evolution of the shear stress during the monotonic shear failure test on sample HDO-1

The evolution of the shear stress during the monotonic shear failure test on sample HDO-1 is plotted on Figure 5.2. The shear stress increased in the sample until it reached a maximum and started decreasing towards zero. A maximum shear stress was observed in all the monotonic shear failure tests. The maximum shear stress that the interface can endure is named the interface shear strength and is noted τ_{max}. The interface shear strength in the sample HDO-1 is 1.04 MPa. The maximum was reached after a time t_{max} = 25.5 s, *i.e.* for a rotation of 0.84 ° that would correspond to 0.5 % of global shear strain in a homogeneous sample with the same dimensions.

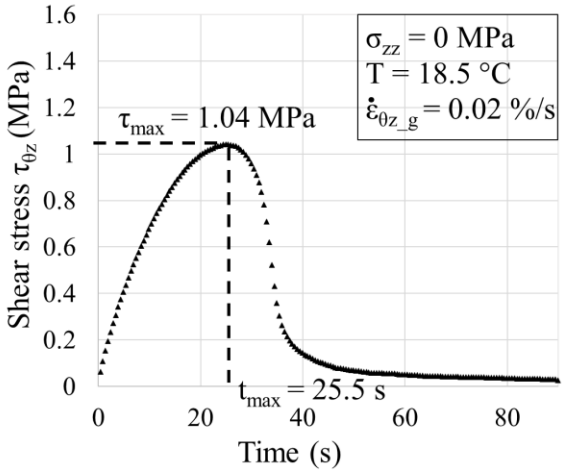

Figure 5.2 - Evolution of the shear stress during the monotonic failure test on sample HDO-1

5.1.3. Evolution of the displacement gaps at the interfaces and of the strain in the bituminous mixtures during the monotonic shear failure test on sample HDO-1

The evolution of the vertical displacement gap and of the horizontal displacement gap at the interface during the monotonic shear failure test on sample HDO-1 is presented in Figure 5.3.

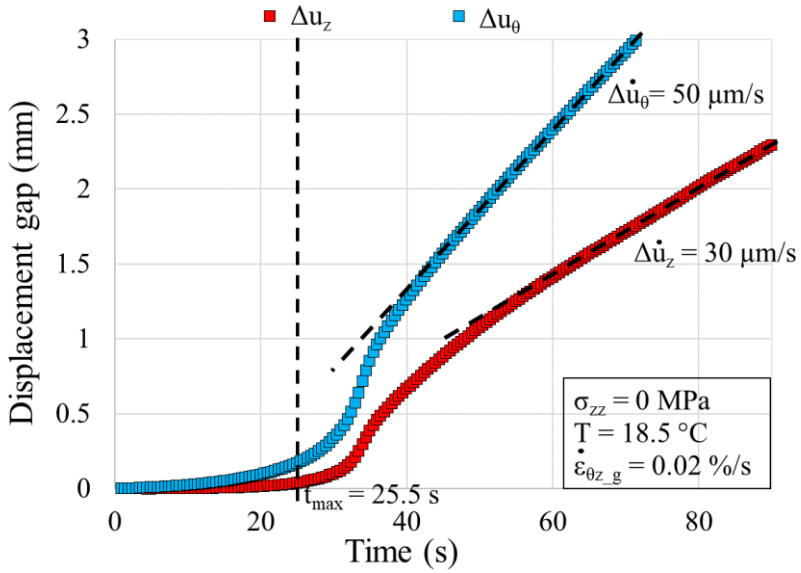

Figure 5.3 - Evolution of the vertical displacement gap and of the horizontal displacement gap at the interface during the monotonic failure test on sample HDO-1

After a slow increase at the beginning of the test, the displacement gaps increased rapidly after the interface had broken. The fact that the vertical displacement gap is positive after the interface failure concurs with the overriding of the aggregates observed on the pictures of the test (Figure 5.1).

At the end of the test, the displacement gaps evolved linearly with the time. At that point, the interface stiffness was nil and the totality of the global rotation was applied to the upper layer of the sample when the lower layer was fixed. The horizontal displacement gap speed was constant and equal to 50 µm/m/s as shown in Figure 5.3. As the displacement gap at the interface is measured on the exterior surface of the sample that is a cylinder with a radius of 8.6 cm, this speed corresponds to a rotation speed of 0.033 °/s which is the one actually imposed during the test.

The vertical displacement gap speed was also constant at the end of the test, equal to 30 µm/m/s. Instead of applying a vertical stress exactly nil, the hydraulic press might have applied a slight tension that translated into a small upward displacement when no stress could be applied anymore.

The horizontal displacement gap obtained when the maximum shear stress is reached is noted Δu_{θ_max} and is equal to 0.18 mm for the test on sample HDO-1. The vertical displacement gap at the maximum shear stress is noted Δu_{z_max} and is equal to 41 µm.

When zooming on the beginning of the test (Figure 5.4), the horizontal displacement gap at the interface did not evolve linearly with time. So the actual displacement speed at the interface was not constant during the failure test. This observation was the same for all the tested samples. As it can be seen in Figure 5.5, the vertical and horizontal displacement gap were not proportional at the beginning of the test.

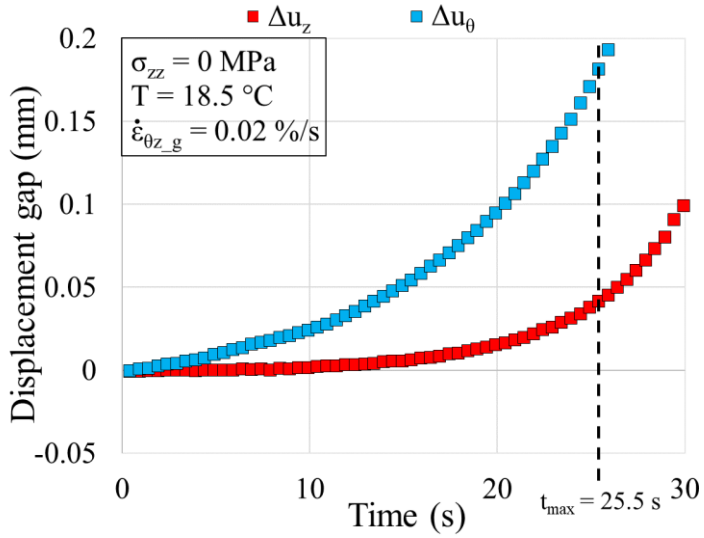

Figure 5.4 - Evolution of the vertical displacement gap and of the horizontal displacement gap at the interface at the beginning of the monotonic failure test on sample HDO-1

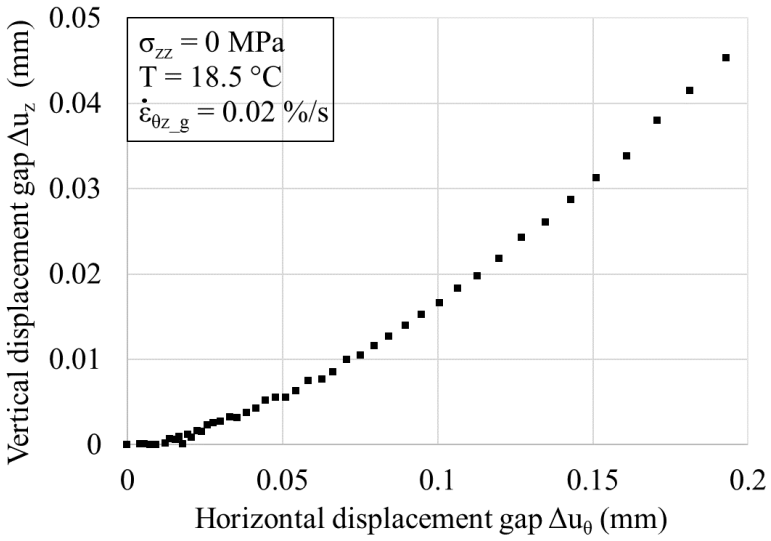

Figure 5.5 - Vertical displacement gap versus horizontal displacement gap at the interface at the beginning of the monotonic failure test on sample HDO-1

The evolution of the vertical strain and of the shear strain in the bituminous mixtures layers during the monotonic shear failure test on sample HDO-1 is presented in Figure 5.6.

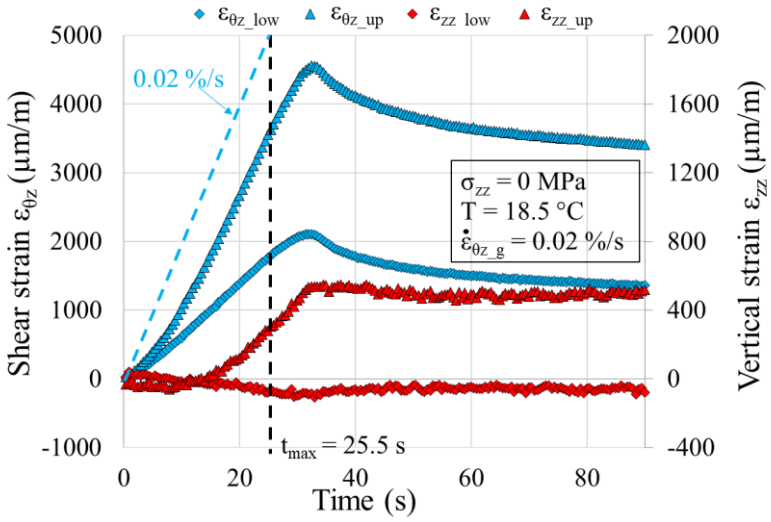

Figure 5.6 - Evolution of the shear strain and of the vertical strain in the bituminous mixtures layers during the monotonic failure test on sample HDO-1

In the first part of the test, the shear strain in the layers increased linearly. The shear strain rate in the layers was inferior to 0.02 %/s (which is the equivalent global shear strain rate applied) because the displacement gap at the interface increased during the test too. The shear strain was more important in the upper layer because the mixture used is less stiff than the one in the lower layer, as it was observed in the small strain domain in Chapter 4.

The shear strain in the layers reached a maximum that happened after the one observed for the shear stress. It can be considered as the moment of actual separation of the layers. After this, a period of strain "recovering" began with nil stresses in the layers. The maximum shear strain is observed at the same time that the shear stress decreased rapidly (Figure 5.2), shortly before the displacement gaps speeds began to be constant (Figure 5.3).

The results obtained with 3D DIC after the failure are to be considered with care, the DIC being inadequate for very large deformation. For an important number of samples, the correlation algorithm did not converge for the pictures taken after the failure. In the curves presented in this chapter, the absence of data after failure is only related to this matter.

5.1.4. Shear stress-horizontal displacement gap ($\tau_{\theta z}$ - Δu_{θ}) curve for monotonic shear failure test on sample HDO-1

The shear stress during the test is plotted versus the horizontal displacement gap in Figure 5.7.

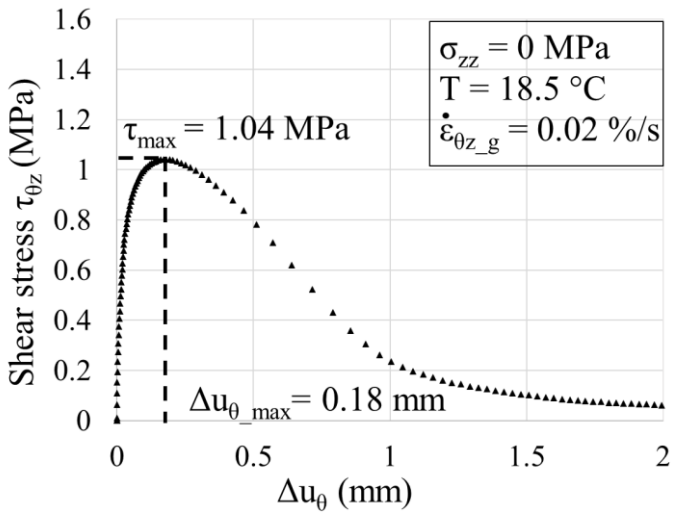

Figure 5.7 - Shear stress versus horizontal displacement gap at the interface during the monotonic failure test on sample HDO-1

The shear stress did not increase linearly with the horizontal displacement gap at the beginning of the test.

The important experimental results for the analysis of the monotonic shear failure test on sample HDO-1 are recapitulated in Table 5.1. The figures presented in this section can be found for all the other samples in Appendix C.

Table 5.1 - Results of the monotonic shear failure test on sample HDO-1

Sample	Upper layer	Lower layer	Tack coat type	Tack coat dosage (g/m²)	Global shear strain rate $\dot{\varepsilon}_{\theta z\_g}$ (%/s)	T (°C)	σ_{zz} (MPa)	τ_{max} (MPa)	Δu_{θ_max} (mm)	Δu_{z_max} (µm)
HDO-1	BBSG3	EME2	Pure Bitumen	450	0.02	18.5	0	1.04	0.18	42

5.2. Influence of the rotation speed on the interface failure behaviour

Three samples of the reference configuration (REFA-3, REFB-1, REFB-2) were tested in order to find the rotation speed that would give, at the aimed temperature of 20 °C, an interface shear strength that would be situated in the middle of the torque cell measurement range. The torque cell measures torque up to 2,000 N.m which represents a shear stress of 2.33 MPa in the 2T3C HCA sample. The tested rotation speeds (expressed in global shear strain rate, calculated as if the sample was made of a homogeneous material) and the results of the monotonic shear failure tests on samples REFA-3, REFB-1 and REFB-2 are presented in Table 5.2.

Table 5.2 - Results of the monotonic shear failure tests on samples REFA-3, REFB-1 and REFB-2

Sample	Upper layer	Lower layer	Tack coat type	Tack coat dosage (g/m²)	Global shear strain rate $\dot{\varepsilon}_{\theta z\_g}$ (%/s)	T (°C)	σ_{zz} (MPa)	τ_{max} (MPa)	Δu_{θ_max} (mm)	Δu_{z_max} (µm)
REFA-3	BBSG3	EME2	Pure Bitumen	350	0.2	18.5	0	2.08	0.19	36
REFB-1	BBSG3	EME2	Pure Bitumen	350	0.067	18.5	0	1.47	0.20	46
REFB-2	BBSG3	EME2	Pure Bitumen	350	0.02	18.5	0	1.06	0.20	47

The horizontal displacement gap at the maximum shear stress was almost the same for all the tested rotation speeds with a value close to 0.20 mm. The vertical displacement gap at the interface for the maximum shear stress was also almost constant, close to 40 µm in all the tests.

The interface shear strength of the samples REFA-3, REFB-1 and REFB-2 are plotted versus the global shear strain rate applied during the test in Figure 5.8.

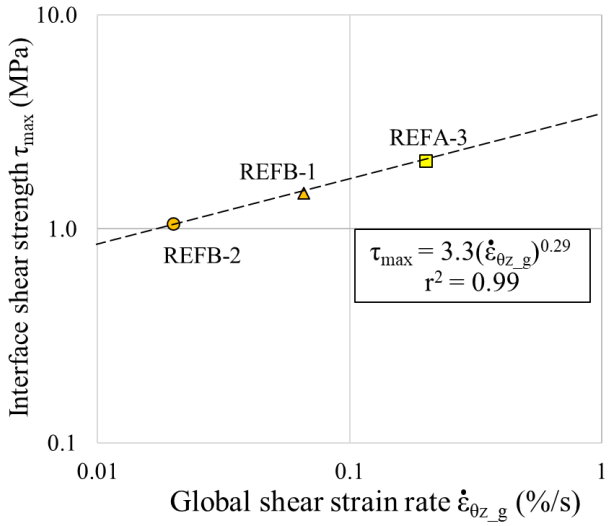

Figure 5.8 - Interface shear strength versus global shear strain rate in the monotonic shear failure tests on samples REFA-3, REFB-1 and REFB-2

The dependency of the interface shear strength with the global shear strain rate can be modelled using a power law, which concurs with previous observations (Diakhaté 2007; Canestrari *et al.* 2013). The interface shear strength of sample REFB-2 corresponded approximately to half of the torque cell measurement range so the global shear strain rate was fixed at 0.02 %/s in the other tests.

The shear stress-horizontal displacement gap curves are plotted in Figure 5.9 for the tests on samples REFA-3, REFB-1 and REFB-2.

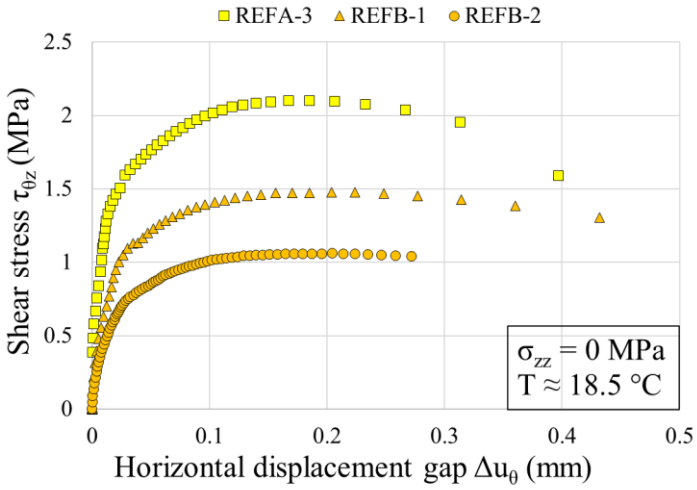

Figure 5.9 - Shear stress versus horizontal displacement gap at the interface during the monotonic failure tests on samples REFA-3, REFB-1 and REFB-2

The vertical displacement gap is plotted versus the horizontal displacement gap at the interface for the beginning of the monotonic shear failure tests on samples REFA-3, REFB-1 and REFB-2 in Figure 5.10. The evolution of the vertical displacement gap with the horizontal displacement gap was similar in the three tests.

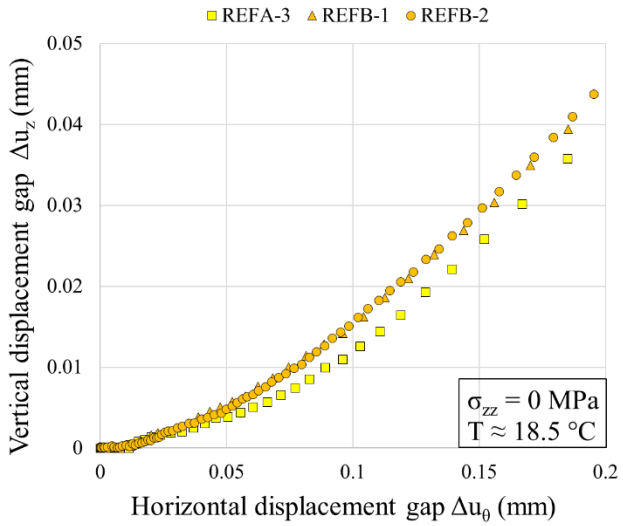

Figure 5.10 - Vertical displacement gap versus horizontal displacement gap at the interface at the beginning of the monotonic failure tests on samples REFA-3, REFB-1 and REFB-2

5.3. Influence of the normal stress on the interface failure behaviour

For three of the tested configurations (REF, D/C, LDO) tests were performed at three different vertical stresses: either 0, 0.25 or 1 MPa. The results of these tests can be found in Table 5.3 where it can be seen that he application of a normal stress increases the interface shear strength and the horizontal displacement gap at the maximum shear stress.

Table 5.3 - Results of the monotonic shear failure tests on configurations REF, D/C and LDO

Sample	Upper layer	Lower layer	Tack coat type	Tack coat dosage (g/m²)	Global shear strain rate $\dot{\varepsilon}_{\theta z\_g}$ (%/s)	T (°C)	σ_{zz} (MPa)	τ_{max} (MPa)	Δu_{θ_max} (mm)	Δu_{z_max} (µm)
REFB-2	BBSG3	EME2	Pure Bitumen	350	0.02	18.5	0	1.06	0.20	47
REFB-3	BBSG3	EME2	Pure Bitumen	350	0.02	18.5	0.25	1.13	0.27	54
REFC-2	BBSG3	EME2	Pure Bitumen	350	0.02	18.7	1	1.47	0.30	27
REFC-3	BBSG3	EME2	Pure Bitumen	350	0.02	18.5	0.25	1.05	0.23	41
D/C-1	BB5	EME2	Pure Bitumen	350	0.02	18.9	0	1.05	0.18	37
D/C-2	BB5	EME2	Pure Bitumen	350	0.02	19	0.25	1.16	0.35	35
D/C-3	BB5	EME2	Pure Bitumen	350	0.02	18.7	1	1.43	0.99	55
LDO-1	BBSG3	EME2	Pure Bitumen	250	0.02	18.7	0	0.85	0.26	38
LDO-2	BBSG3	EME2	Pure Bitumen	250	0.02	18.8	0.25	0.82	0.35	35
LDO-3	BBSG3	EME2	Pure Bitumen	250	0.02	18.8	1	1.05	0.76	31

The interface shear strengths for these configurations are plotted versus the vertical stress during the test in Figure 5.11.

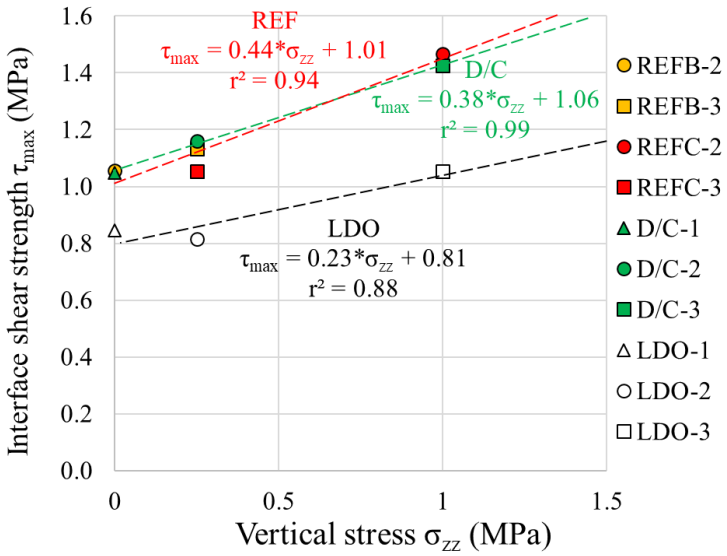

Figure 5.11 - Interface shear strength versus vertical stress for monotonic shear failure tests on configurations REF, D/C and LDO

The evolution of the interface shear strength versus the vertical stress could be modelled using a linear law, which is the Mohr-Coulomb failure criterion, for each of the tested configuration. This observation is in agreement with previous studies of the influence of normal stress on the interface shear strength (Canestrari *et al.* 2005). The cohesion *C* and the angle of internal friction φ, defined in Equation 1.34, are found for each configuration and presented in Table 5.4. The angle of internal friction was between 13 and 24 ° depending on the configuration.

Table 5.4 - Mohr-Coulomb failure criterion constants for configurations REF, D/C and LDO

Configuration	**Upper layer**	**Lower layer**	**Tack coat type**	**Tack coat dosage (g/m²)**	**Global shear strain rate $\dot{\varepsilon}_{\theta z\_g}$ (%/s)**	**Average T (°C)**	**C (MPa)**	**φ (°)**
REF	BBSG3	EME2	Pure Bitumen	350	0.02	18.6	1.01	24
D/C	BB5	EME2	Pure Bitumen	350	0.02	18.9	1.06	21
LDO	BBSG3	EME2	Pure Bitumen	250	0.02	18.8	0.81	13

The vertical displacement gap is plotted versus the horizontal displacement gap at the interface at the beginning of the monotonic shear failure tests on configurations REF, D/C and LDO in Figure 5.12. Higher vertical displacement gaps were observed for the same value of horizontal displacement gap for lower normal stresses. The vertical displacement gap was negative at the beginning of the tests with the vertical stress at 1 MPa before increasing as the rotation took place, showing that the aggregate overriding was preeminent over the contraction of the tack coat due to the normal compressive stress.

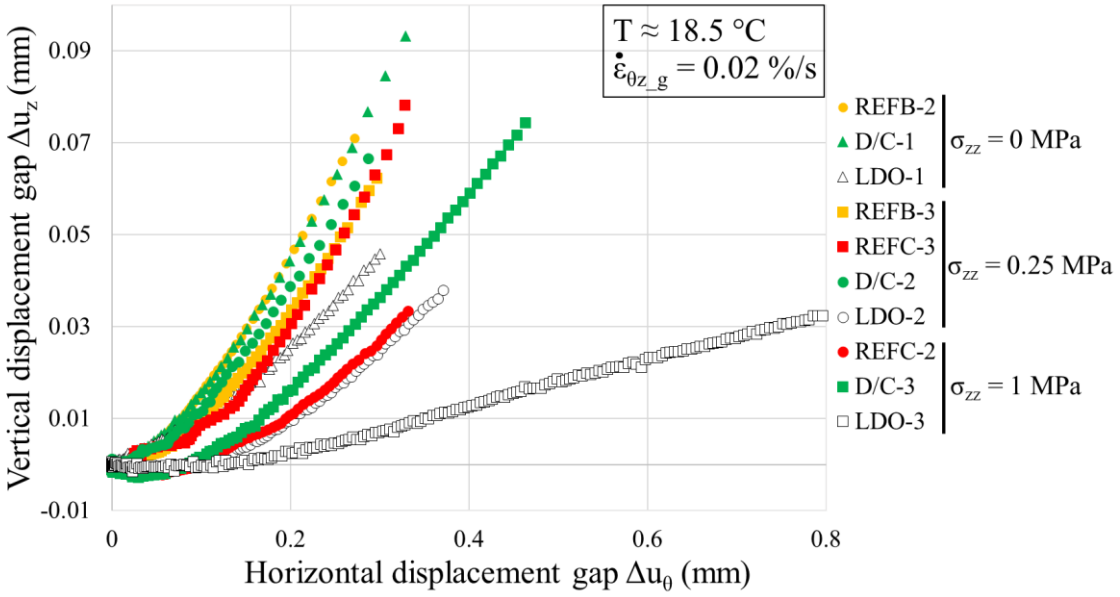

Figure 5.12 - Vertical displacement gap versus horizontal displacement gap at the interface at the beginning of the monotonic failure tests on configurations REF, D/C and LDO

5.4. Influence of the type of bituminous mixtures in the layers on the interface failure behaviour

Four configurations (REF, C/D, D/D, D/C) were used to assess the influence of the bituminous mixture in the layers on the interface failure. Four different mixtures were used in the configurations but the tack coat was the same, made of pure bitumen emulsion applied at a residual dosage of 350 g/m^2. The mixtures had either a continuous aggregate size distribution curve (BBSG3 in the upper layer and EME2 in the lower layer) or a discontinuous one (BB5 in the upper layer and GB5 in the lower layer). The different configurations of mixtures in the upper layer and in the lower layer were tested. The experimental results for the tested configurations are presented in Table 5.5

Table 5.5 - Results of the monotonic shear failure tests on configurations REF, C/D, D/D and D/C

Sample	Upper layer	Lower layer	Tack coat type	Tack coat dosage (g/m^2)	Global shear strain rate $\dot{\varepsilon}_{\theta z\_g}$ (%/s)	T (°C)	σ_{zz} (MPa)	τ_{max} (MPa)	Δu_{θ_max} (mm)	Δu_{z_max} (µm)
REFB-2	BBSG3	EME2	Pure Bitumen	350	0.02	18.5	0	1.06	0.20	47
REFB-3	BBSG3	EME2	Pure Bitumen	350	0.02	18.5	0.25	1.13	0.27	54
REFC-2	BBSG3	EME2	Pure Bitumen	350	0.02	18.7	1	1.47	0.30	27
REFC-3	BBSG3	EME2	Pure Bitumen	350	0.02	18.5	0.25	1.05	0.23	41
C/D-1	BBSG3	GB5	Pure Bitumen	350	0.02	18.6	0	1.25	0.11	24
C/D-2	BBSG3	GB5	Pure Bitumen	350	0.02	18.8	0	1.15	0.15	33
C/D-3	BBSG3	GB5	Pure Bitumen	350	0.02	18.8	1	1.56	0.18	25
D/D-1	BB5	GB5	Pure Bitumen	350	0.02	18.4	0	1.00	0.19	41
D/D-2	BB5	GB5	Pure Bitumen	350	0.02	18.5	0	0.97	0.27	75
D/C-1	BB5	EME2	Pure Bitumen	350	0.02	18.9	0	1.05	0.18	37
D/C-2	BB5	EME2	Pure Bitumen	350	0.02	19	0.25	1.16	0.35	35
D/C-3	BB5	EME2	Pure Bitumen	350	0.02	18.7	1	1.43	0.99	55

The average interface shear strength per configuration is presented in Figure 5.13 for the tests without normal stress and in Figure 5.14 for the tests with normal stress. From Figure 5.13, it can be seen that the configuration C/D presented a higher shear strength that the other ones. The values for the other configurations were almost equal. The strength for configuration C/D (Continuous on Discontinuous) was 13 % higher than for the configuration REF (Continuous on Continuous). This observation concurs with the analysis presented in section 1.3.3 concerning the interlocking effect (Raab *et al.* 2012) where the configuration smooth on rough was the most favourable. The "valleys" in the lower layer are more easily filled by a mixture with a continuous grading curve when the upper layer is compacted at a high temperature than by a mixture with a discontinuous curve. The EME2 mixture had a significantly smaller mean texture depth than the GB5 mixture (section 3.1.2) and this could explain the lowest strength obtained for configurations REF and D/C. The interlocking effect is more visible at high temperatures and low rotation speeds as it is the case in the monotonic shear failure test presented in this study where the failure is always ductile, never brittle. These results are also related to the tack coat dosage. At a smaller dosage, a rough interface increases the interlocking effect but might diminish the bonding brought by the tack coat leading to a weaker strength in the end.

From Figure 5.14, similar observations are made when applying a constant vertical stress during the test: the configuration C/D is more resistant and the other configurations have almost the same bonding strength.

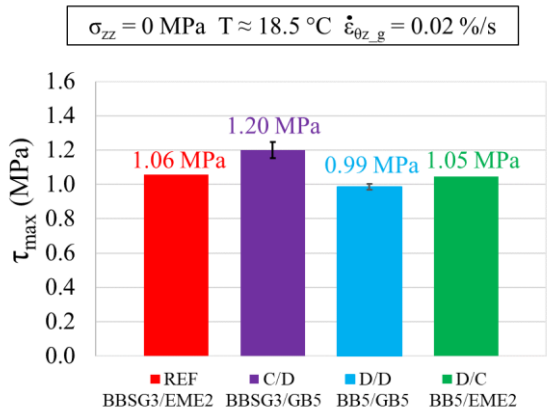

Figure 5.13 - Interface shear strength for monotonic shear failure tests without normal stress on configurations REF, C/D, D/D and D/C

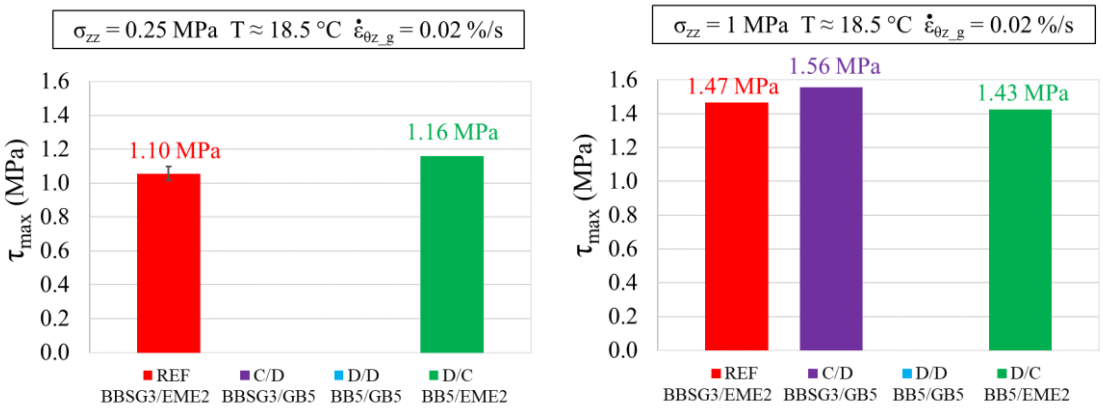

Figure 5.14 - Interface shear strength for monotonic shear failure tests with normal stress on configurations REF, C/D, D/D and D/C

The shear stress-horizontal displacement gap curves for the tests on configurations REF, C/D, D/D and D/C can be found in Figure 5.15. For some of the samples, it looks like the displacement gap decreased during the test when the shear stress was still increasing (very visible on sample D/D-2 on the left of Figure 5.15). This is related to the computation of the horizontal displacement gap that is based on the assumption of homogeneity of strain in the sample (section 2.3.1). For large deformations as in the monotonic shear failure test with 2T3C HCA, strain in the layers was not always homogeneous which influenced the calculated value of the displacement gap at the interface.

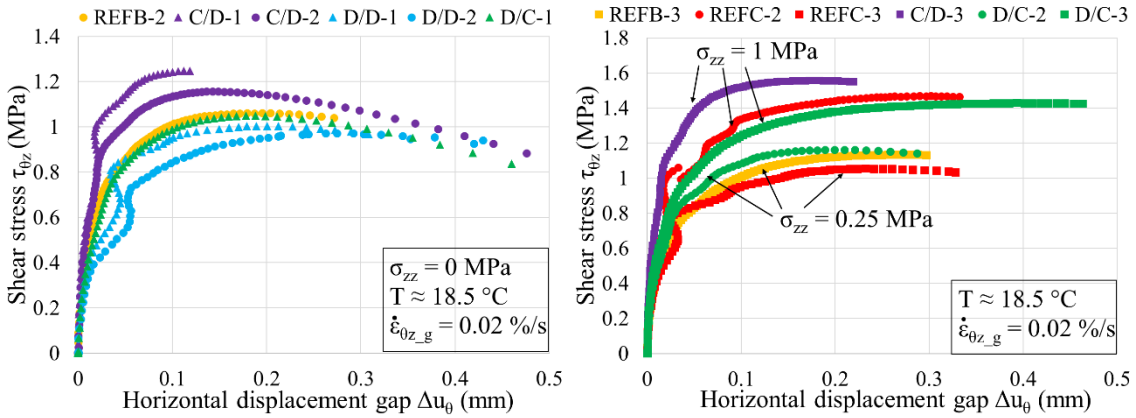

Figure 5.15 - Shear stress versus horizontal displacement gap at the interface during the monotonic shear failure tests on configurations REF, C/D, D/D and D/C (tests without normal stress on the left and tests with normal stress on the right)

The average horizontal displacement gap at the maximum shear stress per configuration is presented in Figure 5.16 for the tests without normal stress and in Figure 5.17 for the tests with normal stress. The average vertical displacement gap at the maximum shear stress per configuration is presented in Figure 5.18 for the tests without normal stress and in Figure 5.19 for the tests with normal stress.

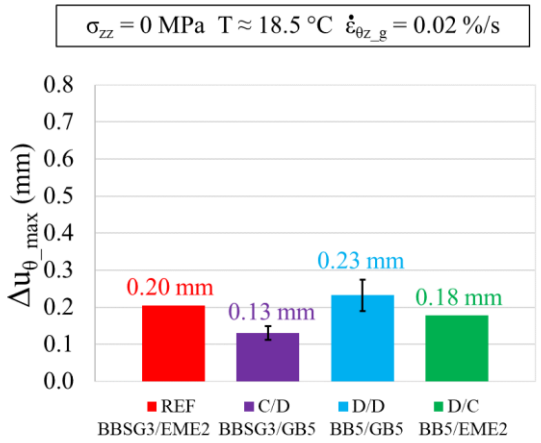

Figure 5.16 - Horizontal displacement gap at maximum shear stress for monotonic shear failure tests without normal stress on configurations REF, C/D, D/D and D/C

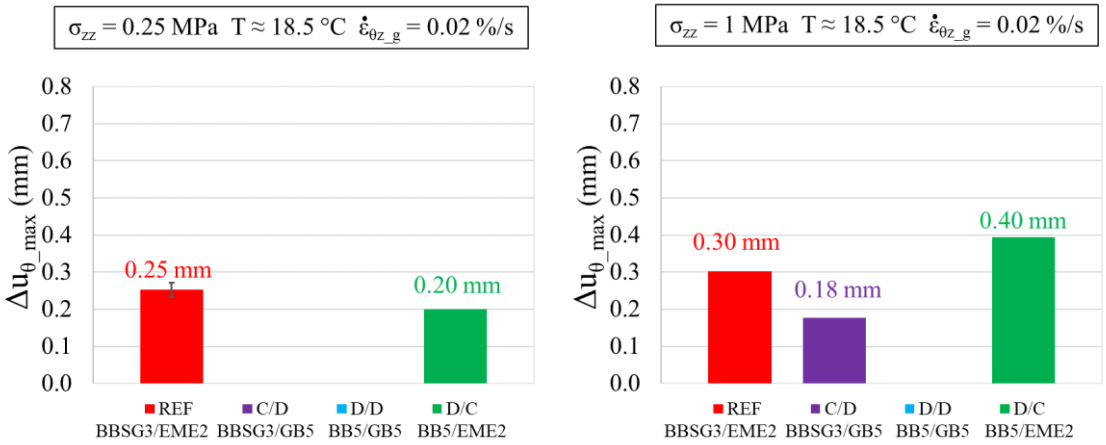

Figure 5.17 - Horizontal displacement gap at maximum shear stress for monotonic shear failure tests with normal stress on configurations REF, C/D, D/D and D/C

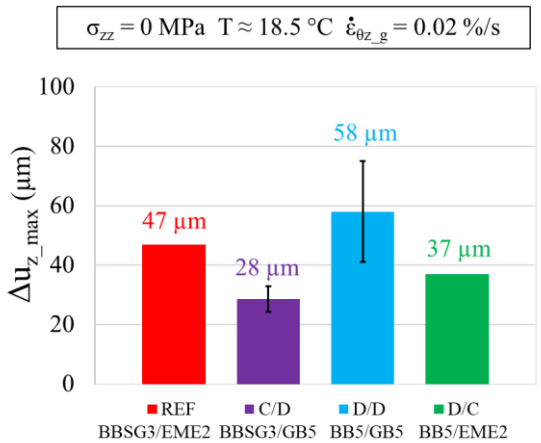

Figure 5.18 - Vertical displacement gap at maximum shear stress for monotonic shear failure tests without normal stress on configurations REF, C/D, D/D and D/C

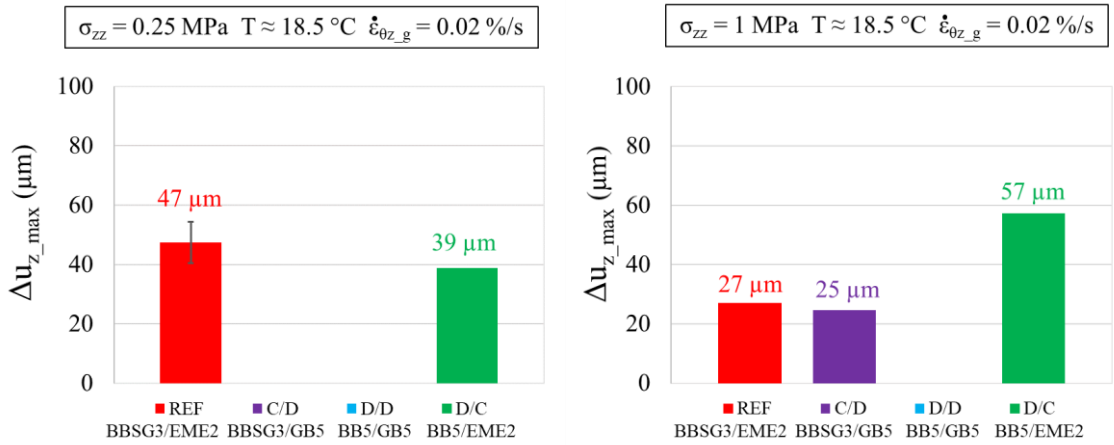

Figure 5.19 - Vertical displacement gap at maximum shear stress for monotonic shear failure tests with normal stress on configurations REF, C/D, D/D and D/C

The vertical and horizontal displacement gaps at the interface at the maximum shear stress were slightly lower in the configuration C/D than for the other configurations. The rigidity of the interface both in the shear and tension-compression mode was thus higher for this configuration, which could be a consequence of aggregate interlocking.

5.5. Influence of the dosage of tack coat on the interface failure behaviour

Three different dosages of tack coat at the interface were tested in the configurations LDO, REF and HDO. The bituminous mixtures in the upper layer (BBSG3) and in the lower layer (EME2) were the same for the three configurations. The tack coat was an emulsion of pure bitumen with a residual binder dosage of 250 g/m^2 for configuration LDO, 350 g/m^2 for REF and 450 g/m^2 for HDO. The experimental results of the monotonic shear failure tests on these configurations are presented in Table 5.6.

Table 5.6 - Results of the monotonic shear failure tests on configurations REF, LDO and HDO

Sample	Upper layer	Lower layer	Tack coat type	Tack coat dosage (g/m^2)	Global shear strain rate $\dot{\varepsilon}_{\theta z\_g}$ (%/s)	T (°C)	σ_{zz} (MPa)	τ_{max} (MPa)	Δu_{θ_max} (mm)	Δu_{z_max} (µm)
REFB-2	BBSG3	EME2	Pure Bitumen	350	0.02	18.5	0	1.06	0.20	47
REFB-3	BBSG3	EME2	Pure Bitumen	350	0.02	18.5	0.25	1.13	0.27	54
REFC-2	BBSG3	EME2	Pure Bitumen	350	0.02	18.7	1	1.47	0.30	27
REFC-3	BBSG3	EME2	Pure Bitumen	350	0.02	18.5	0.25	1.05	0.23	41
LDO-1	BBSG3	EME2	Pure Bitumen	250	0.02	18.7	0	0.85	0.26	38
LDO-2	BBSG3	EME2	Pure Bitumen	250	0.02	18.8	0.25	0.82	0.35	35
LDO-3	BBSG3	EME2	Pure Bitumen	250	0.02	18.8	1	1.05	0.76	31
HDO-1	BBSG3	EME2	Pure Bitumen	450	0.02	18.5	0	1.04	0.18	42
HDO-2	BBSG3	EME2	Pure Bitumen	450	0.02	18.7	0	1.04	0.18	44

The average interface shear strength per configuration is presented in Figure 5.20 for tests without normal stress and in Figure 5.21 for tests with normal stress. The configuration LDO presented the lowest interface shear strength when the values for configurations REF and HDO were close. When no vertical shear strength is applied, the LDO configuration presented an interface shear strength 19 % lower than the reference configuration. When not enough tack coat is applied, the effective contact surface between the layers is reduced, leading to a decreased interface shear strength. It is interesting to

notice that for the bituminous mixtures used in these configurations, the French standard (NF P 98-150-1) recommends a minimal dosage of 250 g/m² when the optimum tack coat dosage seems to be higher (for the temperature and loading speed tested with 2T3C HCA).

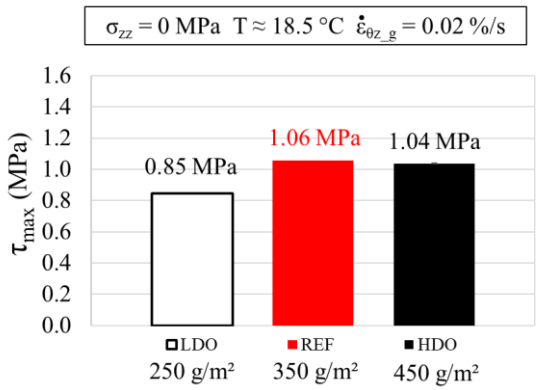

Figure 5.20 - Interface shear strength for monotonic shear failure tests without normal stress on configurations LDO, REF and HDO

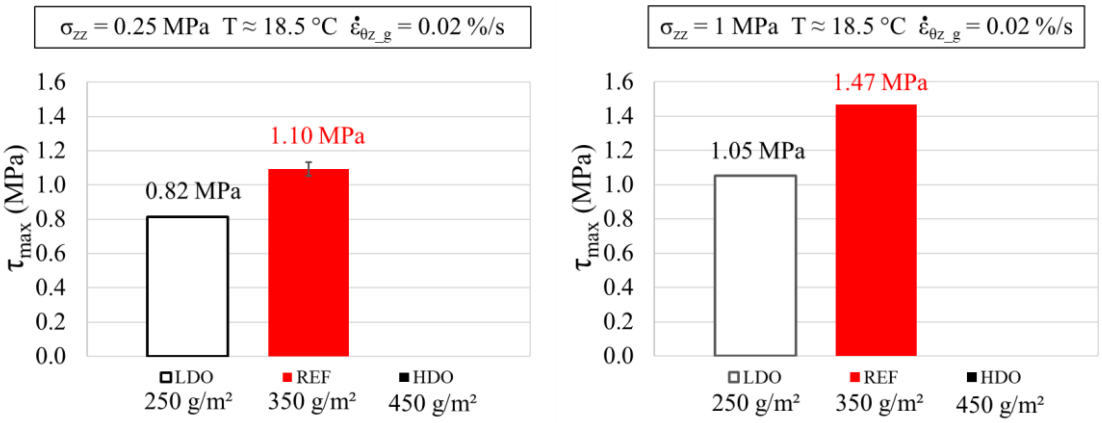

Figure 5.21 - Interface shear strength for monotonic shear failure tests with normal stress on configurations LDO, REF and HDO

The shear stress-horizontal displacement curves for the tests on configurations LDO, REF and HDO are presented in Figure 5.22.

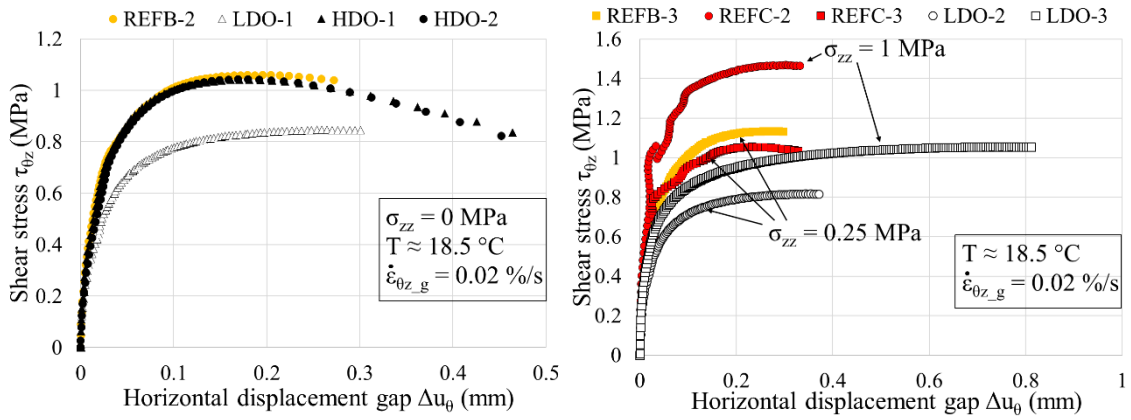

Figure 5.22 - Shear stress versus horizontal displacement gap at the interface during the monotonic shear failure tests on configurations LDO, REF and HDO (tests without normal stress on the left, and tests with normal stress on the right)

The average horizontal displacement gap at the maximum shear stress per configuration is presented in Figure 5.23 for the tests without normal stress and in Figure 5.24 for the tests with normal stress. The average vertical displacement gap at the maximum shear stress per configuration is presented in Figure 5.25 for the tests without normal stress and in Figure 5.26 for the tests with normal stress.

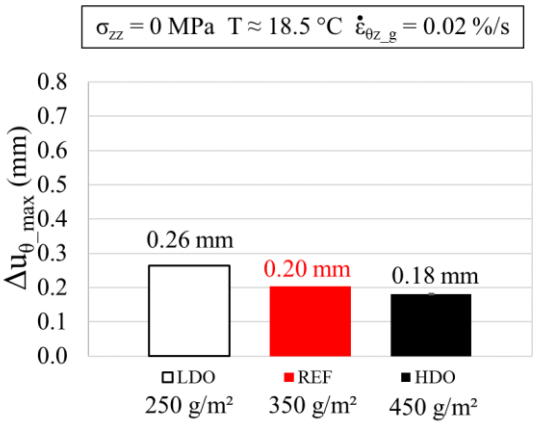

Figure 5.23 - Horizontal displacement gap at maximum shear stress for monotonic shear failure tests without normal stress on configurations LDO, REF and HDO

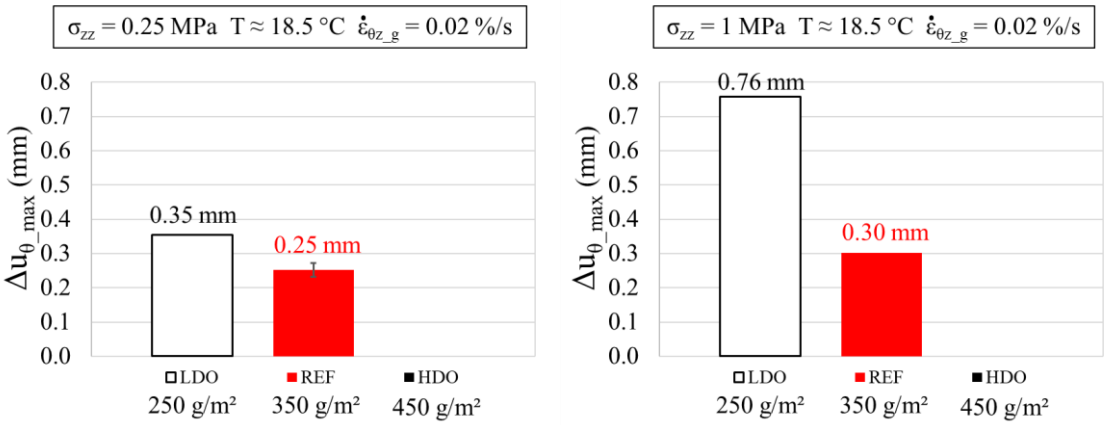

Figure 5.24 - Horizontal displacement gap at maximum shear stress for monotonic shear failure tests with normal stress on configurations LDO, REF and HDO

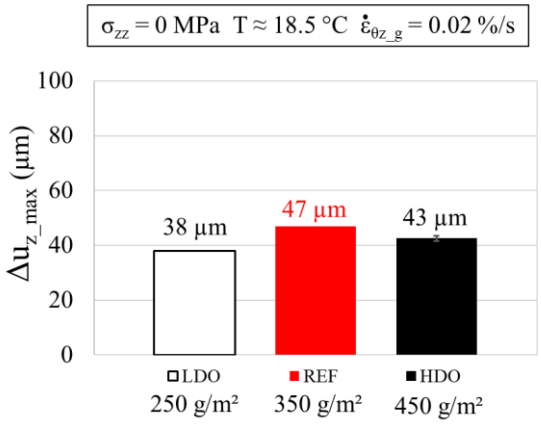

Figure 5.25 - Vertical displacement gap at maximum shear stress for monotonic shear failure tests without normal stress on configurations LDO, REF and HDO

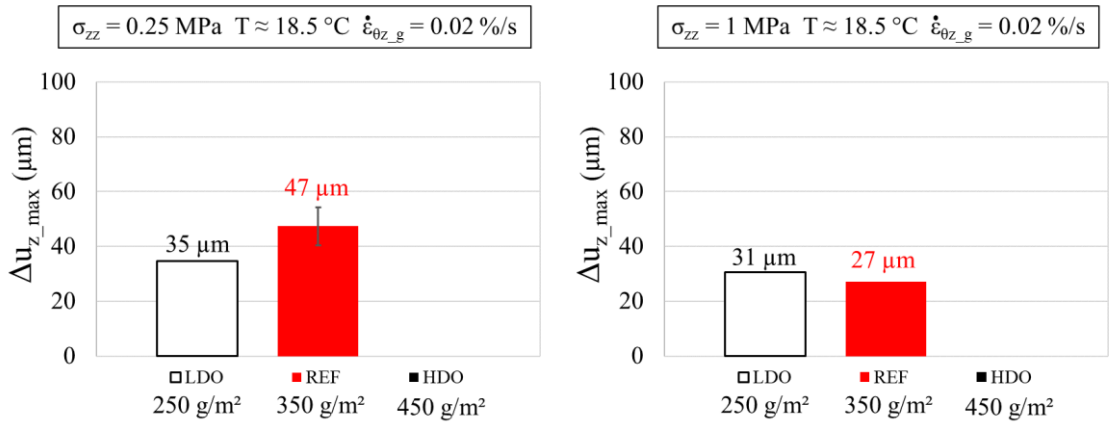

Figure 5.26 - Vertical displacement gap at maximum shear stress for monotonic shear failure tests with normal stress on configurations LDO, REF and HDO

The vertical and horizontal displacement gaps at the maximum shear stress were quite similar for the different dosages of tack coat tested without normal stress.

5.6. Influence of the type of tack coat on the interface failure behaviour

Concerning the influence of the type of tack coat at the interface, the three configurations tested were REF with an emulsion of pure bitumen, SBS with an emulsion of bitumen modified with SBS polymer and LAT with an emulsion of bitumen modified with latex. The bituminous mixtures were the same in the layers (BBSG3 in the upper layer and EME2 in the lower layer). The dosage of residual binder was 350 g/m^2 for all the samples. The results of the monotonic shear failure tests on configurations REF, SBS and LAT are presented in Table 5.7.

Table 5.7 - Results of the monotonic shear failure tests on configurations REF, SBS and LAT

Sample	Upper layer	Lower layer	Tack coat type	Tack coat dosage (g/m^2)	Global shear strain rate $\dot{\varepsilon}_{\theta z\_g}$ (%/s)	T (°C)	σ_{zz} (MPa)	τ_{max} (MPa)	Δu_{θ_max} (mm)	Δu_{z_max} (µm)
REFB-2	BBSG3	EME2	Pure Bitumen	350	0.02	18.5	0	1.06	0.20	47
REFB-3	BBSG3	EME2	Pure Bitumen	350	0.02	18.5	0.25	1.13	0.27	54
REFC-2	BBSG3	EME2	Pure Bitumen	350	0.02	18.7	1	1.47	0.30	27
REFC-3	BBSG3	EME2	Pure Bitumen	350	0.02	18.5	0.25	1.05	0.23	41
SBS-1	BBSG3	EME2	Bitumen modified with SBS	350	0.02	18.5	0	0.92	0.19	41
SBS-2	BBSG3	EME2	Bitumen modified with SBS	350	0.02	18.5	0	0.97	0.26	58
SBS-3	BBSG3	EME2	Bitumen modified with SBS	350	0.02	18.5	1	1.31	0.63	89
LAT-1	BBSG3	EME2	Bitumen modified with latex	350	0.02	18.5	0	1.12	0.17	94
LAT-2	BBSG3	EME2	Bitumen modified with latex	350	0.02	18.5	0	1.06	0.32	101

The average interface shear strength in the configurations REF, SBS and LAT are presented in Figure 5.27. The modification of the bitumen in the emulsion with SBS decreased the interface shear

strength with and without normal stress. The modification of the bitumen with latex did not have any influence on the interface shear strength when no vertical stress was applied.

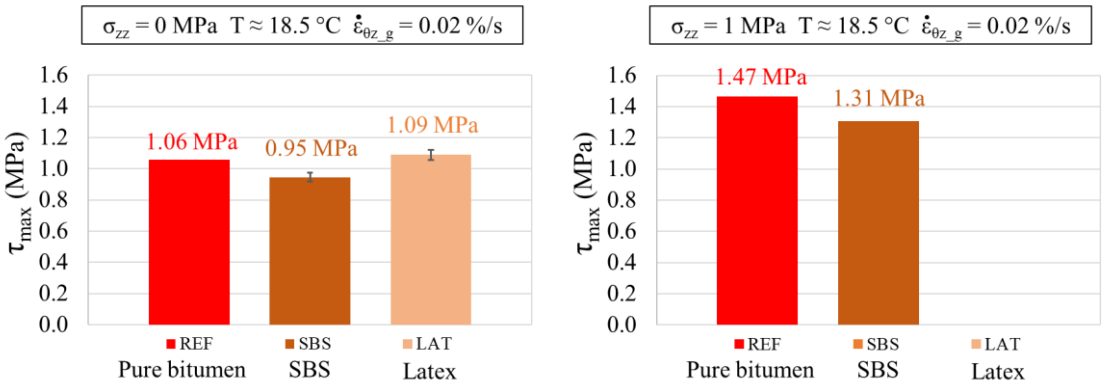

Figure 5.27 - Interface shear strength for monotonic shear failure tests on configurations REF, SBS and LAT (tests without normal stress on the left and tests with normal stress on the right)

The shear stress-horizontal displacement curves for the tests on configurations REF, SBS and LAT are presented in Figure 5.28.

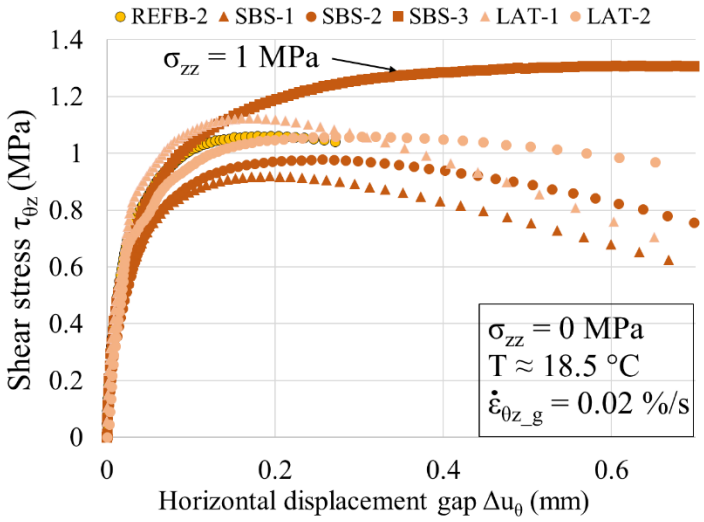

Figure 5.28 - Shear stress versus horizontal displacement gap at the interface during the monotonic shear failure tests on configurations REF, SBS and LAT

The average horizontal displacement gap at the maximum shear stress per configuration is presented in Figure 5.29. The average vertical displacement gap at the maximum shear stress per configuration is presented in Figure 5.30.

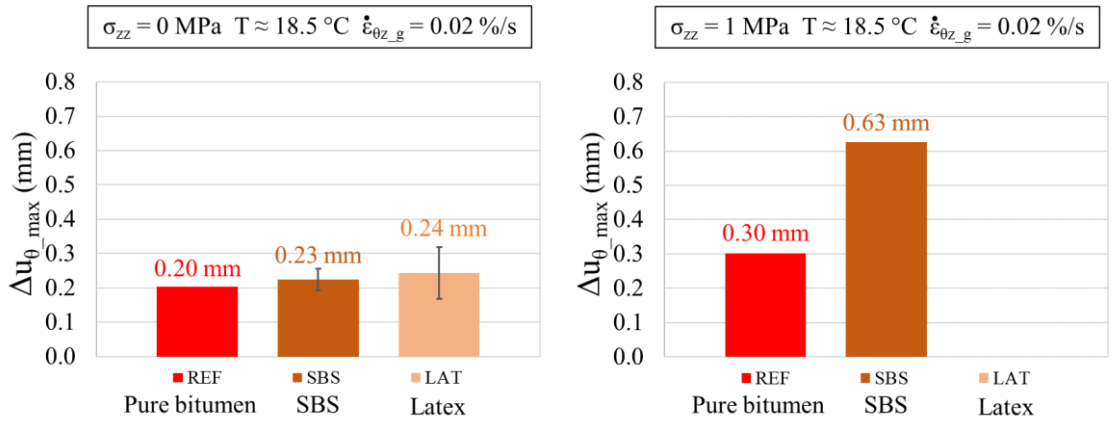

Figure 5.29 - Horizontal displacement gap at the maximum shear stress for monotonic shear failure tests on configurations REF, SBS and LAT (tests without normal stress on the left and tests with normal stress on the right)

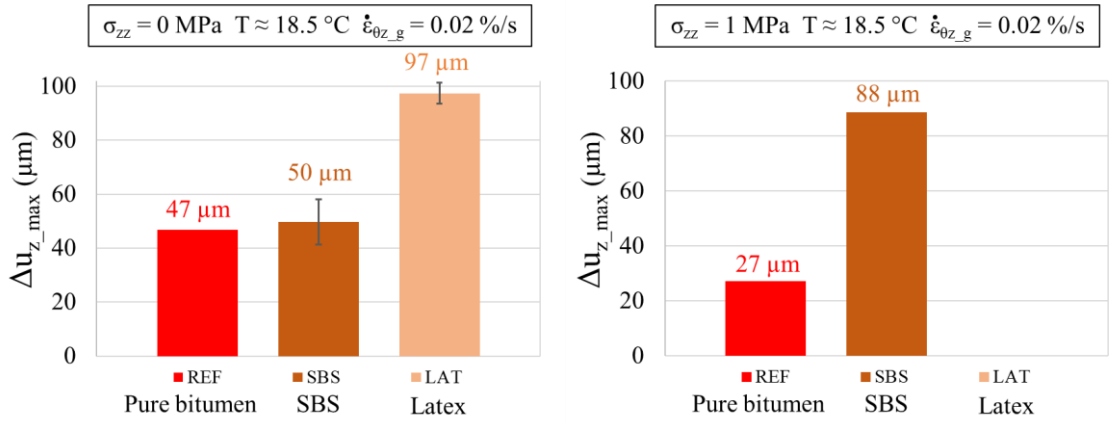

Figure 5.30 - Vertical displacement gap at the maximum shear stress for monotonic shear failure tests on configurations REF, SBS and LAT (tests without normal stress on the left and tests with normal stress on the right)

5.7. Conclusions

From monotonic shear failure tests performed at a constant rotation speed, the failure behaviour of interfaces was observed. The tests were all done at a temperature close to 20 °C.

The increase of shear strain rate induced an increase in the interface shear strength. The dependency of the interface shear strength with the shear strain rate was modelled with a power law.

When increasing the normal stress, the interface shear strength at the interface and the horizontal displacement gap at the maximum shear stress increased. The interfaces could be described using the Mohr-Coulomb failure criterion.

The aggregate interlocking had an effect on the interface failure behaviour. The configuration where a bituminous mixture with a continuous aggregate size distribution curve was compacted on a mixture with a continuous grading curve presented the best interface shear strength.

For interfaces with a tack coat in pure bitumen emulsion, the dosage of 250 g/m^2 of residual binder led to the lowest interface shear strength compared to the application dosages of 350 and 450 g/m^2.

The tack coat with an emulsion of bitumen modified with SBS showed the lowest interface shear strength compared to the emulsion of pure bitumen and to the emulsion of bitumen modified with latex, for which the interface shear strengths were close.

A recapitulation of all the results of the monotonic shear failure tests performed in this campaign can be found in Table 5.8.

Table 5.8 - Results of the monotonic shear failure tests (*the mixture in the upper layer of sample HDO-3 failed before the interface)

Sample	Upper layer	Lower layer	Tack coat type	Tack coat dosage (g/m^2)	Global shear strain rate $\dot{\varepsilon}_{\theta z\_g}$ (%/s)	T (°C)	σ_{zz} (MPa)	τ_{max} (MPa)	Δu_{θ_max} (mm)	Δu_{z_max} (µm)
REFA-3	BBSG3	EME2	Pure Bitumen	350	0.2	18.5	0	2.08	0.19	36
REFB-1	BBSG3	EME2	Pure Bitumen	350	0.067	18.5	0	1.47	0.20	46
REFB-2	BBSG3	EME2	Pure Bitumen	350	0.02	18.5	0	1.06	0.20	47
REFB-3	BBSG3	EME2	Pure Bitumen	350	0.02	18.5	0.25	1.13	0.27	54
REFC-1	BBSG3	EME2	Pure Bitumen	350	0.02	24.0	0	0.86	0.20	46
REFC-2	BBSG3	EME2	Pure Bitumen	350	0.02	18.7	1	1.47	0.30	27
REFC-3	BBSG3	EME2	Pure Bitumen	350	0.02	18.5	0.25	1.05	0.23	41
C/D-1	BBSG3	GB5	Pure Bitumen	350	0.02	18.6	0	1.25	0.11	24
C/D-2	BBSG3	GB5	Pure Bitumen	350	0.02	18.8	0	1.15	0.15	33
C/D-3	BBSG3	GB5	Pure Bitumen	350	0.02	18.8	1	1.56	0.18	25
D/D-1	BB5	GB5	Pure Bitumen	350	0.02	18.4	0	1.00	0.19	41
D/D-2	BB5	GB5	Pure Bitumen	350	0.02	18.5	0	0.97	0.27	75
D/D-3	BB5	GB5	Pure Bitumen	350	0.02	23.9	0	1.28	0.23	42
D/C-1	BB5	EME2	Pure Bitumen	350	0.02	18.9	0	1.05	0.18	37
D/C-2	BB5	EME2	Pure Bitumen	350	0.02	19	0.25	1.16	0.35	35
D/C-3	BB5	EME2	Pure Bitumen	350	0.02	18.7	1	1.43	0.99	55
LDO-1	BBSG3	EME2	Pure Bitumen	250	0.02	18.7	0	0.85	0.26	38
LDO-2	BBSG3	EME2	Pure Bitumen	250	0.02	18.8	0.25	0.82	0.35	35
LDO-3	BBSG3	EME2	Pure Bitumen	250	0.02	18.8	1	1.05	0.76	31
HDO-1	BBSG3	EME2	Pure Bitumen	450	0.02	18.5	0	1.04	0.18	42
HDO-2	BBSG3	EME2	Pure Bitumen	450	0.02	18.7	0	1.04	0.18	44
HDO-3	BBSG3	EME2	Pure Bitumen	450	0.02	18.6	1	X*	X*	X*
SBS-1	BBSG3	EME2	Bitumen modified with SBS	350	0.02	18.5	0	0.92	0.19	41
SBS-2	BBSG3	EME2	Bitumen modified with SBS	350	0.02	18.5	0	0.97	0.26	58
SBS-3	BBSG3	EME2	Bitumen modified with SBS	350	0.02	18.5	1	1.31	0.63	89
LAT-1	BBSG3	EME2	Bitumen modified with latex	350	0.02	18.5	0	1.12	0.17	94
LAT-2	BBSG3	EME2	Bitumen modified with latex	350	0.02	18.5	0	1.06	0.32	101

CONCLUSIONS AND PERSPECTIVES

The purpose of this thesis was the study of interfaces between pavement layers in bituminous mixtures. An innovative experimental device, the 2T3C Hollow Cylinder Apparatus (2T3C HCA), was designed, implemented in the University of Lyon/ENTPE and used to test samples made in laboratory. The thermomechanical behaviour of bituminous mixtures and interfaces could be observed and modelled in the small strain domain. The shear strength of different interface configurations was evaluated from monotonic shear failure tests.

The 2T3C HCA applies torsion and tension-compression, independently or simultaneously, to hollow cylinder samples with two layers and an interface at a controlled temperature. A large variety of stress paths can be tested. The sample dimensions were chosen so that the state of stress is homogeneous in it. The major novelty of the device is the use of an optical measurement technique, the 3D Digital Image Correlation (3D DIC), to obtain the interface mechanical properties. A specific analysis method is introduced in this thesis to obtain the relative displacements between the layers at the interface in the tension-compression mode and in the shear mode. The strain in the bituminous mixtures is also obtained with this method.

An important experimental campaign was conducted using the 2T3C HCA. The main objectives of this campaign were the study of the interfaces behaviour in the small strain domain and the study of the failure of interfaces. Eight different interface configurations were considered with four different bituminous mixtures and three types of tack coat applied at different dosages. A total of 27 samples were tested.

Advanced complex modulus tests were performed on the bi-layered samples. Sinusoidal loadings were applied at four different frequencies (from 0.01 Hz to 0.3 Hz) and at four different temperatures (from 10 °C to 40 °C) both in shear mode (without axial stress) and in tension-compression mode (without shear stress). The cycles were performed in the small strain domain with a global strain amplitude of 200 µm/m (calculated as if the sample was homogeneous). The following conclusions could be drawn from these tests:

- The axial and shear complex moduli of the bituminous mixtures in the small strain domain were obtained with 3D DIC. The four tested mixtures respected the Time-Temperature Superposition Principle (TTSP) both in tension-compression mode and in shear mode. They were modelled using the linear viscoelastic model 2S2P1D. The 2S2P1D model described well the behaviour of the mixtures in tension-compression mode and in shear mode. The absence of experimental values for high frequencies and low temperatures induced difficulties to calibrate accurately the models in this area.
- The axial complex modulus of two of the mixtures obtained with the 2T3C HCA were compared with the results from a tension-compression modulus test on cylindrical samples on these mixtures. Significant differences were observed. They might be explained by the anisotropic behaviour of bituminous mixtures compacted in laboratory or by the difference in air void content.
- Displacement gaps, defined as the relative displacement between the bottom of the upper layer and the top of the lower layer, were found at the level of the interface from the analysis

method of 3D DIC results introduced in this thesis. When sinusoidal loadings were applied, the displacement gaps were also sinusoidal. The observed amplitudes of the vertical displacement gaps were between 0.5 and 4 µm. The observed amplitudes of the horizontal displacement gaps were between 2 and 10 µm.

- The complex interface stiffnesses in the tension-compression mode and in the shear mode were defined and calculated from the advanced complex modulus test results. The eight interface configurations respected the TTSP both in tension-compression mode and in shear mode.
- The behaviour of the interfaces at the tested amplitude was not linear viscoelastic, neither in tension-compression mode nor in shear mode.
- A new model, the DBN_{PDSC} (DBN model with Plastic Dissipation for Small Cycles) model was introduced to describe the interfaces. It is based on the DBN model with the addition of plastic energy dissipation in the elastoplastic elements. This model fitted the interface behaviour both in tension-compression mode and in shear mode. No clear influence of the type of bituminous mixtures in the layers, of the type or of the dosage of tack coat on the interface behaviour in the small strain domain could be identified.
- The behaviour of the interfaces with a tack coat in pure bitumen emulsion could be modelled by the DBN_{PDSC} model using the results of a shear complex modulus test performed on the bitumen of the emulsion with a Dynamic Shear Rheometer.

Still in the small strain domain, a nonlinearity test was conducted on one sample with an interface by applying sinusoidal rotation cycles (0.1 Hz at 20 °C) at different amplitudes. It was observed that:

- For displacement gap amplitudes between 3 and 10 µm, the norm of the shear complex interface stiffness decreased when the amplitude of the cycles increased. The phase angle did not vary significantly.
- The interface got damaged during the nonlinearity test making it impossible to isolate the effect of the value of the displacement gap amplitude on the shear complex interface stiffness.

In addition, an oligocyclic test was performed on the same sample to monitor the evolution of the shear complex interface stiffness subjected to a continuous cyclic loading (0.1 Hz at 20 °C). The amplitude of the cycles was the same than in the advanced complex modulus test. It was found that:

- The norm of the shear complex interface stiffness decreased rapidly at the tested amplitude. The phase angle increased during the test. The norm lost almost 50 % of its value after 50 cycles. This result confirms that the interface behaviour is not linear viscoelastic at this amplitude, and neither was it in the advanced complex modulus test.
- The norm of the shear complex modulus recovered rapidly after the end of the cycles, regaining 90 % of its initial value after only 1 h, and 98 % after 24 h. This proves that reversible phenomena are partially responsible for the loss of norm of shear complex interface stiffness and that they should be taken into account in cyclic testing on interfaces.

After the interfaces were tested in the small strain domain, monotonic shear failure tests were performed to evaluate the interface shear strength of the different configurations. The tests were performed at a constant rotation speed (0.02 %/s, 0.067 %/s or 0.2 %/s in global shear strain rate) with a constant vertical stress (compressive values of 0, 0.25 or 1 MPa). The temperature of the test was the same for all the samples, close to 20 °C. From these tests, it was found that:

- Out of 27 samples, 26 broke at the interface. The shear stress during all the tests reached a maximum value before decreasing, this value defines the interface shear strength.
- For the three different rotation speeds tested on the same interface configuration, the interface shear strength increased with the rotation speed following a power law confirming results from the literature.

- The addition of compressive normal stress during the tests induced an increase of the interface shear strength and of the horizontal displacement gap for which the maximum stress is reached. The Mohr-Coulomb failure criterion was used to model the interface failure behaviour.
- The aggregate interlocking had an effect on the interface failure. The optimal configuration of bituminous mixtures was obtained with a mixture having a continuous aggregate size distribution curve compacted on a mixture with a discontinuous aggregate size distribution curve. This finding concurs with a simple reasoning found in the literature on aggregate interlocking. The other configurations of mixtures showed weaker bond strengths.
- An insufficient dosage of tack coat led to a reduced interface shear strength. The tested dosage of 250 g/m^2 showed worst results than the dosages of 350 g/m^2 and 450 g/m^2, when it is actually the minimum dosage for the tested configuration of mixtures in the French standard.
- The modification of the bitumen used in the emulsion with SBS or with latex did not improve significantly the interface shear strength. It seemed to decrease it for SBS modified emulsion.

Following these conclusions, perspectives for future research are presented hereafter.

- From a slab made in laboratory, only three sample of the 2T3C HCA can be cored. The results obtained in this thesis were obtained with a few number of repetitions and need to be supported by more tests. Coring samples *in situ* (in actual pavements) could be an interesting way of obtaining more samples for the same interface configuration. It would also make it possible to compare the behaviour of damaged interfaces with the ones obtained in laboratory.
- The comparison between 2T3C HCA results for bituminous mixtures and the tension-compression modulus test on cylindrical samples should be performed again on more samples and different mixtures to try and eliminate the anisotropy factor. The tests should also be performed at the same strain amplitude.
- The DBN_{PDSC} model should be able to model the behaviour of bituminous mixtures subjected to medium or high strain amplitude but it has to be verified on existing data or with new tests. The model can be improved to take into account the dependency of the norm of the complex modulus (or complex interface stiffness) with the strain (or displacement gap) amplitude.
- Using the results of the advanced complex modulus test and the modelling of interfaces with the DBN_{PDSC} model, it should be possible to implement a viscoelastic behaviour for interfaces in a finite element model of a pavement. This realistic approach could highlight a possible influence of the interface behaviour on the strain in the layers and thus on the predicted pavement lifetime.
- The 2T3C HCA can be used to perform fatigue tests on the interfaces, which is of uttermost importance in the pavement design. As it is not possible to control the displacement gap amplitude at the interface, tests should be performed at constant stress amplitude. A specific procedure still needs to be designed concerning the acquisition of pictures during the test to limit the amount of data to be treated. A special attention should be paid to the study of reversible phenomena occurring during continuous cyclic loadings to evaluate the interface damage adequately. Thermocouples could be added in the interface to monitor self-heating for instance.
- Only very simple stress paths were studied in this thesis compared to the possibilities of the 2T3C HCA. Many test protocols are worth considering. For instance, it would be interesting to observe the interface under a realistic loading representing a moving vehicle.

REFERENCES

Adam, J.-P. (1989). *La construction romaine: matériaux et techniques*. Paris: Grands Manuels Picard. [in French]

Airey, G. D., Rahimzadeh, B., and Collop, A.C. (2003). "Viscoelastic Linearity Limits for Bituminous Materials." *Materials and Structures*, 36, 643–647. DOI: 10.1007/BF02479495

Allix, O., Ladevéze, P., and Corigliano, A. (1995). "Damage Analysis of Interlaminar Fracture Specimens." *Composite Structures*, 31, 61–74. DOI: 10.1016/0263-8223(95)00002-X.

Al-Qadi, I. L., Loulizi, A., Elseifi, M. and Lahouar. M. (2004). "The Virginia Smart Road: The Impact of Pavement Instrumentation on Understanding Pavement Performance." *Asphalt Paving Technology*, 39.

Alsing, C. (1868). *Improved Asphalt Pavement*. U.S. Patent 77,565 issued 1868.

Arbellot, G. (1973). "La Grande Mutation Des Routes de France Au XVIIIe Siècle." *Annales. Histoire, Sciences Sociales*, 28, 765–791. DOI: 10.3406/ahess.1973.293381. [in French]

Attia, T. (2015). *Comportement Des Matériaux Bitumineux : Essais En Laboratoire En Petites et Grandes Déformations et Modélisation Du Comportement Thermo-Visqueux*. (Unpublished master's dissertation). Ecole Nationale des Travaux Publics de l'Etat. [in French]

Babadopulos, L. F. A. L. (2017). *Phenomena Occurring during Cyclic Loading and Fatigue Tests on Bituminous Materials: Identification and Quantification*. (Unpublished doctoral dissertation). University of Lyon/Ecole Nationale des Travaux Publics de l'Etat.

Babadopulos, L. F. A. L., Orozco G., Sauzéat C., and Di Benedetto, H. (2019). "Reversible Phenomena and Fatigue Damage during Cyclic Loading and Rest Periods on Bitumen." *International Journal of Fatigue*, 124, 303–314. DOI: 10.1016/j.ijfatigue.2019.03.008.

Bae, A., Elseifi, M. A., Button, J., and Patel, N. (2010). "Effects of Temperature on Interface Shear Strength of Emulsified Tack Coats and Its Relationship to Rheological Properties." *Transportation Research Record: Journal of the Transportation Research Board*, 2180, 102–109. DOI: 10.3141/2180-12.

Bailey, D. 1869. *Improved concrete pavement*. U.S. Patent 97,149 issued 1869.

Bazant, Z. (1989). "Measurement of Characteristic Length of Nonlocal Continuum." *Journal of Engineering Mechanics*, 115.

Berthelot, M. (1885). "Route." In *La Grande Encyclopédie: Inventaire Raisonné Des Sciences, Des Lettres et Des Arts*, Paris: Société anonyme de "La Grande encyclopédie." [in French]

Birgisson, B., Montepara, A., Romeo, E., Roncella, R., Roque, R., and Tebaldi, G. (2009). "An Optical Strain Measurement System for Asphalt Mixtures." *Materials and Structures*, 42, 427–441. DOI: 10.1617/s11527-008-9392-8.

Blomberg, J. (2014). "Tack Coat Specifications and Testing." presented at the North Central Asphalt User Producer Group Technical Conference Program, Kansas City, MO.

Boltzmann, L. (1874). “Zur Theorie Der Elastischen Nachwirkung.” *Sitzungsberichte der Mathematisch-Naturwissenschaftlichen Klasse der Kaiserlichen Akademie der Wissenschaften*, 70, 275–306. [in German]

Booij, H. C., and Thoone, G.P.J.M. (1982). “Generalization of Kramers-Kronig Transforms and Some Approximations of Relations between Viscoelastic Quantities.” *Rheologica Acta*, 21, 15–24.

Brown, S. F., Brodrick, B.V., Tekieli, K., and Collop, A.C. (2013). “A Torsional Hollow Cylinder Research Apparatus for Studying the Permanent Deformation Characteristics of Asphalt.” *Road Materials and Pavement Design*, 14, 65–85. DOI: 10.1080/14680629.2013.774747.

Brühwiler, E., and Wittmann, F. H. (1990). “The Wedge Splitting Test, a New Method of Performing Stable Fracture Mechanics Tests.” *Engineering Fracture Mechanics*, 35, 117–25. DOI: 10.1016/0013-7944(90)90189-N.

Burmister, D. M. (1945). “The General Theory of Stresses and Displacements in Layered Soil Systems. II.” *Journal of Applied Physics*, 16, 126–127. DOI: 10.1063/1.1707562.

Buttlar, W. G., Al-Khateeb, G. G., and Bozkurt, D. (1999). “Development of a hollow cylinder tensile tester to obtain mechanical properties of bituminous paving mixtures” *Association of Asphalt Paving Technologists Proceedings*, 68, 369–403.

Canestrari, F., and Santagata, E. (2005). “Temperature Effects on the Shear Behaviour of Tack Coat Emulsions Used in Flexible Pavements.” *International Journal of Pavement Engineering*, 6, 39–46. DOI: 10.1080/10298430500068720.

Canestrari, F., Belogi, L., Ferrotti, G., and Graziani, A. (2015). “Shear and Flexural Characterization of Grid-Reinforced Asphalt Pavements and Relation with Field Distress Evolution.” *Materials and Structures*, 48, 959–975. DOI: 10.1617/s11527-013-0207-1.

Canestrari, F., Ferrotti, G. and Graziani, A. (2016). “Shear Failure Characterization of Time–Temperature Sensitive Interfaces.” *Mechanics of Time-Dependent Materials*, 20, 405–419. DOI: 10.1007/s11043-016-9299-7.

Canestrari, F., Ferrotti, G., Lu, X., Millien, A., Partl, M.N., Petit, C., Phelipot-Mardelé, A., Piber, H., and Raab, C. (2013). “Mechanical Testing of Interlayer Bonding in Asphalt Pavements.” In *Advances in Interlaboratory Testing and Evaluation of Bituminous Materials*, 303–360. Dordrecht: Springer Netherlands. DOI: 10.1007/978-94-007-5104-0_6.

Canestrari, F., Ferrotti, G., Partl, M.N. and Santagata, E. (2005). “Advanced Testing and Characterization of Interlayer Shear Resistance.” *Transportation Research Record: Journal of the Transportation Research Board*, 1929, 69–78. DOI: 10.3141/1929-09.

Cazacliu, B. (1996). *Comportement Des Sables En Petites et Moyennes Déformations - Prototype d’essai de Torsion, Compression, Confinement Sur Cylindre Creux*. (Unpublished doctoral dissertation) Ecole Centrale de Paris. [in French]

Cho, S.-H., Safavizadeh, S.A., and Kim, R. Y. (2017). “Verification of the Applicability of the Time–Temperature Superposition Principle to Interface Shear Stiffness and Strength of GlasGrid-Reinforced Asphalt Mixtures.” *Road Materials and Pavement Design*, 18, 766–784. DOI: 10.1080/14680629.2016.1189350.

Cho, S.-H., and Kim, R., Y. (2016). “Verification of Time–Temperature Superposition Principle for Shear Bond Failure of Interlayers in Asphalt Pavements.” *Transportation Research Record: Journal of the Transportation Research Board*, 2590, 18–27. DOI: 10.3141/2590-03.

Clec'h, P. (2010). *Comportement Des Enrobés Bitumineux Sous Sollicitation Multidirectionnelle*. (Unpublished doctoral dissertation). INSA Lyon. [in French]

Collop, A.C., Sutanto, M.H., Airey, G.D. and Elliott, R.C. (2009). "Shear Bond Strength between Asphalt Layers for Laboratory Prepared Samples and Field Cores." *Construction and Building Materials*, 23, 2251–2258. DOI: 10.1016/j.conbuildmat.2008.11.017.

Collop, A.C., Sutanto, M.H., and Elliott, R.C. (2011). "Development of an Automatic Torque Test to Measure the Shear Bond Strength between Asphalt." *Construction and Building Materials*, 25, 623–629. DOI: 10.1016/j.conbuildmat.2010.07.030.

Corté, J.-F., and Di Benedetto, H. (2004). *Matériaux routiers bitumeux 1: description et propriétés des constituants*. Paris: Hermès Science Publications. [in French]

D'Andrea, A., Russo, S., and Tozzo, C. (2013). "Interlayer Shear Testing under Combined State of Stress." *Advanced Materials Research*, 723, 381–388. DOI: 10.4028/www.scientific.net/AMR.723.381.

D'Andrea, A., and Tozzo, C. (2016a). "Dynamic Tests on Bituminous Layers Interface." *Materials and Structures*, 49, 917–928. DOI: 10.1617/s11527-015-0548-z.

D'Andrea, A., and Tozzo, C. (2016b). "Interface Stress State in the Most Common Shear Tests." *Construction and Building Materials*, 107, 341–355. DOI: 10.1016/j.conbuildmat.2016.01.016.

D'Andrea, A., Tozzo, C., Boschetto, A., and Bottini, L. (2013). "Interface Roughness Parameters and Shear Strength." *Modern Applied Science*, 7, DOI: 10.5539/mas.v7n10p1.

De Smedt, J. (1870). *Improvement in laying asphalt or concrete pavement or roads*. U.S. Patent 103,581 issued 1870.

Destrée, A., De Visscher, J. and Vanelstraete, A. (2012). "Evaluation of Tack Coat Performance for Thin and Ultra-Thin Asphalt Pavements." presented at the 5th Eurasphalt & Eurobitume Congress, Istanbul.

Di Benedetto, H., and Corté J.-F. (2005). *Matériaux routiers bitumeux 2: constitution et propriétés thermomécaniques des mélanges*. Paris: Hermès Science Publications. [in French]

Di Benedetto, H., Gabet, T., Grenfell, J., Perraton, D., Sauzéat, C. and Bodin, D. (2013). "Mechanical Testing of Bituminous Mixtures." In *Advances in Interlaboratory Testing and Evaluation of Bituminous Materials: State-of-the-Art Report of the RILEM Technical Committee 206-ATB*, 143–256. Dordrecht: Springer Netherlands. DOI: 10.1007/978-94-007-5104-0_4.

Di Benedetto, H., Neifar M., Sauzéat, C., and Olard, F. (2007). "Three-Dimensional Thermo-Viscoplastic Behaviour of Bituminous Materials: The DBN Model." *Road Materials and Pavement Design*, 8, 285–315. DOI: 10.1080/14680629.2007.9690076.

Di Benedetto, H., Olard, F., Sauzéat, C., and Delaporte, B. (2004). "Linear Viscoelastic Behaviour of Bituminous Materials: From Binders to Mixes." *Road Materials and Pavement Design*, 5, 163–202. DOI: 10.1080/14680629.2004.9689992.

Di Benedetto, H., Sauzéat, C. and Clec'h, P. (2016). "Anisotropy of Bituminous Mixtures in the Linear Viscoelastic Domain." *Mechanics of Time-Dependent Materials*, 20, 281–297.

Diakhaté, M., Millien, A., Petit, C., Phelipot-Mardelé, A., and Pouteau, B. (2011). "Experimental Investigation of Tack Coat Fatigue Performance: Towards an Improved Lifetime Assessment of

Pavement Structure Interfaces." *Construction and Building Materials*, 25, 1123–1133. DOI: 10.1016/j.conbuildmat.2010.06.064.

Diakhaté, M. (2007). *Fatigue et Comportement Des Couches d'accrochage Dans Les Structures de Chaussée*. (Unpublished doctoral dissertation). Université de Limoges. [in French]

Diakhate, M., Phelipot, A., Millien, A. and Petit, C. (2006). "Shear Fatigue Behaviour of Tack Coats in Pavements." *Road Materials and Pavement Design*, 7, 201–222. DOI: 10.1080/14680629.2006.9690033.

Duttine, A., Di Benedetto, H., Bang, D.P.V., and Ezaoui, A. (2007). "Anisotropic Small Strain Elastic Properties of Sands and Mixture of Sand-Clay Measured by Dynamic and Static Methods." *Soils and Foundations*, 47, 457–472.

Ech, M., Yotte, S., Morel, S., Breysse, D., and Pourteau, B. (2007). "Laboratory Evaluation of Pavement Macrotexture Durability." *Revue Européenne de Génie Civil*, 11, 643–662. DOI: 10.3166/regc.11.643-662.

Eitner, U., Köntges, M., and Brendel, R. (2010). "Use of Digital Image Correlation Technique to Determine Thermomechanical Deformations in Photovoltaic Laminates: Measurements and Accuracy." *Solar Energy Materials and Solar Cells*, 94, 1346–1351. DOI: 10.1016/j.solmat.2010.03.028.

Ferrotti, G., Canestrari, F., Pasquini, E. and Virgili, A. (2012). "Experimental Evaluation of the Influence of Surface Coating on Fiberglass Geogrid Performance in Asphalt Pavements." *Geotextiles and Geomembranes*, 34, 11–18. DOI: 10.1016/j.geotexmem.2012.02.011.

Ferrotti, G., D'Andrea, A., Maliszewski, M., Partl, M.N., Raab, C., Sangiorgi, C., and Canestrari, F. (2016). "Inter-Laboratory Shear Evaluation of Reinforced Bituminous Interfaces." In *8th RILEM International Symposium on Testing and Characterization of Sustainable and Innovative Bituminous Materials*, 309–21. Dordrecht: Springer Netherlands. DOI: 10.1007/978-94-017-7342-3_25.

Freire, R.A., Di Benedetto, H., Sauzéat, C., Pouget, S., and Lesueur, D. (2018). "Linear Viscoelastic Behaviour of Geogrids Interface within Bituminous Mixtures." *KSCE Journal of Civil Engineering*, 22, 2082–2088. DOI: 10.1007/s12205-018-1696-9.

Gaborit, P., Sauzéat, C., Di Benedetto, H., Pouget, S., Olard, F., and Claude, A. (2014). "Investigation of Highway Pavements Using In-Situ Strain Sensors." In *Sustainability, Eco-Efficiency, and Conservation in Transportation Infrastructure Asset Management*, 331–337. CRC Press. DOI: 10.1201/b16730-49.

Gayte, P. (2016). *Modélisation Du Comportement Thermo-Viscoplastique Des Enrobés Bitumineux*. (Unpublished doctoral dissertation). Ecole Nationale des Travaux Publics de l'Etat. [in French]

Gayte, P., Di Benedetto, H., Sauzéat, C., and Nguyen, Q.T. (2016). "Influence of Transient Effects for Analysis of Complex Modulus Tests on Bituminous Mixtures." *Road Materials and Pavement Design*, 17, 271–289. DOI:10.1080/14680629.2015.1067246.

Gitman, I.M., Askes, H., and Sluys, L.J. (2007). "Representative Volume: Existence and Size Determination." *Engineering Fracture Mechanics*, 74, 2518–2534. DOI: 10.1016/j.engfracmech.2006.12.021.

Godard, E., Yvinec, B., Dony, A., and Koutiri, I. (2015). "Collage Des Couches d'Enrobés Bitumineux." *Revue Générale Des Routes et de l'aménagement*, 4141, 60–69. [in French]

Graziani, A., Canestrari, F., Cardone, F., and Ferrotti, G. (2017). "Time–Temperature Superposition Principle for Interlayer Shear Strength of Bituminous Pavements." *Road Materials and Pavement Design,* 18, 12–25. DOI: 10.1080/14680629.2017.1304247.

Grellet, D., Doré, G., Chupin, O., and Piau, J.-M. (2018). "Highlighting of the Viscoelastic Behaviour of Interfaces in Asphalt Pavements – a Possible Origin to Top-down Cracking." *Road Materials and Pavement Design,* 19, 581–590. DOI: 10.1080/14680629.2018.1418721.

Highways England. (2019). *Manual of Contract Documents of Highways Works Volume 1: Specification for Highway Works Series 900: Bituminous Bound Materials*.

Hight, D. W., Gens, A., and Symes, M.J. (1983). "The Development of a New Hollow Cylinder Apparatus for Investigating the Effects of Principal Stress Rotation in Soils." *Géotechnique*, 33, 355-383. DOI: 10.1680/geot.1983.33.4.355.

Hooley, E. P. (1903). *Improvements in the Means for and the Method of "Tarring" Broken Slag, Macadam, and similar Materials.* GB190207796, filed 1902 and issued 1903.

Hristov, B. (2018a). "Master Function for Analytical Determination of the Interlayer Bond Shear Stiffness and Fatigue Functions for Asphalt Pavements." *MATEC Web of Conferences,* 251. DOI: 10.1051/matecconf/201825101001.

Hristov, B. (2018b). "Influence of Different Interface Properties on the Interlayer Bond Shear Stiffness." *IOP Conference Series: Materials Science and Engineering*, 365. DOI: 10.1088/1757-899X/365/3/032056.

Hughes, D. A. B. (1986). *Polymer Grid Reinforcement of Asphalt Pavements*. (Unpublished doctoral dissertation). University of Nottingham.

Hun, M. (2012). *Influence de l'eau Sur Le Décollement d'une Interface Par Flexion d'un Bicouche de Chaussée Urbaine*. (Unpublished doctoral dissertation). Ecole Centrale de Nantes. [in French]

Isailović, I., Falchetto, A.C. and Wistuba, M. (2017). "Fatigue Investigation on Asphalt Mixture Layers' Interface." *Road Materials and Pavement Design*, 18, 514–534. DOI: 10.1080/14680629.2017.1389087.

Ktari, R. (2016). "Mécanismes et Modélisations Des Dégradations Des Interfaces Entre Couches de Chaussées." (Unpublished doctoral dissertation). Université de Limoges. [in French]

Ktari, R., Fouchal, F., Millien, A. and Petit, C. (2017). "Surface Roughness: A Key Parameter in Pavement Interface Design." *European Journal of Environmental and Civil Engineering*, 21, 27–42. DOI: 10.1080/19648189.2017.1304284.

Ktari, R., Millien, A., Fouchal, F., Pop, I.-O., and Petit, C. (2016). "Pavement Interface Damage Behavior in Tension Monotonic Loading." *Construction and Building Materials,* 106, 430–442. DOI: 10.1016/j.conbuildmat.2015.12.020.

LCPC. (1995). "Méthode d'essai LPC N°41 : Ovalisation Exécution et Exploitation Des Mesures". Ministère de l'Equipement, des Transports et du Tourisme. [in French]

LCPC. (1996a). "Méthode d'essai LPC N°42 : Application d'un Radar Pulsé Monostatique à l'auscultation Des Chaussées". Ministère de l'Equipement, des Transports et du Tourisme. [in French]

LCPC. (1996b). "Méthode d'essai LPC N°43 : Exécution et Exploitation Des Carottages de Chaussées". Ministère de l'Equipement, des Transports et du Tourisme. [in French]

LCPC. (1998). *Catalogue Des Dégradations de Surface Des Chaussées*. Ministère de l'Equipement, des Transports et du Logement. [in French]

LCPC and SETRA. (1994). *Conception et Dimensionnement Des Structures de Chaussée*. Ministère de l'Equipement, des Transports et du Tourisme. [in French]

Léandry, I., Brèque, C., and Valle, V. (2012). "Calibration of a Structured-Light Projection System: Development to Large Dimension Objects." *Optics and Lasers in Engineering*, 50, 373–379. DOI: 10.1016/j.optlaseng.2011.10.020.

Lee, S. J. (2008). "Mechanical Performance and Crack Retardation Study of a Fiberglass-Grid-Reinforced Asphalt Concrete System." *Canadian Journal of Civil Engineering*, 35, 1042–1049. DOI: 10.1139/L08-049.

Lesueur, D. (2002). "La Rhéologie Des Bitumes: Principes et Modification." *Rhéologie*,1–30. [in French]

Leutner, R. (1979). "Untersuchung Des Schichtenverbundes Beim Bituminosen Oberbau." *Bitumen*, 41, 84–91. [in German]

Linsbauer, H.N., and Tschegg, E.K. (1986). "Fracture Energy Determination of Concrete with Cube-Shaped Specimens." *Zement Und Beton*, 31, 38–40.

Lyons, J. S., Liu, J., and Sutton, M.A. (1996). "High-Temperature Deformation Measurements Using Digital-Image Correlation." *Experimental Mechanics*, 36, 64–70. DOI: 10.1007/BF02328699.

Mangiafico, S. (2014). *Linear Viscoelastic Properties and Fatigue of Bituminous Mixtures Produced with Reclaimed Asphalt Pavement and Corresponding Binder Blends*. (Unpublished doctoral dissertation) Ecole Nationale des Travaux Publics de l'Etat.

Mangiafico, S., Babadopulos, L. F. A. L., Sauzéat, C. and Di Benedetto, H. (2017). "Nonlinearity of Bituminous Mixtures." *Mechanics of Time-Dependent Materials*, 29-49. DOI: 10.1007/s11043-017-9350-3.

McAdam, J. L. (1819). *A Practical Essay on the Scientific Repair and Preservation of Public Roads*. Quebec: John Neilson.

McAdam, J.L. (1821). *Remarks on the Present System of Road Making with Observations, Deduced from Practice and Experience, with a View to a Revision of the Existing Laws, and the Introduction of Improvement in the Method of Making, Repairing, and Preserving Roads, and Defending the Road Funds from Misapplication*. London: Longman, Hurst, Rees, Orme and Brown.

Meunier, Y. (1986). *Le Décollement Des Couches de Revêtement de Chaussées*. SETRA.

Mohammad, L. N., Elseifi, M.A., Bae, A., Nachiketa, P., Button, J. and Scherocman, J.A. (2012). *Optimization of Tack Coat for HMA Placement*. Washington, D.C.: Transportation Research Board.

Mohammad, L.N., Raqib, M., and Huang, B. (2002). "Influence of Asphalt Tack Coat Materials on Interface Shear Strength." *Transportation Research Record: Journal of the Transportation Research Board*, 1789, 56–65. DOI: 10.3141/1789-06.

Molenaar, A.A.A., Heerkens, J.C.P. and Verhoeven J.H.M. (1986). "Effects of Stress Absorbing Membrane Interlayers." presented to the 1986 Annual Meeting of the Association of Asphalt Paving Technologists.

NCHRP. (2004). *Design guide, mechanistic empirical design of new and rehabilitated pavement.*

Neifar, M., and Di Benedetto, H. (2001). “Thermo-Viscoplastic Law for Bituminous Mixes.” *Road Materials and Pavement Design*, 2, 71–95. DOI: 10.1080/14680629.2001.9689894.

NF EN 12697-33+A1:2007 “Mélange Bitumineux - Méthodes d’essai Pour Mélange Hydrocarboné à Chaud - Partie 33 : Confection d’éprouvettes Au Compacteur de Plaque.” [in French]

NF EN 13036-1 - “Caractéristiques de Surface Des Routes et Aérodromes — Méthodes d’essai — Partie 1 : Mesurage de La Profondeur de Macrotexture de La Surface d’un Revêtement à l’aide d’une Technique Volumétrique à La Tâche”. [in French]

NF P 98-150-1 - “Exécution Des Assises de Chaussées, Couches de Liaison et Couches de Roulement. Partie 1 : Mélanges Bitumineux - Constituants, Formulation, Fabrication, Transport, Mise En Oeuvre et Contrôle Sur Chantier.” [in French]

NF P-98-203-1 Décembre 1997 “Essais Relatifs Aux Chaussées - Déformations Dans Les Couches de Chaussées - Partie 1 : Essai d’ovalisation.” [in French]

Olard, F., and Di Benedetto, H. (2003). “General ‘2S2P1D’ Model and Relation Between the Linear Viscoelastic Behaviours of Bituminous Binders and Mixes.” *Road Materials and Pavement Design*, 4, 185–224. DOI: 10.1080/14680629.2003.9689946.

Pasquini, E., Bocci, M., Ferrotti, G., and Canestrari, F. (2013). “Laboratory Characterisation and Field Validation of Geogrid-Reinforced Asphalt Pavements.” *Road Materials and Pavement Design*, 14, 17–35. DOI: 10.1080/14680629.2012.735797.

Miró Recasens, R., Martínez, A., Pérez Jiménez, F. (2005). “Assessing Heat-Adhesive Emulsions for Tack Coats.” *Proceedings of the ICE - Transport*, 158, 45–51. DOI: 10.1680/tran.2005.158.1.45.

Petit, C., Chabot, A., Destrée, A., and Raab, C. (2018). “Recommendation of RILEM TC 241-MCD on Interface Debonding Testing in Pavements.” *Materials and Structures*, 51. DOI: 10.1617/s11527-018-1223-y.

Petit, C., Diakhaté, M., Millien, A., Phelipot-Mardelé, A., and Pouteau, B. (2009). “Pavement Design for Curved Road Sections: Fatigue Performance of Interfaces and Longitudinal Top-down Cracking in Multilayered Pavements.” *Road Materials and Pavement Design*, 10, 609–624.

Pinto, M., Gupta, S., and Shukla, A. (2015). “Study of Implosion of Carbon/Epoxy Composite Hollow Cylinders Using 3-D Digital Image Correlation.” *Composite Structures*, 119, 272–286. DOI: 10.1016/j.compstruct.2014.08.040.

Pouget, S. (2011). “Influence Des Propriétés Élastiques Ou Viscoélastiques Des Revêtements Sur Le Comportement Des Ponts à Dalle Orthotrope.” (Unpublished doctoral dissertation). Ecole Nationale des Travaux Publics de l’Etat. [in French]

Pouget, S., Sauzéat, C., Di Benedetto, H., and Olard, F. (2012). “Viscous Energy Dissipation in Asphalt Pavement Structures and Implication for Vehicle Fuel Consumption.” *Journal of Materials in Civil Engineering*, 24, 568–576. DOI: 10.1061/(ASCE)MT.1943-5533.0000414.

Raab, C., Partl, M.N., Fourquet, E., and Abd El Halim, A.O. (2017). “Static and Cyclic Evaluation of Interlayer Bonding.” In *Bearing Capacity of Roads, Railways and Airfields*, 1511–1516. CRC Press. DOI: 10.1201/9781315100333-216.

Raab, C., Partl, M.N., and Abd El Halim, A.O. (2009). “Evaluation of Interlayer Shear Bond Devices for Asphalt Pavements.” *The Baltic Journal of Road and Bridge Engineering*, 4, 186–195. DOI: 10.3846/1822-427X.2009.4.186-195.

Raab, C., Abd El Halim, A.O., and Partl, M.N. (2012). "Interlayer Bond Testing Using a Model Material." *Construction and Building Materials*, 26, 190–199. DOI: 10.1016/j.conbuildmat.2011.06.009.

Raab, C., and Partl., M.N. (2004). "Effect of Tack Coats on Interlayer Shear Bond of Pavements." In *Proceedings of the 8th Conference on Asphalt Pavements for Southern Africa* (CAPSA'04).

Raposeiras, A. C., Vega-Zamanillo, A., Calzada-Pérez, M.A., and Castro-Fresno, D. (2012). "Influence of Surface Macro-Texture and Binder Dosage on the Adhesion between Bituminous Pavement Layers." *Construction and Building Materials*, 28, 187–192. DOI: 10.1016/j.conbuildmat.2011.08.029.

Romanoschi, S.A. (1999). *Characterization of Pavement Layer Interfaces*. (Unpublished doctoral dissertation). Baton Rouge: Louisiana State University.

Romanoschi, S. A., and Metcalf, J.B. (2001). "Characterization of Asphalt Concrete Layer Interfaces." *Transportation Research Record: Journal of the Transportation Research Board*, 1778, 132–139. DOI: 10.3141/1778-16.

Romeo, E. (2013). "Two-Dimensional Digital Image Correlation for Asphalt Mixture Characterisation: Interest and Limitations." *Road Materials and Pavement Design*, 14, 747–763. DOI: 10.1080/14680629.2013.815128.

Romero, P., and Masad, E. (2001). "Relationship between the Representative Volume Element and Mechanical Properties of Asphalt Concrete." *Journal of Materials in Civil Engineering*, 13.

Rueda, E. J., Caro, S., Caicedo, B., and Monroy, J. (2017). "A New Approach for the Advanced Mechanical Characterisation of Asphalt Mixtures Using the Hollow Cylinder Methodology." *Measurement*, 103, 333–342. DOI: 10.1016/j.measurement.2017.02.048.

Sadoun, A., Broutin, M., and Simonin, J.-M. (2016). "Assessment of HWD Ability to Detect Debonding of Pavement Layer Interfaces." In *8th RILEM International Conference on Mechanisms of Cracking and Debonding in Pavements*, 763–69. Dordrecht: Springer Netherlands. DOI: 10.1007/978-94-024-0867-6_106.

Safavizadeh, S.A., and Kim, R.Y. (2014). "Mode II Fatigue and Reflective Cracking Performance of GlasGrid-Reinforced Asphalt Concrete under Repeated Loading." In *Asphalt Pavements*, 1893–1902. CRC Press. DOI: 10.1201/b17219-228.

Safavizadeh, S.A. (2015). *Fatigue and Fracture Characterization of GlasGrid Reinforced Asphalt Concrete Pavement.* (Unpublished doctoral dissertation). North Carolina State University.

Salençon, J. (2009). *Viscoélasticité pour le calcul des structures*. Palaiseau: Éd. de l'École polytechnique : Les Presses des Ponts et chaussées. [in French]

Sauzéat, C. (2003). *Comportement Du Sable Dans Le Domaine Des Petites et Moyennes Déformations : Rotations 'd'axes' et Effets Visqueux*. (Unpublished doctoral thesis) Institut National des Sciences Appliquées de Lyon. [in French]

Sayao, A., and Vaid, Y. P. (1991). "A Critical Assessment of Stress Nonuniformities in Hollow Cylinder Test Specimens." *Soils and Foundations*, 31, 60–72. DOI: 10.3208/sandf1972.31.60.

Sayegh, G. (1965). *Contribution à l'étude Des Propriétés Viscoélastiques Des Bitumes Purs et Des Bétons Bitumineux*. (Unpublished doctoral dissertation). Université de Paris. [in French]

Sholar, G. A., Page, G.C., Musselman, J.A., Upshaw, P.B., and Moseley, H.L. (2004). "Preliminary Investigation of a Test Method to Evaluate Bond Strength of Bituminous Tack Coats (with Discussion)." *Journal of the Association of Asphalt Paving Technologists*, 73.

Sousa, J. B. (1986). *Dynamic Properties of Materials for Pavement Design*. (Unpublished doctoral thesis) University of California, Berkeley.

STAC. (2014). *Auscultation Des Chaussées Souples Aéronautiques Au HWD Guide Technique*. Direction Générale de l'Aviation Civile. [in French]

Sutton, M. A., McNeill, S.R., Helm, J.D., and Chao, Y.J. (2000). "Advances in Two-Dimensional and Three-Dimensional Computer Vision." In *Photomechanics*, 323–372. Springer. DOI: 10.1007/3-540-48800-6_10.

The Highways Agency. (2006). "Section 2 Pavement Design and Construction Part 3 Pavement Design." In *Design Manual for Roads and Bridges*. Vol. 7.

The New Encyclopaedia Britannica. (2006). Chicago, IL: Encyclopedia Britannica, Inc.

Tiouajni, S. (2013). *Etude Du Comportement Des Sables Avec Analyse de La Coaxialité : Expérimentation et Modélisation*. (Unpublished doctoral thesis) University of Lyon/ENTPE. [in French]

Tozzo, C., Fiore, N., and D'Andrea, A. (2014). "Dynamic Shear Tests for the Evaluation of the Effect of the Normal Load on the Interface Fatigue Resistance." *Construction and Building Materials*, 61, 200–205. DOI: 10.1016/j.conbuildmat.2014.03.010.

Tozzo, C., Fiore, N., and D'Andrea, A. (2016). "Investigation of Dilatancy Effects on Asphalt Interface Shear Strength." In *8th RILEM International Symposium on Testing and Characterization of Sustainable and Innovative Bituminous Materials*, 335–346. Dordrecht: Springer Netherlands. DOI: 10.1007/978-94-017-7342-3_27.

Tschegg, E.K., Kroyer G., Tan, D.-M., Stanzl-Tschegg, S.E., and Litzka, J. (1995). "Investigation of Bonding between Asphalt Layers on Road Construction." *Journal of Transportation Engineering*, 121, 309–316. DOI: 10.1061/(ASCE)0733-947X(1995)121:4(309).

Uzan, J., Livneh, M., and Eshed, Y. (1978). "Investigation of Adhesion Properties between Asphaltic-Concrete Layers."*Association of Asphalt Paving Technologists Proceedings*, 47:495–521.

Van Vliet, M. (2000). *Size Effect in Tensile Fracture of Concrete and Rock*. (Unpublished doctoral thesis) Technische Universiteit Delft.

West, R.C., Zhang, J., and Moore, J. (2005). "Evaluation of Bond Strength between Pavement Layers." NCAT Report, 05–08.

Williams, M.L., Landel, R.F. and Ferry, J.D. (1955). "The Temperature Dependence of Relaxation Mechanisms in Amorphous Polymers and Other Glass-Forming Liquids." *Journal of the American Chemical Society*, 77, 3701–3707. DOI: 10.1021/ja01619a008.

Zofka, A., Maliszewski, M., Bernier, A., Josen, A., Vaitkus, A., and Kleizienė, R. (2015). "Advanced Shear Tester for Evaluation of Asphalt Concrete under Constant Normal Stiffness Conditions." *Road Materials and Pavement Design*, 16, 187–210. DOI: 10.1080/14680629.2015.1029690.

Zofka, A., Maliszewski, M., and Maliszewska, D. (2017). “Glass and Carbon Geogrid Reinforcement of Asphalt Mixtures.” *Road Materials and Pavement Design*, 18, 471–490. DOI: 10.1080/14680629.2016.1266775.

TABLE OF FIGURES

TABLE OF TABLES

APPENDICES

APPENDIX A

Advanced complex modulus test results for bituminous mixtures and interfaces

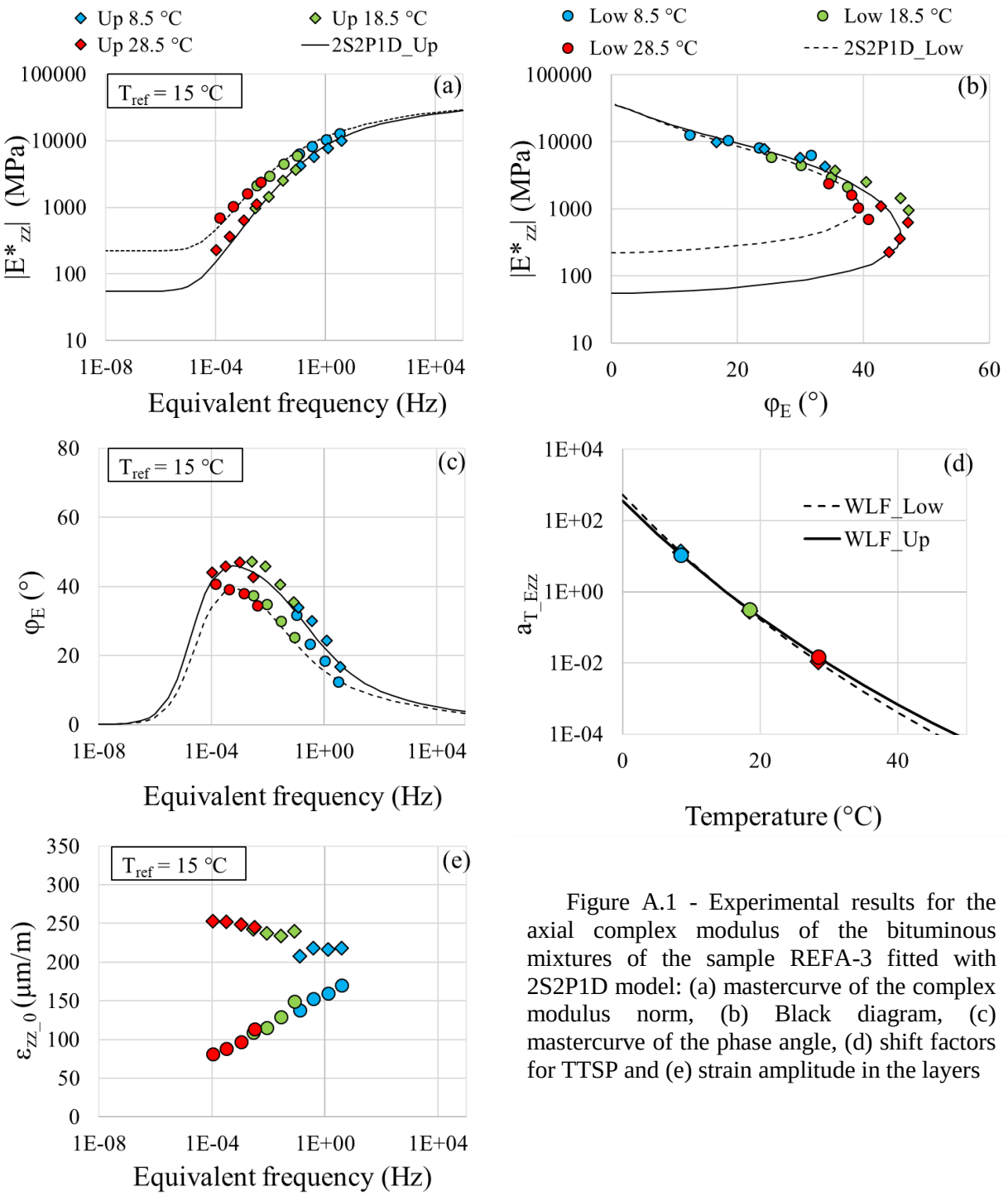

Figure A.1 - Experimental results for the axial complex modulus of the bituminous mixtures of the sample REFA-3 fitted with 2S2P1D model: (a) mastercurve of the complex modulus norm, (b) Black diagram, (c) mastercurve of the phase angle, (d) shift factors for TTSP and (e) strain amplitude in the layers

Table A.1 - 2S2P1D constants and WLF equation coefficients for sample REFA-3

Layer	Mixture	E_{00} (MPa)	E_0 (MPa)	k	h	δ	τ_E (s)	β	T_{ref} (°C)	C_1	C_2
Upper	BBSG3	55	37000	0.168	0.55	2	0.08	200	15	21.2	131.4
Lower	EME2	220	37000	0.168	0.55	2.3	0.5	90	15	19.8	131.6

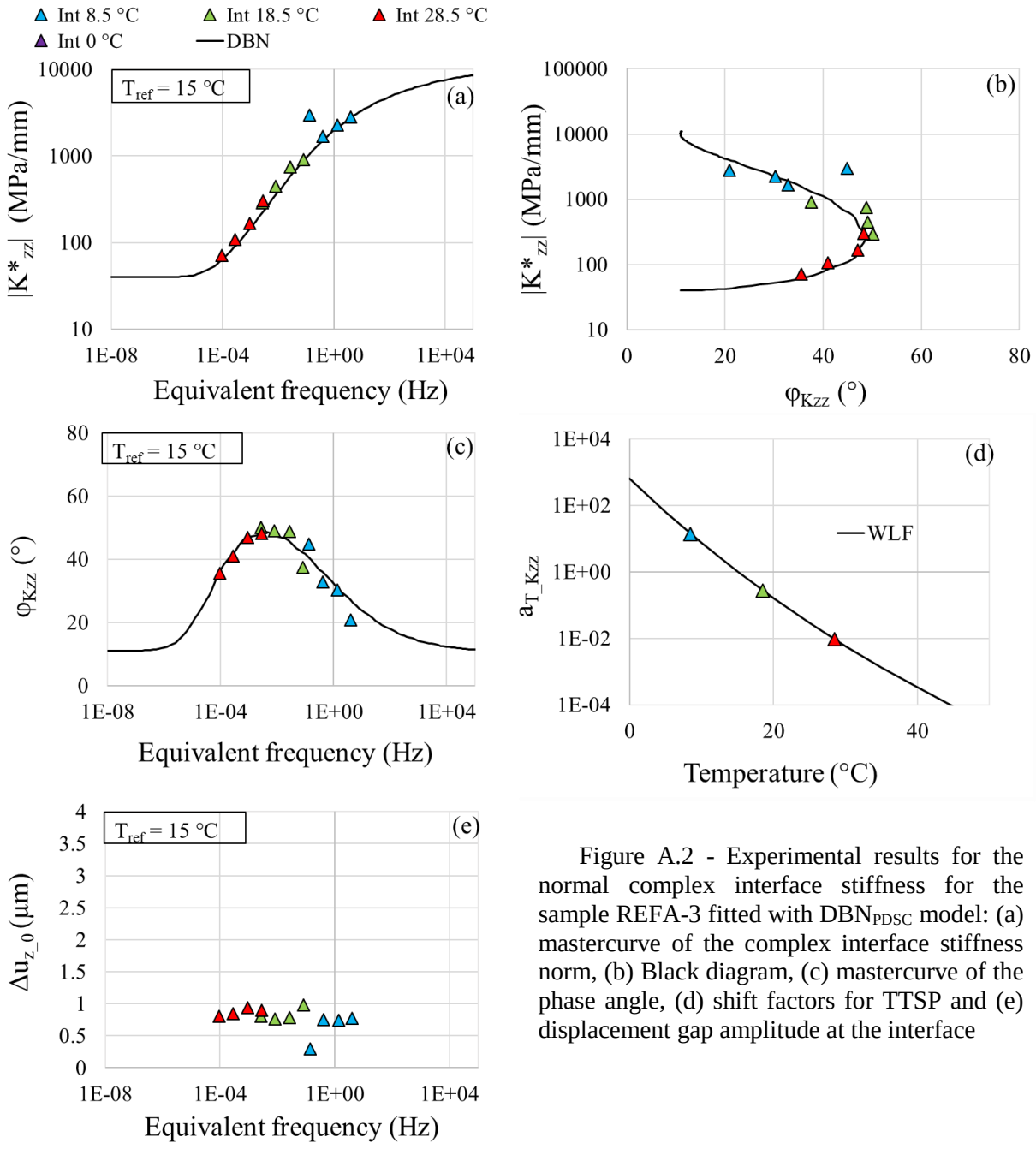

Figure A.2 - Experimental results for the normal complex interface stiffness for the sample REFA-3 fitted with DBN_{PDSC} model: (a) mastercurve of the complex interface stiffness norm, (b) Black diagram, (c) mastercurve of the phase angle, (d) shift factors for TTSP and (e) displacement gap amplitude at the interface

Table A.2 - 2S2P1D constants, DBN_{PDSC} constant φ_{NL} and WLF equation coefficients for sample REFA-3

K_{zz_00} (MPa)	K_{zz_0} (MPa)	k	h	δ	τ_{Kzz} (s)	β	φ_{NL}(°)	T_{ref} (°C)	C_1	C_2
40	11000	0.2	0.53	2.3	0.06	300	11	15	21.8	131.3

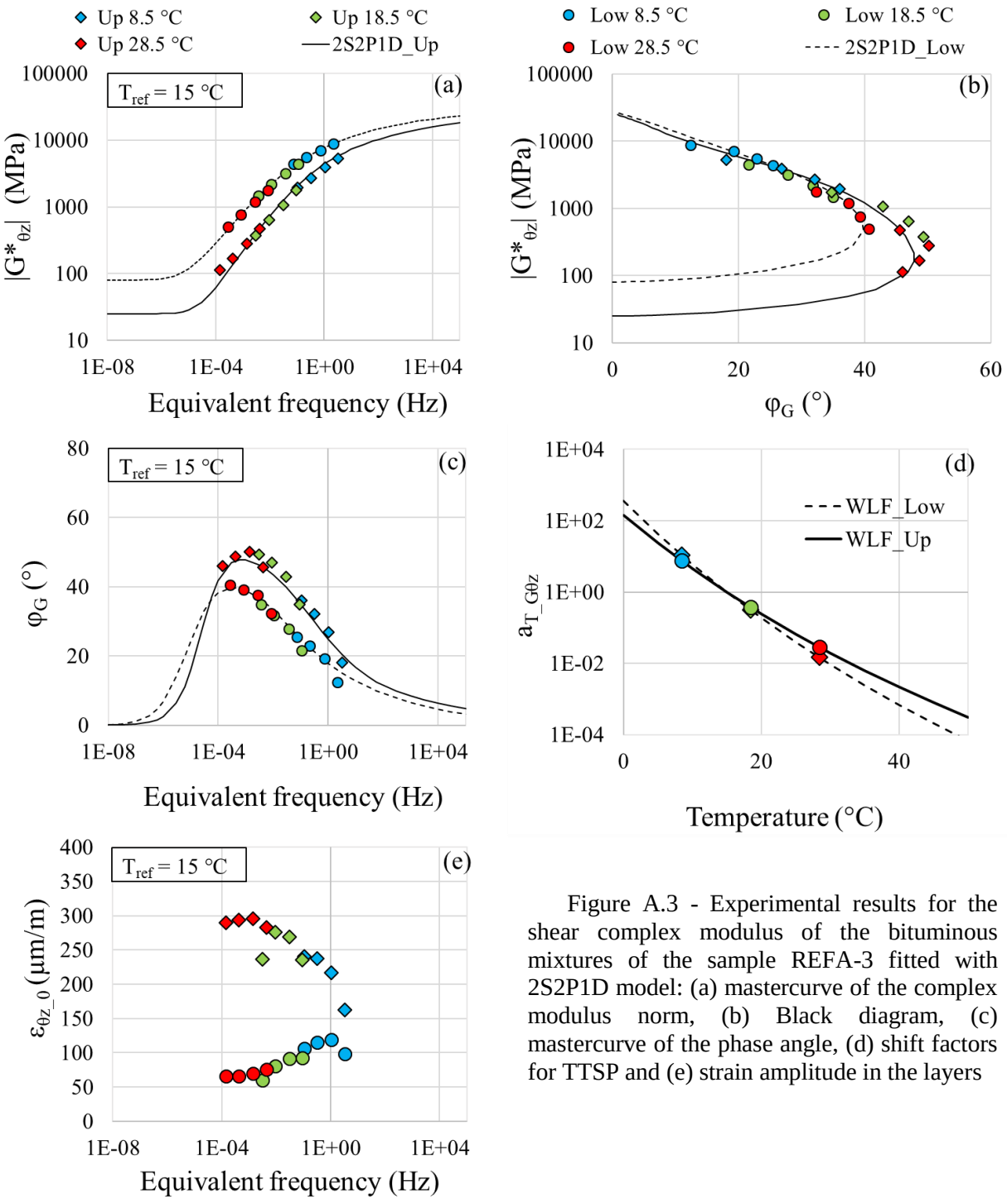

Figure A.3 - Experimental results for the shear complex modulus of the bituminous mixtures of the sample REFA-3 fitted with 2S2P1D model: (a) mastercurve of the complex modulus norm, (b) Black diagram, (c) mastercurve of the phase angle, (d) shift factors for TTSP and (e) strain amplitude in the layers

Table A.3 - 2S2P1D constants and WLF equation coefficients for sample REFA-3

Layer	Mixture	G_{00} (MPa)	G_0 (MPa)	k	h	δ	τ_G (s)	β	T_{ref} (°C)	C_1	C_2
Upper	BBSG3	25	26000	0.172	0.56	2.5	0.04	200	15	19.8	131.6
Lower	EME2	80	27500	0.2	0.55	2.6	0.4	250	15	16.8	132.1

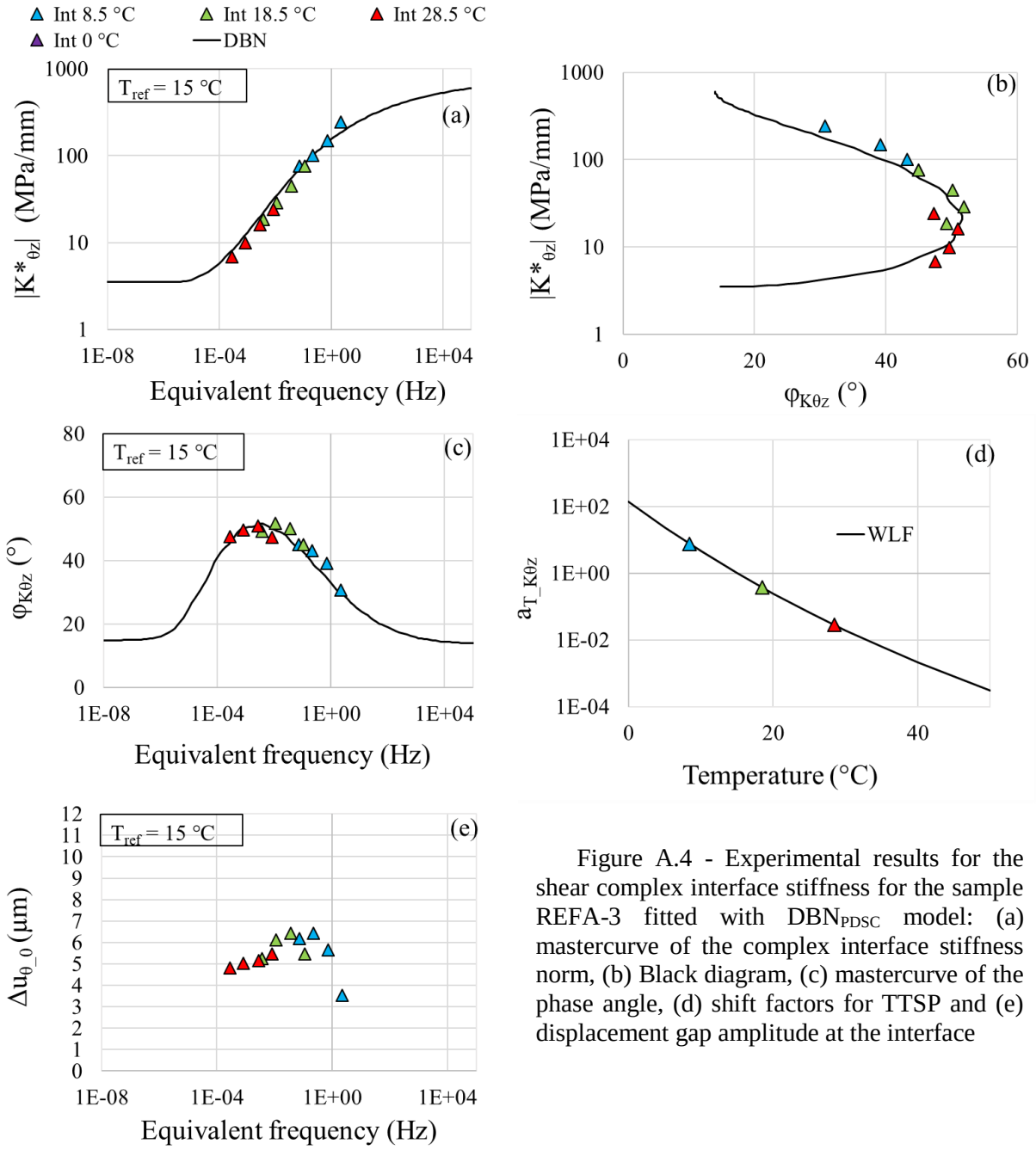

Figure A.4 - Experimental results for the shear complex interface stiffness for the sample REFA-3 fitted with DBN_{PDSC} model: (a) mastercurve of the complex interface stiffness norm, (b) Black diagram, (c) mastercurve of the phase angle, (d) shift factors for TTSP and (e) displacement gap amplitude at the interface

Table A.4 - 2S2P1D constants, DBN_{PDSC} constant φ_{NL} and WLF equation coefficients for sample REFA-3

K_{0z_00} (MPa)	K_{0z_0} (MPa)	k	h	δ	τ_{K0z} (s)	β	φ_{NL}(°)	T_{ref} (°C)	C_1	C_2
3.5	750	0.2	0.53	2.3	0.1	300	15	15	16.8	132.0

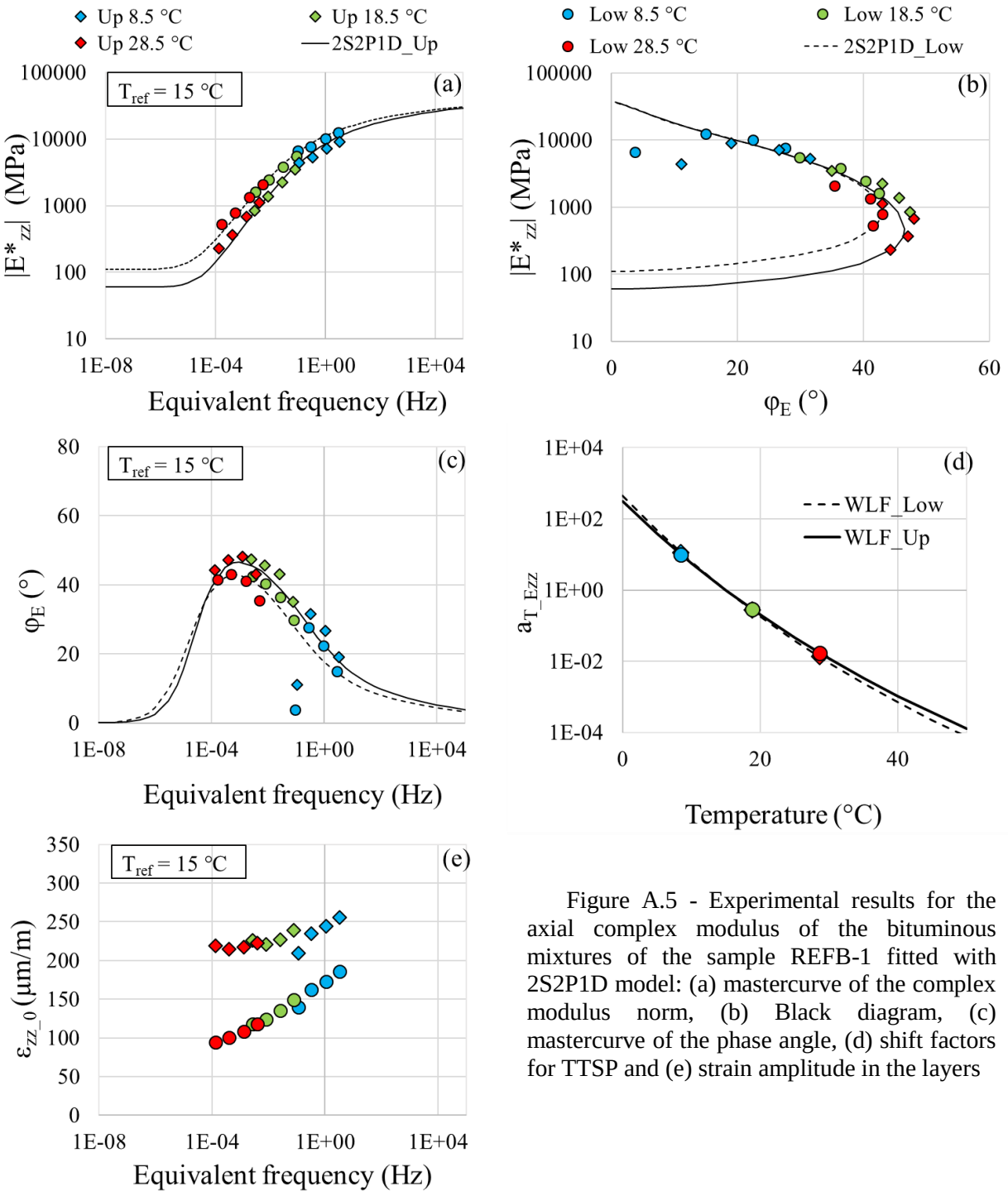

Figure A.5 - Experimental results for the axial complex modulus of the bituminous mixtures of the sample REFB-1 fitted with 2S2P1D model: (a) mastercurve of the complex modulus norm, (b) Black diagram, (c) mastercurve of the phase angle, (d) shift factors for TTSP and (e) strain amplitude in the layers

Table A.5 - 2S2P1D constants and WLF equation coefficients for sample REFB-1

Layer	Mixture	E_{00} (MPa)	E_0 (MPa)	k	h	δ	τ_E (s)	β	T_{ref} (°C)	C_1	C_2
Upper	BBSG3	60	38000	0.174	0.57	2.15	0.09	160	15	17.7	115.1
Lower	EME2	110	38000	0.172	0.57	2.1	0.3	200	15	16.7	115.3

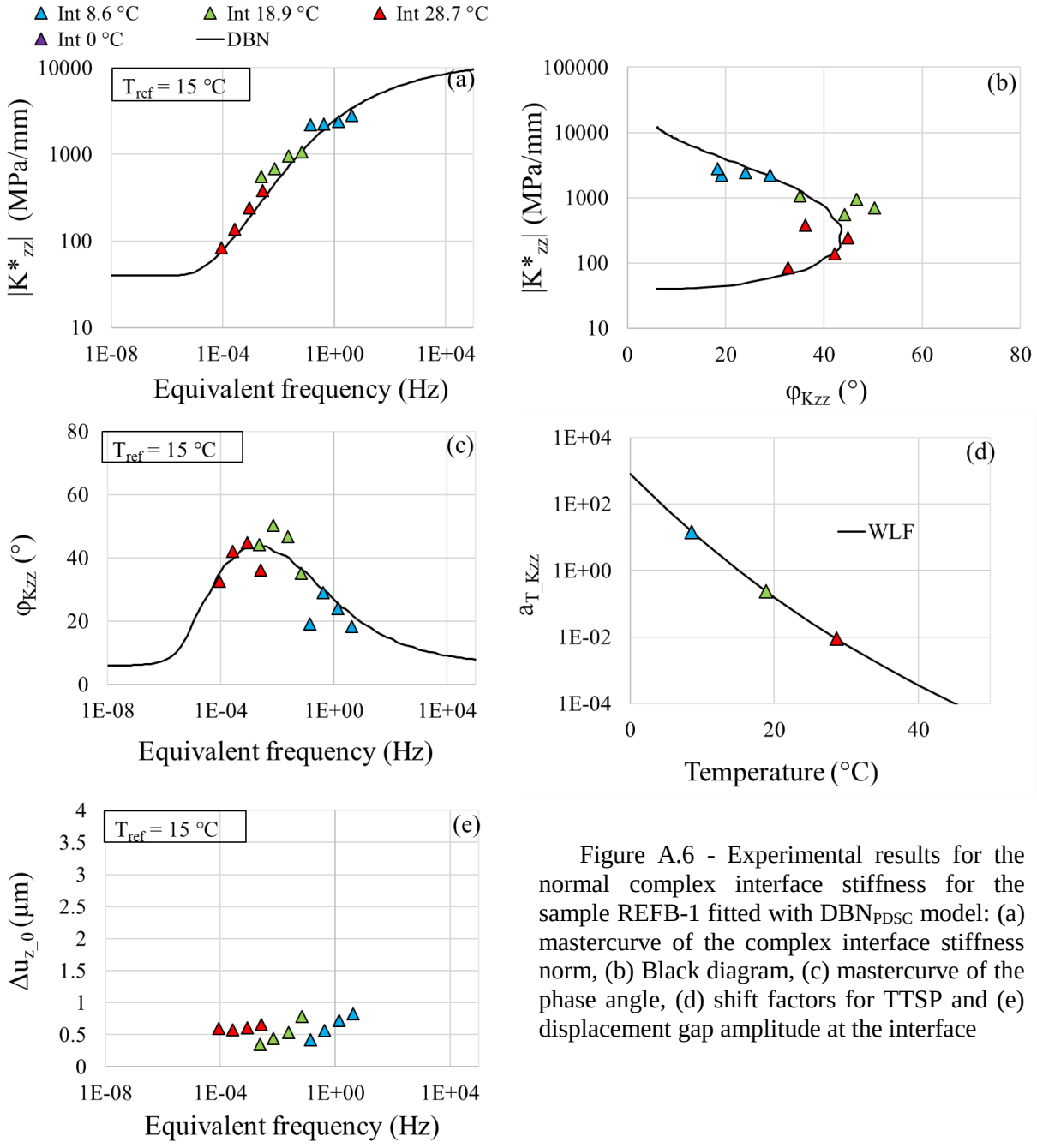

Figure A.6 - Experimental results for the normal complex interface stiffness for the sample REFB-1 fitted with DBN_{PDSC} model: (a) mastercurve of the complex interface stiffness norm, (b) Black diagram, (c) mastercurve of the phase angle, (d) shift factors for TTSP and (e) displacement gap amplitude at the interface

Table A.6 - 2S2P1D constants, DBN_{PDSC} constant φ_{NL} and WLF equation coefficients for sample REFB-1

K_{zz_00} (MPa)	K_{zz_0} (MPa)	k	h	δ	τ_{Kzz} (s)	β	φ_{NL}(°)	T_{ref} (°C)	C_1	C_2
40	12000	0.2	0.53	2.3	0.1	300	6	15	19.3	115.0

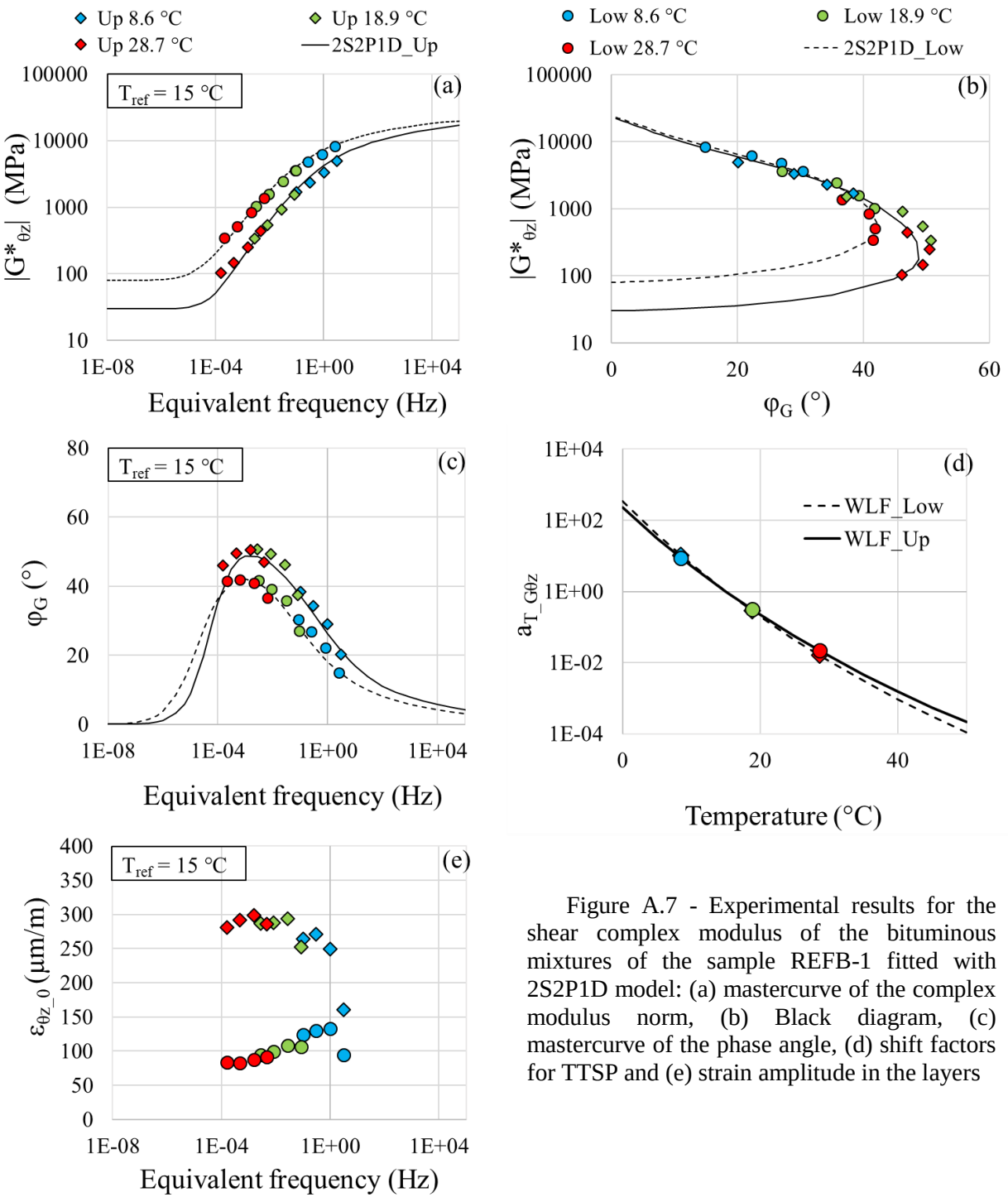

Figure A.7 - Experimental results for the shear complex modulus of the bituminous mixtures of the sample REFB-1 fitted with 2S2P1D model: (a) mastercurve of the complex modulus norm, (b) Black diagram, (c) mastercurve of the phase angle, (d) shift factors for TTSP and (e) strain amplitude in the layers

Table A.7 - 2S2P1D constants and WLF equation coefficients for sample REFB-1

Layer	Mixture	G_{00} (MPa)	G_0 (MPa)	k	h	δ	τ_G (s)	β	T_{ref} (°C)	C_1	C_2
Upper	BBSG3	30	23000	0.172	0.57	2.1	0.04	120	15	17.0	115.3
Lower	EME2	80	24000	0.18	0.57	2	0.3	200	15	15.8	115.4

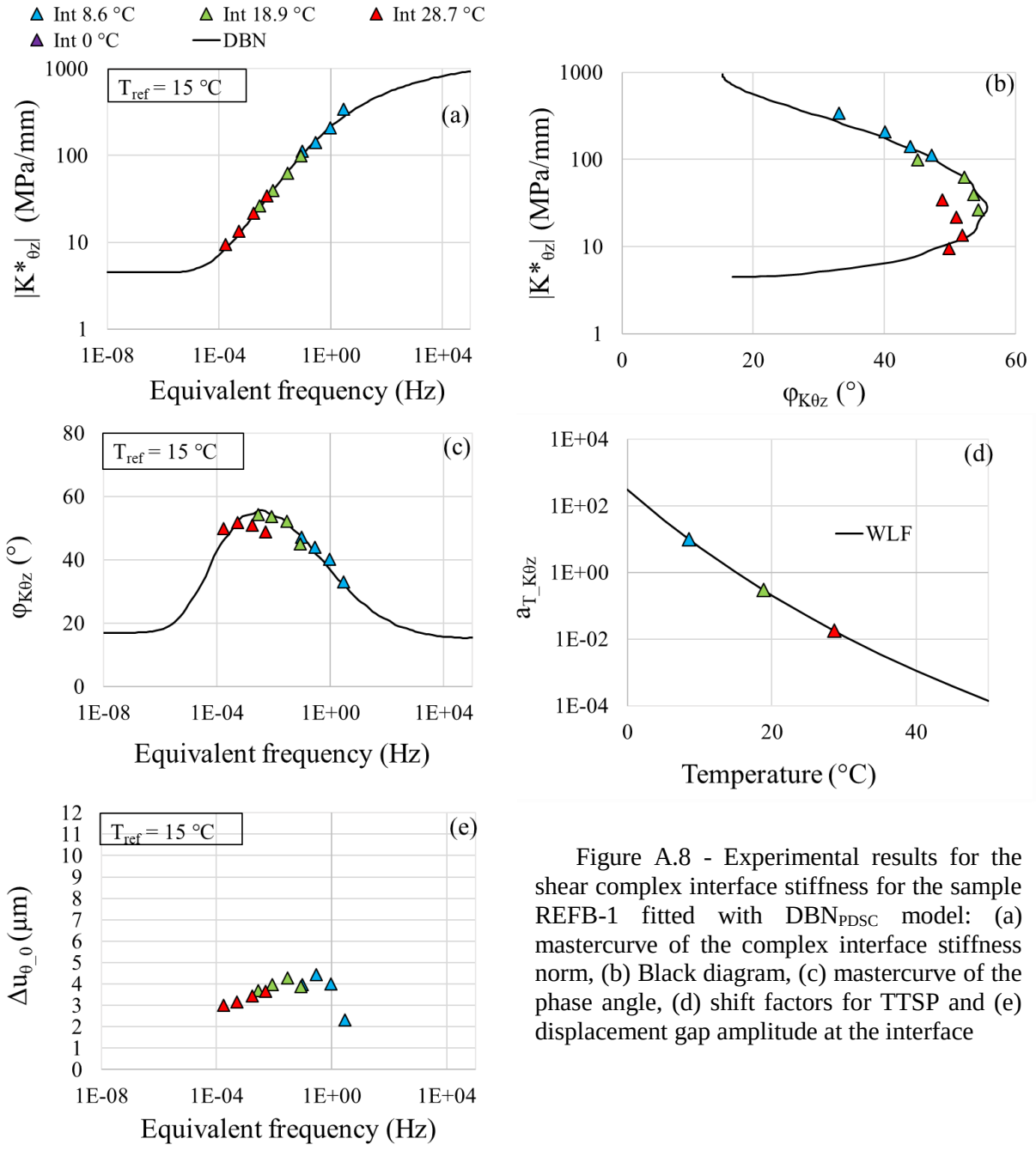

Figure A.8 - Experimental results for the shear complex interface stiffness for the sample REFB-1 fitted with DBN_{PDSC} model: (a) mastercurve of the complex interface stiffness norm, (b) Black diagram, (c) mastercurve of the phase angle, (d) shift factors for TTSP and (e) displacement gap amplitude at the interface

Table A.8 - 2S2P1D constants, DBN_{PDSC} constant φ_{NL} and WLF equation coefficients for sample REFB-1

K_{0z_00} (MPa)	K_{0z_0} (MPa)	k	h	δ	τ_{K0z} (s)	β	φ_{NL}(°)	T_{ref} (°C)	C_1	C_2
4.5	1200	0.2	0.53	2.3	0.06	300	17	15	16.6	115.3

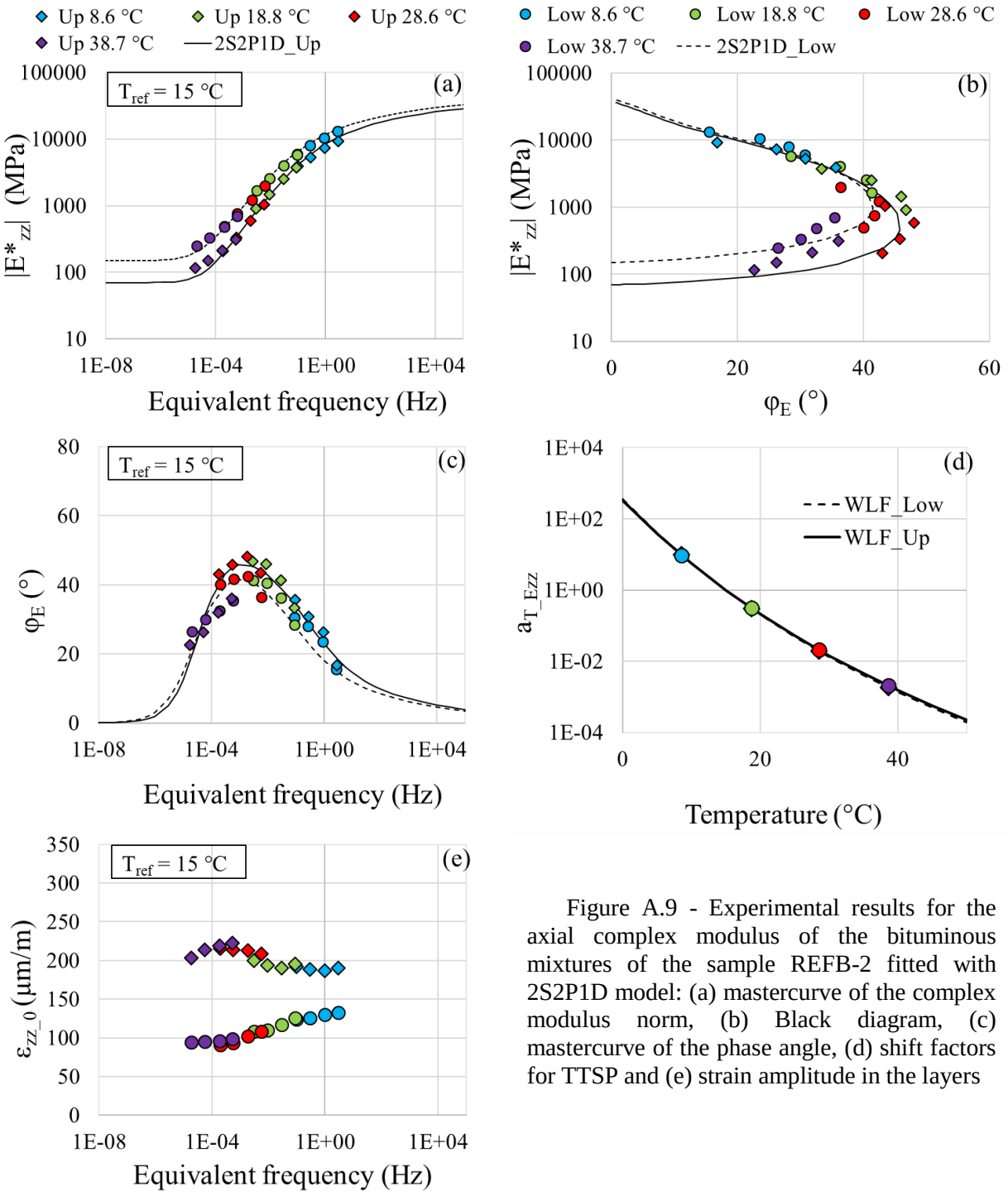

Figure A.9 - Experimental results for the axial complex modulus of the bituminous mixtures of the sample REFB-2 fitted with 2S2P1D model: (a) mastercurve of the complex modulus norm, (b) Black diagram, (c) mastercurve of the phase angle, (d) shift factors for TTSP and (e) strain amplitude in the layers

Table A.9 - 2S2P1D constants and WLF equation coefficients for sample REFB-2

Layer	Mixture	E_{00} (MPa)	E_0 (MPa)	k	h	δ	τ_E (s)	β	T_{ref} (°C)	C_1	C_2
Upper	BBSG3	70	38000	0.17	0.57	2.1	0.08	160	15	14.0	97.2
Lower	EME2	150	42000	0.17	0.57	2.2	0.25	200	15	13.8	97.5

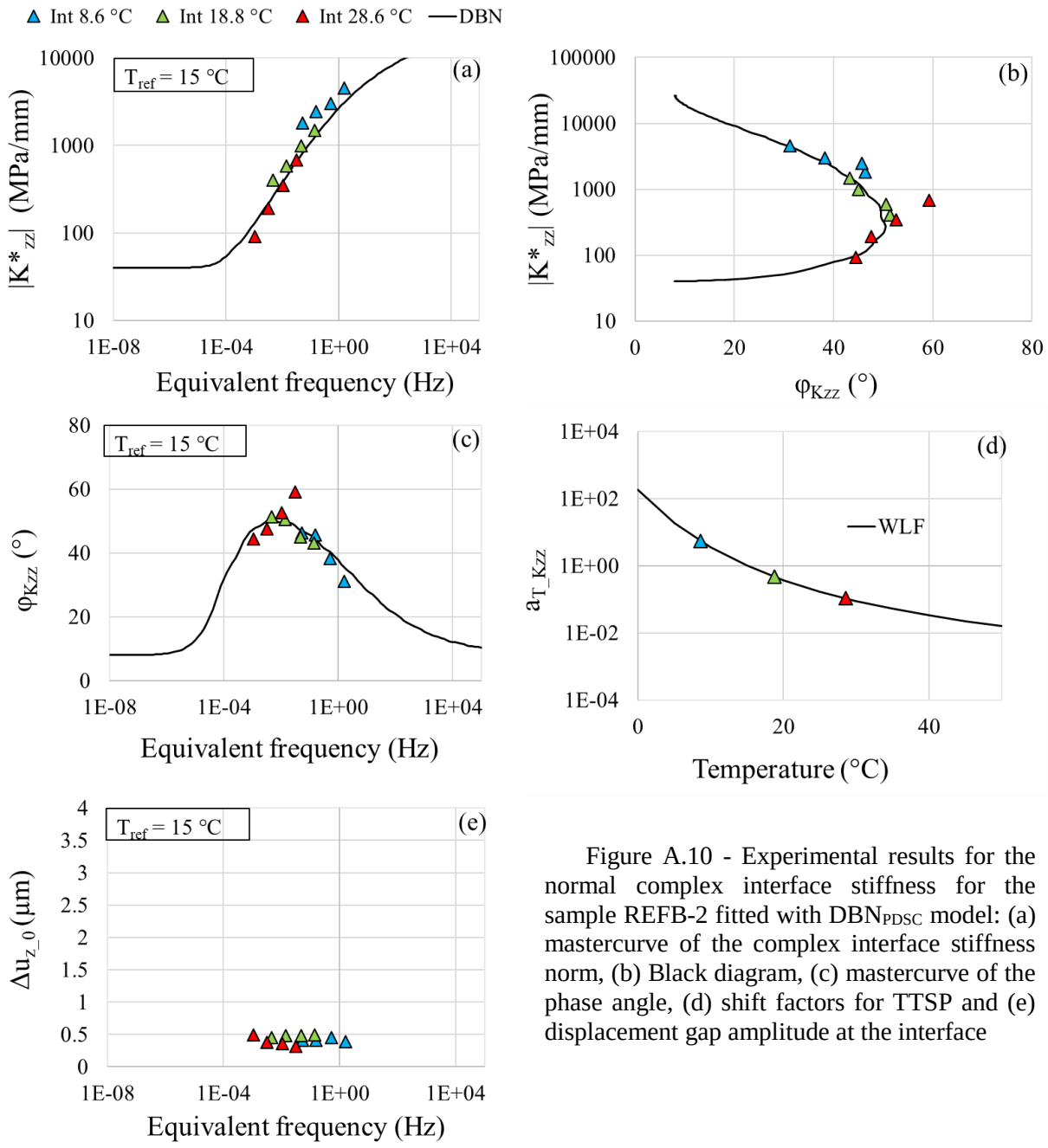

Figure A.10 - Experimental results for the normal complex interface stiffness for the sample REFB-2 fitted with DBN_{PDSC} model: (a) mastercurve of the complex interface stiffness norm, (b) Black diagram, (c) mastercurve of the phase angle, (d) shift factors for TTSP and (e) displacement gap amplitude at the interface

Table A.10 - 2S2P1D constants, DBN_{PDSC} constant φ_{NL} and WLF equation coefficients for sample REFB-2

K_{zz_00} (MPa)	K_{zz_0} (MPa)	k	h	δ	τ_{Kzz} (s)	β	φ_{NL}(°)	T_{ref} (°C)	C_1	C_2
40	26000	0.2	0.53	2.3	0.01	300	8	15	3.9	40.5

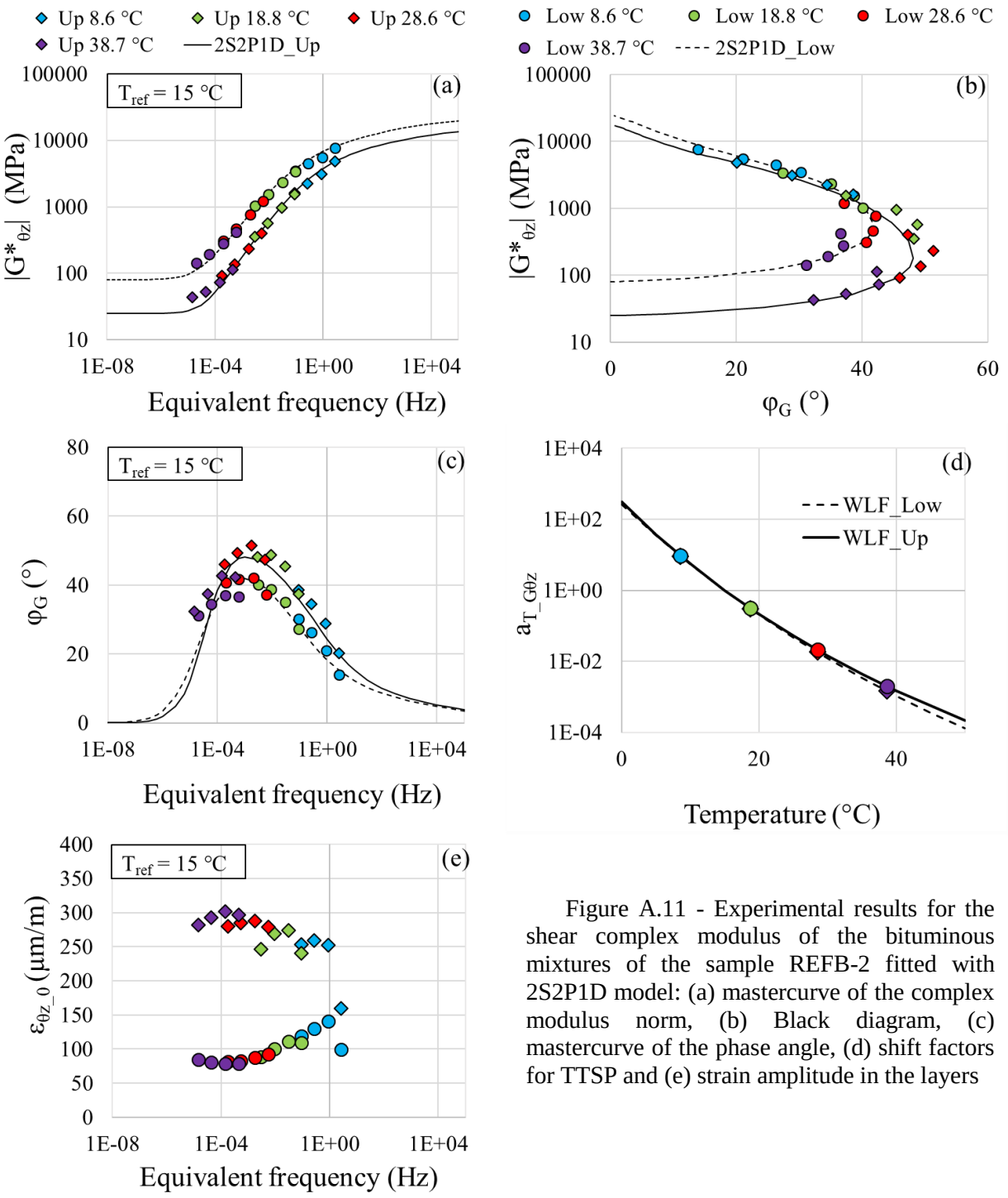

Figure A.11 - Experimental results for the shear complex modulus of the bituminous mixtures of the sample REFB-2 fitted with 2S2P1D model: (a) mastercurve of the complex modulus norm, (b) Black diagram, (c) mastercurve of the phase angle, (d) shift factors for TTSP and (e) strain amplitude in the layers

Table A.11 - 2S2P1D constants and WLF equation coefficients for sample REFB-2

Layer	Mixture	G_{00} (MPa)	G_0 (MPa)	k	h	δ	τ_G (s)	β	T_{ref} (°C)	C_1	C_2
Upper	BBSG3	25	18000	0.166	0.57	2	0.06	140	15	17.8	125.1
Lower	EME2	80	25000	0.174	0.57	2.3	0.25	200	15	14.0	99.1

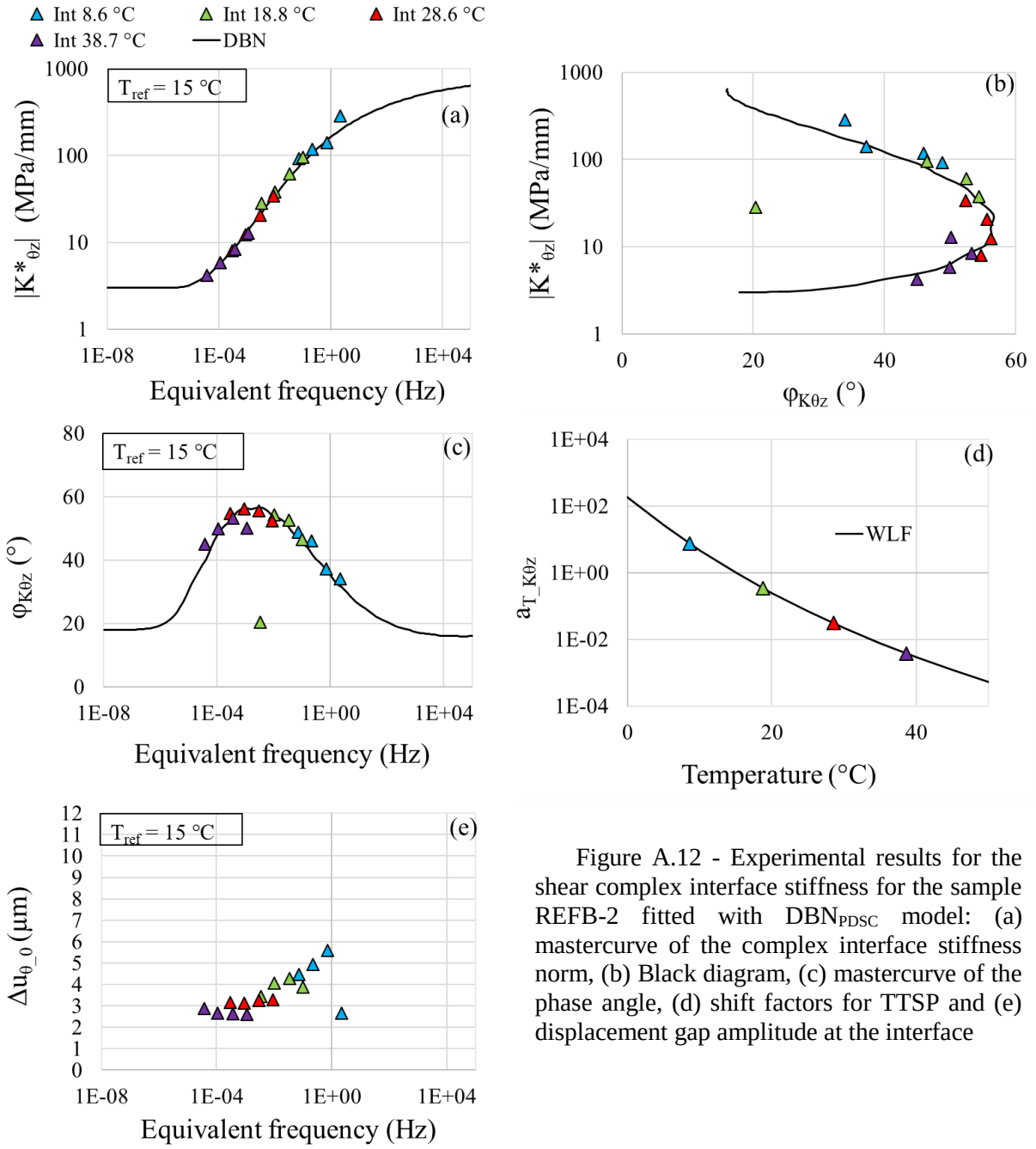

Figure A.12 - Experimental results for the shear complex interface stiffness for the sample REFB-2 fitted with DBN_{PDSC} model: (a) mastercurve of the complex interface stiffness norm, (b) Black diagram, (c) mastercurve of the phase angle, (d) shift factors for TTSP and (e) displacement gap amplitude at the interface

Table A.12 - 2S2P1D constants, DBN_{PDSC} constant φ_{NL} and WLF equation coefficients for sample REFB-2

K_{0z_00} (MPa)	K_{0z_0} (MPa)	k	h	δ	τ_{K0z} (s)	β	φ_{NL}(°)	T_{ref} (°C)	C_1	C_2
3	800	0.2	0.53	2.3	0.1	300	18	15	12.5	97.8

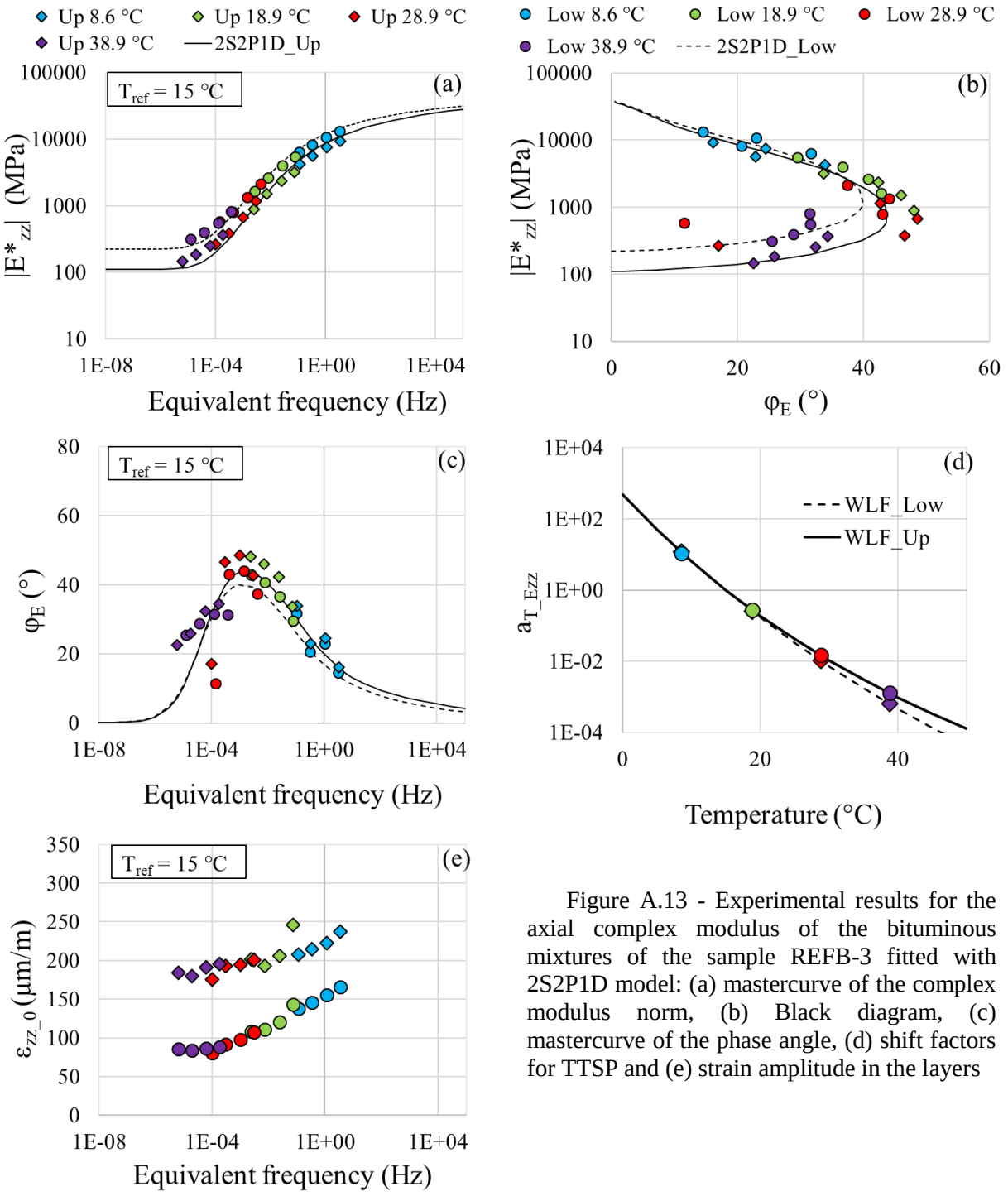

Figure A.13 - Experimental results for the axial complex modulus of the bituminous mixtures of the sample REFB-3 fitted with 2S2P1D model: (a) mastercurve of the complex modulus norm, (b) Black diagram, (c) mastercurve of the phase angle, (d) shift factors for TTSP and (e) strain amplitude in the layers

Table A.13 - 2S2P1D constants and WLF equation coefficients for sample REFB-3

Layer	Mixture	E_{00} (MPa)	E_0 (MPa)	k	h	δ	τ_E (s)	β	T_{ref} (°C)	C_1	C_2
Upper	BBSG3	110	38000	0.17	0.59	2.6	0.15	130	15	20.8	131.0
Lower	EME2	220	39000	0.17	0.57	2.1	0.35	120	15	14.7	96.7

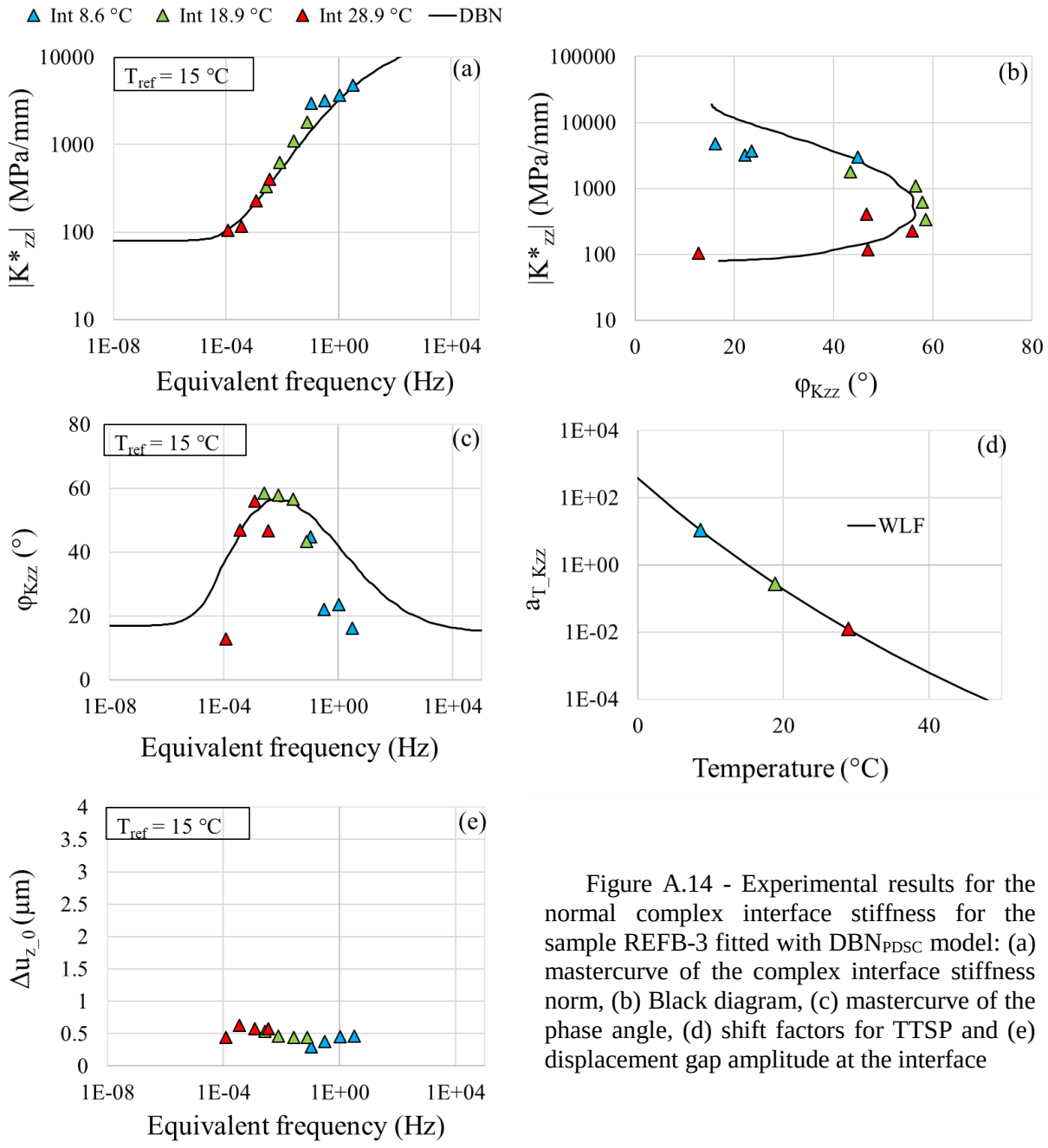

Figure A.14 - Experimental results for the normal complex interface stiffness for the sample REFB-3 fitted with DBN_{PDSC} model: (a) mastercurve of the complex interface stiffness norm, (b) Black diagram, (c) mastercurve of the phase angle, (d) shift factors for TTSP and (e) displacement gap amplitude at the interface

Table A.14 - 2S2P1D constants, DBN_{PDSC} constant φ_{NL} and WLF equation coefficients for sample REFB-3

K_{zz_00} (MPa)	K_{zz_0} (MPa)	k	h	δ	τ_{Kzz} (s)	β	φ_{NL}(°)	T_{ref} (°C)	C_1	C_2
80	25000	0.2	0.53	2.3	0.02	300	17	15	20.0	130.9

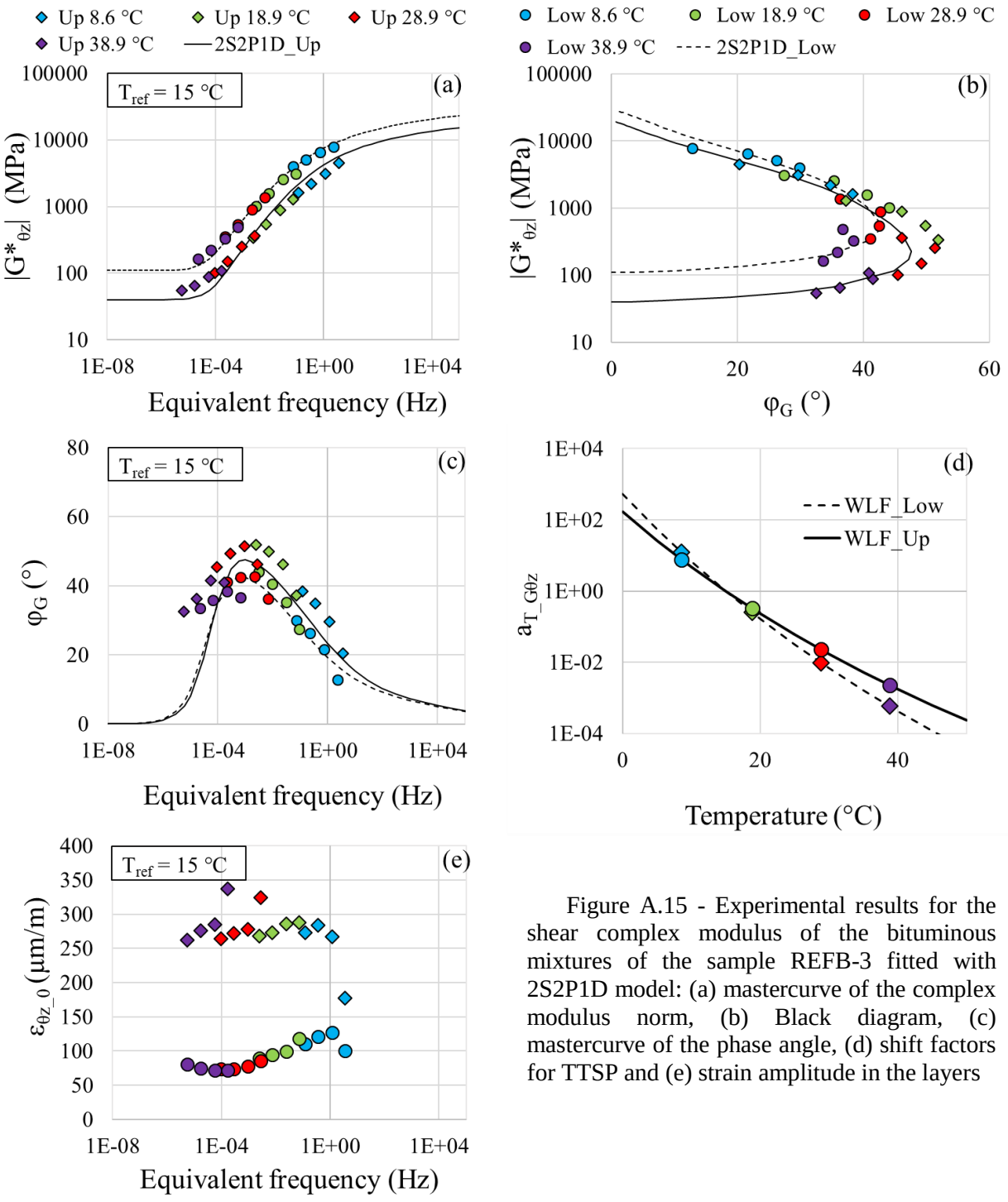

Figure A.15 - Experimental results for the shear complex modulus of the bituminous mixtures of the sample REFB-3 fitted with 2S2P1D model: (a) mastercurve of the complex modulus norm, (b) Black diagram, (c) mastercurve of the phase angle, (d) shift factors for TTSP and (e) strain amplitude in the layers

Table A.15 - 2S2P1D constants and WLF equation coefficients for sample REFB-3

Layer	Mixture	G_{00} (MPa)	G_0 (MPa)	k	h	δ	τ_G (s)	β	T_{ref} (°C)	C_1	C_2
Upper	BBSG3	40	20000	0.17	0.54	2	0.06	100	15	21.1	130.9
Lower	EME2	110	30000	0.17	0.53	2.2	0.15	100	15	17.3	131.5

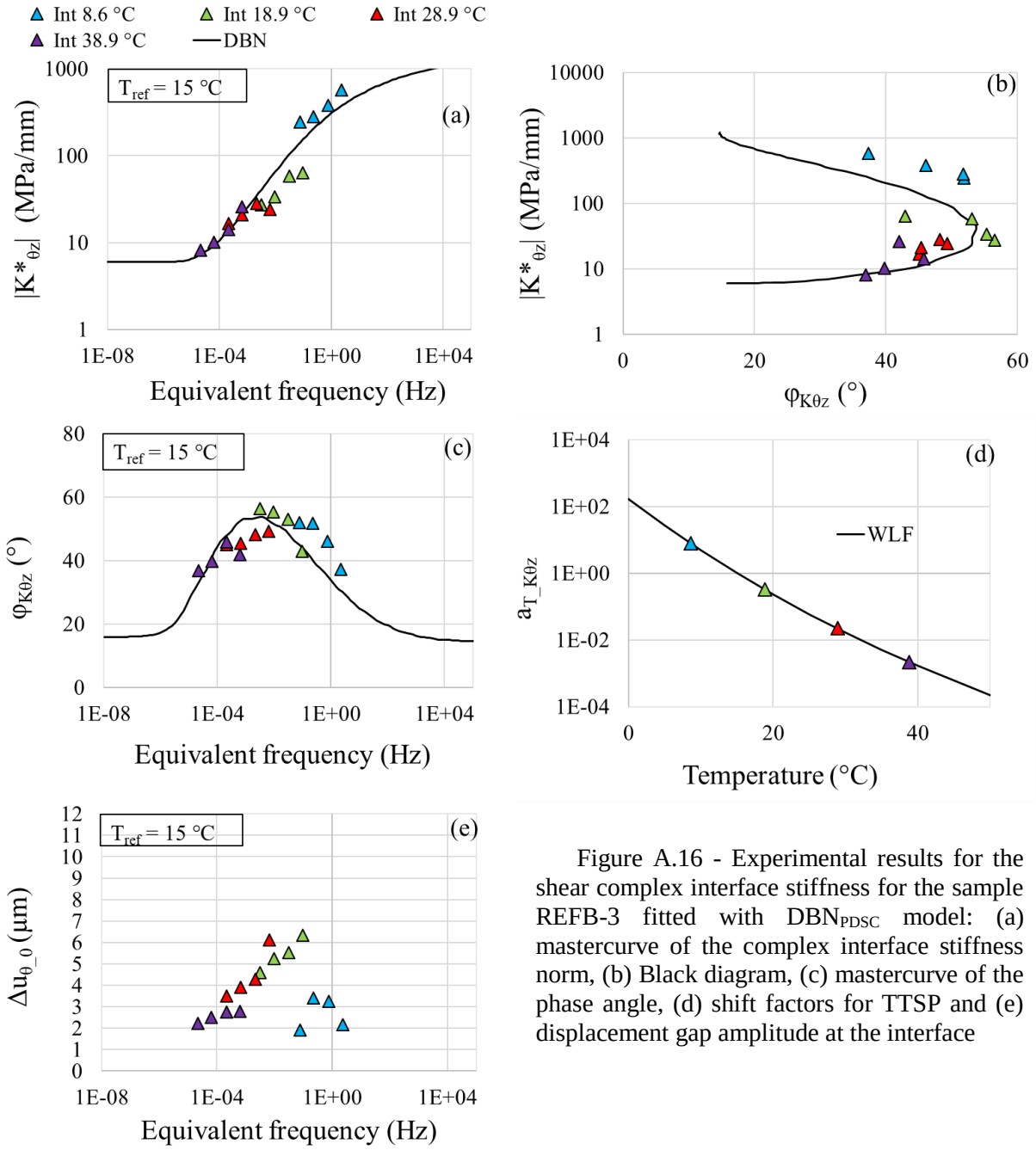

Figure A.16 - Experimental results for the shear complex interface stiffness for the sample REFB-3 fitted with DBN_{PDSC} model: (a) mastercurve of the complex interface stiffness norm, (b) Black diagram, (c) mastercurve of the phase angle, (d) shift factors for TTSP and (e) displacement gap amplitude at the interface

Table A.16 - 2S2P1D constants, DBN_{PDSC} constant φ_{NL} and WLF equation coefficients for sample REFB-3

K_{0z_00} (MPa)	K_{0z_0} (MPa)	k	h	δ	τ_{K0z} (s)	β	φ_{NL}(°)	T_{ref} (°C)	C_1	C_2
6	1500	0.2	0.53	2.3	0.1	300	16	15	17.3	131.3

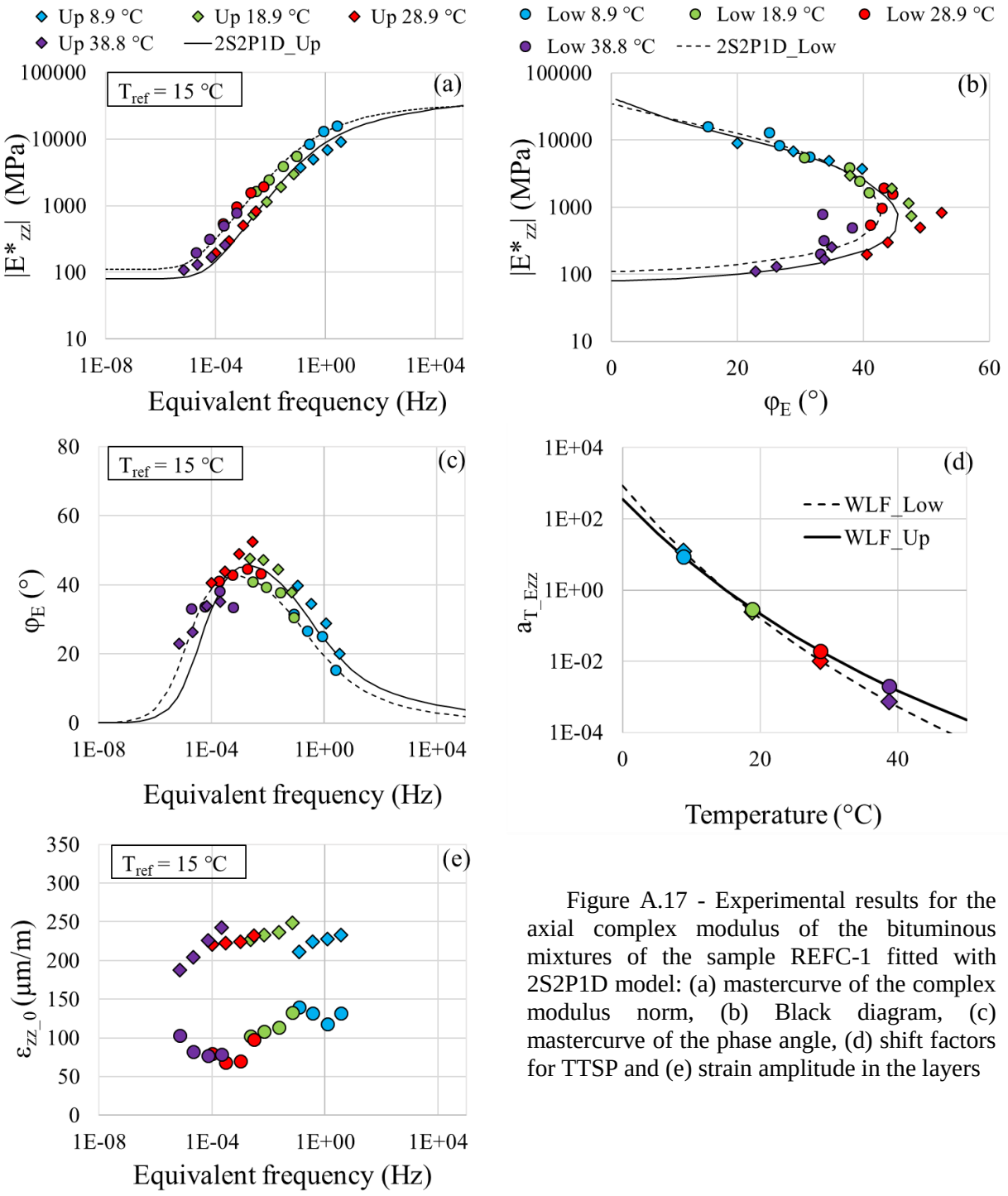

Figure A.17 - Experimental results for the axial complex modulus of the bituminous mixtures of the sample REFC-1 fitted with 2S2P1D model: (a) mastercurve of the complex modulus norm, (b) Black diagram, (c) mastercurve of the phase angle, (d) shift factors for TTSP and (e) strain amplitude in the layers

Table A.17 - 2S2P1D constants and WLF equation coefficients for sample REFC-1

Layer	Mixture	E_{00} (MPa)	E_0 (MPa)	k	h	δ	τ_E (s)	β	T_{ref} (°C)	C_1	C_2
Upper	BBSG3	80	42000	0.168	0.57	2	0.06	180	15	15.8	95.9
Lower	EME2	110	35000	0.19	0.54	1.2	0.25	200	15	13.5	94.2

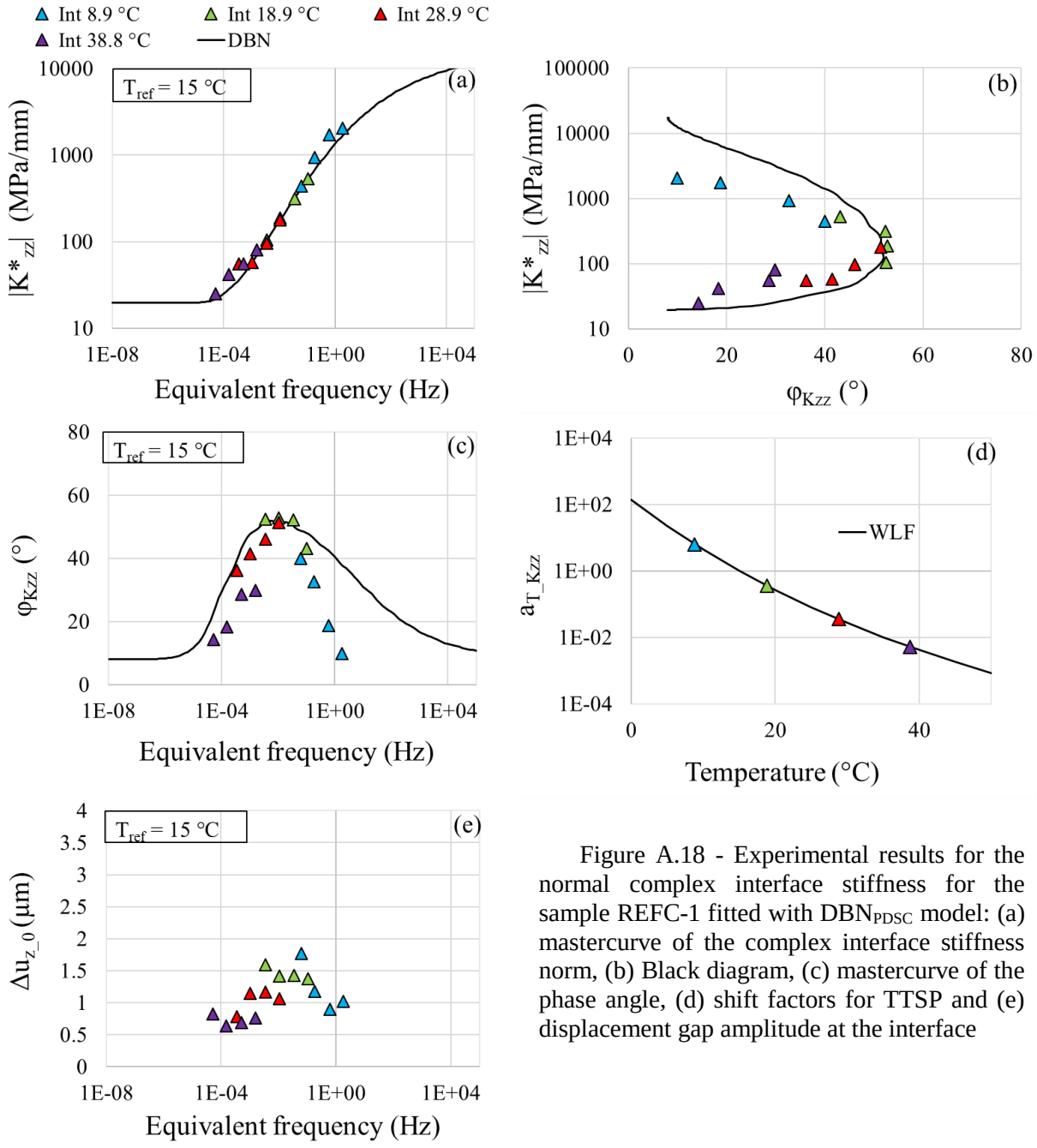

Figure A.18 - Experimental results for the normal complex interface stiffness for the sample REFC-1 fitted with DBN_{PDSC} model: (a) mastercurve of the complex interface stiffness norm, (b) Black diagram, (c) mastercurve of the phase angle, (d) shift factors for TTSP and (e) displacement gap amplitude at the interface

Table A.18 - 2S2P1D constants, DBN_{PDSC} constant φ_{NL} and WLF equation coefficients for sample REFC-1

K_{zz_00} (MPa)	K_{zz_0} (MPa)	k	h	δ	τ_{Kzz} (s)	β	φ_{NL}(°)	T_{ref} (°C)	C_1	C_2
20	17000	0.2	0.53	2.3	0.005	300	8	15	11.4	94.4

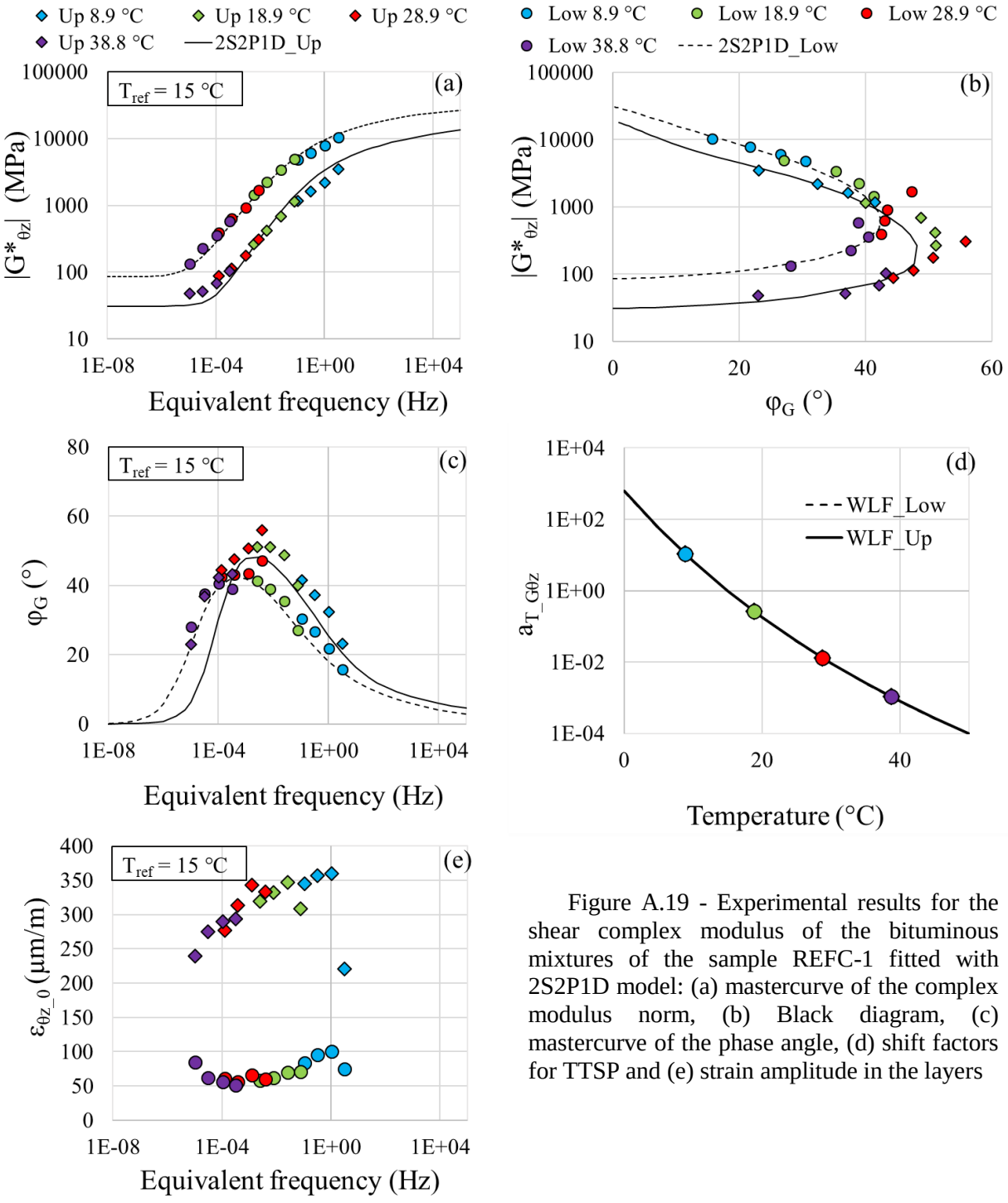

Figure A.19 - Experimental results for the shear complex modulus of the bituminous mixtures of the sample REFC-1 fitted with 2S2P1D model: (a) mastercurve of the complex modulus norm, (b) Black diagram, (c) mastercurve of the phase angle, (d) shift factors for TTSP and (e) strain amplitude in the layers

Table A.19 - 2S2P1D constants and WLF equation coefficients for sample REFC-1

Layer	Mixture	G_{00} (MPa)	G_0 (MPa)	k	h	δ	τ_G (s)	β	T_{ref} (°C)	C_1	C_2
Upper	BBSG3	31	19000	0.164	0.57	2.3	0.04	100	15	14.8	94.7
Lower	EME2	85	31000	0.2	0.57	2.2	0.4	200	15	14.8	94.7

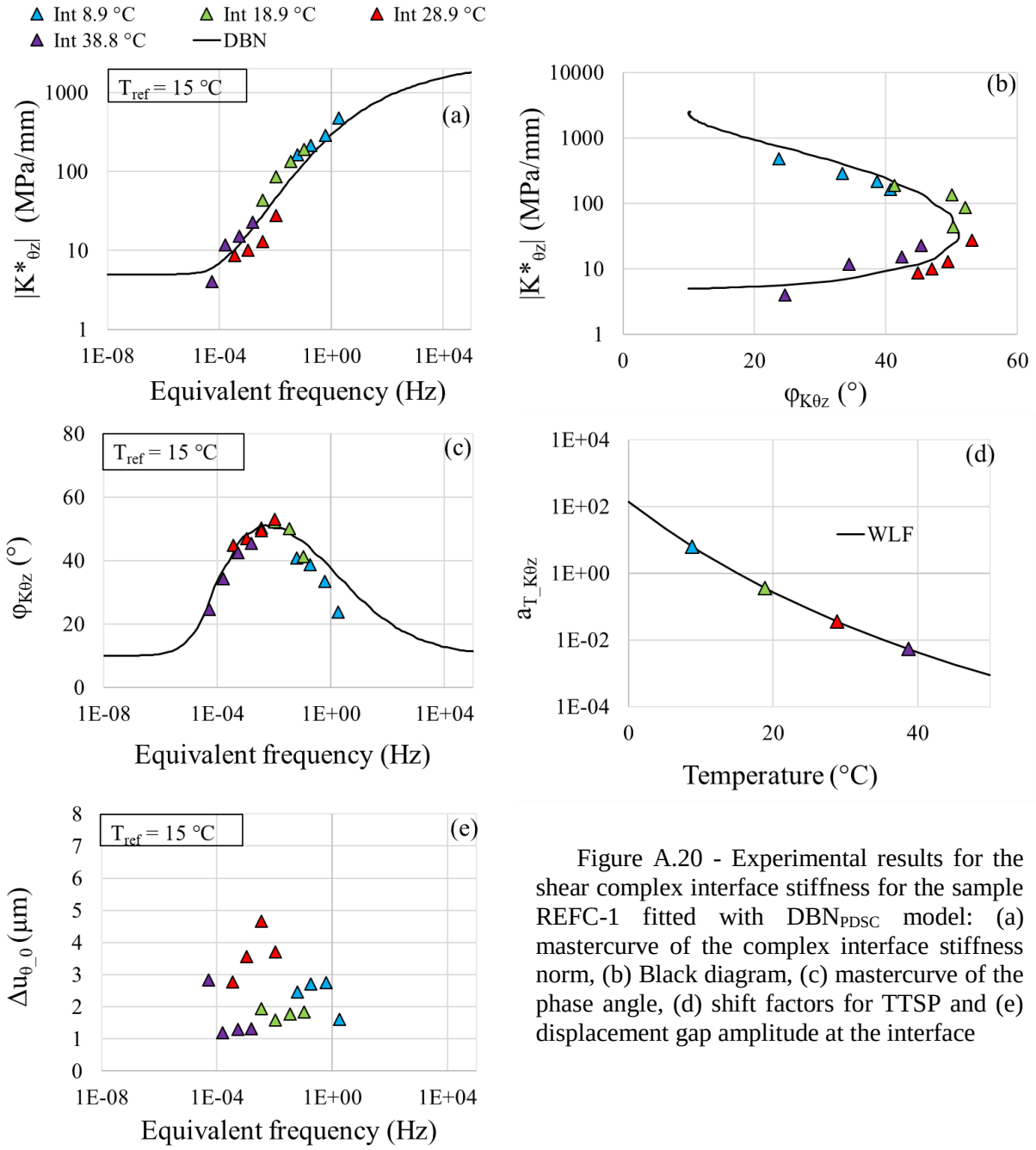

Figure A.20 - Experimental results for the shear complex interface stiffness for the sample REFC-1 fitted with DBN_{PDSC} model: (a) mastercurve of the complex interface stiffness norm, (b) Black diagram, (c) mastercurve of the phase angle, (d) shift factors for TTSP and (e) displacement gap amplitude at the interface

Table A.20 - 2S2P1D constants, DBN_{PDSC} constant φ_{NL} and WLF equation coefficients for sample REFC-1

K_{0z_00} (MPa)	K_{0z_0} (MPa)	k	h	δ	τ_{K0z} (s)	β	φ_{NL}(°)	T_{ref} (°C)	C_1	C_2
5	2500	0.2	0.53	2.3	0.015	300	10	15	16.8	132.0

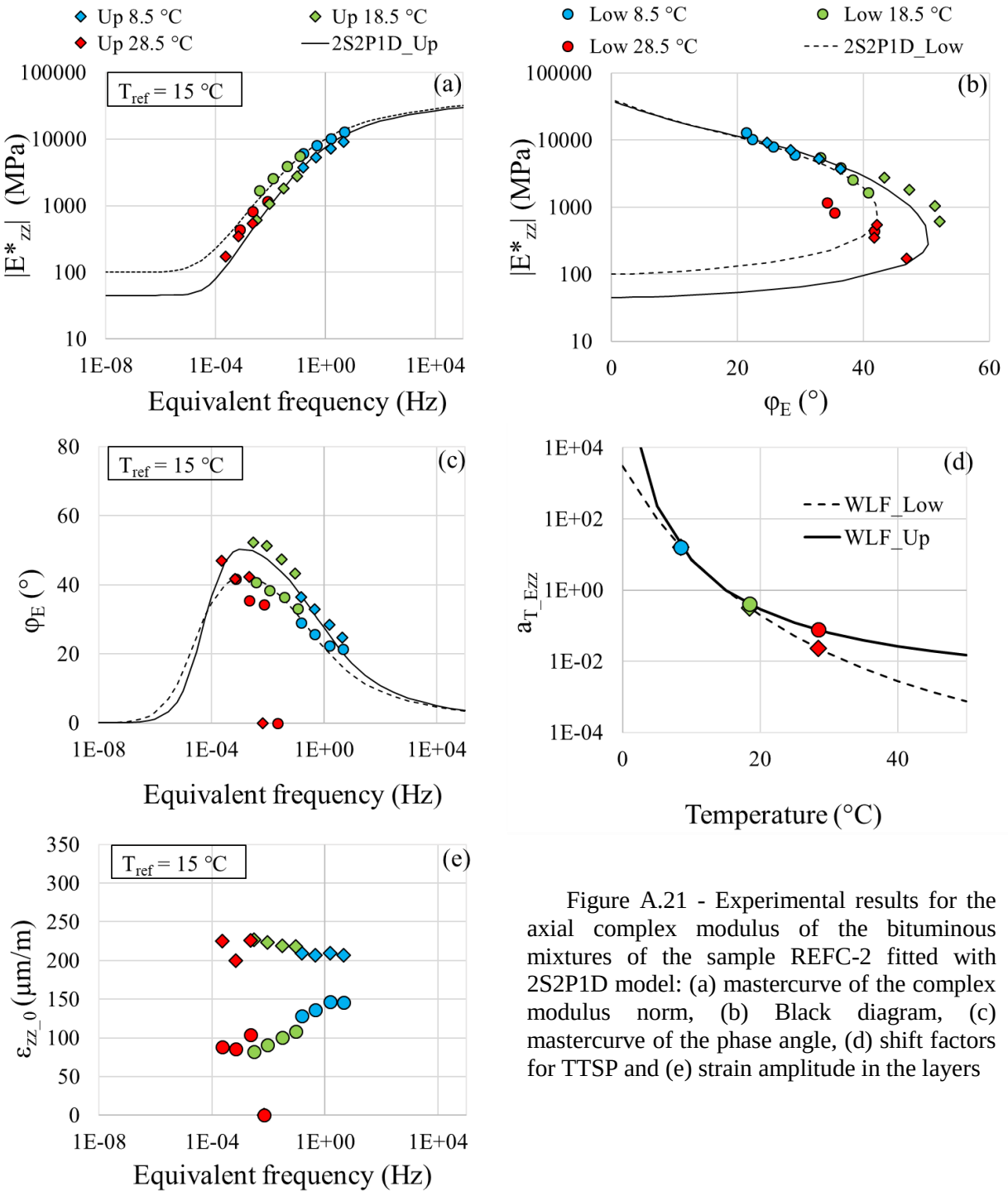

Figure A.21 - Experimental results for the axial complex modulus of the bituminous mixtures of the sample REFC-2 fitted with 2S2P1D model: (a) mastercurve of the complex modulus norm, (b) Black diagram, (c) mastercurve of the phase angle, (d) shift factors for TTSP and (e) strain amplitude in the layers

Table A.21 - 2S2P1D constants and WLF equation coefficients for sample REFC-2

Layer	Mixture	E_{00} (MPa)	E_0 (MPa)	k	h	δ	τ_E (s)	β	T_{ref} (°C)	C_1	C_2
Upper	BBSG3	45	38000	0.176	0.57	1.7	0.04	110	15	7.3	46.3
Lower	EME2	100	40000	0.17	0.55	1.8	0.1	300	15	3.0	22.8

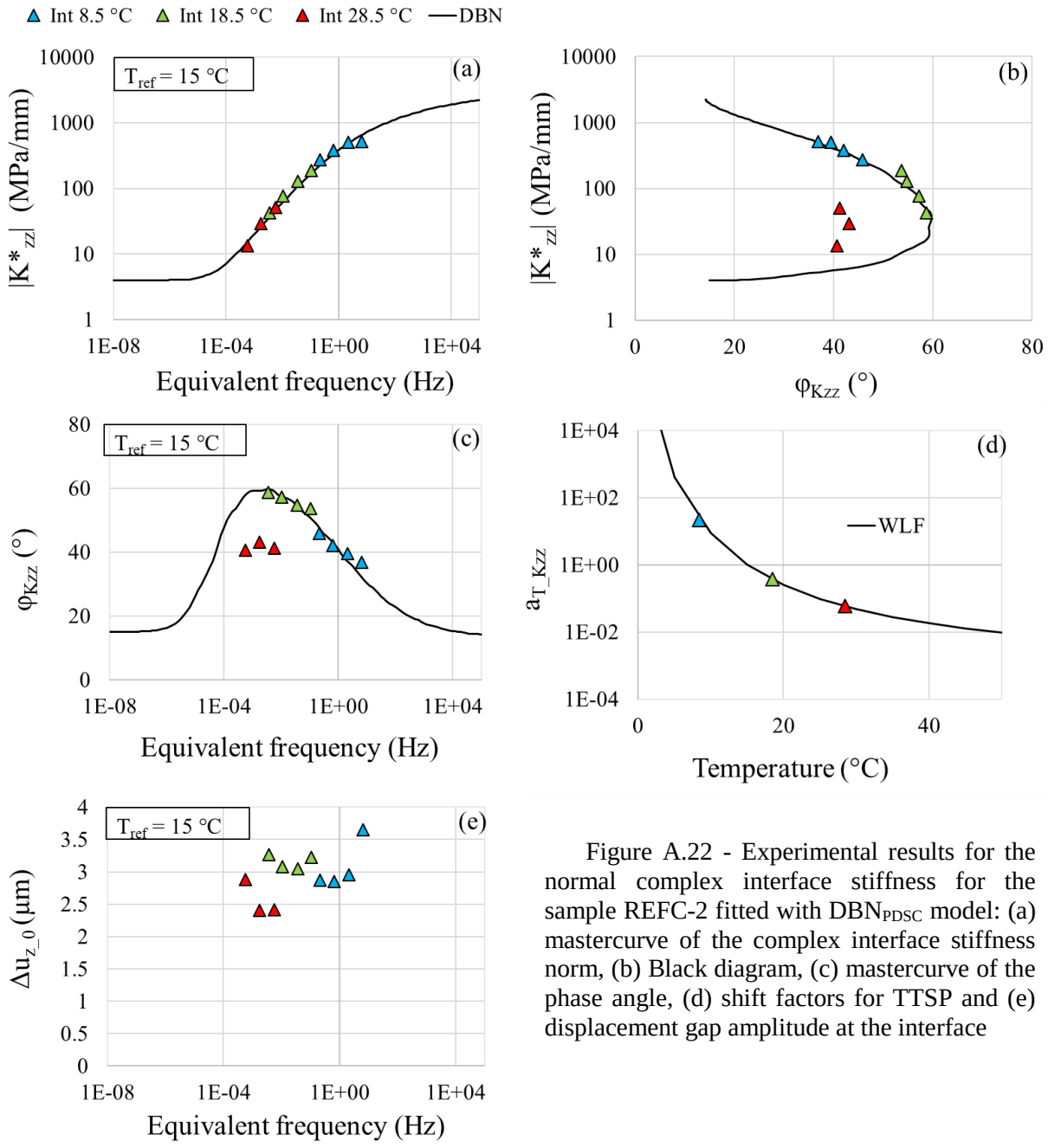

Figure A.22 - Experimental results for the normal complex interface stiffness for the sample REFC-2 fitted with DBN_{PDSC} model: (a) mastercurve of the complex interface stiffness norm, (b) Black diagram, (c) mastercurve of the phase angle, (d) shift factors for TTSP and (e) displacement gap amplitude at the interface

Table A.22 - 2S2P1D constants, DBN_{PDSC} constant φ_{NL} and WLF equation coefficients for sample REFC-2

K_{zz_00} (MPa)	K_{zz_0} (MPa)	k	h	δ	τ_{Kzz} (s)	β	φ_{NL}(°)	T_{ref} (°C)	C_1	C_2
4	3000	0.2	0.53	2.3	0.02	300	15	15	3.3	22.7

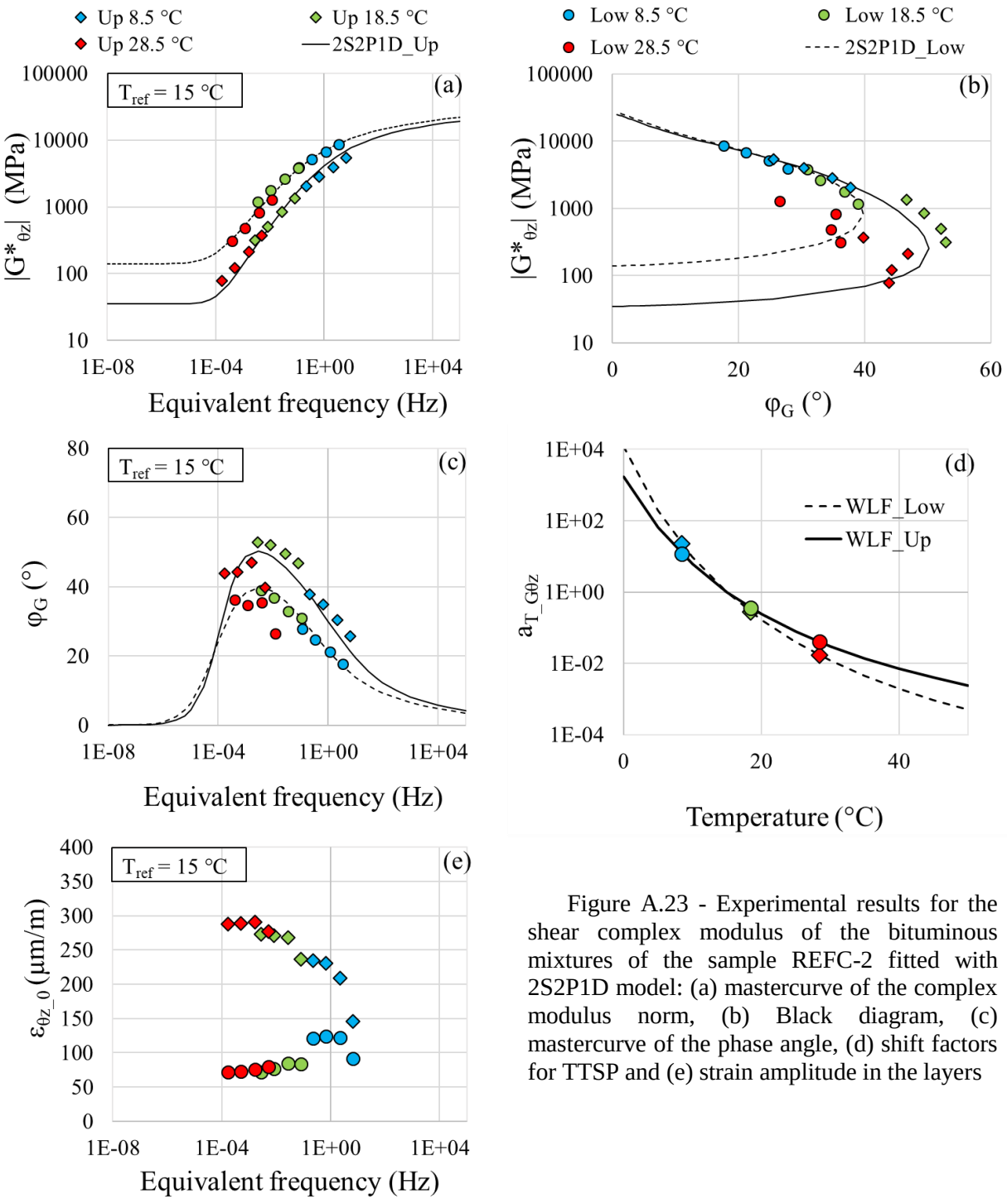

Figure A.23 - Experimental results for the shear complex modulus of the bituminous mixtures of the sample REFC-2 fitted with 2S2P1D model: (a) mastercurve of the complex modulus norm, (b) Black diagram, (c) mastercurve of the phase angle, (d) shift factors for TTSP and (e) strain amplitude in the layers

Table A.23 - 2S2P1D constants and WLF equation coefficients for sample REFC-2

Layer	Mixture	G_{00} (MPa)	G_0 (MPa)	k	h	δ	τ_G (s)	β	T_{ref} (°C)	C_1	C_2
Upper	BBSG3	35	26000	0.17	0.56	1.8	0.02	100	15	7.2	41.4
Lower	EME2	140	28000	0.17	0.55	1.9	0.1	160	15	5.7	41.5

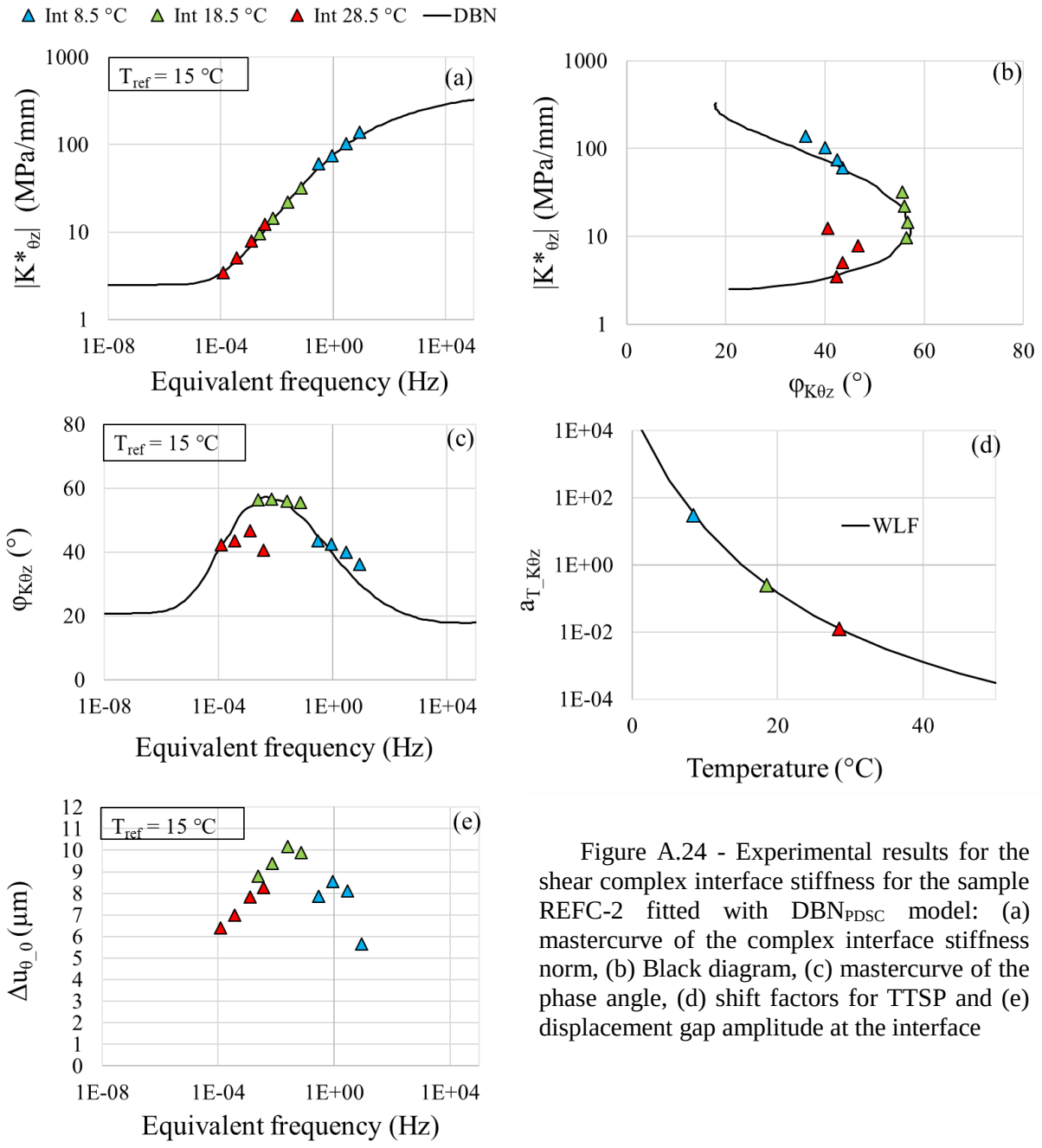

Figure A.24 - Experimental results for the shear complex interface stiffness for the sample REFC-2 fitted with DBN_{PDSC} model: (a) mastercurve of the complex interface stiffness norm, (b) Black diagram, (c) mastercurve of the phase angle, (d) shift factors for TTSP and (e) displacement gap amplitude at the interface

Table A.24 - 2S2P1D constants, DBN_{PDSC} constant φ_{NL} and WLF equation coefficients for sample REFC-2

K_{0z_00} (MPa)	K_{0z_0} (MPa)	k	h	δ	τ_{K0z} (s)	β	φ_{NL}(°)	T_{ref} (°C)	C_1	C_2
2.5	420	0.2	0.53	2.3	0.06	300	21	15	7.5	39.7

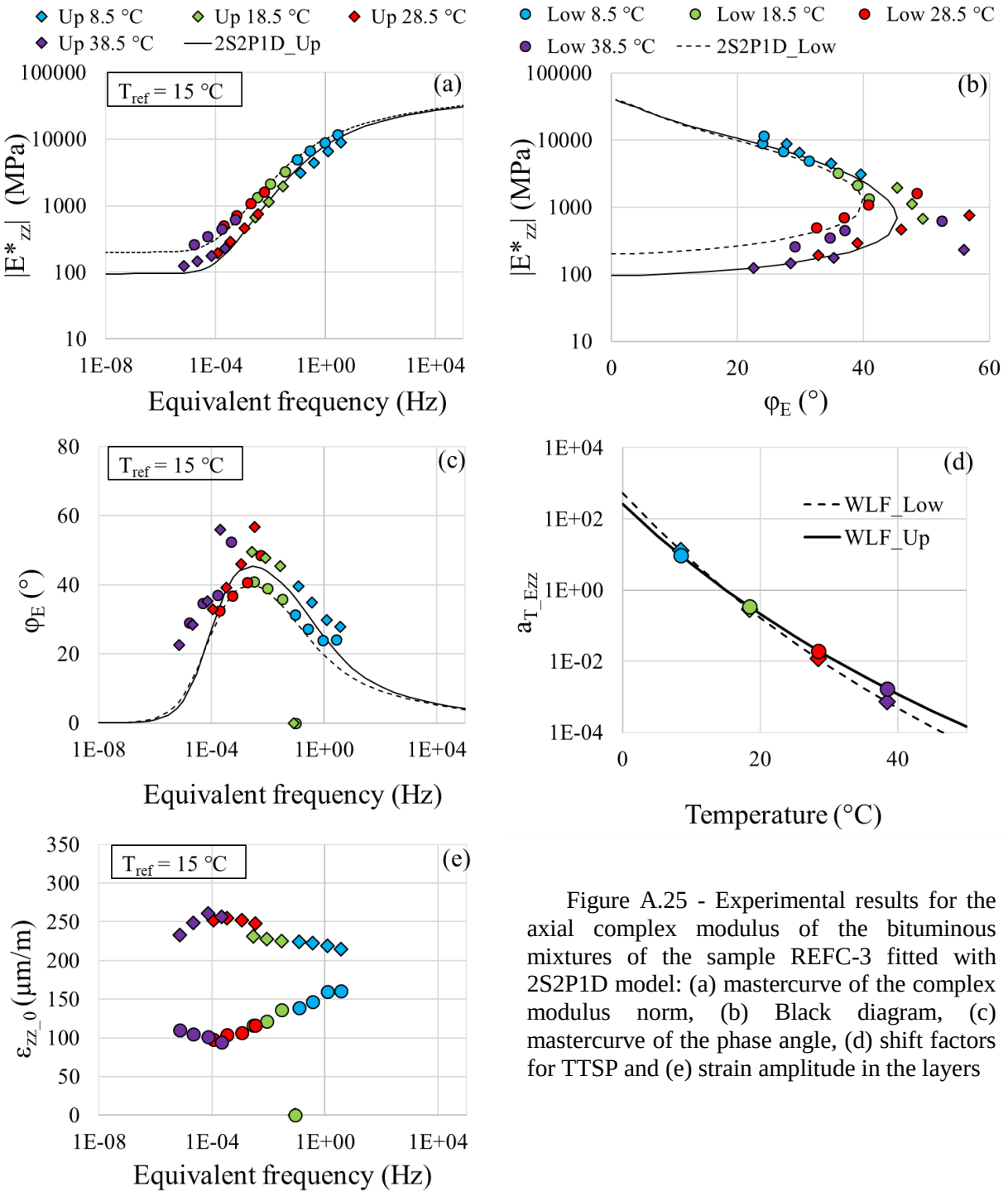

Figure A.25 - Experimental results for the axial complex modulus of the bituminous mixtures of the sample REFC-3 fitted with 2S2P1D model: (a) mastercurve of the complex modulus norm, (b) Black diagram, (c) mastercurve of the phase angle, (d) shift factors for TTSP and (e) strain amplitude in the layers

Table A.25 - 2S2P1D constants and WLF equation coefficients for sample REFC-3

Layer	Mixture	E_{00} (MPa)	E_0 (MPa)	k	h	δ	τ_E (s)	β	T_{ref} (°C)	C_1	C_2
Upper	BBSG3	95	41000	0.17	0.57	2.1	0.05	130	15	19.5	122.3
Lower	EME2	200	42000	0.17	0.57	2.4	0.15	150	15	17.3	122.5

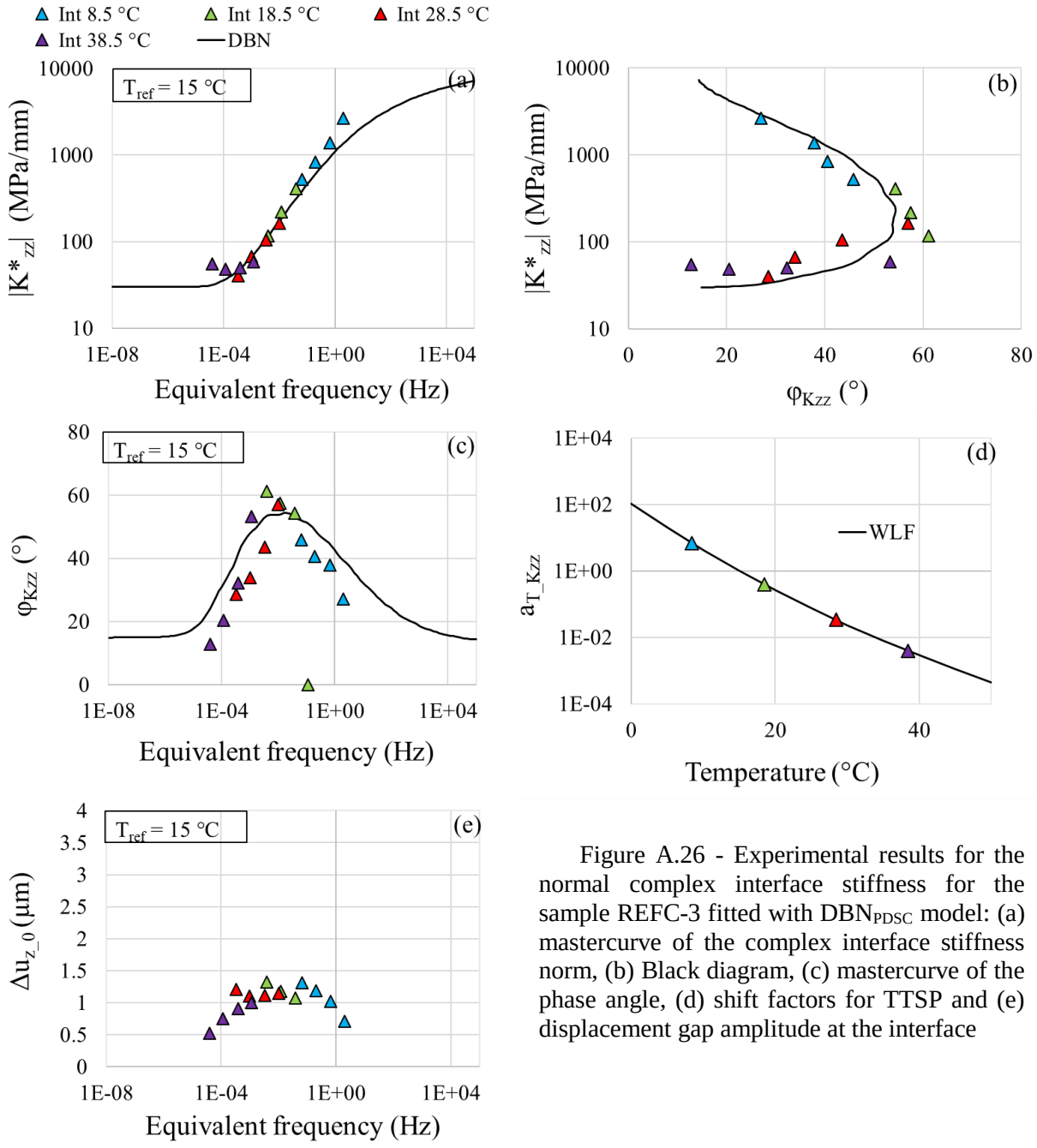

Figure A.26 - Experimental results for the normal complex interface stiffness for the sample REFC-3 fitted with DBN_{PDSC} model: (a) mastercurve of the complex interface stiffness norm, (b) Black diagram, (c) mastercurve of the phase angle, (d) shift factors for TTSP and (e) displacement gap amplitude at the interface

Table A.26 - 2S2P1D constants, DBN_{PDSC} constant φ_{NL} and WLF equation coefficients for sample REFC-3

K_{zz_00} (MPa)	K_{zz_0} (MPa)	k	h	δ	τ_{Kzz} (s)	β	φ_{NL}(°)	T_{ref} (°C)	C_1	C_2
30	10000	0.2	0.53	2.3	0.012	300	15	15	16.2	134.2

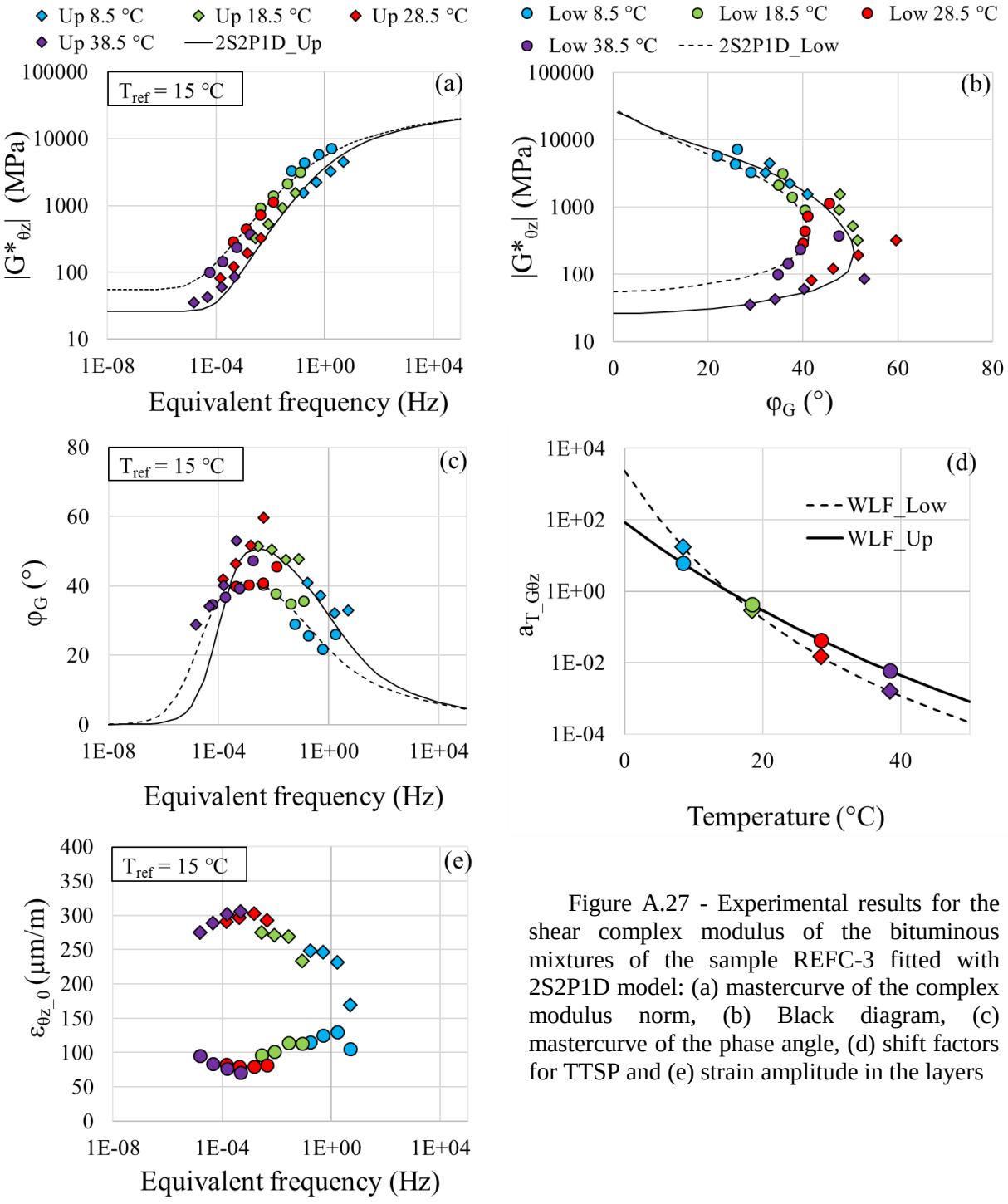

Figure A.27 - Experimental results for the shear complex modulus of the bituminous mixtures of the sample REFC-3 fitted with 2S2P1D model: (a) mastercurve of the complex modulus norm, (b) Black diagram, (c) mastercurve of the phase angle, (d) shift factors for TTSP and (e) strain amplitude in the layers

Table A.27 - 2S2P1D constants and WLF equation coefficients for sample REFC-3

Layer	Mixture	G_{00} (MPa)	G_0 (MPa)	k	h	δ	τ_G (s)	β	T_{ref} (°C)	C_1	C_2
Upper	BBSG3	26	27000	0.176	0.57	2	0.015	120	15	9.8	58.6
Lower	EME2	55	28000	0.17	0.54	2.5	0.07	400	15	14.3	126.6

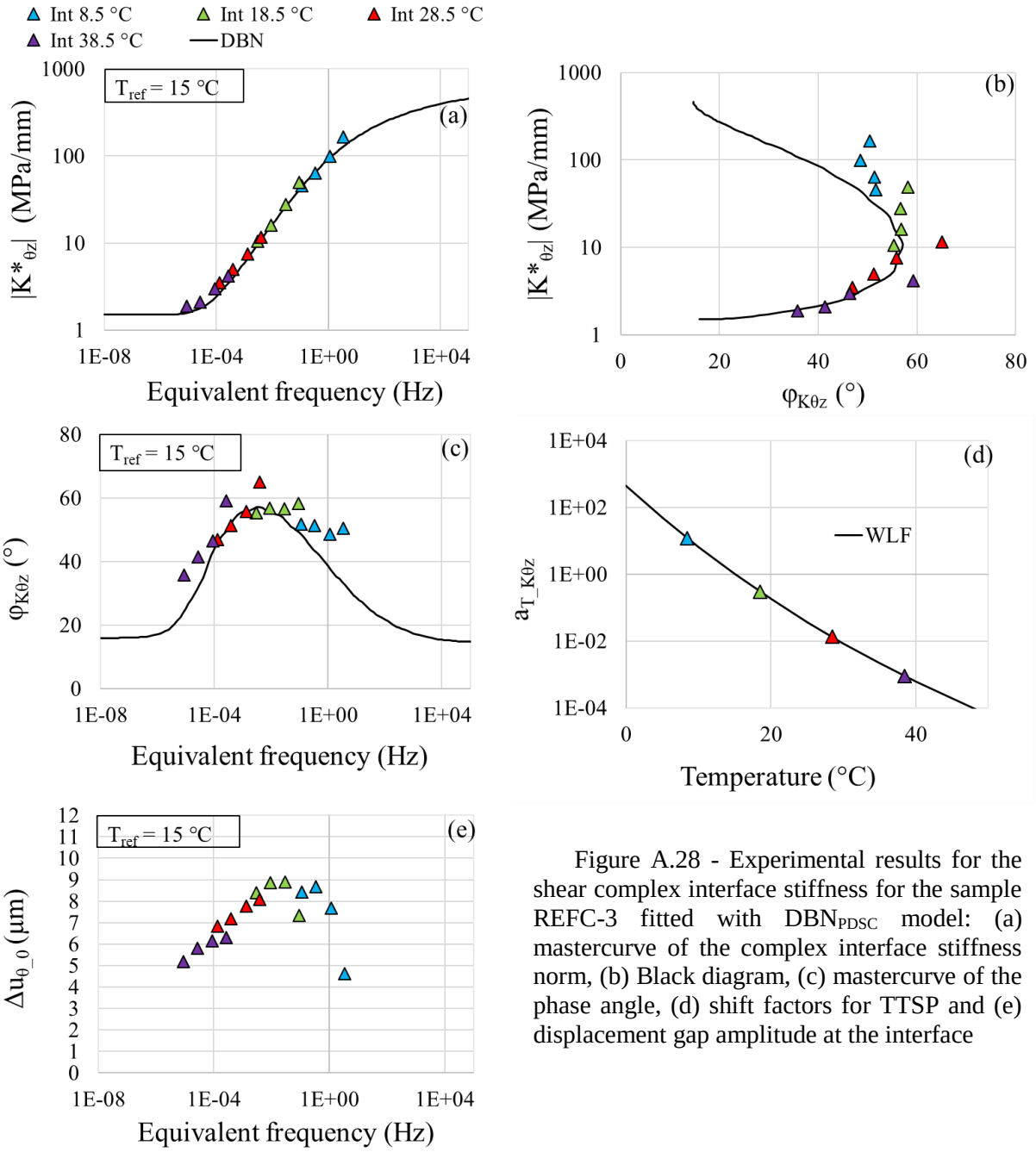

Figure A.28 - Experimental results for the shear complex interface stiffness for the sample REFC-3 fitted with DBN_{PDSC} model: (a) mastercurve of the complex interface stiffness norm, (b) Black diagram, (c) mastercurve of the phase angle, (d) shift factors for TTSP and (e) displacement gap amplitude at the interface

Table A.28 - 2S2P1D constants, DBN_{PDSC} constant φ_{NL} and WLF equation coefficients for sample REFC-3

K_{0z_00} (MPa)	K_{0z_0} (MPa)	k	h	δ	τ_{K0z} (s)	β	φ_{NL}(°)	T_{ref} (°C)	C_1	C_2
1.5	600	0.2	0.53	2.3	0.036	300	16	15	12.5	97.8

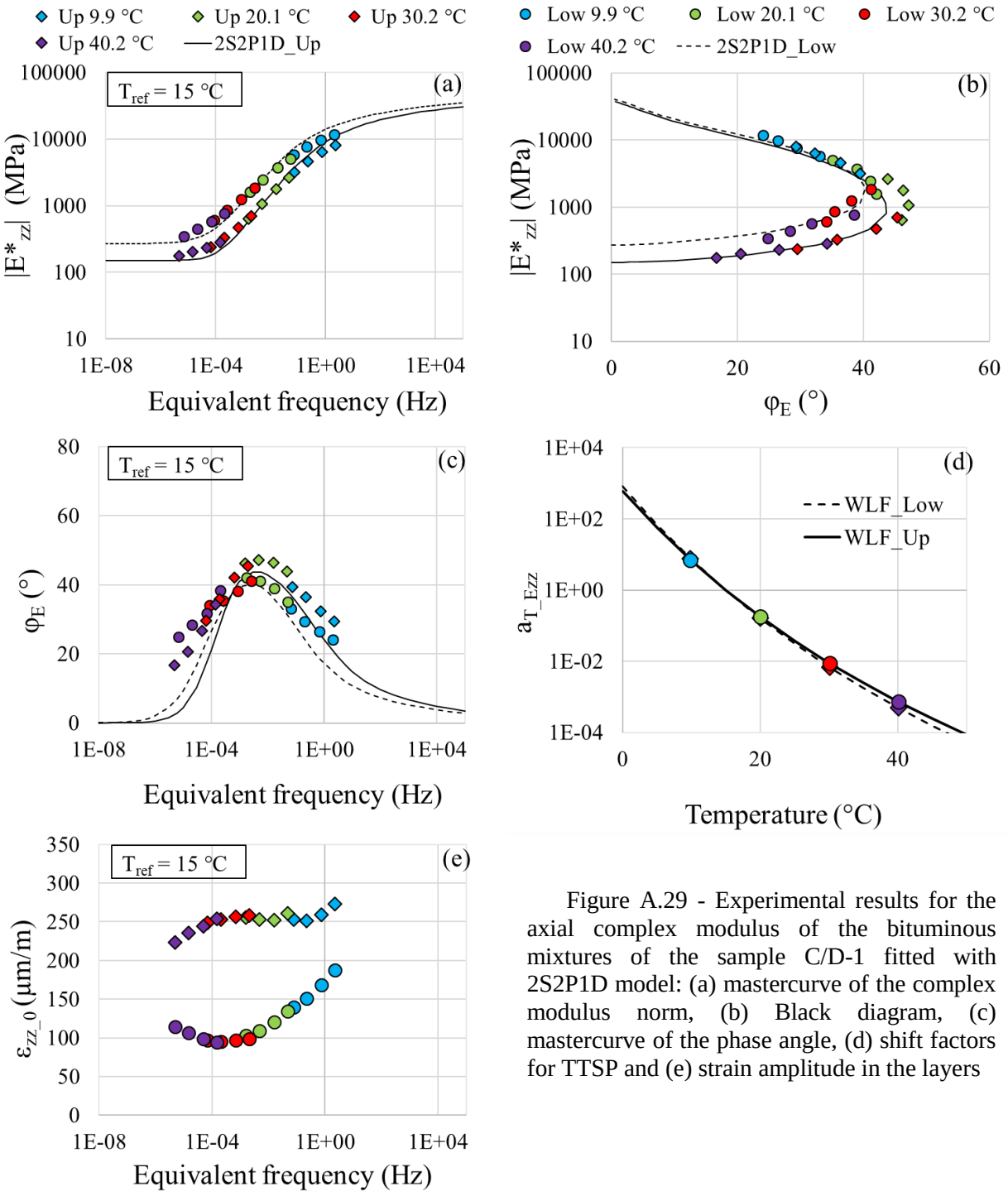

Figure A.29 - Experimental results for the axial complex modulus of the bituminous mixtures of the sample C/D-1 fitted with 2S2P1D model: (a) mastercurve of the complex modulus norm, (b) Black diagram, (c) mastercurve of the phase angle, (d) shift factors for TTSP and (e) strain amplitude in the layers

Table A.29 - 2S2P1D constants and WLF equation coefficients for sample C/D-1

Layer	Mixture	E_{00} (MPa)	E_0 (MPa)	k	h	δ	τ_E (s)	β	T_{ref} (°C)	C_1	C_2
Upper	BBSG3	150	39000	0.17	0.57	1.8	0.07	100	15	16.3	98.9
Lower	GB5	270	42000	0.17	0.59	1.8	0.35	200	15	15.5	99.0

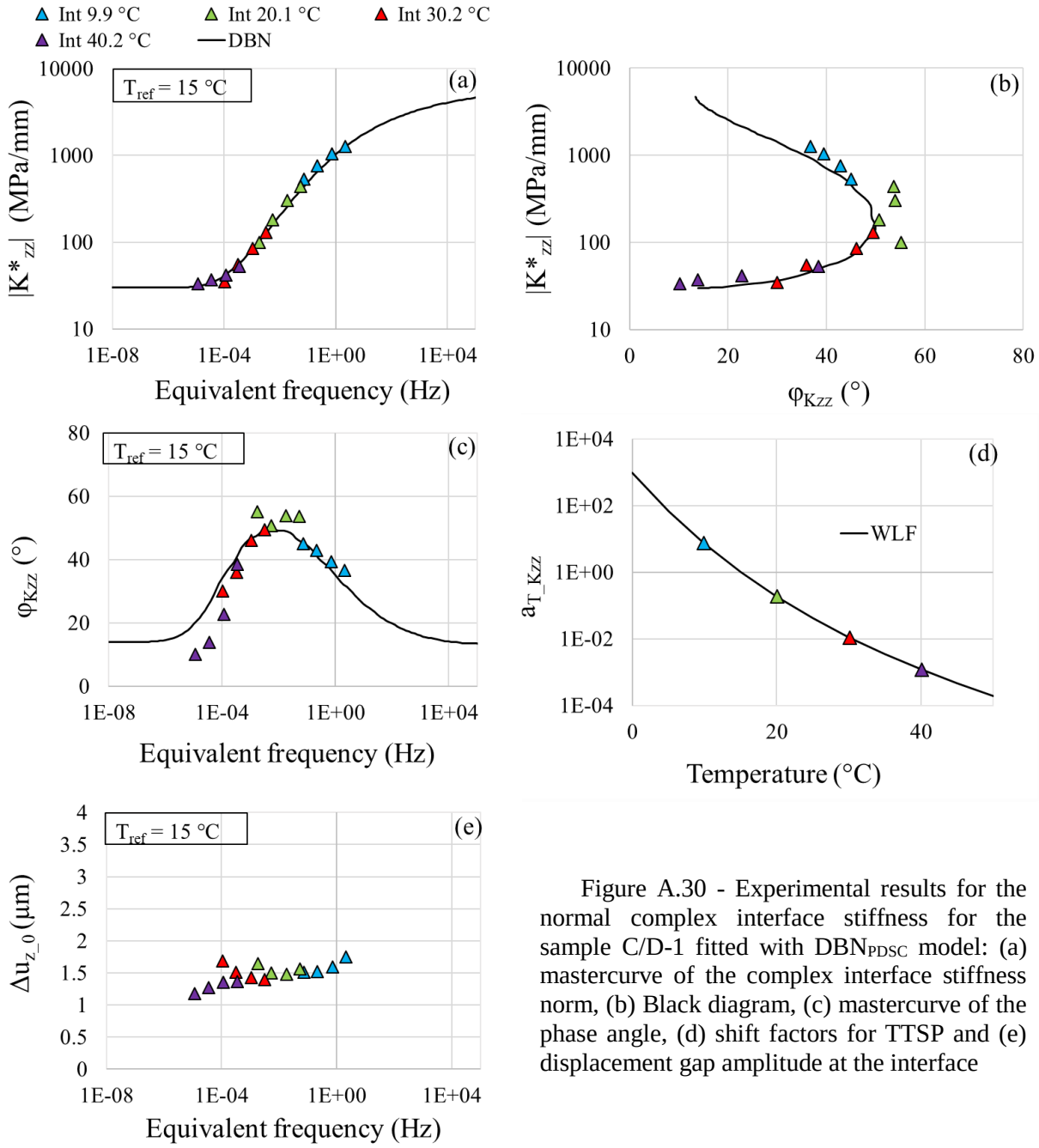

Figure A.30 - Experimental results for the normal complex interface stiffness for the sample C/D-1 fitted with DBN_{PDSC} model: (a) mastercurve of the complex interface stiffness norm, (b) Black diagram, (c) mastercurve of the phase angle, (d) shift factors for TTSP and (e) displacement gap amplitude at the interface

Table A.30 - 2S2P1D constants, DBN_{PDSC} constant φ_{NL} and WLF equation coefficients for sample C/D-1

K_{zz_00} (MPa)	K_{zz_0} (MPa)	k	h	δ	τ_{Kzz} (s)	β	φ_{NL}(°)	T_{ref} (°C)	C_1	C_2
30	6000	0.2	0.53	2.3	0.05	300	14	15	11.3	71.7

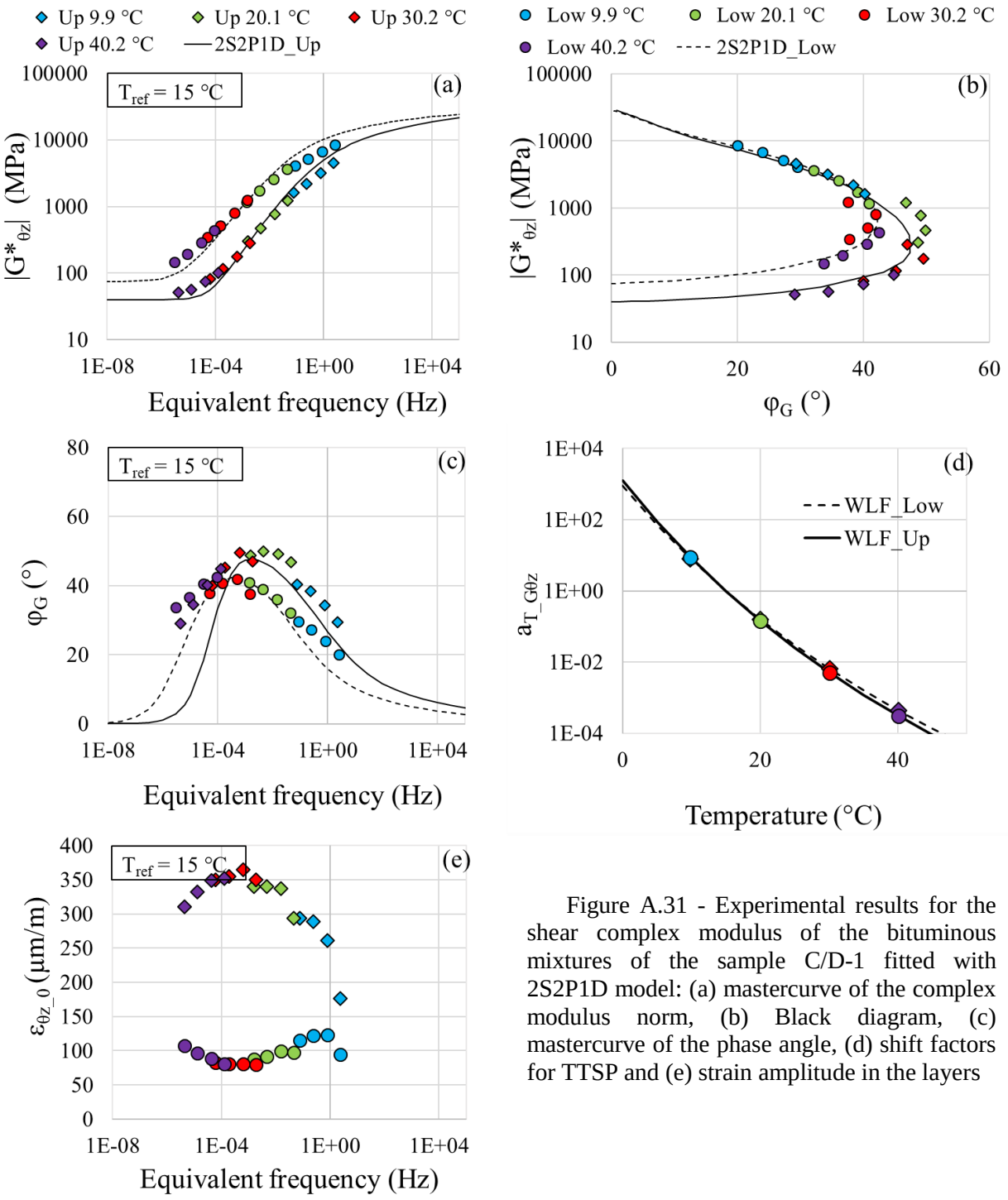

Figure A.31 - Experimental results for the shear complex modulus of the bituminous mixtures of the sample C/D-1 fitted with 2S2P1D model: (a) mastercurve of the complex modulus norm, (b) Black diagram, (c) mastercurve of the phase angle, (d) shift factors for TTSP and (e) strain amplitude in the layers

Table A.31 - 2S2P1D constants and WLF equation coefficients for sample C/D-1

Layer	Mixture	G_{00} (MPa)	G_0 (MPa)	k	h	δ	τ_G (s)	β	T_{ref} (°C)	C_1	C_2
Upper	BBSG3	40	30000	0.17	0.56	2.2	0.03	150	15	16.6	98.9
Lower	GB5	75	29000	0.17	0.56	1.8	0.5	400	15	17.3	98.8

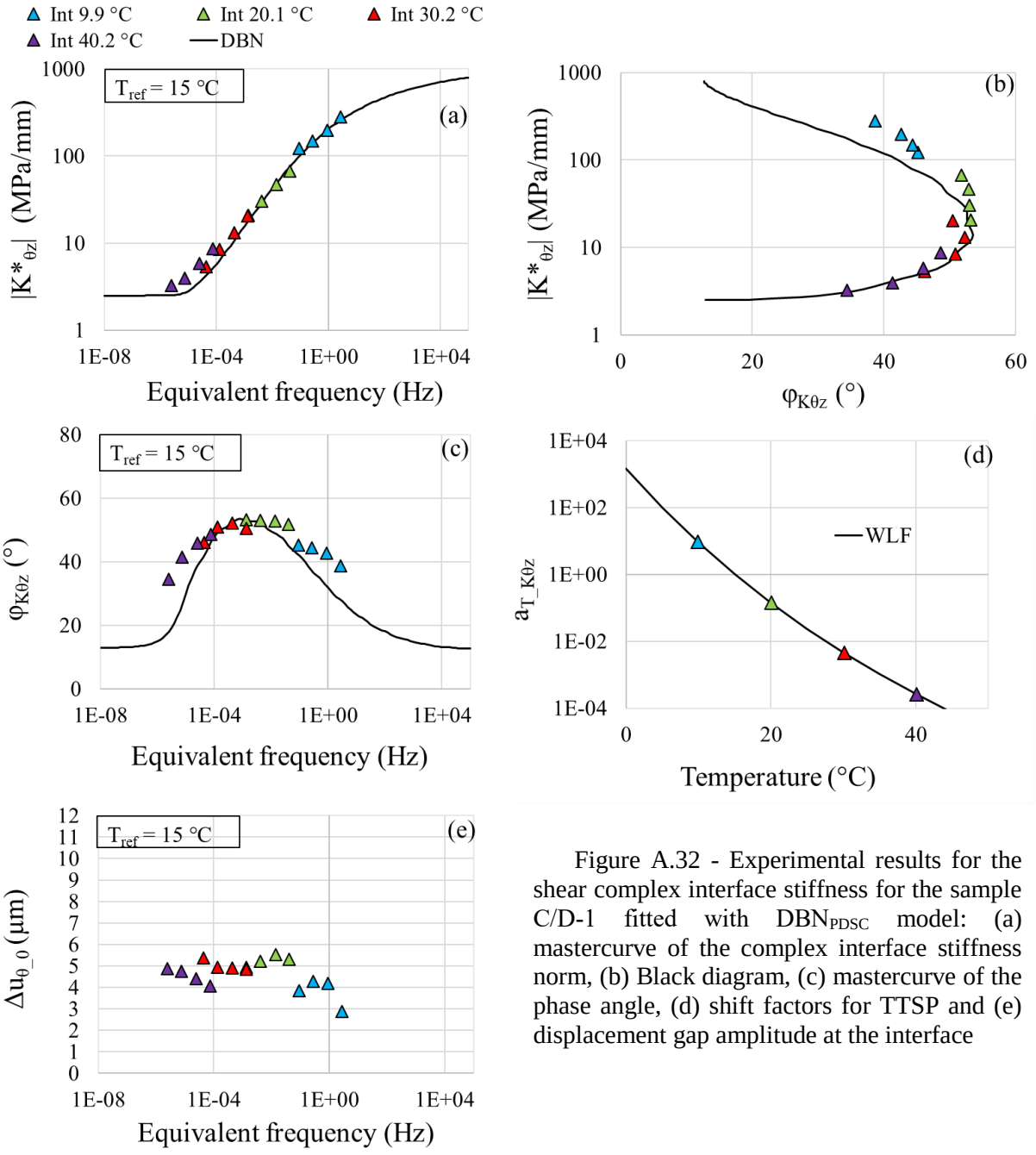

Figure A.32 - Experimental results for the shear complex interface stiffness for the sample C/D-1 fitted with DBN_{PDSC} model: (a) mastercurve of the complex interface stiffness norm, (b) Black diagram, (c) mastercurve of the phase angle, (d) shift factors for TTSP and (e) displacement gap amplitude at the interface

Table A.32 - 2S2P1D constants, DBN_{PDSC} constant φ_{NL} and WLF equation coefficients for sample C/D-1

K_{0z_00} (MPa)	K_{0z_0} (MPa)	k	h	δ	τ_{K0z} (s)	β	φ_{NL}(°)	T_{ref} (°C)	C_1	C_2
2.5	1000	0.2	0.53	2.3	0.1	300	13	15	17.7	98.7

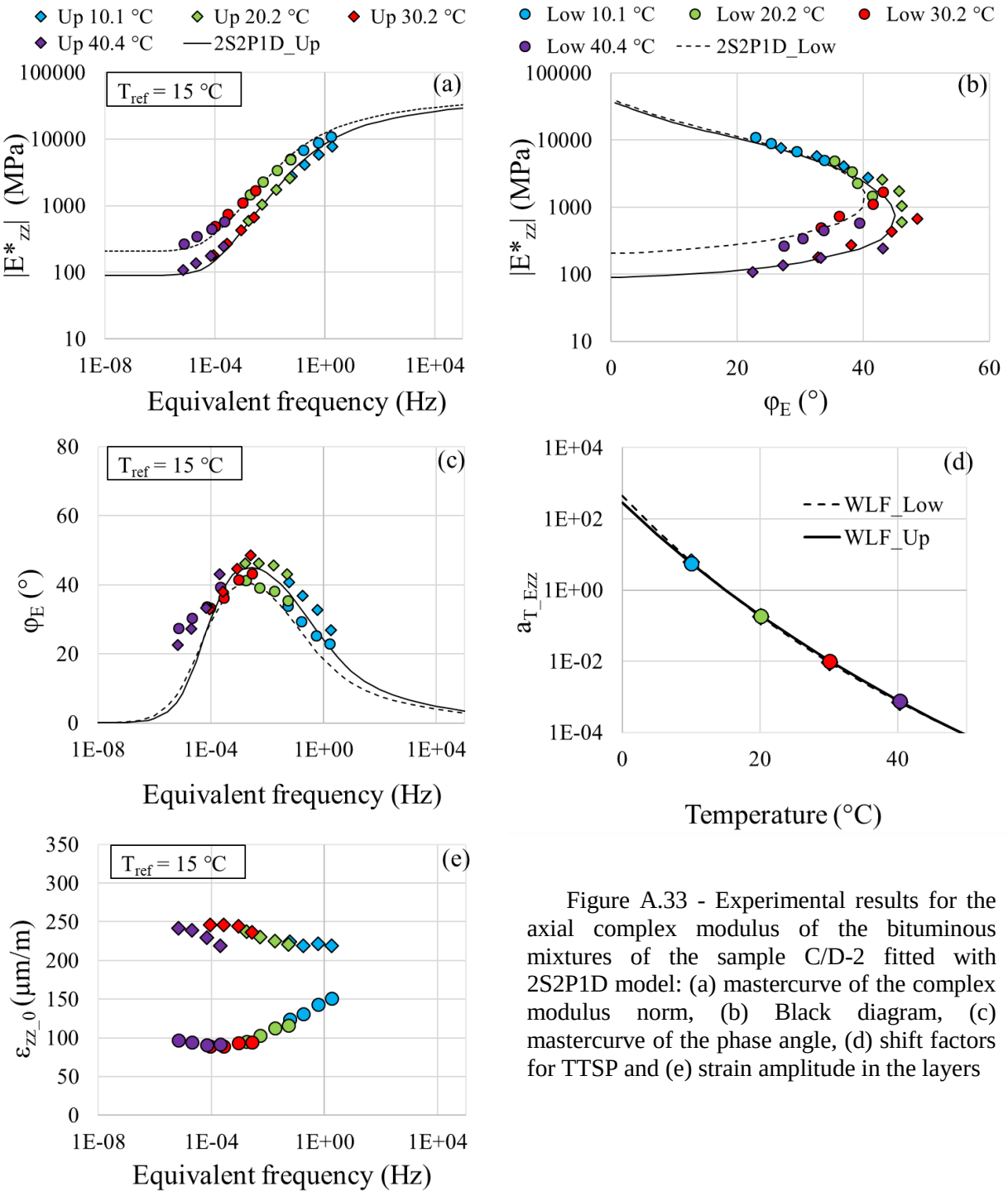

Figure A.33 - Experimental results for the axial complex modulus of the bituminous mixtures of the sample C/D-2 fitted with 2S2P1D model: (a) mastercurve of the complex modulus norm, (b) Black diagram, (c) mastercurve of the phase angle, (d) shift factors for TTSP and (e) strain amplitude in the layers

Table A.33 - 2S2P1D constants and WLF equation coefficients for sample C/D-2

Layer	Mixture	E_{00} (MPa)	E_0 (MPa)	k	h	δ	τ_E (s)	β	T_{ref} (°C)	C_1	C_2
Upper	BBSG3	90	37000	0.17	0.57	1.8	0.07	150	15	17.0	111.4
Lower	GB5	205	40000	0.17	0.57	1.8	0.25	200	15	20.3	138.9

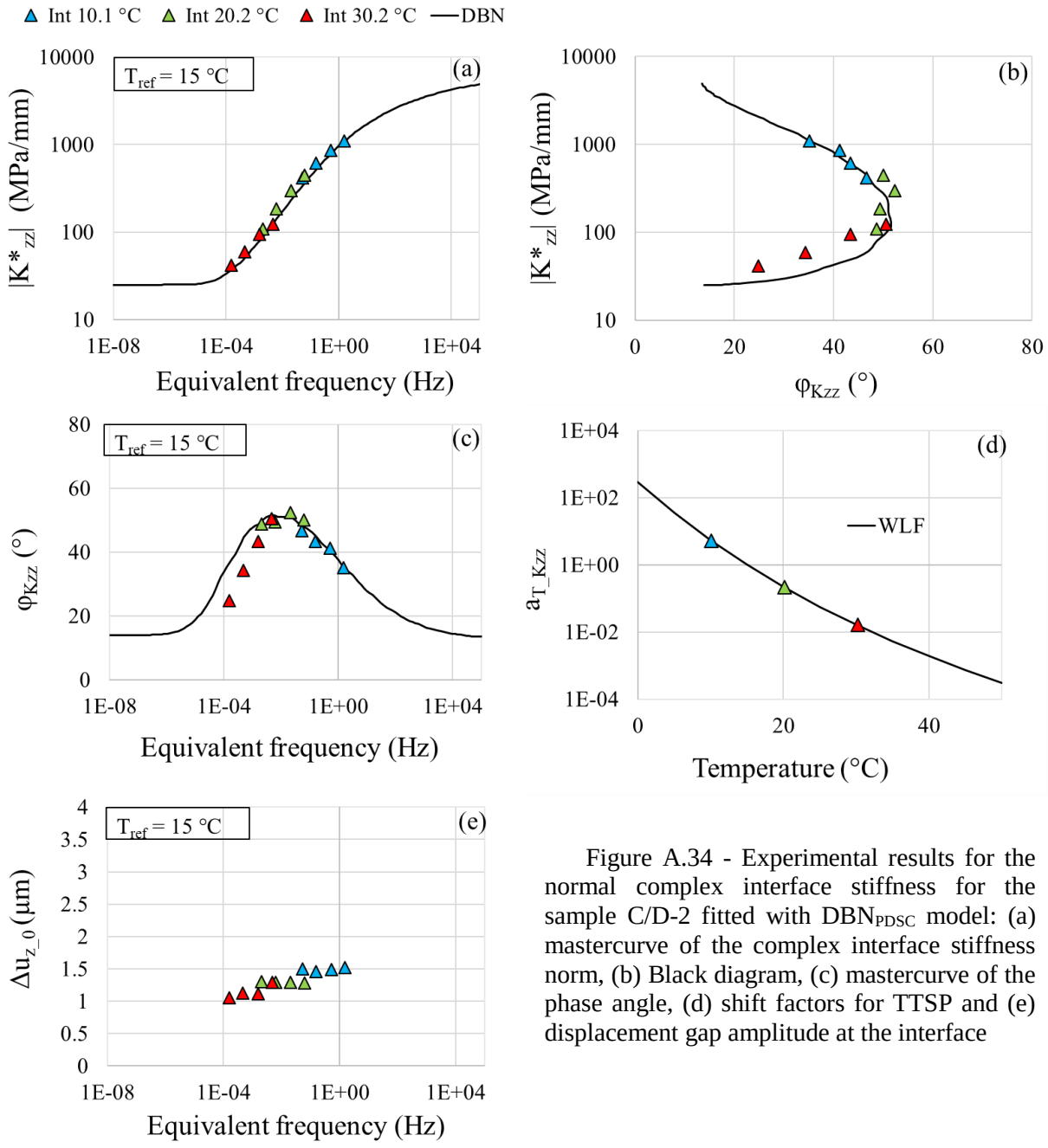

Figure A.34 - Experimental results for the normal complex interface stiffness for the sample C/D-2 fitted with DBN_{PDSC} model: (a) mastercurve of the complex interface stiffness norm, (b) Black diagram, (c) mastercurve of the phase angle, (d) shift factors for TTSP and (e) displacement gap amplitude at the interface

Table A.34 - 2S2P1D constants, DBN_{PDSC} constant φ_{NL} and WLF equation coefficients for sample C/D-2

K_{zz_00} (MPa)	K_{zz_0} (MPa)	k	h	δ	τ_{Kzz} (s)	β	φ_{NL}(°)	T_{ref} (°C)	C_1	C_2
25	6500	0.2	0.53	2.3	0.03	300	14	15	12.8	92.9

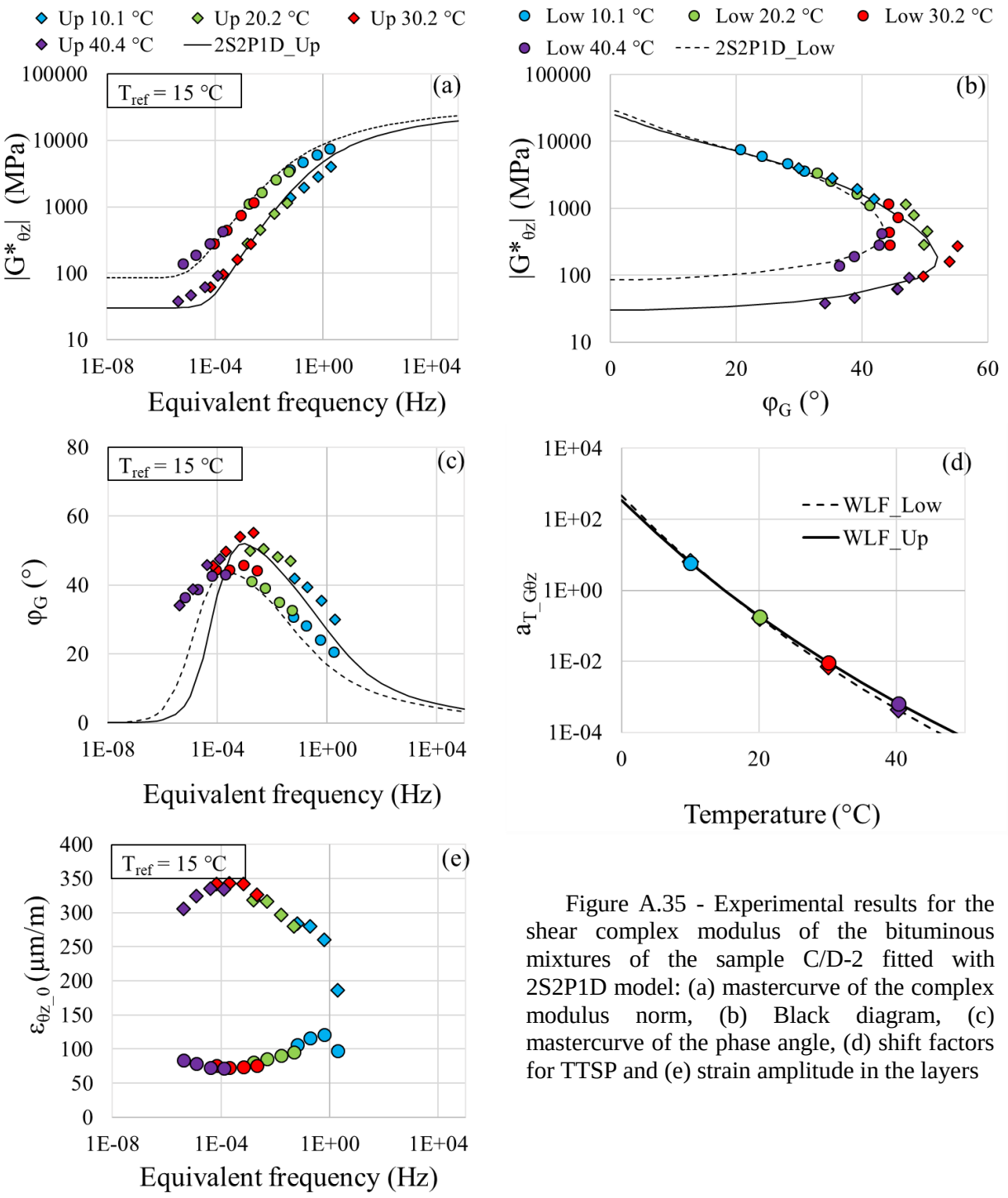

Figure A.35 - Experimental results for the shear complex modulus of the bituminous mixtures of the sample C/D-2 fitted with 2S2P1D model: (a) mastercurve of the complex modulus norm, (b) Black diagram, (c) mastercurve of the phase angle, (d) shift factors for TTSP and (e) strain amplitude in the layers

Table A.35 - 2S2P1D constants and WLF equation coefficients for sample C/D-2

Layer	Mixture	G_{00} (MPa)	G_0 (MPa)	k	h	δ	τ_G (s)	β	T_{ref} (°C)	C_1	C_2
Upper	BBSG3	30	26000	0.17	0.54	1.8	0.03	100	15	21.4	134.9
Lower	GB5	85	30000	0.165	0.53	2.1	0.3	130	15	20.2	135.1

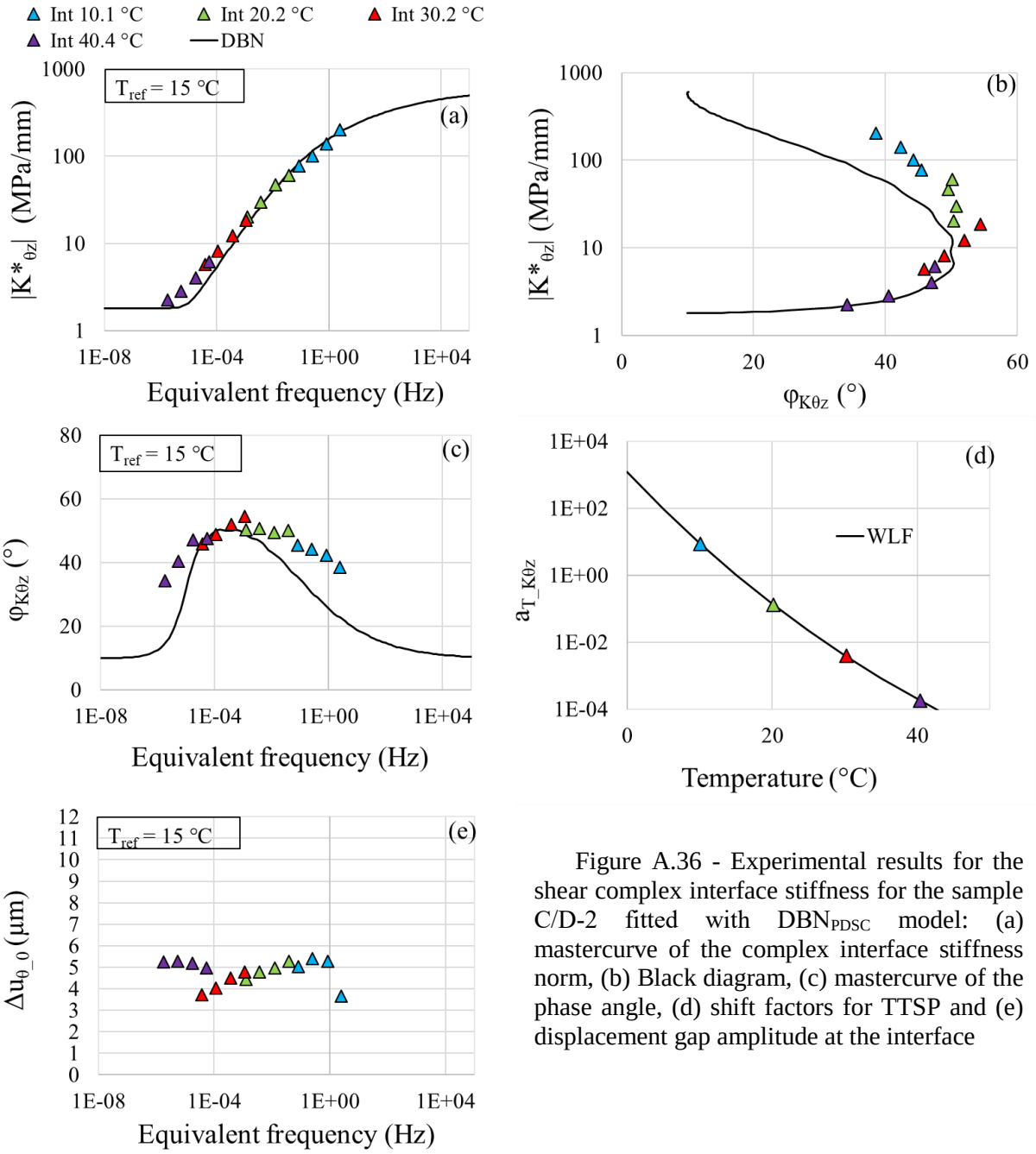

Figure A.36 - Experimental results for the shear complex interface stiffness for the sample C/D-2 fitted with DBN_{PDSC} model: (a) mastercurve of the complex interface stiffness norm, (b) Black diagram, (c) mastercurve of the phase angle, (d) shift factors for TTSP and (e) displacement gap amplitude at the interface

Table A.36- 2S2P1D constants, DBN_{PDSC} constant φ_{NL} and WLF equation coefficients for sample C/D-2

K_{0z_00} (MPa)	K_{0z_0} (MPa)	k	h	δ	τ_{K0z} (s)	β	φ_{NL}(°)	T_{ref} (°C)	C_1	C_2
1.8	600	0.2	0.53	2.3	0.3	300	10	15	21.0	116.9

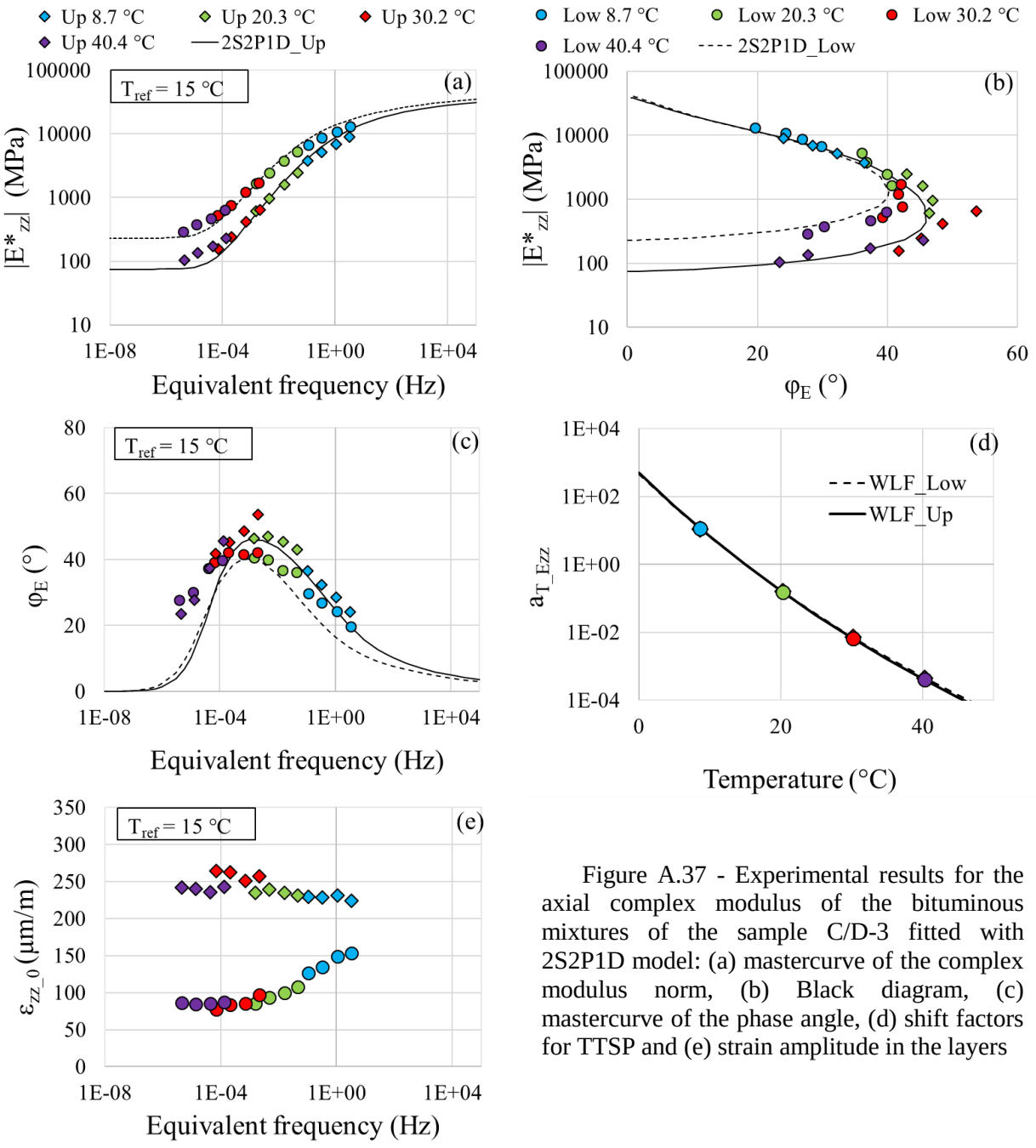

Figure A.37 - Experimental results for the axial complex modulus of the bituminous mixtures of the sample C/D-3 fitted with 2S2P1D model: (a) mastercurve of the complex modulus norm, (b) Black diagram, (c) mastercurve of the phase angle, (d) shift factors for TTSP and (e) strain amplitude in the layers

Table A.37 - 2S2P1D constants and WLF equation coefficients for sample C/D-3

Layer	Mixture	E_{00} (MPa)	E_0 (MPa)	k	h	δ	τ_E (s)	β	T_{ref} (°C)	C_1	C_2
Upper	BBSG3	75	40000	0.176	0.56	1.8	0.06	150	15	20.8	131.9
Lower	GB5	230	43000	0.17	0.56	2	0.4	120	15	21.1	131.9

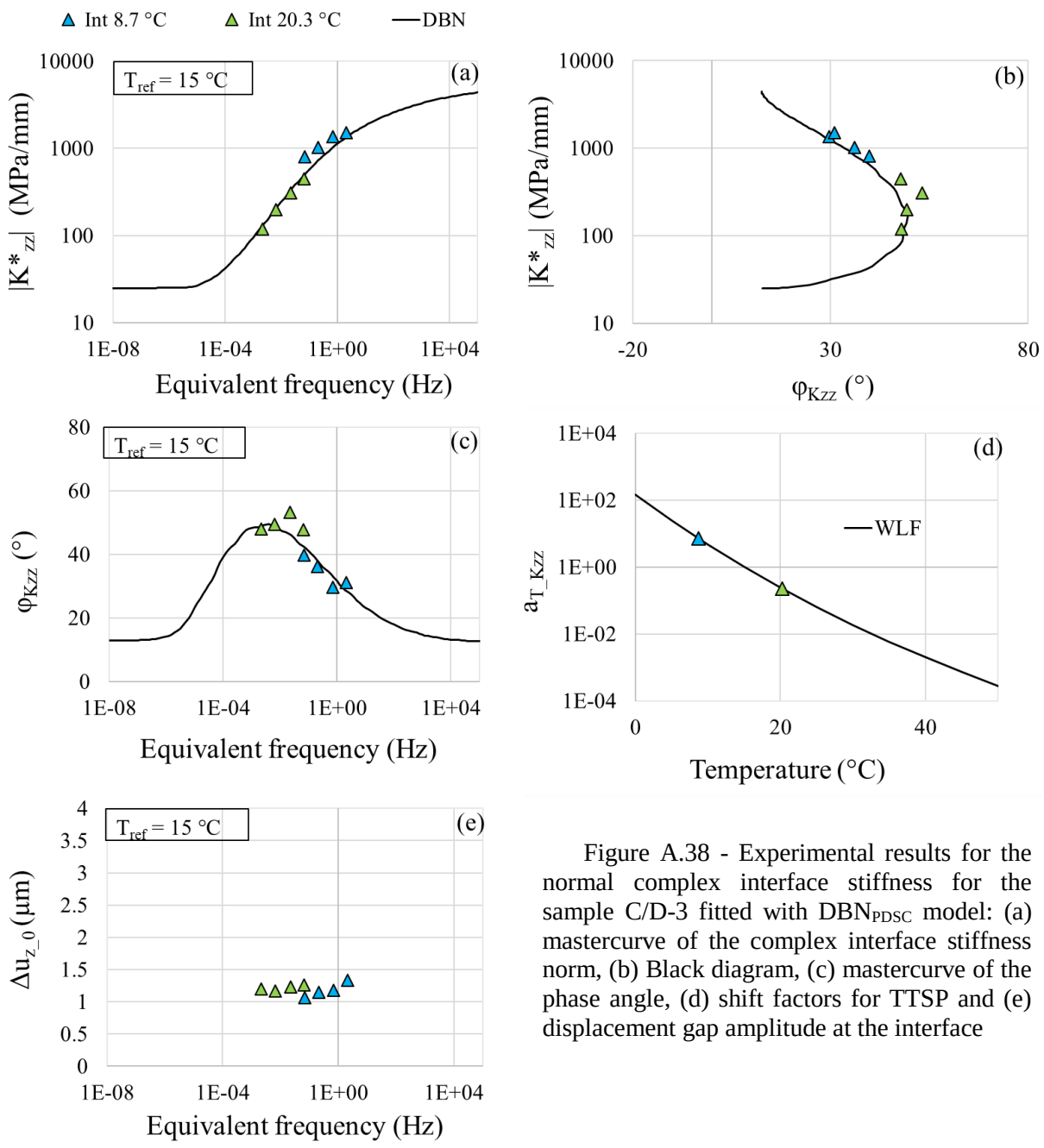

Figure A.38 - Experimental results for the normal complex interface stiffness for the sample C/D-3 fitted with DBN_{PDSC} model: (a) mastercurve of the complex interface stiffness norm, (b) Black diagram, (c) mastercurve of the phase angle, (d) shift factors for TTSP and (e) displacement gap amplitude at the interface

Table A.38 - 2S2P1D constants, DBN_{PDSC} constant φ_{NL} and WLF equation coefficients for sample C/D-3

K_{zz_00} (MPa)	K_{zz_0} (MPa)	k	h	δ	τ_{Kzz} (s)	β	φ_{NL}(°)	T_{ref} (°C)	C_1	C_2
25	5500	0.2	0.53	2.3	0.1	300	13	15	17.0	132.5

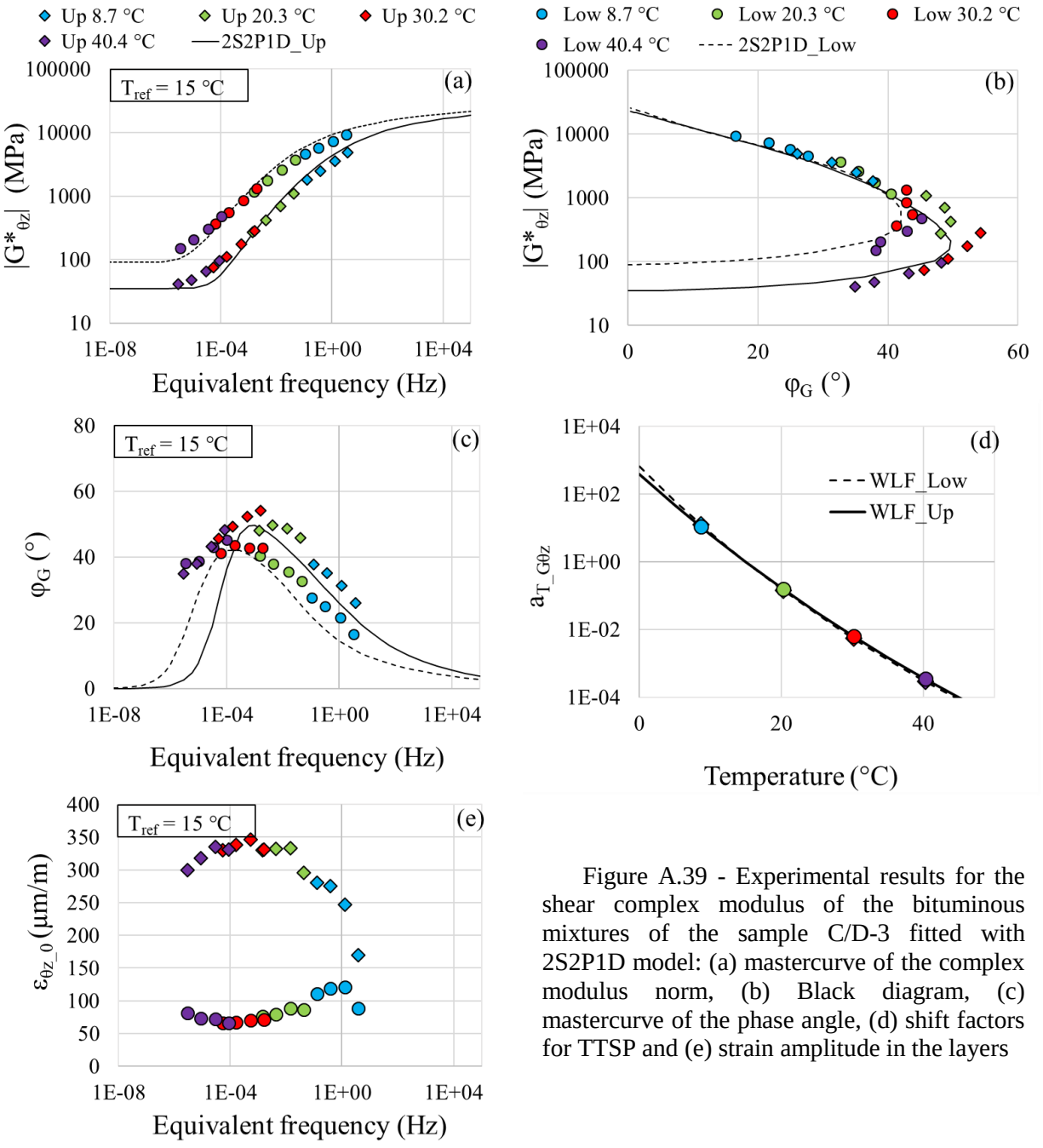

Figure A.39 - Experimental results for the shear complex modulus of the bituminous mixtures of the sample C/D-3 fitted with 2S2P1D model: (a) mastercurve of the complex modulus norm, (b) Black diagram, (c) mastercurve of the phase angle, (d) shift factors for TTSP and (e) strain amplitude in the layers

Table A.39 - 2S2P1D constants and WLF equation coefficients for sample C/D-3

Layer	Mixture	G_{00} (MPa)	G_0 (MPa)	k	h	δ	τ_G (s)	β	T_{ref} (°C)	C_1	C_2
Upper	BBSG3	35	23000	0.2	0.53	1.9	0.04	100	15	21.9	131.7
Lower	GB5	90	26000	0.17	0.54	2	0.8	130	15	26.2	166.4

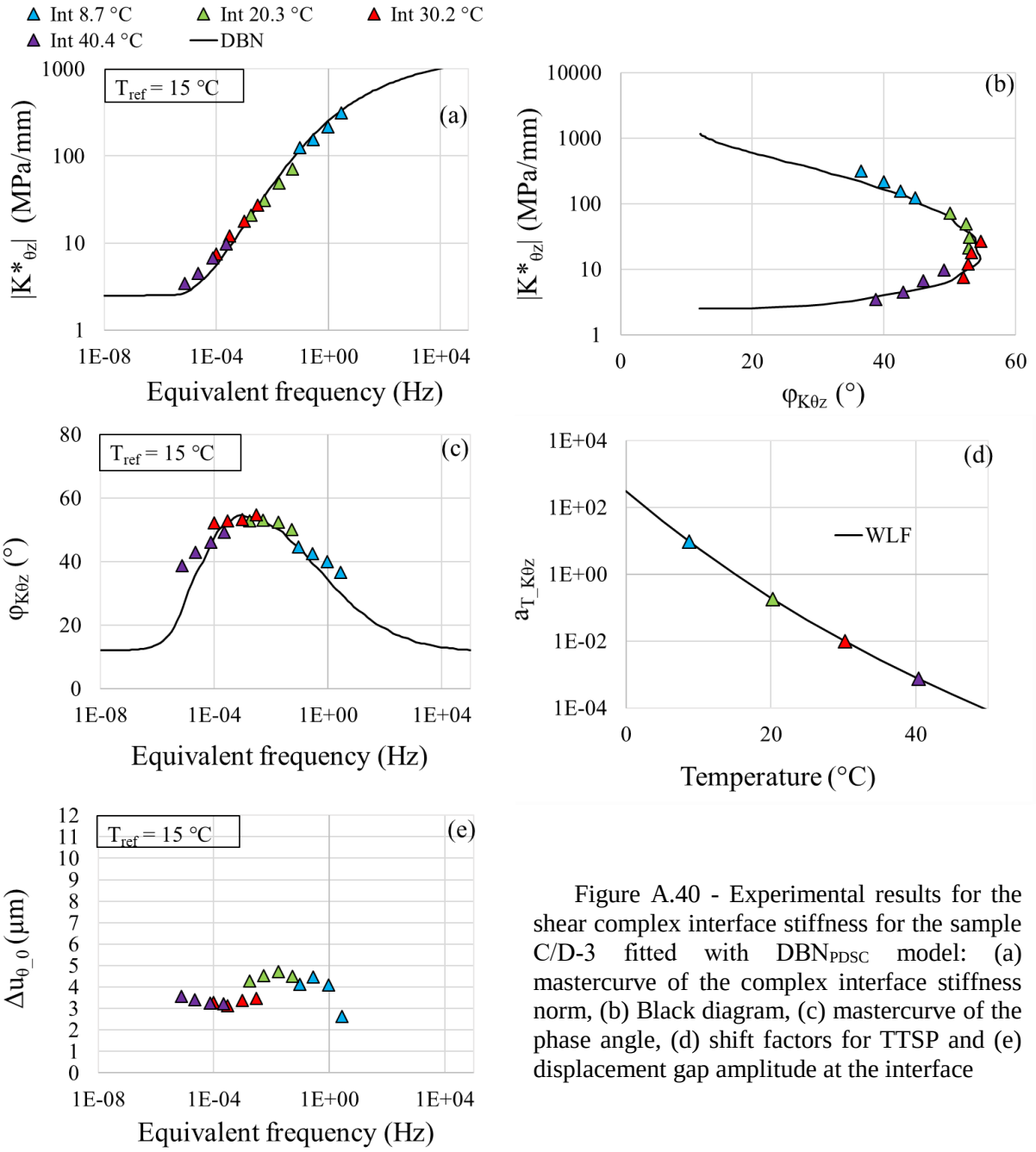

Figure A.40 - Experimental results for the shear complex interface stiffness for the sample C/D-3 fitted with DBN_{PDSC} model: (a) mastercurve of the complex interface stiffness norm, (b) Black diagram, (c) mastercurve of the phase angle, (d) shift factors for TTSP and (e) displacement gap amplitude at the interface

Table A.40 - 2S2P1D constants, DBN_{PDSC} constant φ_{NL} and WLF equation coefficients for sample C/D-3

$K_{\theta z\_00}$ (MPa)	$K_{\theta z\_0}$ (MPa)	k	h	δ	$\tau_{K\theta z}$ (s)	β	φ_{NL}(°)	T_{ref} (°C)	C_1	C_2
2.5	1500	0.2	0.53	2.3	0.05	300	12	15	19.4	132.3

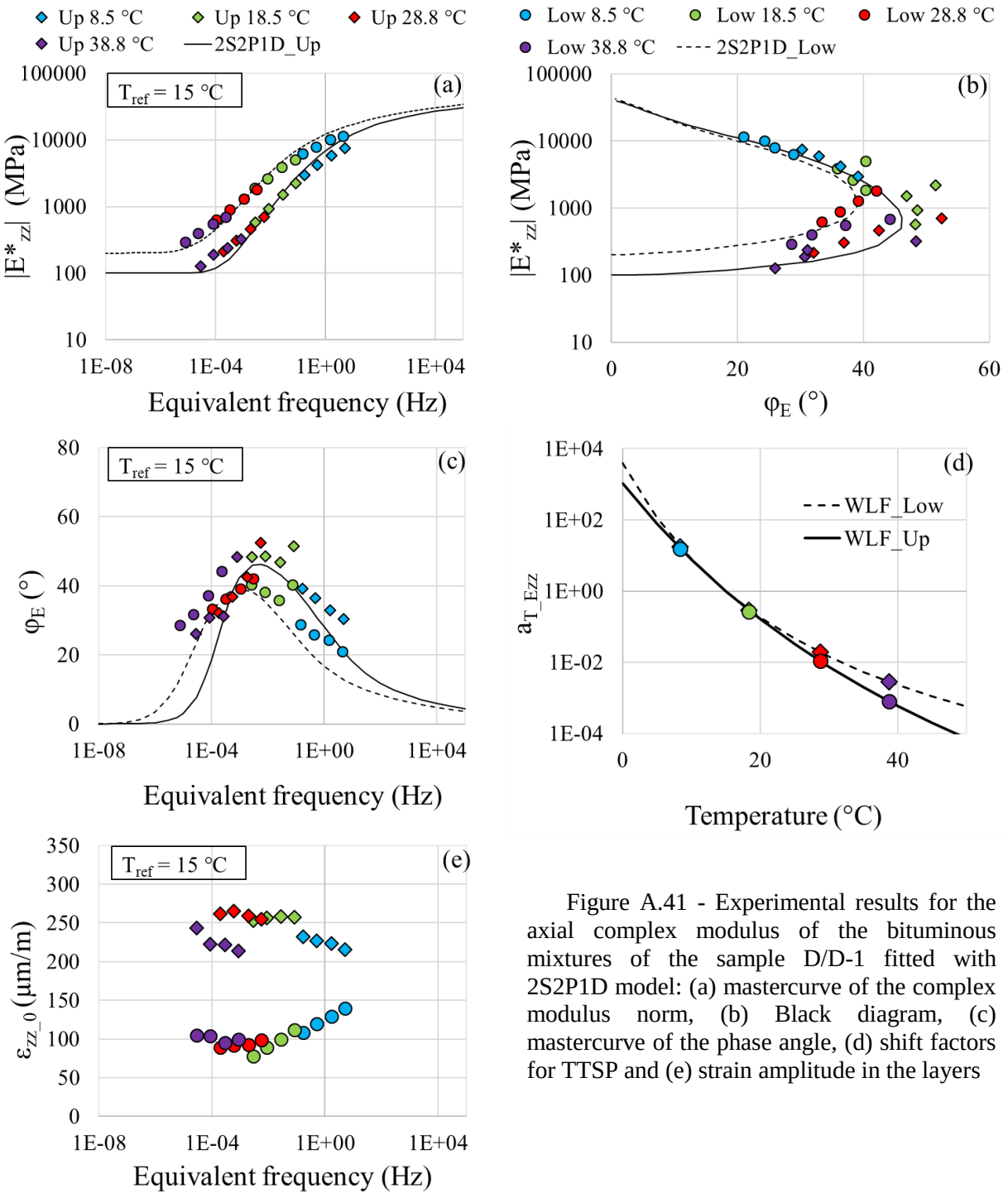

Figure A.41 - Experimental results for the axial complex modulus of the bituminous mixtures of the sample D/D-1 fitted with 2S2P1D model: (a) mastercurve of the complex modulus norm, (b) Black diagram, (c) mastercurve of the phase angle, (d) shift factors for TTSP and (e) strain amplitude in the layers

Table A.41 - 2S2P1D constants and WLF equation coefficients for sample D/D-1

Layer	Mixture	E_{00} (MPa)	E_0 (MPa)	k	h	δ	τ_E (s)	β	T_{ref} (°C)	C_1	C_2
Upper	BB5	100	42000	0.17	0.56	2	0.025	100	15	7.5	46.2
Lower	GB5	200	44000	0.17	0.57	2.5	0.35	250	15	14.4	86.3

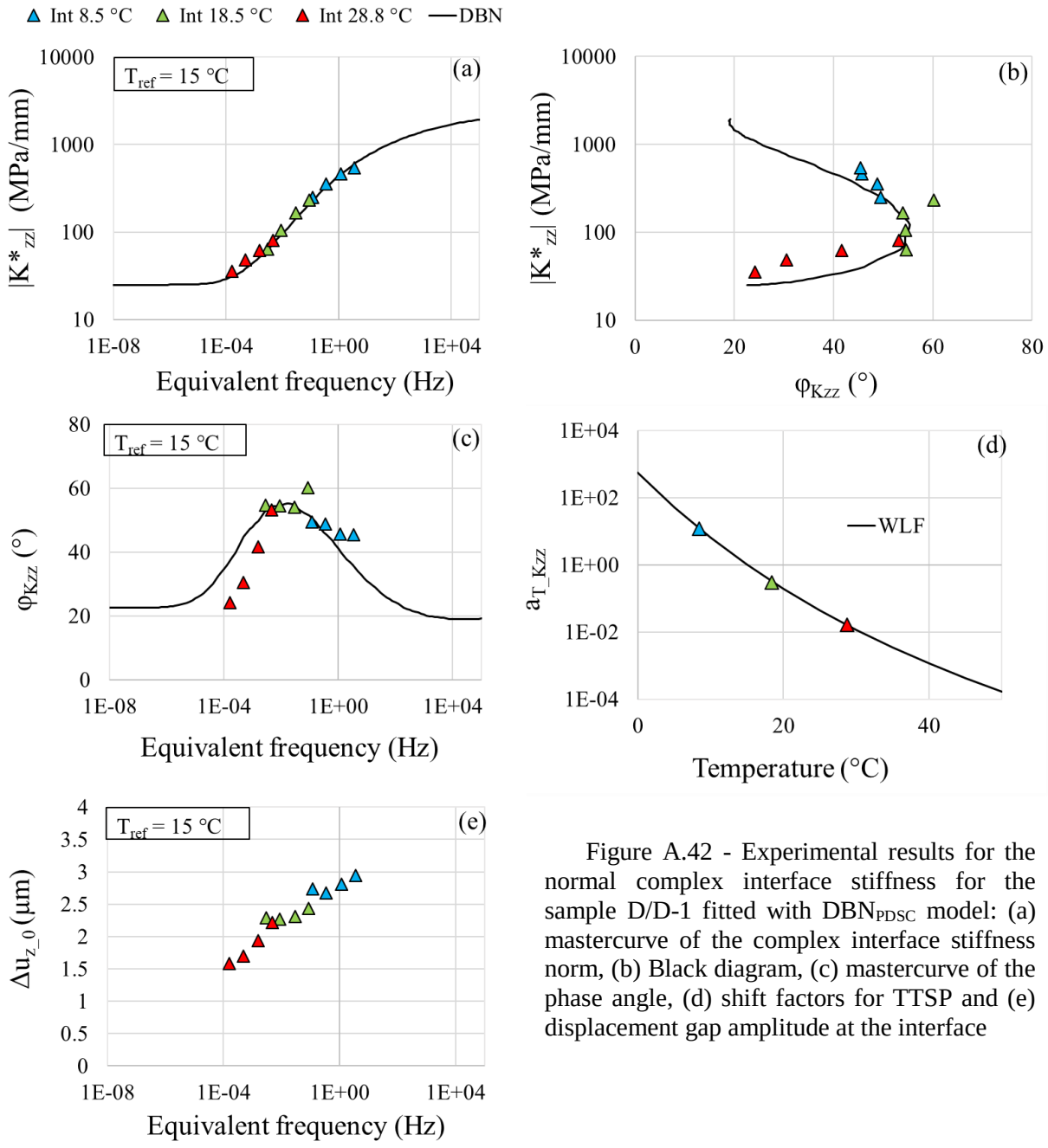

Figure A.42 - Experimental results for the normal complex interface stiffness for the sample D/D-1 fitted with DBN_{PDSC} model: (a) mastercurve of the complex interface stiffness norm, (b) Black diagram, (c) mastercurve of the phase angle, (d) shift factors for TTSP and (e) displacement gap amplitude at the interface

Table A.42 - 2S2P1D constants, DBN_{PDSC} constant φ_{NL} and WLF equation coefficients for sample D/D-1

K_{zz_00} (MPa)	K_{zz_0} (MPa)	k	h	δ	τ_{Kzz} (s)	β	φ_{NL}(°)	T_{ref} (°C)	C_1	C_2
25	2500	0.2	0.53	2.3	0.05	300	23	15	13.1	86.4

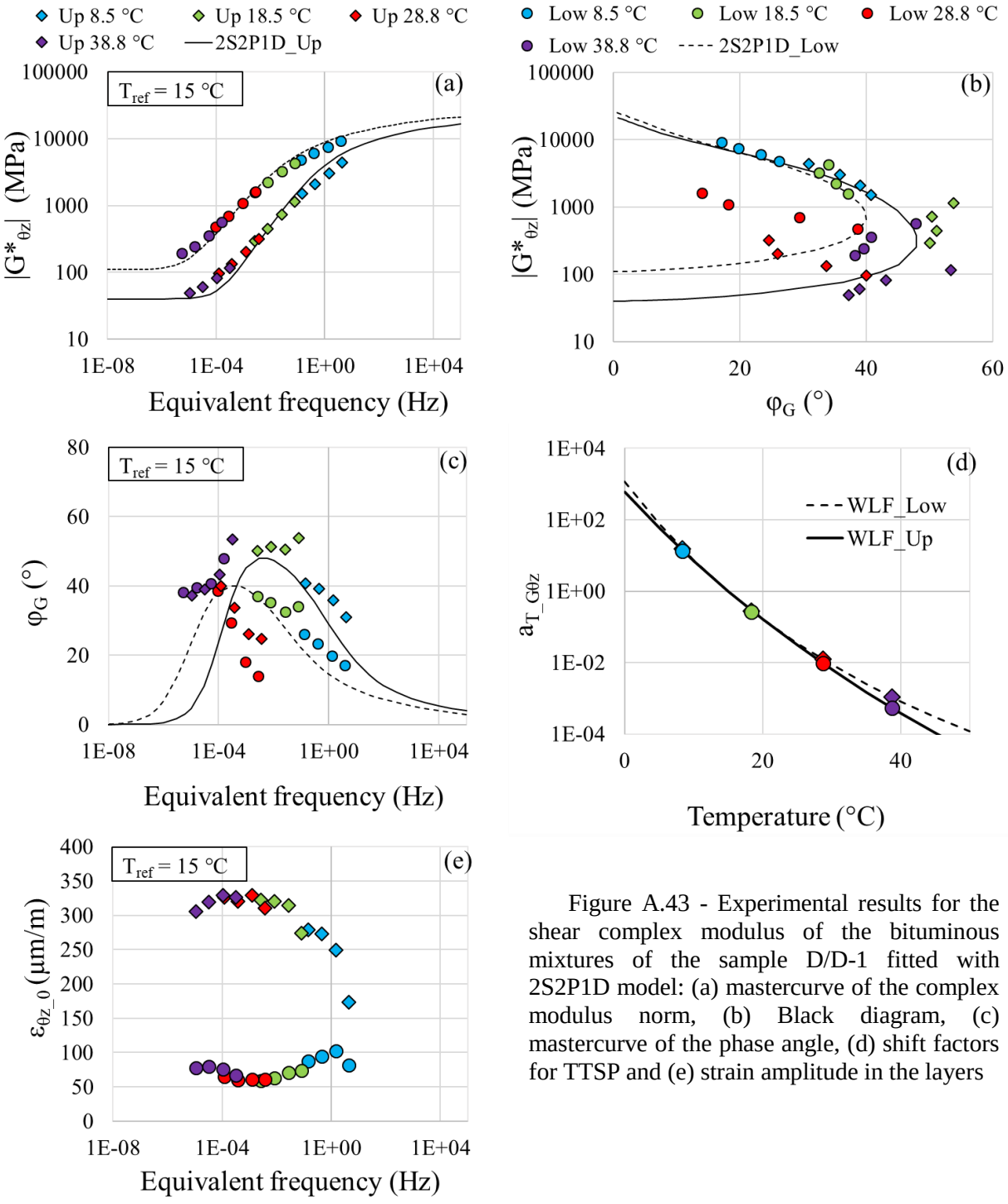

Figure A.43 - Experimental results for the shear complex modulus of the bituminous mixtures of the sample D/D-1 fitted with 2S2P1D model: (a) mastercurve of the complex modulus norm, (b) Black diagram, (c) mastercurve of the phase angle, (d) shift factors for TTSP and (e) strain amplitude in the layers

Table A.43 - 2S2P1D constants and WLF equation coefficients for sample D/D-1

Layer	Mixture	G_{00} (MPa)	G_0 (MPa)	k	h	δ	τ_G (s)	β	T_{ref} (°C)	C_1	C_2
Upper	BB5	40	22000	0.17	0.58	1.8	0.03	110	15	12.4	75.7
Lower	GB5	110	26000	0.17	0.56	2.2	0.8	200	15	21.1	129.1

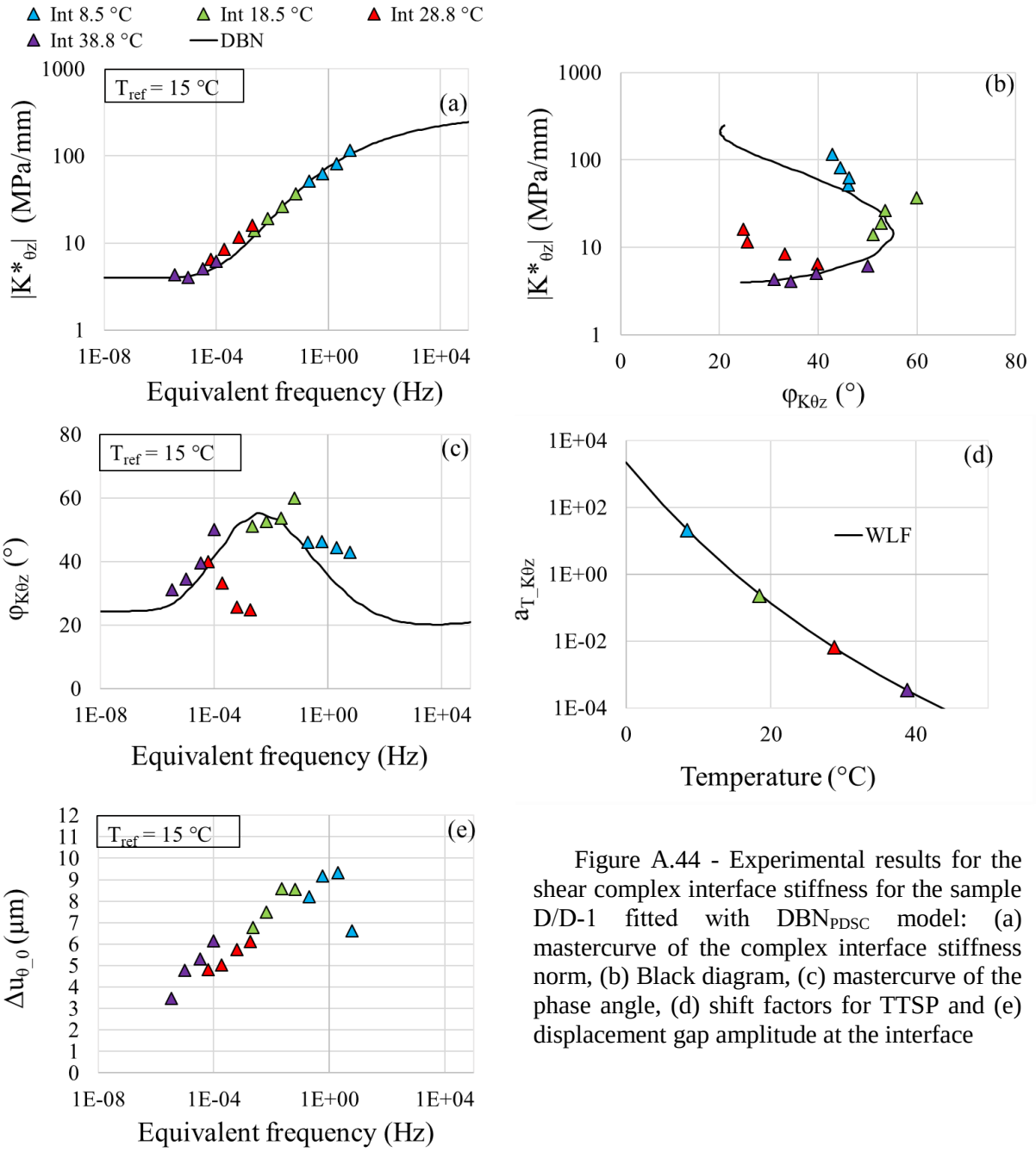

Figure A.44 - Experimental results for the shear complex interface stiffness for the sample D/D-1 fitted with DBN_{PDSC} model: (a) mastercurve of the complex interface stiffness norm, (b) Black diagram, (c) mastercurve of the phase angle, (d) shift factors for TTSP and (e) displacement gap amplitude at the interface

Table A.44 - 2S2P1D constants, DBN_{PDSC} constant φ_{NL} and WLF equation coefficients for sample D/D-1

K_{0z_00} (MPa)	K_{0z_0} (MPa)	k	h	δ	τ_{K0z} (s)	β	φ_{NL}(°)	T_{ref} (°C)	C_1	C_2
4	300	0.2	0.53	2.3	0.2	300	25	15	16.3	88.2

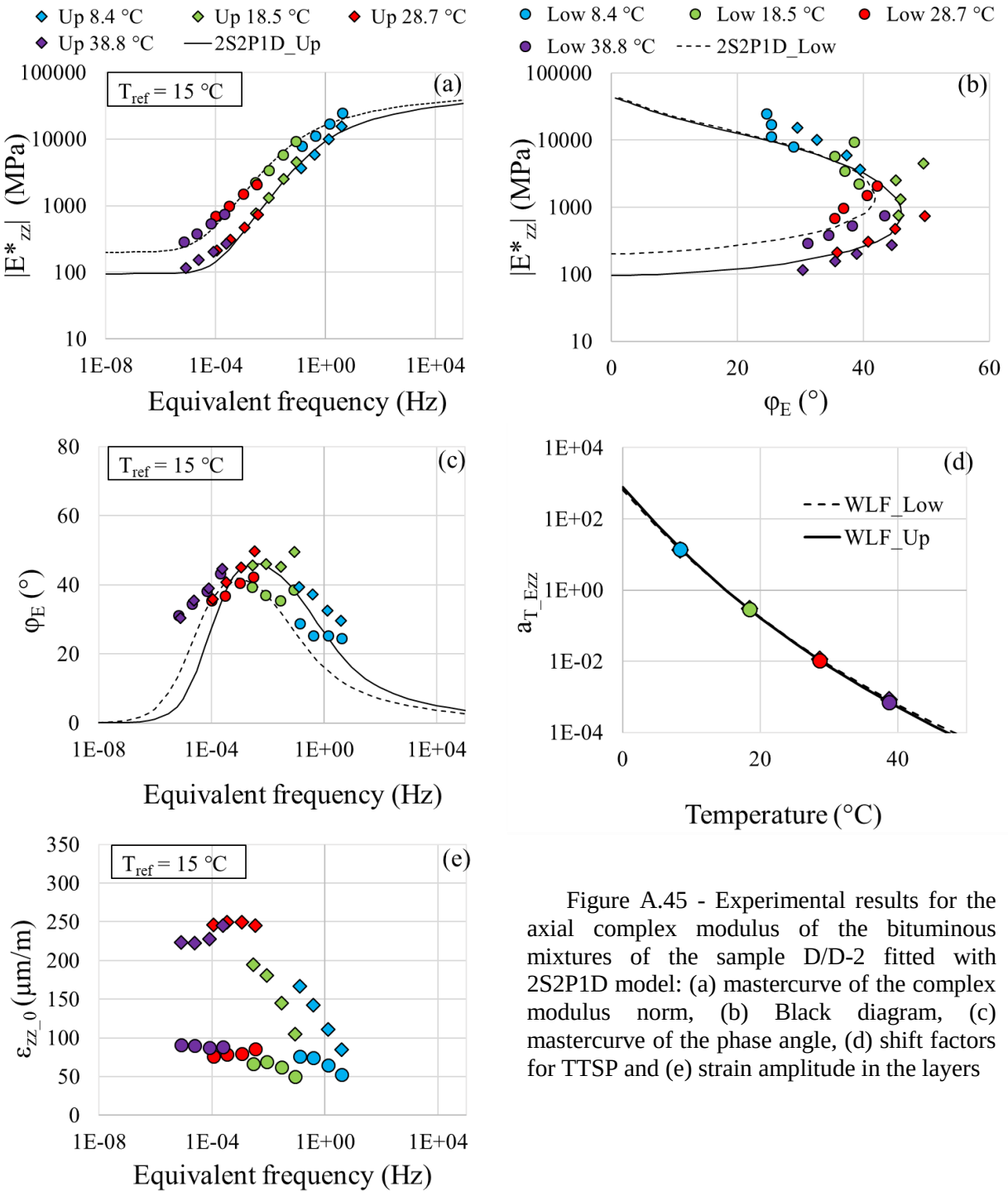

Figure A.45 - Experimental results for the axial complex modulus of the bituminous mixtures of the sample D/D-2 fitted with 2S2P1D model: (a) mastercurve of the complex modulus norm, (b) Black diagram, (c) mastercurve of the phase angle, (d) shift factors for TTSP and (e) strain amplitude in the layers

Table A.45 - 2S2P1D constants and WLF equation coefficients for sample D/D-2

Layer	Mixture	E_{00} (MPa)	E_0 (MPa)	k	h	δ	τ_E (s)	β	T_{ref} (°C)	C_1	C_2
Upper	BB5	95	44000	0.17	0.58	1.8	0.05	150	15	16.2	101.4
Lower	GB5	200	46000	0.17	0.58	1.8	0.5	200	15	16.6	101.3

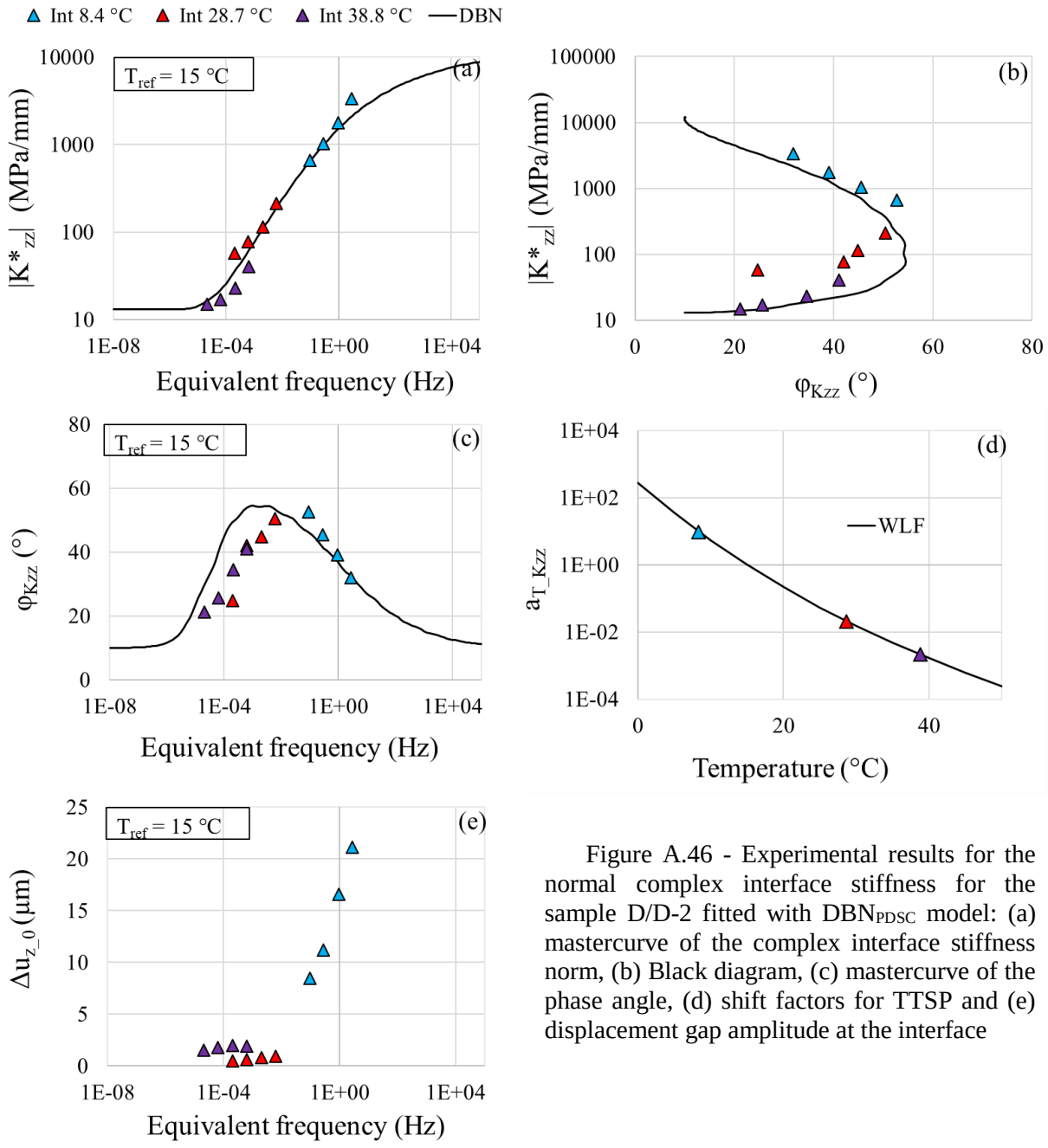

Figure A.46 - Experimental results for the normal complex interface stiffness for the sample D/D-2 fitted with DBN_{PDSC} model: (a) mastercurve of the complex interface stiffness norm, (b) Black diagram, (c) mastercurve of the phase angle, (d) shift factors for TTSP and (e) displacement gap amplitude at the interface

Table A.46 - 2S2P1D constants, DBN_{PDSC} constant φ_{NL} and WLF equation coefficients for sample D/D-2

K_{zz_00} (MPa)	K_{zz_0} (MPa)	k	h	δ	τ_{Kzz} (s)	β	φ_{NL}(°)	T_{ref} (°C)	C_1	C_2
13	12000	0.2	0.53	2.3	0.02	300	10	15	14.0	100.5

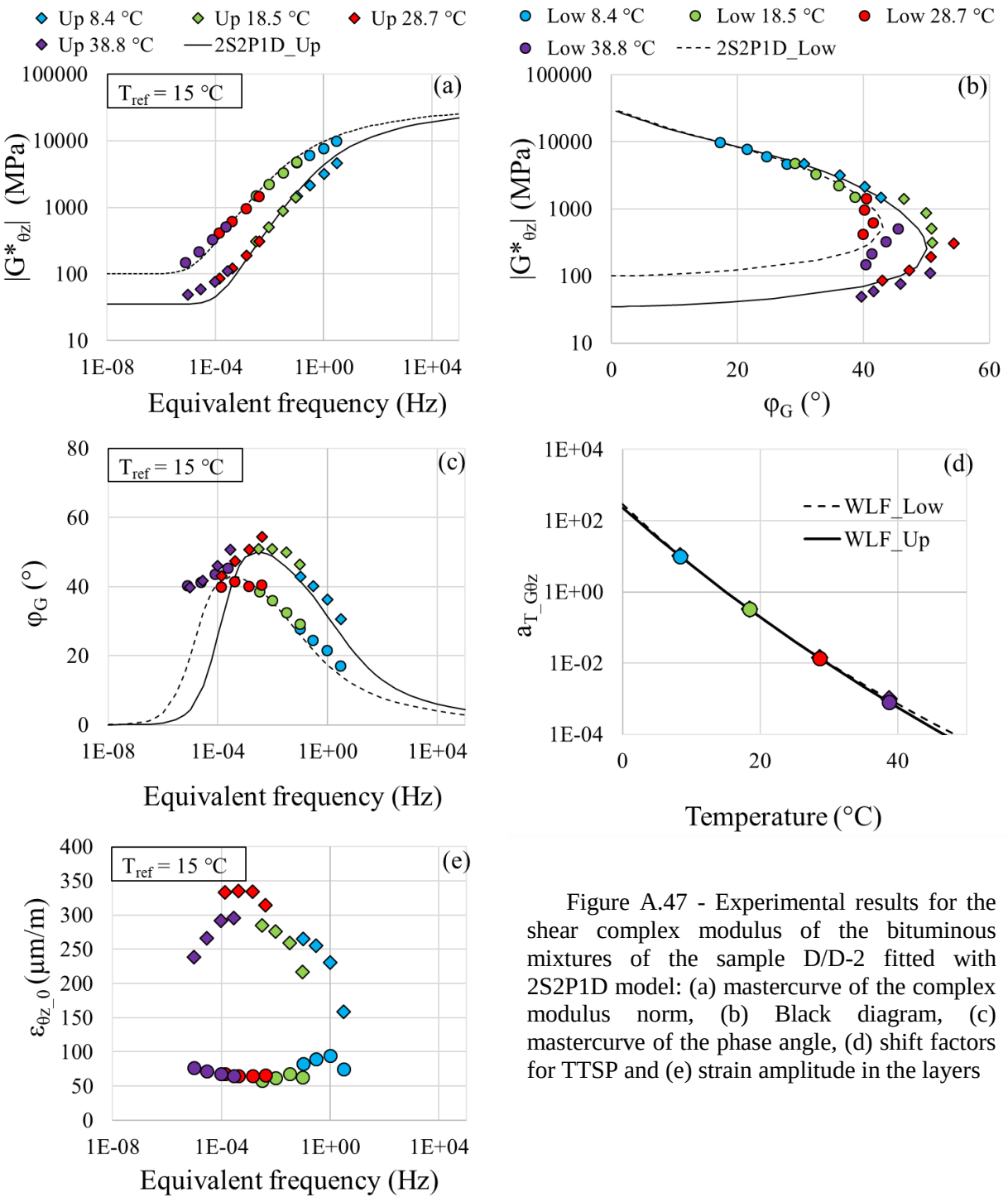

Figure A.47 - Experimental results for the shear complex modulus of the bituminous mixtures of the sample D/D-2 fitted with 2S2P1D model: (a) mastercurve of the complex modulus norm, (b) Black diagram, (c) mastercurve of the phase angle, (d) shift factors for TTSP and (e) strain amplitude in the layers

Table A.47 - 2S2P1D constants and WLF equation coefficients for sample D/D-2

Layer	Mixture	G_{00} (MPa)	G_0 (MPa)	k	h	δ	τ_G (s)	β	T_{ref} (°C)	C_1	C_2
Upper	BB5	35	30000	0.17	0.56	1.8	0.015	120	15	21.7	146.8
Lower	GB5	100	31000	0.17	0.53	1.8	0.3	130	15	30.1	206.3

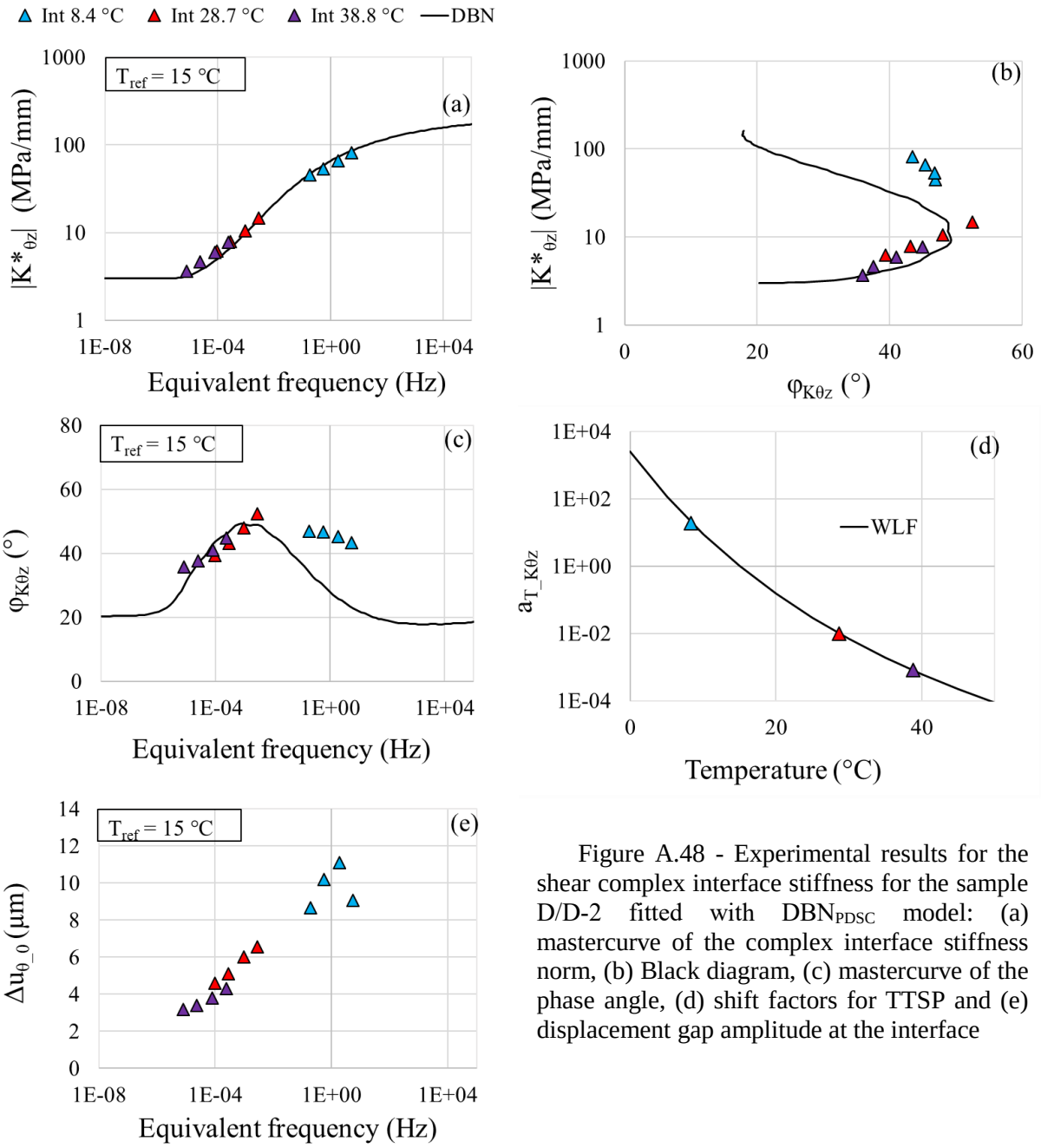

Figure A.48 - Experimental results for the shear complex interface stiffness for the sample D/D-2 fitted with DBN_{PDSC} model: (a) mastercurve of the complex interface stiffness norm, (b) Black diagram, (c) mastercurve of the phase angle, (d) shift factors for TTSP and (e) displacement gap amplitude at the interface

Table A.48 - 2S2P1D constants, DBN_{PDSC} constant φ_{NL} and WLF equation coefficients for sample D/D-2

K_{0z_00} (MPa)	K_{0z_0} (MPa)	k	h	δ	τ_{K0z} (s)	β	φ_{NL}(°)	T_{ref} (°C)	C_1	C_2
3	200	0.2	0.53	2.3	0.8	300	21	15	11.9	67.2

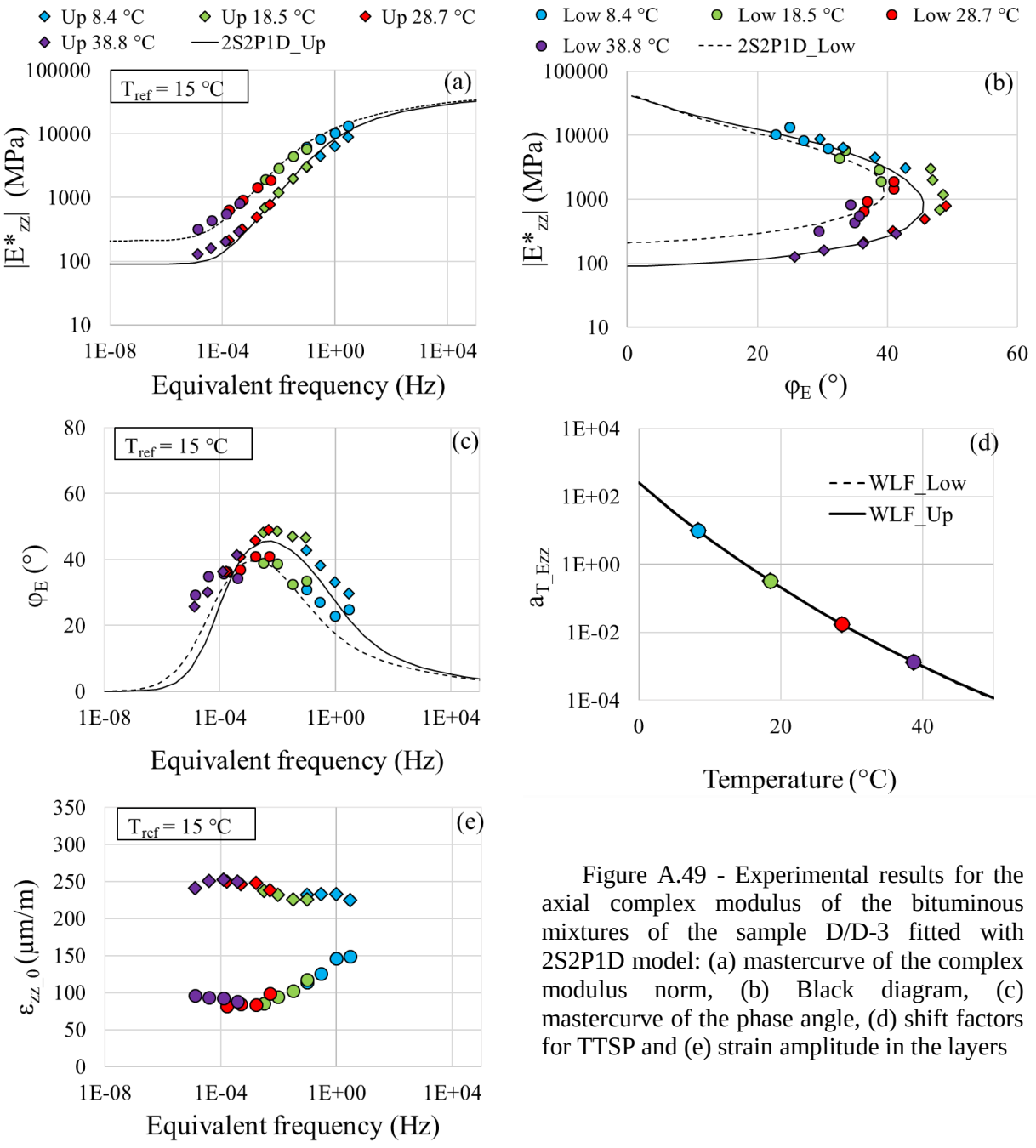

Figure A.49 - Experimental results for the axial complex modulus of the bituminous mixtures of the sample D/D-3 fitted with 2S2P1D model: (a) mastercurve of the complex modulus norm, (b) Black diagram, (c) mastercurve of the phase angle, (d) shift factors for TTSP and (e) strain amplitude in the layers

Table A.49 - 2S2P1D constants and WLF equation coefficients for sample D/D-3

Layer	Mixture	E_{00} (MPa)	E_0 (MPa)	k	h	δ	τ_E (s)	β	T_{ref} (°C)	C_1	C_2
Upper	BB5	90	43000	0.17	0.58	1.8	0.04	200	130	19.2	133.9
Lower	GB5	210	44000	0.17	0.58	2.3	0.3	300	15	19.0	133.9

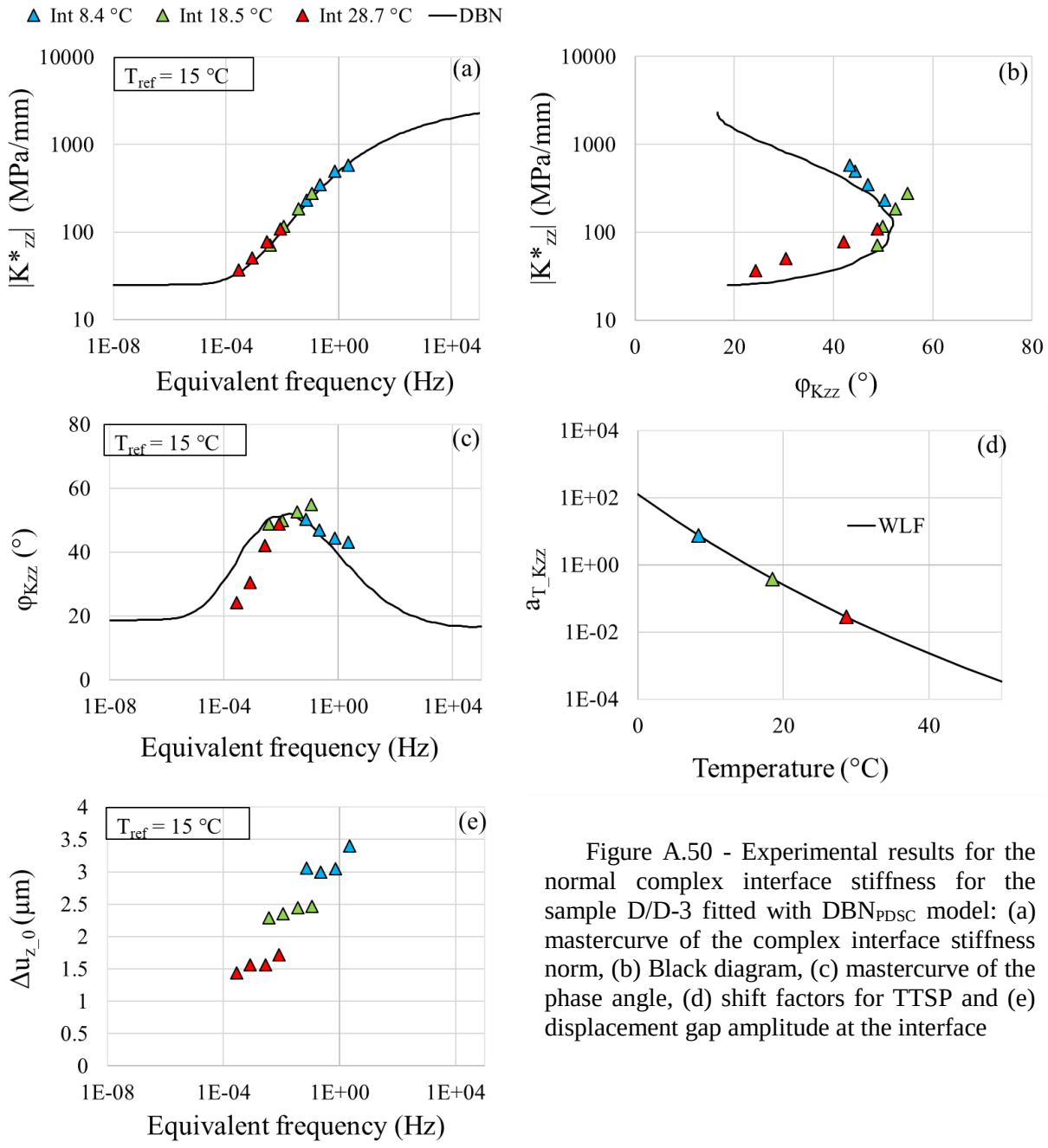

Figure A.50 - Experimental results for the normal complex interface stiffness for the sample D/D-3 fitted with DBN_{PDSC} model: (a) mastercurve of the complex interface stiffness norm, (b) Black diagram, (c) mastercurve of the phase angle, (d) shift factors for TTSP and (e) displacement gap amplitude at the interface

Table A.50 - 2S2P1D constants, DBN_{PDSC} constant φ_{NL} and WLF equation coefficients for sample D/D-3

K_{zz_00} (MPa)	K_{zz_0} (MPa)	k	h	δ	τ_{Kzz} (s)	β	φ_{NL}(°)	T_{ref} (°C)	C_1	C_2
25	3000	0.2	0.53	2.3	0.04	300	19	15	16.8	134.1

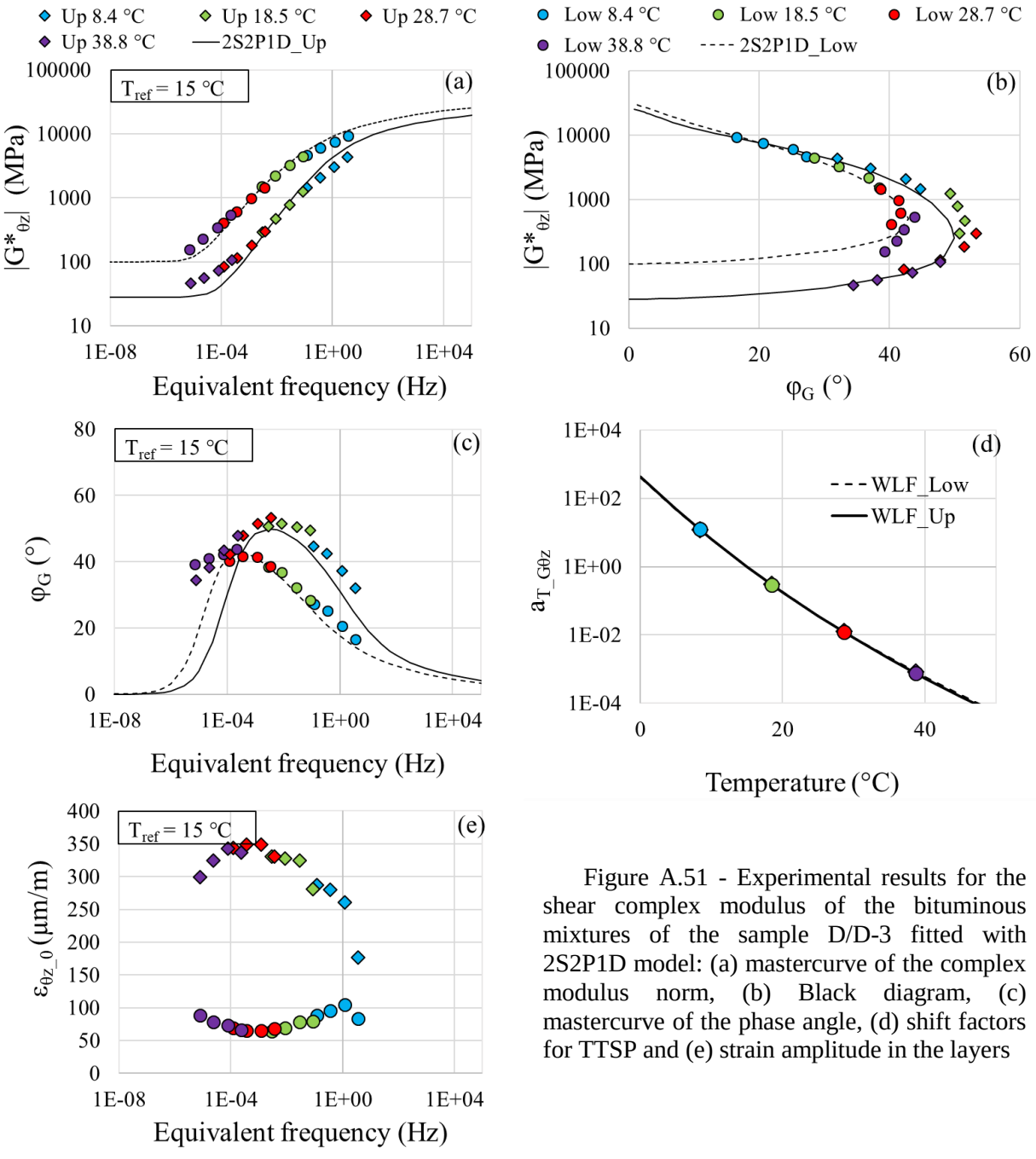

Figure A.51 - Experimental results for the shear complex modulus of the bituminous mixtures of the sample D/D-3 fitted with 2S2P1D model: (a) mastercurve of the complex modulus norm, (b) Black diagram, (c) mastercurve of the phase angle, (d) shift factors for TTSP and (e) strain amplitude in the layers

Table A.51 - 2S2P1D constants and WLF equation coefficients for sample D/D-3

Layer	Mixture	G_{00} (MPa)	G_0 (MPa)	k	h	δ	τ_G (s)	β	T_{ref} (°C)	C_1	C_2
Upper	BB5	28	27000	0.16	0.58	1.8	0.02	150	15	20.2	131.5
Lower	GB5	100	32000	0.17	0.52	2.1	0.25	130	15	20.5	131.5

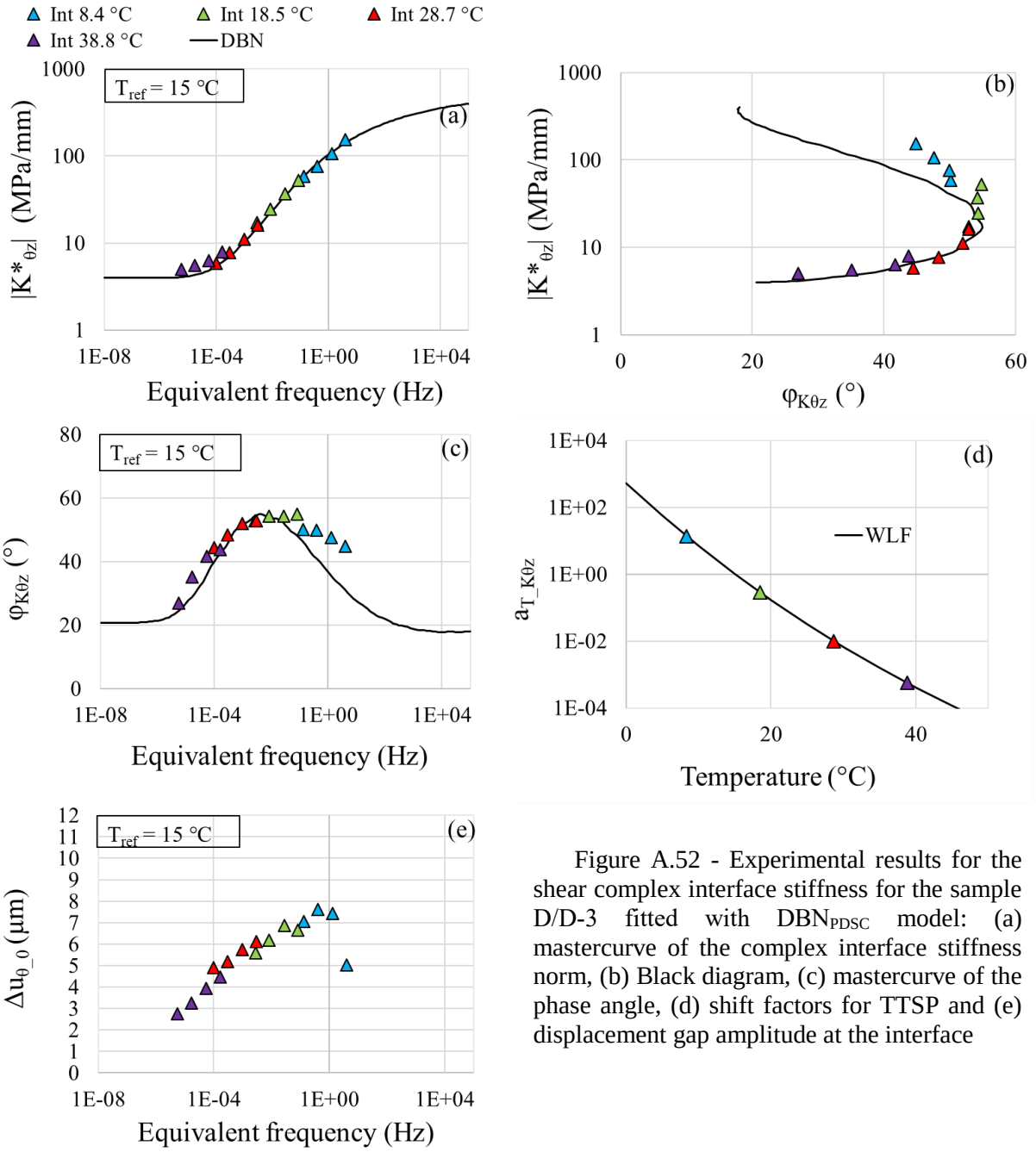

Figure A.52 - Experimental results for the shear complex interface stiffness for the sample D/D-3 fitted with DBN_{PDSC} model: (a) mastercurve of the complex interface stiffness norm, (b) Black diagram, (c) mastercurve of the phase angle, (d) shift factors for TTSP and (e) displacement gap amplitude at the interface

Table A.52 - 2S2P1D constants, DBN_{PDSC} constant φ_{NL} and WLF equation coefficients for sample D/D-3

K_{0z_00} (MPa)	K_{0z_0} (MPa)	k	h	δ	τ_{K0z} (s)	β	φ_{NL}(°)	T_{ref} (°C)	C_1	C_2
4	500	0.2	0.53	2.3	0.1	300	21	15	21.2	131.4

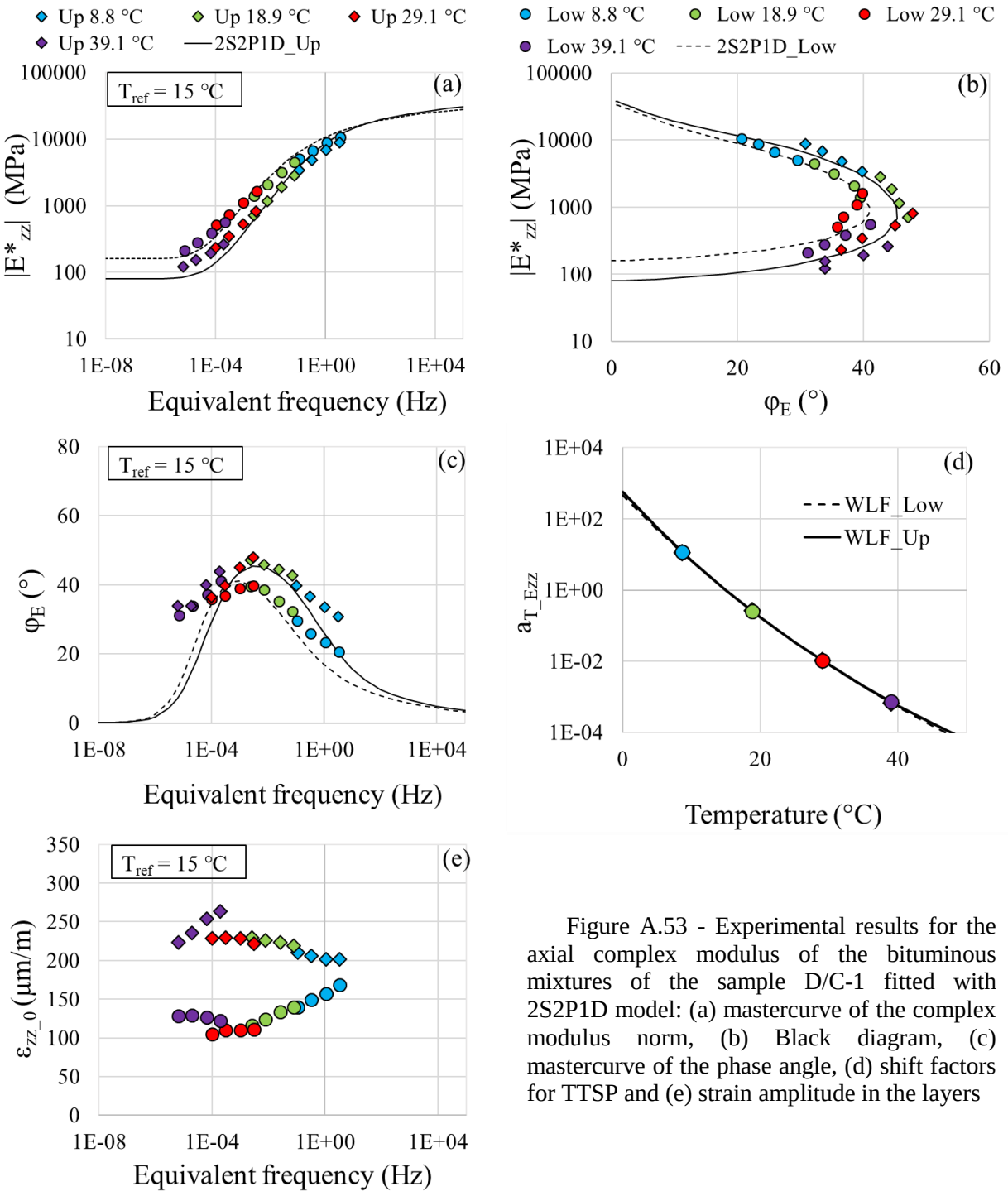

Figure A.53 - Experimental results for the axial complex modulus of the bituminous mixtures of the sample D/C-1 fitted with 2S2P1D model: (a) mastercurve of the complex modulus norm, (b) Black diagram, (c) mastercurve of the phase angle, (d) shift factors for TTSP and (e) strain amplitude in the layers

Table A.53 - 2S2P1D constants and WLF equation coefficients for sample D/C-1

Layer	Mixture	E_{00} (MPa)	E_0 (MPa)	k	h	δ	τ_E (s)	β	T_{ref} (°C)	C_1	C_2
Upper	BB5	80	40000	0.16	0.58	1.7	0.05	300	15	19.8	125.6
Lower	EME2	160	35000	0.17	0.56	2.1	0.35	120	15	17.5	109.9

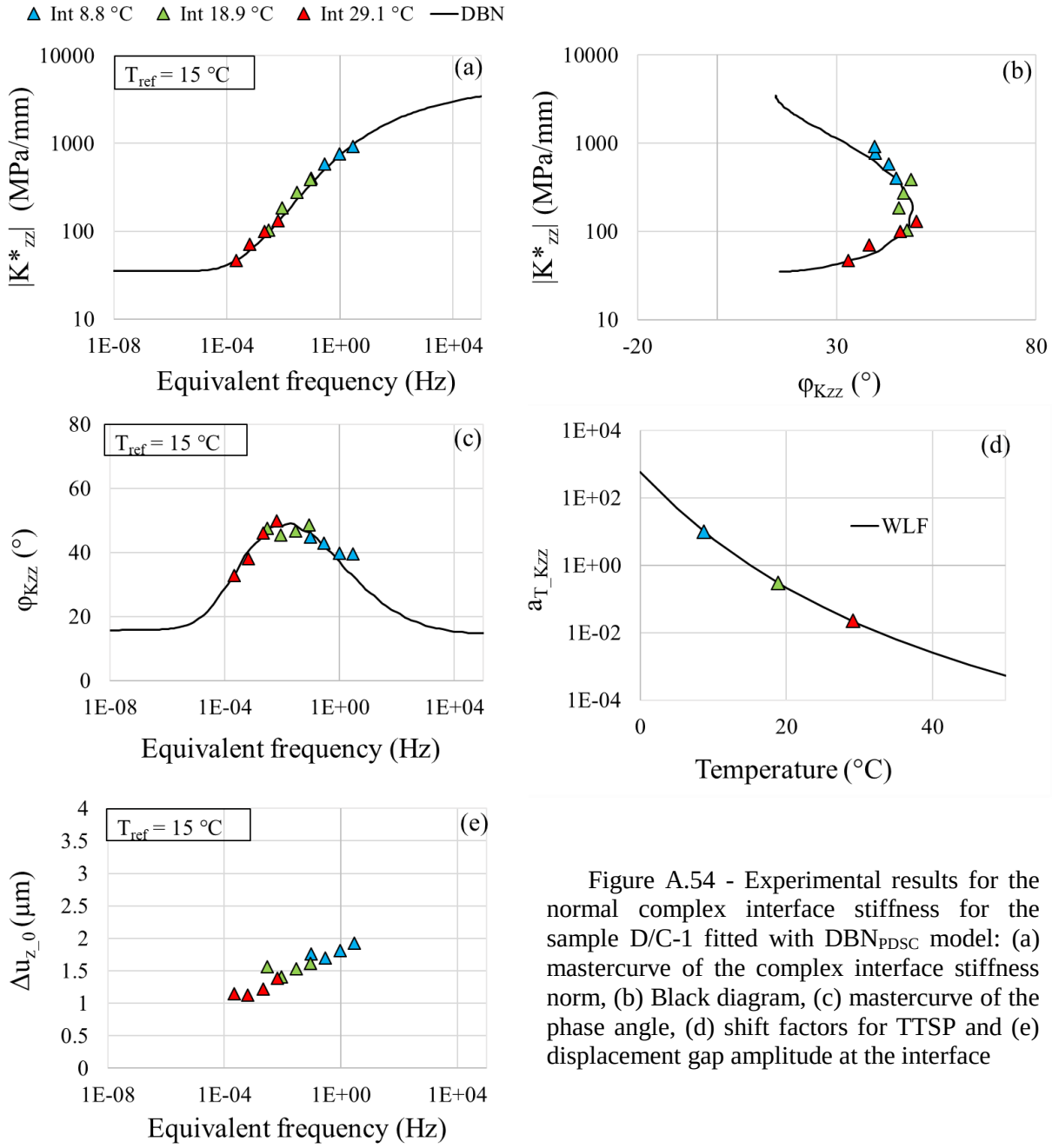

Figure A.54 - Experimental results for the normal complex interface stiffness for the sample D/C-1 fitted with DBN_{PDSC} model: (a) mastercurve of the complex interface stiffness norm, (b) Black diagram, (c) mastercurve of the phase angle, (d) shift factors for TTSP and (e) displacement gap amplitude at the interface

Table A.54 - 2S2P1D constants, DBN_{PDSC} constant φ_{NL} and WLF equation coefficients for sample D/C-1

K_{zz_00} (MPa)	K_{zz_0} (MPa)	k	h	δ	τ_{Kzz} (s)	β	φ_{NL}(°)	T_{ref} (°C)	C_1	C_2
35	4500	0.2	0.53	2.3	0.04	300	16	15	9.5	66.3

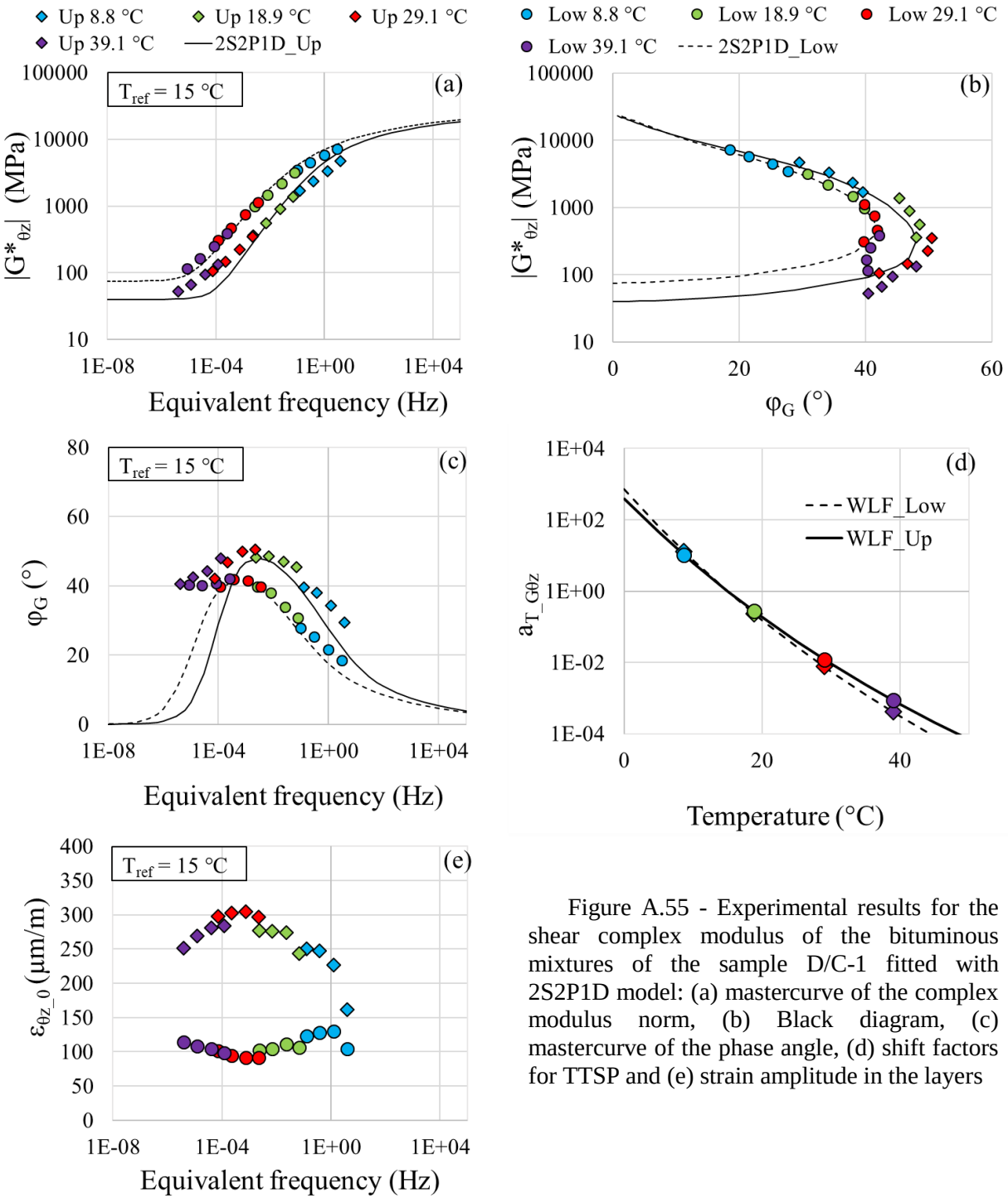

Figure A.55 - Experimental results for the shear complex modulus of the bituminous mixtures of the sample D/C-1 fitted with 2S2P1D model: (a) mastercurve of the complex modulus norm, (b) Black diagram, (c) mastercurve of the phase angle, (d) shift factors for TTSP and (e) strain amplitude in the layers

Table A.55 - 2S2P1D constants and WLF equation coefficients for sample D/C-1

Layer	Mixture	G_{00} (MPa)	G_0 (MPa)	k	h	δ	τ_G (s)	β	T_{ref} (°C)	C_1	C_2
Upper	BB5	40	24000	0.17	0.57	1.8	0.035	120	15	21.0	125.0
Lower	EME2	75	25000	0.17	0.55	2.2	0.28	200	15	18.9	124.6

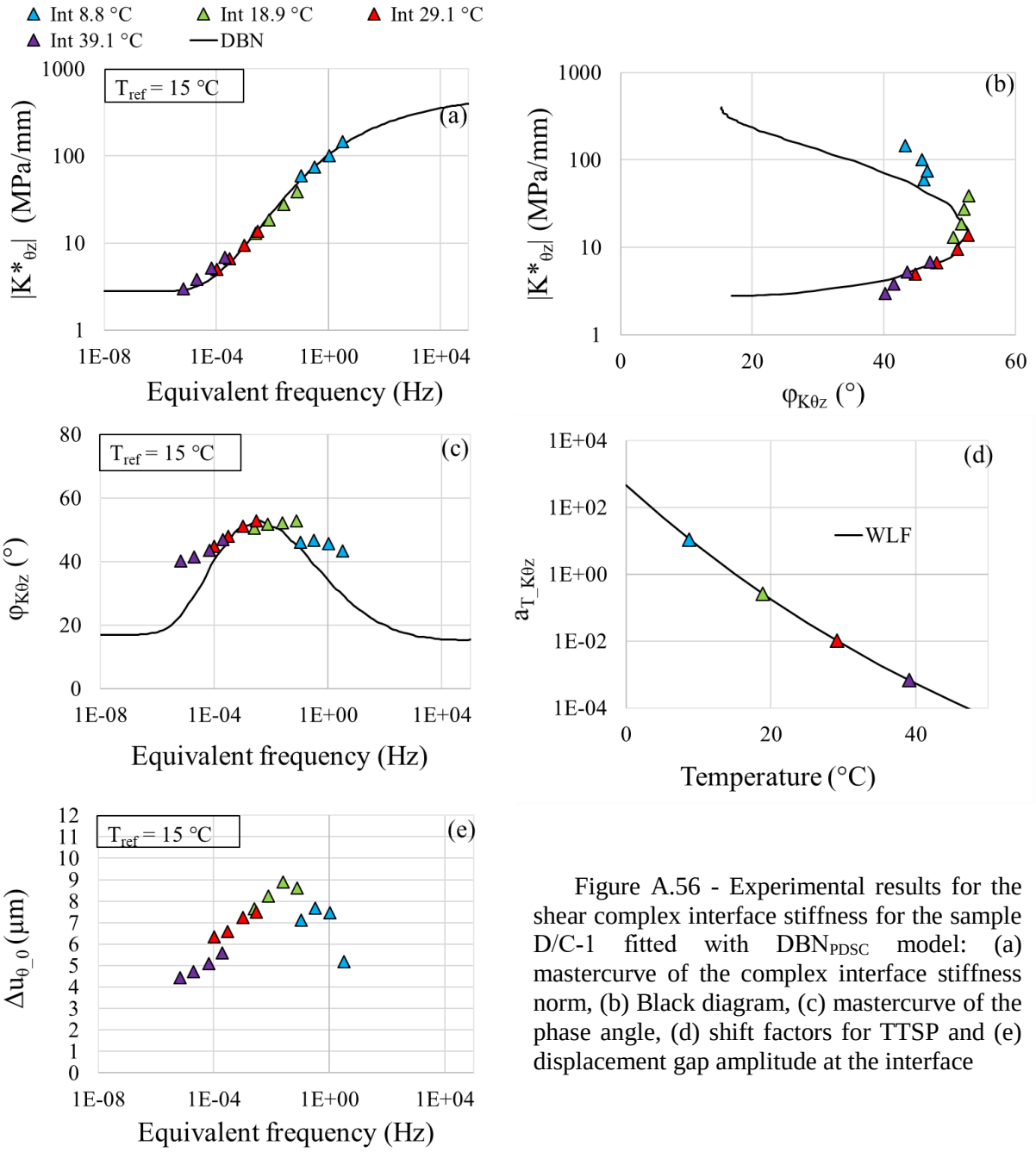

Figure A.56 - Experimental results for the shear complex interface stiffness for the sample D/C-1 fitted with DBN_{PDSC} model: (a) mastercurve of the complex interface stiffness norm, (b) Black diagram, (c) mastercurve of the phase angle, (d) shift factors for TTSP and (e) displacement gap amplitude at the interface

Table A.56 - 2S2P1D constants, DBN_{PDSC} constant φ_{NL} and WLF equation coefficients for sample D/C-1

K_{0z_00} (MPa)	K_{0z_0} (MPa)	k	h	δ	τ_{K0z} (s)	β	φ_{NL}(°)	T_{ref} (°C)	C_1	C_2
2.8	500	0.2	0.53	2.3	0.1	300	17	15	19.7	125.7

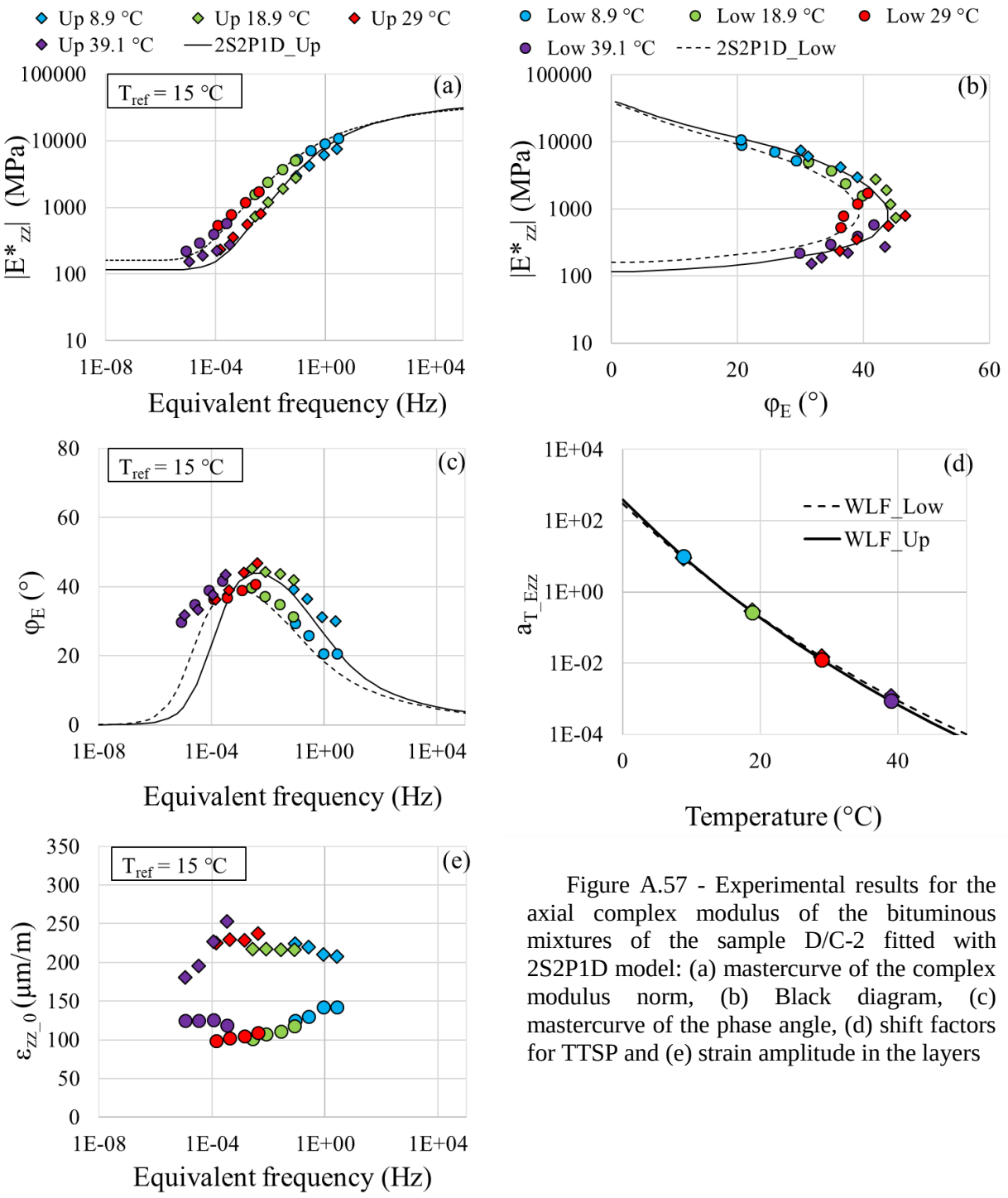

Figure A.57 - Experimental results for the axial complex modulus of the bituminous mixtures of the sample D/C-2 fitted with 2S2P1D model: (a) mastercurve of the complex modulus norm, (b) Black diagram, (c) mastercurve of the phase angle, (d) shift factors for TTSP and (e) strain amplitude in the layers

Table A.57 - 2S2P1D constants and WLF equation coefficients for sample D/C-2

Layer	Mixture	E_{00} (MPa)	E_0 (MPa)	k	h	δ	τ_E (s)	β	T_{ref} (°C)	C_1	C_2
Upper	BB5	115	41000	0.17	0.56	1.8	0.04	150	15	18.3	125.7
Lower	EME2	160	38000	0.17	0.53	2.1	0.2	180	15	19.1	125.3

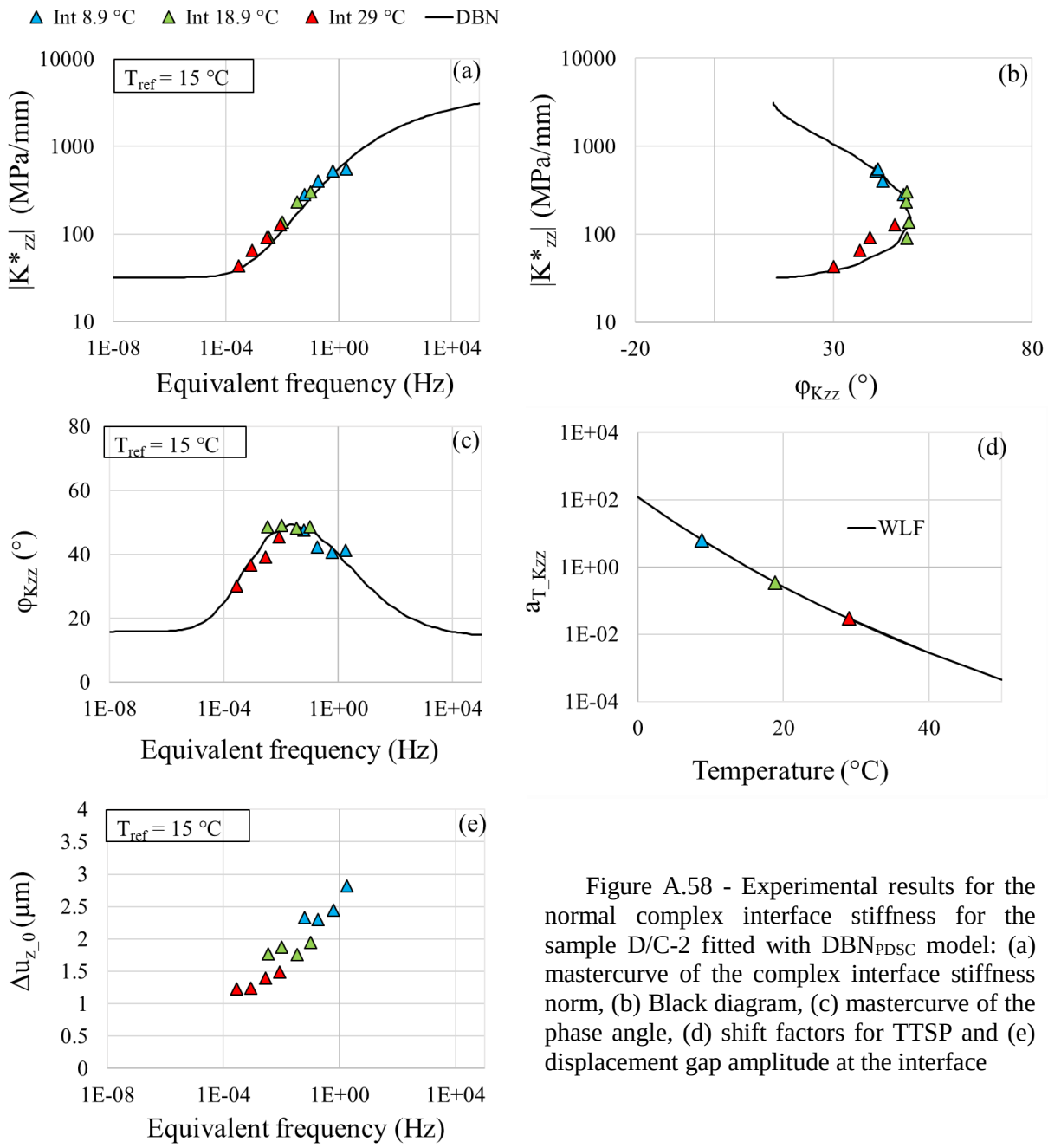

Figure A.58 - Experimental results for the normal complex interface stiffness for the sample D/C-2 fitted with DBN_{PDSC} model: (a) mastercurve of the complex interface stiffness norm, (b) Black diagram, (c) mastercurve of the phase angle, (d) shift factors for TTSP and (e) displacement gap amplitude at the interface

Table A.58 - 2S2P1D constants, DBN_{PDSC} constant φ_{NL} and WLF equation coefficients for sample D/C-2

K_{zz_00} (MPa)	K_{zz_0} (MPa)	k	h	δ	τ_{Kzz} (s)	β	φ_{NL}(°)	T_{ref} (°C)	C_1	C_2
32	4200	0.2	0.53	2.3	0.02	300	16	15	15.4	126.1

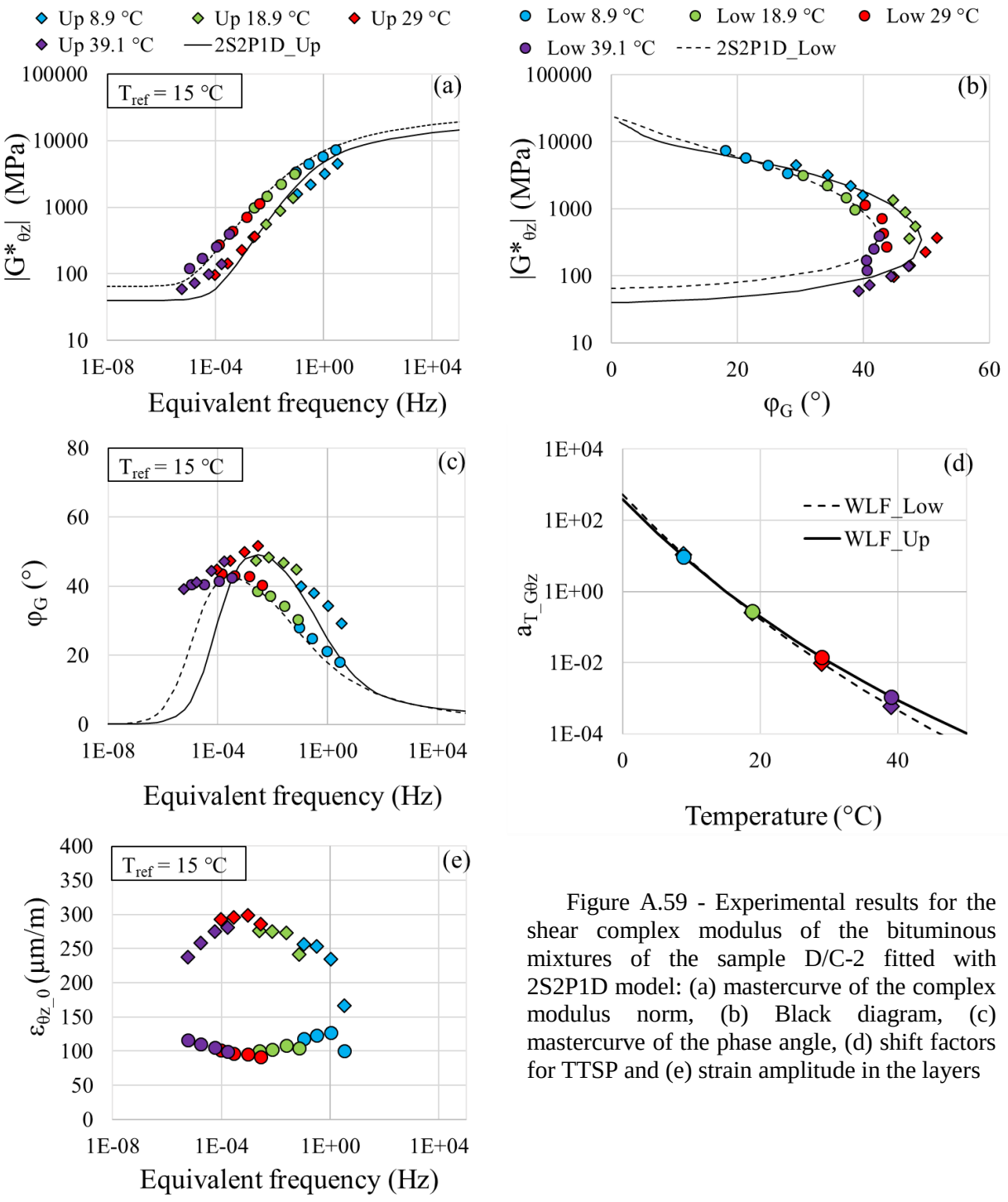

Figure A.59 - Experimental results for the shear complex modulus of the bituminous mixtures of the sample D/C-2 fitted with 2S2P1D model: (a) mastercurve of the complex modulus norm, (b) Black diagram, (c) mastercurve of the phase angle, (d) shift factors for TTSP and (e) strain amplitude in the layers

Table A.59 - 2S2P1D constants and WLF equation coefficients for sample D/C-2

Layer	Mixture	G_{00} (MPa)	G_0 (MPa)	k	h	δ	τ_G (s)	β	T_{ref} (°C)	C_1	C_2
Upper	BB5	40	22000	0.12	0.58	1.8	0.05	100	15	20.1	125.6
Lower	EME2	65	24000	0.17	0.53	2	0.25	180	15	16.8	112.7

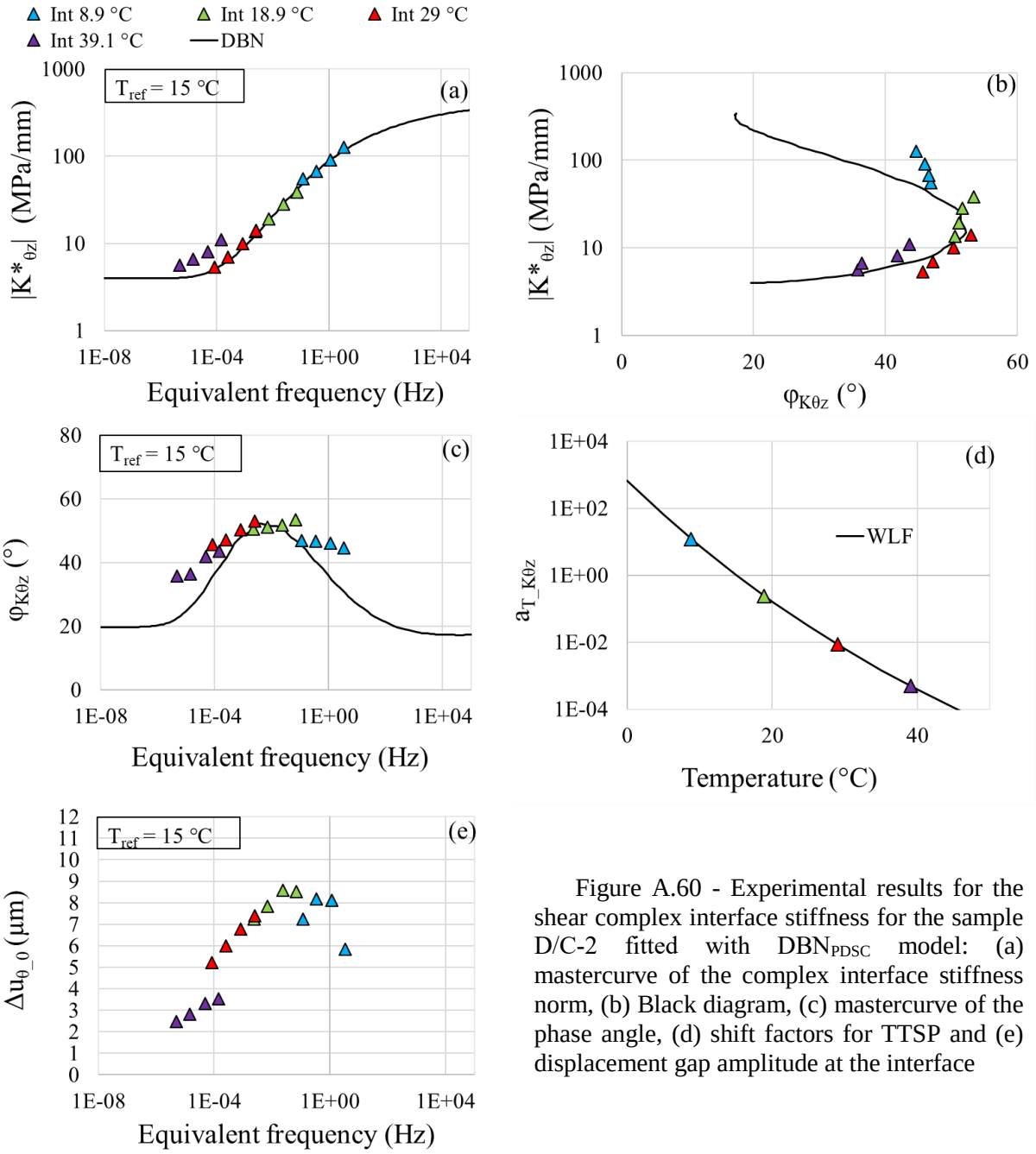

Figure A.60 - Experimental results for the shear complex interface stiffness for the sample D/C-2 fitted with DBN_{PDSC} model: (a) mastercurve of the complex interface stiffness norm, (b) Black diagram, (c) mastercurve of the phase angle, (d) shift factors for TTSP and (e) displacement gap amplitude at the interface

Table A.60 - 2S2P1D constants, DBN_{PDSC} constant φ_{NL} and WLF equation coefficients for sample D/C-2

$K_{\theta z\_00}$ (MPa)	$K_{\theta z\_0}$ (MPa)	k	h	δ	$\tau_{K\theta z}$ (s)	β	φ_{NL}(°)	T_{ref} (°C)	C_1	C_2
4	425	0.2	0.53	2.3	0.1	300	20	15	19.9	120.8

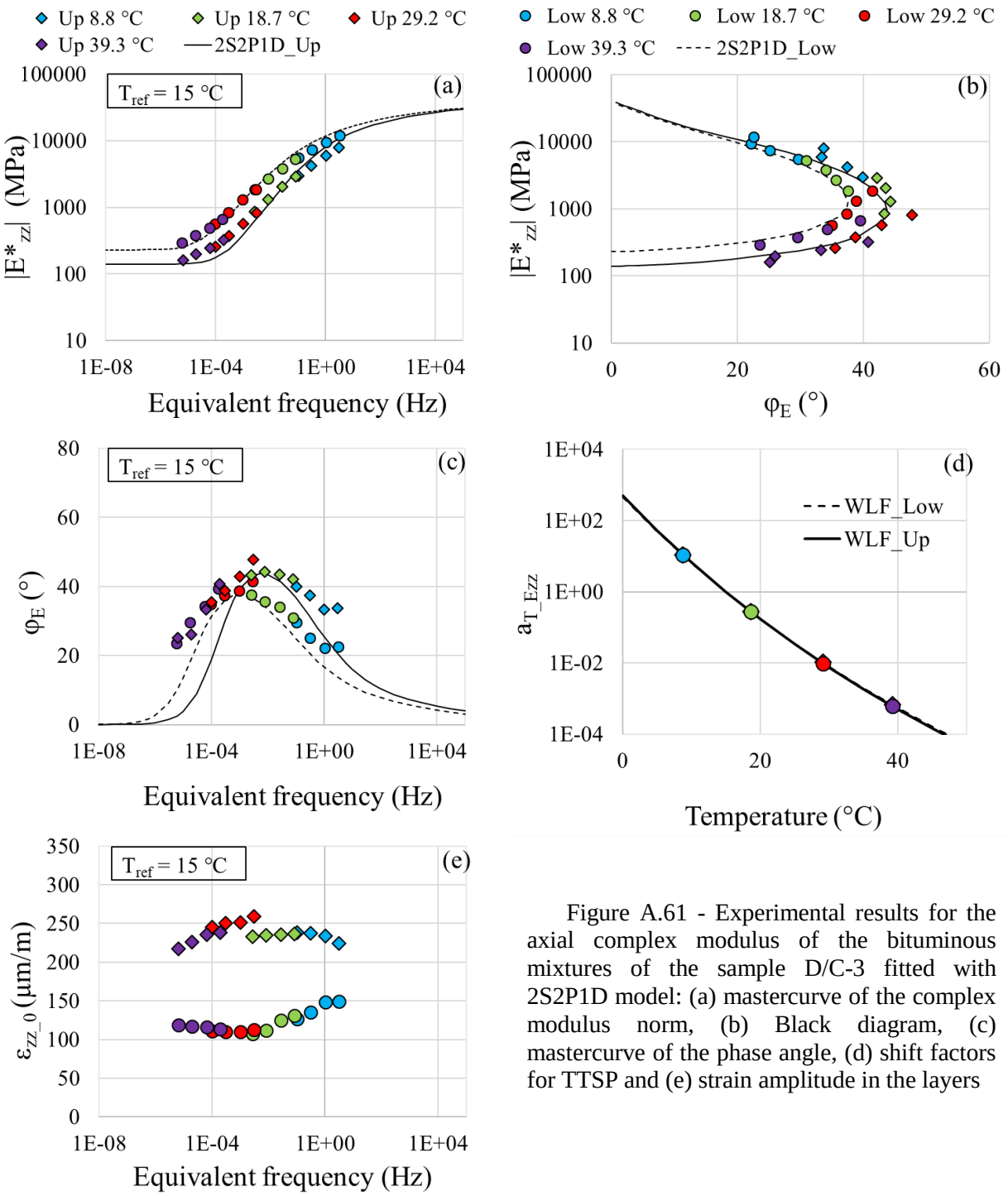

Figure A.61 - Experimental results for the axial complex modulus of the bituminous mixtures of the sample D/C-3 fitted with 2S2P1D model: (a) mastercurve of the complex modulus norm, (b) Black diagram, (c) mastercurve of the phase angle, (d) shift factors for TTSP and (e) strain amplitude in the layers

Table A.61 - 2S2P1D constants and WLF equation coefficients for sample D/C-3

Layer	Mixture	E_{00} (MPa)	E_0 (MPa)	k	h	δ	τ_E (s)	β	T_{ref} (°C)	C_1	C_2
Upper	BB5	140	40000	0.17	0.58	2	0.05	120	15	19.7	125.8
Lower	EME2	230	38000	0.17	0.54	2	0.35	180	15	19.9	125.8

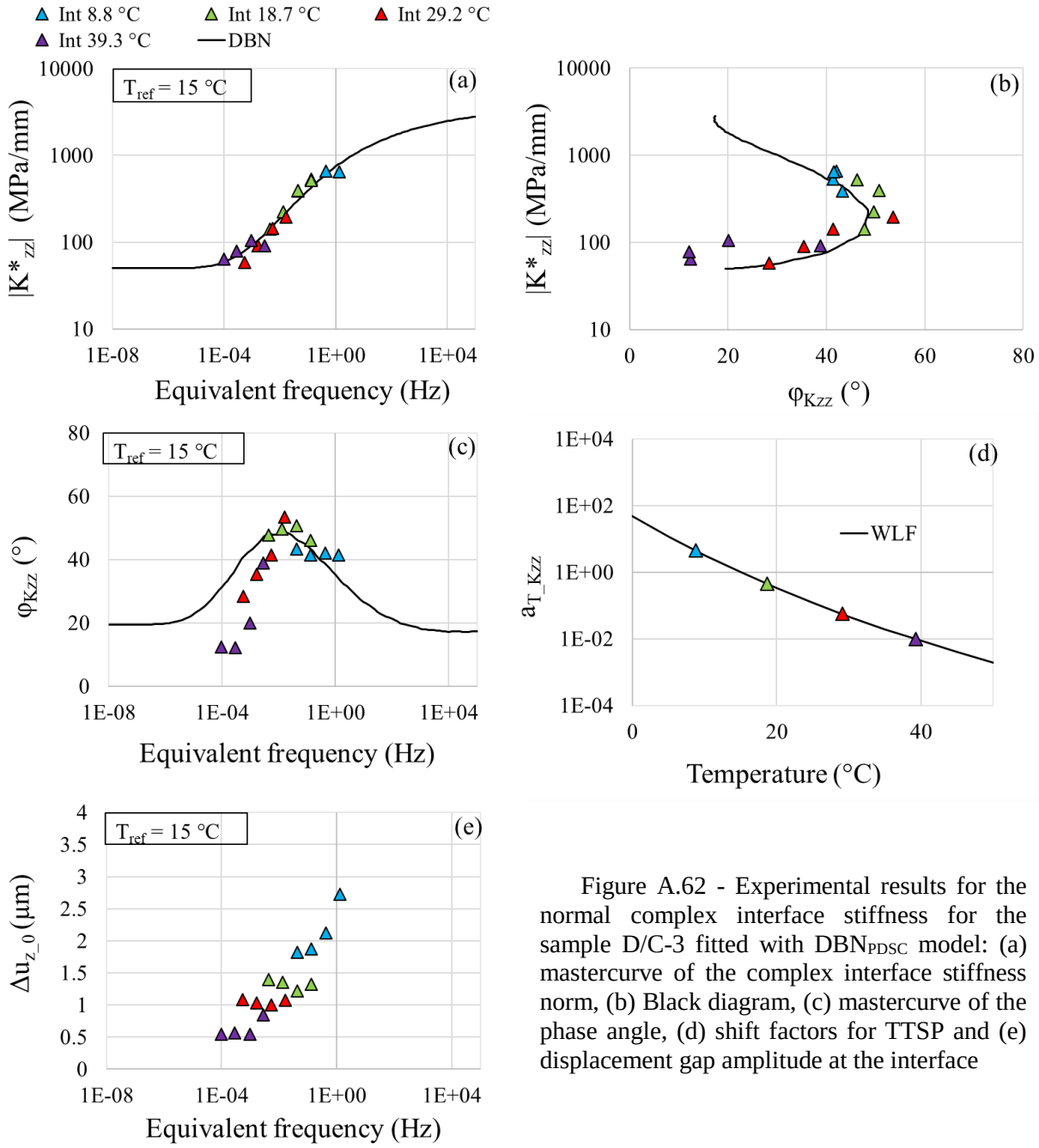

Figure A.62 - Experimental results for the normal complex interface stiffness for the sample D/C-3 fitted with DBN_{PDSC} model: (a) mastercurve of the complex interface stiffness norm, (b) Black diagram, (c) mastercurve of the phase angle, (d) shift factors for TTSP and (e) displacement gap amplitude at the interface

Table A.62 - 2S2P1D constants, DBN_{PDSC} constant φ_{NL} and WLF equation coefficients for sample D/C-3

K_{zz_00} (MPa)	K_{zz_0} (MPa)	k	h	δ	τ_{Kzz} (s)	β	φ_{NL}(°)	T_{ref} (°C)	C_1	C_2
50	3500	0.2	0.53	2.3	0.1	300	20	15	15.4	126.1

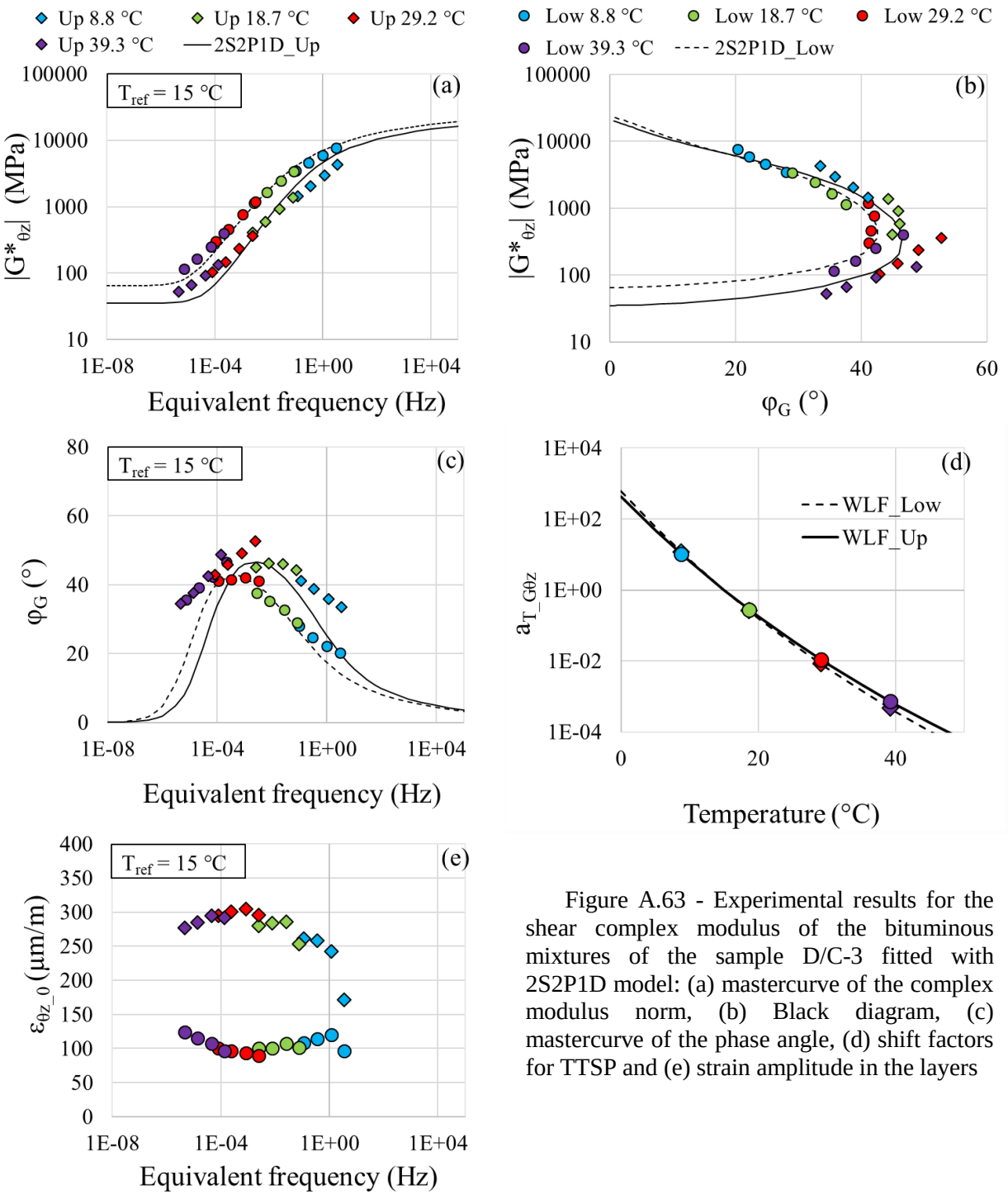

Figure A.63 - Experimental results for the shear complex modulus of the bituminous mixtures of the sample D/C-3 fitted with 2S2P1D model: (a) mastercurve of the complex modulus norm, (b) Black diagram, (c) mastercurve of the phase angle, (d) shift factors for TTSP and (e) strain amplitude in the layers

Table A.63 - 2S2P1D constants and WLF equation coefficients for sample D/C-3

Layer	Mixture	G_{00} (MPa)	G_0 (MPa)	k	h	δ	τ_G (s)	β	T_{ref} (°C)	C_1	C_2
Upper	BB5	35	21000	0.17	0.58	1.8	0.06	200	15	20.6	125.7
Lower	EME2	65	24000	0.17	0.55	2.1	0.3	180	15	19.4	125.8

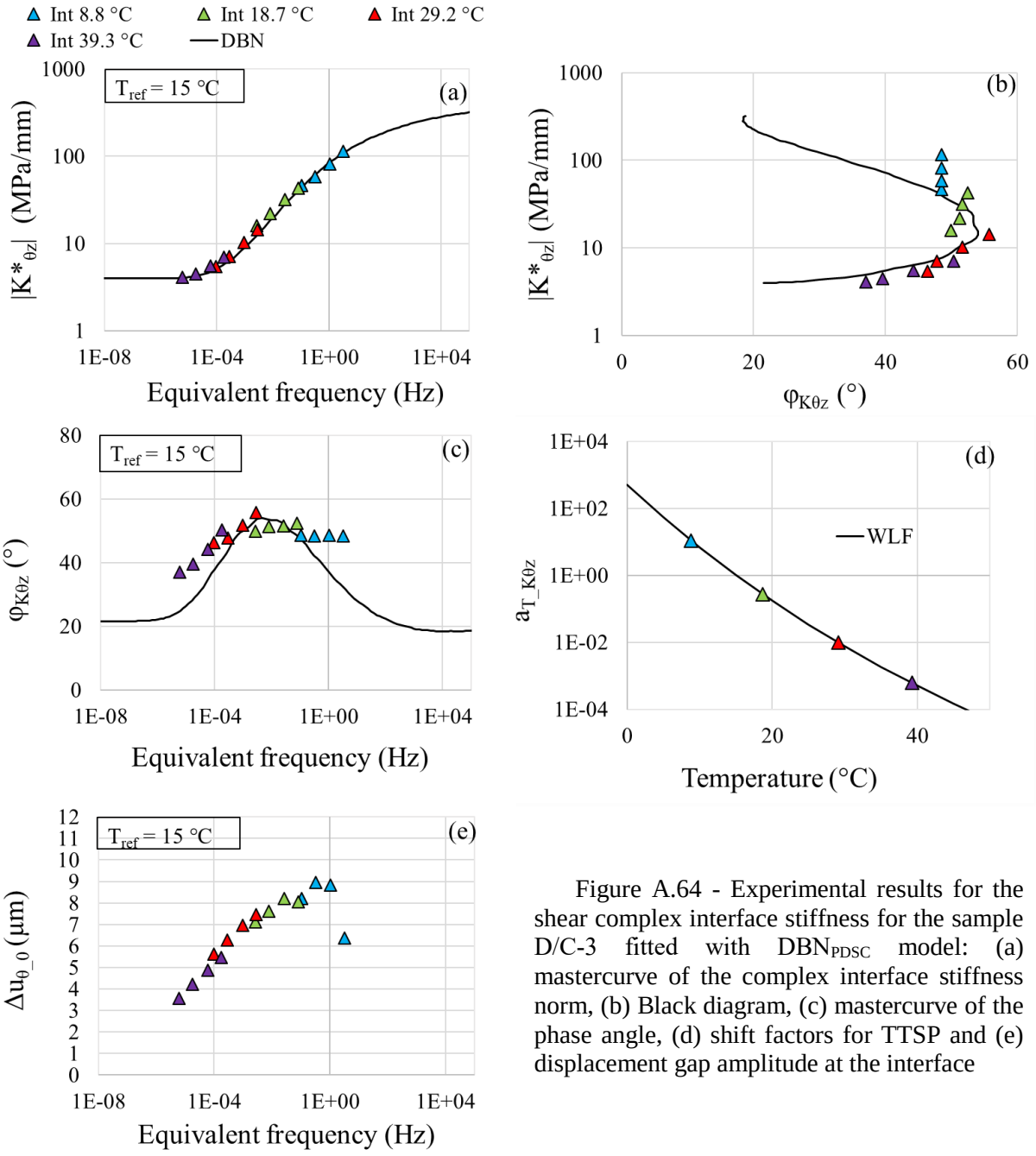

Figure A.64 - Experimental results for the shear complex interface stiffness for the sample D/C-3 fitted with DBN_{PDSC} model: (a) mastercurve of the complex interface stiffness norm, (b) Black diagram, (c) mastercurve of the phase angle, (d) shift factors for TTSP and (e) displacement gap amplitude at the interface

Table A.64 - 2S2P1D constants, DBN_{PDSC} constant φ_{NL} and WLF equation coefficients for sample D/C-3

$K_{\theta z\_00}$ (MPa)	$K_{\theta z\_0}$ (MPa)	k	h	δ	$\tau_{K\theta z}$ (s)	β	φ_{NL}(°)	T_{ref} (°C)	C_1	C_2
4	400	0.2	0.53	2.3	0.1	300	22	15	19.9	125.8

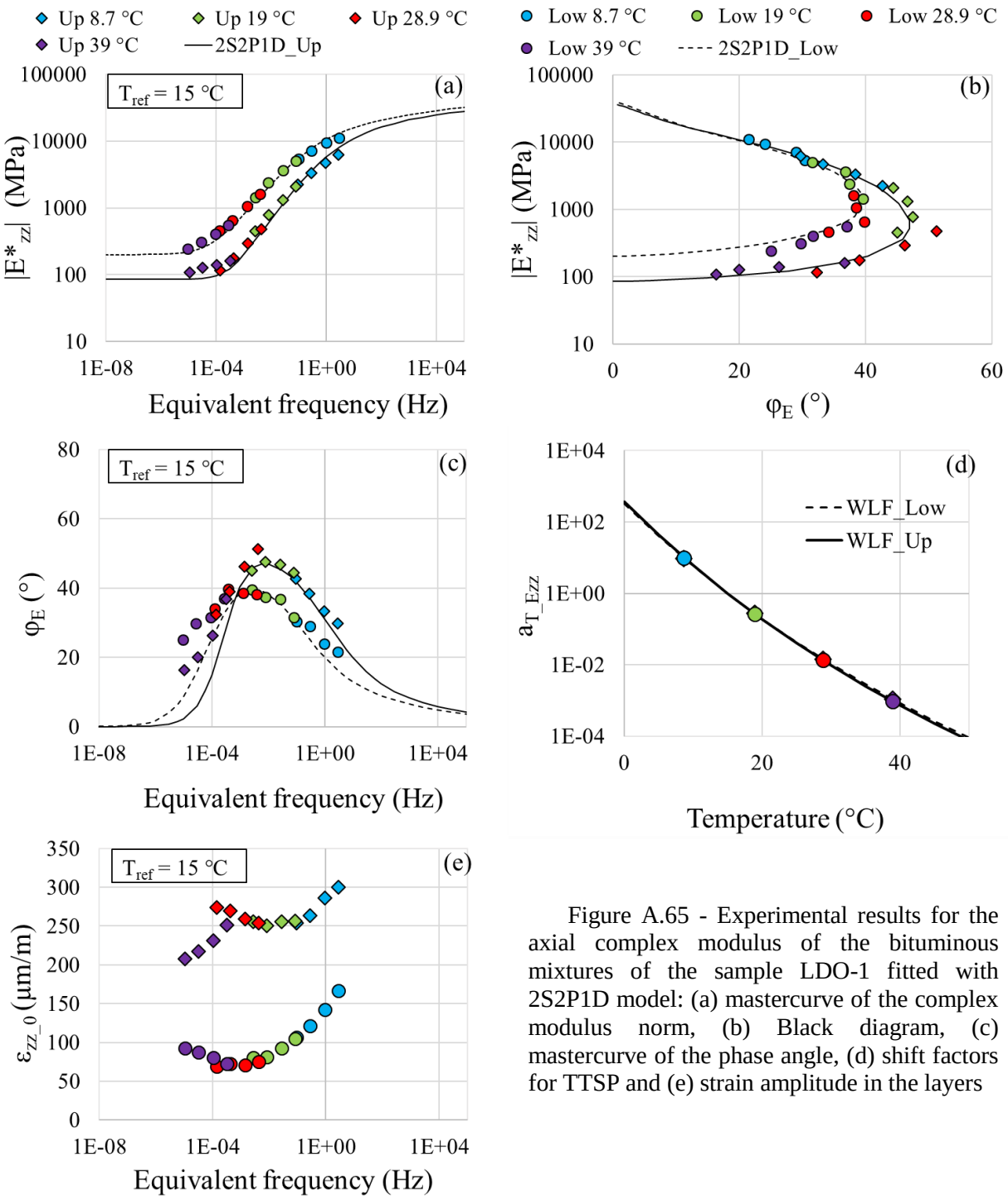

Figure A.65 - Experimental results for the axial complex modulus of the bituminous mixtures of the sample LDO-1 fitted with 2S2P1D model: (a) mastercurve of the complex modulus norm, (b) Black diagram, (c) mastercurve of the phase angle, (d) shift factors for TTSP and (e) strain amplitude in the layers

Table A.65 - 2S2P1D constants and WLF equation coefficients for sample LDO-1

Layer	Mixture	E_{00} (MPa)	E_0 (MPa)	k	h	δ	τ_E (s)	β	T_{ref} (°C)	C_1	C_2
Upper	BBSG3	85	38000	0.17	0.57	1.8	0.018	100	15	18.5	125.3
Lower	EME2	200	41000	0.17	0.57	2.1	0.15	250	15	18.8	124.9

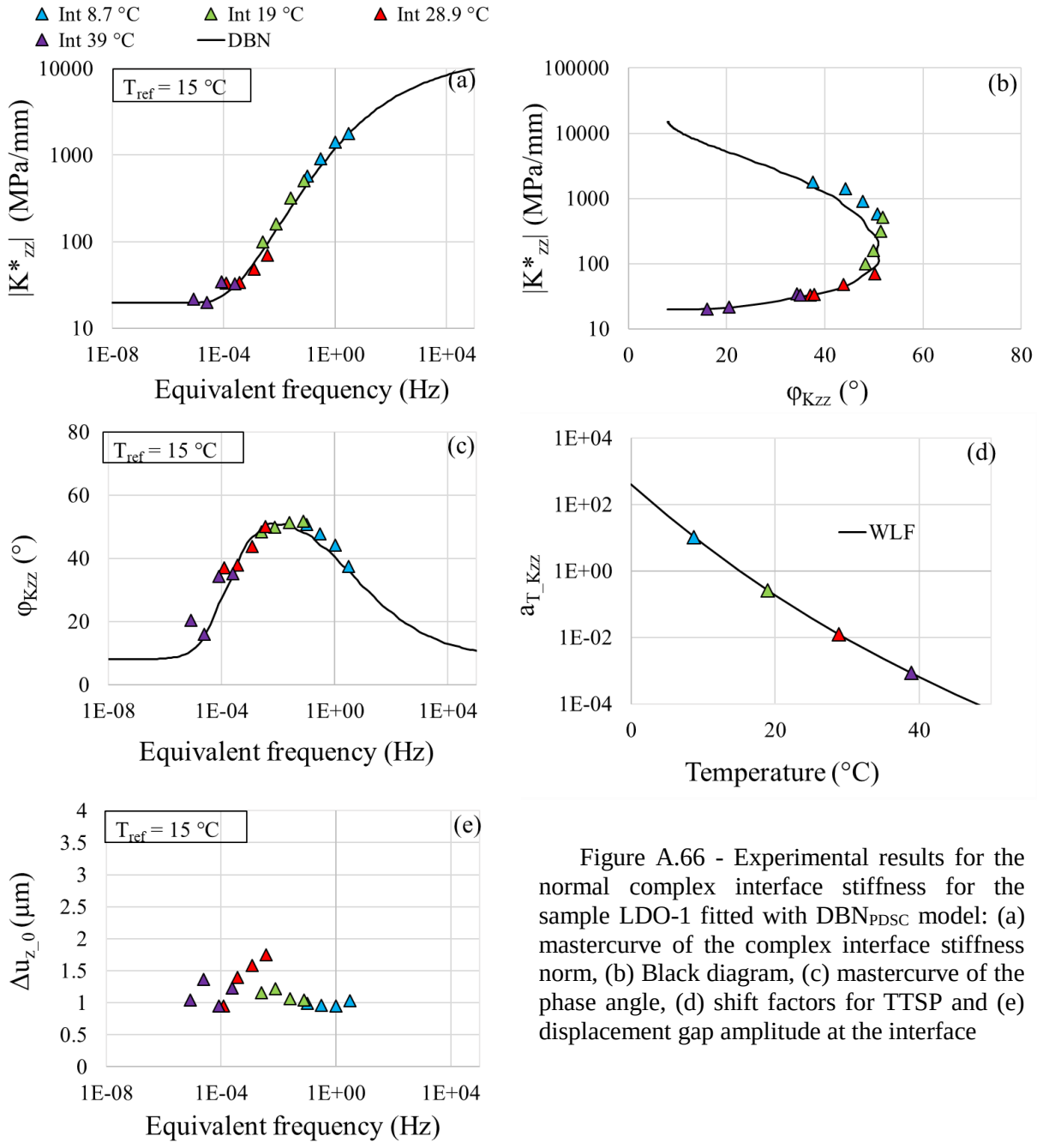

Figure A.66 - Experimental results for the normal complex interface stiffness for the sample LDO-1 fitted with DBN_{PDSC} model: (a) mastercurve of the complex interface stiffness norm, (b) Black diagram, (c) mastercurve of the phase angle, (d) shift factors for TTSP and (e) displacement gap amplitude at the interface

Table A.66 - 2S2P1D constants, DBN_{PDSC} constant φ_{NL} and WLF equation coefficients for sample LDO-1

K_{zz_00} (MPa)	K_{zz_0} (MPa)	k	h	δ	τ_{Kzz} (s)	β	φ_{NL}(°)	T_{ref} (°C)	C_1	C_2
20	15000	0.2	0.53	2.3	0.005	300	8	15	19.2	125.6

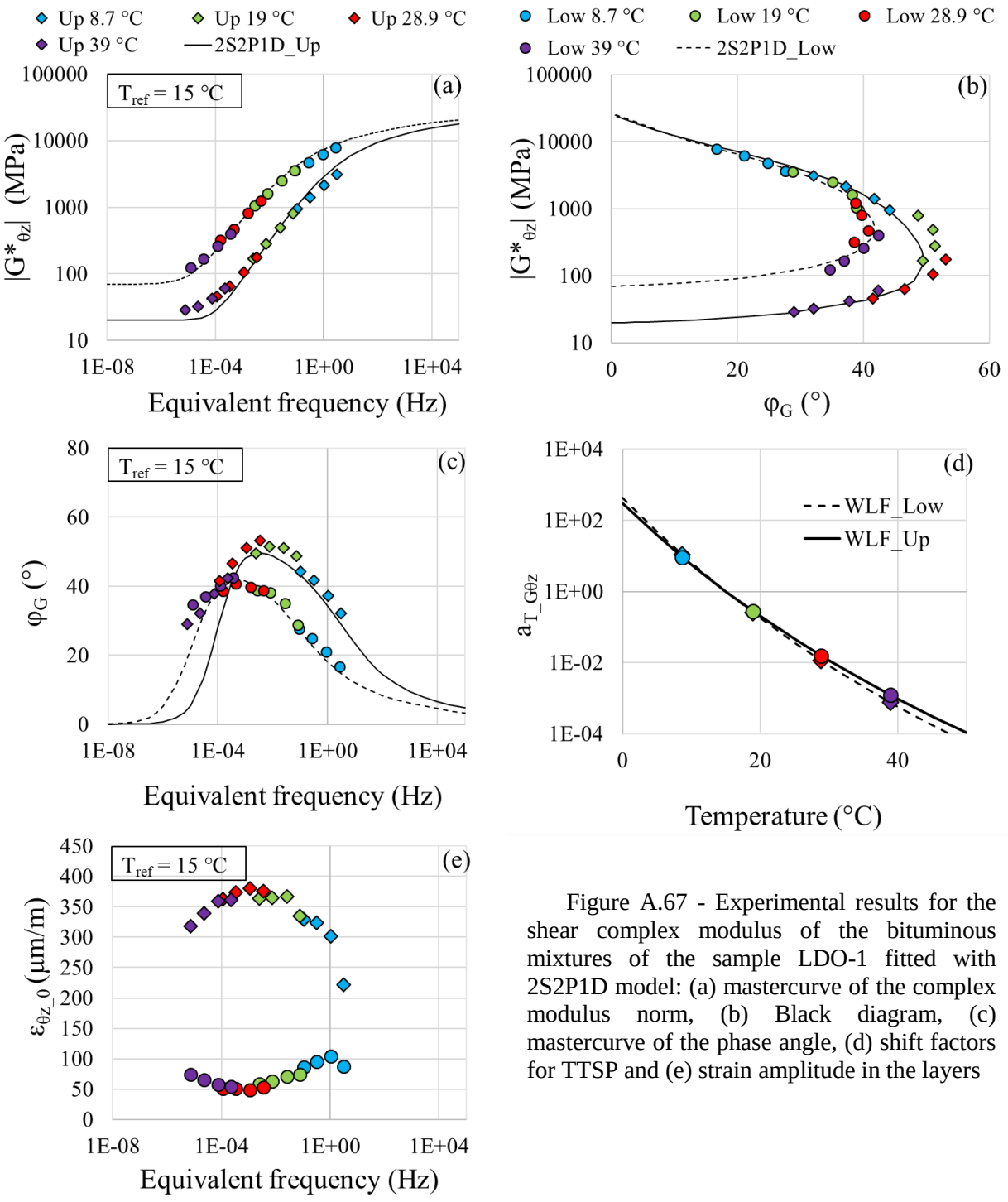

Figure A.67 - Experimental results for the shear complex modulus of the bituminous mixtures of the sample LDO-1 fitted with 2S2P1D model: (a) mastercurve of the complex modulus norm, (b) Black diagram, (c) mastercurve of the phase angle, (d) shift factors for TTSP and (e) strain amplitude in the layers

Table A.67 - 2S2P1D constants and WLF equation coefficients for sample LDO-1

Layer	Mixture	G_{00} (MPa)	G_0 (MPa)	k	h	δ	τ_G (s)	β	T_{ref} (°C)	C_1	C_2
Upper	BBSG3	20	25000	0.17	0.56	1.8	0.008	200	15	19.5	125.6
Lower	EME2	70	26000	0.17	0.55	2.1	0.25	250	15	18.2	125.3

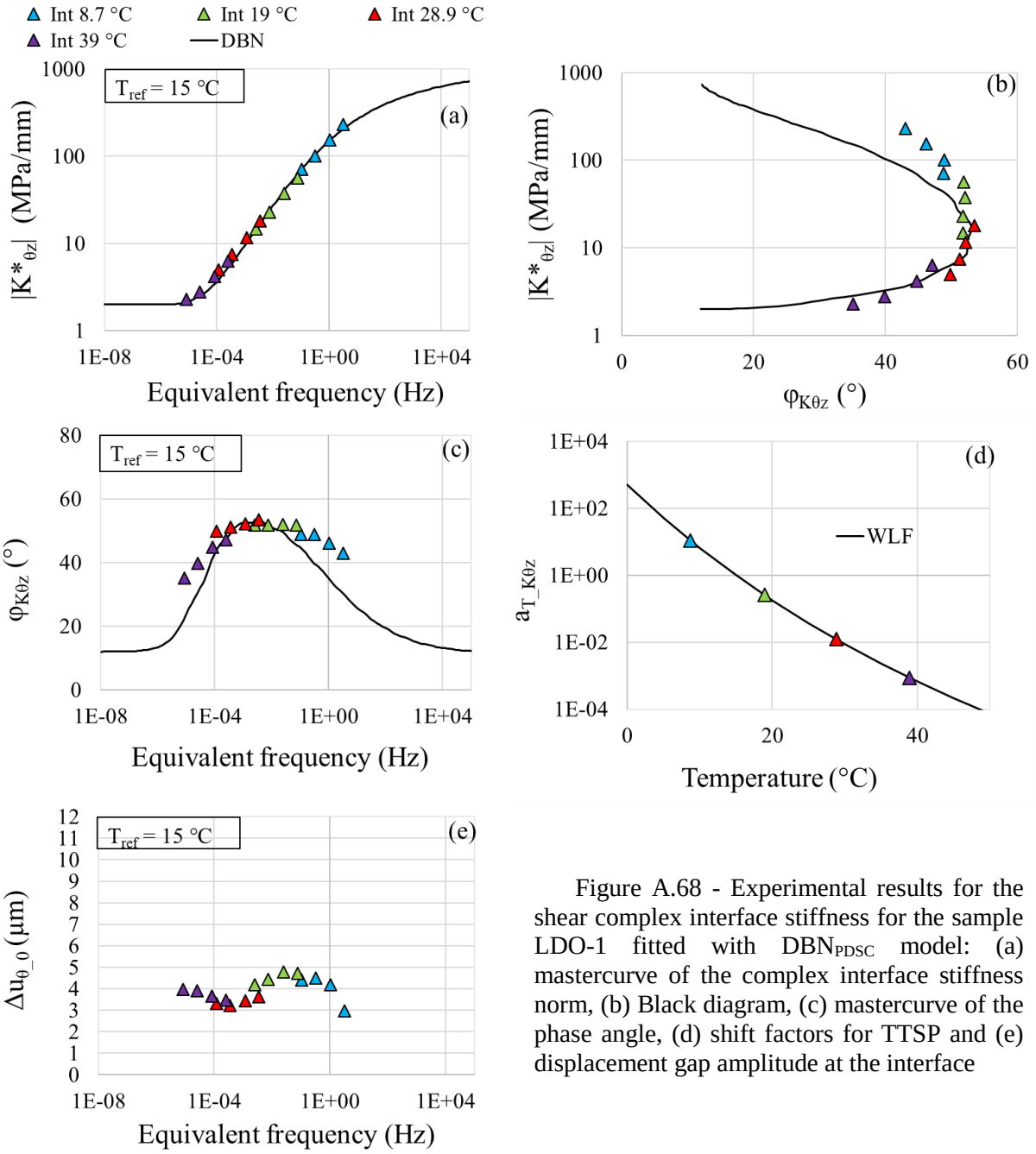

Figure A.68 - Experimental results for the shear complex interface stiffness for the sample LDO-1 fitted with DBN_{PDSC} model: (a) mastercurve of the complex interface stiffness norm, (b) Black diagram, (c) mastercurve of the phase angle, (d) shift factors for TTSP and (e) displacement gap amplitude at the interface

Table A.68 - 2S2P1D constants, DBN_{PDSC} constant φ_{NL} and WLF equation coefficients for sample LDO-1

K_{0z_00} (MPa)	K_{0z_0} (MPa)	k	h	δ	τ_{K0z} (s)	β	φ_{NL}(°)	T_{ref} (°C)	C_1	C_2
2	950	0.2	0.53	2.3	0.04	300	12	15	17.3	110.9

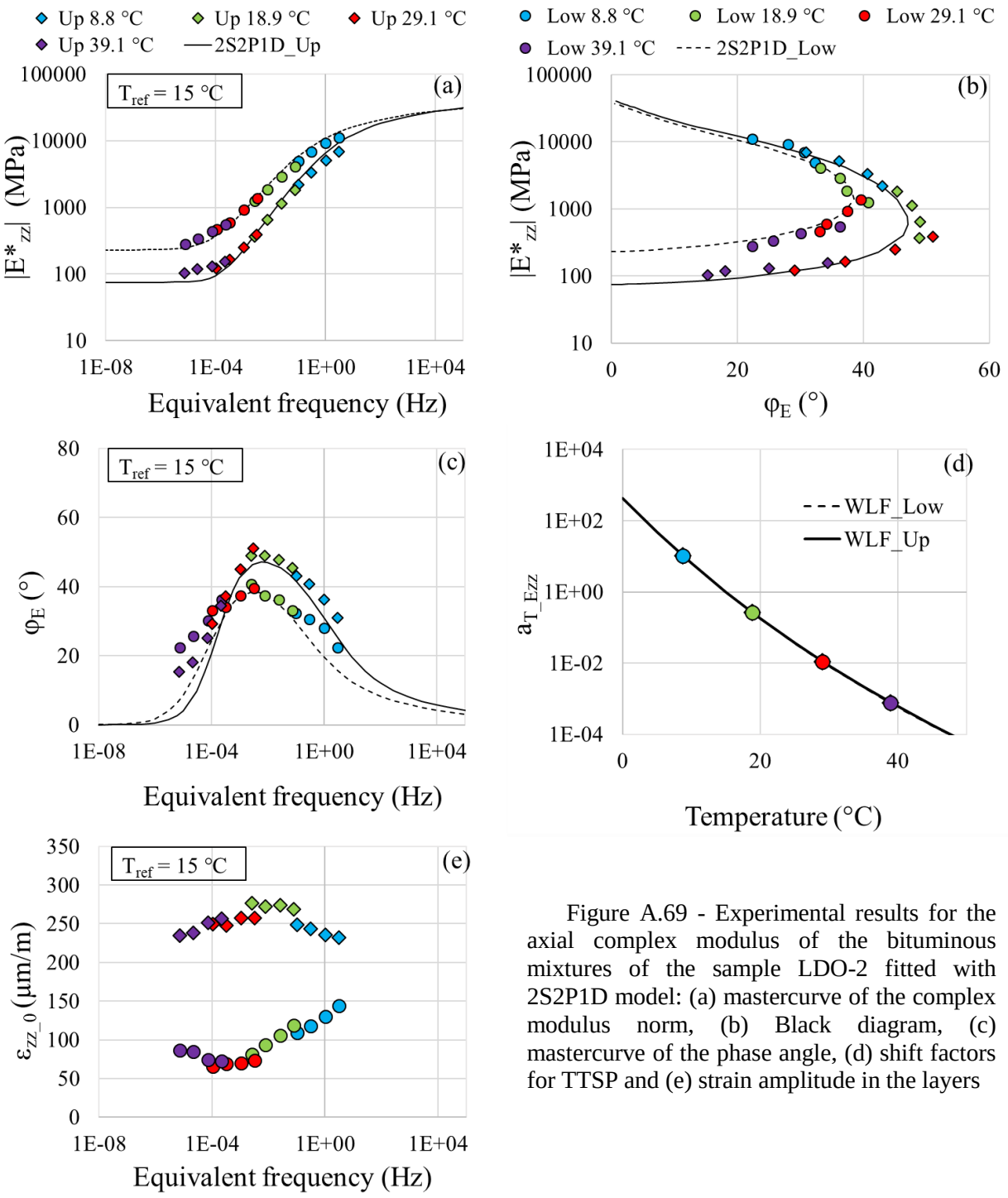

Figure A.69 - Experimental results for the axial complex modulus of the bituminous mixtures of the sample LDO-2 fitted with 2S2P1D model: (a) mastercurve of the complex modulus norm, (b) Black diagram, (c) mastercurve of the phase angle, (d) shift factors for TTSP and (e) strain amplitude in the layers

Table A.69 - 2S2P1D constants and WLF equation coefficients for sample LDO-2

Layer	Mixture	E_{00} (MPa)	E_0 (MPa)	k	h	δ	τ_E (s)	β	T_{ref} (°C)	C_1	C_2
Upper	BBSG3	75	42000	0.17	0.58	1.8	0.02	150	15	19.6	126.7
Lower	EME2	230	38000	0.17	0.56	1.8	0.17	280	15	19.5	126.2

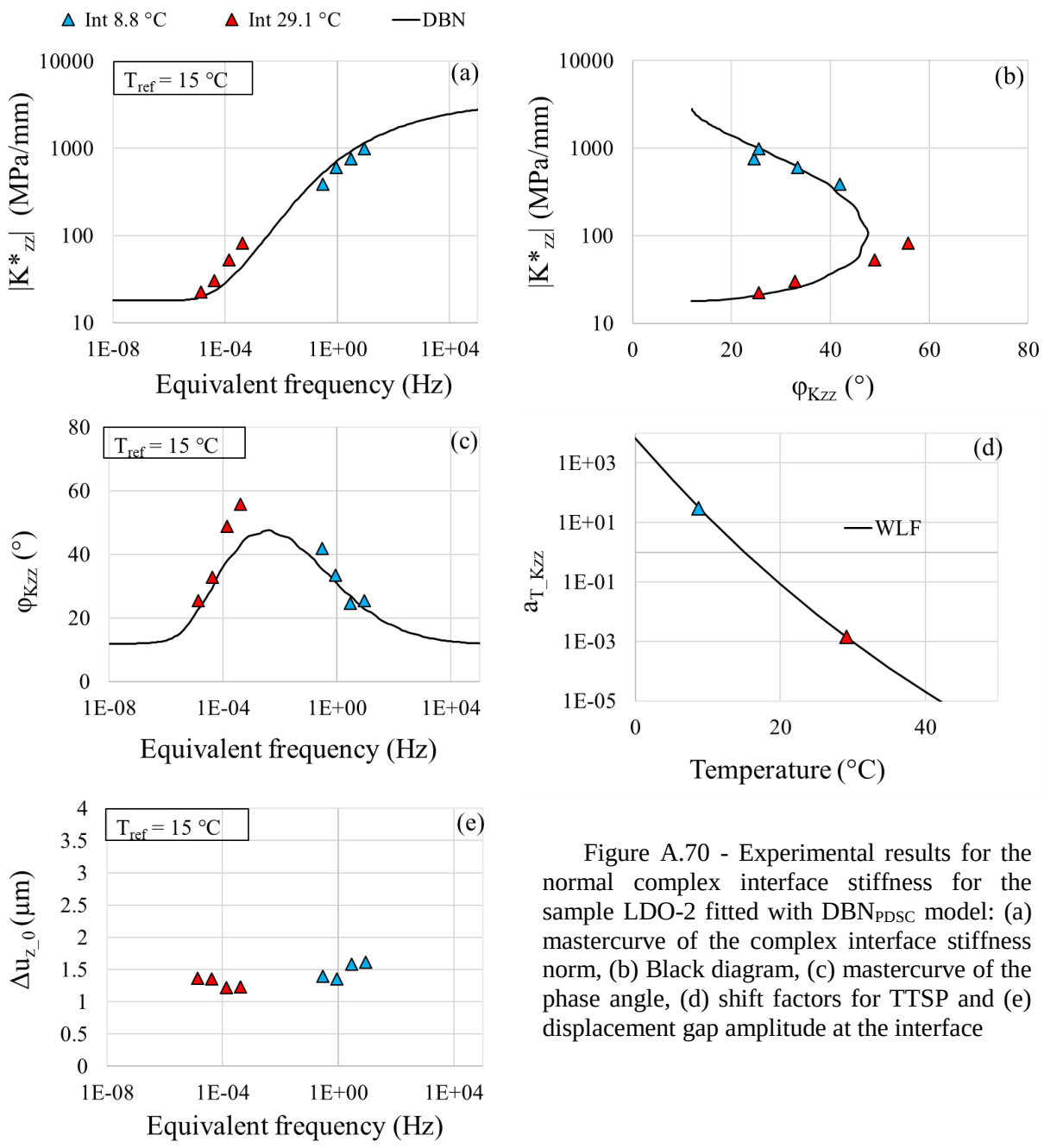

Figure A.70 - Experimental results for the normal complex interface stiffness for the sample LDO-2 fitted with DBN_{PDSC} model: (a) mastercurve of the complex interface stiffness norm, (b) Black diagram, (c) mastercurve of the phase angle, (d) shift factors for TTSP and (e) displacement gap amplitude at the interface

Table A.70 - 2S2P1D constants, DBN_{PDSC} constant φ_{NL} and WLF equation coefficients for sample LDO-2

K_{zz_00} (MPa)	K_{zz_0} (MPa)	k	h	δ	τ_{Kzz} (s)	β	φ_{NL}(°)	T_{ref} (°C)	C_1	C_2
18	3500	0.2	0.53	2.3	0.1	300	12	15	28.5	126.5

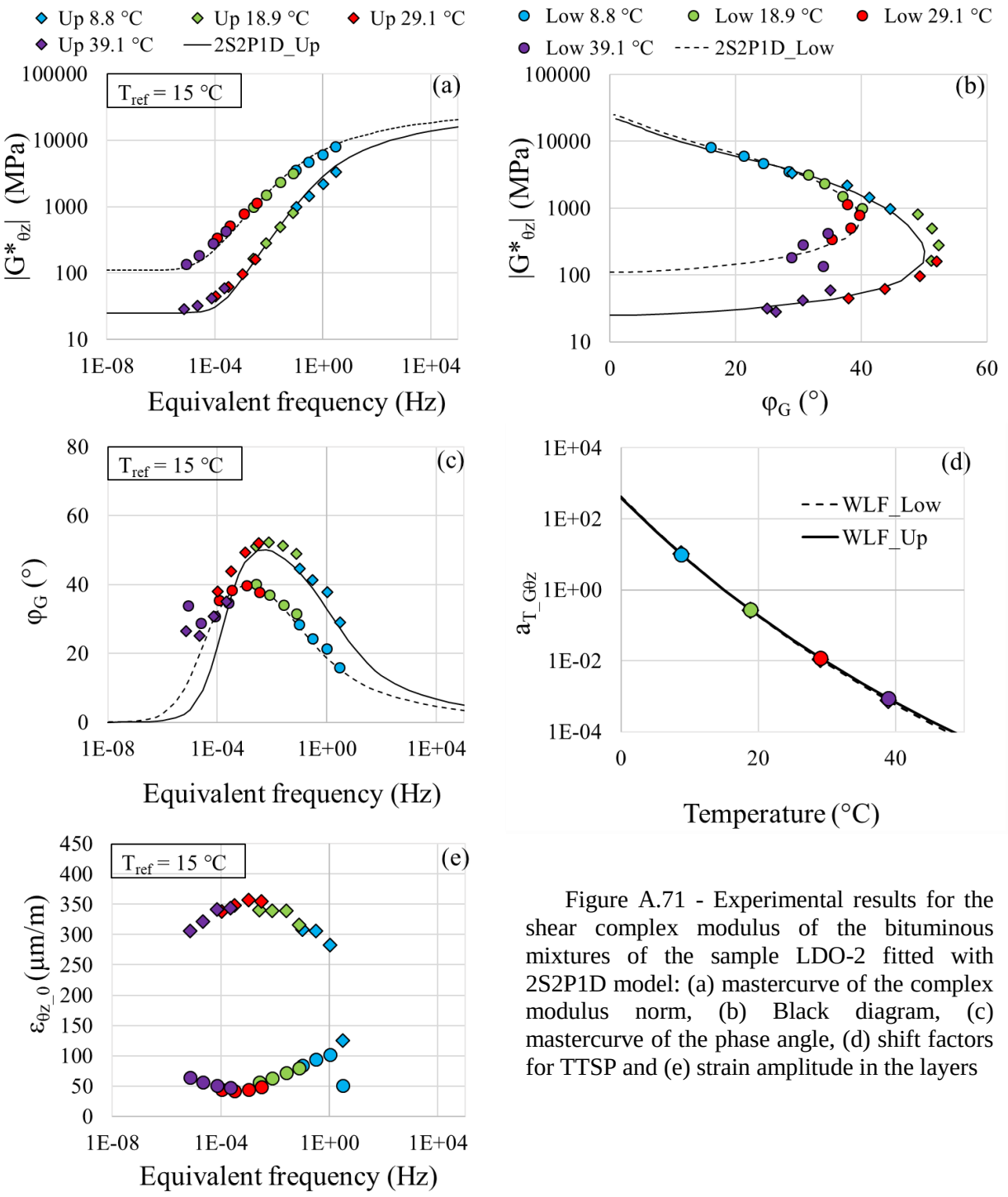

Figure A.71 - Experimental results for the shear complex modulus of the bituminous mixtures of the sample LDO-2 fitted with 2S2P1D model: (a) mastercurve of the complex modulus norm, (b) Black diagram, (c) mastercurve of the phase angle, (d) shift factors for TTSP and (e) strain amplitude in the layers

Table A.71 - 2S2P1D constants and WLF equation coefficients for sample LDO-2

Layer	Mixture	G_{00} (MPa)	G_0 (MPa)	k	h	δ	τ_G (s)	β	T_{ref} (°C)	C_1	C_2
Upper	BBSG3	25	23000	0.17	0.58	2.1	0.012	120	15	19.6	126.2
Lower	EME2	110	26000	0.17	0.55	2.1	0.2	200	15	19.2	126.3

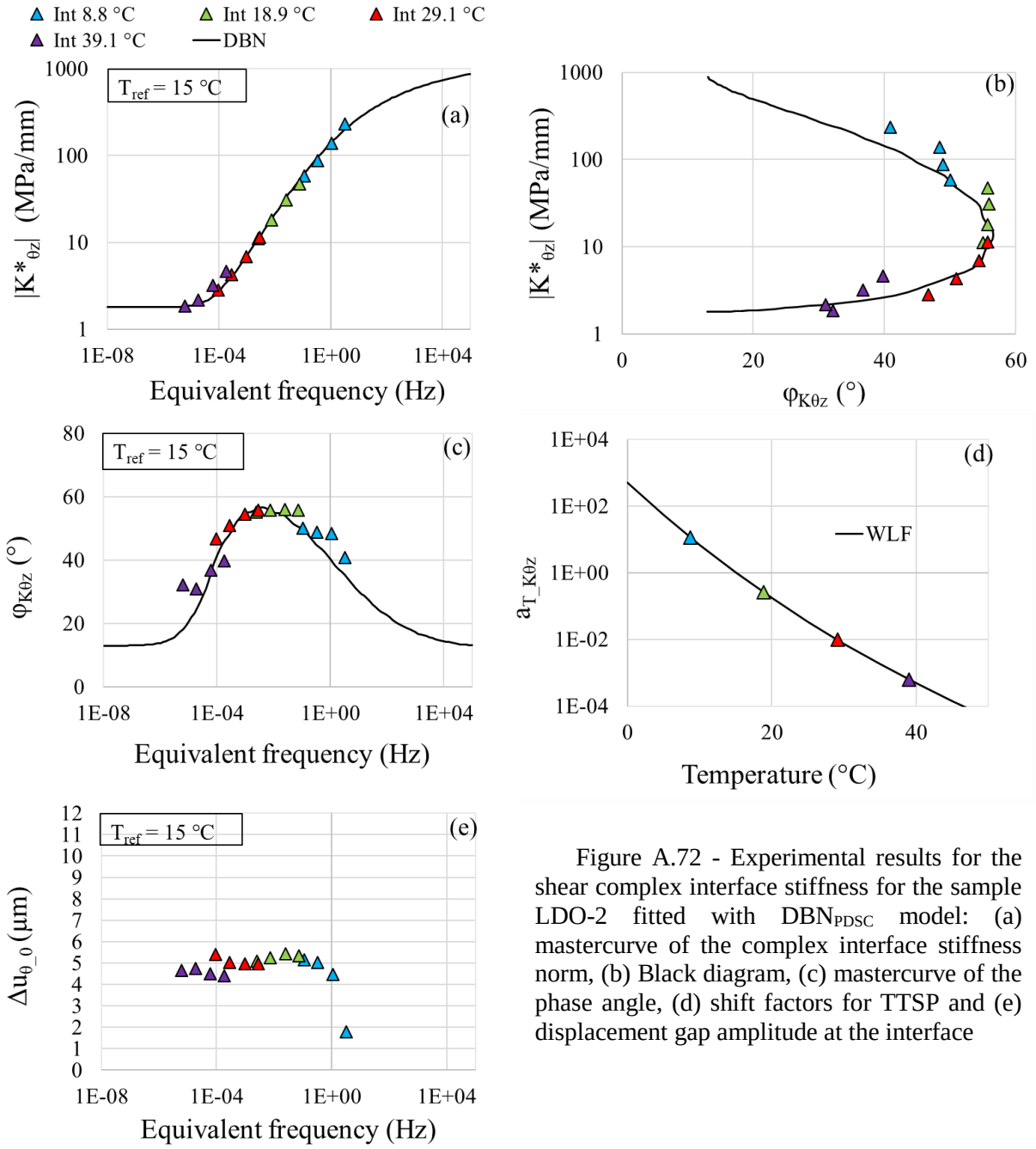

Figure A.72 - Experimental results for the shear complex interface stiffness for the sample LDO-2 fitted with DBN_{PDSC} model: (a) mastercurve of the complex interface stiffness norm, (b) Black diagram, (c) mastercurve of the phase angle, (d) shift factors for TTSP and (e) displacement gap amplitude at the interface

Table A.72 - 2S2P1D constants, DBN_{PDSC} constant φ_{NL} and WLF equation coefficients for sample LDO-2

K_{0z_00} (MPa)	K_{0z_0} (MPa)	k	h	δ	τ_{K0z} (s)	β	φ_{NL}(°)	T_{ref} (°C)	C_1	C_2
1.8	1200	0.2	0.53	2.3	0.015	300	13	15	20.0	126.0

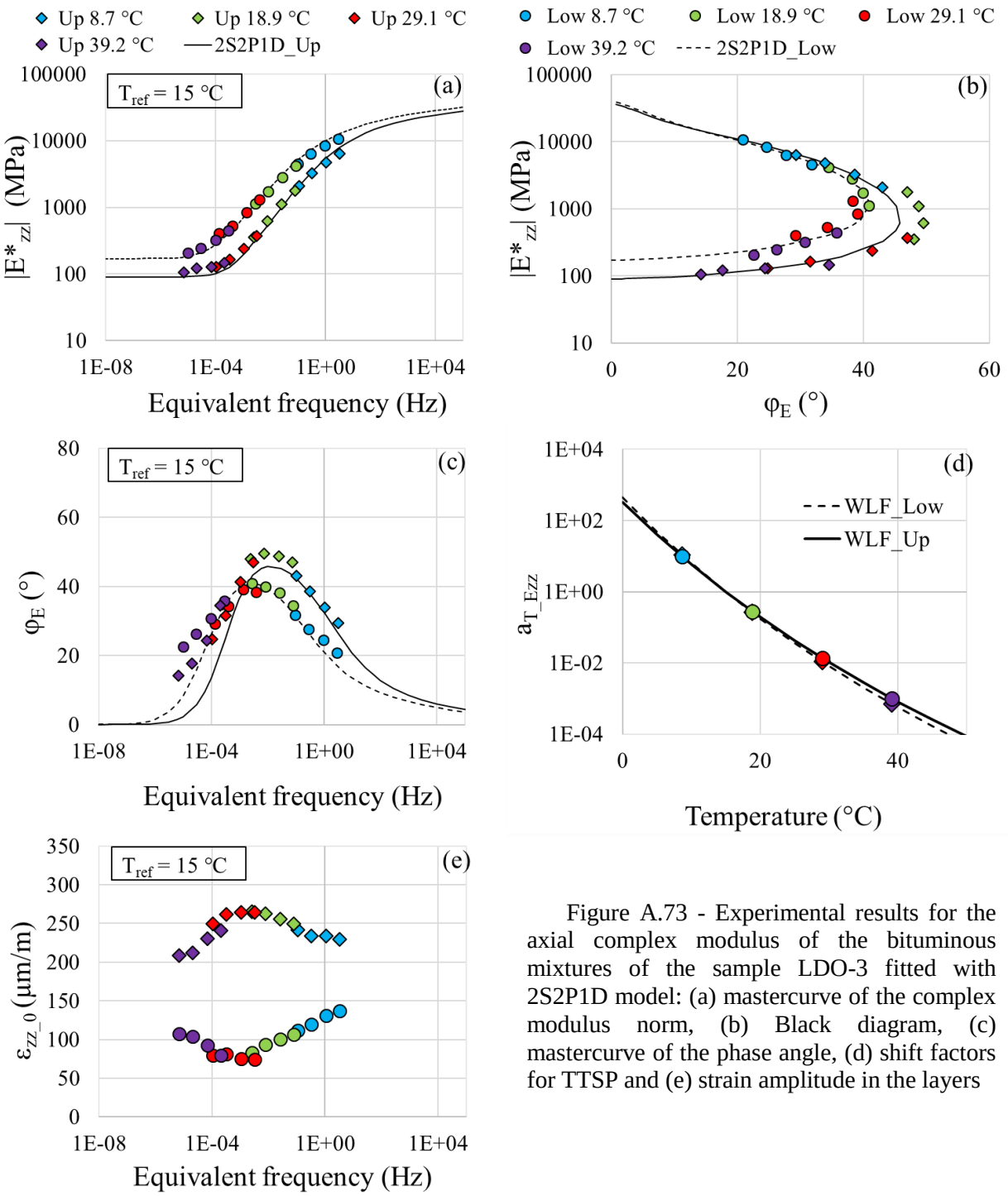

Figure A.73 - Experimental results for the axial complex modulus of the bituminous mixtures of the sample LDO-3 fitted with 2S2P1D model: (a) mastercurve of the complex modulus norm, (b) Black diagram, (c) mastercurve of the phase angle, (d) shift factors for TTSP and (e) strain amplitude in the layers

Table A.73 - 2S2P1D constants and WLF equation coefficients for sample LDO-3

Layer	Mixture	E_{00} (MPa)	E_0 (MPa)	k	h	δ	τ_E (s)	β	T_{ref} (°C)	C_1	C_2
Upper	BBSG3	90	38000	0.17	0.58	1.8	0.015	140	15	19.6	126.2
Lower	EME2	170	41000	0.17	0.57	2.1	0.12	200	15	18.7	126.3

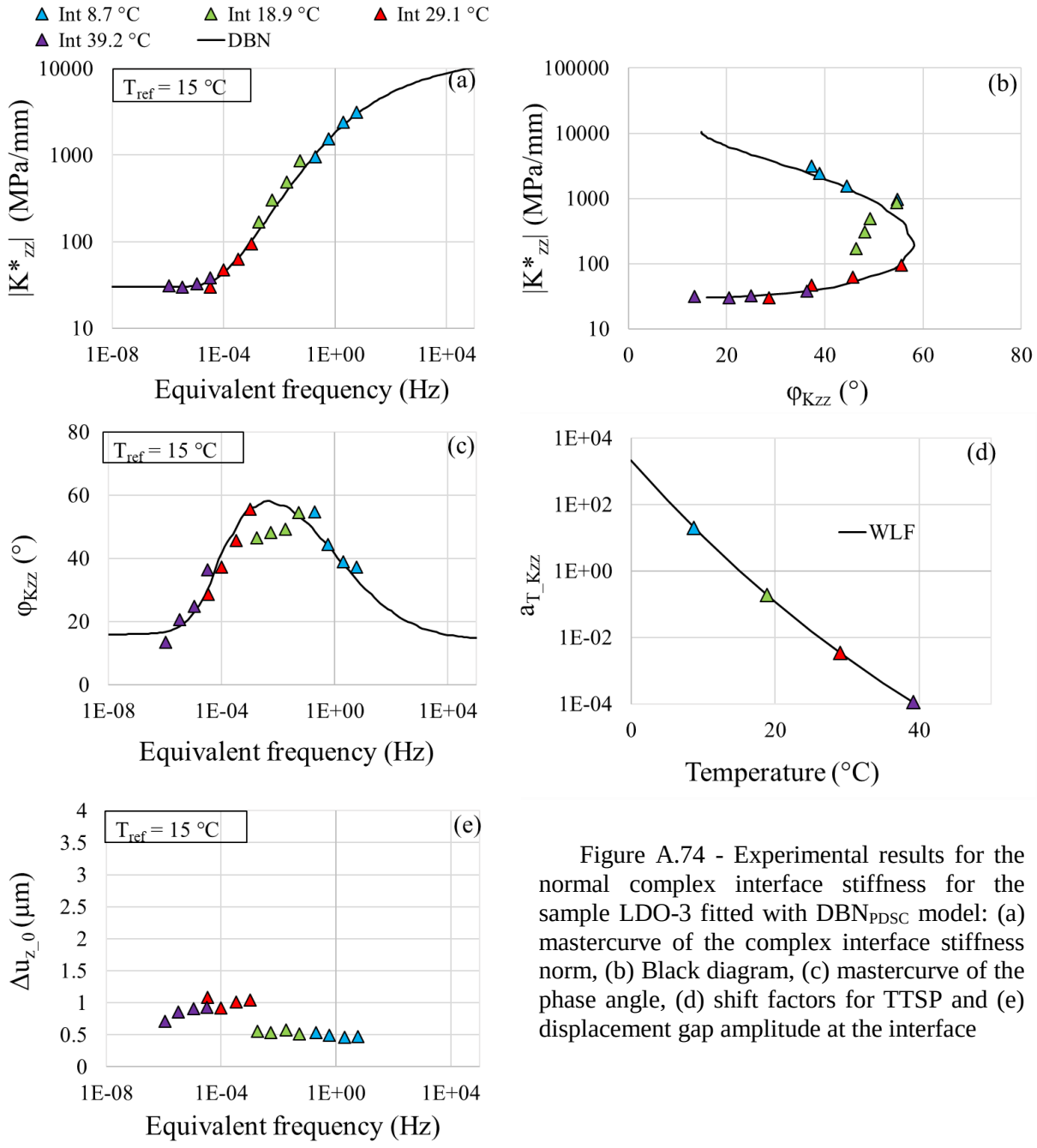

Figure A.74 - Experimental results for the normal complex interface stiffness for the sample LDO-3 fitted with DBN_{PDSC} model: (a) mastercurve of the complex interface stiffness norm, (b) Black diagram, (c) mastercurve of the phase angle, (d) shift factors for TTSP and (e) displacement gap amplitude at the interface

Table A.74 - 2S2P1D constants, DBN_{PDSC} constant φ_{NL} and WLF equation coefficients for sample LDO-3

K_{zz_00} (MPa)	K_{zz_0} (MPa)	k	h	δ	τ_{Kzz} (s)	β	φ_{NL}(°)	T_{ref} (°C)	C_1	C_2
30	14000	0.2	0.53	2.3	0.02	300	16	15	24.5	125.6

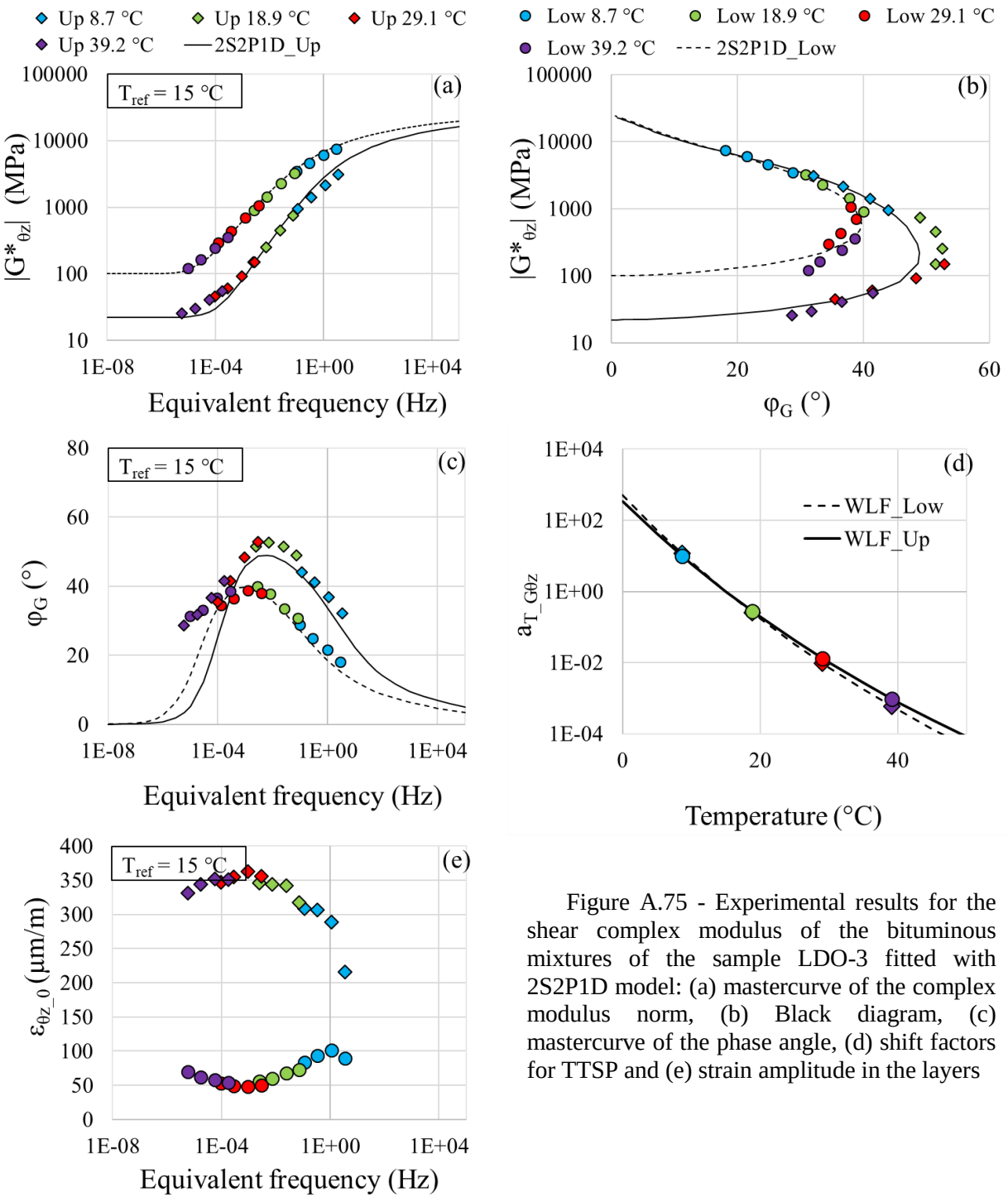

Figure A.75 - Experimental results for the shear complex modulus of the bituminous mixtures of the sample LDO-3 fitted with 2S2P1D model: (a) mastercurve of the complex modulus norm, (b) Black diagram, (c) mastercurve of the phase angle, (d) shift factors for TTSP and (e) strain amplitude in the layers

Table A.75 - 2S2P1D constants and WLF equation coefficients for sample LDO-3

Layer	Mixture	G_{00} (MPa)	G_0 (MPa)	k	h	δ	τ_G (s)	β	T_{ref} (°C)	C_1	C_2
Upper	BBSG3	22	24000	0.17	0.58	2.1	0.01	200	15	20.0	125.7
Lower	EME2	100	25000	0.17	0.54	2.1	0.2	200	15	18.8	125.9

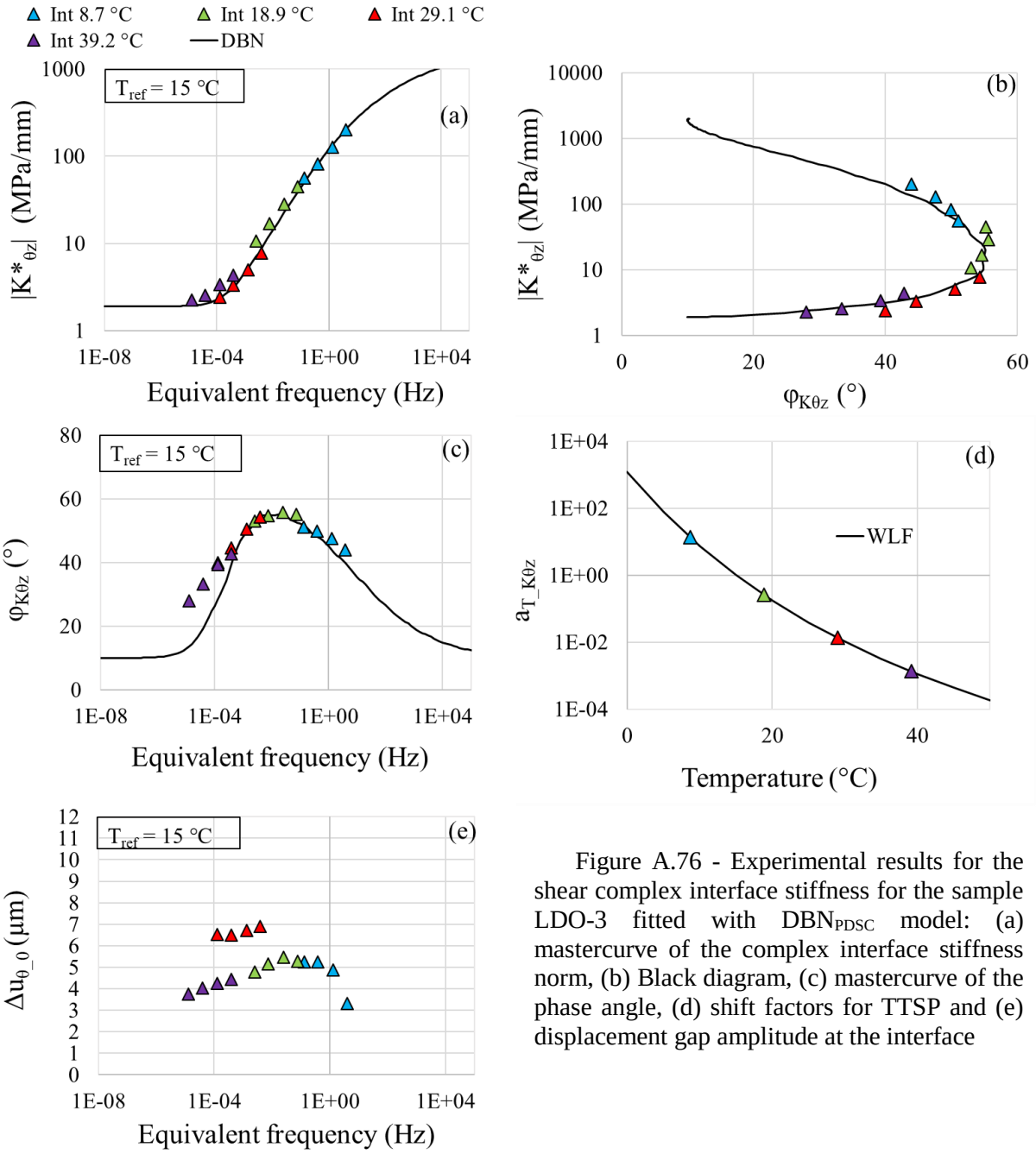

Figure A.76 - Experimental results for the shear complex interface stiffness for the sample LDO-3 fitted with DBN_{PDSC} model: (a) mastercurve of the complex interface stiffness norm, (b) Black diagram, (c) mastercurve of the phase angle, (d) shift factors for TTSP and (e) displacement gap amplitude at the interface

Table A.76 - 2S2P1D constants, DBN_{PDSC} constant φ_{NL} and WLF equation coefficients for sample LDO-3

K_{0z_00} (MPa)	K_{0z_0} (MPa)	k	h	δ	τ_{K0z} (s)	β	φ_{NL}(°)	T_{ref} (°C)	C_1	C_2
2	2000	0.2	0.53	2.3	0.0025	300	10	15	11.1	68.7

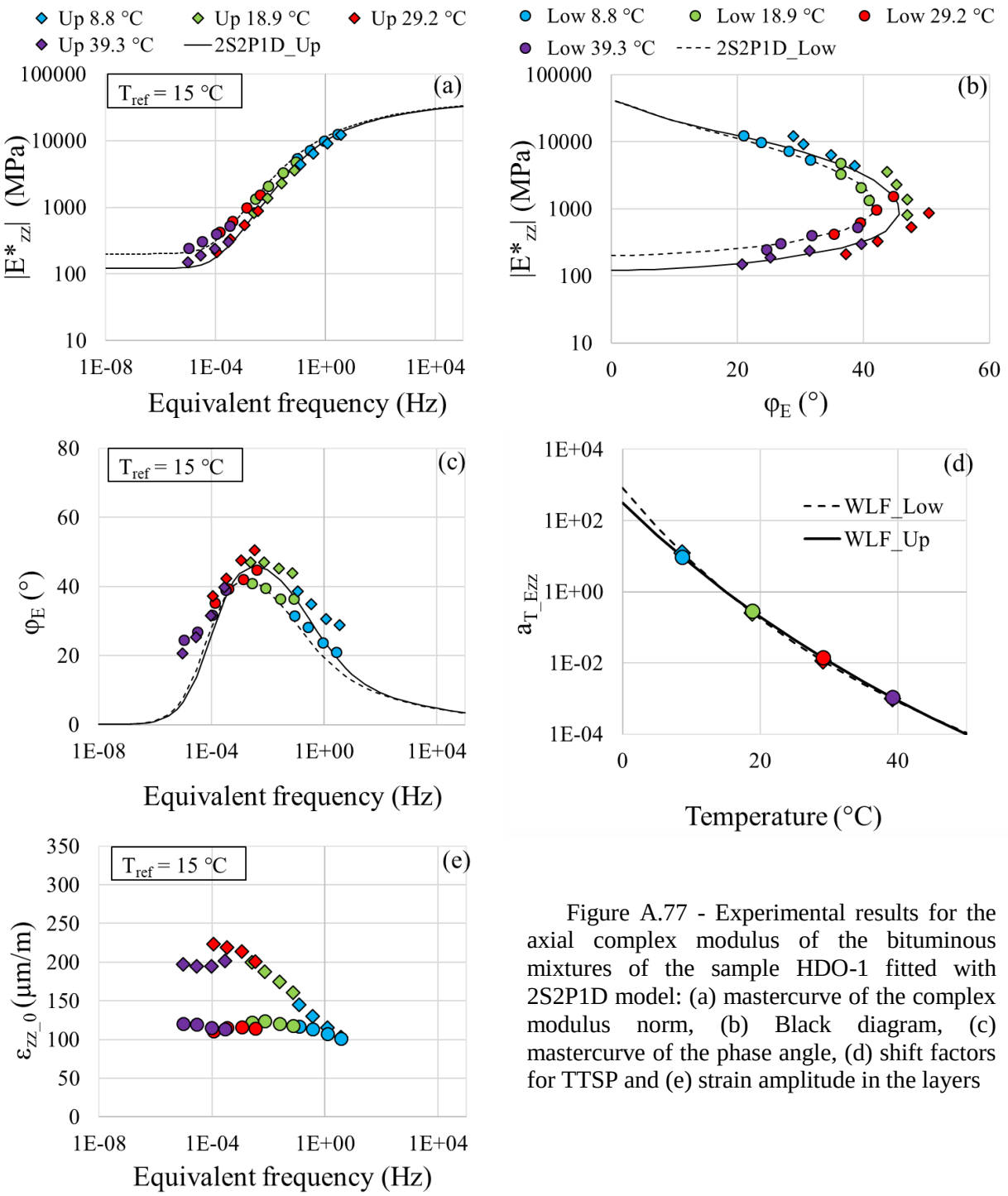

Figure A.77 - Experimental results for the axial complex modulus of the bituminous mixtures of the sample HDO-1 fitted with 2S2P1D model: (a) mastercurve of the complex modulus norm, (b) Black diagram, (c) mastercurve of the phase angle, (d) shift factors for TTSP and (e) strain amplitude in the layers

Table A.77 - 2S2P1D constants and WLF equation coefficients for sample HDO-1

Layer	Mixture	E_{00} (MPa)	E_0 (MPa)	k	h	δ	τ_E (s)	β	T_{ref} (°C)	C_1	C_2
Upper	BBSG3	120	42000	0.17	0.59	1.8	0.08	120	15	13.4	83.8
Lower	EME2	200	42000	0.18	0.57	2.1	0.2	90	15	18.4	125.8

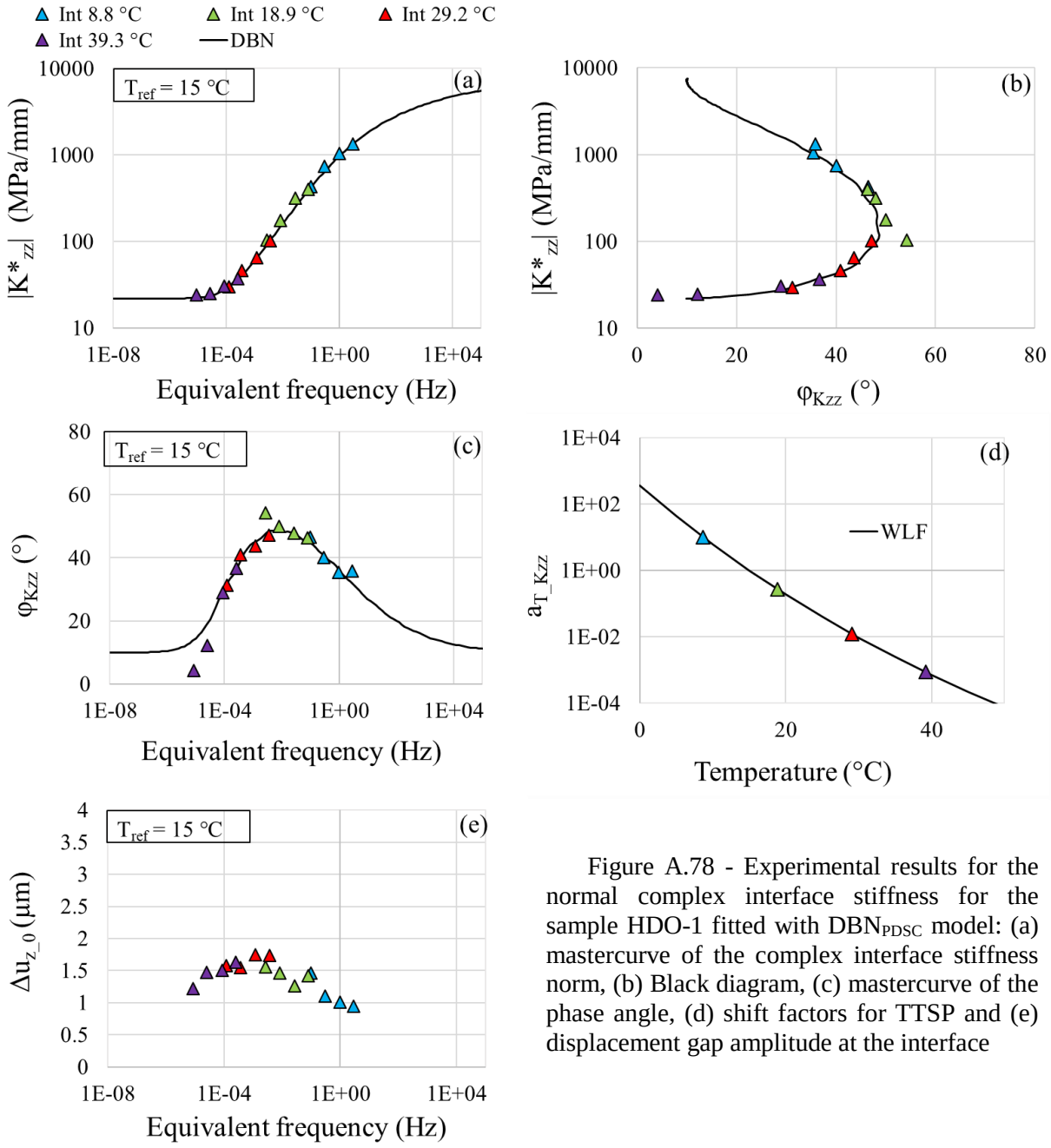

Figure A.78 - Experimental results for the normal complex interface stiffness for the sample HDO-1 fitted with DBN_{PDSC} model: (a) mastercurve of the complex interface stiffness norm, (b) Black diagram, (c) mastercurve of the phase angle, (d) shift factors for TTSP and (e) displacement gap amplitude at the interface

Table A.78 - 2S2P1D constants, DBN_{PDSC} constant φ_{NL} and WLF equation coefficients for sample HDO-1

K_{zz_00} (MPa)	K_{zz_0} (MPa)	k	h	δ	τ_{Kzz} (s)	β	φ_{NL}(°)	T_{ref} (°C)	C_1	C_2
22	7500	0.2	0.53	2.3	0.02	300	10	15	19.1	126.7

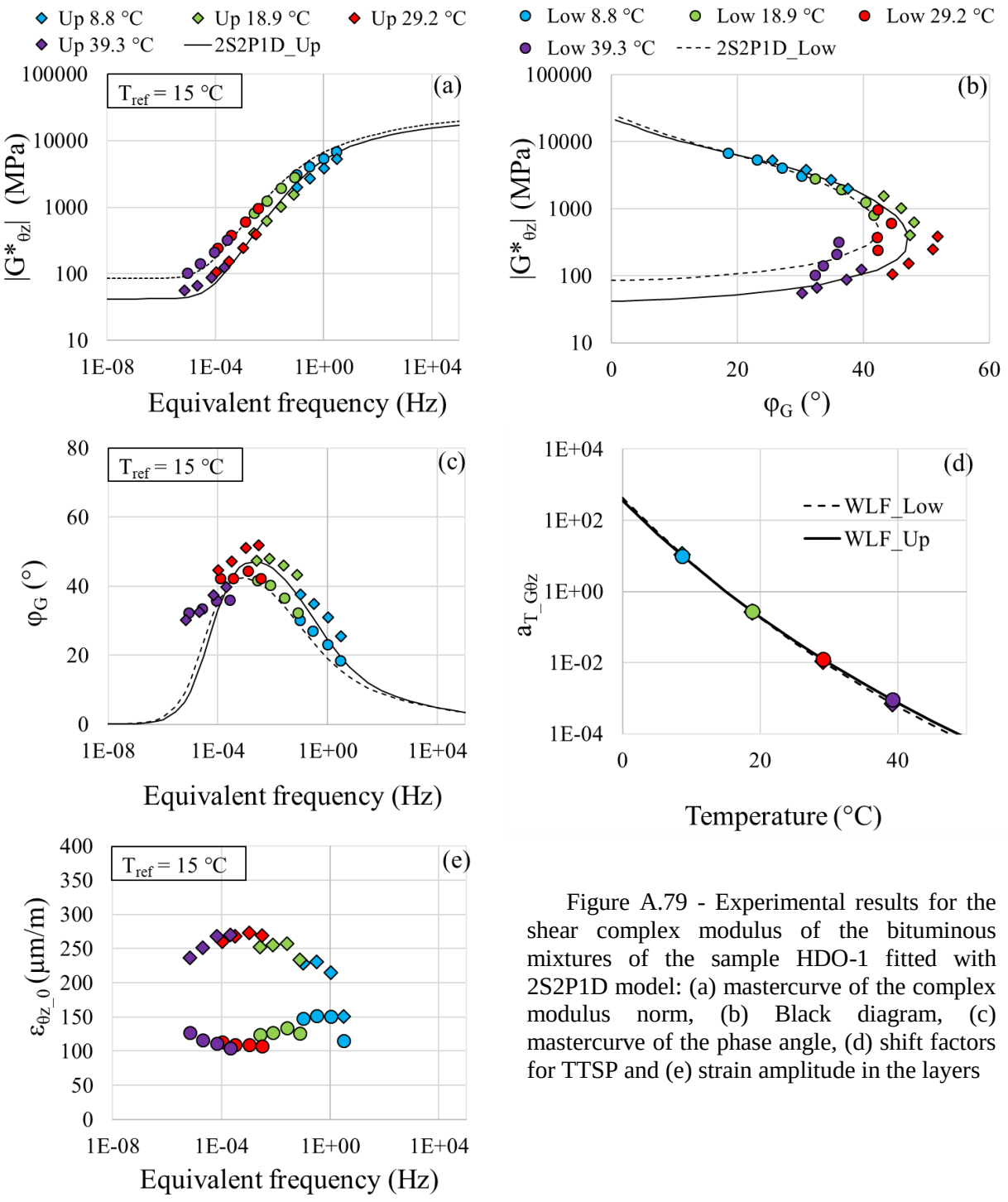

Figure A.79 - Experimental results for the shear complex modulus of the bituminous mixtures of the sample HDO-1 fitted with 2S2P1D model: (a) mastercurve of the complex modulus norm, (b) Black diagram, (c) mastercurve of the phase angle, (d) shift factors for TTSP and (e) strain amplitude in the layers

Table A.79 - 2S2P1D constants and WLF equation coefficients for sample HDO-1

Layer	Mixture	G_{00} (MPa)	G_0 (MPa)	k	h	δ	τ_G (s)	β	T_{ref} (°C)	C_1	C_2
Upper	BBSG3	42	22000	0.17	0.58	1.8	0.07	130	15	19.6	126.2
Lower	EME2	85	25000	0.17	0.55	2.1	0.18	130	15	18.9	126.1

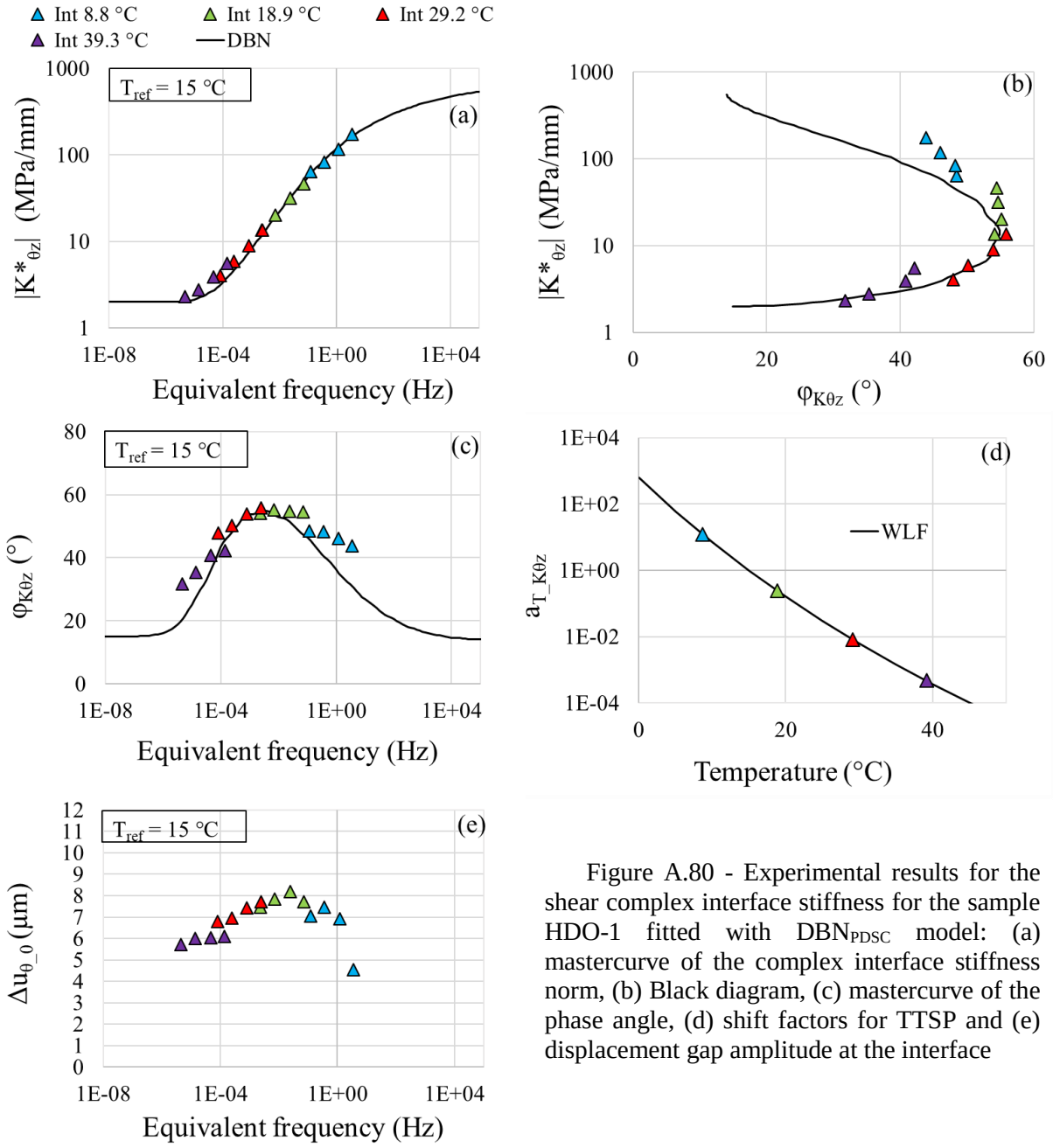

Figure A.80 - Experimental results for the shear complex interface stiffness for the sample HDO-1 fitted with DBN_{PDSC} model: (a) mastercurve of the complex interface stiffness norm, (b) Black diagram, (c) mastercurve of the phase angle, (d) shift factors for TTSP and (e) displacement gap amplitude at the interface

Table A.80 - 2S2P1D constants, DBN_{PDSC} constant φ_{NL} and WLF equation coefficients for sample HDO-1

K_{0z_00} (MPa)	K_{0z_0} (MPa)	k	h	δ	τ_{K0z} (s)	β	φ_{NL}(°)	T_{ref} (°C)	C_1	C_2
2	700	0.2	0.53	2.3	0.05	300	15	15	20.7	126.5

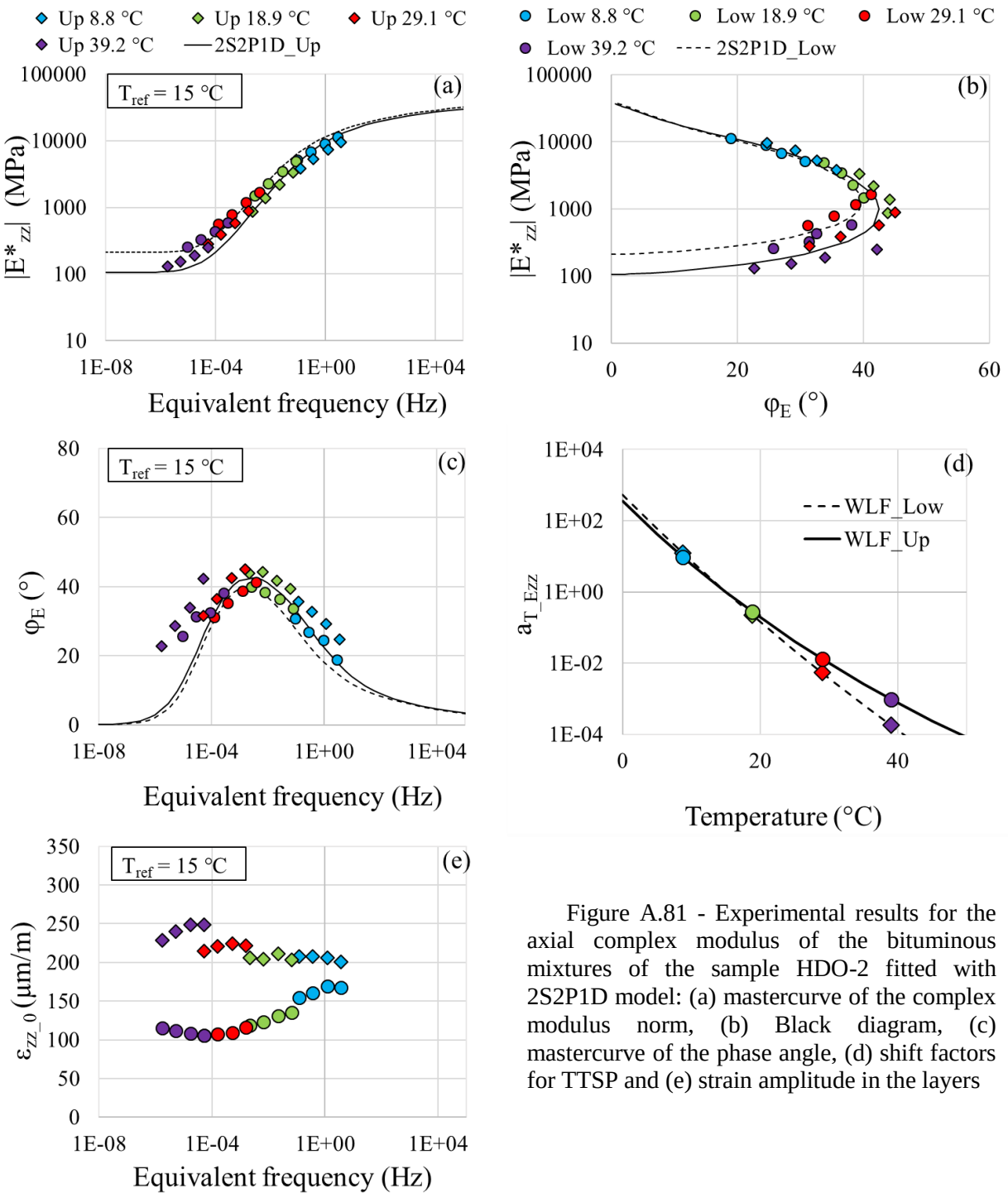

Figure A.81 - Experimental results for the axial complex modulus of the bituminous mixtures of the sample HDO-2 fitted with 2S2P1D model: (a) mastercurve of the complex modulus norm, (b) Black diagram, (c) mastercurve of the phase angle, (d) shift factors for TTSP and (e) strain amplitude in the layers

Table A.81 - 2S2P1D constants and WLF equation coefficients for sample HDO-2

Layer	Mixture	E_{00} (MPa)	E_0 (MPa)	k	h	δ	τ_E (s)	β	T_{ref} (°C)	C_1	C_2
Upper	BBSG3	105	38000	0.17	0.57	1.8	0.1	450	15	41.4	242.1
Lower	EME2	210	40000	0.17	0.57	2.1	0.25	180	15	18.8	125.7

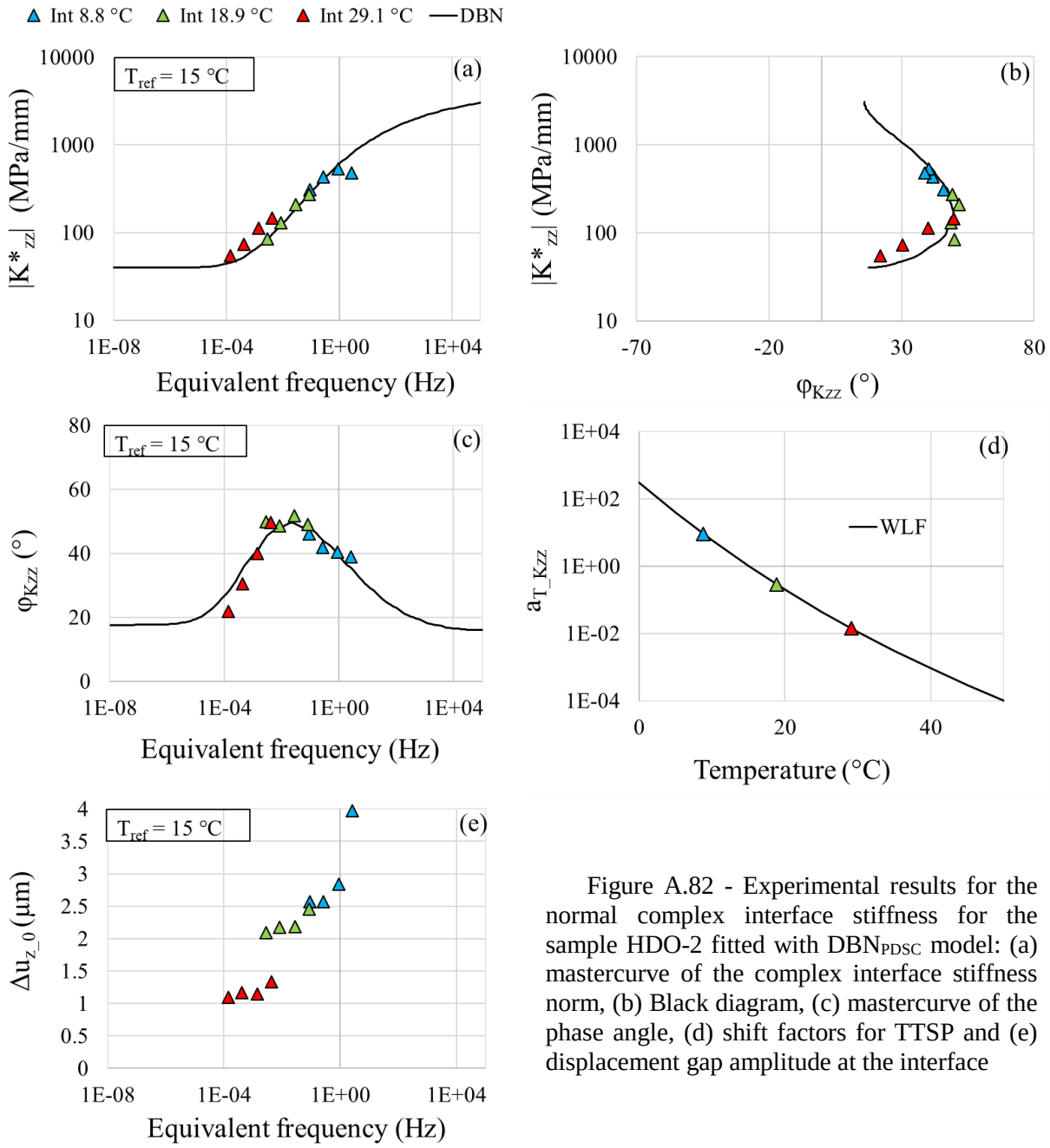

Figure A.82 - Experimental results for the normal complex interface stiffness for the sample HDO-2 fitted with DBN_{PDSC} model: (a) mastercurve of the complex interface stiffness norm, (b) Black diagram, (c) mastercurve of the phase angle, (d) shift factors for TTSP and (e) displacement gap amplitude at the interface

Table A.82 - 2S2P1D constants, DBN_{PDSC} constant φ_{NL} and WLF equation coefficients for sample HDO-2

K_{zz_00} (MPa)	K_{zz_0} (MPa)	k	h	δ	τ_{Kzz} (s)	β	φ_{NL}(°)	T_{ref} (°C)	C_1	C_2
40	4000	0.2	0.53	2.3	0.03	300	18	15	18.4	126.4

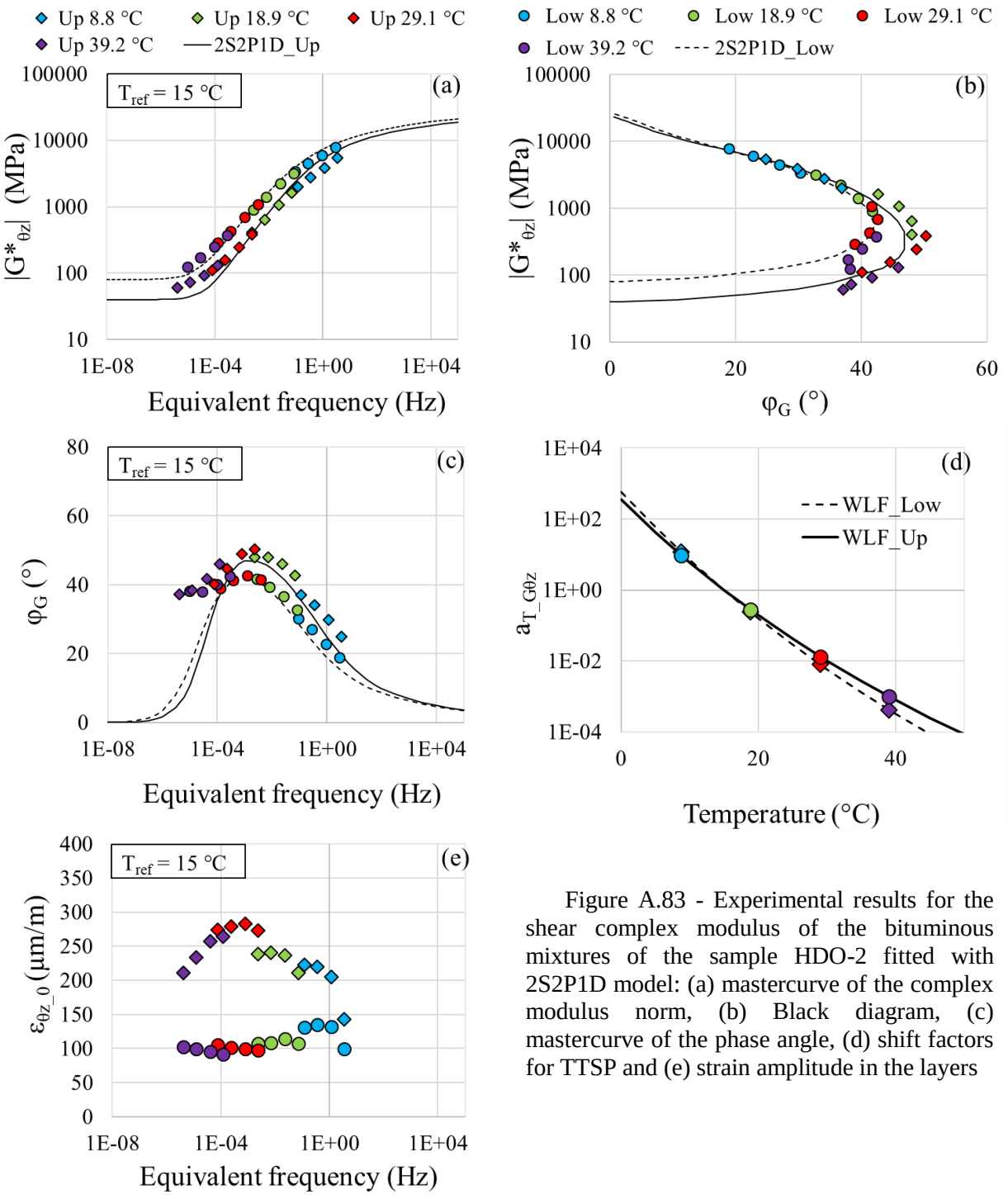

Figure A.83 - Experimental results for the shear complex modulus of the bituminous mixtures of the sample HDO-2 fitted with 2S2P1D model: (a) mastercurve of the complex modulus norm, (b) Black diagram, (c) mastercurve of the phase angle, (d) shift factors for TTSP and (e) strain amplitude in the layers

Table A.83 - 2S2P1D constants and WLF equation coefficients for sample HDO-2

Layer	Mixture	G_{00} (MPa)	G_0 (MPa)	k	h	δ	τ_G (s)	β	T_{ref} (°C)	C_1	C_2
Upper	BBSG3	40	24000	0.17	0.57	1.8	0.06	150	15	22.7	137.8
Lower	EME2	80	27000	0.17	0.56	2.1	0.2	220	15	18.4	123.2

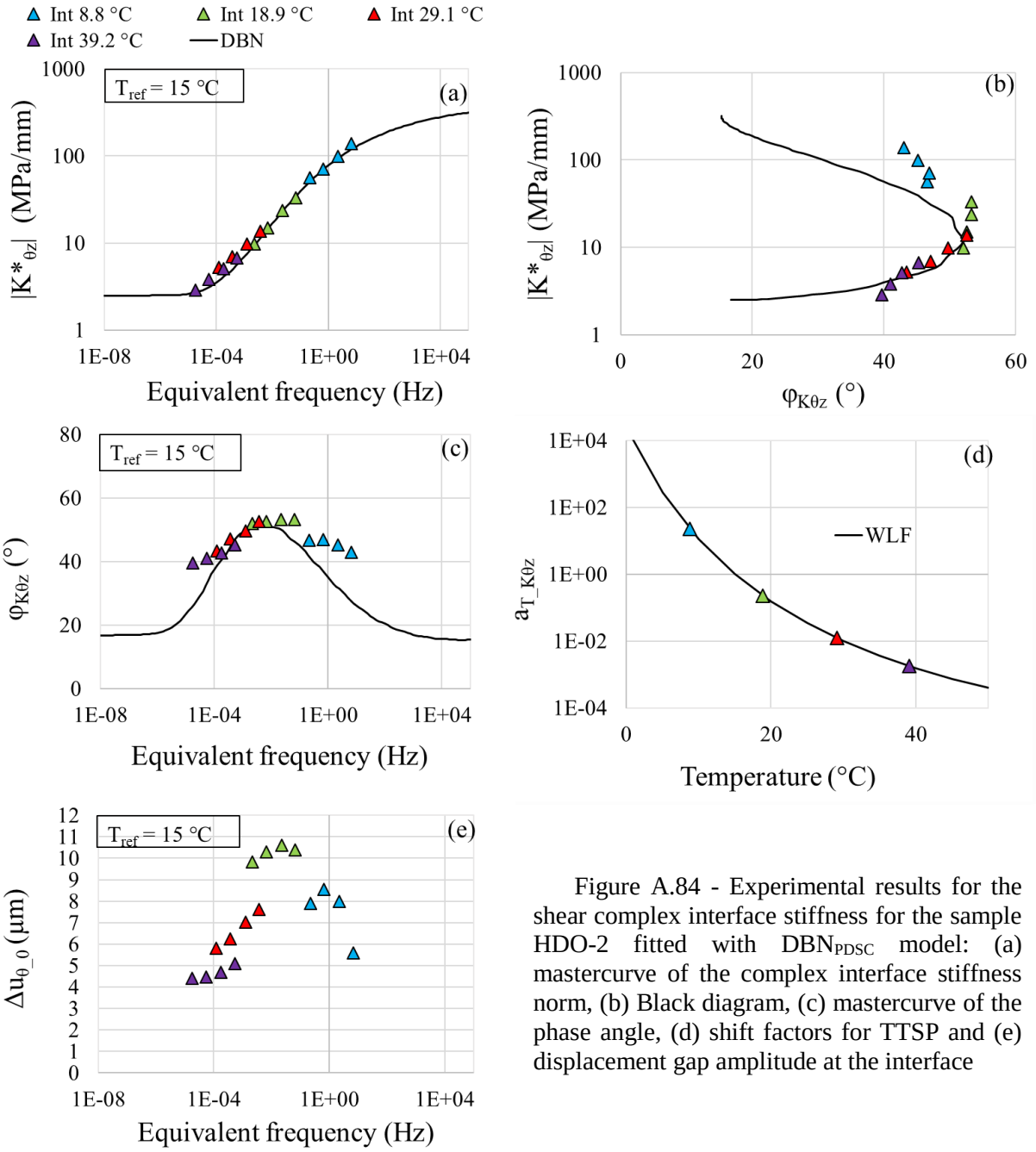

Figure A.84 - Experimental results for the shear complex interface stiffness for the sample HDO-2 fitted with DBN_{PDSC} model: (a) mastercurve of the complex interface stiffness norm, (b) Black diagram, (c) mastercurve of the phase angle, (d) shift factors for TTSP and (e) displacement gap amplitude at the interface

Table A.84 - 2S2P1D constants, DBN_{PDSC} constant φ_{NL} and WLF equation coefficients for sample HDO-2

$K_{\theta z\_00}$ (MPa)	$K_{\theta z\_0}$ (MPa)	k	h	δ	$\tau_{K\theta z}$ (s)	β	φ_{NL}(°)	T_{ref} (°C)	C_1	C_2
2.5	400	0.2	0.53	2.3	0.08	300	17	15	7.3	39.7

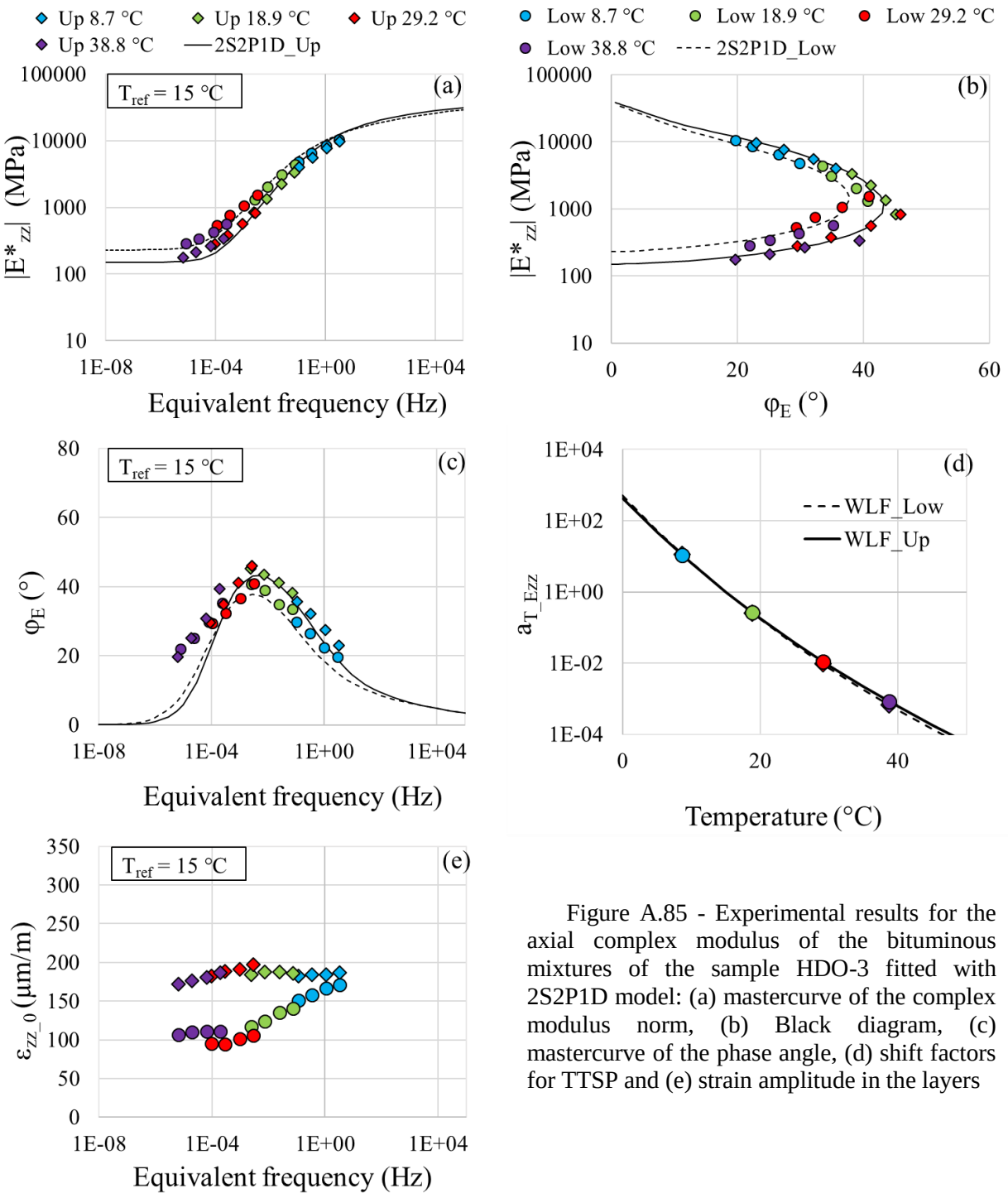

Figure A.85 - Experimental results for the axial complex modulus of the bituminous mixtures of the sample HDO-3 fitted with 2S2P1D model: (a) mastercurve of the complex modulus norm, (b) Black diagram, (c) mastercurve of the phase angle, (d) shift factors for TTSP and (e) strain amplitude in the layers

Table A.85 - 2S2P1D constants and WLF equation coefficients for sample HDO-3

Layer	Mixture	E_{00} (MPa)	E_0 (MPa)	k	h	δ	τ_E (s)	β	T_{ref} (°C)	C_1	C_2
Upper	BBSG3	150	40000	0.17	0.58	1.8	0.08	150	15	20.0	125.7
Lower	EME2	230	37000	0.17	0.57	2.2	0.22	300	15	19.5	126.2

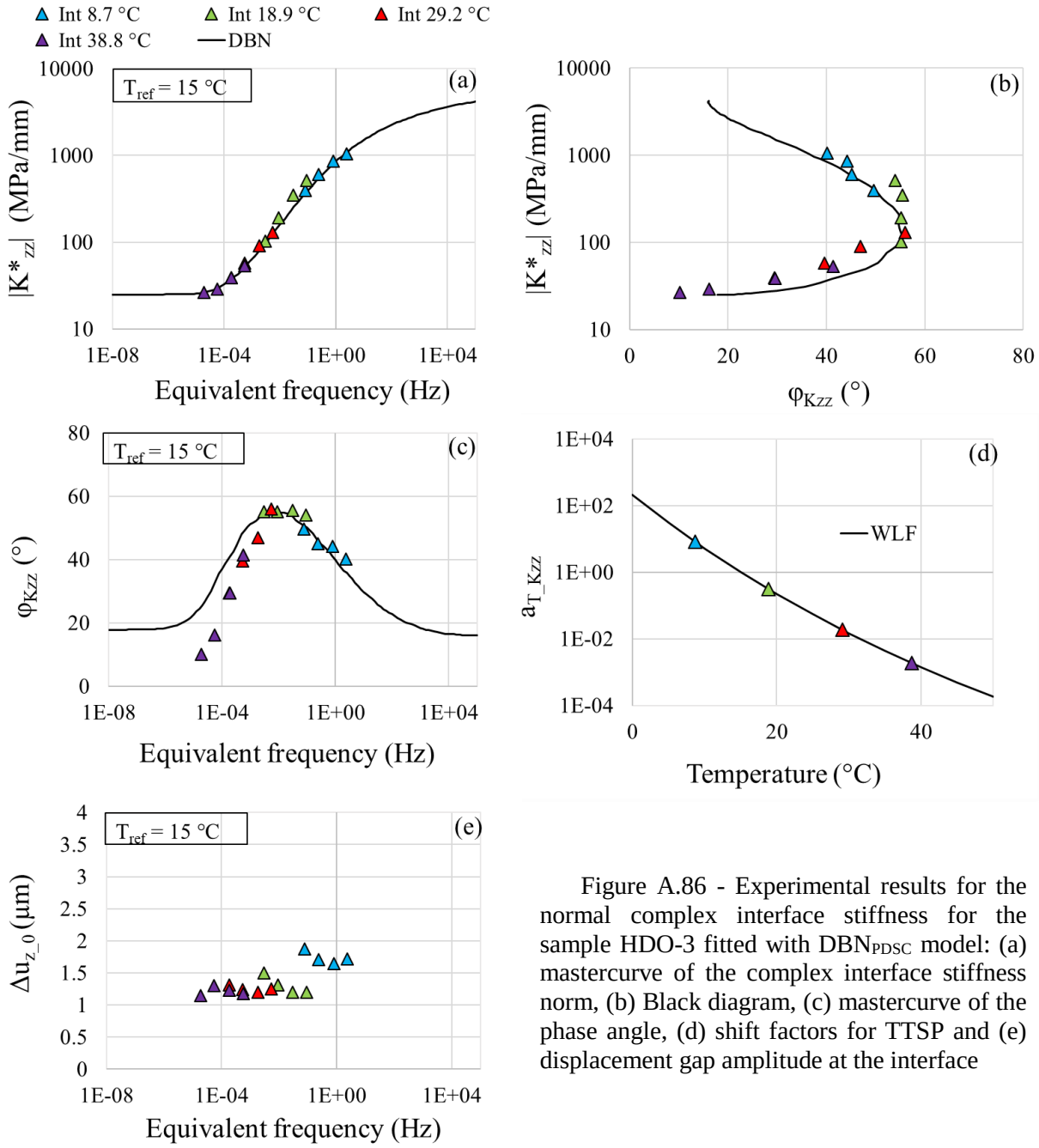

Figure A.86 - Experimental results for the normal complex interface stiffness for the sample HDO-3 fitted with DBN_{PDSC} model: (a) mastercurve of the complex interface stiffness norm, (b) Black diagram, (c) mastercurve of the phase angle, (d) shift factors for TTSP and (e) displacement gap amplitude at the interface

Table A.86 - 2S2P1D constants, DBN_{PDSC} constant φ_{NL} and WLF equation coefficients for sample HDO-3

K_{zz_00} (MPa)	K_{zz_0} (MPa)	k	h	δ	τ_{Kzz} (s)	β	φ_{NL}(°)	T_{ref} (°C)	C_1	C_2
25	500	0.2	0.53	2.3	0.035	300	18	15	17.3	126.5

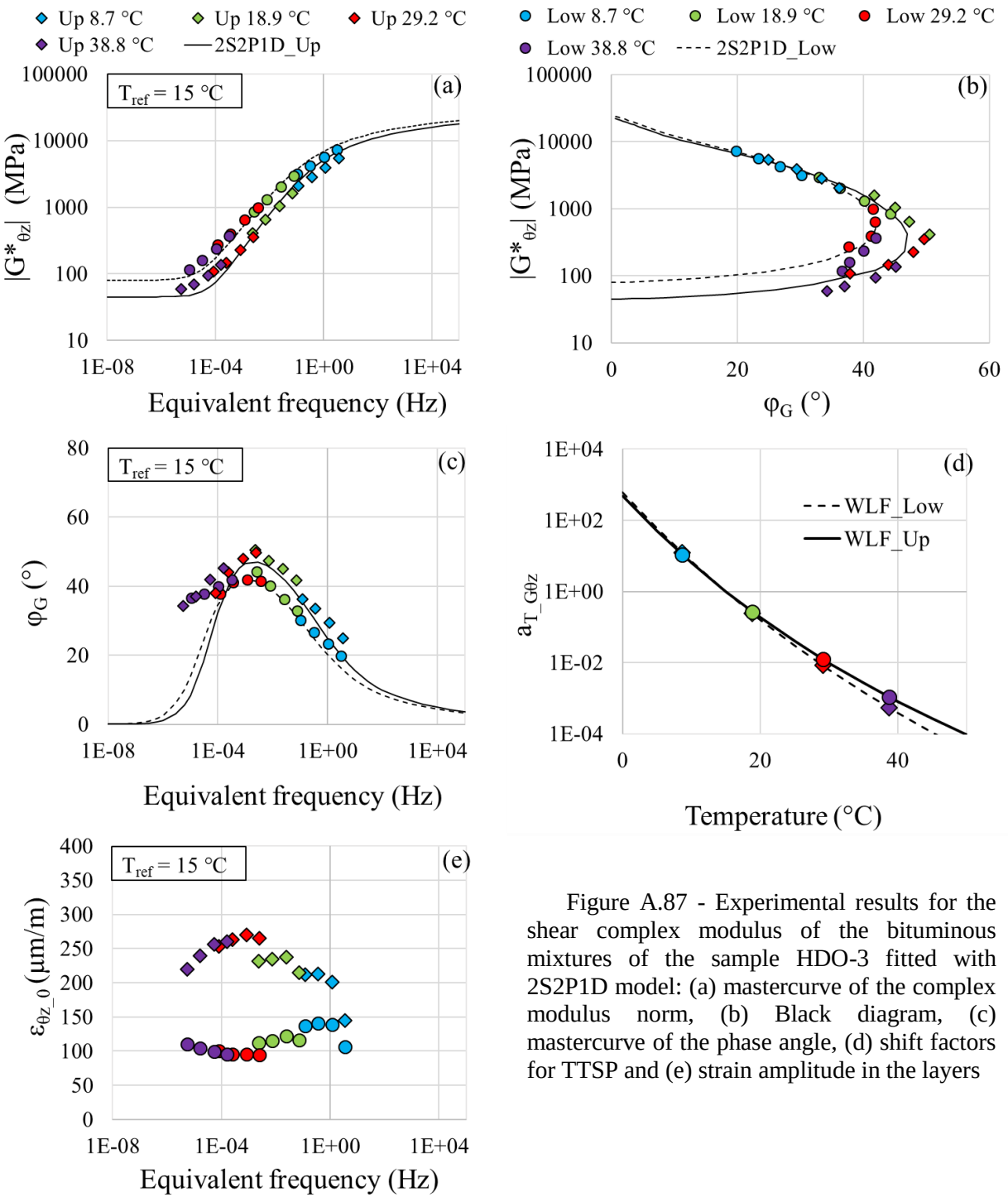

Figure A.87 - Experimental results for the shear complex modulus of the bituminous mixtures of the sample HDO-3 fitted with 2S2P1D model: (a) mastercurve of the complex modulus norm, (b) Black diagram, (c) mastercurve of the phase angle, (d) shift factors for TTSP and (e) strain amplitude in the layers

Table A.87 - 2S2P1D constants and WLF equation coefficients for sample HDO-3

Layer	Mixture	G_{00} (MPa)	G_0 (MPa)	k	h	δ	τ_G (s)	β	T_{ref} (°C)	C_1	C_2
Upper	BBSG3	45	23000	0.17	0.57	1.8	0.06	120	15	20.5	125.6
Lower	EME2	80	25000	0.17	0.55	1.8	0.15	200	15	16.0	104.2

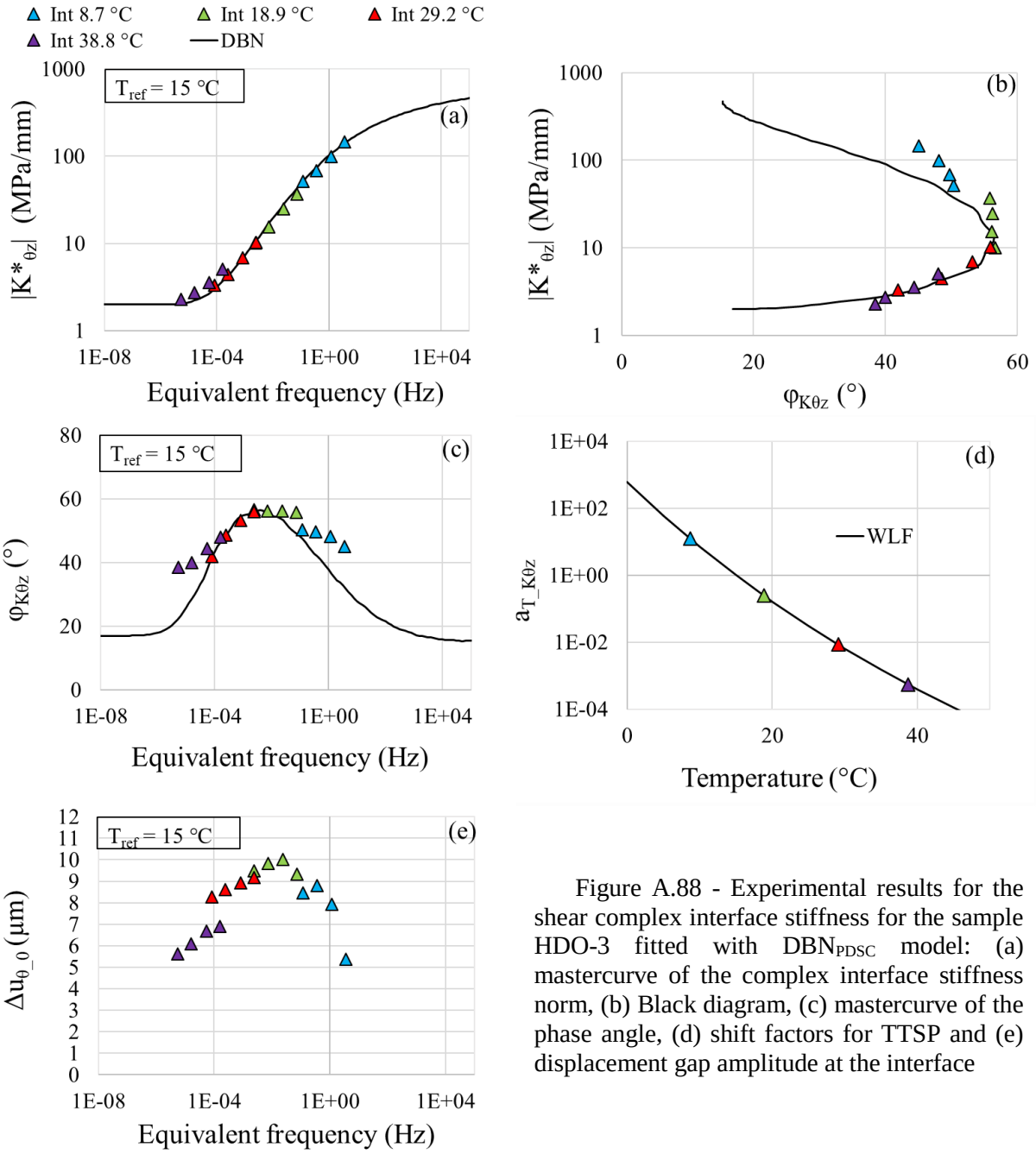

Figure A.88 - Experimental results for the shear complex interface stiffness for the sample HDO-3 fitted with DBN_{PDSC} model: (a) mastercurve of the complex interface stiffness norm, (b) Black diagram, (c) mastercurve of the phase angle, (d) shift factors for TTSP and (e) displacement gap amplitude at the interface

Table A.88 - 2S2P1D constants, DBN_{PDSC} constant φ_{NL} and WLF equation coefficients for sample HDO-3

$K_{\theta z\_00}$ (MPa)	$K_{\theta z\_0}$ (MPa)	k	h	δ	$\tau_{K\theta z}$ (s)	β	φ_{NL}(°)	T_{ref} (°C)	C_1	C_2
2	600	0.2	0.53	2.3	0.05	300	17	15	20.6	126.1

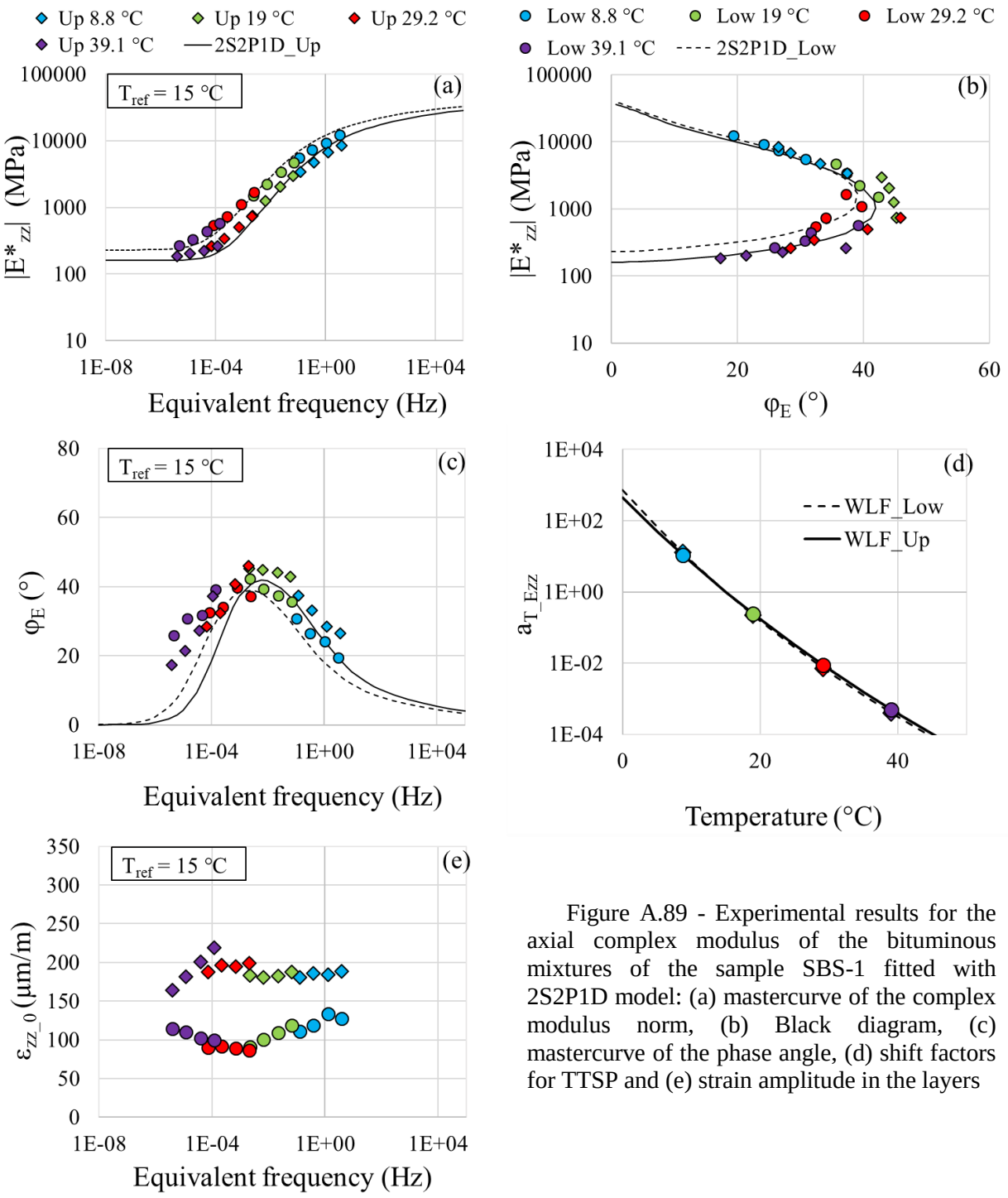

Figure A.89 - Experimental results for the axial complex modulus of the bituminous mixtures of the sample SBS-1 fitted with 2S2P1D model: (a) mastercurve of the complex modulus norm, (b) Black diagram, (c) mastercurve of the phase angle, (d) shift factors for TTSP and (e) strain amplitude in the layers

Table A.89 - 2S2P1D constants and WLF equation coefficients for sample SBS-1

Layer	Mixture	E_{00} (MPa)	E_0 (MPa)	k	h	δ	τ_E (s)	β	T_{ref} (°C)	C_1	C_2
Upper	BBSG3	160	38000	0.17	0.58	2.1	0.06	150	15	21.1	125.4
Lower	EME2	230	41000	0.17	0.57	2	0.25	250	15	24.6	154.4

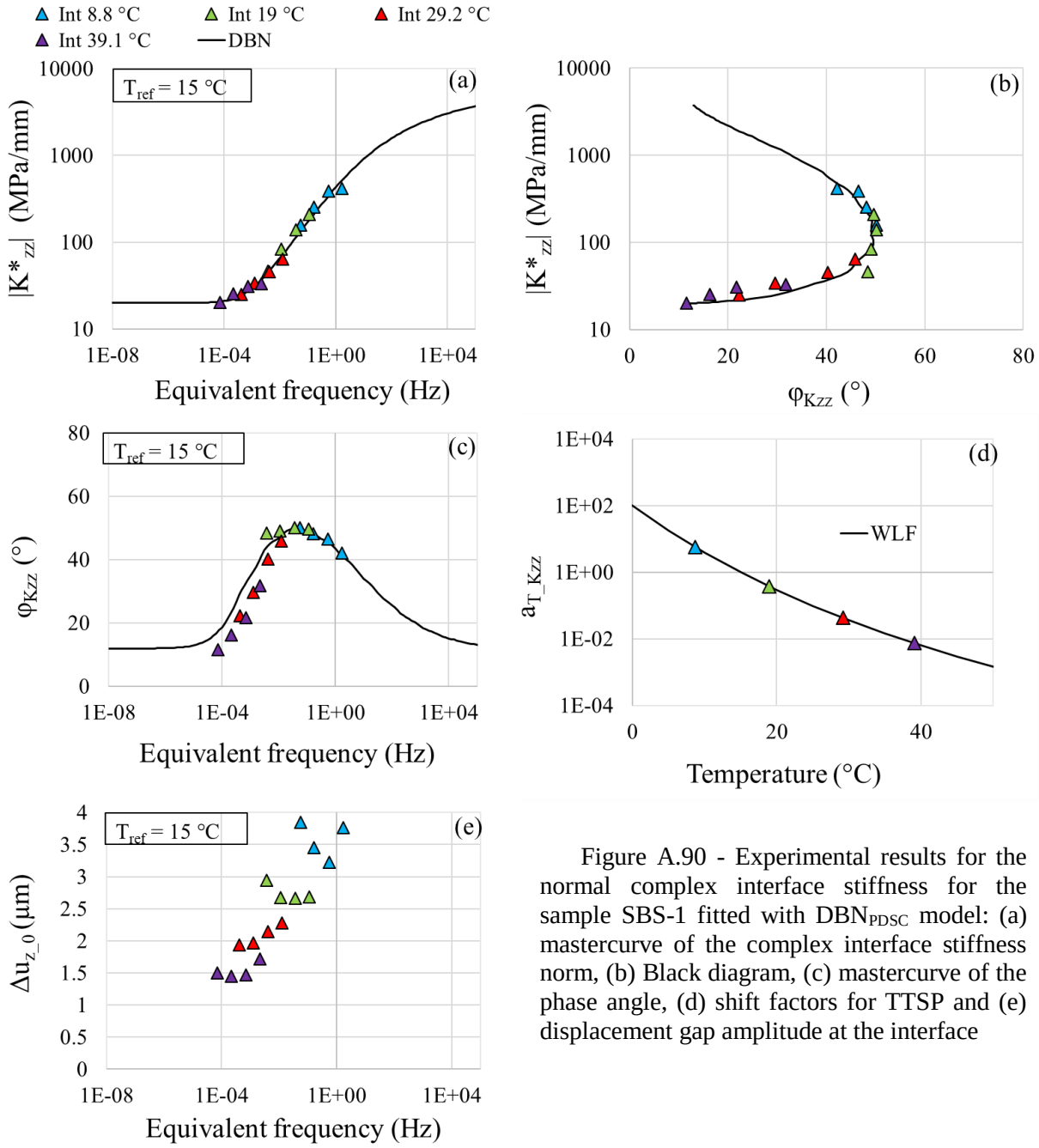

Figure A.90 - Experimental results for the normal complex interface stiffness for the sample SBS-1 fitted with DBN_{PDSC} model: (a) mastercurve of the complex interface stiffness norm, (b) Black diagram, (c) mastercurve of the phase angle, (d) shift factors for TTSP and (e) displacement gap amplitude at the interface

Table A.90 - 2S2P1D constants, DBN_{PDSC} constant φ_{NL} and WLF equation coefficients for sample SBS-1

K_{zz_00} (MPa)	K_{zz_0} (MPa)	k	h	δ	τ_{Kzz} (s)	β	φ_{NL}(°)	T_{ref} (°C)	C_1	C_2
20	5500	0.2	0.53	2.3	0.0045	300	12	15	10.4	92.9

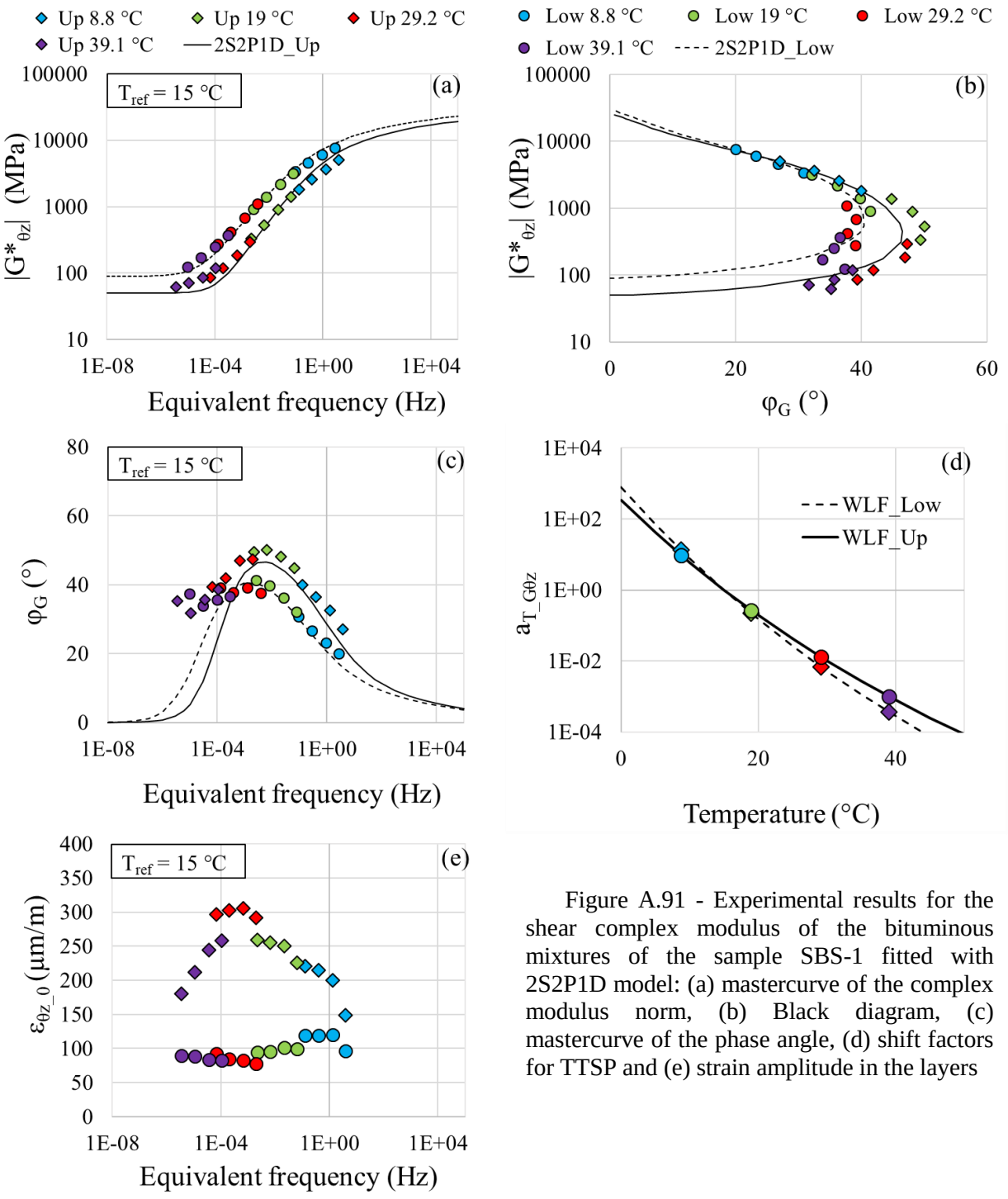

Figure A.91 - Experimental results for the shear complex modulus of the bituminous mixtures of the sample SBS-1 fitted with 2S2P1D model: (a) mastercurve of the complex modulus norm, (b) Black diagram, (c) mastercurve of the phase angle, (d) shift factors for TTSP and (e) strain amplitude in the layers

Table A.91 - 2S2P1D constants and WLF equation coefficients for sample SBS-1

Layer	Mixture	G_{00} (MPa)	G_0 (MPa)	k	h	δ	τ_G (s)	β	T_{ref} (°C)	C_1	C_2
Upper	BBSG3	50	26000	0.17	0.58	1.9	0.03	150	15	21.3	124.8
Lower	EME2	90	30000	0.17	0.55	2.1	0.12	350	15	18.7	125.7

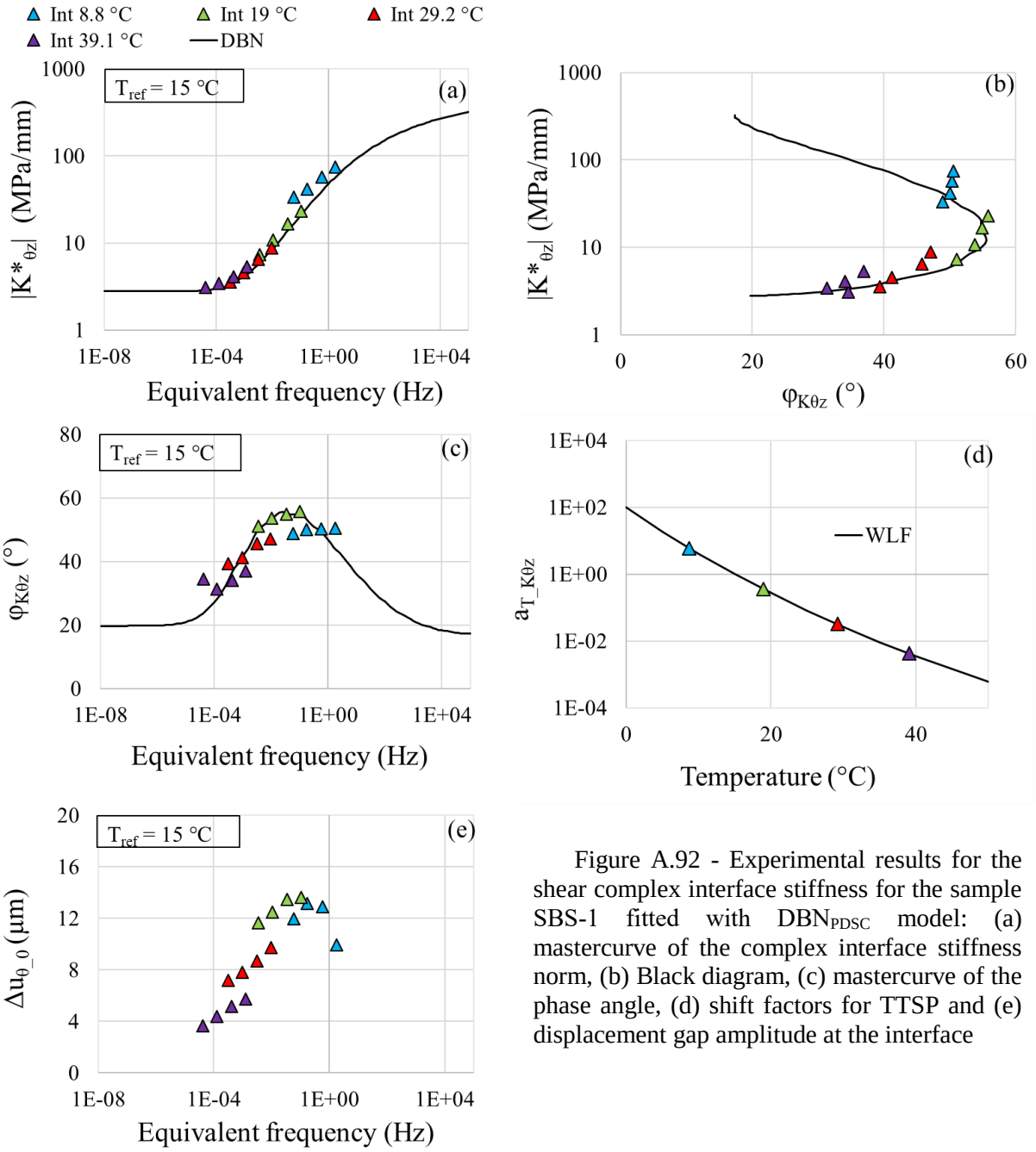

Figure A.92 - Experimental results for the shear complex interface stiffness for the sample SBS-1 fitted with DBN_{PDSC} model: (a) mastercurve of the complex interface stiffness norm, (b) Black diagram, (c) mastercurve of the phase angle, (d) shift factors for TTSP and (e) displacement gap amplitude at the interface

Table A.92 - 2S2P1D constants, DBN_{PDSC} constant φ_{NL} and WLF equation coefficients for sample SBS-1

K_{0z_00} (MPa)	K_{0z_0} (MPa)	k	h	δ	τ_{K0z} (s)	β	φ_{NL}(°)	T_{ref} (°C)	C_1	C_2
2.8	450	0.2	0.53	2.3	0.01	300	20	15	14.8	125.9

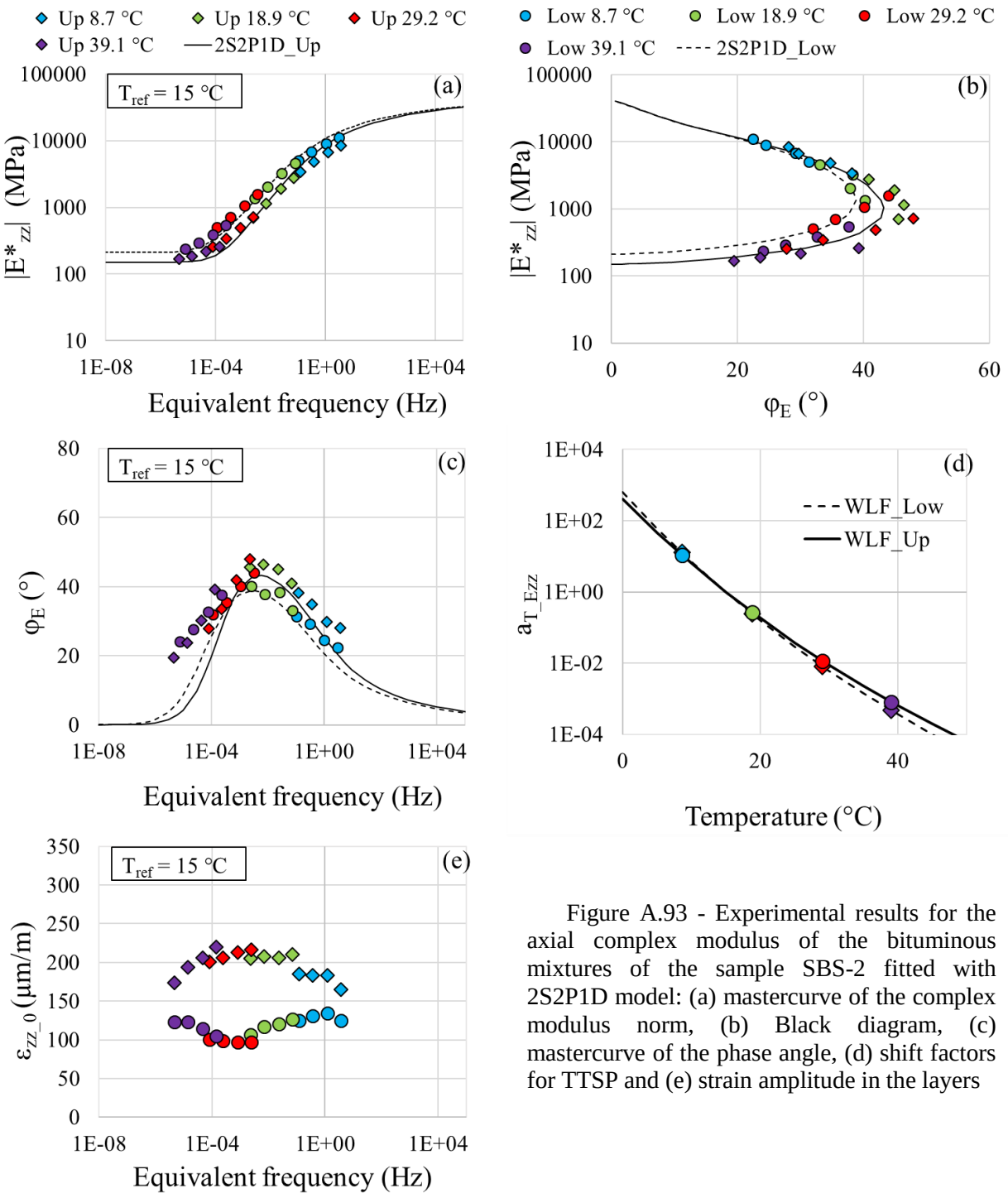

Figure A.93 - Experimental results for the axial complex modulus of the bituminous mixtures of the sample SBS-2 fitted with 2S2P1D model: (a) mastercurve of the complex modulus norm, (b) Black diagram, (c) mastercurve of the phase angle, (d) shift factors for TTSP and (e) strain amplitude in the layers

Table A.93 - 2S2P1D constants and WLF equation coefficients for sample SBS-2

Layer	Mixture	E_{00} (MPa)	E_0 (MPa)	k	h	δ	τ_E (s)	β	T_{ref} (°C)	C_1	C_2
Upper	BBSG3	150	42000	0.17	0.57	1.9	0.05	130	15	20.7	125.5
Lower	EME2	210	42000	0.17	0.55	1.9	0.12	250	15	19.2	125.1

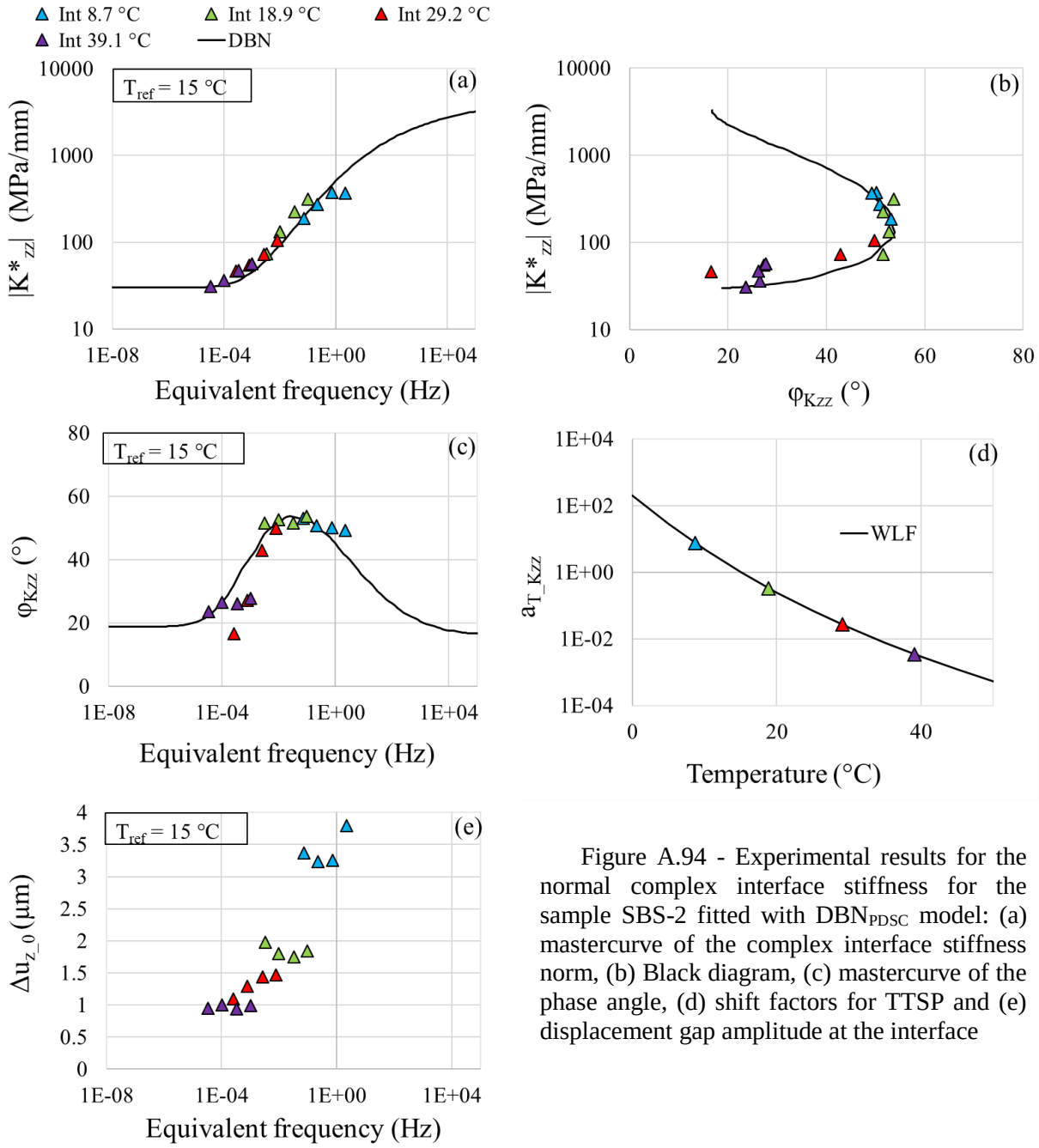

Figure A.94 - Experimental results for the normal complex interface stiffness for the sample SBS-2 fitted with DBN_{PDSC} model: (a) mastercurve of the complex interface stiffness norm, (b) Black diagram, (c) mastercurve of the phase angle, (d) shift factors for TTSP and (e) displacement gap amplitude at the interface

Table A.94 - 2S2P1D constants, DBN_{PDSC} constant φ_{NL} and WLF equation coefficients for sample SBS-2

K_{zz_00} (MPa)	K_{zz_0} (MPa)	k	h	δ	τ_{Kzz} (s)	β	φ_{NL}(°)	T_{ref} (°C)	C_1	C_2
30	4500	0.2	0.53	2.3	0.012	300	19	15	12.0	93.5

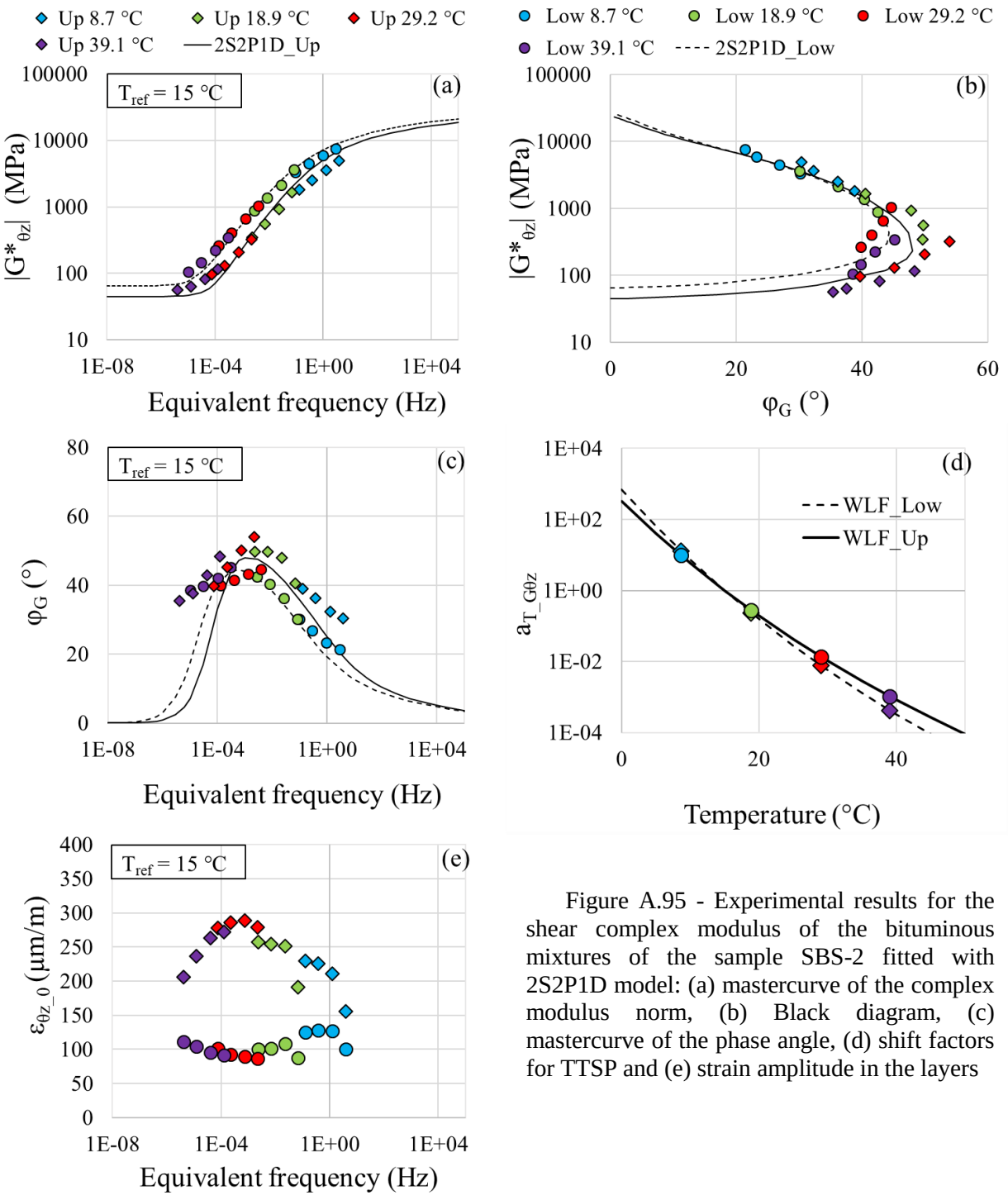

Figure A.95 - Experimental results for the shear complex modulus of the bituminous mixtures of the sample SBS-2 fitted with 2S2P1D model: (a) mastercurve of the complex modulus norm, (b) Black diagram, (c) mastercurve of the phase angle, (d) shift factors for TTSP and (e) strain amplitude in the layers

Table A.95 - 2S2P1D constants and WLF equation coefficients for sample SBS-2

Layer	Mixture	G_{00} (MPa)	G_0 (MPa)	k	h	δ	τ_G (s)	β	T_{ref} (°C)	C_1	C_2
Upper	BBSG3	45	24000	0.17	0.55	1.8	0.05	100	15	20.9	125.0
Lower	EME2	65	27000	0.17	0.55	2.1	0.18	140	15	18.4	124.7

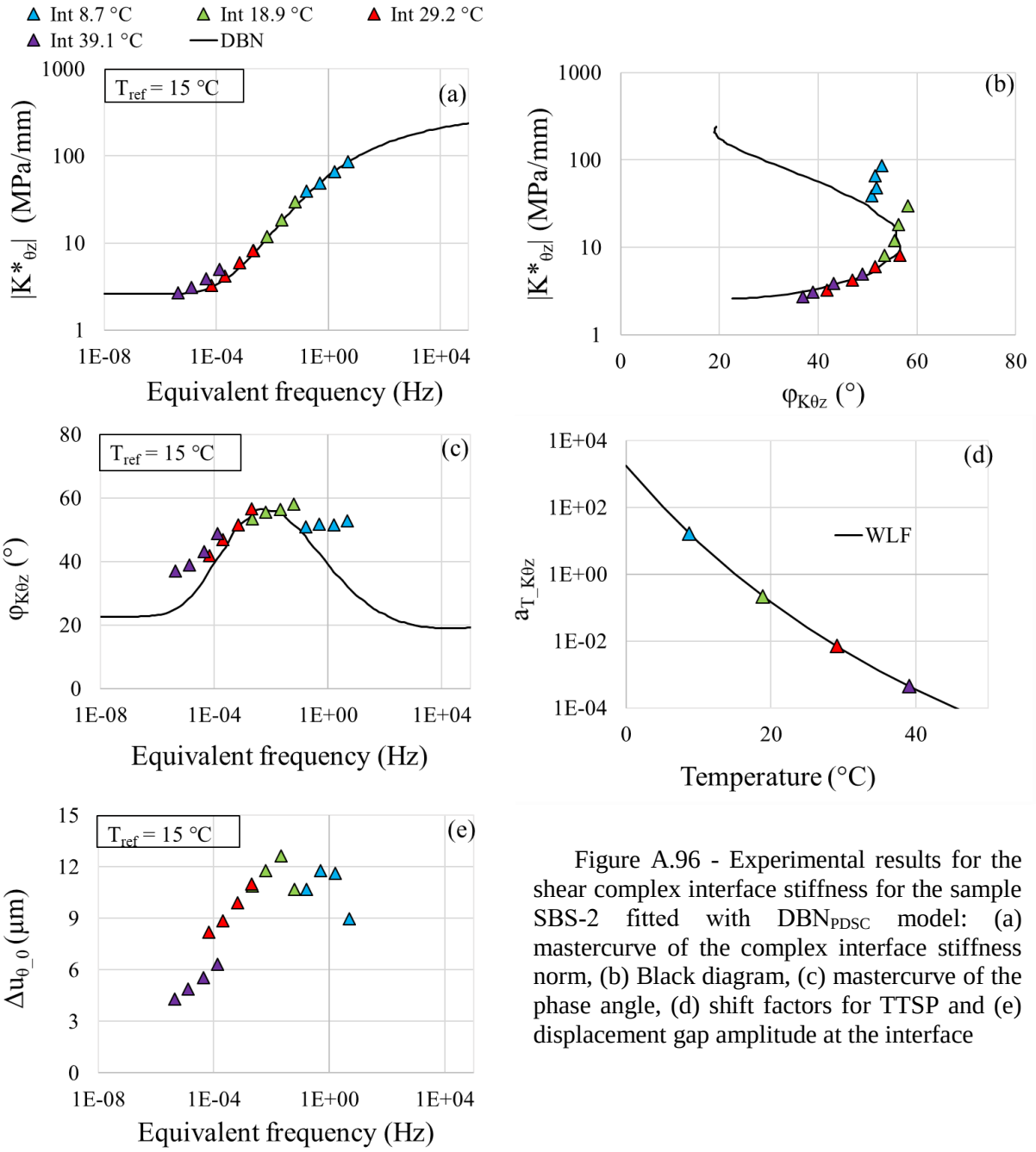

Figure A.96 - Experimental results for the shear complex interface stiffness for the sample SBS-2 fitted with DBN_{PDSC} model: (a) mastercurve of the complex interface stiffness norm, (b) Black diagram, (c) mastercurve of the phase angle, (d) shift factors for TTSP and (e) displacement gap amplitude at the interface

Table A.96 - 2S2P1D constants, DBN_{PDSC} constant φ_{NL} and WLF equation coefficients for sample SBS-2

K_{0z_00} (MPa)	K_{0z_0} (MPa)	k	h	δ	τ_{K0z} (s)	β	φ_{NL}(°)	T_{ref} (°C)	C_1	C_2
2.6	300	0.2	0.53	2.3	0.08	300	23	15	15.2	85.4

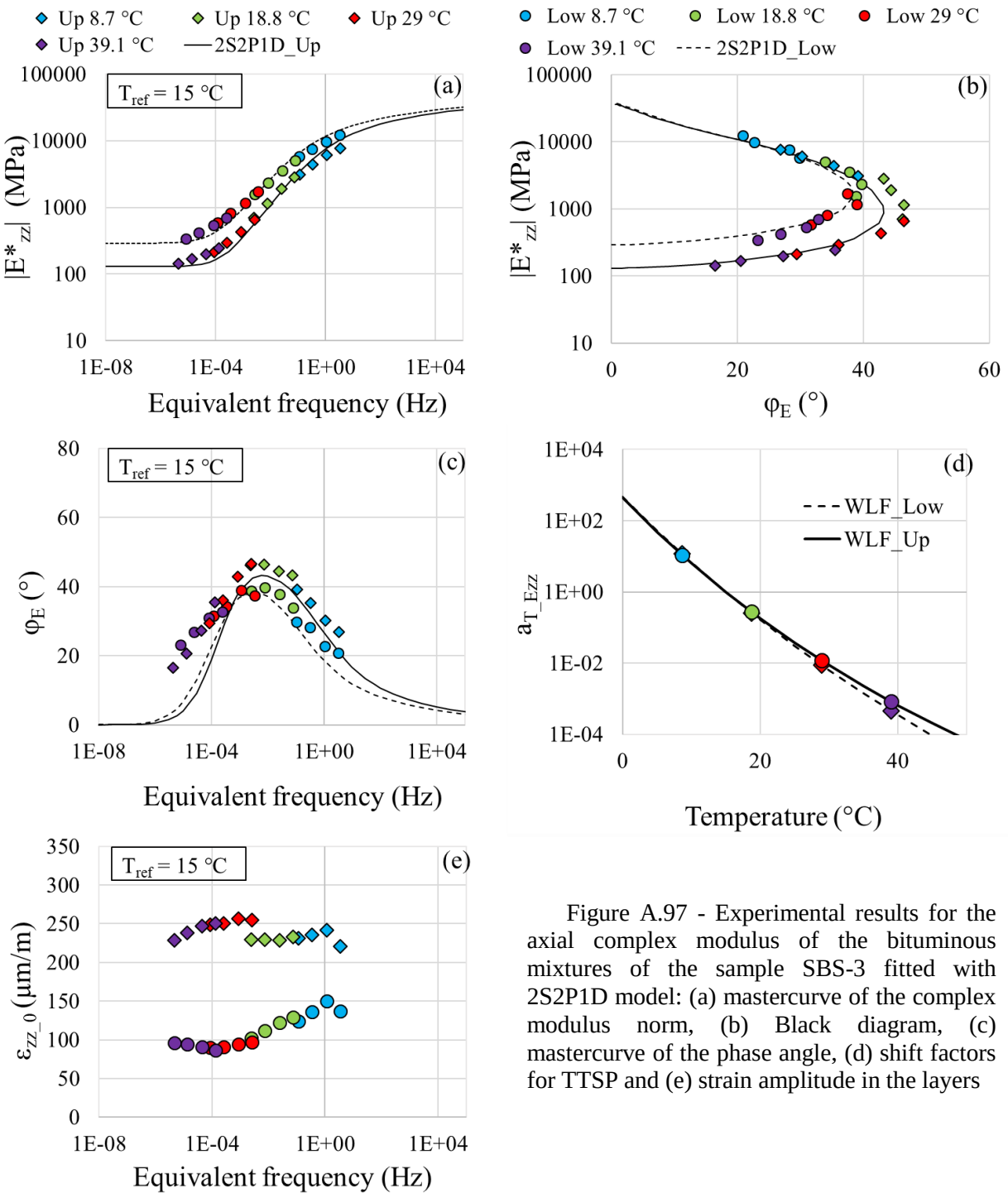

Figure A.97 - Experimental results for the axial complex modulus of the bituminous mixtures of the sample SBS-3 fitted with 2S2P1D model: (a) mastercurve of the complex modulus norm, (b) Black diagram, (c) mastercurve of the phase angle, (d) shift factors for TTSP and (e) strain amplitude in the layers

Table A.97 - 2S2P1D constants and WLF equation coefficients for sample SBS-3

Layer	Mixture	E_{00} (MPa)	E_0 (MPa)	k	h	δ	τ_E (s)	β	T_{ref} (°C)	C_1	C_2
Upper	BBSG3	130	38000	0.17	0.57	1.8	0.04	150	15	24.6	153.4
Lower	EME2	290	39500	0.17	0.57	1.9	0.22	150	15	18.3	118.9

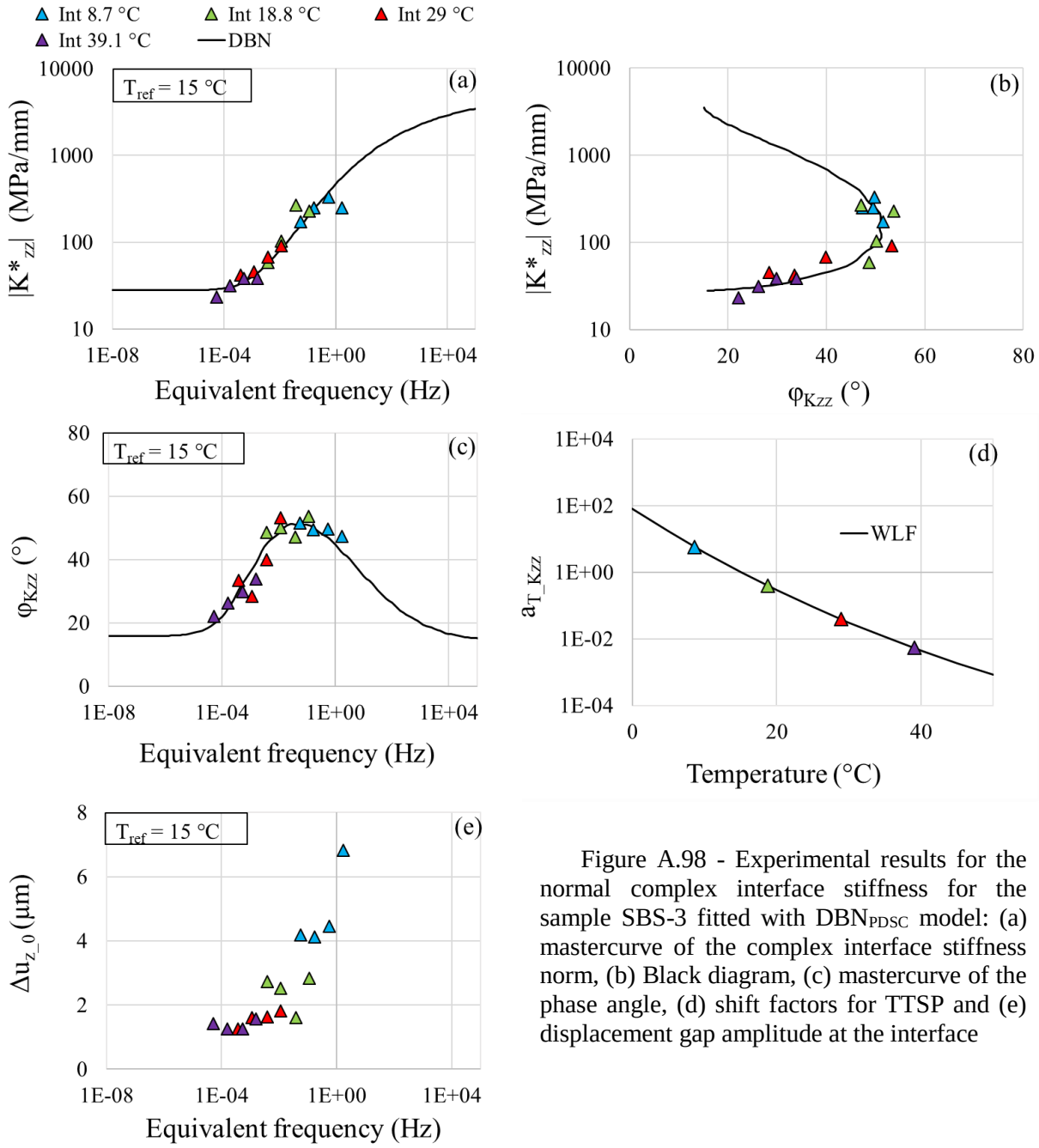

Figure A.98 - Experimental results for the normal complex interface stiffness for the sample SBS-3 fitted with DBN_{PDSC} model: (a) mastercurve of the complex interface stiffness norm, (b) Black diagram, (c) mastercurve of the phase angle, (d) shift factors for TTSP and (e) displacement gap amplitude at the interface

Table A.98 - 2S2P1D constants, DBN_{PDSC} constant φ_{NL} and WLF equation coefficients for sample SBS-3

K_{zz_00} (MPa)	K_{zz_0} (MPa)	k	h	δ	τ_{Kzz} (s)	β	φ_{NL}(°)	T_{ref} (°C)	C_1	C_2
28	5000	0.2	0.53	2.3	0.007	300	16	15	14.3	126.7

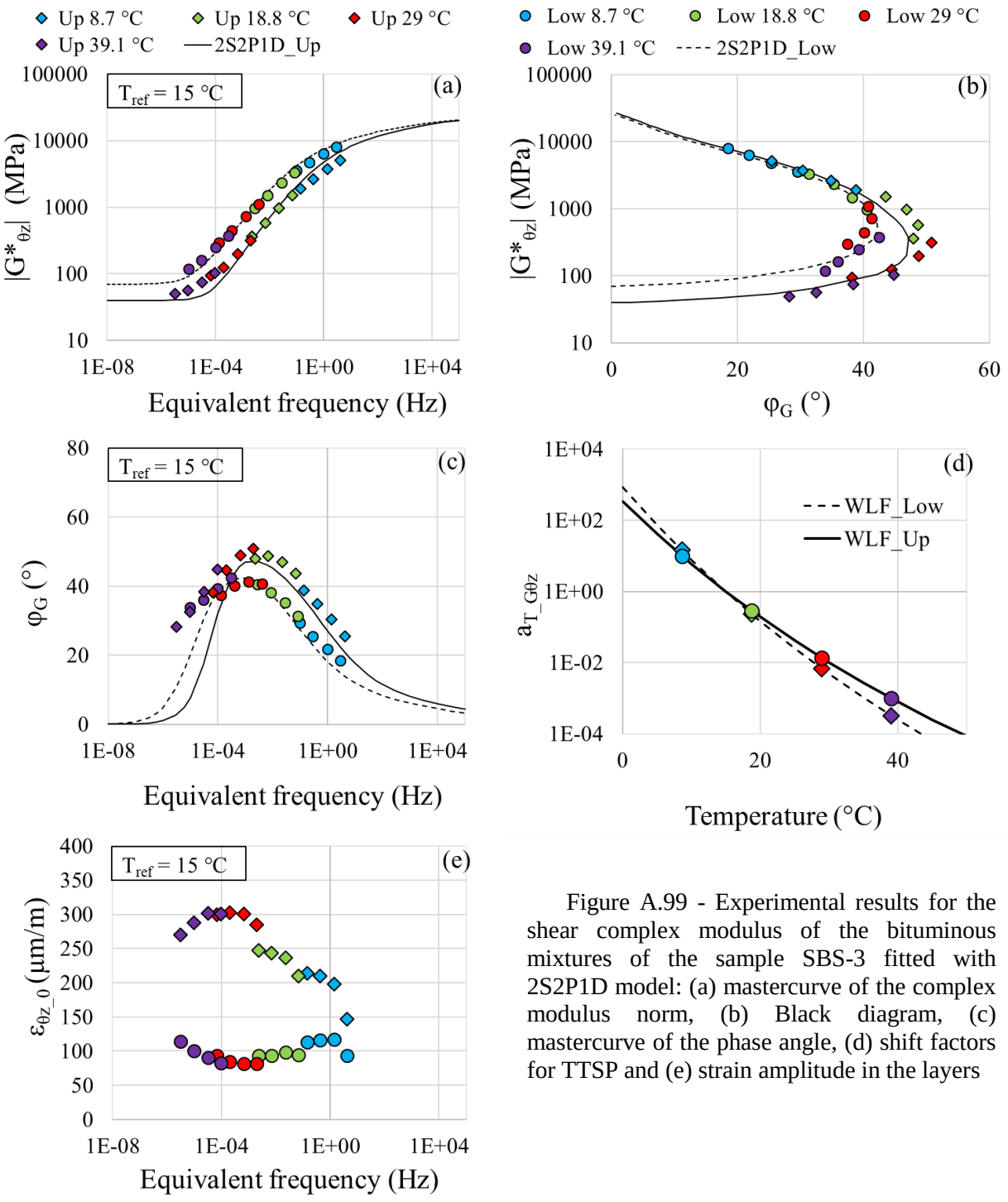

Figure A.99 - Experimental results for the shear complex modulus of the bituminous mixtures of the sample SBS-3 fitted with 2S2P1D model: (a) mastercurve of the complex modulus norm, (b) Black diagram, (c) mastercurve of the phase angle, (d) shift factors for TTSP and (e) strain amplitude in the layers

Table A.99 - 2S2P1D constants and WLF equation coefficients for sample SBS-3

Layer	Mixture	G_{00} (MPa)	G_0 (MPa)	k	h	δ	τ_G (s)	β	T_{ref} (°C)	C_1	C_2
Upper	BBSG3	40	28000	0.17	0.56	2.1	0.03	150	15	22.0	127.5
Lower	EME2	70	26000	0.17	0.56	2.1	0.25	250	15	18.6	125.4

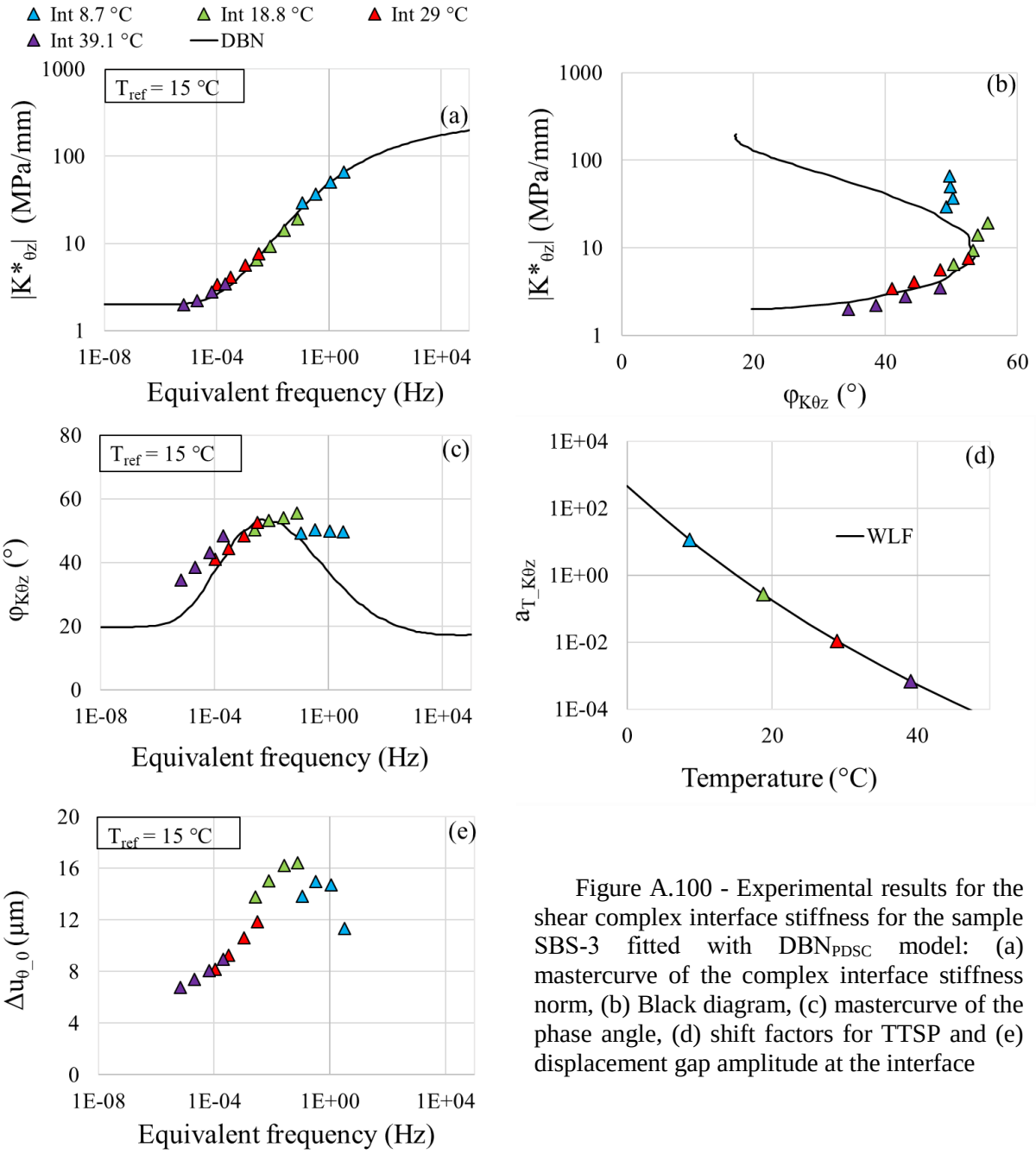

Figure A.100 - Experimental results for the shear complex interface stiffness for the sample SBS-3 fitted with DBN_{PDSC} model: (a) mastercurve of the complex interface stiffness norm, (b) Black diagram, (c) mastercurve of the phase angle, (d) shift factors for TTSP and (e) displacement gap amplitude at the interface

Table A.100 - 2S2P1D constants, DBN_{PDSC} constant φ_{NL} and WLF equation coefficients for sample SBS-3

K_{0z_00} (MPa)	K_{0z_0} (MPa)	k	h	δ	τ_{K0z} (s)	β	φ_{NL}(°)	T_{ref} (°C)	C_1	C_2
2	250	0.2	0.53	2.3	0.08	300	20	15	19.7	125.7

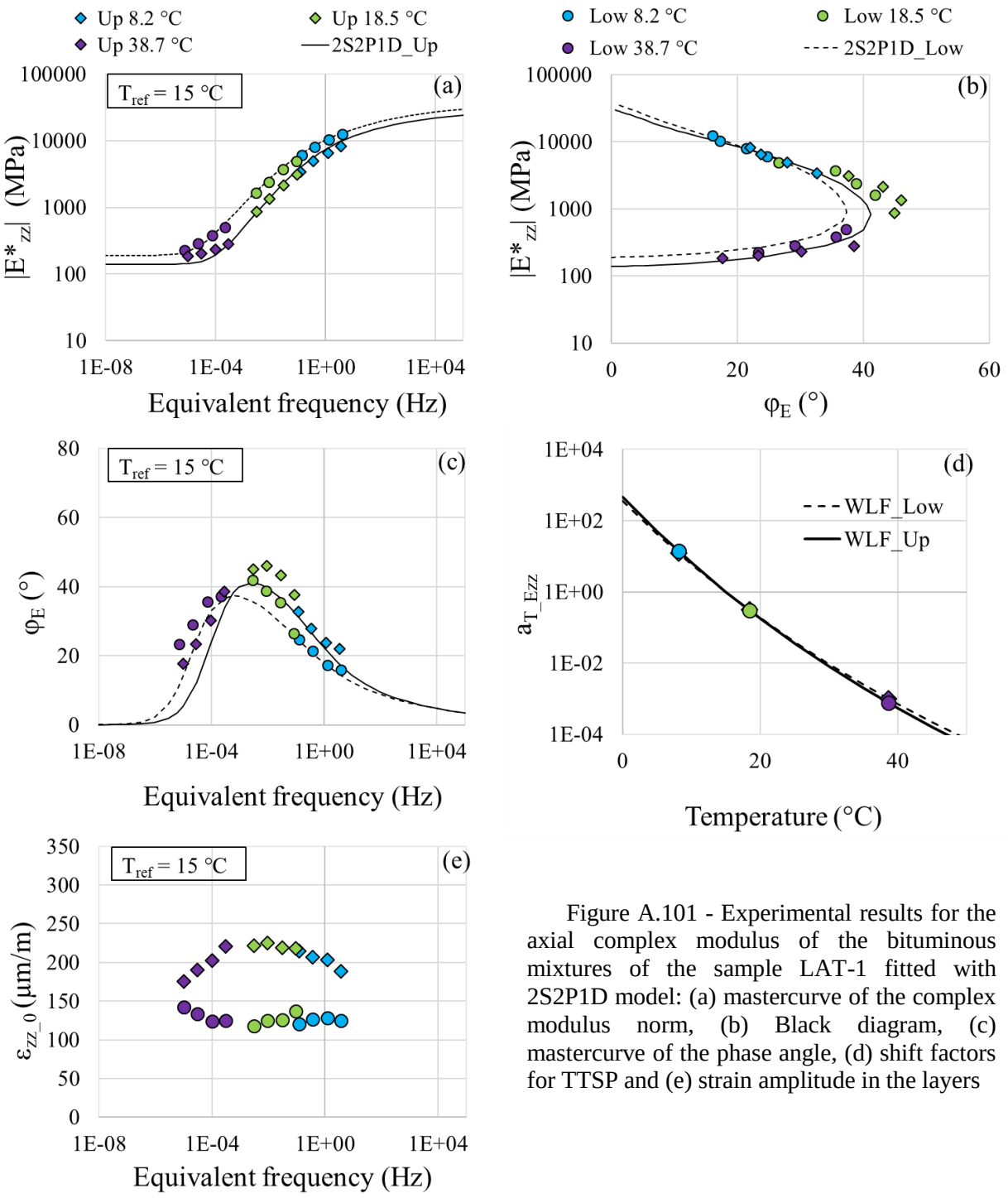

Figure A.101 - Experimental results for the axial complex modulus of the bituminous mixtures of the sample LAT-1 fitted with 2S2P1D model: (a) mastercurve of the complex modulus norm, (b) Black diagram, (c) mastercurve of the phase angle, (d) shift factors for TTSP and (e) strain amplitude in the layers

Table A.101 - 2S2P1D constants and WLF equation coefficients for sample LAT-1

Layer	Mixture	E_{00} (MPa)	E_0 (MPa)	k	h	δ	τ_E (s)	β	T_{ref} (°C)	C_1	C_2
Upper	BBSG3	140	31000	0.17	0.54	1.8	0.08	120	15	19.0	126.1
Lower	EME2	190	38000	0.17	0.51	2.1	0.2	200	15	19.8	126.0

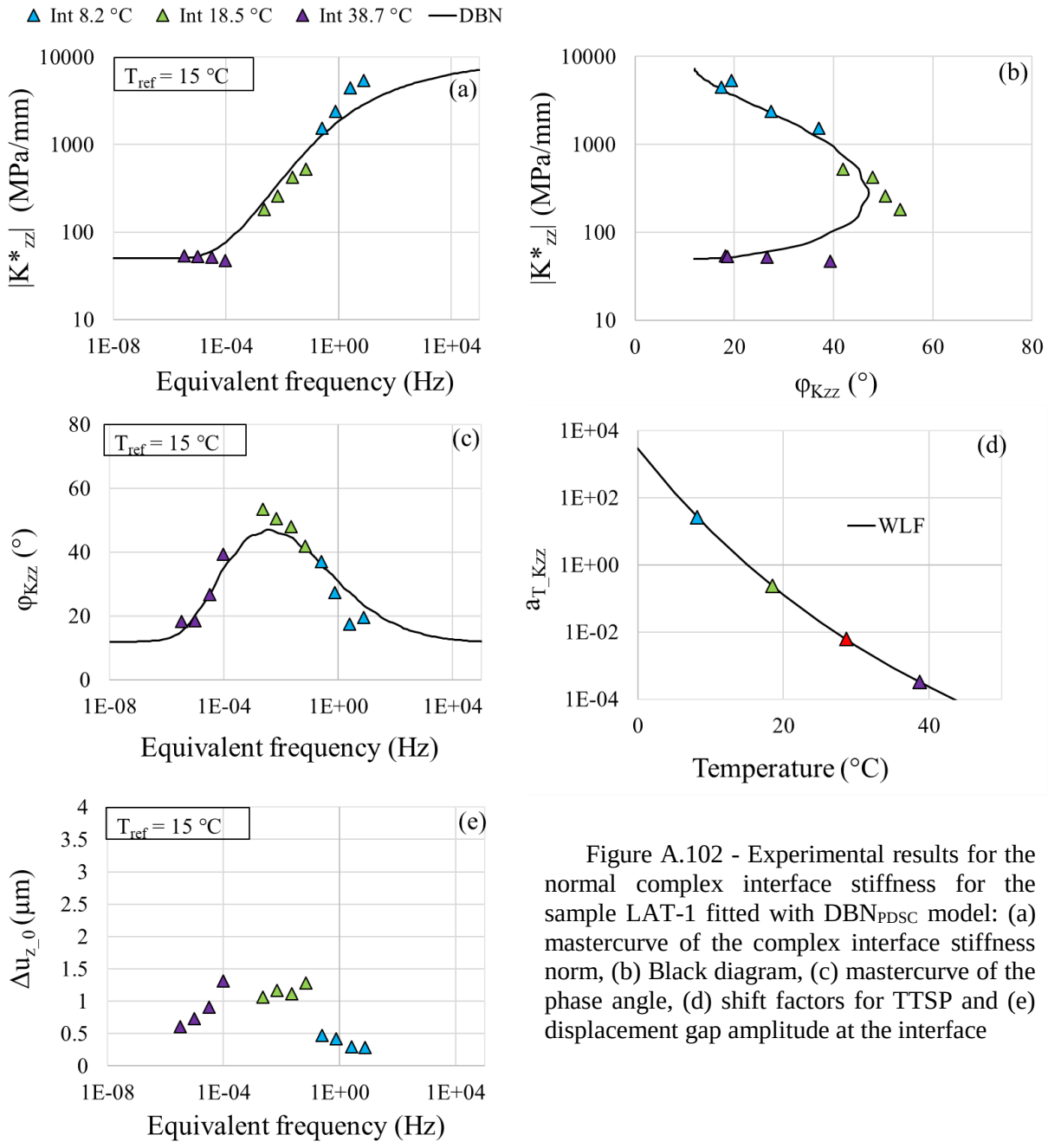

Figure A.102 - Experimental results for the normal complex interface stiffness for the sample LAT-1 fitted with DBN_{PDSC} model: (a) mastercurve of the complex interface stiffness norm, (b) Black diagram, (c) mastercurve of the phase angle, (d) shift factors for TTSP and (e) displacement gap amplitude at the interface

Table A.102 - 2S2P1D constants, DBN_{PDSC} constant φ_{NL} and WLF equation coefficients for sample LAT-1

K_{zz_00} (MPa)	K_{zz_0} (MPa)	k	h	δ	τ_{Kzz} (s)	β	φ_{NL}(°)	T_{ref} (°C)	C_1	C_2
50	9000	0.2	0.53	2.3	0.1	300	12	15	15.7	82.8

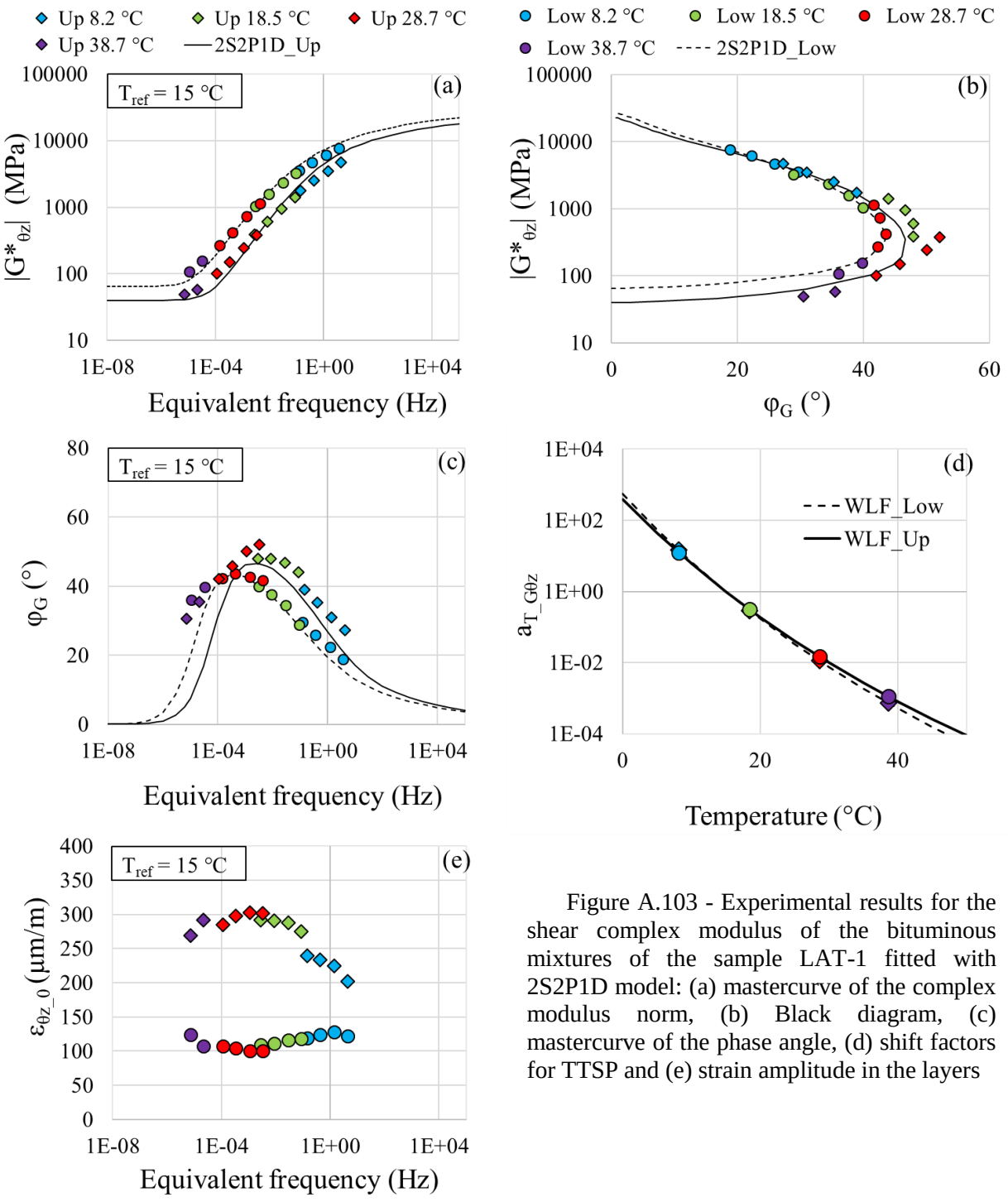

Figure A.103 - Experimental results for the shear complex modulus of the bituminous mixtures of the sample LAT-1 fitted with 2S2P1D model: (a) mastercurve of the complex modulus norm, (b) Black diagram, (c) mastercurve of the phase angle, (d) shift factors for TTSP and (e) strain amplitude in the layers

Table A.103 - 2S2P1D constants and WLF equation coefficients for sample LAT-1

Layer	Mixture	G_{00} (MPa)	G_0 (MPa)	k	h	δ	τ_G (s)	β	T_{ref} (°C)	C_1	C_2
Upper	BBSG3	40	24000	0.17	0.56	1.9	0.035	150	15	18.6	116.6
Lower	EME2	65	28500	0.17	0.53	2.1	0.15	180	15	17.5	116.7

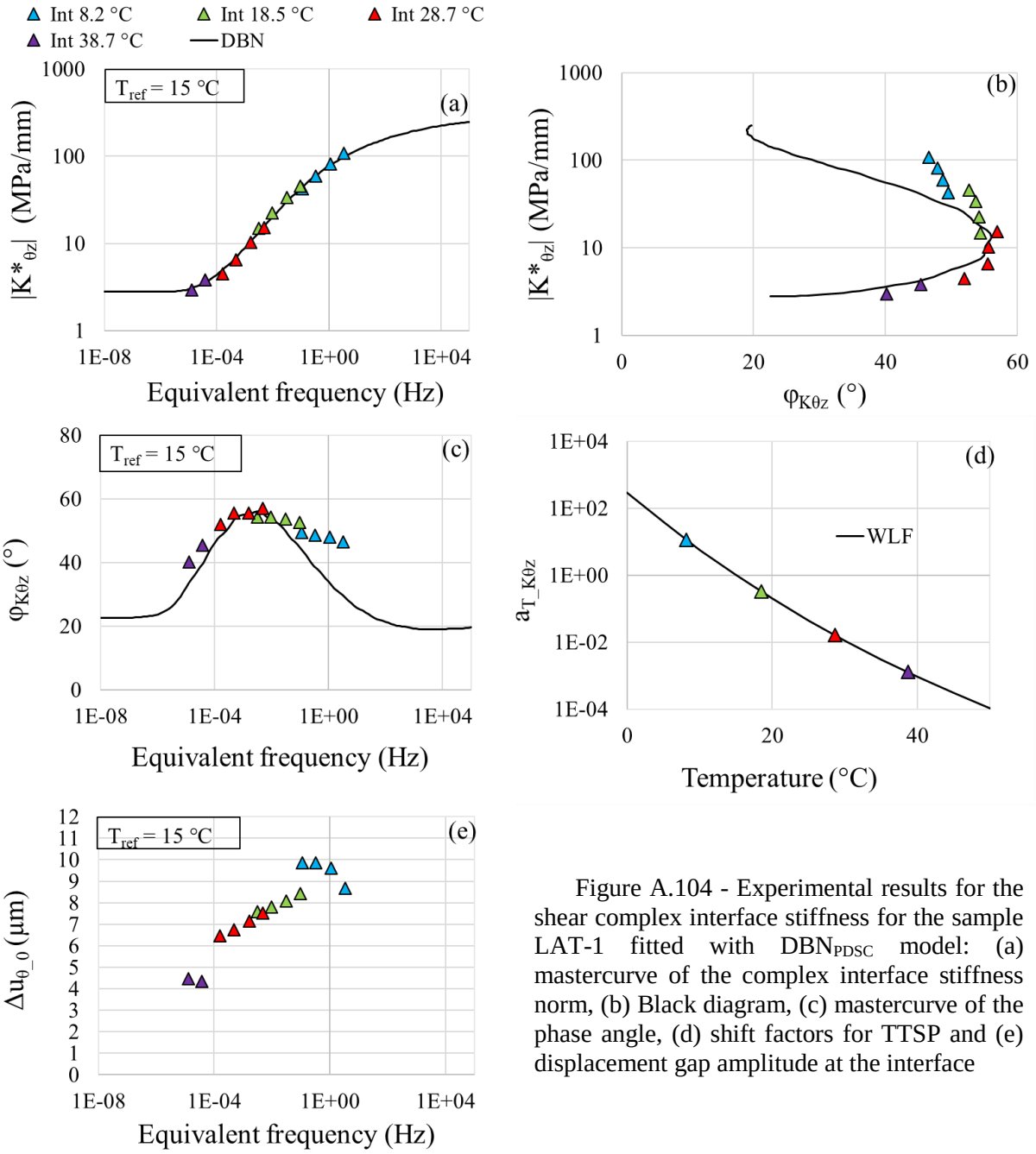

Figure A.104 - Experimental results for the shear complex interface stiffness for the sample LAT-1 fitted with DBN_{PDSC} model: (a) mastercurve of the complex interface stiffness norm, (b) Black diagram, (c) mastercurve of the phase angle, (d) shift factors for TTSP and (e) displacement gap amplitude at the interface

Table A.104 - 2S2P1D constants, DBN_{PDSC} constant φ_{NL} and WLF equation coefficients for sample LAT-1

$K_{\theta z\_00}$ (MPa)	$K_{\theta z\_0}$ (MPa)	k	h	δ	$\tau_{K\theta z}$ (s)	β	φ_{NL}(°)	T_{ref} (°C)	C_1	C_2
2.8	300	0.2	0.53	2.3	0.4	300	23	15	18.3	126.2

APPENDIX B

DBN_{PDSC} model constants for the interfaces

Table B.1 - DBN_{PDSC} constants of the complex interface stiffnesses for sample REFA-3

	Sample REFA-3 (K^*_{zz})		**Sample REFA-3 ($K^*_{\theta z}$)**	
	φ_{NL} = 11 °		**φ_{NL} = 15 °**	
Element number	**K_{zzi} (MPa/mm)**	**η_i (MPa.s/mm)**	**$K_{\theta zi}$ (MPa/mm)**	**η_i (MPa.s/mm)**
0	1.1E+04	X	7.5E+02	X
1	2.1E+06	1.9E-08	1.6E+05	1.4E-09
2	2.4E+06	1.2E-07	1.8E+05	9.3E-09
3	2.2E+06	6.3E-07	1.6E+05	4.7E-08
4	2.0E+06	3.3E-06	1.5E+05	2.5E-07
5	1.2E+06	1.1E-05	9.2E+04	8.5E-07
6	9.5E+05	5.0E-05	7.2E+04	3.8E-06
7	6.3E+05	1.9E-04	4.7E+04	1.4E-05
8	4.6E+05	7.8E-04	3.5E+04	5.9E-05
9	3.2E+05	3.0E-03	2.4E+04	2.3E-04
10	2.3E+05	1.2E-02	1.7E+04	9.3E-04
11	1.6E+05	4.8E-02	1.2E+04	3.7E-03
12	1.1E+05	1.9E-01	8.5E+03	1.5E-02
13	7.7E+04	7.5E-01	5.9E+03	5.7E-02
14	5.3E+04	2.9E+00	4.0E+03	2.2E-01
15	3.5E+04	1.1E+01	2.7E+03	8.5E-01
16	2.3E+04	4.0E+01	1.8E+03	3.2E+00
17	1.4E+04	1.4E+02	1.1E+03	1.1E+01
18	7.9E+03	4.5E+02	6.4E+02	3.7E+01
19	4.2E+03	1.3E+03	3.5E+02	1.1E+02
20	2.0E+03	3.7E+03	1.7E+02	3.2E+02
21	9.3E+02	9.6E+03	8.1E+01	8.4E+02
22	4.1E+02	2.4E+04	3.6E+01	2.1E+03
23	1.8E+02	5.9E+04	1.7E+01	5.5E+03
24	1.0E+02	2.0E+05	9.8E+00	1.8E+04
25	1.9E+02	2.0E+06	1.4E+01	1.5E+05

Table B.2 - DBN_{PDSC} constants of the normal complex interface stiffness for samples of slab REFB

	Sample REFB-1		**Sample REFB-2**		**Sample REFB-3**	
	φ_{NL} = 6 °		**φ_{NL} = 8 °**		**φ_{NL} = 17 °**	
Element number	**K_{zzi} (MPa/mm)**	**η_i (MPa.s/mm)**	**K_{zzi} (MPa/mm)**	**η_i (MPa.s/mm)**	**K_{zzi} (MPa/mm)**	**η_i (MPa.s/mm)**
0	1.2E+04	X	2.6E+04	X	2.5E+04	X
1	2.6E+06	2.3E-08	3.5E+06	3.1E-08	3.9E+06	3.5E-08
2	2.9E+06	1.5E-07	4.0E+06	2.0E-07	4.4E+06	2.2E-07
3	2.6E+06	7.6E-07	3.6E+06	1.0E-06	4.0E+06	1.1E-06
4	2.4E+06	4.0E-06	3.3E+06	5.4E-06	3.7E+06	6.0E-06
5	1.5E+06	1.4E-05	2.0E+06	1.9E-05	2.2E+06	2.0E-05
6	1.1E+06	6.0E-05	1.6E+06	8.2E-05	1.7E+06	9.1E-05
7	7.6E+05	2.2E-04	1.0E+06	3.1E-04	1.1E+06	3.4E-04
8	5.6E+05	9.4E-04	7.6E+05	1.3E-03	8.4E+05	1.4E-03
9	3.8E+05	3.6E-03	5.2E+05	5.0E-03	5.8E+05	5.5E-03
10	2.8E+05	1.5E-02	3.7E+05	2.0E-02	4.1E+05	2.2E-02
11	1.9E+05	5.8E-02	2.6E+05	7.9E-02	2.9E+05	8.7E-02
12	1.4E+05	2.3E-01	1.8E+05	3.1E-01	2.0E+05	3.5E-01
13	9.4E+04	9.1E-01	1.2E+05	1.2E+00	1.4E+05	1.3E+00
14	6.5E+04	3.6E+00	8.2E+04	4.5E+00	9.3E+04	5.2E+00
15	4.3E+04	1.4E+01	5.2E+04	1.6E+01	6.1E+04	1.9E+01
16	2.8E+04	5.0E+01	3.2E+04	5.7E+01	3.8E+04	6.7E+01
17	1.8E+04	1.8E+02	1.8E+04	1.8E+02	2.2E+04	2.2E+02
18	1.0E+04	5.8E+02	9.5E+03	5.4E+02	1.2E+04	6.9E+02
19	5.5E+03	1.8E+03	4.6E+03	1.5E+03	6.0E+03	1.9E+03
20	2.8E+03	5.0E+03	2.1E+03	3.8E+03	2.8E+03	5.2E+03
21	1.3E+03	1.3E+04	8.9E+02	9.2E+03	1.2E+03	1.3E+04
22	5.7E+02	3.3E+04	3.6E+02	2.1E+04	5.3E+02	3.1E+04
23	2.4E+02	8.0E+04	1.3E+02	4.5E+04	2.5E+02	8.2E+04
24	1.2E+02	2.2E+05	8.7E+01	1.6E+05	2.3E+02	4.2E+05
25	1.1E+02	1.2E+06	8.4E+02	8.9E+06	1.7E+03	1.8E+07

Table B.3 - DBN_{PDSC} constants of the shear complex interface stiffness for samples of slab REFB

	Sample REFB-1		**Sample REFB-2**		**Sample REFB-3**	
	φ_{NL} = 17 °		**φ_{NL} = 18 °**		**φ_{NL} = 16 °**	
Element number	**$K_{\theta zi}$ (MPa/mm)**	**η_i (MPa.s/mm)**	**$K_{\theta zi}$ (MPa/mm)**	**η_i (MPa.s/mm)**	**$K_{\theta zi}$ (MPa/mm)**	**η_i (MPa.s/mm)**
0	1.2E+03	X	8.0E+02	X	1.5E+03	X
1	2.3E+05	2.1E-09	1.7E+05	1.5E-09	3.2E+05	2.9E-09
2	2.6E+05	1.3E-08	1.9E+05	9.9E-09	3.6E+05	1.9E-08
3	2.4E+05	6.8E-08	1.8E+05	5.1E-08	3.3E+05	9.5E-08
4	2.2E+05	3.6E-07	1.6E+05	2.7E-07	3.0E+05	5.0E-07
5	1.3E+05	1.2E-06	9.8E+04	9.1E-07	1.8E+05	1.7E-06
6	1.0E+05	5.4E-06	7.7E+04	4.0E-06	1.4E+05	7.5E-06
7	6.8E+04	2.0E-05	5.1E+04	1.5E-05	9.5E+04	2.8E-05
8	5.1E+04	8.5E-05	3.7E+04	6.3E-05	7.0E+04	1.2E-04
9	3.5E+04	3.3E-04	2.6E+04	2.4E-04	4.8E+04	4.6E-04
10	2.5E+04	1.3E-03	1.8E+04	9.9E-04	3.5E+04	1.9E-03
11	1.7E+04	5.3E-03	1.3E+04	3.9E-03	2.4E+04	7.3E-03
12	1.2E+04	2.1E-02	9.0E+03	1.6E-02	1.7E+04	2.9E-02
13	8.4E+03	8.2E-02	6.2E+03	6.1E-02	1.2E+04	1.1E-01
14	5.8E+03	3.2E-01	4.3E+03	2.4E-01	8.1E+03	4.5E-01
15	3.8E+03	1.2E+00	2.9E+03	9.1E-01	5.4E+03	1.7E+00
16	2.5E+03	4.4E+00	1.9E+03	3.4E+00	3.5E+03	6.3E+00
17	1.5E+03	1.5E+01	1.2E+03	1.2E+01	2.2E+03	2.2E+01
18	8.6E+02	4.9E+01	6.8E+02	3.9E+01	1.3E+03	7.3E+01
19	4.6E+02	1.5E+02	3.7E+02	1.2E+02	6.9E+02	2.2E+02
20	2.2E+02	4.1E+02	1.8E+02	3.4E+02	3.5E+02	6.3E+02
21	1.0E+02	1.1E+03	8.6E+01	8.9E+02	1.6E+02	1.7E+03
22	4.5E+01	2.6E+03	3.8E+01	2.2E+03	7.2E+01	4.2E+03
23	2.0E+01	6.5E+03	1.7E+01	5.5E+03	3.2E+01	1.0E+04
24	1.2E+01	2.2E+04	8.5E+00	1.6E+04	1.7E+01	3.2E+04
25	2.3E+01	2.4E+05	9.5E+00	1.0E+05	2.1E+01	2.2E+05

Table B.4 - DBN_{PDSC} constants of the normal complex interface stiffness for samples of slab REFC

	Sample REFC-1		**Sample REFC-2**		**Sample REFC-3**	
	φ_{NL} = 8 °		**φ_{NL} = 15 °**		**φ_{NL} = 15 °**	
Element number	**K_{zzi} (MPa/mm)**	**η_i (MPa.s/mm)**	**K_{zzi} (MPa/mm)**	**η_i (MPa.s/mm)**	**K_{zzi} (MPa/mm)**	**η_i (MPa.s/mm)**
0	1.7E+04	X	3.0E+03	X	1.0E+04	X
1	2.0E+06	1.8E-08	4.6E+05	4.2E-09	1.4E+06	1.3E-08
2	2.3E+06	1.2E-07	5.3E+05	2.7E-08	1.6E+06	8.1E-08
3	2.0E+06	5.9E-07	4.7E+05	1.4E-07	1.4E+06	4.1E-07
4	1.9E+06	3.1E-06	4.4E+05	7.2E-07	1.3E+06	2.2E-06
5	1.1E+06	1.1E-05	2.6E+05	2.5E-06	8.0E+05	7.4E-06
6	8.9E+05	4.7E-05	2.1E+05	1.1E-05	6.3E+05	3.3E-05
7	5.9E+05	1.7E-04	1.4E+05	4.1E-05	4.1E+05	1.2E-04
8	4.3E+05	7.3E-04	1.0E+05	1.7E-04	3.0E+05	5.1E-04
9	3.0E+05	2.8E-03	6.9E+04	6.6E-04	2.1E+05	2.0E-03
10	2.1E+05	1.1E-02	5.0E+04	2.7E-03	1.5E+05	8.0E-03
11	1.5E+05	4.4E-02	3.4E+04	1.0E-02	1.0E+05	3.1E-02
12	1.0E+05	1.7E-01	2.4E+04	4.2E-02	7.2E+04	1.2E-01
13	6.8E+04	6.7E-01	1.6E+04	1.6E-01	4.9E+04	4.8E-01
14	4.5E+04	2.5E+00	1.1E+04	6.2E-01	3.3E+04	1.8E+00
15	2.8E+04	8.9E+00	7.3E+03	2.3E+00	2.1E+04	6.7E+00
16	1.7E+04	3.0E+01	4.5E+03	8.0E+00	1.3E+04	2.3E+01
17	9.2E+03	9.3E+01	2.6E+03	2.7E+01	7.5E+03	7.5E+01
18	4.7E+03	2.7E+02	1.4E+03	8.1E+01	4.0E+03	2.3E+02
19	2.2E+03	7.1E+02	7.2E+02	2.3E+02	1.9E+03	6.3E+02
20	9.8E+02	1.8E+03	3.3E+02	6.1E+02	8.9E+02	1.6E+03
21	4.1E+02	4.2E+03	1.5E+02	1.5E+03	3.9E+02	4.0E+03
22	1.5E+02	9.1E+03	6.0E+01	3.5E+03	1.6E+02	9.6E+03
23	5.5E+01	1.8E+04	2.2E+01	7.4E+03	8.1E+01	2.7E+04
24	4.7E+01	8.8E+04	9.0E+00	1.7E+04	1.0E+02	1.9E+05
25	1.5E+03	1.6E+07	1.5E+01	1.6E+05	2.9E+03	3.1E+07

Table B.5 - DBN_{PDSC} constants of the shear complex interface stiffness for samples of slab REFC

	Sample REFC-1		**Sample REFC-2**		**Sample REFC-3**	
	φ_{NL} = 10 °		**φ_{NL} = 21 °**		**φ_{NL} = 16 °**	
Element number	**$K_{\theta zi}$ (MPa/mm)**	**η_i (MPa.s/mm)**	**$K_{\theta zi}$ (MPa/mm)**	**η_i (MPa.s/mm)**	**$K_{\theta zi}$ (MPa/mm)**	**η_i (MPa.s/mm)**
0	2.5E+03	X	4.2E+02	X	6.0E+02	X
1	3.6E+05	3.3E-09	8.1E+04	7.3E-10	1.0E+05	9.4E-10
2	4.1E+05	2.1E-08	9.2E+04	4.7E-09	1.2E+05	6.0E-09
3	3.7E+05	1.1E-07	8.3E+04	2.4E-08	1.1E+05	3.1E-08
4	3.5E+05	5.7E-07	7.7E+04	1.3E-07	9.9E+04	1.6E-07
5	2.1E+05	1.9E-06	4.6E+04	4.3E-07	6.0E+04	5.5E-07
6	1.6E+05	8.6E-06	3.6E+04	1.9E-06	4.7E+04	2.5E-06
7	1.1E+05	3.2E-05	2.4E+04	7.1E-06	3.1E+04	9.2E-06
8	8.0E+04	1.3E-04	1.8E+04	3.0E-05	2.3E+04	3.8E-05
9	5.4E+04	5.2E-04	1.2E+04	1.2E-04	1.6E+04	1.5E-04
10	3.9E+04	2.1E-03	8.7E+03	4.7E-04	1.1E+04	6.0E-04
11	2.7E+04	8.2E-03	6.1E+03	1.8E-03	7.8E+03	2.4E-03
12	1.9E+04	3.3E-02	4.3E+03	7.4E-03	5.5E+03	9.4E-03
13	1.3E+04	1.3E-01	2.9E+03	2.9E-02	3.7E+03	3.7E-02
14	8.7E+03	4.8E-01	2.0E+03	1.1E-01	2.6E+03	1.4E-01
15	5.6E+03	1.8E+00	1.4E+03	4.2E-01	1.7E+03	5.3E-01
16	3.5E+03	6.2E+00	8.7E+02	1.5E+00	1.1E+03	1.9E+00
17	2.0E+03	2.0E+01	5.3E+02	5.4E+00	6.4E+02	6.5E+00
18	1.1E+03	6.1E+01	3.1E+02	1.7E+01	3.6E+02	2.0E+01
19	5.3E+02	1.7E+02	1.6E+02	5.2E+01	1.8E+02	5.9E+01
20	2.4E+02	4.5E+02	7.9E+01	1.4E+02	8.8E+01	1.6E+02
21	1.1E+02	1.1E+03	3.7E+01	3.8E+02	3.9E+01	4.1E+02
22	4.3E+01	2.5E+03	1.7E+01	9.8E+02	1.7E+01	9.8E+02
23	1.7E+01	5.8E+03	8.7E+00	2.9E+03	6.9E+00	2.3E+03
24	1.1E+01	2.1E+04	7.8E+00	1.5E+04	3.6E+00	6.8E+03
25	7.0E+01	7.4E+05	2.5E+01	2.6E+05	7.4E+00	7.9E+04

Table B.6 - DBN_{PDSC} constants of the normal complex interface stiffness for samples of slab C/D

	Sample C/D-1		**Sample C/D-2**		**Sample C/D-3**	
	φ_{NL} = 14 °		**φ_{NL} = 14 °**		**φ_{NL} = 13 °**	
Element number	**K_{zzi} (MPa/mm)**	**η_i (MPa.s/mm)**	**K_{zzi} (MPa/mm)**	**η_i (MPa.s/mm)**	**K_{zzi} (MPa/mm)**	**η_i (MPa.s/mm)**
0	6.0E+03	X	6.5E+03	X	5.5E+03	X
1	1.1E+06	1.0E-08	1.1E+06	9.8E-09	1.2E+06	1.1E-08
2	1.3E+06	6.5E-08	1.2E+06	6.3E-08	1.3E+06	6.8E-08
3	1.1E+06	3.3E-07	1.1E+06	3.2E-07	1.2E+06	3.5E-07
4	1.1E+06	1.7E-06	1.0E+06	1.7E-06	1.1E+06	1.8E-06
5	6.4E+05	5.9E-06	6.2E+05	5.8E-06	6.7E+05	6.2E-06
6	5.0E+05	2.6E-05	4.9E+05	2.6E-05	5.3E+05	2.8E-05
7	3.3E+05	9.8E-05	3.2E+05	9.6E-05	3.5E+05	1.0E-04
8	2.4E+05	4.1E-04	2.4E+05	4.0E-04	2.6E+05	4.3E-04
9	1.7E+05	1.6E-03	1.6E+05	1.6E-03	1.8E+05	1.7E-03
10	1.2E+05	6.5E-03	1.2E+05	6.3E-03	1.3E+05	6.8E-03
11	8.3E+04	2.5E-02	8.1E+04	2.5E-02	8.8E+04	2.7E-02
12	5.9E+04	1.0E-01	5.7E+04	9.9E-02	6.2E+04	1.1E-01
13	4.0E+04	4.0E-01	3.9E+04	3.8E-01	4.3E+04	4.2E-01
14	2.8E+04	1.5E+00	2.7E+04	1.5E+00	3.0E+04	1.6E+00
15	1.8E+04	5.8E+00	1.8E+04	5.5E+00	2.0E+04	6.2E+00
16	1.2E+04	2.1E+01	1.1E+04	2.0E+01	1.3E+04	2.3E+01
17	7.2E+03	7.2E+01	6.6E+03	6.6E+01	8.1E+03	8.1E+01
18	4.1E+03	2.3E+02	3.7E+03	2.1E+02	4.7E+03	2.7E+02
19	2.1E+03	6.9E+02	1.9E+03	6.0E+02	2.6E+03	8.2E+02
20	1.0E+03	1.9E+03	8.9E+02	1.6E+03	1.3E+03	2.3E+03
21	4.8E+02	4.9E+03	4.0E+02	4.1E+03	6.0E+02	6.2E+03
22	2.1E+02	1.2E+04	1.7E+02	1.0E+04	2.7E+02	1.6E+04
23	1.1E+02	3.5E+04	8.2E+01	2.7E+04	1.2E+02	4.0E+04
24	8.8E+01	1.6E+05	7.1E+01	1.3E+05	7.0E+01	1.3E+05
25	2.9E+02	3.1E+06	3.4E+02	3.6E+06	9.9E+01	1.1E+06

Table B.7 - DBN_{PDSC} constants of the shear complex interface stiffness for samples of slab C/D

	Sample C/D-1		**Sample C/D-2**		**Sample C/D-3**	
	φ_{NL} = 13 °		**φ_{NL} = 10 °**		**φ_{NL} = 12 °**	
Element number	**$K_{\theta zi}$ (MPa/mm)**	**η_i (MPa.s/mm)**	**$K_{\theta zi}$ (MPa/mm)**	**η_i (MPa.s/mm)**	**$K_{\theta zi}$ (MPa/mm)**	**η_i (MPa.s/mm)**
0	1.0E+03	X	6.0E+02	X	1.5E+03	X
1	2.1E+05	1.9E-09	1.6E+05	1.4E-09	2.8E+05	2.5E-09
2	2.4E+05	1.2E-08	1.8E+05	9.2E-09	3.2E+05	1.6E-08
3	2.2E+05	6.3E-08	1.6E+05	4.7E-08	2.9E+05	8.2E-08
4	2.0E+05	3.3E-07	1.5E+05	2.5E-07	2.6E+05	4.3E-07
5	1.2E+05	1.1E-06	9.1E+04	8.5E-07	1.6E+05	1.5E-06
6	9.6E+04	5.0E-06	7.2E+04	3.8E-06	1.2E+05	6.5E-06
7	6.3E+04	1.9E-05	4.7E+04	1.4E-05	8.2E+04	2.4E-05
8	4.7E+04	7.8E-05	3.5E+04	5.9E-05	6.1E+04	1.0E-04
9	3.2E+04	3.0E-04	2.4E+04	2.3E-04	4.2E+04	4.0E-04
10	2.3E+04	1.2E-03	1.7E+04	9.3E-04	3.0E+04	1.6E-03
11	1.6E+04	4.9E-03	1.2E+04	3.6E-03	2.1E+04	6.3E-03
12	1.1E+04	1.9E-02	8.5E+03	1.5E-02	1.5E+04	2.5E-02
13	7.8E+03	7.6E-02	5.9E+03	5.8E-02	1.0E+04	9.8E-02
14	5.4E+03	3.0E-01	4.1E+03	2.3E-01	6.9E+03	3.8E-01
15	3.6E+03	1.1E+00	2.8E+03	8.7E-01	4.6E+03	1.4E+00
16	2.4E+03	4.2E+00	1.9E+03	3.3E+00	2.9E+03	5.2E+00
17	1.5E+03	1.5E+01	1.2E+03	1.2E+01	1.8E+03	1.8E+01
18	8.5E+02	4.8E+01	7.3E+02	4.1E+01	1.0E+03	5.7E+01
19	4.6E+02	1.5E+02	4.1E+02	1.3E+02	5.2E+02	1.7E+02
20	2.3E+02	4.2E+02	2.2E+02	3.9E+02	2.5E+02	4.6E+02
21	1.1E+02	1.1E+03	1.0E+02	1.1E+03	1.1E+02	1.2E+03
22	4.6E+01	2.7E+03	4.8E+01	2.8E+03	4.8E+01	2.8E+03
23	1.9E+01	6.4E+03	2.1E+01	6.8E+03	1.9E+01	6.4E+03
24	8.2E+00	1.5E+04	8.7E+00	1.6E+04	7.5E+00	1.4E+04
25	5.4E+00	5.7E+04	2.9E+00	3.0E+04	5.7E+00	6.0E+04

Table B.8 - DBN_{PDSC} constants of the normal complex interface stiffness for samples of slab D/D

	Sample D/D-1		**Sample D/D-2**		**Sample D/D-3**	
	φ_{NL} = 23 °		**φ_{NL} = 10 °**		**φ_{NL} = 19 °**	
Element number	**K_{zzi} (MPa/mm)**	**η_i (MPa.s/mm)**	**K_{zzi} (MPa/mm)**	**η_i (MPa.s/mm)**	**K_{zzi} (MPa/mm)**	**η_i (MPa.s/mm)**
0	2.5E+03	X	1.2E+04	X	3.0E+03	X
1	4.7E+05	4.2E-09	1.9E+06	1.7E-08	5.4E+05	4.8E-09
2	5.3E+05	2.7E-08	2.1E+06	1.1E-07	6.1E+05	3.1E-08
3	4.8E+05	1.4E-07	1.9E+06	5.5E-07	5.5E+05	1.6E-07
4	4.4E+05	7.3E-07	1.8E+06	2.9E-06	5.1E+05	8.3E-07
5	2.7E+05	2.5E-06	1.1E+06	9.8E-06	3.1E+05	2.8E-06
6	2.1E+05	1.1E-05	8.3E+05	4.4E-05	2.4E+05	1.3E-05
7	1.4E+05	4.1E-05	5.5E+05	1.6E-04	1.6E+05	4.7E-05
8	1.0E+05	1.7E-04	4.0E+05	6.8E-04	1.2E+05	2.0E-04
9	7.0E+04	6.7E-04	2.8E+05	2.6E-03	8.0E+04	7.6E-04
10	5.0E+04	2.7E-03	2.0E+05	1.1E-02	5.8E+04	3.1E-03
11	3.5E+04	1.1E-02	1.4E+05	4.2E-02	4.0E+04	1.2E-02
12	2.5E+04	4.3E-02	9.6E+04	1.7E-01	2.8E+04	4.9E-02
13	1.7E+04	1.7E-01	6.6E+04	6.4E-01	1.9E+04	1.9E-01
14	1.2E+04	6.5E-01	4.5E+04	2.5E+00	1.3E+04	7.3E-01
15	7.8E+03	2.4E+00	2.9E+04	9.1E+00	8.8E+03	2.8E+00
16	5.0E+03	8.9E+00	1.8E+04	3.2E+01	5.6E+03	1.0E+01
17	3.1E+03	3.1E+01	1.1E+04	1.1E+02	3.4E+03	3.4E+01
18	1.7E+03	9.9E+01	5.7E+03	3.3E+02	1.9E+03	1.1E+02
19	9.2E+02	3.0E+02	2.9E+03	9.2E+02	1.0E+03	3.2E+02
20	4.6E+02	8.3E+02	1.3E+03	2.4E+03	4.9E+02	8.9E+02
21	2.2E+02	2.3E+03	5.8E+02	6.0E+03	2.3E+02	2.4E+03
22	1.1E+02	6.5E+03	2.4E+02	1.4E+04	1.1E+02	6.7E+03
23	8.2E+01	2.7E+04	8.8E+01	2.9E+04	7.9E+01	2.6E+04
24	1.3E+02	2.5E+05	3.2E+01	5.9E+04	1.3E+02	2.3E+05
25	6.4E+02	6.8E+06	3.8E+01	4.0E+05	7.0E+02	7.5E+06

Table B.9 - DBN_{PDSC} constants of the shear complex interface stiffness for samples of slab D/D

	Sample D/D-1		**Sample D/D-2**		**Sample D/D-3**	
	φ_{NL} = 25 °		**φ_{NL} = 21 °**		**φ_{NL} = 21 °**	
Element number	**$K_{\theta zi}$ (MPa/mm)**	**η_i (MPa.s/mm)**	**$K_{\theta zi}$ (MPa/mm)**	**η_i (MPa.s/mm)**	**$K_{\theta zi}$ (MPa/mm)**	**η_i (MPa.s/mm)**
0	3.0E+02	X	2.0E+02	X	5.0E+02	X
1	7.4E+04	6.7E-10	6.5E+04	5.9E-10	1.1E+05	9.7E-10
2	8.4E+04	4.3E-09	7.4E+04	3.8E-09	1.2E+05	6.2E-09
3	7.6E+04	2.2E-08	6.7E+04	1.9E-08	1.1E+05	3.2E-08
4	7.1E+04	1.2E-07	6.2E+04	1.0E-07	1.0E+05	1.7E-07
5	4.3E+04	3.9E-07	3.7E+04	3.5E-07	6.1E+04	5.7E-07
6	3.3E+04	1.7E-06	2.9E+04	1.5E-06	4.8E+04	2.5E-06
7	2.2E+04	6.5E-06	1.9E+04	5.8E-06	3.2E+04	9.4E-06
8	1.6E+04	2.7E-05	1.4E+04	2.4E-05	2.3E+04	3.9E-05
9	1.1E+04	1.1E-04	9.8E+03	9.4E-05	1.6E+04	1.5E-04
10	8.0E+03	4.3E-04	7.1E+03	3.8E-04	1.2E+04	6.2E-04
11	5.6E+03	1.7E-03	4.9E+03	1.5E-03	8.0E+03	2.4E-03
12	4.0E+03	6.8E-03	3.5E+03	6.1E-03	5.7E+03	9.8E-03
13	2.7E+03	2.7E-02	2.4E+03	2.4E-02	3.9E+03	3.8E-02
14	1.9E+03	1.1E-01	1.7E+03	9.5E-02	2.7E+03	1.5E-01
15	1.3E+03	4.1E-01	1.2E+03	3.7E-01	1.8E+03	5.7E-01
16	8.7E+02	1.5E+00	8.0E+02	1.4E+00	1.2E+03	2.1E+00
17	5.5E+02	5.5E+00	5.3E+02	5.3E+00	7.4E+02	7.5E+00
18	3.3E+02	1.9E+01	3.4E+02	1.9E+01	4.4E+02	2.5E+01
19	1.9E+02	6.1E+01	2.0E+02	6.5E+01	2.4E+02	7.6E+01
20	9.9E+01	1.8E+02	1.1E+02	2.0E+02	1.2E+02	2.2E+02
21	4.9E+01	5.1E+02	5.8E+01	6.0E+02	5.7E+01	5.9E+02
22	2.5E+01	1.4E+03	2.9E+01	1.7E+03	2.7E+01	1.6E+03
23	1.5E+01	4.9E+03	1.5E+01	5.1E+03	1.4E+01	4.8E+03
24	1.5E+01	2.9E+04	1.1E+01	2.0E+04	1.3E+01	2.5E+04
25	3.3E+01	3.5E+05	1.1E+01	1.1E+05	3.4E+01	3.6E+05

Table B.10 - DBN_{PDSC} constants of the normal complex interface stiffness for samples of slab D/C

	Sample D/C-1		**Sample D/C-2**		**Sample D/C-3**	
	φ_{NL} = 16 °		**φ_{NL} = 16 °**		**φ_{NL} = 20 °**	
Element number	**K_{zzi} (MPa/mm)**	**η_i (MPa.s/mm)**	**K_{zzi} (MPa/mm)**	**η_i (MPa.s/mm)**	**K_{zzi} (MPa/mm)**	**η_i (MPa.s/mm)**
0	4.5E+03	X	4.2E+03	X	3.5E+03	X
1	8.0E+05	7.2E-09	6.5E+05	5.9E-09	7.5E+05	6.8E-09
2	9.1E+05	4.7E-08	7.4E+05	3.8E-08	8.6E+05	4.4E-08
3	8.2E+05	2.4E-07	6.7E+05	1.9E-07	7.7E+05	2.2E-07
4	7.6E+05	1.2E-06	6.2E+05	1.0E-06	7.2E+05	1.2E-06
5	4.6E+05	4.3E-06	3.7E+05	3.5E-06	4.3E+05	4.0E-06
6	3.6E+05	1.9E-05	2.9E+05	1.5E-05	3.4E+05	1.8E-05
7	2.4E+05	7.1E-05	1.9E+05	5.7E-05	2.2E+05	6.6E-05
8	1.8E+05	3.0E-04	1.4E+05	2.4E-04	1.7E+05	2.8E-04
9	1.2E+05	1.1E-03	9.8E+04	9.3E-04	1.1E+05	1.1E-03
10	8.6E+04	4.7E-03	7.0E+04	3.8E-03	8.2E+04	4.4E-03
11	6.0E+04	1.8E-02	4.8E+04	1.5E-02	5.7E+04	1.7E-02
12	4.2E+04	7.3E-02	3.4E+04	5.9E-02	4.0E+04	6.9E-02
13	2.9E+04	2.8E-01	2.3E+04	2.3E-01	2.8E+04	2.7E-01
14	2.0E+04	1.1E+00	1.6E+04	8.8E-01	1.9E+04	1.1E+00
15	1.3E+04	4.1E+00	1.0E+04	3.2E+00	1.3E+04	4.1E+00
16	8.4E+03	1.5E+01	6.5E+03	1.1E+01	8.5E+03	1.5E+01
17	5.1E+03	5.1E+01	3.8E+03	3.8E+01	5.3E+03	5.4E+01
18	2.9E+03	1.6E+02	2.1E+03	1.2E+02	3.1E+03	1.8E+02
19	1.5E+03	4.8E+02	1.1E+03	3.4E+02	1.7E+03	5.6E+02
20	7.3E+02	1.3E+03	5.0E+02	9.1E+02	8.9E+02	1.6E+03
21	3.4E+02	3.5E+03	2.3E+02	2.4E+03	4.4E+02	4.5E+03
22	1.7E+02	9.7E+03	1.2E+02	7.1E+03	2.3E+02	1.4E+04
23	1.1E+02	3.6E+04	1.0E+02	3.4E+04	1.8E+02	5.8E+04
24	1.6E+02	3.0E+05	2.4E+02	4.6E+05	2.7E+02	5.0E+05
25	9.0E+02	9.6E+06	2.3E+03	2.4E+07	8.8E+02	9.3E+06

Table B.11 - DBN_{PDSC} constants of the shear complex interface stiffness for samples of slab D/C

	Sample D/C-1		**Sample D/C-2**		**Sample D/C-3**	
	φ_{NL} = 17 °		**φ_{NL} = 20 °**		**φ_{NL} = 22 °**	
Element number	**$K_{\theta zi}$ (MPa/mm)**	**η_i (MPa.s/mm)**	**$K_{\theta zi}$ (MPa/mm)**	**η_i (MPa.s/mm)**	**$K_{\theta zi}$ (MPa/mm)**	**η_i (MPa.s/mm)**
0	5.0E+02	X	4.3E+02	X	4.0E+02	X
1	1.1E+05	9.6E-10	9.1E+04	8.2E-10	8.6E+04	7.7E-10
2	1.2E+05	6.2E-09	1.0E+05	5.3E-09	9.8E+04	5.0E-09
3	1.1E+05	3.2E-08	9.4E+04	2.7E-08	8.8E+04	2.5E-08
4	1.0E+05	1.7E-07	8.7E+04	1.4E-07	8.2E+04	1.3E-07
5	6.1E+04	5.7E-07	5.2E+04	4.8E-07	4.9E+04	4.6E-07
6	4.8E+04	2.5E-06	4.1E+04	2.1E-06	3.9E+04	2.0E-06
7	3.2E+04	9.4E-06	2.7E+04	8.0E-06	2.5E+04	7.5E-06
8	2.3E+04	3.9E-05	2.0E+04	3.4E-05	1.9E+04	3.2E-05
9	1.6E+04	1.5E-04	1.4E+04	1.3E-04	1.3E+04	1.2E-04
10	1.2E+04	6.2E-04	9.8E+03	5.3E-04	9.3E+03	5.0E-04
11	8.0E+03	2.4E-03	6.8E+03	2.1E-03	6.4E+03	2.0E-03
12	5.7E+03	9.8E-03	4.8E+03	8.3E-03	4.6E+03	7.9E-03
13	3.9E+03	3.8E-02	3.3E+03	3.3E-02	3.2E+03	3.1E-02
14	2.7E+03	1.5E-01	2.3E+03	1.3E-01	2.2E+03	1.2E-01
15	1.8E+03	5.7E-01	1.6E+03	4.9E-01	1.5E+03	4.6E-01
16	1.2E+03	2.1E+00	1.0E+03	1.8E+00	9.6E+02	1.7E+00
17	7.4E+02	7.4E+00	6.4E+02	6.4E+00	6.0E+02	6.0E+00
18	4.3E+02	2.5E+01	3.7E+02	2.1E+01	3.5E+02	2.0E+01
19	2.3E+02	7.5E+01	2.0E+02	6.5E+01	1.9E+02	6.2E+01
20	1.2E+02	2.1E+02	1.0E+02	1.9E+02	9.7E+01	1.8E+02
21	5.5E+01	5.7E+02	4.9E+01	5.1E+02	4.7E+01	4.8E+02
22	2.5E+01	1.5E+03	2.4E+01	1.4E+03	2.3E+01	1.3E+03
23	1.2E+01	3.9E+03	1.4E+01	4.6E+03	1.4E+01	4.6E+03
24	8.0E+00	1.5E+04	1.5E+01	2.8E+04	1.5E+01	2.9E+04
25	1.5E+01	1.5E+05	4.2E+01	4.4E+05	4.5E+01	4.8E+05

Table B.12 - DBN_{PDSC} constants of the normal complex interface stiffness for samples of slab LDO

	Sample LDO-1		**Sample LDO -2**		**Sample LDO-3**	
	φ_{NL} = 8 °		**φ_{NL} = 12 °**		**φ_{NL} = 16 °**	
Element number	**K_{zzi} (MPa/mm)**	**η_i (MPa.s/mm)**	**K_{zzi} (MPa/mm)**	**η_i (MPa.s/mm)**	**K_{zzi} (MPa/mm)**	**η_i (MPa.s/mm)**
0	1.5E+04	X	3.5E+03	X	1.4E+04	X
1	1.8E+06	1.6E-08	7.5E+05	6.7E-09	2.2E+06	1.9E-08
2	2.0E+06	1.0E-07	8.5E+05	4.3E-08	2.5E+06	1.3E-07
3	1.8E+06	5.2E-07	7.7E+05	2.2E-07	2.2E+06	6.4E-07
4	1.7E+06	2.7E-06	7.1E+05	1.2E-06	2.1E+06	3.4E-06
5	1.0E+06	9.3E-06	4.3E+05	4.0E-06	1.2E+06	1.1E-05
6	7.9E+05	4.1E-05	3.4E+05	1.8E-05	9.7E+05	5.1E-05
7	5.2E+05	1.5E-04	2.2E+05	6.6E-05	6.4E+05	1.9E-04
8	3.8E+05	6.4E-04	1.6E+05	2.8E-04	4.7E+05	7.9E-04
9	2.6E+05	2.5E-03	1.1E+05	1.1E-03	3.2E+05	3.1E-03
10	1.9E+05	1.0E-02	8.1E+04	4.3E-03	2.3E+05	1.2E-02
11	1.3E+05	3.9E-02	5.6E+04	1.7E-02	1.6E+05	4.9E-02
12	8.9E+04	1.5E-01	4.0E+04	6.8E-02	1.1E+05	1.9E-01
13	6.0E+04	5.9E-01	2.7E+04	2.7E-01	7.7E+04	7.5E-01
14	4.0E+04	2.2E+00	1.9E+04	1.0E+00	5.2E+04	2.9E+00
15	2.5E+04	7.8E+00	1.3E+04	4.0E+00	3.4E+04	1.1E+01
16	1.5E+04	2.6E+01	8.3E+03	1.5E+01	2.1E+04	3.8E+01
17	8.1E+03	8.2E+01	5.2E+03	5.2E+01	1.2E+04	1.2E+02
18	4.1E+03	2.4E+02	3.0E+03	1.7E+02	6.7E+03	3.8E+02
19	1.9E+03	6.3E+02	1.6E+03	5.2E+02	3.4E+03	1.1E+03
20	8.6E+02	1.6E+03	8.2E+02	1.5E+03	1.6E+03	2.9E+03
21	3.6E+02	3.7E+03	3.8E+02	3.9E+03	6.9E+02	7.1E+03
22	1.4E+02	8.0E+03	1.7E+02	1.0E+04	2.8E+02	1.7E+04
23	5.2E+01	1.7E+04	8.0E+01	2.6E+04	1.1E+02	3.8E+04
24	5.3E+01	9.9E+04	5.1E+01	9.5E+04	6.9E+01	1.3E+05
25	3.5E+03	3.7E+07	8.4E+01	8.9E+05	2.7E+02	2.8E+06

Table B.13 - DBN_{PDSC} constants of the shear complex interface stiffness for samples of slab LDO

	Sample LDO-1		**Sample LDO-2**		**Sample LDO-3**	
	φ_{NL} = 12 °		**φ_{NL} = 13 °**		**φ_{NL} = 10 °**	
Element number	**$K_{\theta zi}$ (MPa/mm)**	**η_i (MPa.s/mm)**	**$K_{\theta zi}$ (MPa/mm)**	**η_i (MPa.s/mm)**	**$K_{\theta zi}$ (MPa/mm)**	**η_i (MPa.s/mm)**
0	9.5E+02	X	1.2E+03	X	2.0E+03	X
1	1.7E+05	1.5E-09	1.7E+05	1.6E-09	2.0E+05	1.8E-09
2	1.9E+05	9.8E-09	2.0E+05	1.0E-08	2.3E+05	1.2E-08
3	1.7E+05	5.0E-08	1.8E+05	5.2E-08	2.1E+05	6.0E-08
4	1.6E+05	2.6E-07	1.7E+05	2.7E-07	1.9E+05	3.2E-07
5	9.6E+04	8.9E-07	1.0E+05	9.3E-07	1.2E+05	1.1E-06
6	7.6E+04	4.0E-06	7.8E+04	4.1E-06	9.1E+04	4.8E-06
7	5.0E+04	1.5E-05	5.2E+04	1.5E-05	6.0E+04	1.8E-05
8	3.7E+04	6.2E-05	3.8E+04	6.4E-05	4.4E+04	7.4E-05
9	2.5E+04	2.4E-04	2.6E+04	2.5E-04	3.0E+04	2.9E-04
10	1.8E+04	9.8E-04	1.9E+04	1.0E-03	2.2E+04	1.2E-03
11	1.3E+04	3.8E-03	1.3E+04	3.9E-03	1.5E+04	4.5E-03
12	8.8E+03	1.5E-02	9.1E+03	1.6E-02	1.0E+04	1.8E-02
13	6.1E+03	5.9E-02	6.2E+03	6.0E-02	6.8E+03	6.7E-02
14	4.1E+03	2.3E-01	4.2E+03	2.3E-01	4.4E+03	2.5E-01
15	2.7E+03	8.6E-01	2.7E+03	8.4E-01	2.7E+03	8.5E-01
16	1.7E+03	3.1E+00	1.7E+03	3.0E+00	1.6E+03	2.8E+00
17	1.0E+03	1.1E+01	9.6E+02	9.7E+00	8.3E+02	8.4E+00
18	5.9E+02	3.3E+01	5.1E+02	2.9E+01	4.1E+02	2.3E+01
19	3.0E+02	9.8E+01	2.5E+02	8.2E+01	1.9E+02	6.1E+01
20	1.5E+02	2.6E+02	1.2E+02	2.1E+02	8.1E+01	1.5E+02
21	6.5E+01	6.7E+02	5.1E+01	5.2E+02	3.3E+01	3.4E+02
22	2.8E+01	1.6E+03	2.1E+01	1.2E+03	1.2E+01	6.9E+02
23	1.1E+01	3.7E+03	7.7E+00	2.6E+03	4.3E+00	1.4E+03
24	5.0E+00	9.4E+03	3.8E+00	7.1E+03	6.9E+00	1.3E+04
25	6.9E+00	7.4E+04	1.3E+01	1.4E+05	1.0E+02	1.1E+06

Table B.14 - DBN_{PDSC} constants of the normal complex interface stiffness for samples of slab HDO

	Sample HDO-1		**Sample HDO -2**		**Sample HDO-3**	
	φ_{NL} = 10 °		**φ_{NL} = 18 °**		**φ_{NL} = 18 °**	
Element number	**K_{zzi} (MPa/mm)**	**η_i (MPa.s/mm)**	**K_{zzi} (MPa/mm)**	**η_i (MPa.s/mm)**	**K_{zzi} (MPa/mm)**	**η_i (MPa.s/mm)**
0	7.5E+03	X	4.0E+03	X	5.5E+03	X
1	1.2E+06	1.0E-08	6.8E+05	6.1E-09	9.5E+05	8.6E-09
2	1.3E+06	6.7E-08	7.7E+05	3.9E-08	1.1E+06	5.5E-08
3	1.2E+06	3.4E-07	6.9E+05	2.0E-07	9.8E+05	2.8E-07
4	1.1E+06	1.8E-06	6.4E+05	1.1E-06	9.1E+05	1.5E-06
5	6.6E+05	6.1E-06	3.9E+05	3.6E-06	5.5E+05	5.0E-06
6	5.2E+05	2.7E-05	3.0E+05	1.6E-05	4.3E+05	2.2E-05
7	3.4E+05	1.0E-04	2.0E+05	5.9E-05	2.8E+05	8.4E-05
8	2.5E+05	4.3E-04	1.5E+05	2.5E-04	2.1E+05	3.5E-04
9	1.7E+05	1.6E-03	1.0E+05	9.6E-04	1.4E+05	1.4E-03
10	1.2E+05	6.7E-03	7.3E+04	3.9E-03	1.0E+05	5.5E-03
11	8.6E+04	2.6E-02	5.0E+04	1.5E-02	7.1E+04	2.2E-02
12	6.0E+04	1.0E-01	3.5E+04	6.1E-02	5.0E+04	8.6E-02
13	4.1E+04	4.0E-01	2.4E+04	2.4E-01	3.4E+04	3.4E-01
14	2.8E+04	1.5E+00	1.7E+04	9.2E-01	2.3E+04	1.3E+00
15	1.8E+04	5.7E+00	1.1E+04	3.4E+00	1.5E+04	4.8E+00
16	1.1E+04	2.0E+01	7.0E+03	1.2E+01	9.8E+03	1.7E+01
17	6.7E+03	6.7E+01	4.2E+03	4.2E+01	5.9E+03	5.9E+01
18	3.6E+03	2.1E+02	2.3E+03	1.3E+02	3.3E+03	1.9E+02
19	1.8E+03	5.8E+02	1.2E+03	3.9E+02	1.7E+03	5.5E+02
20	8.5E+02	1.5E+03	5.9E+02	1.1E+03	8.1E+02	1.5E+03
21	3.7E+02	3.8E+03	2.8E+02	2.9E+03	3.7E+02	3.8E+03
22	1.6E+02	9.2E+03	1.5E+02	9.0E+03	1.6E+02	9.5E+03
23	7.0E+01	2.3E+04	1.4E+02	4.5E+04	8.1E+01	2.7E+04
24	5.9E+01	1.1E+05	3.1E+02	5.8E+05	7.6E+01	1.4E+05
25	3.9E+02	4.1E+06	2.0E+03	2.1E+07	3.5E+02	3.7E+06

Table B.15 - DBN_{PDSC} constants of the shear complex interface stiffness for samples of slab HDO

	Sample HDO-1		**Sample HDO-2**		**Sample HDO-3**	
	φ_{NL} = 15 °		**φ_{NL} = 17 °**		**φ_{NL} = 17 °**	
Element number	**$K_{\theta zi}$ (MPa/mm)**	**η_i (MPa.s/mm)**	**$K_{\theta zi}$ (MPa/mm)**	**η_i (MPa.s/mm)**	**$K_{\theta zi}$ (MPa/mm)**	**η_i (MPa.s/mm)**
0	7.0E+02	X	4.0E+02	X	6.0E+02	X
1	1.3E+05	1.2E-09	8.2E+04	7.4E-10	1.1E+05	1.0E-09
2	1.5E+05	7.5E-09	9.3E+04	4.7E-09	1.3E+05	6.5E-09
3	1.3E+05	3.8E-08	8.4E+04	2.4E-08	1.1E+05	3.3E-08
4	1.2E+05	2.0E-07	7.8E+04	1.3E-07	1.1E+05	1.7E-07
5	7.4E+04	6.9E-07	4.7E+04	4.3E-07	6.4E+04	5.9E-07
6	5.8E+04	3.1E-06	3.7E+04	1.9E-06	5.0E+04	2.6E-06
7	3.8E+04	1.1E-05	2.4E+04	7.2E-06	3.3E+04	9.8E-06
8	2.8E+04	4.8E-05	1.8E+04	3.0E-05	2.4E+04	4.1E-05
9	1.9E+04	1.8E-04	1.2E+04	1.2E-04	1.7E+04	1.6E-04
10	1.4E+04	7.5E-04	8.8E+03	4.8E-04	1.2E+04	6.5E-04
11	9.7E+03	3.0E-03	6.1E+03	1.9E-03	8.3E+03	2.5E-03
12	6.8E+03	1.2E-02	4.3E+03	7.5E-03	5.9E+03	1.0E-02
13	4.7E+03	4.6E-02	3.0E+03	2.9E-02	4.0E+03	3.9E-02
14	3.2E+03	1.8E-01	2.1E+03	1.1E-01	2.8E+03	1.5E-01
15	2.1E+03	6.7E-01	1.4E+03	4.3E-01	1.8E+03	5.8E-01
16	1.4E+03	2.4E+00	9.0E+02	1.6E+00	1.2E+03	2.1E+00
17	8.3E+02	8.4E+00	5.5E+02	5.6E+00	7.1E+02	7.2E+00
18	4.7E+02	2.7E+01	3.2E+02	1.8E+01	4.0E+02	2.3E+01
19	2.5E+02	7.9E+01	1.7E+02	5.6E+01	2.1E+02	6.8E+01
20	1.2E+02	2.2E+02	8.6E+01	1.6E+02	1.0E+02	1.9E+02
21	5.4E+01	5.6E+02	4.0E+01	4.1E+02	4.6E+01	4.8E+02
22	2.3E+01	1.4E+03	1.8E+01	1.1E+03	2.0E+01	1.2E+03
23	9.8E+00	3.2E+03	9.3E+00	3.1E+03	8.7E+00	2.9E+03
24	5.1E+00	9.5E+03	7.6E+00	1.4E+04	5.1E+00	9.6E+03
25	8.3E+00	8.8E+04	1.9E+01	2.0E+05	1.0E+01	1.1E+05

Table B.16 - DBN_{PDSC} constants of the normal complex interface stiffness for samples of slab SBS

	Sample SBS-1		**Sample SBS -2**		**Sample SBS-3**	
	φ_{NL} = 12 °		**φ_{NL} = 19 °**		**φ_{NL} = 16 °**	
Element number	**K_{zzi} (MPa/mm)**	**η_i (MPa.s/mm)**	**K_{zzi} (MPa/mm)**	**η_i (MPa.s/mm)**	**K_{zzi} (MPa/mm)**	**η_i (MPa.s/mm)**
0	5.5E+03	X	4.5E+03	X	5.0E+03	X
1	6.3E+05	5.7E-09	6.3E+05	5.7E-09	6.3E+05	5.7E-09
2	7.2E+05	3.7E-08	7.2E+05	3.7E-08	7.1E+05	3.6E-08
3	6.5E+05	1.9E-07	6.5E+05	1.9E-07	6.4E+05	1.9E-07
4	6.0E+05	9.8E-07	6.0E+05	9.8E-07	6.0E+05	9.8E-07
5	3.6E+05	3.3E-06	3.6E+05	3.3E-06	3.6E+05	3.3E-06
6	2.8E+05	1.5E-05	2.8E+05	1.5E-05	2.8E+05	1.5E-05
7	1.9E+05	5.5E-05	1.9E+05	5.5E-05	1.9E+05	5.5E-05
8	1.4E+05	2.3E-04	1.4E+05	2.3E-04	1.4E+05	2.3E-04
9	9.4E+04	8.9E-04	9.4E+04	9.0E-04	9.4E+04	8.9E-04
10	6.7E+04	3.6E-03	6.8E+04	3.6E-03	6.7E+04	3.6E-03
11	4.6E+04	1.4E-02	4.7E+04	1.4E-02	4.6E+04	1.4E-02
12	3.2E+04	5.5E-02	3.3E+04	5.6E-02	3.2E+04	5.6E-02
13	2.2E+04	2.1E-01	2.2E+04	2.2E-01	2.2E+04	2.1E-01
14	1.4E+04	7.9E-01	1.5E+04	8.3E-01	1.5E+04	8.1E-01
15	9.0E+03	2.8E+00	9.7E+03	3.0E+00	9.3E+03	2.9E+00
16	5.3E+03	9.4E+00	6.0E+03	1.1E+01	5.6E+03	9.9E+00
17	2.9E+03	2.9E+01	3.4E+03	3.4E+01	3.1E+03	3.2E+01
18	1.5E+03	8.4E+01	1.8E+03	1.0E+02	1.6E+03	9.3E+01
19	7.0E+02	2.2E+02	9.0E+02	2.9E+02	7.9E+02	2.5E+02
20	3.1E+02	5.7E+02	4.2E+02	7.7E+02	3.6E+02	6.6E+02
21	1.3E+02	1.4E+03	2.0E+02	2.0E+03	1.6E+02	1.7E+03
22	6.4E+01	3.7E+03	1.0E+02	6.1E+03	8.9E+01	5.2E+03
23	5.7E+01	1.9E+04	9.7E+01	3.2E+04	9.5E+01	3.1E+04
24	3.6E+02	6.8E+05	3.3E+02	6.1E+05	5.1E+02	9.6E+05
25	3.7E+03	3.9E+07	3.9E+03	4.1E+07	4.1E+03	4.4E+07

Table B.17 - DBN_{PDSC} constants of the shear complex interface stiffness for samples of slab SBS

	Sample SBS-1		**Sample SBS-2**		**Sample SBS-3**	
	φ_{NL} = 20 °		**φ_{NL} = 23 °**		**φ_{NL} = 20 °**	
Element number	**$K_{\theta zi}$ (MPa/mm)**	**η_i (MPa.s/mm)**	**$K_{\theta zi}$ (MPa/mm)**	**η_i (MPa.s/mm)**	**$K_{\theta zi}$ (MPa/mm)**	**η_i (MPa.s/mm)**
0	4.5E+02	X	3.0E+02	X	2.5E+02	X
1	6.1E+04	5.5E-10	6.2E+04	5.5E-10	5.1E+04	4.6E-10
2	6.9E+04	3.5E-09	7.0E+04	3.6E-09	5.8E+04	3.0E-09
3	6.2E+04	1.8E-08	6.3E+04	1.8E-08	5.3E+04	1.5E-08
4	5.8E+04	9.4E-08	5.9E+04	9.6E-08	4.9E+04	8.0E-08
5	3.5E+04	3.2E-07	3.5E+04	3.3E-07	2.9E+04	2.7E-07
6	2.7E+04	1.4E-06	2.8E+04	1.4E-06	2.3E+04	1.2E-06
7	1.8E+04	5.3E-06	1.8E+04	5.4E-06	1.5E+04	4.5E-06
8	1.3E+04	2.2E-05	1.3E+04	2.3E-05	1.1E+04	1.9E-05
9	9.1E+03	8.6E-05	9.2E+03	8.8E-05	7.7E+03	7.3E-05
10	6.5E+03	3.5E-04	6.6E+03	3.6E-04	5.5E+03	3.0E-04
11	4.5E+03	1.4E-03	4.6E+03	1.4E-03	3.8E+03	1.2E-03
12	3.1E+03	5.4E-03	3.3E+03	5.6E-03	2.7E+03	4.7E-03
13	2.1E+03	2.1E-02	2.2E+03	2.2E-02	1.9E+03	1.8E-02
14	1.4E+03	7.9E-02	1.6E+03	8.6E-02	1.3E+03	7.1E-02
15	9.2E+02	2.9E-01	1.0E+03	3.3E-01	8.7E+02	2.7E-01
16	5.6E+02	1.0E+00	6.8E+02	1.2E+00	5.6E+02	1.0E+00
17	3.2E+02	3.2E+00	4.2E+02	4.2E+00	3.5E+02	3.5E+00
18	1.7E+02	9.7E+00	2.4E+02	1.4E+01	2.0E+02	1.2E+01
19	8.3E+01	2.7E+01	1.3E+02	4.2E+01	1.1E+02	3.5E+01
20	3.9E+01	7.0E+01	6.6E+01	1.2E+02	5.4E+01	9.9E+01
21	1.8E+01	1.8E+02	3.1E+01	3.2E+02	2.6E+01	2.7E+02
22	9.4E+00	5.5E+02	1.5E+01	8.8E+02	1.2E+01	7.1E+02
23	9.1E+00	3.0E+03	8.8E+00	2.9E+03	6.9E+00	2.3E+03
24	3.5E+01	6.5E+04	9.7E+00	1.8E+04	7.0E+00	1.3E+04
25	4.1E+02	4.4E+06	3.1E+01	3.3E+05	2.2E+01	2.3E+05

Table B.18 - DBN_{PDSC} constants of the complex interface stiffnesses for sample LAT-1

	Sample LAT-1 (K^*_{zz})		**Sample LAT-1 ($K^*_{\theta z}$)**	
	φ_{NL} = 12 °		**φ_{NL} = 23 °**	
Element number	**K_{zzi} (MPa/mm)**	**η_i (MPa.s/mm)**	**$K_{\theta zi}$ (MPa/mm)**	**η_i (MPa.s/mm)**
0	9.0E+03	X	3.0E+02	X
1	1.9E+06	1.7E-08	7.7E+04	7.0E-10
2	2.2E+06	1.1E-07	8.8E+04	4.5E-09
3	2.0E+06	5.7E-07	7.9E+04	2.3E-08
4	1.8E+06	3.0E-06	7.4E+04	1.2E-07
5	1.1E+06	1.0E-05	4.4E+04	4.1E-07
6	8.6E+05	4.5E-05	3.5E+04	1.8E-06
7	5.7E+05	1.7E-04	2.3E+04	6.8E-06
8	4.2E+05	7.1E-04	1.7E+04	2.8E-05
9	2.9E+05	2.7E-03	1.2E+04	1.1E-04
10	2.1E+05	1.1E-02	8.4E+03	4.5E-04
11	1.4E+05	4.4E-02	5.8E+03	1.8E-03
12	1.0E+05	1.8E-01	4.1E+03	7.1E-03
13	7.0E+04	6.9E-01	2.9E+03	2.8E-02
14	4.9E+04	2.7E+00	2.0E+03	1.1E-01
15	3.3E+04	1.0E+01	1.4E+03	4.2E-01
16	2.1E+04	3.8E+01	9.0E+02	1.6E+00
17	1.3E+04	1.3E+02	5.8E+02	5.8E+00
18	7.8E+03	4.4E+02	3.5E+02	2.0E+01
19	4.2E+03	1.4E+03	2.0E+02	6.4E+01
20	2.1E+03	3.8E+03	1.0E+02	1.9E+02
21	9.9E+02	1.0E+04	5.2E+01	5.3E+02
22	4.5E+02	2.6E+04	2.4E+01	1.4E+03
23	2.1E+02	7.0E+04	1.2E+01	4.1E+03
24	1.4E+02	2.7E+05	9.0E+00	1.7E+04
25	2.6E+02	2.7E+06	1.3E+01	1.3E+05

APPENDIX C

Monotonic shear failure tests results

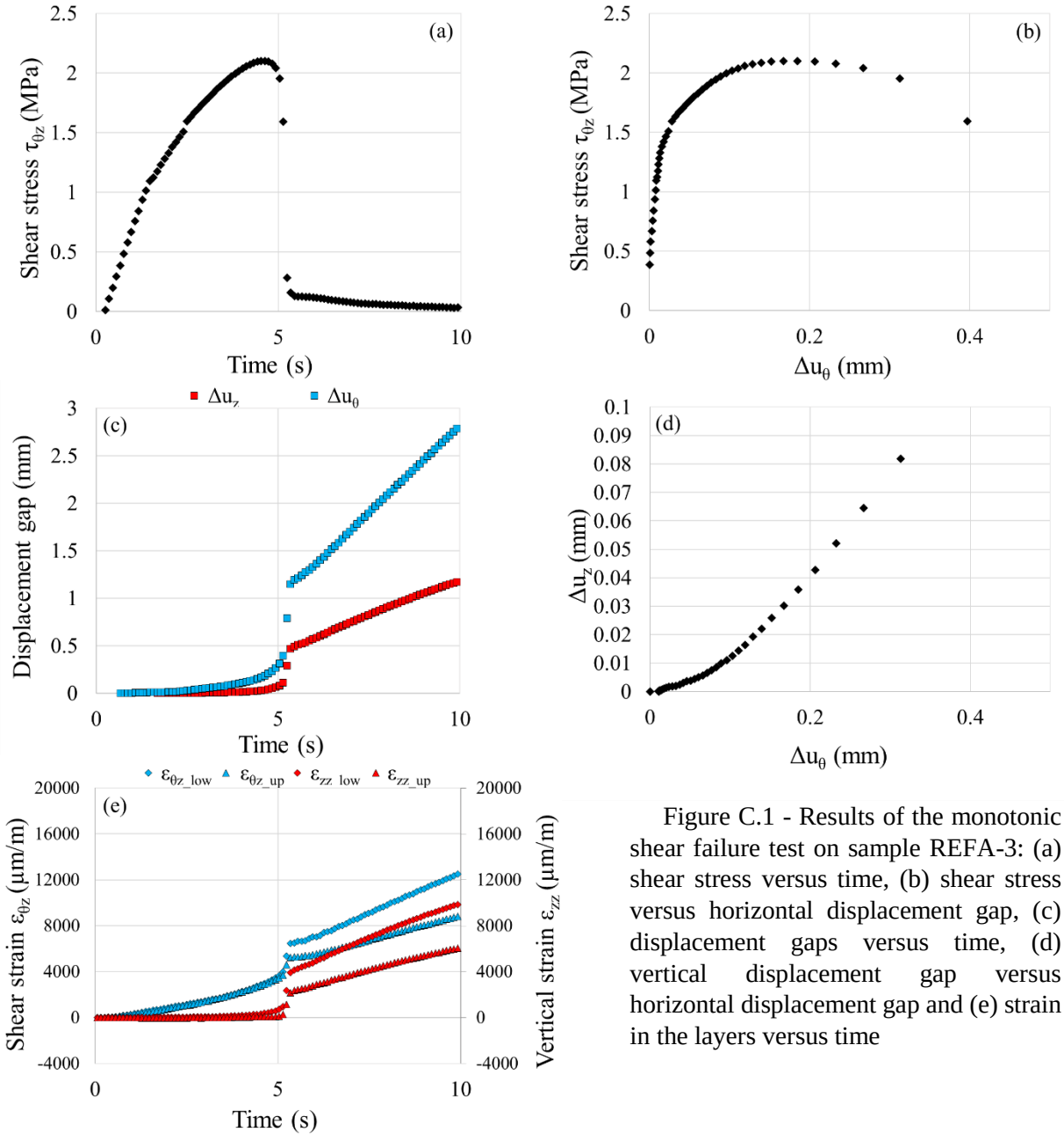

Figure C.1 - Results of the monotonic shear failure test on sample REFA-3: (a) shear stress versus time, (b) shear stress versus horizontal displacement gap, (c) displacement gaps versus time, (d) vertical displacement gap versus horizontal displacement gap and (e) strain in the layers versus time

Table C.1 - Results of the monotonic shear failure test on sample REFA-3

Sample	**Upper layer**	**Lower layer**	**Tack coat type**	**Tack coat dosage (g/m^2)**	**Global shear strain rate $\dot{\varepsilon}_{\theta z\_g}$ (%/s)**	**T (°C)**	**σ_{zz} (MPa)**	**τ_{max} (MPa)**	**Δu_{θ_max} (mm)**	**Δu_{z_max} (µm)**
REFA-3	BBSG3	EME2	Pure Bitumen	350	0.2	18.5	0	2.08	0.19	36

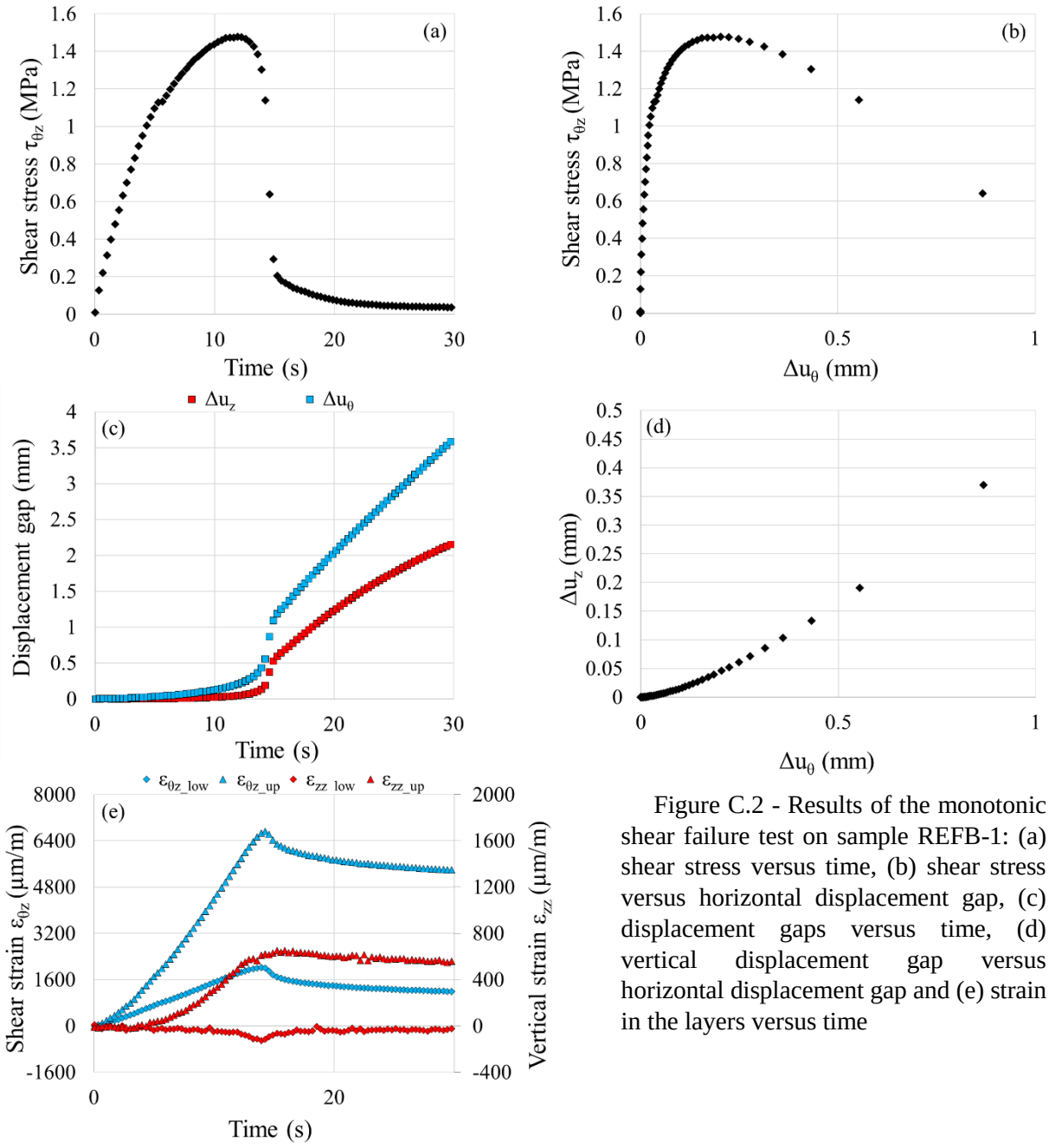

Figure C.2 - Results of the monotonic shear failure test on sample REFB-1: (a) shear stress versus time, (b) shear stress versus horizontal displacement gap, (c) displacement gaps versus time, (d) vertical displacement gap versus horizontal displacement gap and (e) strain in the layers versus time

Table C.2 - Results of the monotonic shear failure test on sample REFB-1

Sample	**Upper layer**	**Lower layer**	**Tack coat type**	**Tack coat dosage (g/m^2)**	**Global shear strain rate $\dot{\varepsilon}_{\theta z\_g}$ (%/s)**	**T (°C)**	**σ_{zz} (MPa)**	**τ_{max} (MPa)**	**Δu_{θ_max} (mm)**	**Δu_{z_max} (µm)**
REFB-1	BBSG3	EME2	Pure Bitumen	350	0.067	18.5	0	1.47	0.20	46

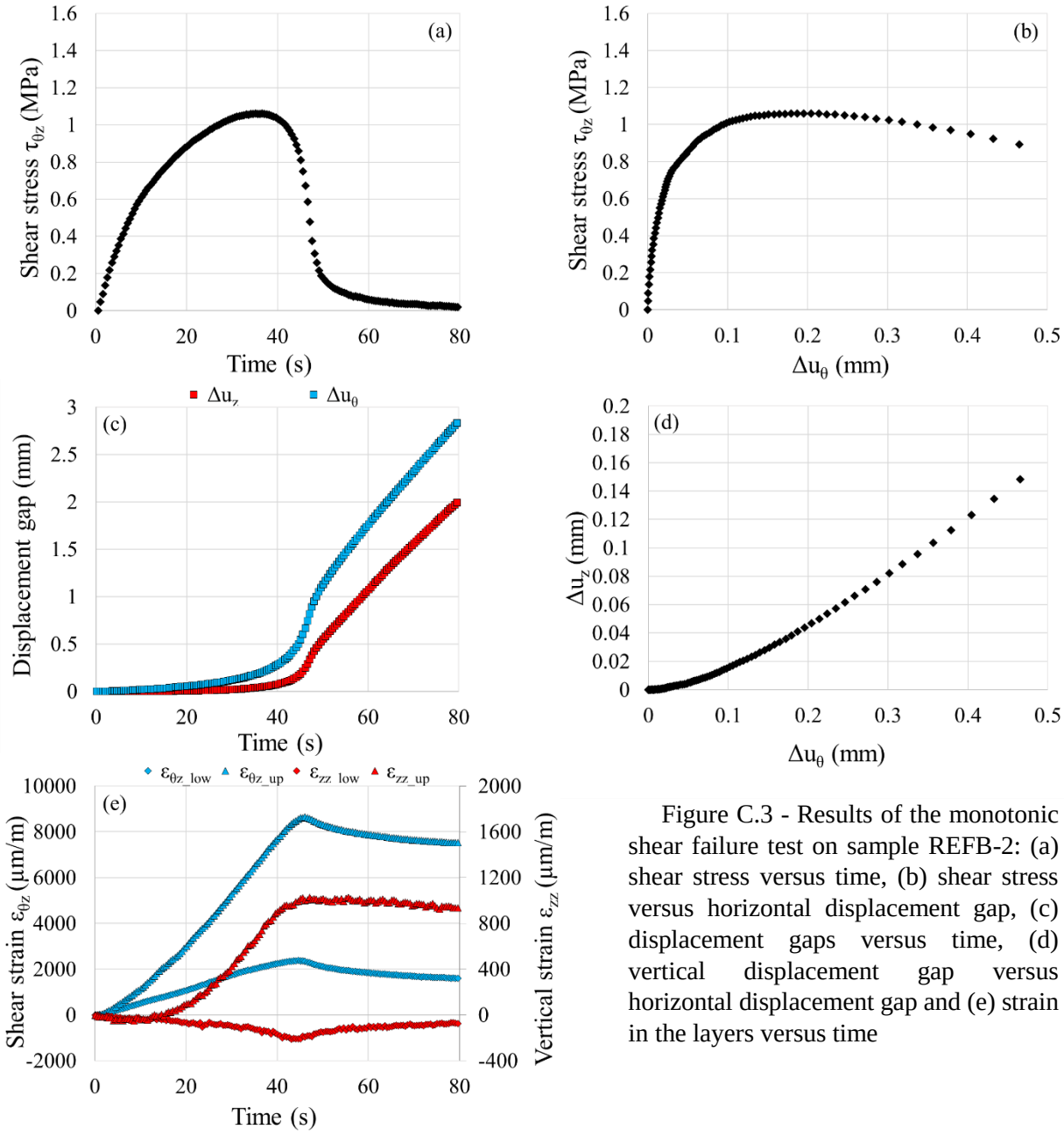

Figure C.3 - Results of the monotonic shear failure test on sample REFB-2: (a) shear stress versus time, (b) shear stress versus horizontal displacement gap, (c) displacement gaps versus time, (d) vertical displacement gap versus horizontal displacement gap and (e) strain in the layers versus time

Table C.3 - Results of the monotonic shear failure test on sample REFB-2

Sample	**Upper layer**	**Lower layer**	**Tack coat type**	**Tack coat dosage (g/m^2)**	**Global shear strain rate $\dot{\varepsilon}_{\theta z\_g}$ (%/s)**	**T (°C)**	**σ_{zz} (MPa)**	**τ_{max} (MPa)**	**Δu_{θ_max} (mm)**	**Δu_{z_max} (µm)**
REFB-2	BBSG3	EME2	Pure Bitumen	350	0.02	18.5	0	1.06	0.20	47

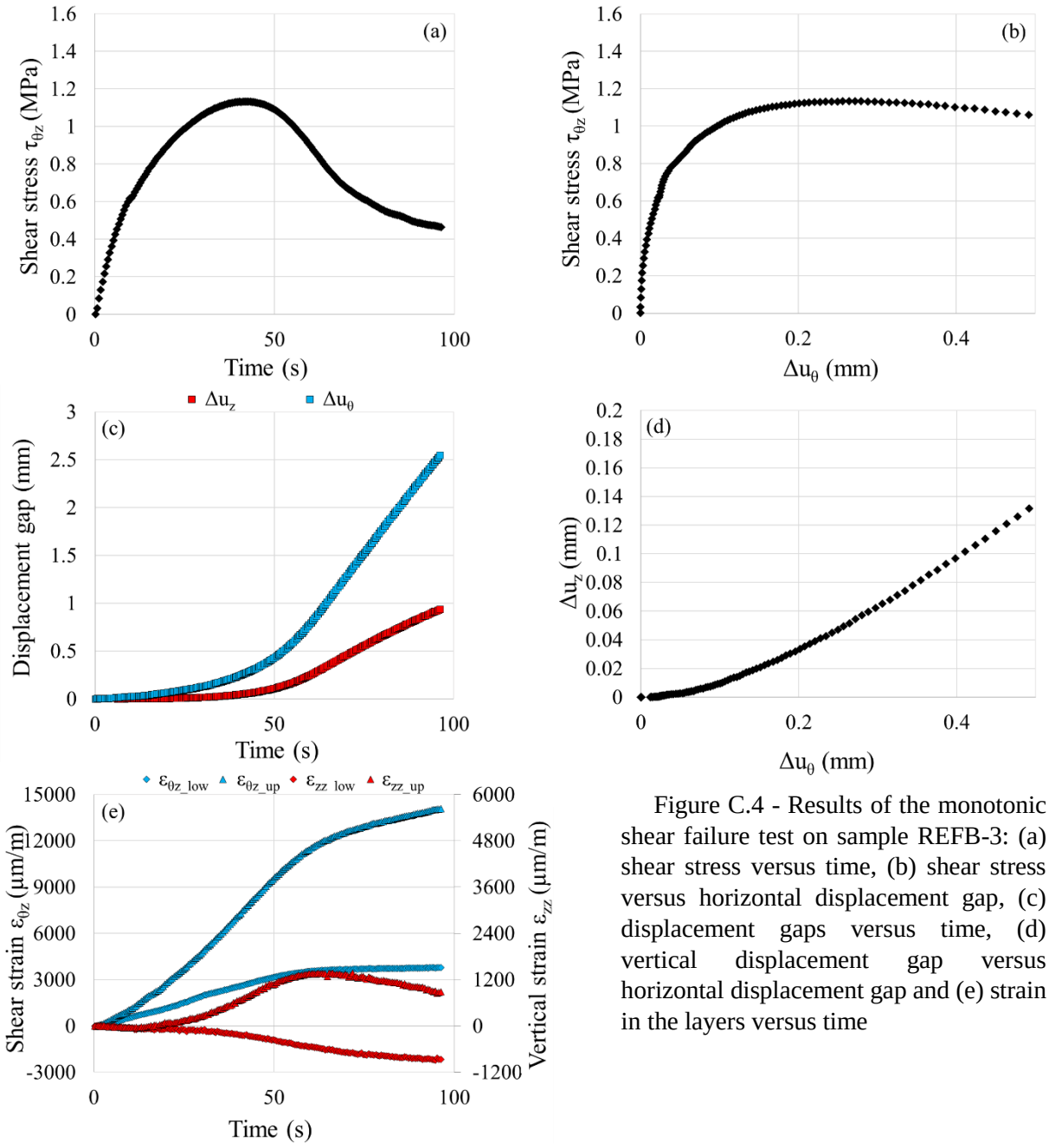

Figure C.4 - Results of the monotonic shear failure test on sample REFB-3: (a) shear stress versus time, (b) shear stress versus horizontal displacement gap, (c) displacement gaps versus time, (d) vertical displacement gap versus horizontal displacement gap and (e) strain in the layers versus time

Table C.4 - Results of the monotonic shear failure test on sample REFB-3

Sample	**Upper layer**	**Lower layer**	**Tack coat type**	**Tack coat dosage (g/m^2)**	**Global shear strain rate $\dot{\varepsilon}_{\theta z\_g}$ (%/s)**	**T (°C)**	**σ_{zz} (MPa)**	**τ_{max} (MPa)**	**Δu_{θ_max} (mm)**	**Δu_{z_max} (µm)**
REFB-3	BBSG3	EME2	Pure Bitumen	350	0.02	18.5	0.25	1.13	0.27	54

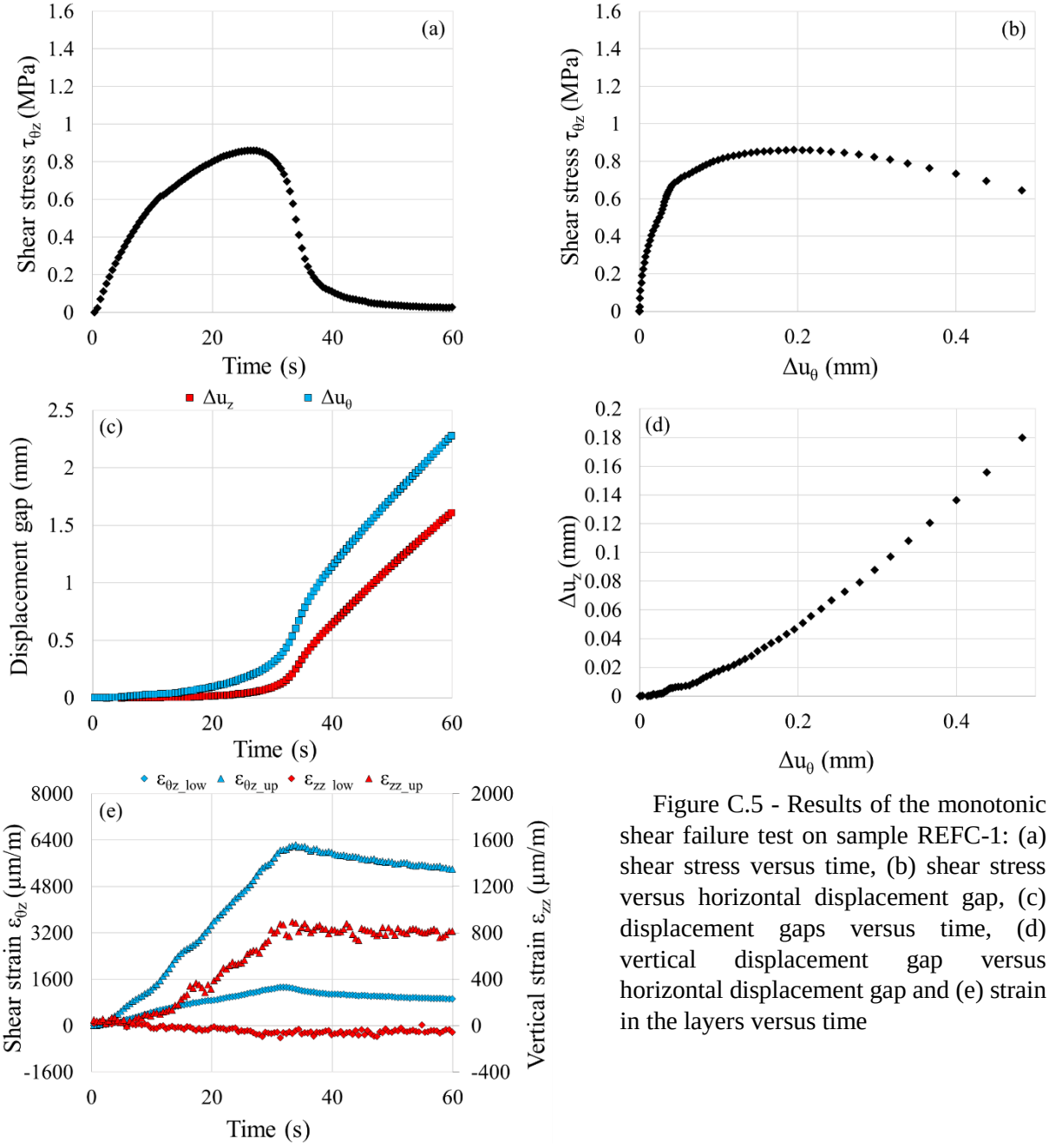

Figure C.5 - Results of the monotonic shear failure test on sample REFC-1: (a) shear stress versus time, (b) shear stress versus horizontal displacement gap, (c) displacement gaps versus time, (d) vertical displacement gap versus horizontal displacement gap and (e) strain in the layers versus time

Table C.5 - Results of the monotonic shear failure test on sample REFC-1

Sample	**Upper layer**	**Lower layer**	**Tack coat type**	**Tack coat dosage (g/m^2)**	**Global shear strain rate $\dot{\varepsilon}_{\theta z\_g}$ (%/s)**	**T (°C)**	**σ_{zz} (MPa)**	**τ_{max} (MPa)**	**Δu_{θ_max} (mm)**	**Δu_{z_max} (µm)**
REFC-1	BBSG3	EME2	Pure Bitumen	350	0.02	24.0	0	0.86	0.20	46

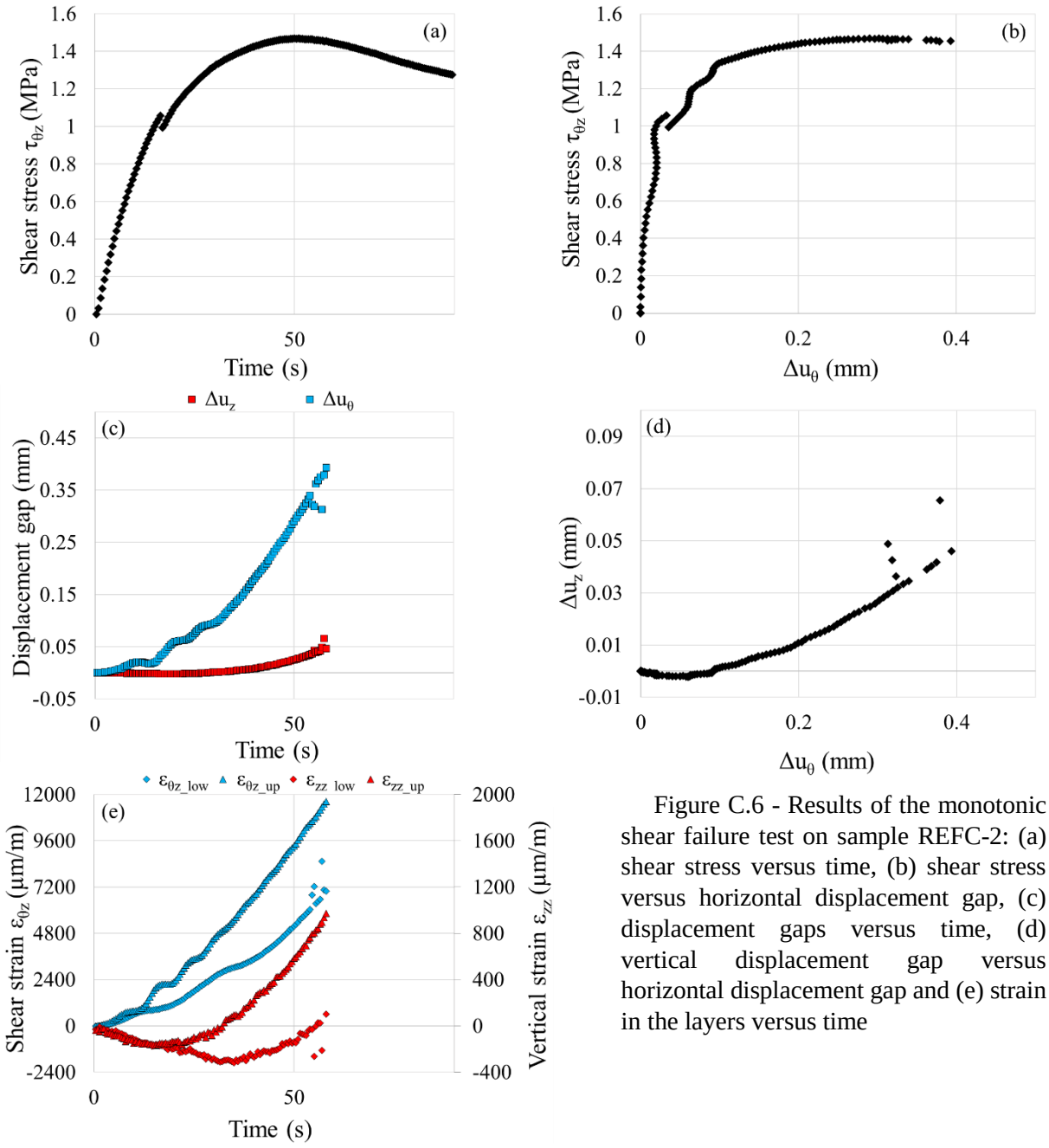

Figure C.6 - Results of the monotonic shear failure test on sample REFC-2: (a) shear stress versus time, (b) shear stress versus horizontal displacement gap, (c) displacement gaps versus time, (d) vertical displacement gap versus horizontal displacement gap and (e) strain in the layers versus time

Table C.6 - Results of the monotonic shear failure test on sample REFC-2

Sample	**Upper layer**	**Lower layer**	**Tack coat type**	**Tack coat dosage (g/m^2)**	**Global shear strain rate $\dot{\varepsilon}_{\theta z\_g}$ (%/s)**	**T (°C)**	**σ_{zz} (MPa)**	**τ_{max} (MPa)**	**Δu_{θ_max} (mm)**	**Δu_{z_max} (µm)**
REFC-2	BBSG3	EME2	Pure Bitumen	350	0.02	18.7	1	1.47	0.30	27

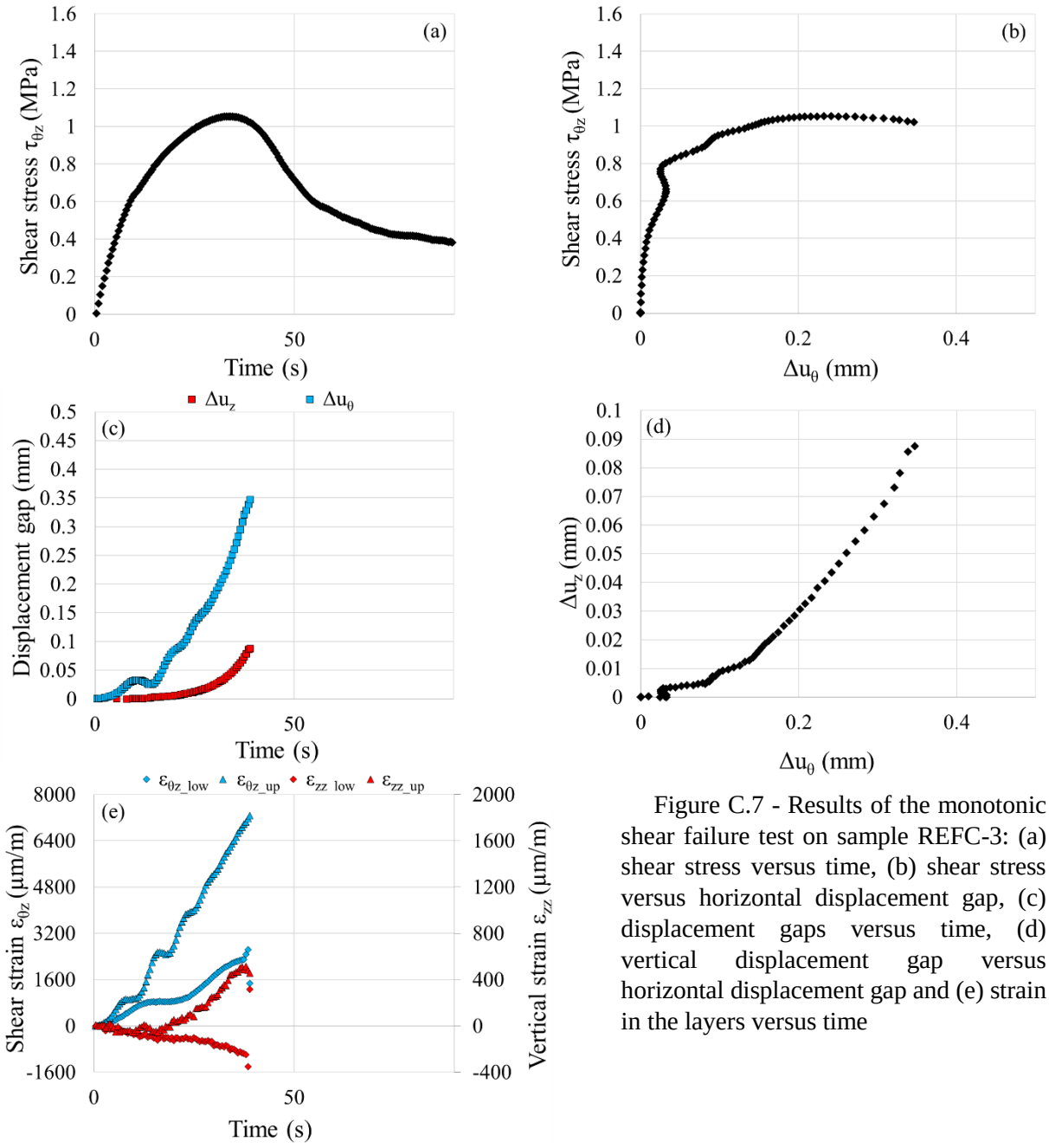

Figure C.7 - Results of the monotonic shear failure test on sample REFC-3: (a) shear stress versus time, (b) shear stress versus horizontal displacement gap, (c) displacement gaps versus time, (d) vertical displacement gap versus horizontal displacement gap and (e) strain in the layers versus time

Table C.7 - Results of the monotonic shear failure test on sample REFC-3

Sample	**Upper layer**	**Lower layer**	**Tack coat type**	**Tack coat dosage (g/m^2)**	**Global shear strain rate $\dot{\varepsilon}_{\theta z\_g}$ (%/s)**	**T (°C)**	**σ_{zz} (MPa)**	**τ_{max} (MPa)**	**Δu_{θ_max} (mm)**	**Δu_{z_max} (µm)**
REFC-3	BBSG3	EME2	Pure Bitumen	350	0.02	18.5	0.25	1.05	0.23	41

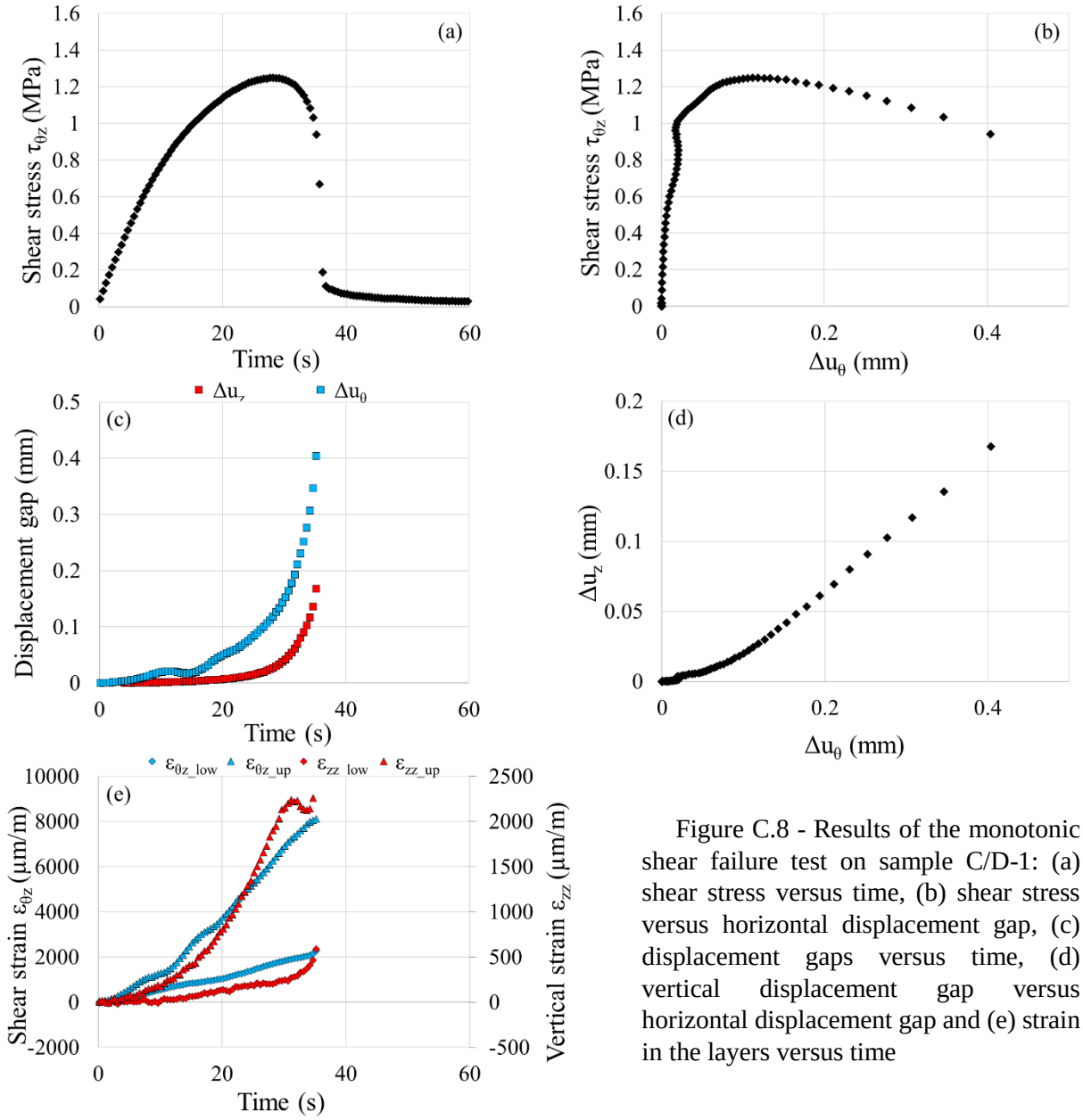

Figure C.8 - Results of the monotonic shear failure test on sample C/D-1: (a) shear stress versus time, (b) shear stress versus horizontal displacement gap, (c) displacement gaps versus time, (d) vertical displacement gap versus horizontal displacement gap and (e) strain in the layers versus time

Table C.8 - Results of the monotonic shear failure test on sample C/D-1

Sample	**Upper layer**	**Lower layer**	**Tack coat type**	**Tack coat dosage (g/m^2)**	**Global shear strain rate $\dot{\varepsilon}_{\theta z\_g}$ (%/s)**	**T (°C)**	**σ_{zz} (MPa)**	**τ_{max} (MPa)**	**Δu_{θ_max} (mm)**	**Δu_{z_max} (µm)**
C/D-1	BBSG3	GB5	Pure Bitumen	350	0.02	18.6	0	1.25	0.11	24

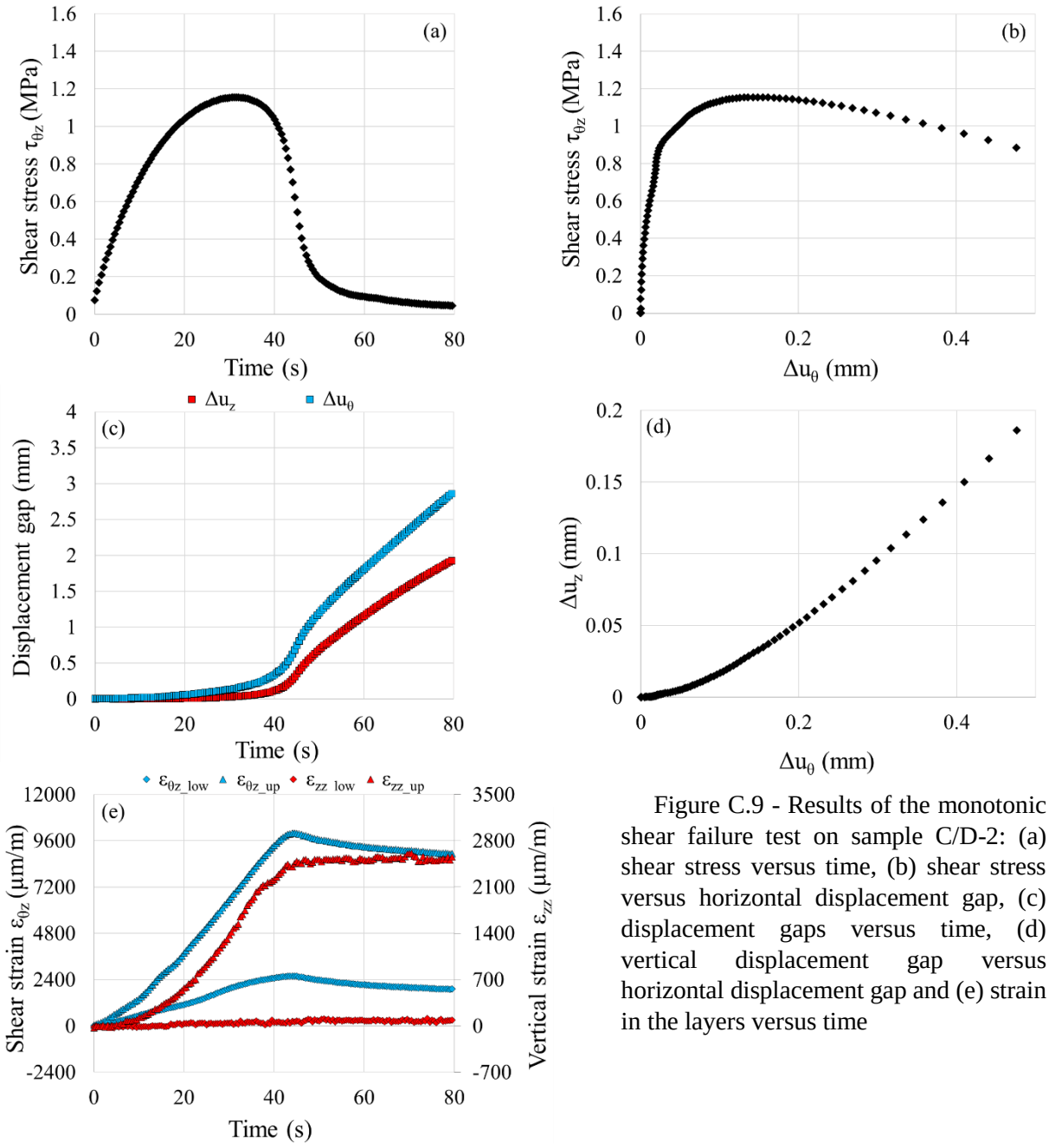

Figure C.9 - Results of the monotonic shear failure test on sample C/D-2: (a) shear stress versus time, (b) shear stress versus horizontal displacement gap, (c) displacement gaps versus time, (d) vertical displacement gap versus horizontal displacement gap and (e) strain in the layers versus time

Table C.9 - Results of the monotonic shear failure test on sample C/D-2

Sample	**Upper layer**	**Lower layer**	**Tack coat type**	**Tack coat dosage (g/m^2)**	**Global shear strain rate $\dot{\varepsilon}_{\theta z\_g}$ (%/s)**	**T (°C)**	**σ_{zz} (MPa)**	**τ_{max} (MPa)**	**Δu_{θ_max} (mm)**	**Δu_{z_max} (µm)**
C/D-2	BBSG3	GB5	Pure Bitumen	350	0.02	18.8	0	1.15	0.15	33

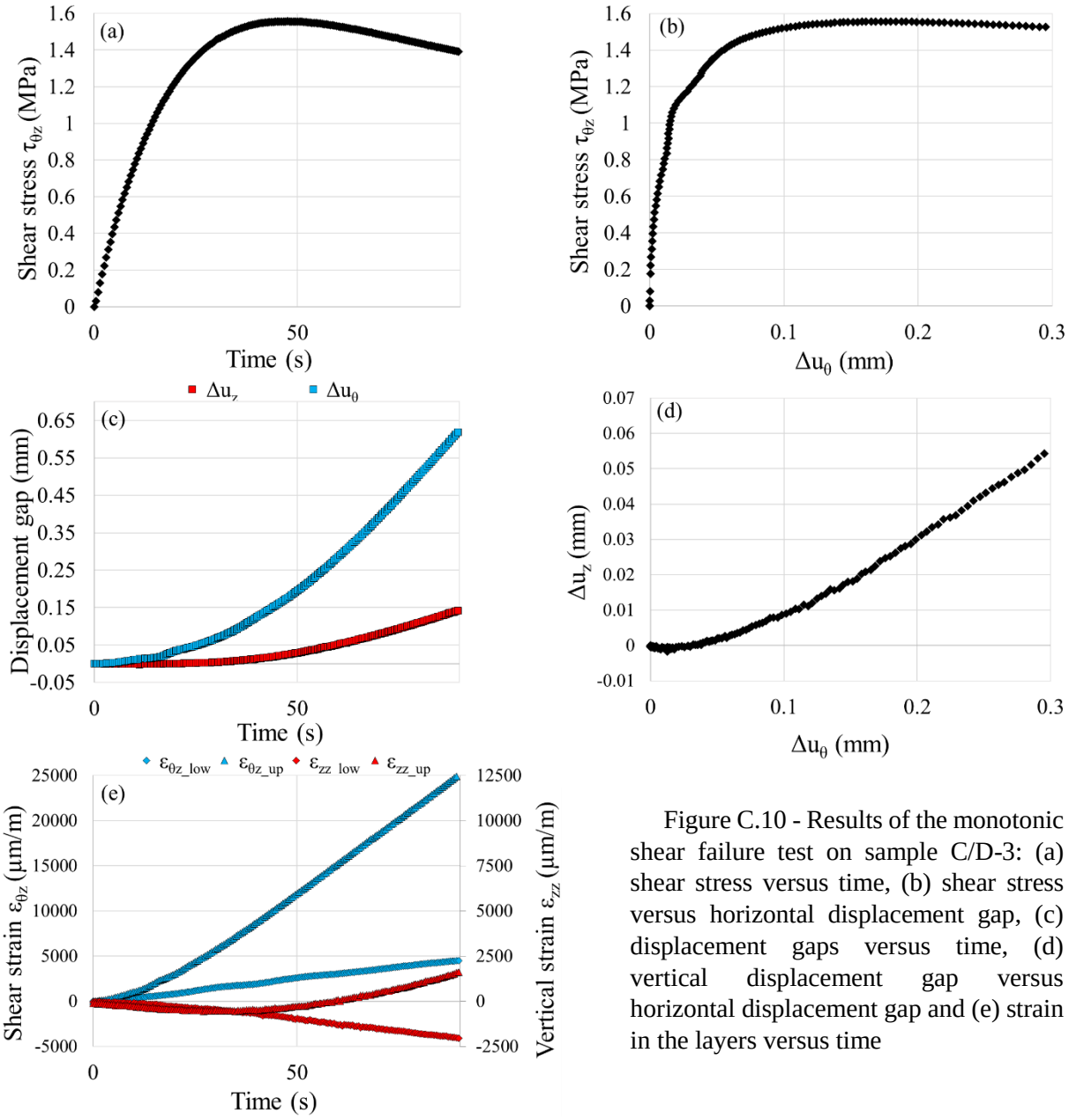

Figure C.10 - Results of the monotonic shear failure test on sample C/D-3: (a) shear stress versus time, (b) shear stress versus horizontal displacement gap, (c) displacement gaps versus time, (d) vertical displacement gap versus horizontal displacement gap and (e) strain in the layers versus time

Table C.10 - Results of the monotonic shear failure test on sample C/D-3

Sample	**Upper layer**	**Lower layer**	**Tack coat type**	**Tack coat dosage (g/m^2)**	**Global shear strain rate $\dot{\varepsilon}_{\theta z\_g}$ (%/s)**	**T (°C)**	**σ_{zz} (MPa)**	**τ_{max} (MPa)**	**Δu_{θ_max} (mm)**	**Δu_{z_max} (µm)**
C/D-3	BBSG3	GB5	Pure Bitumen	350	0.02	18.8	1	1.56	0.18	25

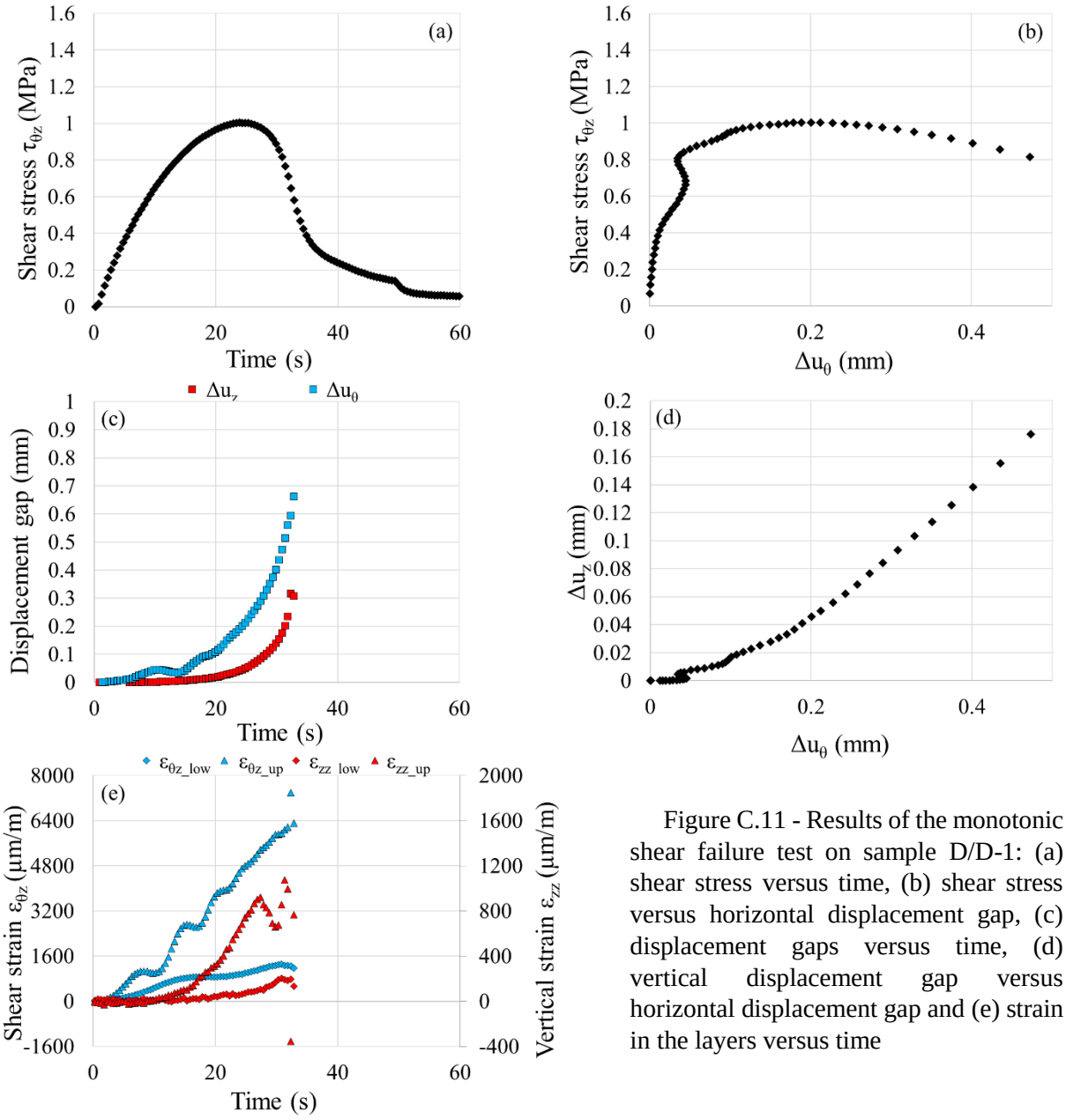

Figure C.11 - Results of the monotonic shear failure test on sample D/D-1: (a) shear stress versus time, (b) shear stress versus horizontal displacement gap, (c) displacement gaps versus time, (d) vertical displacement gap versus horizontal displacement gap and (e) strain in the layers versus time

Table C.11 - Results of the monotonic shear failure test on sample D/D-1

Sample	**Upper layer**	**Lower layer**	**Tack coat type**	**Tack coat dosage (g/m^2)**	**Global shear strain rate $\dot{\varepsilon}_{\theta z\_g}$ (%/s)**	**T (°C)**	**σ_{zz} (MPa)**	**τ_{max} (MPa)**	**Δu_{θ_max} (mm)**	**Δu_{z_max} (µm)**
D/D-1	BB5	GB5	Pure Bitumen	350	0.02	18.4	0	1.00	0.19	41

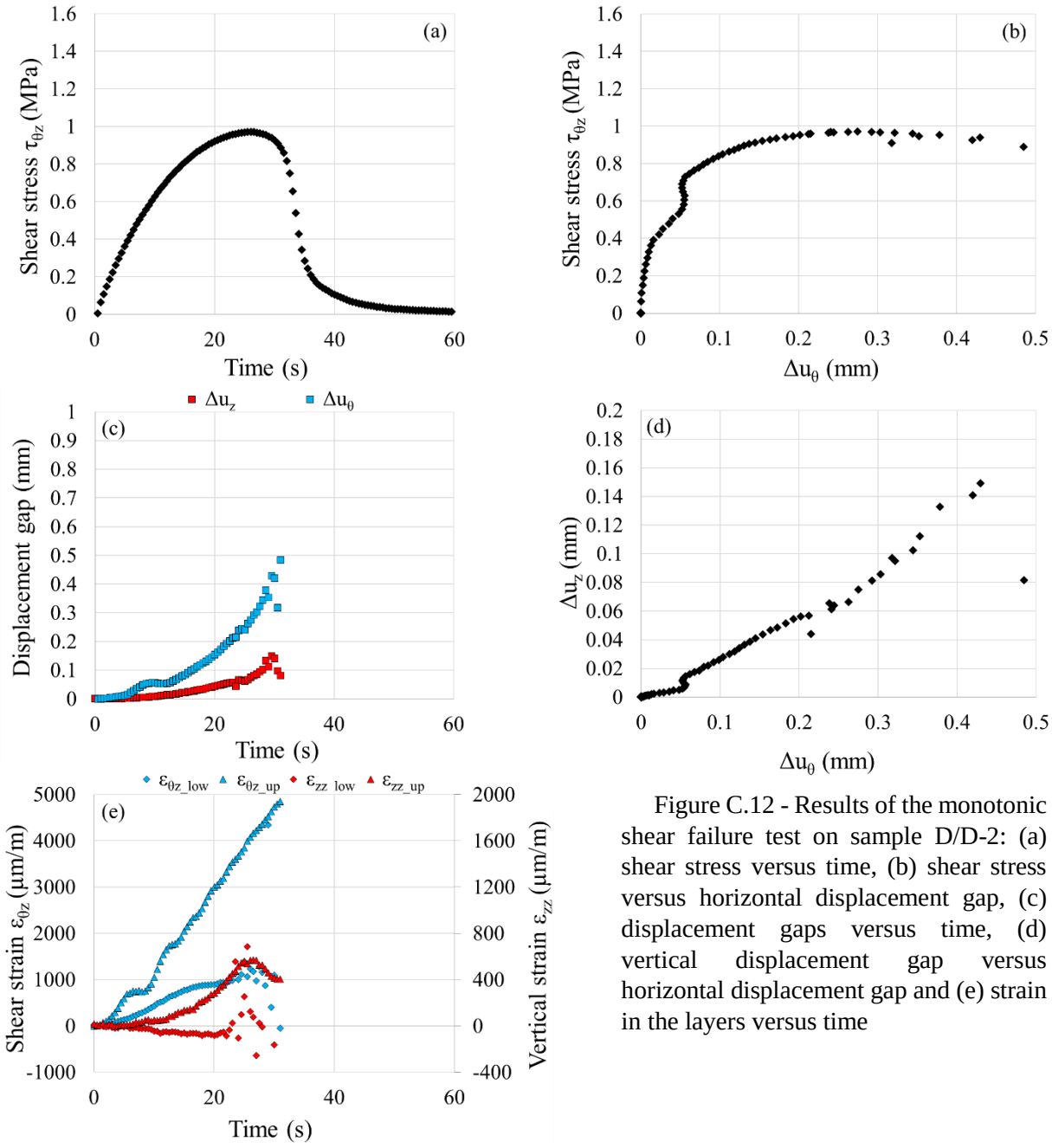

Figure C.12 - Results of the monotonic shear failure test on sample D/D-2: (a) shear stress versus time, (b) shear stress versus horizontal displacement gap, (c) displacement gaps versus time, (d) vertical displacement gap versus horizontal displacement gap and (e) strain in the layers versus time

Table C.12 - Results of the monotonic shear failure test on sample D/D-2

Sample	**Upper layer**	**Lower layer**	**Tack coat type**	**Tack coat dosage (g/m^2)**	**Global shear strain rate $\dot{\varepsilon}_{\theta z\_g}$ (%/s)**	**T (°C)**	**σ_{zz} (MPa)**	**τ_{max} (MPa)**	**Δu_{θ_max} (mm)**	**Δu_{z_max} (µm)**
D/D-2	BB5	GB5	Pure Bitumen	350	0.02	18.5	0	0.97	0.27	75

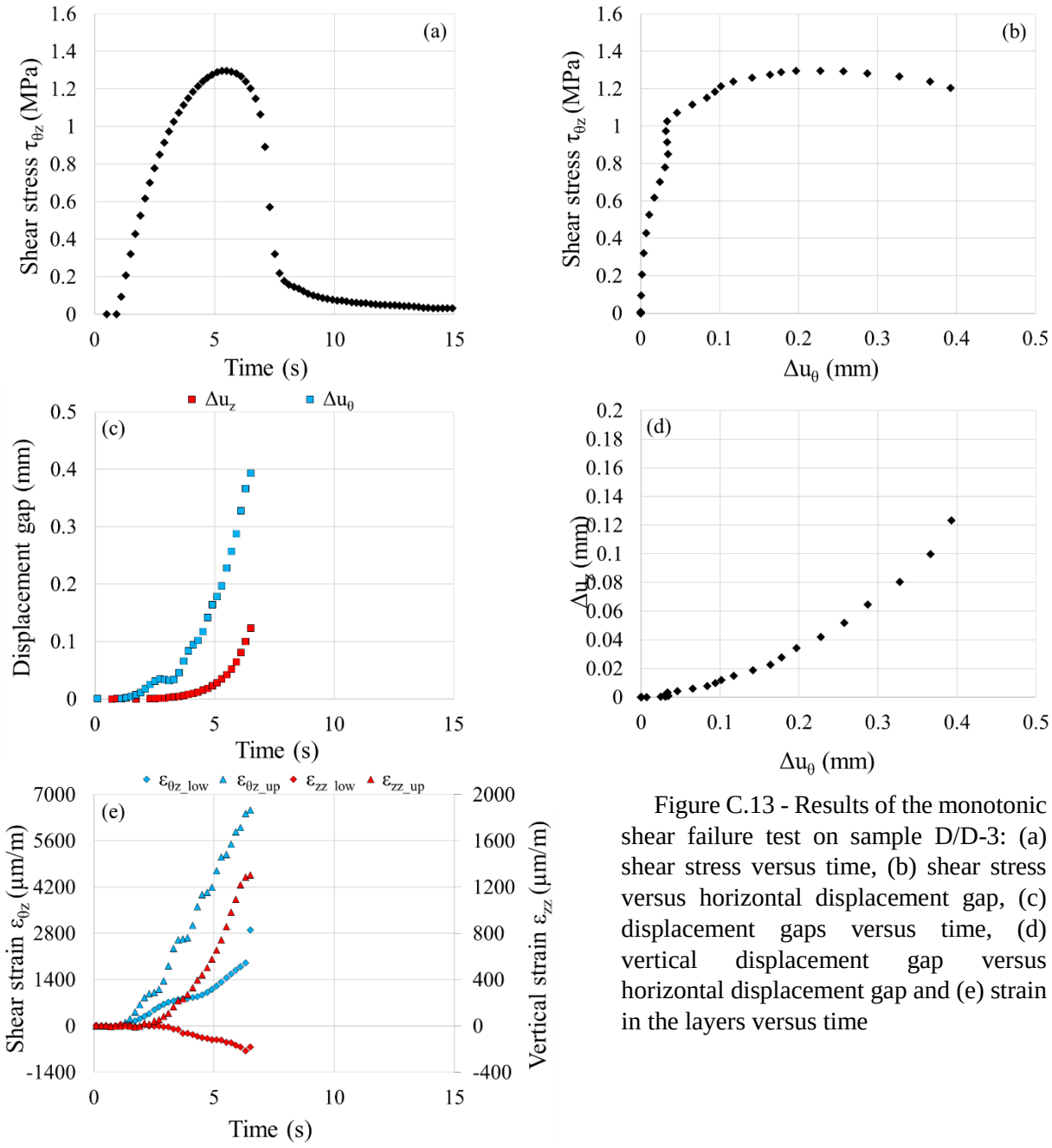

Figure C.13 - Results of the monotonic shear failure test on sample D/D-3: (a) shear stress versus time, (b) shear stress versus horizontal displacement gap, (c) displacement gaps versus time, (d) vertical displacement gap versus horizontal displacement gap and (e) strain in the layers versus time

Table C.13 - Results of the monotonic shear failure test on sample D/D-3

Sample	**Upper layer**	**Lower layer**	**Tack coat type**	**Tack coat dosage (g/m^2)**	**Global shear strain rate $\dot{\varepsilon}_{\theta z\_g}$ (%/s)**	**T (°C)**	**σ_{zz} (MPa)**	**τ_{max} (MPa)**	**Δu_{θ_max} (mm)**	**Δu_{z_max} (µm)**
D/D-3	BB5	GB5	Pure Bitumen	350	0.02	23.9	0	1.28	0.23	42

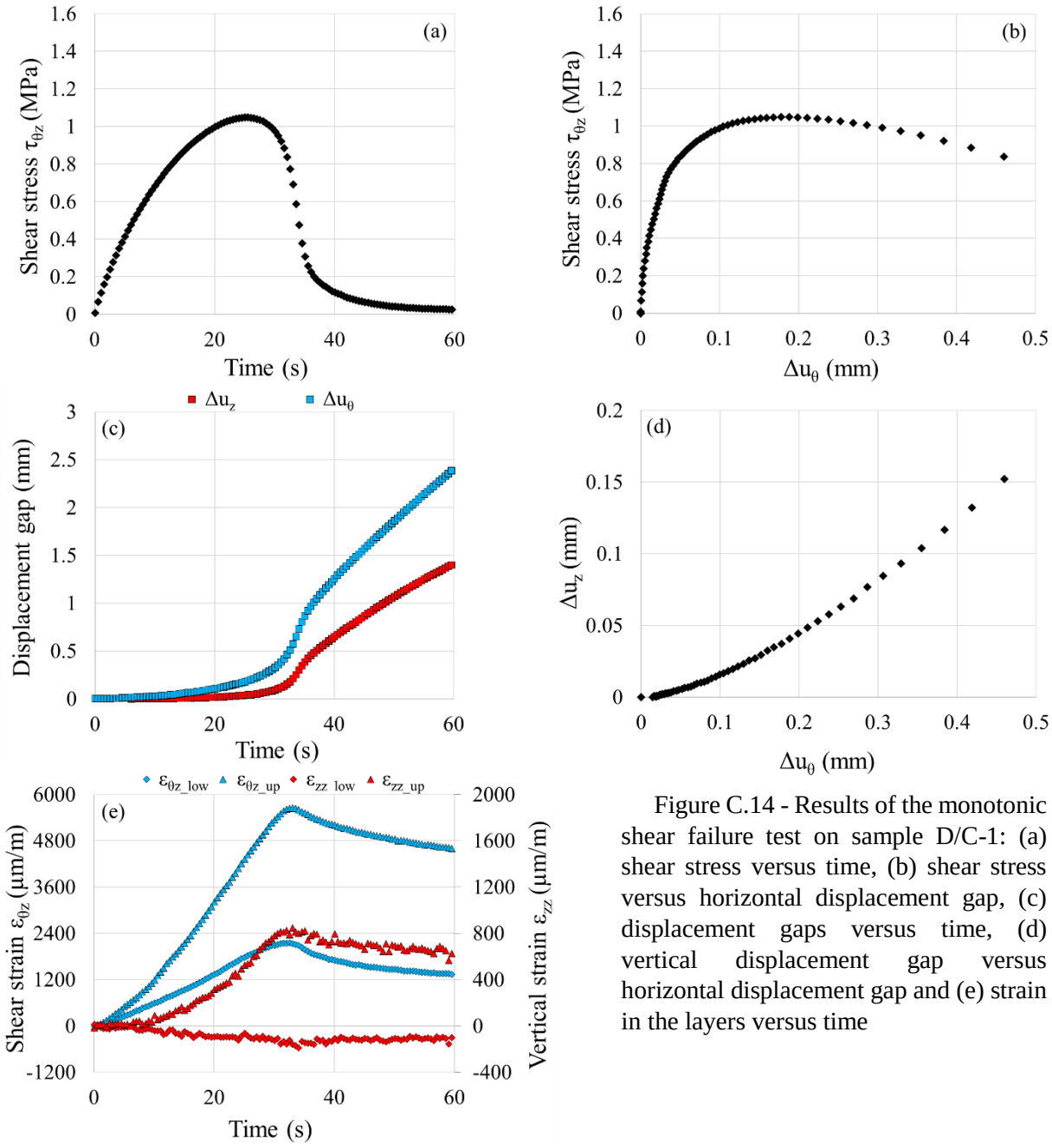

Figure C.14 - Results of the monotonic shear failure test on sample D/C-1: (a) shear stress versus time, (b) shear stress versus horizontal displacement gap, (c) displacement gaps versus time, (d) vertical displacement gap versus horizontal displacement gap and (e) strain in the layers versus time

Table C.14 - Results of the monotonic shear failure test on sample D/C-1

Sample	**Upper layer**	**Lower layer**	**Tack coat type**	**Tack coat dosage (g/m^2)**	**Global shear strain rate $\dot{\varepsilon}_{\theta z\_g}$ (%/s)**	**T (°C)**	**σ_{zz} (MPa)**	**τ_{max} (MPa)**	**Δu_{θ_max} (mm)**	**Δu_{z_max} (µm)**
D/C-1	BB5	EME2	Pure Bitumen	350	0.02	18.9	0	1.05	0.18	37

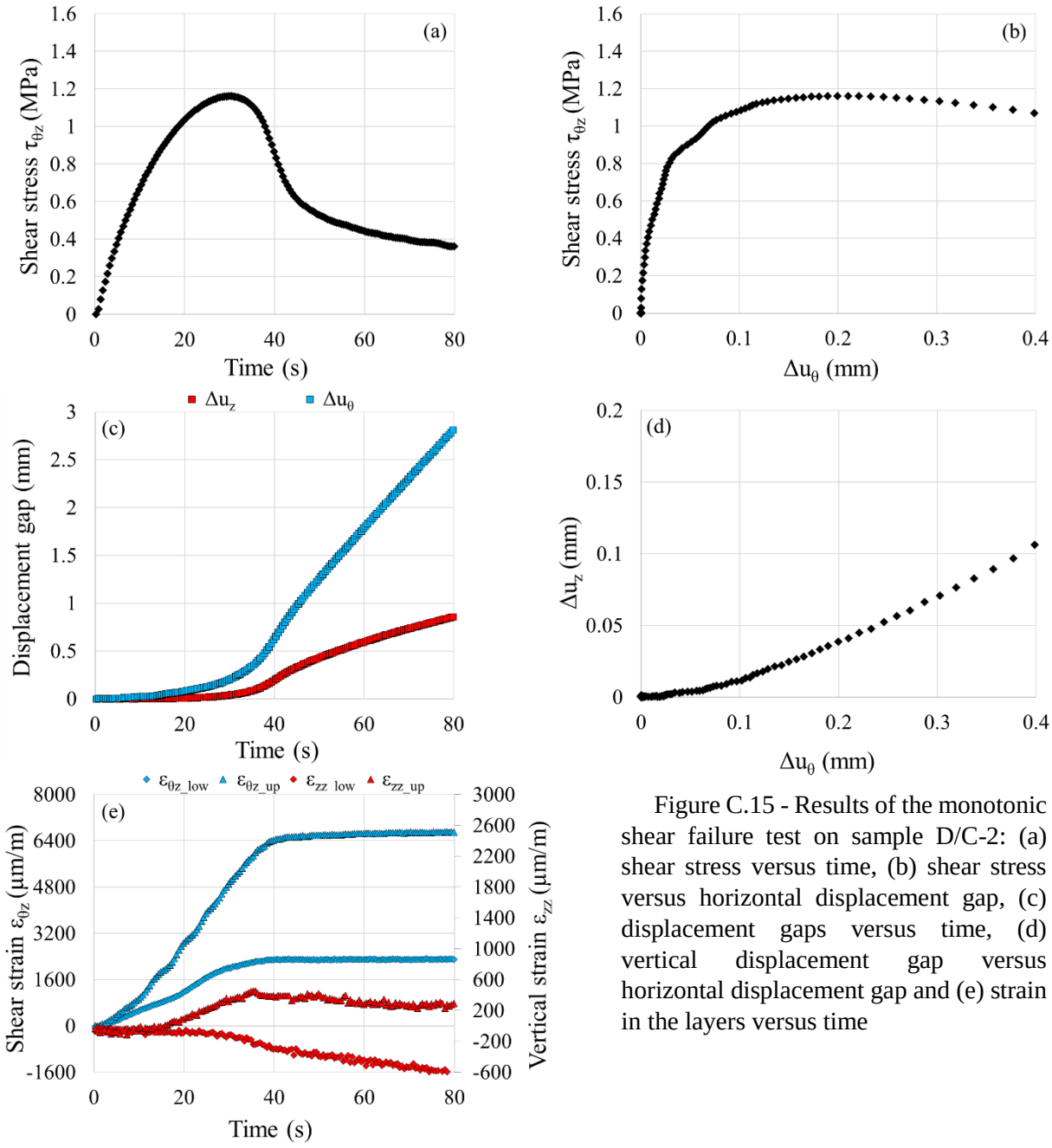

Figure C.15 - Results of the monotonic shear failure test on sample D/C-2: (a) shear stress versus time, (b) shear stress versus horizontal displacement gap, (c) displacement gaps versus time, (d) vertical displacement gap versus horizontal displacement gap and (e) strain in the layers versus time

Table C.15 - Results of the monotonic shear failure test on sample D/C-2

Sample	**Upper layer**	**Lower layer**	**Tack coat type**	**Tack coat dosage (g/m^2)**	**Global shear strain rate $\dot{\varepsilon}_{\theta z\_g}$ (%/s)**	**T (°C)**	**σ_{zz} (MPa)**	**τ_{max} (MPa)**	**Δu_{θ_max} (mm)**	**Δu_{z_max} (µm)**
D/C-2	BB5	EME2	Pure Bitumen	350	0.02	19	0.25	1.16	0.35	35

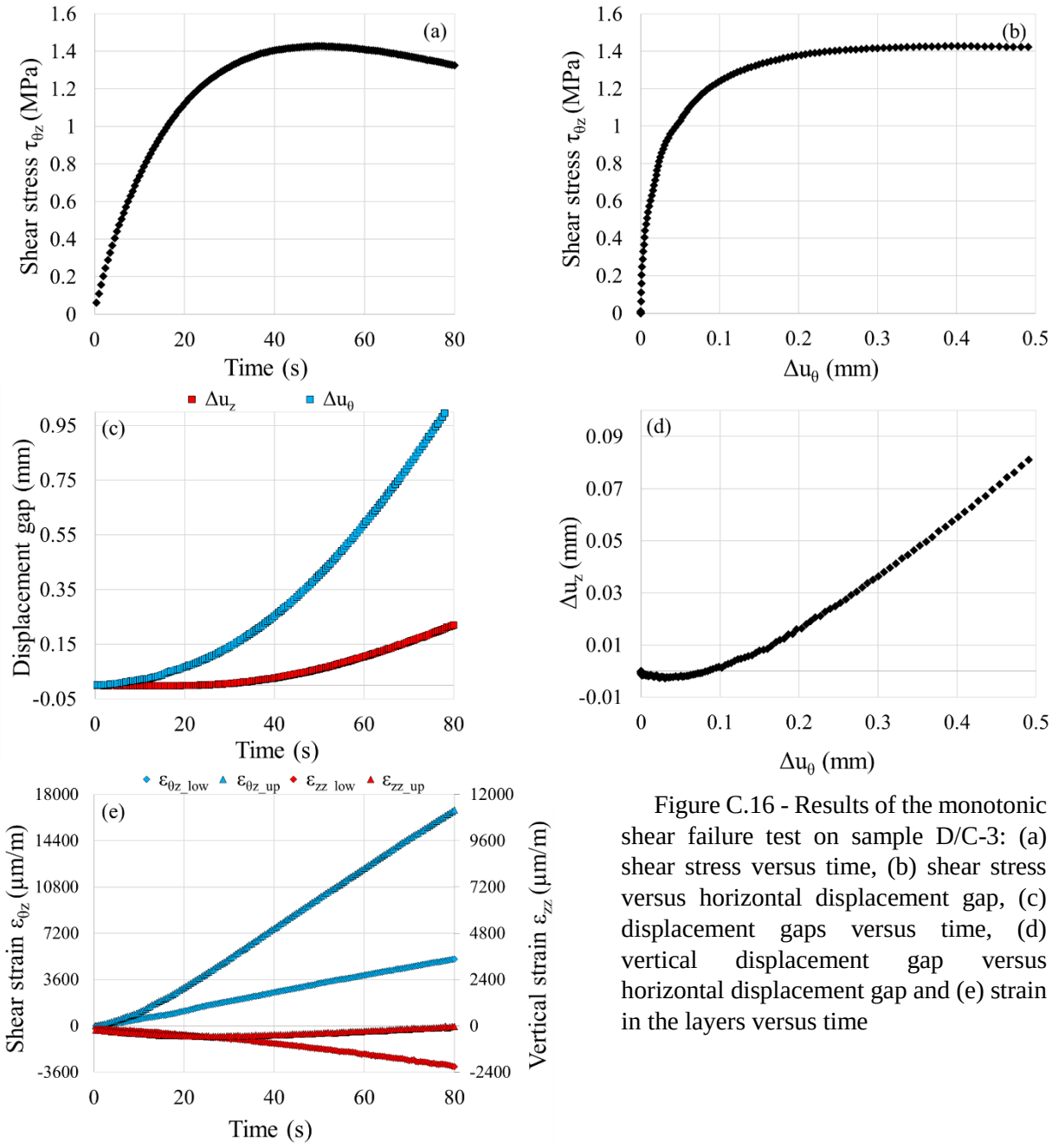

Figure C.16 - Results of the monotonic shear failure test on sample D/C-3: (a) shear stress versus time, (b) shear stress versus horizontal displacement gap, (c) displacement gaps versus time, (d) vertical displacement gap versus horizontal displacement gap and (e) strain in the layers versus time

Table C.16 - Results of the monotonic shear failure test on sample D/C-3

Sample	**Upper layer**	**Lower layer**	**Tack coat type**	**Tack coat dosage (g/m^2)**	**Global shear strain rate $\dot{\varepsilon}_{\theta z\_g}$ (%/s)**	**T (°C)**	**σ_{zz} (MPa)**	**τ_{max} (MPa)**	**Δu_{θ_max} (mm)**	**Δu_{z_max} (µm)**
D/C-3	BB5	EME2	Pure Bitumen	350	0.02	18.7	1	1.43	0.99	55

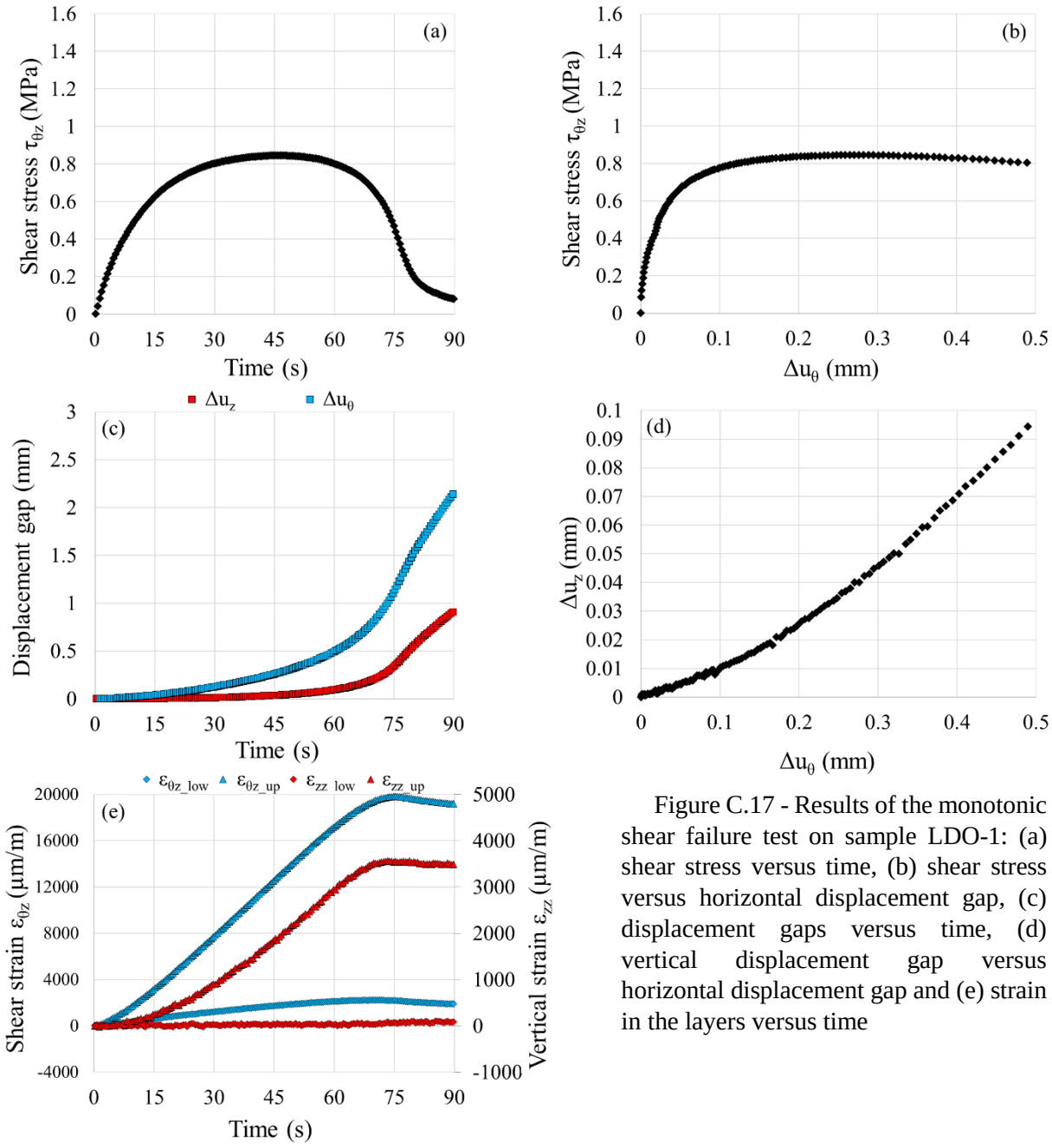

Figure C.17 - Results of the monotonic shear failure test on sample LDO-1: (a) shear stress versus time, (b) shear stress versus horizontal displacement gap, (c) displacement gaps versus time, (d) vertical displacement gap versus horizontal displacement gap and (e) strain in the layers versus time

Table C.17 - Results of the monotonic shear failure test on sample LDO-1

Sample	**Upper layer**	**Lower layer**	**Tack coat type**	**Tack coat dosage (g/m^2)**	**Global shear strain rate $\dot{\varepsilon}_{\theta z\_g}$ (%/s)**	**T (°C)**	**σ_{zz} (MPa)**	**τ_{max} (MPa)**	**Δu_{θ_max} (mm)**	**Δu_{z_max} (µm)**
LDO-1	BBSG3	EME2	Pure Bitumen	250	0.02	18.7	0	0.85	0.26	38

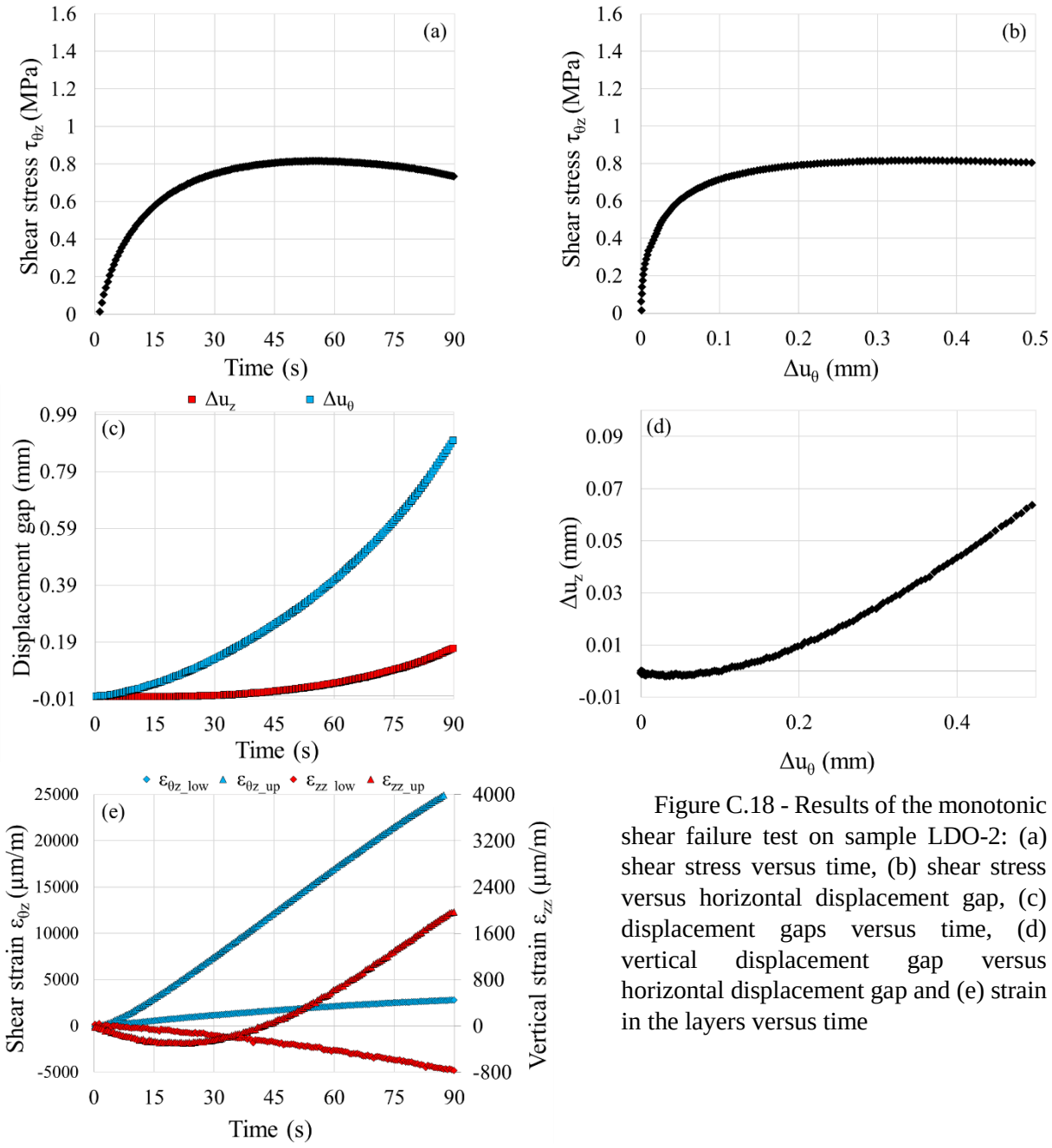

Figure C.18 - Results of the monotonic shear failure test on sample LDO-2: (a) shear stress versus time, (b) shear stress versus horizontal displacement gap, (c) displacement gaps versus time, (d) vertical displacement gap versus horizontal displacement gap and (e) strain in the layers versus time

Table C.18 - Results of the monotonic shear failure test on sample LDO-2

Sample	**Upper layer**	**Lower layer**	**Tack coat type**	**Tack coat dosage (g/m^2)**	**Global shear strain rate $\dot{\varepsilon}_{\theta z\_g}$ (%/s)**	**T (°C)**	**σ_{zz} (MPa)**	**τ_{max} (MPa)**	**Δu_{θ_max} (mm)**	**Δu_{z_max} (µm)**
LDO-2	BBSG3	EME2	Pure Bitumen	250	0.02	18.8	0.25	0.82	0.35	35

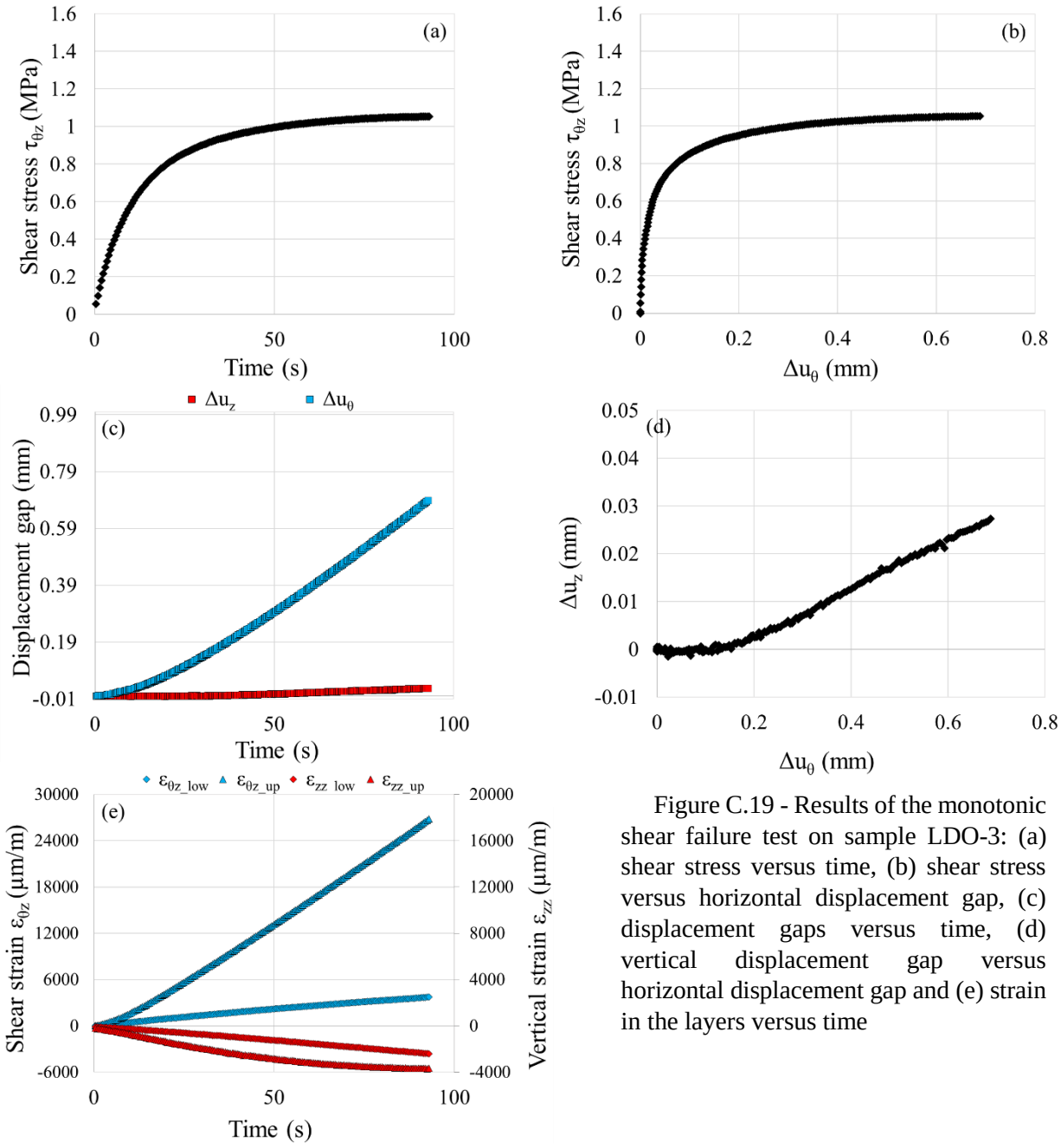

Figure C.19 - Results of the monotonic shear failure test on sample LDO-3: (a) shear stress versus time, (b) shear stress versus horizontal displacement gap, (c) displacement gaps versus time, (d) vertical displacement gap versus horizontal displacement gap and (e) strain in the layers versus time

Table C.19 - Results of the monotonic shear failure test on sample LDO-3

Sample	**Upper layer**	**Lower layer**	**Tack coat type**	**Tack coat dosage (g/m^2)**	**Global shear strain rate $\dot{\varepsilon}_{\theta z\_g}$ (%/s)**	**T (°C)**	**σ_{zz} (MPa)**	**τ_{max} (MPa)**	**Δu_{θ_max} (mm)**	**Δu_{z_max} (µm)**
LDO-3	BBSG3	EME2	Pure Bitumen	250	0.02	18.8	1	1.05	0.76	31

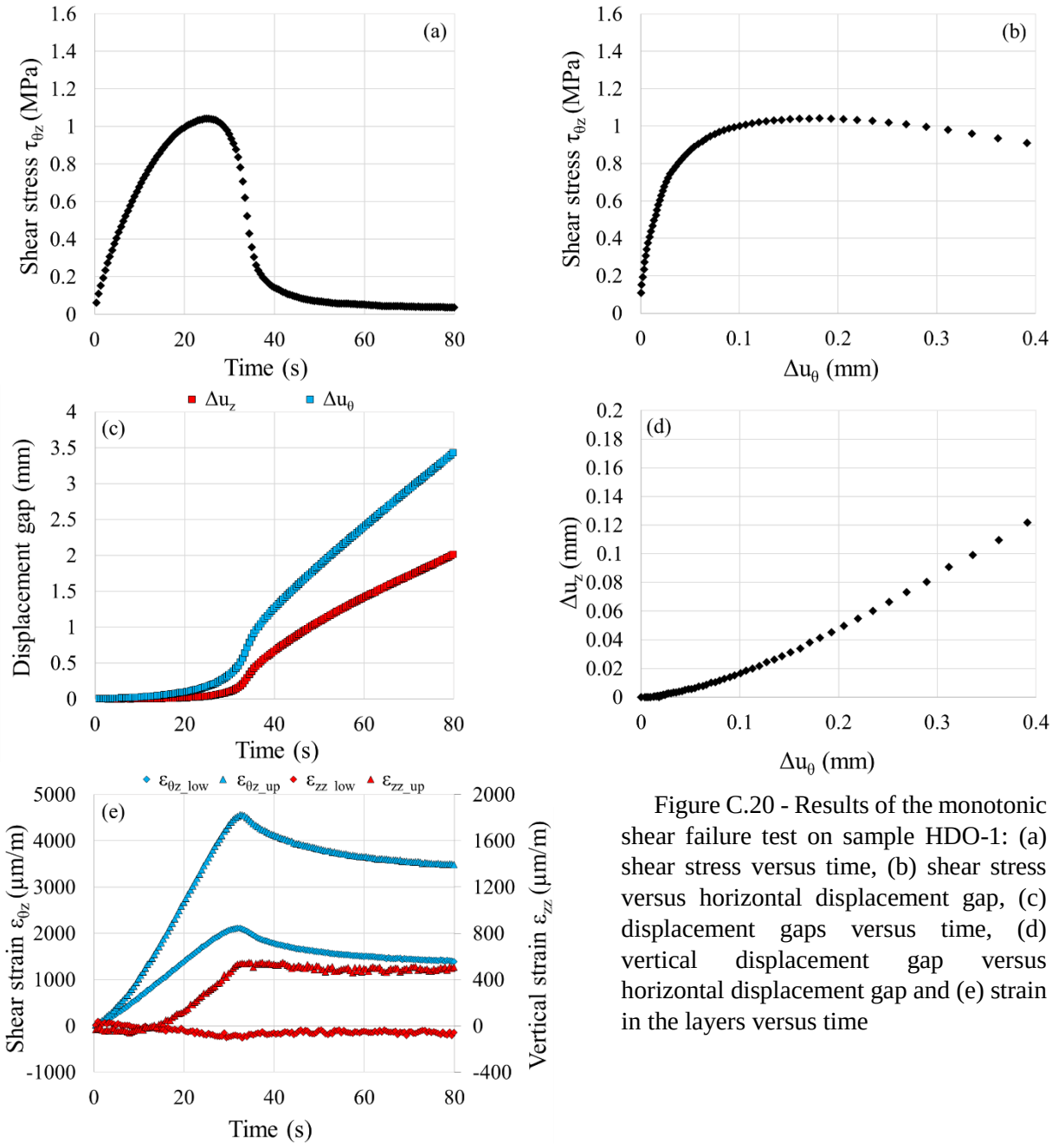

Figure C.20 - Results of the monotonic shear failure test on sample HDO-1: (a) shear stress versus time, (b) shear stress versus horizontal displacement gap, (c) displacement gaps versus time, (d) vertical displacement gap versus horizontal displacement gap and (e) strain in the layers versus time

Table C.20 - Results of the monotonic shear failure test on sample HDO-1

Sample	**Upper layer**	**Lower layer**	**Tack coat type**	**Tack coat dosage (g/m^2)**	**Global shear strain rate $\dot{\varepsilon}_{\theta z\_g}$ (%/s)**	**T (°C)**	**σ_{zz} (MPa)**	**τ_{max} (MPa)**	**Δu_{θ_max} (mm)**	**Δu_{z_max} (µm)**
HDO-1	BBSG3	EME2	Pure Bitumen	450	0.02	18.5	0	1.04	0.18	42

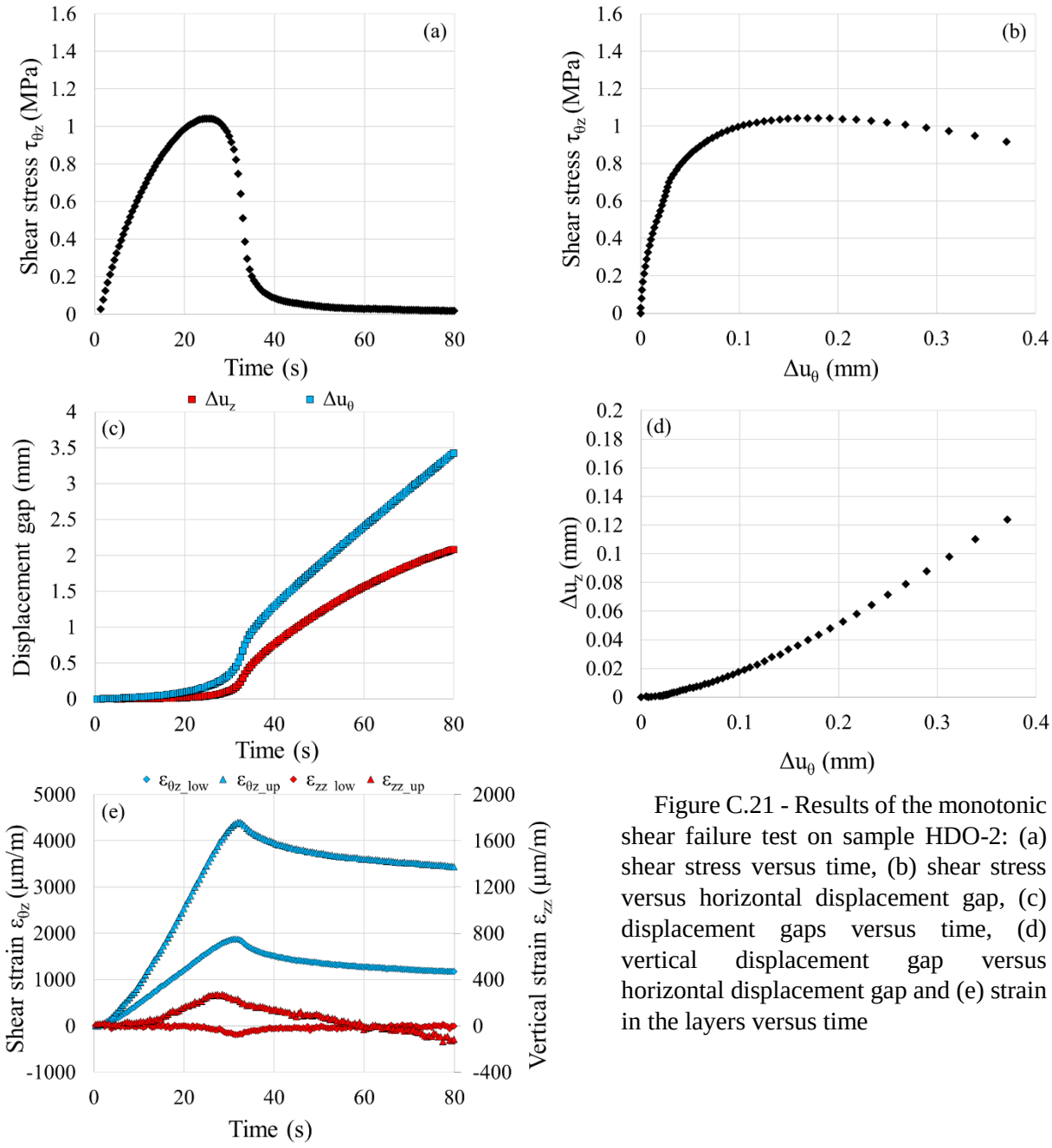

Figure C.21 - Results of the monotonic shear failure test on sample HDO-2: (a) shear stress versus time, (b) shear stress versus horizontal displacement gap, (c) displacement gaps versus time, (d) vertical displacement gap versus horizontal displacement gap and (e) strain in the layers versus time

Table C.21 - Results of the monotonic shear failure test on sample HDO-2

Sample	**Upper layer**	**Lower layer**	**Tack coat type**	**Tack coat dosage (g/m^2)**	**Global shear strain rate $\dot{\varepsilon}_{\theta z\_g}$ (%/s)**	**T (°C)**	**σ_{zz} (MPa)**	**τ_{max} (MPa)**	**Δu_{θ_max} (mm)**	**Δu_{z_max} (µm)**
HDO-2	BBSG3	EME2	Pure Bitumen	450	0.02	18.7	0	1.04	0.18	44

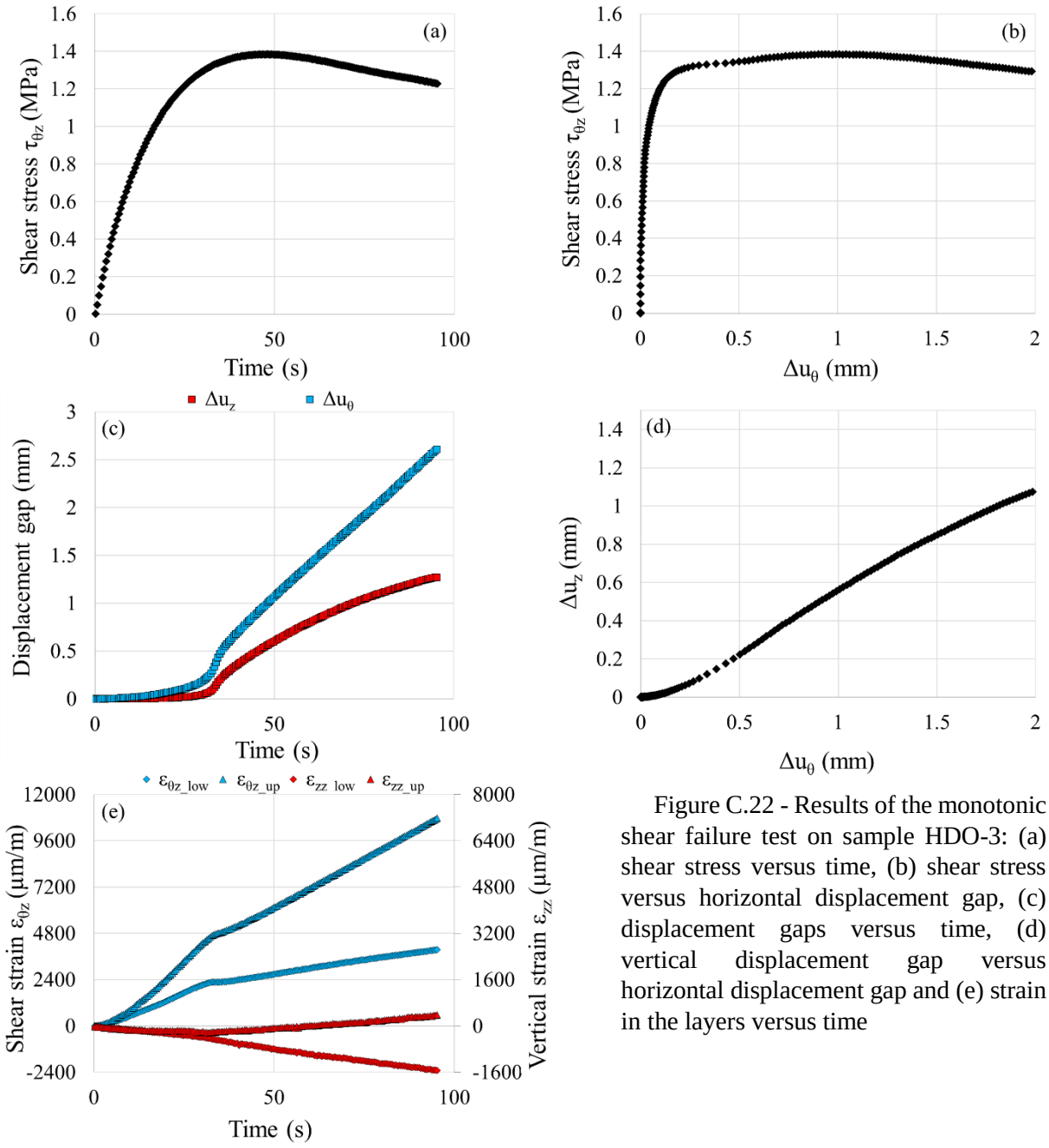

Figure C.22 - Results of the monotonic shear failure test on sample HDO-3: (a) shear stress versus time, (b) shear stress versus horizontal displacement gap, (c) displacement gaps versus time, (d) vertical displacement gap versus horizontal displacement gap and (e) strain in the layers versus time

Table C.22 - Results of the monotonic shear failure test on sample HDO-3 (the bituminous mixture in the upper layer failed before the interface in this test)

Sample	**Upper layer**	**Lower layer**	**Tack coat type**	**Tack coat dosage (g/m^2)**	**Global shear strain rate $\dot{\varepsilon}_{\theta z\_g}$ (%/s)**	**T (°C)**	**σ_{zz} (MPa)**	**τ_{max} (MPa)**	**Δu_{θ_max} (mm)**	**Δu_{z_max} (µm)**
HDO-3	BBSG3	EME2	Pure Bitumen	450	0.02	18.6	1	1.38*	0.99*	554*

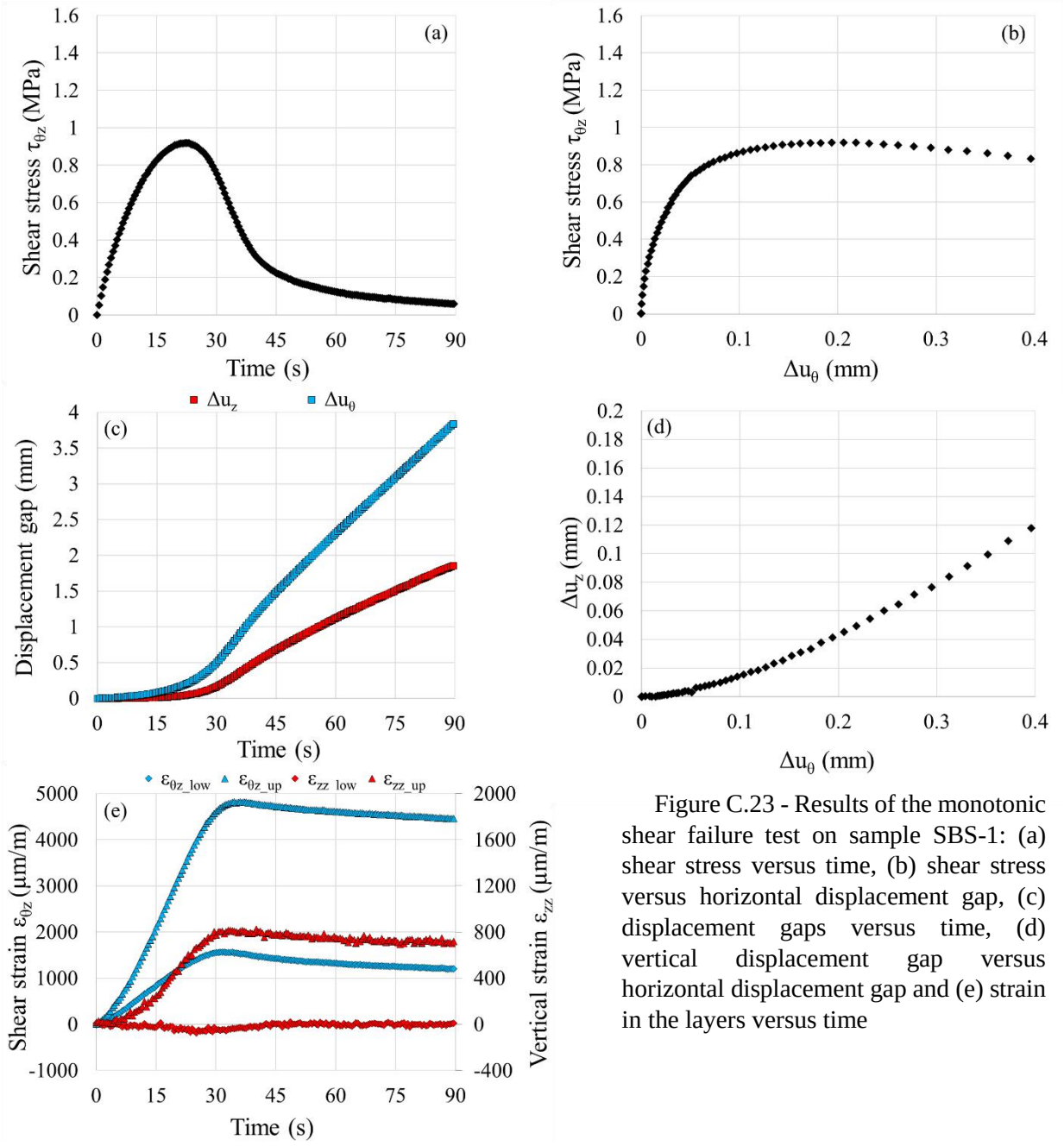

Figure C.23 - Results of the monotonic shear failure test on sample SBS-1: (a) shear stress versus time, (b) shear stress versus horizontal displacement gap, (c) displacement gaps versus time, (d) vertical displacement gap versus horizontal displacement gap and (e) strain in the layers versus time

Table C.23 - Results of the monotonic shear failure test on sample SBS-1

Sample	**Upper layer**	**Lower layer**	**Tack coat type**	**Tack coat dosage (g/m^2)**	**Global shear strain rate $\dot{\varepsilon}_{\theta z\_g}$ (%/s)**	**T (°C)**	**σ_{zz} (MPa)**	**τ_{max} (MPa)**	**Δu_{θ_max} (mm)**	**Δu_{z_max} (µm)**
SBS-1	BBSG3	EME2	Bitumen modified with SBS	350	0.02	18.5	0	0.92	0.19	41

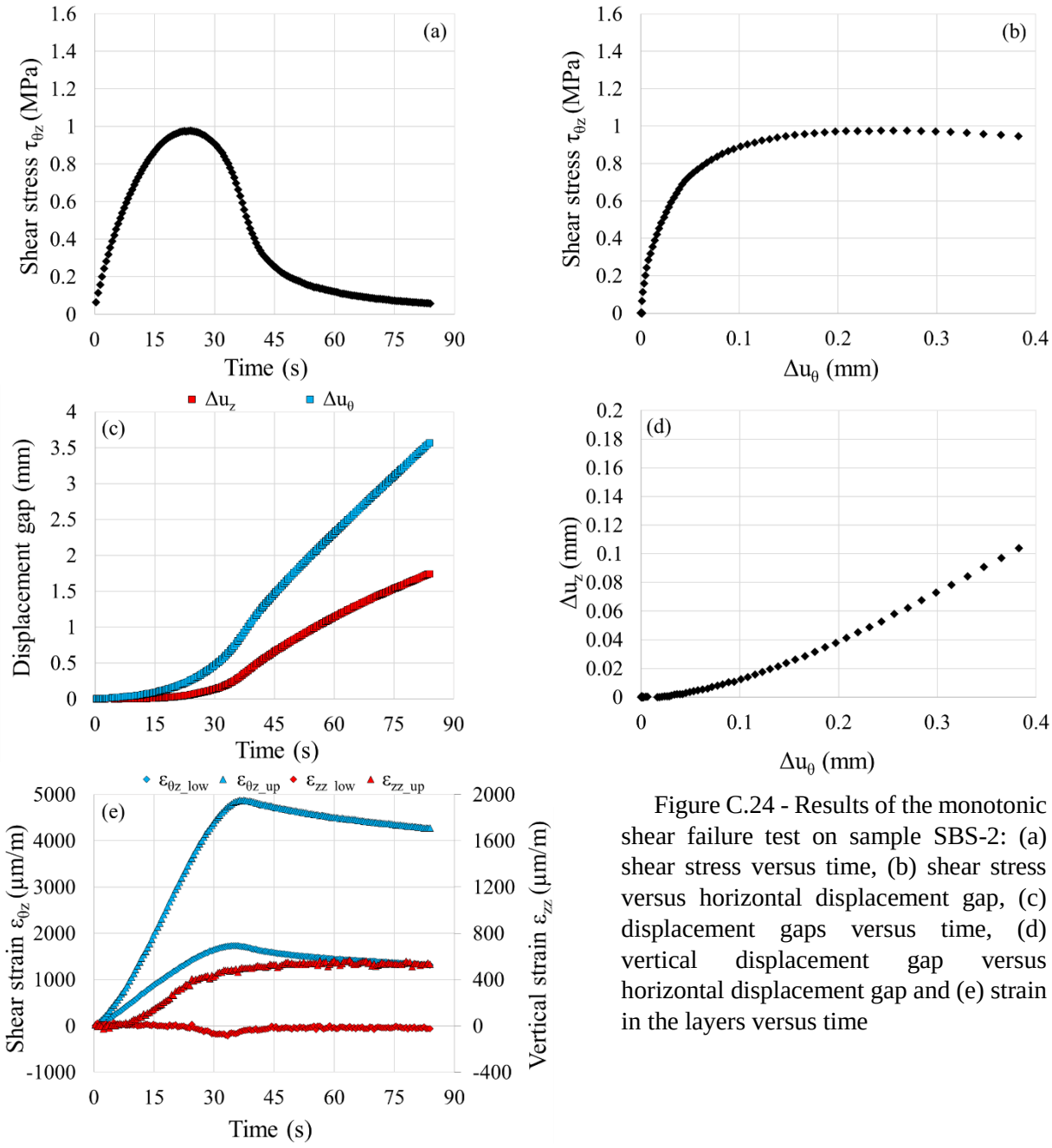

Figure C.24 - Results of the monotonic shear failure test on sample SBS-2: (a) shear stress versus time, (b) shear stress versus horizontal displacement gap, (c) displacement gaps versus time, (d) vertical displacement gap versus horizontal displacement gap and (e) strain in the layers versus time

Table C.24 - Results of the monotonic shear failure test on sample SBS-2

Sample	Upper layer	Lower layer	Tack coat type	Tack coat dosage (g/m^2)	Global shear strain rate $\dot{\varepsilon}_{\theta z\_g}$ (%/s)	T (°C)	σ_{zz} (MPa)	τ_{max} (MPa)	Δu_{θ_max} (mm)	Δu_{z_max} (µm)
SBS-2	BBSG3	EME2	Bitumen modified with SBS	350	0.02	18.5	0	0.97	0.26	58

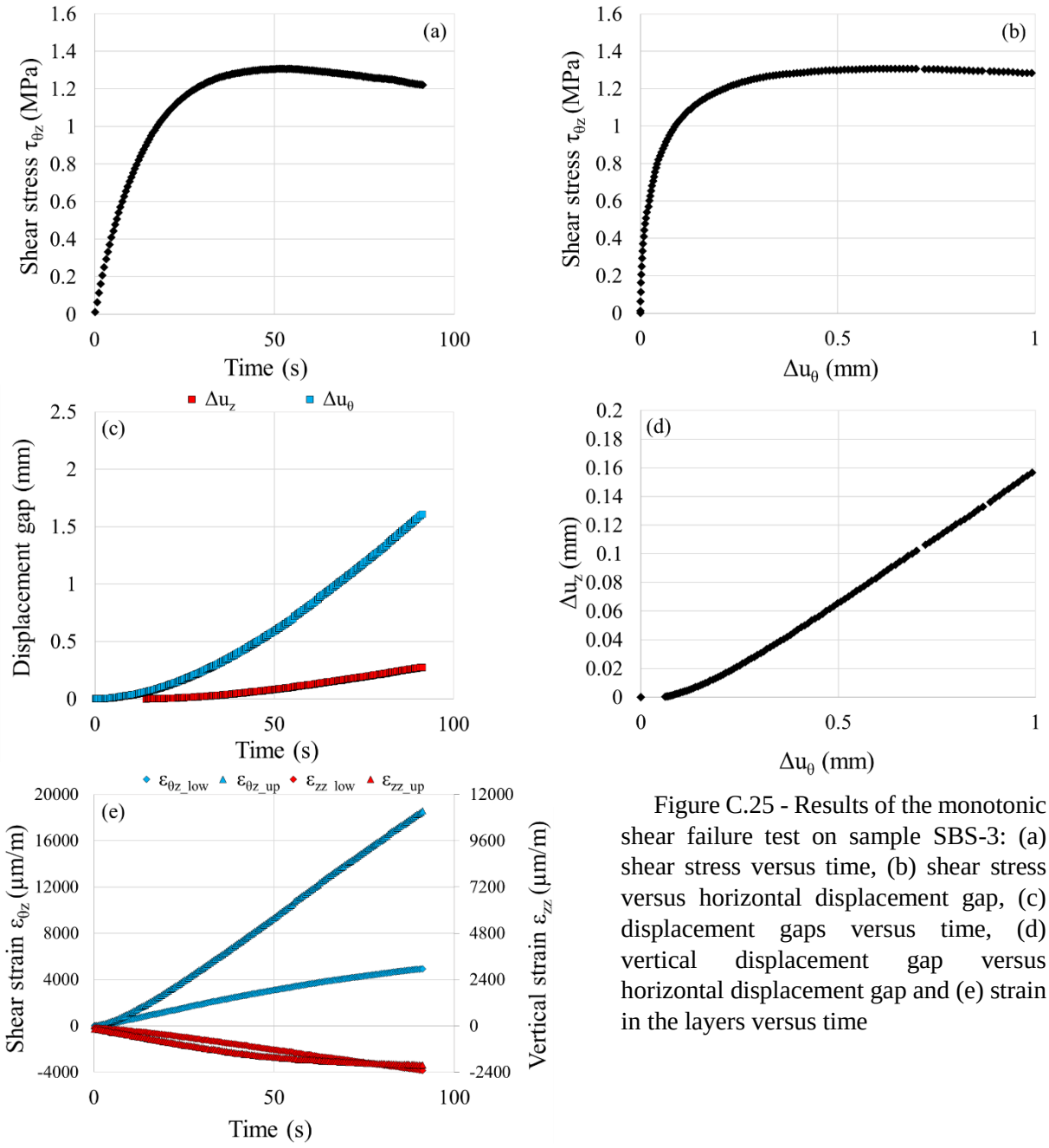

Figure C.25 - Results of the monotonic shear failure test on sample SBS-3: (a) shear stress versus time, (b) shear stress versus horizontal displacement gap, (c) displacement gaps versus time, (d) vertical displacement gap versus horizontal displacement gap and (e) strain in the layers versus time

Table C.25 - Results of the monotonic shear failure test on sample SBS-3

Sample	**Upper layer**	**Lower layer**	**Tack coat type**	**Tack coat dosage (g/m^2)**	**Global shear strain rate $\dot{\varepsilon}_{\theta z\_g}$ (%/s)**	**T (°C)**	**σ_{zz} (MPa)**	**τ_{max} (MPa)**	**Δu_{θ_max} (mm)**	**Δu_{z_max} (µm)**
SBS-3	BBSG3	EME2	Bitumen modified with SBS	350	0.02	18.5	1	1.31	0.63	89

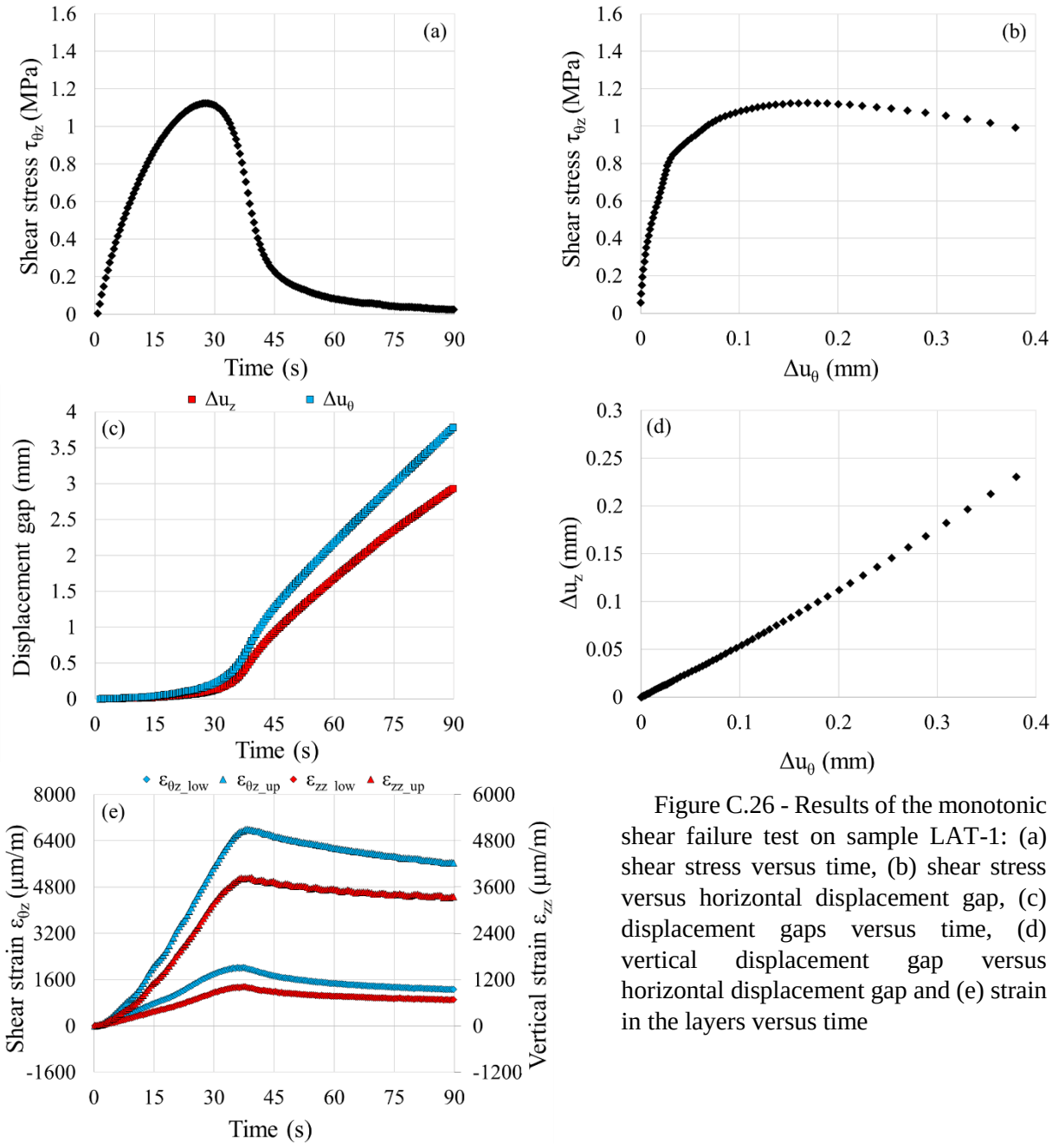

Figure C.26 - Results of the monotonic shear failure test on sample LAT-1: (a) shear stress versus time, (b) shear stress versus horizontal displacement gap, (c) displacement gaps versus time, (d) vertical displacement gap versus horizontal displacement gap and (e) strain in the layers versus time

Table C.26 - Results of the monotonic shear failure test on sample LAT-1

Sample	**Upper layer**	**Lower layer**	**Tack coat type**	**Tack coat dosage (g/m^2)**	**Global shear strain rate $\dot{\varepsilon}_{\theta z\_g}$ (%/s)**	**T (°C)**	**σ_{zz} (MPa)**	**τ_{max} (MPa)**	**Δu_{θ_max} (mm)**	**Δu_{z_max} (µm)**
LAT-1	BBSG3	EME2	Bitumen modified with latex	350	0.02	18.5	0	1.12	0.17	94

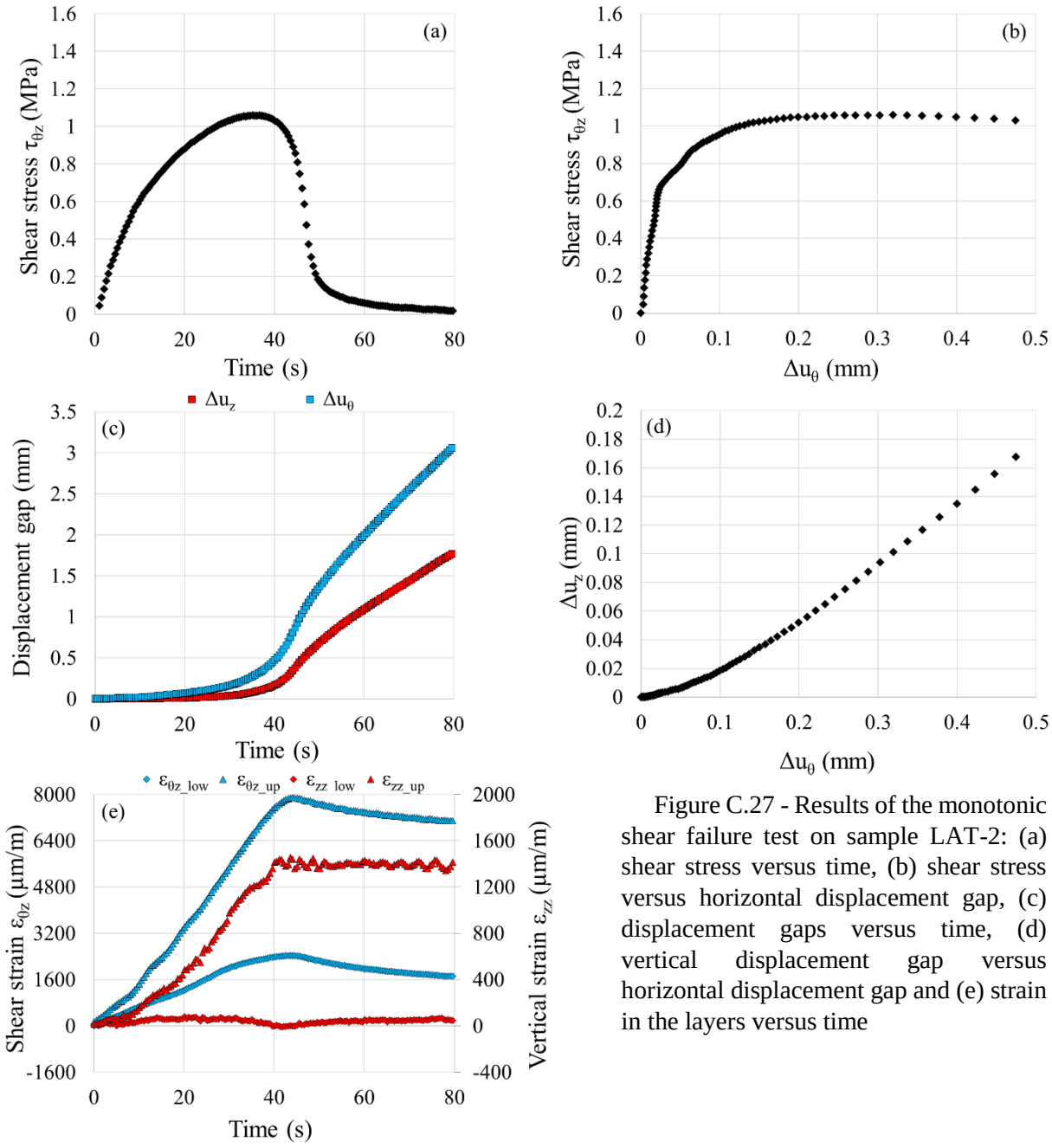

Figure C.27 - Results of the monotonic shear failure test on sample LAT-2: (a) shear stress versus time, (b) shear stress versus horizontal displacement gap, (c) displacement gaps versus time, (d) vertical displacement gap versus horizontal displacement gap and (e) strain in the layers versus time

Table C.27 - Results of the monotonic shear failure test on sample LAT-2

Sample	**Upper layer**	**Lower layer**	**Tack coat type**	**Tack coat dosage (g/m^2)**	**Global shear strain rate $\dot{\varepsilon}_{\theta z\_g}$ (%/s)**	**T (°C)**	**σ_{zz} (MPa)**	**τ_{max} (MPa)**	**Δu_{θ_max} (mm)**	**Δu_{z_max} (µm)**
LAT-2	BBSG3	EME2	Bitumen modified with latex	350	0.02	18.5	0	1.06	0.32	101